

The Mechanical Response of a Passive-Dynamic Ankle-Foot-Orthosis and its Interaction with the Lower Limb during Gait

Kirstie Edwards

Dissertation submitted in fulfilment of the requirements for the degree of:

Doctor of philosophy

Department of Bioengineering, Imperial College London

December 2021

ABSTRACT

The prescription of a passive dynamic ankle foot orthosis (PD-AFO), trademarked the Momentum, has improved functional outcome for many patients, though not all. The design features of the PD-AFO that account for this improvement, and the changes the PD-AFO introduces into gait, are not fully understood. This thesis aims to establish how the PD-AFO alters the external and internal loading of the foot during gait.

Gait analysis was used to evaluate changes in external loading of the foot when wearing the PD-AFO (possible offloading). It was demonstrated that the PD-AFO reduced loading in the foot when walking, with maximum offloading seen during early stance. A novel methodology, using strain gauges, demonstrated the struts' energy storage and return (ESAR) characteristics and ability to provide propulsive power during late stance.

Finite element (FE) modelling was used to evaluate internal loading of the foot. A comprehensive development process was undertaken to build FE models of the foot and PD-AFO. By running multiple simulations of the FE model of the PD-AFO, design components whose mechanical characteristics may significantly alter gait were highlighted, such as the alignment of the posterior struts.

The FE models of the foot and PD-AFO were combined to model the loading at a point during early stance; comparable results with data recorded experimentally was achieved. Simulation results demonstrated greater relative reduction in contact stresses, compared to contact force, at the subtalar joint. This suggested that PD-AFO's influence on the subtalar joint angle may be an important design feature in the PD-AFO's success.

This research may help to predict who may be successfully aided by the PD-AFO, target research on design components that influence the mechanical response of the PD-AFO; and indicate potential long-term adverse effects of using the device as a result of changes to gait.

DECLARATION OF ORIGINALITY

I declare that the work within this thesis is my own, and all other work is appropriately referenced.

COPYRIGHT DECLARATION

The copyright of this thesis rests with the author. Unless otherwise indicated, its contents are licensed under a Creative Commons Attribution-Non Commercial 4.0 International Licence (CC BY-NC).

Under this licence, you may copy and redistribute the material in any medium or format. You may also create and distribute modified versions of the work. This is on the condition that: you credit the author and do not use it, or any derivative works, for a commercial purpose. When reusing or sharing this work, ensure you make the licence terms clear to others by naming the licence and linking to the licence text. Where a work has been adapted, you should indicate that the work has been changed and describe those changes. Please seek permission from the copyright holder for uses of this work that are not included in this licence or permitted under UK Copyright Law.

ACKNOWLEDGEMENTS

This work would not have been possible without several key people. Firstly, I would like to thank my supervisors Dr Spyros Masouros and Dr Arul Ramasamy. Spyros' unwavering support, along with his knowledge and guidance, have played a vital role in the completion of this thesis.

In addition, I would like to thank my colleagues for the laughter, the positivity, and the runs through Hyde Park. In particular, I would like to thank Dr Grigorios Grigoriadis, Dr Dilen Carpanen and Dr Louise McMenemy for their help and friendship throughout this work.

I would also like to thank the Royal British Legion for their funding, providing me with the opportunity to complete this research. I would like to thank Blatchford for their provision of the Momentum brace, and support throughout my research.

Lastly, I would like to thank my family and friends for their support; those friends whom I met whilst completing this research, provided laughs and support as we navigated the process together. A special mention must also go to Immy, my oldest friend, whose 'positivity' helped me reach the finish line.

And finally, to Thomas, who has stood by me throughout this all; he has encouraged me, listened to me and remained my rock. I will be forever grateful.

CONTENTS

Abstract	2
Declaration of Originality	3
Copyright Declaration.....	3
Acknowledgements	4
Contents	5
Table of Figures	12
Abbreviations	28
1 Introduction.....	30
1.1 Scope of thesis	30
1.2 Clinical problem.....	31
1.3 Treatment pathway.....	31
1.4 Aim and Objectives.....	33
1.5 Thesis Structure.....	33
2 Functional Anatomy of the Foot and Ankle.....	35
2.1 Anatomical coordinate system	35
2.2 Components	36
2.2.1 Bones.....	36
2.2.2 Ligaments and Plantar Fascia	38
2.2.3 Cartilage	39
2.2.4 Muscles	39
2.3 Movement and Rotation.....	40
2.3.2 Coordinate system of the ankle joint complex.....	41
2.4 Gait.....	42
2.5 Gait analysis	45
2.6 Conclusion	46
3 PD-AFO Literature	47
3.1 Introduction.....	47
3.2 PD-AFO Development.....	48

3.2.1	PD-AFO Design.....	49
3.3	Performance	51
3.3.1	Influencing Factors	52
3.3.2	Gait Analysis.....	57
3.3.3	Joint Kinetics and Kinematics.....	57
3.3.4	GRF and Plantar Pressure	60
3.3.5	Limitations	62
3.4	Design and Mechanical Response.....	63
3.4.1	Strut Manufacture and Stiffness.....	65
3.4.2	Alignment.....	67
3.4.3	Bending axis.....	68
3.4.4	Heel Wedge Properties.....	69
3.4.5	Limitations	69
3.5	Conclusion	70
4	Material Behaviour of the Components of the PD-AFO	71
4.1	Introduction.....	71
4.2	Carbon-fibre Layers	72
4.2.1	Literature Review and Analysis.....	73
4.2.2	Sensitivity analyses.....	77
4.2.3	Results	79
4.3	Discussion	81
4.4	Strut Composite.....	81
4.4.1	Experimental protocol.....	82
4.4.2	Experimental results.....	85
4.4.3	Sensitivity analyses.....	86
4.4.4	Sensitivity analyses results.....	88
4.4.5	Discussion	89
4.5	Heel Wedge and Foams	90
4.5.1	Experimental protocol.....	91

4.5.2	Results	93
4.5.3	Discussion	96
4.6	Conclusion	96
5	Limb Loading During Gait	97
5.1	Introduction	98
5.2	Literature	101
5.2.1	Plantarflexion and Peak Forces	101
5.2.2	Dorsiflexion Moment	102
5.2.3	Propulsive Forces	103
5.2.4	Loading of the Limb	103
5.2.5	Limitations	104
5.3	Methods and materials	105
5.3.1	Manufacture	105
5.3.2	Gait Trials	106
5.3.3	Post-Processing	107
5.4	Results	111
5.4.1	Overall Limb Loading	111
5.4.2	Regional Loading of the Lower Limb	119
5.4.3	PD-AFO gait across 4 days	128
5.5	Discussion	129
5.5.1	Combined Peak Loads	129
5.5.2	Lower Limb Peak Loads and Peak Pressures	131
5.5.3	Loading ratio	132
5.6	Limitations	133
5.7	Conclusion	134
6	Energy Storage Characteristics	135
6.1	Introduction	135
6.2	Methodology	139
6.2.1	Strain Gauge Reliability and Accuracy	139

6.2.2	Efficiency	141
6.2.3	Instrumented Gait Trials	142
6.3	Results.....	146
6.3.1	Strain Gauge Reliability and Accuracy.....	146
6.3.2	Efficiency	150
6.3.3	Instrumented Gait Trials	151
6.3.4	Energy and Power	155
6.4	Discussion	157
6.4.1	Strain Gauge Reliability and Accuracy.....	158
6.4.2	Efficiency	158
6.4.3	Strain gauges	159
6.4.4	Energy and Power	160
6.5	Limitations	162
6.6	Conclusion	162
7	FE Model of PD-AFO.....	164
7.1	Introduction.....	164
7.2	Previous FE Models of AFOs	165
7.3	Methodology	170
7.3.1	Geometry.....	170
7.3.2	Mesh and model set up.....	171
7.3.3	Material Properties.....	171
7.3.4	Model Calibration and Validation.....	172
7.3.5	Mechanical Response.....	176
7.3.6	Sensitivity analysis on device-design parameters	180
7.4	Results.....	187
7.4.1	Model Calibration and Validation.....	188
7.4.2	Mechanical Response.....	191
7.4.3	Design Sensitivity	193
7.5	Discussion	200

7.5.1	Model Calibration and Validation.....	200
7.5.2	Mechanical Response.....	200
7.5.3	Design Sensitivity	201
7.6	Conclusion	203
8	Lower Limb FE Model	204
8.1	Introduction.....	204
8.2	Previous FE models of the lower limb.....	205
8.2.1	Geometry.....	205
8.2.2	Tissue components.....	206
8.2.3	Material Properties.....	212
8.2.4	Comparison to Experimental Data.....	216
8.2.5	Summary	217
8.3	Methodology	218
8.3.1	Geometry generation.....	218
8.3.2	Material Behaviour	224
8.3.3	Contact	225
8.3.4	Initial Position and Boundary Conditions.....	225
8.3.5	Comparison to experimental data	227
8.3.6	Sensitivity Analysis.....	228
8.4	Results.....	230
8.4.1	Comparison to Experimental data.....	231
8.4.2	Contact Stresses	232
8.4.3	Sensitivity Analysis.....	233
8.5	Discussion	237
8.5.1	Calibration and comparison to experimental data.....	237
8.5.2	Limitations	238
8.6	Conclusion	239
9	Combined Model.....	240
9.1	Introduction.....	240

9.1.1	Previous FE models	241
9.1.2	Calf Mechanical Properties.....	243
9.2	Methodology	245
9.2.1	Orientating the PD-AFO and lower limb models	245
9.2.2	Geometry and Contact	245
9.2.3	Boundary Conditions	249
9.2.4	Model Outputs.....	250
9.3	Results.....	250
9.3.1	Calf Properties.....	250
9.3.2	Comparison of the FE combined models to experimental data	251
9.3.3	Comparison of lower limb loading with and without the PD-AFO.....	254
9.4	Discussion	257
9.4.1	Comparison to Experimental Data.....	257
9.4.2	Comparison with and without the PD-AFO.....	258
9.4.3	Limitations	259
9.5	Conclusion	260
10	Summary and Future Work.....	261
10.1	Summary	261
10.2	Discussion and Future Work.....	264
10.3	Conclusions	268
11	References.....	270
12	Appendices.....	280
12.1	Appendix A	280
12.1.1	Carbon fibre sensitivity analyses	280
12.1.2	Compliance	285
12.1.3	Macauley's Beam Theory	286
12.1.4	Strain Rate Sensitivity of the Struts	288
12.1.5	Sample Strut Measurements.....	289
12.1.6	Composite Strut Force-Displacement Curves.....	290

12.1.7	Buckling.....	291
12.1.8	Ogden Material Formulation.....	291
12.1.9	Foam Stress Strain Curves	293
12.2	Appendix B	295
12.2.1	Copy of Consent Form.....	295
12.2.2	Total Ground Reaction Force and Plantar Force	296
12.2.3	Loading Ratio Error	300
12.2.4	Plantar Pressures	303
12.3	Appendix C	310
12.3.1	Zero strain gauge error.....	310
12.3.2	Force-displacement Curves efficiency.....	312
12.3.3	Mediolateral SGs.....	313
12.4	Appendix D	315
12.4.1	Compliance	315
12.4.2	Design Sensitivity	316
12.5	Appendix E	317
12.5.1	Ligaments.....	317
12.5.2	Lower Limb Only Simulation	320
12.5.3	Cartilage Contact Stress	321
12.6	Appendix F.....	323
12.6.1	Limb in PD-AFO Model.....	323
12.6.2	Tibia cross-sectional area.....	325
12.6.3	Calf Contact	326
12.6.4	Contact Stresses	328
12.7	Appendix G.....	330

TABLE OF FIGURES

Figure 1.2.1: A calcaneal blast fracture observed in the limb [3]. Image reproduced with permission from the rights holder Wolters Kluwer.	31
Figure 1.3.1: The (a) IDEO produced for the US military [18] and the (b) B.O.B produced for the UK military. Image (a) reproduced with permission from the rights holder Wolter Kluwer.	32
Figure 2.1.1: (a) Planes of motion (x-y plane is named transverse plane, y-z plane is named coronal plane (or frontal), x-z plane is named sagittal plane). (b) Clockwise rotation about x, in the coronal plane, is described as inversion (anticlockwise as eversion). Clockwise rotation about y, in the sagittal plane, is described as plantarflexion (anticlockwise as dorsiflexion). Clockwise rotation about z, in the transverse plane, is described as internal rotation (anticlockwise as external rotation).....	36
Figure 2.2.1: Bones of the foot as viewed from the dorsal surface. Image reproduced is open access [23].	37
Figure 2.2.2: Ligaments in the foot, from (a) the lateral aspect and (b) the medial aspect. Images reproduced are open access [23].	38
Figure 2.2.3: The cartilage on the surface of the left talus viewed from (a) a proximal aspect (b) a lateral aspect. Images reproduced are open access [23].....	39
Figure 2.3.1: On the left is the lower limb, viewed from the lateral side, labelled with the anatomical landmarks used to describe the three planes of the ankle joint complex. On the right is the frontal view. The ankle joint complex is in the neutral position. MM – medial malleolus, LM – lateral malleolus, MC – medial point on border of medial tibial condyle, LC lateral point on lateral tibial condyle, TT – tibial tuberosity, IM – inter-malleolar point located at midpoint of MM and LM, IC – inter-condylar point located at midpoint of MC and LC. XYZ shows the tibia coordinate system and the xyz coordinate system shows the calcaneus coordinate system.[27] Image reproduced with permission of the rights holder, Elsevier.	42
Figure 2.4.1: The sub-phases of the gait cycle for the left foot on the top row and right foot on the bottom row.. 0% of the cycle, in this case, is based upon the gait cycle of the left limb. The sub-phases of the stance phase are initial contact (0-2%), loading response (2-10%), midstance (10-30%), terminal stance (30-50%) and pre-swing (50-60%). The sub-phases of swing phase are: initial swing (60-70%), mid-swing (70-85%) and terminal swing (85-100%).[30].	43
Figure 2.5.1: Standard ground reaction force (GRF) for healthy walking gait during stance phase	46
Figure 3.2.1: The PD-AFO and its components (Momentum [®] provided and manufactured by Blatchford).	50
Figure 3.2.2: Cuff region of the PD-AFO (the Momentum [®] provided by Blatchford, UK).....	51
Figure 3.3.1: Data from Bedigrew et al. demonstrating improvements seen in functional outcome measures, including A) four square step test B) timed stair ascent C) self-selected walking velocity (SSV) and D) 20m shuttle run, at the start (week 0), middle (week 4) and end (week 8) of the RTR run	

programme [21]. Image reproduced with permission from the rightsholder Wolters Kluwer Health, Inc.....	53
Figure 3.3.2: Adapted from Hill et al. showing the percentage of late amputations in each diagnostic category [49]	56
Figure 3.3.3: Data acquired by Esposito et al. demonstrating the ground reaction forces in the vertical direction, the anteroposterior (AP) direction and the mediolateral (ML) direction, (in PD-AFOs of 3 different strut stiffnesses) compared to healthy controls [56]. Image reproduced with permission from the rights holder Wolters Kluwer Health, Inc	61
Figure 3.4.1: A study by Wach et al. evaluating the stiffness of 4 different AFOs at three points in gait: Midstance, (MSt) Terminal Stance (TSt) and Pre-swing (PSw) [63]. Image reproduced with permission from the rights holder ASME.....	64
Figure 3.4.2: Figure reproduced from Esposito et al. showing an selective laser sintered posterior strut [56]. Image reproduced with permission from the rights holder Wolters Kluwer Health.	66
Figure 3.4.3: A study by Brown et al.; changes in joint kinematics and kinetics during walking, following changes in strut alignment. The shapes indicate a significant difference between 2 alignments: Δ -between the dorsiflexed and neutral alignment, \bullet - between the dorsiflexion and plantarflexed alignment, \square - between the neutral and plantarflexed alignment. Image reproduced with permission from the Rightsholder Elsevier [38].....	67
Figure 3.4.4: The 3 selective laser sintered posterior struts used in studies by Ranz et al. and Esposito et al. examining the changes in gait during walking and running, as the bending axis changes [39, 54]. Image reproduced with permission from the rights holder, Elsevier [54]	68
Figure 4.2.1: Carbon-fibre layers sensitivity analysis geometry and boundary conditions in compression. The red lines indicate the location where nodes were fixed in 1 degree of freedom, where δ indicates the displacement at that point. Each end of the sample was compressed 0.5mm. The primary direction of the Young's Modulus was in x.....	78
<i>Figure 4.2.2: Carbon-fibre layers sensitivity analysis geometry and boundary conditions in bending. The red cross indicates the nodes fixed in 2 degrees of freedom, where δ indicates the displacement at that point. The top 2 cylindrical surfaces displaced the layer downwards, whilst the bottom 2 cylindrical surfaces remained fixed. The primary direction of the Young's Modulus was in x.</i>	79
Figure 4.2.3: The sensitivity of the bending and compressive stiffness in the primary direction (s) of the Young's Modulus (E_1 , E_2) of (a) carbon-twill (b) uni-directional carbon fibre and (c) aramid. ΔK . is the change with respect to the baseline stiffness.	80
Figure 4.4.1 (a) Schematic showing experimental set-up for compression where δ_{input} was the applied displacement; the fixture consisted of two flat surfaces between which the sample was place unconstrained (b) Image showing same experimental set-up, with strain gauges	83

Figure 4.4.2: Schematic showing experimental set-up for 4-point bend test (bending), the fixture consisted of 4 rounded surfaces constrained relative to one another; $a = 6\text{mm}$, $L = 18\text{mm}$ (b) Image showing same experimental set-up. δ_{input} was the applied displacement..... 84

Figure 4.4.3: Process to determine the appropriate statistical test for each comparison coded in Python 85

Figure 4.4.4: The Young's modulus (E) calculated across all 3 samples for both compression and bending ($n = 36$). The median Young's modulus in compression was calculated to be 34.45GPa and in bending 36.92GPa. The mean Young's modulus $\pm 1\text{SD}$ in compression was $33.77 \pm 2.96\text{GPa}$, and $36.65 \pm 1.18\text{GPa}$ in bending. *indicates a statistical difference for $p < 0.05$, using a Wilcoxon signed rank test. 86

Figure 4.4.5: The FE model used to analyse the sensitivity of Poisson's ratio and assumption of isotropy on the posterior strut in (a) compression and (b) bending. (a) The sample is compressed between two rigid surfaces. The red dashed line indicates the long axis; this was fixed in x and z , where δ indicates the displacement at that point. The centre of the sample, indicated by the solid red line was fixed in y to prevent rigid body motion. (b) The top 2 cylindrical surfaces displaced the sample downwards, whilst the bottom 2 cylindrical surfaces remained fixed. The red cross indicates a boundary condition preventing motion in x and z directions..... 87

Figure 4.4.6: Sensitivity of (a) orthotropy of the Young's Modulus (E_2, E_3) and (b) the Poisson's ratio (ν) on the bending and compressive stiffness relative to the baseline stiffness. ΔK is the change with respect to the baseline stiffness. 89

Figure 4.5.1: (a) A schematic of the experimental test set-up showing the applied displacement, δ_{input} , and (b) an image of the fixtures and a thick foam sample set up in the uniaxial materials testing machine 91

Figure 4.5.2: An axi-symmetric FE model of the polyurethane foam sample. The horizontal red line indicates symmetry. δ is the displacement applied to the rigid line (orange vertical line), compressing the foam..... 93

Figure 4.5.3: Experimental stress-strain curve for Foam A and Foam B. The shaded area denotes 1 SD..... 94

Figure 4.5.4: The force-displacement curves recorded during the experimental compression tests of the foams samples and obtained via the FE simulation for (a) the polyurethane foam (b) Foam A and (c) Foam B 95

Figure 5.1.1: Location of where plantar force and ground reaction force (GRF) would be recorded, modelling the limb and PD-AFO as springs 100

Figure 5.2.1: Results from Stewart et al. showing the averaged peak plantar pressures (coloured patches) and the CoP progression line in red, in the affected (injured) and unaffected foot when (a) not wearing the PD-AFO on the affected foot and (b) wearing the PD-AFO on the affected foot [59]. Image reproduced with permission from the copyright holder Wolters Kluwer Health..... 102

Figure 5.3.1: (a) Initial fitting using plaster cast (b) Assessment of fit by orthotist.....	105
Figure 5.3.2 PD-AFO as worn by the subject (a) without and (b) with trainers.....	106
Figure 5.3.3: Alignment and windowing of PEDAR and force plate data. ‘L’ indicates a measurement for the left foot and ‘R’ indicates a measurement for the right foot. ‘insole’ is the plantar force recorded by the PEDAR sensors. FP 1 and FP 2 are the ground reaction forces recorded by the force plates. A subscript 0 indicates the start (0%) of the gait cycle chosen for that limb and a subscript 100 indicates the end (100%) of the gait cycle chosen.	108
Figure 5.3.4: Map of 99 discrete pressure sensors in the PEDAR, divided into 8 regions.....	110
Figure 5.3.5: Process to determine the appropriate statistical test for each comparison coded in Python	111
Figure 5.4.1: The mean, normalised, ground reaction force (GRF) normalised to body weight (BW), as recorded by the force plates, for the left and right limbs during the control gait and the PD-AFO and shod limb during PD-AFO gait in each direction. The shaded area around the mean value denotes one standard deviation. For the mediolateral GRF, a positive value indicates a laterally directed force and a negative value indicates a medially directed force. For the anteroposterior GRF, a positive value indicates a braking force and a negative value indicates a propulsive force.	113
Figure 5.4.2: The peak medial GRF, normalised to body weight (BW), recorded during terminal stance and pre-swing, in each of the 4 limbs. * indicates a statistical difference for $p < 0.05$ using a paired t-test.....	114
Figure 5.4.3: (a) The peak, braking GRF, normalised to body weight (BW), and (b) the peak propulsive GRF seen in all limbs. *indicates a statistical difference for $p < 0.05$ using a paired t-test.	115
Figure 5.4.4: The peak vertical GRF, normalised to body weight (BW), recorded by all limbs during (a) weight acceptance and (b) push off. * indicates a statistical difference for $p < 0.05$ using a paired t-test.	116
Figure 5.4.5: Total (a) GRF and (b) plantar force, both normalised to body weight (BW), for all limbs through the gait cycle	117
Figure 5.4.6: The plantar force at (a) weight acceptance (b) midstance and (c) push off as a percentage of the total GRF recorded for each limb. * indicates a statistical difference for $p < 0.05$ using a paired t-test.	118
Figure 5.4.7: The dark grey region shows the loading experienced by the PD-AFO limb (the plantar force normalised to body weight (BW)). The light grey region indicates the loading experienced by the PD-AFO. The summation of both areas gives the total GRF. The dotted line indicates the calculated error, used to account for the measurement techniques from the PEDAR sensors and force plates. The data labels indicate the percentage of total load +/- calculated error, at weight acceptance, midstance and push off.	119

Figure 5.4.8: The centre of pressure (CoP) for each limb throughout the gait cycle. The percentages indicate the point of the gait cycle at which this CoP was reached. The CoP readings not located on the insole are erroneous as the foot strikes the ground. 120

Figure 5.4.9: Peak Plantar Pressure in each limb, normalised for body weight, throughout the gait cycle 121

Figure 5.4.10: The normalised, plantar pressure in (a) the greater toe (b) the lesser toe (c) the medial forefoot (d) the lateral forefoot (e) the medial midfoot (f) the lateral midfoot (g) the medial hindfoot (h) the lateral hindfoot, throughout the stance phase of the gait cycle, for both the control gait and PD-AFO gait. As viewed the figures are presented in the respective regions of a right footprint, with the medial regions demonstrated on the left hand side of the page, and the lateral regions to the right hand side. The toe regions are represented in at the top of the page, and the hindfoot regions at the bottom. 123

Figure 5.4.11: The peak plantar pressure, normalised for body weight, at weight acceptance in the (a) medial and (b) lateral hindfoot region. * indicates a statistical difference for $p < 0.05$ using a paired t-test. 124

Figure 5.4.12: The mean plantar pressure at midstance, normalised for body weight, in (a) the medial and (b) the lateral midfoot. * indicates a statistical difference for $p < 0.05$, using a paired t-test between the shod limb and PD-AFO limb and a Wilcoxon signed rank test between the left control and right control. 125

Figure 5.4.13: The peak plantar pressure, normalised for body weight, at push off in the (a) medial and (b) the lateral hindfoot region. * indicates a statistical difference for $p < 0.05$ using a paired t-test between the PD-AFO limb and the shod limb, and using a Wilcoxon signed rank test between the left control and the right control. 126

Figure 5.4.14: The peak plantar pressures experienced at push off in each limb, normalised for body weight, in the (a) medial forefoot region, (b) the lateral forefoot region, (c) the greater toe and (d) the lesser toes. * indicates a statistical difference for $p < 0.05$ using a paired t-test in all cases except between plantar pressure in the medial forefoot region between the left control and right control where a Wilcoxon signed rank test was used. 127

Figure 5.4.15: The peak GRF in the (a) PD-AFO limb and (b) shod limb and the peak plantar force in (c) PD-AFO limb and (d) shod limb at weight acceptance (n=5). * indicates a statistical difference for $p < 0.05$, using a paired t-test. 128

Figure 5.4.16: The peak GRF in the (a) PD-AFO limb and (b) the shod limb and the peak plantar force in (c) PD-AFO limb and (d) shod limb at push off (n=5). * indicates a statistical difference for $p < 0.05$ using a paired t-test. 129

Figure 6.1.1: The ankle power (W) of the combined limb-PD-AFO system, normalised to body weight, during (a) walking with 3 different posterior strut stiffnesses and a healthy control [56] and

during (b) running with 3 prescribed bending axis location of the posterior struts [54]. Images reproduced with permission from the rights holder [(a) Wolter Hu (b) Elsevier]. 137

Figure 6.1.2: Strut deflections in the sagittal plane seen during mechanical testing of 4 different AFOs, including the US military version of the PD-AFO, the IDEO, at 3 points in gait: Midstance (MSt), Terminal Stance (Tst) and Pre-swing (PSw) [63]. Image reproduced with permission from the rights holder ASME. 138

Figure 6.2.1 Schematic showing strain gauges on samples at 2 sites (1 and 2), located at 90° to one another (at locations j, k, l, m) in the; (a) orientation for compression tests (b) orientation for bending tests..... 139

Figure 6.2.2: A custom made strain gauge attachment to help ensure consistent strain-gauge placement. This attachment fitted around the sample of each posterior strut to indicate the location and orientation for each strain gauge. 140

Figure 6.2.3: Experimental test set-ups used to validate the strain gauge attachments in (a) compression and (b) 4-point bending..... 140

Figure 6.2.4: Schematic showing the location of the 4 sites where strain gauges were attached as measured from the posterior, proximal surface of the base of the struts. It is a rear view of the orthotic. At each site there are 4 strain gauges. ‘MS’ indicates the site on the medial strut, and ‘LS’ indicates the site on the lateral strut. ‘P’ and ‘D’ indicate whether it is a proximal or a distal site. 143

Figure 6.2.5: The axial strain distribution in a cross section where y indicates an increased distance from the neutral axis (NA). The strain distribution in (a) is for bending, in (b) is for compression and in (c) is the superposition of both bending and compression. The **cross-sectional** view in (d) represents the posterior strut cross section and its neutral axis, with the 2 crosses illustrating where the strain gauges were placed. 144

Figure 6.3.1: Change in strain over time (strain rate) during compression as recorded by 8 strain gauges(SGs) on 3 samples, and as calculated by the force-displacement curve recorded by the materials testing machine. The median strain rate for samples 1, 2, and 3 was -0.0007863 s^{-1} , -0.0006332 s^{-1} , and -0.0006560 s^{-1} respectively. The median strain rate, as calculated by the materials testing machine readings was -0.0007586 s^{-1} . *p indicates the p value calculated using an unpaired t-test with the significance level set at $\alpha=0.05$ 147

Figure 6.3.2: Change in absolute strain over time, across 3 samples during 4-point-bending. The strain was recorded by 2 strain gauges (SGs) on 2 sides (where ϵ_k and ϵ_m are the strain gauges top and bottom as indicated in Figure 6.2.1b) of the sample. The median absolute value of strain over time for the bottom strain gauges was 0.0005435 s^{-1} . and for the top strain gauges was 0.0005490 s^{-1} 148

Figure 6.3.3: Change in the absolute value of strain over time during bending, as recorded by 4 strain gauges (those located on the side of the samples during the 4-point-bend test: ϵ_j and ϵ_l) on 3 samples, and the maximum change in strain over time as calculated by the force displacement curve recorded

by the materials testing machine. The median strain rate for samples 1, 2, and 3 was $3.112 \times 10^{-6} \text{ s}^{-1}$, $1.991 \times 10^{-6} \text{ s}^{-1}$, $1.089 \times 10^{-5} \text{ s}^{-1}$ respectively.	149
Figure 6.3.4: The force-displacement curve recorded during 4 point-bending for 1 sample during loading and unloading. The linear regression models fitted to the loading and unloading curve between 0.2 mm and the maximum displacement are shown.	150
Figure 6.3.5: The efficiency, η , calculated from each sample ($n=12$) from 4-point bending. The median efficiency recorded by sample 1 was 0.967, by sample 2 was 0.971 and by sample 3 was 0.969. *p indicates the p value calculated using an unpaired t-test with $\alpha=0.05$	151
Figure 6.3.6: The mean strain values during walking on (a) the posterior side of the struts and (b) the anterior side of the struts: on the medial strut, at the proximal (MS_P) and distal sites (MS_D); and on the lateral strut, at the proximal (LS_P) and distal sites (LS_D). The shaded areas show 1 standard deviation.	153
Figure 6.3.7: The mean strain values recorded during running on (a) the posterior side of the struts and (b) the anterior side of the struts: on the medial strut, at the proximal (MS_P) and distal site (MS_D); and on the lateral strut, at the proximal (LS_P) and distal site (LS_D). The shaded area shows 1 standard deviation.	154
Figure 6.3.8: (a) Strain energy stored within the posterior struts during walking gait. The shaded region is the propagated error from all measurements used to calculate the energy. (b) Power consumed and generated by the posterior struts. The efficiency of the posterior struts was accounted for to give the true values of power. The small, dotted lines indicate the true power when calculated with the values of energy \pm propagated error.....	156
Figure 6.3.9: (a) Strain energy stored within the posterior struts during running gait. The shaded region is the propagated error from all measurements used to calculate the energy. (b) Power dissipated and generated by the posterior struts. The efficiency was accounted to give true values of power of posterior struts. The small, dotted lines indicate the true power when calculated with the values of energy \pm propagated error.....	157
Figure 6.4.1 Diagram showing the changes in the shape of the struts throughout the gait cycle. The magnitudes of displacement are not to scale, and timings within the gait cycle are approximate. The first letter described the proximal (P) /distal (D) location of the strain gauge, and the second letter, describes the posterior (P) /anterior(A) location.....	159
Figure 6.4.2: Total ground reaction force, normalised for body weight, during walking gait, as described in Chapter 5.....	160
Figure 7.2.1: An FE model of a PD-AFO by Schrank et al. with a surrogate tibia, of length R, fixed at the 'ankle joint centre' (AJC) demonstrating how the model simulated an experimental testing set-up. A force, F, was applied to the proximal end of the surrogate tibia and the rotational stiffness determined by the change in angle, θ , of the tibia [105]. The plot shows vertical displacement with	

blue indicating minimal displacement and red indicating the greatest displacement. Image reproduced with permission from the rights holder the American Society of Mechanical Engineers ASME 166

Figure 7.2.2: Experimental set-up, with surrogate limb, used by Ielapi et al. to test the rotational stiffness of an AFO. A linear motor drives the surrogate tibia in the anteroposterior direction [107]. Image reproduced is Open Access. 167

Figure 7.2.3: (a) An AFO loaded at the plantar aspect of its footplate in an experimental set-up with the boundary conditions shown in the FE model. (b) The different regions of the AFO shown in the FE model. Images reproduced from Zou et al. [94] are open access. 169

Figure 7.3.1: Process to develop the geometry of FE model of the PD-AFO 170

Figure 7.3.2: The local coordinate systems assigned to the carbon fibre regions. The black arrow indicates the prescribed direction of E_1 , normal to the page (for all components) prescribes the direction of E_2 and the grey arrow indicates the direction of E_3 172

Figure 7.3.3: The (a) schematic and (b) experimental set-up used to test for validation the PD-AFO FE model.. The schematic demonstrates the 0° orientation of the PD-AFO, with posterior struts sitting within the x-z plane and normal to the ground (parallel to z). The force was measured at the same point as δ_{input} 174

Figure 7.3.4: The boundary conditions, in red, applied to the control node of the cuff contact body during the FE validation, where δ indicates displacement in that direction, and R indicates rotation about that axis. The location of the two surfaces, representing the point of contact of the screws, is shown, and the control node is located centrally between them. 175

Figure 7.3.5: The top figures show the whole PD-AFO, and the bottom illustrate a region of the PD-AFO partly invisible to show the area, in yellow, over which the total force was applied at (a) early stance - 10% of the gait cycle and (b) late stance – 50% of the gait cycle. ‘A’ indicates the anterior direction, ‘P’, the posterior direction, ‘M’, the medial direction and ‘L’, the lateral direction 177

Figure 7.3.6: The boundary conditions applied to the PD-AFO model, for both (a) early stance (10% of the gait cycle) and (b) late stance (50% of the gait cycle). The red, solid line represents the angle of the long axis of the tibia compared to the vertical at the start of the analysis (the initial shank-to-vertical angle, θ_i) and the red, dotted line indicates the final position of the tibia compared to the vertical (the final shank-to-vertical angle described as θ_f). $\delta=0$ indicates that region is fixed in all directions. 178

Figure 7.3.7: Shank-to-vertical angle throughout the gait cycle when wearing 3 different heel heights according to a study by Owens et al. [123]. Image reproduced with permission from the rights holder Sage Publications, Open Access. 179

Figure 7.3.8: The expanded view baseline model is shown in (a) with the region that is considered built-in to the posterior cuff and the base. The strut model is shown in (b) with the alterations made to the posterior struts, replacing the built-in region with rigid strut inserts. These rigid inserts were glued

to the posterior cuff and base. The strut caps were glued to the posterior struts and had the same control node as the rigid inserts, so did not move relative to one another during the simulation..... 181

Figure 7.3.9: Rotation of the toe region in the sagittal plane relative to the long axis of the posterior struts to give (a) dorsiflexed angle of 4° relative to baseline (b) neutral toe position as prescribed of 2° dorsiflexed relative to the long axis of the posterior struts and (c) plantarflexed angle of 4° relative to baseline and rotation of the distal base portion to give (d) dorsiflexed position of 4° relative to baseline (e) baseline position as prescribed as prescribed at 3° plantar flexion relative to the long axis of the posterior struts (f) plantarflexed by 4° relative to baseline..... 184

Figure 7.3.10: Rotation of the posterior struts to (a) plantarflexed position of 4° relative to baseline (b) baseline position as prescribed with posterior aspect of base and long axis of posterior struts in plane (c) dorsiflexed by 4° relative to baseline and rotation of the cuff to (d) plantarflexed position of 4° relative to baseline (e) baseline position as prescribed with posterior aspect of cuff and long axis of posterior struts in plane (f) dorsiflexed by 4° relative to baseline 185

Figure 7.3.11: Changing the cross sectional areas of the struts by (a) -40% of the base line area (b) baseline value and (c) +40% of the baseline area. Altering the second moment of area - in the sagittal plane - of the struts, whilst maintaining the cross-sectional area, to give a second moment of area of (d) 567mm^4 (e) 944mm^4 and (f) 1323mm^4 about the sagittal plane neutral axis, SP-NA. Altering the diameter of the lateral (L) and medial (M) posterior struts to give (g) an increase in 40% diameter of the medial strut and 40% reduction of the lateral strut diameter, (h) the baseline diameters, and (i) an increase in lateral strut diameter by 40% and a decrease in medial strut diameter by 40%. All dimensions are in mm. 186

Figure 7.4.1: Mesh convergence analysis on the PD-AFO FE model. The model reaction force and peak equivalent Von Mises Stress. 187

Figure 7.4.2: Mean force-displacement curve, ± 1 SD, for 5 tests for the experimental, validation set-up..... 188

Figure 7.4.3: The (a) experimental and (b) computational compression testing of the PD-AFO showing the device at full compression with 400 N. The location of the maximum value of Von Mises stress recorded in each component during the FE simulation is shown in (i) the lateral strut (ii) the medial strut (iii) the posterior cuff and, (iv) the proximal region of the base (v) the distal region of the base..... 189

Figure 7.4.4: The force-displacement (disp) curve recorded during the experimental set-up and the force-displacement curves calculated by the FE simulation. The solid red line indicates the force-displacement curve obtained using the mean material properties. The steeper and shallower dotted red lines indicate the force-displacement curves obtained using the maximum and minimum material properties, respectively. 190

Figure 7.4.5: Ratio of strain energy recorded by the FE model within each component of the PD-AFO upon completion of both the early stance and late stance simulation. 191

Figure 7.4.6: The equivalent Von Mises stress in the PD-AFO at (a) early stance with (i) 59MPa on the lateral strut, (ii) 58MPa on the medial strut and (iii) 8 MPa on the insert for the medial strut in the posterior cuff and (b) late stance with (i) 82MPa on the medial strut (ii) 75MPa on the medial strut and (iii) 47MPa on the insert for the medial strut in the posterior cuff, and within the base alone at (c) early stance with (i) 86MPa (ii) 10MPa and (iii) 7MPa and (d) late stance with (i) 107MPa on the insert for the lateral strut in the base (ii) 38MPa and (iii) 22MPa. 192

Figure 7.4.7: Influence of the Young’s modulus of the posterior struts, when varied by $\pm 40\%$, on the rotational stiffness and strain energy stored in the posterior struts, when compared to the baseline model. ES: early stance, simulation 10% of the gait cycle; LS: late stance, simulation 50% of the gait cycle 194

Figure 7.4.8: Influence of the carbon fibre material properties on the rotational stiffness and strain energy stored in the posterior struts, when compared to the baseline model. The parameters changed were (a) the Young’s Moduli of all carbon fibre layers used in the base and the cuff by $\pm 40\%$ (b) the addition (add.) and removal (rem.) of aramid from all areas within the base (c) the Young’s Moduli of the uni-directional carbon fibre in the base and cuff by $\pm 40\%$ and (d) the Young’s Moduli of the carbon twill carbon fibre in the base and the cuff by $\pm 40\%$. ES: early stance, simulation 10% of the gait cycle; LS: late stance, simulation 50% of the gait cycle..... 195

Figure 7.4.9: Influence of the base alignment on the rotational stiffness and strain energy stored in the posterior struts, when compared to the baseline model. The parameters changed were (a) the alignment of plantar region of the toe region relative to the posterior struts by $\pm 4^\circ$ (b) the alignment of plantar region of the whole base relative to the posterior struts $\pm 4^\circ$. (Plan. indicates the mode plantarflexed alignment and dors. indicates the more dorsiflexed alignment.) ES: early stance, simulation 10% of the gait cycle; LS: late stance, simulation 50% of the gait cycle. 196

Figure 7.4.10: Influence of the strut and cuff alignment on the rotational stiffness and strain energy stored in the posterior struts, when compared to the baseline model. The parameters changed were (a) the relative alignment of the struts and cuff to the ground by $\pm 4^\circ$ (b) the relative alignment of the cuff to the posterior struts by $\pm 4^\circ$. (Plan. indicates the plantarflexed alignment, and dors. the dorsiflexed alignment.). ES: early stance, simulation 10% of the gait cycle; LS: late stance, simulation 50% of the gait cycle. 197

Figure 7.4.11: Influence of the strut cross-sectional area on the rotational stiffness and strain energy stored in the posterior struts, when compared to the baseline model. The parameters changed were (a) the strut cross-sectional area by $\pm 40\%$ (b) the second moment of area by $\pm 40\%$ in the sagittal plane (c) uneven strut cross-sectional areas (with med+ indicating the medial strut had a larger cross-sectional area and lat+ indicating the lateral strut had a larger cross-sectional area). ES: early stance, simulation 10% of the gait cycle; LS: late stance, simulation 50% of the gait cycle. 199

Figure 8.2.1: Validation results reported by Chen et al. (noted as ‘current study’), comparing the ground reaction force (GRF) and the plantar-fascia tension (FT) to 2 cadaveric studies (Erdemer 2004

and Sharkey 1998) in literature, throughout different instances of the gait cycle [146]. Image reproduced with permission from Sage Publications, Open Access.....	207
Figure 8.2.2: The maximum dorsiflexion experienced in the (a) rigid model and (b) deformable model [147]. Images reproduced with permission from the rights holder Society of Automotive Engineers.	208
Figure 8.2.3: FE model developed by Akrami et al. showing the soft tissue (transparent), along with a meshed plantar fascia, 30 bones, 1814 line elements representing 85 ligaments and 74 cartilage layers [131]. Image reproduced with Open-Access.....	210
Figure 8.3.1: Schematic showing foot as scanned using MRI	218
Figure 8.3.2: Segmentation process of the MRI scans for the calcaneus with (a) 2D slice (b) Region Growing tool to create 3D geometry (c) final smoothed 3D volume	219
Figure 8.3.3: The methodology to create cartilage surfaces. First a surface was created at the midpoint between the 2 exterior surfaces of the bones, demonstrated by the green dashed line in 2D in (a). The cartilage was then extended to this surface from both bones to form two layers of cartilage. This is shown in 2D in (b).	220
Figure 8.3.4 The orientation of the lower limb as scanned compared to the neutral orientation as defined by Wu et al. [27] in the (a) transverse, (b) frontal and (c) sagittal planes.....	221
Figure 8.3.5: The blue region, as indicated, is the location of a thin, rigid surface to represent the constraining effect of the skin tissue proximal the fat pad. All points in contact with the surface were fixed relative to one another but otherwise free to translate and rotate.	222
Figure 8.3.6: Ligaments modelled as springs (shown by red lines) within the FE model and their insertion points viewed from the (a) medial side and (b) the lateral side. The lateral side, (b), also shows the point at which the Achilles Tendon was considered to act.	223
Figure 8.3.7: The rotation of the model to the initial position, to give the desired shank-to-vertical angle, and the boundary conditions imposed on the simulation. F indicates a force in that direction, δ indicates the displacement in that direction, and R indicates the rotation about that axis.	226
Figure 8.3.8: The stress within the Achilles tendon throughout gait at different walking speeds [175]. The stresses seen in the Achilles tendon of the younger cohort are shown on the left and of the older cohort are shown in the right. Image reproduced with permission from the rights holder Elsevier... ..	227
Figure 8.3.9: Simplified, fat pad only, model to evaluate the sensitivity of the floor material properties and fat pad properties on the plantar pressure. The distal phalanges (light blue) and the calcaneus (green) were considered to rotate about the ankle joint, indicated as the origin, O. F indicates a force in that direction, δ indicates the displacement in that direction, and R indicates the rotation about that axis.	229
Figure 8.4.1: The lower limb FE model viewed from the medial side in (a) the initial position and (b) its final position after application of boundary conditions to mimic 10% of the gait cycle, between loading response and midstance.....	230

Figure 8.4.2: The plantar pressure in the left foot at the selected point in gait, as recorded during (a) the gait analysis described in Chapter 5 and (b) the FE simulation. The foot is split into 2 regions, the hindfoot region, and the midfoot and forefoot region. The light grey region indicates the value of plantar pressure is off of the scale..... 231

Figure 8.4.3: The relative magnitude of mean plantar pressures $\pm 1SD$ (indicated by the dashed line) recorded experimentally and simulated computationally, in the hindfoot region, and in the midfoot and forefoot regions. 232

Figure 8.4.4: Contact normal stress at (a) the talocrural joint and (b) the subtalar joint when simulating 10% of the gait cycle..... 233

Figure 8.4.5: The plantar pressure distribution obtained from the FE whole model with (a) the baseline properties and boundary conditions (b) the baseline Young’s modulus of cartilage altered by -20% (c) the baseline Young’s modulus of cartilage altered by +20% (d) the baseline Achilles tendon force altered by -20% and (d) the baseline Achilles tendon force altered by+20%..... 234

Figure 8.4.6: The contact stress at the talocrural joint (on the talus’ cartilage) from the FE whole model with (a) the baseline properties and boundary conditions (b) the baseline Young’s modulus of cartilage altered by -20% (c) the baseline Young’s modulus of cartilage altered by +20% (d) the baseline Achilles tendon force altered by -20% and (d) the baseline Achilles tendon force altered by+20% 235

Figure 8.4.7: The plantar pressure distribution obtained from the fat pad only, FE model with (a) the baseline properties and boundary conditions (b) the addition of a deformable floor with leather properties (c) the addition of a deformable floor with aluminium properties (d) the fat pad Young’s modulus decreased by 20%, and (e) with the fat pad Young’s modulus increased by 20%..... 236

Figure 9.1.1: The areas of contact between the lower limb and the PD-AFO and how these can change at different points in gait. This includes the (a) cuff-tibia contact shown in green, which varies between contact between the posterior cuff and posterior calf during early stance and the anterior cuff and anterior aspect of the tibia during late stance. Additionally, there is (b) contact between the sole and fat pad shown in red. 241

Figure 9.1.2: A solid model of an AFO combined with an AFO and insole [183]. Reproduced with permission from the rightsholder Taylor and Francis. 242

Figure 9.1.3: FE model of a lower limb in an AFO [183]. Image reproduced is in the public domain. 243

Figure 9.2.1: The connection of the tibia to the posterior cuff shown with (a) the whole model and (b) the posterior cuff with 30 springs, shown in red, used to model the calf muscle. 15 of the springs act in the vertical direction only, and 15 in the anteroposterior direction only. 246

Figure 9.2.2: FE model boundary conditions used to determine the suitable stiffness for the springs to represent the contact between the calf and the PD-AFO. The tibia was fixed in all degrees of freedom. The contact region was a rigid surface, in contact with the calf, and positioned in 3 locations, distal

(left), central (middle) and proximal (right). A total displacement, δ_{total} of up to 20 mm was applied to the control node. x: lateral direction, y: posterior direction, z: proximal direction. δ indicates the displacement in that direction, and R indicates the rotation about that axis.	247
Figure 9.2.3: The spring model, with (a) the contact points between the 30 springs and the interior surface of the cuff and (b) the boundary conditions applied, where δ_{total} was the resultant displacement of up to 20mm. δ indicates the displacement in that direction, and R indicates the rotation about that axis.	248
Figure 9.2.4: The initial position of the combined limb-PD-AFO model and the boundary conditions applied to mimic 10% of the gait cycle. F indicates a force in that direction, δ indicates the displacement in that direction, and R indicates the rotation about that axis.	249
Figure 9.3.1: The force-displacement curves as recorded from compression of the meshed calf and the spring replacement model when run with 4 sets of material properties.	251
Figure 9.3.2: FE model of the limb and PD-AFO in (a) the initial position and (b) upon completion of the simulation at 10% of the gait cycle.	251
Figure 9.3.3: The ratio of load between the limb and PD-AFO as calculated by the FE simulation and during the experimental gait analysis. The dotted lines represent the experimental corridor, accounting for difference in measurement between the PEDAR sensors and force plates.	252
Figure 9.3.4: The plantar pressure obtained (a) experimentally in the PD-AFO gait analysis described in chapter 5 and (b) from the FE simulation of the limb when wearing the PD-AFO. The foot is split into 2 regions, the hindfoot region, and the midfoot and forefoot region. The light grey region indicates the value of plantar pressure is off the scale.	253
Figure 9.3.5: The relative magnitude of mean plantar pressures recorded, both experimentally and computationally, in the hindfoot region of the foot, and the midfoot and forefoot region of the foot, during PD-AFO gait.	254
Figure 9.3.6: The joint loads when the lower limb is simulated with and without the PD-AFO, normalised for the total force applied in each model.	255
Figure 9.3.7: Contact normal stresses at the (a) talocrural joint and (b) subtalar joint at 10% of the gait cycle with the limb in the PD-AFO	256
Figure 9.3.8: The mean contact normal stress at the major joints, evaluated in the lower limb only model and the combined limb-PD-AFO model. The contact stresses are normalised for the total force applied in each model.	257
Figure 12.1.1: The sensitivity of the compressive stiffness in the primary direction of carbon-twill to (a) Young's modulus, E_1 , (b) Young's modulus, E_3 , (c) shear moduli, G_{13} and G_{23} , (d) Poisson's ratio, ν_{12} , and (e) the Poisson's ratio, ν_{13} and ν_{23}	282
Figure 12.1.2: The sensitivity of the compressive stiffness in the primary direction of uni-directional carbon-fibre to (a) Young's modulus, E_1 , (b) Young's modulus, E_2 , (c) shear moduli, G_{13} and G_{23} , (d) Poisson's ratio, ν_{23} , and (e) the Poisson's ratio, ν_{12} and ν_{13}	283

Figure 12.1.3: The sensitivity of the compressive stiffness in the primary direction of aramid to (a) Young's modulus, E_1 , (b) Young's modulus, E_3 , (c) shear moduli, G_{13} and G_{23} , (d) Poisson's ratio, ν_{12} , and (e) the Poisson's ratio, ν_{13} and ν_{23} .	284
Figure 12.1.4 (a) Schematic of set up showing that the displacement y , is a function of the distance x as prescribed by figure (b) showing a close-up of the bending comparing the displacement δ_{input} and y	286
Figure 12.1.5: Young's modulus calculated in compression, of 1 sample ($n=5$) at 4 different strain rates, For each rate respectively (0.030/s, 0.059/s, 0.119/s, 0.234/s)) the median Young's modulus calculated is 28.84GPa, 32.02GPa, 32.60GPa, 31.91GPa. *p indicates a statistical difference calculated from an unpaired t-test	288
Figure 12.1.6: Young's modulus calculated in bending, of 1 sample ($n=5$) at 4 different displacement rates, For each rate respectively (0.095mm/s, 0.19mm/s, 0.38mm/s, 0.75mm/s) the median Young's modulus calculated is 31.93GPa, 32.95GPa, 32.69GPa, and 32.42GPa. *p indicates a statistical difference calculated from an unpaired t-test	289
Figure 12.1.7: 1 Force-displacement curves for each of the 3 samples of composite strut in (a) compression and (b) bending	290
Figure 12.1.8: Stress-strain curve recorded during compression of samples of polyurethane used in manufacture of the heel wedge and fitted 2-term Ogden model. The shaded area denotes 1 SD	293
Figure 12.1.9: Mean experimental stress-strain curve for Foam A and Foam B, as calculated from the recorded force-displacement curves and Ogden model fitted to the combined dataset. The shaded area denotes 1 SD.	294
Figure 12.2.1: The mean, normalised plantar force $\pm 1SD$ as calculated by the PEDAR sensor and the total ground reaction force as calculated by the force plates for (a) the left limb and (b) the right limb during control gait, and (c) the PD-AFO limb and (d) the shod limb for the PD-AFO gait.	296
Figure 12.2.2: The plantar force, as measured by the PEDAR sensors and the total GRF as measured by the force plates at weight acceptance in (a) the left limb (b) the right limb (c) the PD-AFO limb and (d) the shod limb. * indicates a statistical difference for $p < 0.05$ for paired T-Test	297
Figure 12.2.3: The plantar force, as measured by the PEDAR sensors and the total GRF as measured by the force plates at midstance in (a) the left limb (b) the right limb (c) the PD-AFO limb and (d) the shod limb. * indicates a statistical difference for $p < 0.05$ for paired T-Test	298
Figure 12.2.4: The plantar force, as measured by the PEDAR sensors and the total GRF as measured by the force plates at push off in (a) the left limb (b) the right limb (c) the PD-AFO limb and (d) the shod limb. * indicates a statistical difference for $p < 0.05$ for paired T-Test	299
Figure 12.2.5: Underestimation of the plantar force compared to the GRF in the shod limb, left limb and right limb, and the mean values of these errors throughout gait.	300
Figure 12.2.6: The total GRF recorded by all limbs during (a) weight acceptance (b) midstance (c) push-off.	301

Figure 12.2.7: The peak plantar force recorded by all limbs during (a) weight acceptance (b) midstance and c) push off.	302
Figure 12.2.8: The plantar pressure in the medial hindfoot at (a) weight acceptance (b) midstance (c) push off. † indicates the figure is shown in the main text.	303
Figure 12.2.9: The plantar pressure in the lateral midfoot at (a) weight acceptance (b) midstance (c) push off. † indicates the figure is shown in the main text.	304
Figure 12.2.10: The plantar pressure in the medial midfoot at (a) weight acceptance (b) midstance (c) push off. † indicates the figure is shown in the main text.	305
Figure 12.2.11: The plantar pressure in the lateral forefoot at (a) weight acceptance (b) midstance (c) push off. † indicates the figure is shown in the main text.	306
Figure 12.2.12: The plantar pressure in the medial forefoot at (a) weight acceptance (b) midstance (c) push off. † indicates the figure is shown in the main text.	307
Figure 12.2.13: The plantar pressure in the lesser toe (lateral) at (a) weight acceptance (b) midstance (c) push off. † indicates the figure is shown in the main text.	308
Figure 12.2.14: The plantar pressure in the greater toe (medial) at (a) weight acceptance (b) midstance (c) push off. † indicates the figure is shown in the main text.	309
Figure 12.3.1: In (a) the raw strain gauge readings recording during the strain gauge reliability tests and (b) these strains adjusted for the zero error.	311
Figure 12.3.2: The force-displacement curves of 12 test repeats of 4-point-bending used to establish the efficiency of sample 1.	312
Figure 12.3.3: The mean strain values $\pm 1SD$ at (a) the lateral side of the struts and (b) the medial side of the struts: on the medial strut, at the proximal (MS_P) and distal location (MS_D); and on the lateral strut, at the proximal (LS_P) and distal location (LS_D)	314
Figure 12.5.1: The lower Limb only upon completion of simulation at 10% of the gait cycle	320
Figure 12.5.2: The contact normal stress on the talar cartilage surfaces, observed during the FE simulation of the lower limb only, at 10% of the gait cycle.	321
Figure 12.5.3: The contact normal stress on the calcaneal cartilage surfaces, observed during the FE simulation of the lower limb only, at 10% of the gait cycle	322
Figure 12.6.1: Views of the FE model of the lower limb within the PD-AFO positioned to simulate 10% of the gait cycle.	324
Figure 12.6.2: The equivalent Von Mises stress observed following compression of the idealised meshed calf with (a) Avril 2010 properties, (b) Dai 1999 properties, (c) maximum values in the range provided by Lima et al. and (d) minimum values in the range provided by Lima et al.	326
Figure 12.6.3: The force-displacement curve used to define the material properties of the spring in the combined PD-AFO – lower limb FE model.	327
Figure 12.6.4: The contact normal stress on the talar cartilage surfaces, observed during the FE simulation at 10% of the gait cycle for the lower limb when in the PD-AFO.	328

Figure 12.6.5: The contact normal stress on the calcaneal cartilage surfaces, observed during the FE simulation for 10% of the gait cycle for the lower limb when in the PD-AFO.	329
Figure 12.7.1: Permission to reproduce Figure 1.2.1 in Chapter 1 [3].	330
Figure 12.7.2: Permission to reproduce Figure 1.3.1 in chapter 1 [18]	331
Figure 12.7.3: Permission to reproduce Figure 2.3.1Chapter 2[27].	333
Figure 12.7.4: Permission to reproduce Figure 3.3.1 in Chapter 3 [21].	334
Figure 12.7.5: Permission to reproduce Figure 3.3.3 and Figure 3.4.2 in Chapter 3 [56].	335
Figure 12.7.6: Permission to reproduce Figure 3.4.1 in Chapter 3 and Figure 6.1.2 in Chapter 6 [63].	336
Figure 12.7.7: Permission to reproduce Figure 3.4.3 in Chapter 3.[38].	337
Figure 12.7.8: Permission to reproduce Figure 3.4.4 in Chapter 3 [54].	338
Figure 12.7.9: Permission to reproduce Figure 5.2.1 in Chapter 5 [59].	339
Figure 12.7.10: Permission to reproduce Figure 6.1.1a in Chapter 6 [56].....	340
Figure 12.7.11: Permission to reproduce Figure 6.1.1b in Chapter 6 [54].	341
Figure 12.7.12: Permission to reproduce Figure 7.2.1 in Chapter 7 [105].	342
Figure 12.7.13: Permission to reproduce Fig 1.2.2a and Fig1.2.2b in Chapter 8 [147].....	343
Figure 12.7.14: Permission to reproduce Fig 1.3.9 in chapter 8 [175].	344
Figure 12.7.15: Permission to reproduce Figure 9.1.3 in chapter 9[183]	345

ABBREVIATIONS

Abbreviation	Description
PD-AFO	Passive dynamic ankle foot orthosis
AFO	Ankle foot orthosis
GRF	Ground reaction force
ESAR	Energy storage and return
FE	Finite element
BTK	Below the knee
LEAP	Lower Extremity Assessment Project
METALS	Military Extremity Trauma Amputation/Limb Salvage
SIP	Sickness impact profile
B.O.B	British offloading brace
IDEO	Intrepid Dynamic Exoskeletal Orthosis
EMG	Electromyography
ROM	Range of motion
RTR	Return to run
RTD	Return to duty
PTOA	Post-traumatic osteoarthritis
SLS	Selective laser sintering
LEFS	Lower Extremity Functional Scale
PPM	Physical Performance Measures
SMFA	Short Musculoskeletal Function Assessment
CF	Carbon fibre
CT	Carbon twill
UD	Uni-directional
SD	Standard Deviation
CoP	Centre of pressure
ML	Mediolateral
AP	Anteroposterior
BW	Body weight
FP	Force Plate
CT	Computer
MRI	Magnetic Resonance Imaging
CAD	Computer aided design

1 INTRODUCTION

1.1 SCOPE OF THESIS

This thesis examines a novel rehabilitation device: a passive, dynamic ankle-foot orthosis (PD-AFO) trademarked the MomentumTM, that has been prescribed to UK military personnel following serious foot and ankle injuries. Whilst the device has been shown to improve functional outcome for many patients, facilitating their return to high level activity such as running, there is a remainder who do not benefit from prescription of the PD-AFO. The design parameters believed to be responsible for improved functional outcomes for patients have not been studied rigorously. This thesis seeks to investigate the theorised functional design features of the PD-AFO, including offloading and energy storage and return (ESAR), to help ascertain how the PD-AFO alters the joint kinetics of the foot and ankle and why the PD-AFO works for certain patients but not others. By developing computational models of the PD-AFO and the lower limb, along with experimental analyses, this thesis (a) evaluates the effects on both internal and external loading of the limb as a result of wearing the PD-AFO; and (b) identifies critical design components that would have the greatest influence on the performance of the PD-AFO. These models can be the basis for predicting which patients are likely to experience improved functional outcome from this device, and can be used to predict potential long-term adverse effects from its use, and can guide design improvements to elongate the device's longevity and widen the cohort of patients likely to benefit from it.

1.2 CLINICAL PROBLEM

In the last 20 years, conflicts in Iraq (Operation Telic) and Afghanistan (Operation Herrick) have resulted in a large number of extremity injuries due to the use of improvised explosive devices (IEDs) by insurgents. In Operation Herrick alone, more than 5000 injuries involved the use of IEDs [1]; 50% of all injuries were to the extremities, with 11.5% of all injuries being to the foot and ankle [2]. Due to the nature of blast injuries, there are often associated comorbidities, leading to a complicated overall prognosis [3]. One particularly severe, but common, injury is the calcaneal fracture, such as that seen in Figure 1.2.1; a study of 114 patients reported that 87% of ankle and foot injuries included such fractures [4]. These calcaneal fractures are life changing with survivors suffering from ongoing pain and limited opportunities to return to service [5]. Depending on severity, some patients require amputation; Bennet et al. estimated that, from 2003-2014, 52.7% of all ankle and foot injuries to UK service personnel resulted in such surgery [4]. Advances in surgical techniques, as well as a reduction in overall mortality, have, however, made limb salvage an option for more patients than previously possible who have such traumatic lower limb injuries, [6].



Figure 1.2.1: A calcaneal blast fracture observed in the limb [3]. Image reproduced with permission from the rights holder Wolters Kluwer.

1.3 TREATMENT PATHWAY

As treatments for serious lower limb injuries have improved there has been debate, dating back to before the development of the PD-AFO, on the best treatment method to follow, with literature inconclusive on whether limb salvage or amputation is preferential in the long term [6-11]. Georgiadis et al. directly compared limb salvage to below-the-knee (BTK) amputations, the operation that would be performed on unsuccessful limb-salvage patients. BTK patients have the best results of all amputees [12], with fewer operations, shorter recovery times and generally more functionality than those undergoing limb salvage [10]. The Lower Extremity Assessment Project (LEAP) study, a series

of papers published on a civilian cohort, reported poor functional outcome associated with both treatment pathways [13, 14], with patient success highly dependent on factors such as socioeconomic status, race and self-efficacy [14]. The outcomes of both pathways were also found to be worse at 84 months than 24 months, a fact that the authors attributed to decreased mental health scores associated with long term disability [14]. Both Doukas at al. and Sheean et al. found that limb-salvage patients had lower mental health scores than amputees [7, 15]. Based on data from civilian injuries, limb salvage was found to reduce the overall medical cost compared to limb amputation [16].

To facilitate limb salvage and restore functionality following severe lower limb injuries during the recent conflicts, a PD-AFO was produced by the US Army [17], named the Intrepid Dynamic Exoskeletal Orthosis (IDEO) or ExoSym™, shown in Figure 1.3.1a. The UK military provides a similar PD-AFO named the British Offloading Brace (B.O.B) or Momentum®, shown in Figure 1.3.1b, with minor alterations to the US version thought not to alter functionality.

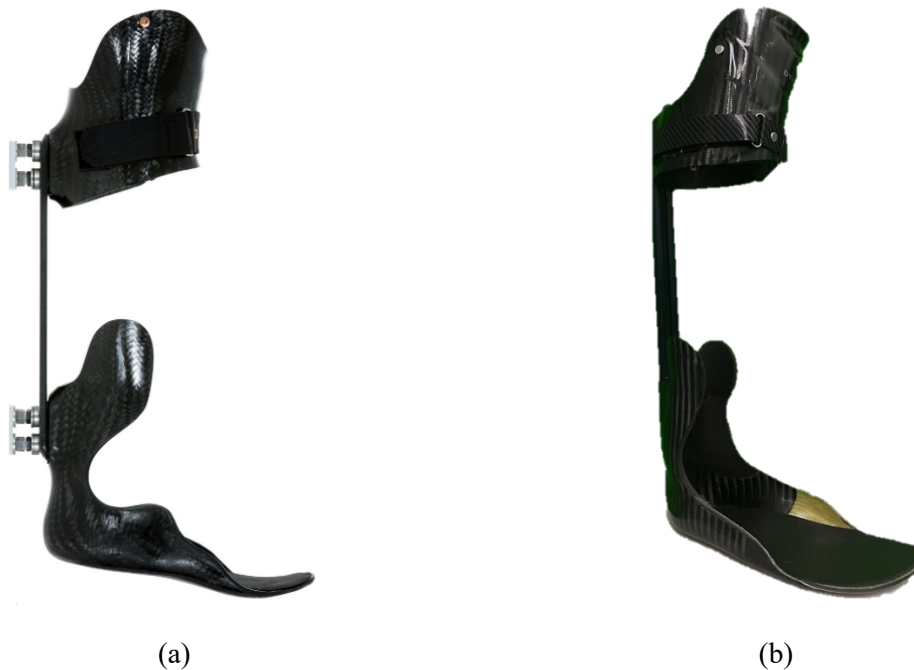


Figure 1.3.1: The (a) IDEO produced for the US military [18] and the (b) B.O.B produced for the UK military. Image (a) reproduced with permission from the rights holder Wolter Kluwer.

The PD-AFO was developed with the aim of reducing the number of limb-salvage patients requesting late amputations; this highly driven and athletic cohort were witnessing fellow personnel with amputations recover at a seemingly faster rate, hitting important ‘landmarks’ such as running earlier, whilst they were otherwise still struggling to walk without pain [17, 19, 20]. The PD-AFO is not successful for all patients, and retrospective cohort studies have, so far, not pre-determined for whom the PD-AFO would or would not work. Understanding this would ensure patients are directed to the best treatment pathway as early on in their recovery as possible.

The PD-AFO was designed based on a number of concepts from different AFOs. Whilst prescription of the device has been shown in the literature to improve functional outcome for patients, it is not yet fully understood which design aspects of the PD-AFO are the most pivotal in its success [21, 22]. Across literature the PD-AFO has been hypothesised to have several design characteristics including ESAR to aid with propulsion during gait, the ability to limit plantarflexion of the foot and the ability to offload the foot and ankle. Offloading is where some of the force exerted on the foot and ankle during gait, is diverted to a region of the leg proximal to the foot and ankle by aid of a device, thereby reducing the forces experienced by the joints.

Despite literature demonstrating the success of the PD-AFO [21], a lack of understanding remains as to whether all of the proposed design characteristics of the PD-AFO, such as offloading and ESAR characteristics, happen during gait. Understanding whether these mechanisms do occur, and to what extent, is important both in terms of fitting of the device and helping to estimate possible long-term effects of the PD-AFO. Additionally, evaluating the changes in internal and external loading, caused by use of the PD-AFO, may allow insight as to why the PD-AFO improves the functional outcome for certain patients but not for others. This will help direct patients to the most suitable treatment pathway, and guide alterations to the design of the PD-AFO to fine tune the device to meet patients' needs.

1.4 AIM AND OBJECTIVES

The aim of this thesis is to characterise the mechanical response of the PD-AFO, and understand how the PD-AFO alters the internal and external loading of the lower limb during gait. This is achieved through a combination of experimental and computational analyses. The thesis has the following objectives:

1. Characterise the PD-AFO's overall mechanical behaviour and the behaviour of individual components of the PD-AFO
2. Understand how the PD-AFO varies the loading on the limb during gait and quantify to what extent offloading of the limb occurs (if any).
3. Evaluate the energy storage and return characteristics of the PD-AFO and quantify the propulsive power the PD-AFO may provide.
4. Understand the significant design components of the PD-AFO, and evaluate those design aspects most likely to alter gait.
5. Establish how the PD-AFO alters the internal loading of the limb.

1.5 THESIS STRUCTURE

This section briefly describes the structure of the thesis. Chapter 2 describes the functional anatomy of the foot and ankle, along with clinical descriptions of its movement. It also details the gait cycle, the

rotations experienced by the foot and ankle during the cycle and the possible experimental methods that can be used to analyse this.

Chapter 3 moves on to review the PD-AFO literature. It begins by detailing the features of the PD-AFO, along with how it came to be prescribed. The chapter evaluates the current success of the PD-AFO, highlighting the improvements observed in several functional outcomes. It also describes the changes that the PD-AFO has made to certain aspects of gait, and highlights aspects of gait that have not been the main focus of the studies currently available in literature. Finally, the chapter assesses design analyses of the PD-AFO, undertaken with gait studies, highlighting important features of the PD-AFO and areas where further work is needed.

Chapter 4 determines the material behaviour of the components of the PD-AFO using a combination of literature, experimental testing and FE modelling. A sensitivity analysis is performed to determine the limitations incurred by the assumptions made.

In chapters 5 and 6 gait analysis is undertaken with a healthy subject. In chapter 5 the subject walks with and without the PD-AFO and the forces and pressures observed during gait are quantified and compared to evaluate how the PD-AFO alters external loading of the limb, and to determine whether offloading of the limb does occur as hypothesised.

In chapter 6 the gait analysis focusses on characterising the behaviour of the PD-AFO's posterior struts during running and walking. The ability of the struts to store and return energy is quantified, and this is used to calculate the possible power generation and dissipation.

Chapter 7 describes the development of an FE model of the PD-AFO, with material properties assigned from chapter 4. The FE model is used to evaluate the mechanical response of the PD-AFO at two points in gait. A design sensitivity is also performed on several design aspects, evaluating those components that are influential to the response of the PD-AFO.

Chapter 8 describes the methodology used to develop the FE model of the lower limb, discussing the most appropriate simplifications and assumptions that can be used, whilst still ensuring a useful output from the simulation. Additionally, the FE simulation of the lower limb, at the chosen point in gait (during early stance at 10% of the gait cycle) is compared to experimental data.

In chapter 9 the model of the PD-AFO developed in chapter 7, and of the lower limb developed in chapter 8, are combined. The chapter describes the development of the combined model, and defines the contact interactions between the 2 bodies. The results obtained from the simulation of the lower limb alone, and of the combined PD-AFO and lower limb are compared, evaluating the contact stresses between cartilage pairs, and the loading at major joints.

Finally, chapter 10 summarises and discusses the work conducted within this thesis, and suggests possible future studies that could be undertaken to develop it further.

2 FUNCTIONAL ANATOMY OF THE FOOT AND ANKLE

This chapter describes the anatomy of the foot and ankle, including the bones, muscles, and tendons. It also gives details of the joints within the foot and how to clinically describe their rotations. The role of these movements during healthy gait are explained, along with descriptions of methodologies used to analyse gait.

2.1 ANATOMICAL COORDINATE SYSTEM

A standard right-hand Cartesian coordinate system can be used to describe the relative location or motion of the human body (Figure 2.1.1a). The coordinate system prescribes 3 planes through the body: coronal plane, sagittal plane, and transverse plane. Relative positions/translations can be described in relation to the coordinate system:

- a) Anterior movement is described by an increase in $|x|$ (posterior movement by a decrease in $|x|$)
- b) Lateral movement is described by an increase in $|y|$ (medial movement by a decrease in $|y|$),
- c) Distal movement is described by an increase in $|z|$ (proximal movement by a decrease in $|z|$).

A local coordinate system, with the origin located at the centre of a joint, can be used to describe the relative rotations of bones to one another around that joint. Of particular interest for this thesis is the coordinate system located at the talocrural joint (see section 2.3). This can be used to describe inversion and eversion, plantarflexion and dorsiflexion, and internal and external rotation ((Figure 2.1.1b). Internal rotation is also known as adduction and external rotation is known as abduction. For the talocrural joint, the range of motion (ROM) in the sagittal plane is much greater than that possible in the transverse and coronal planes.

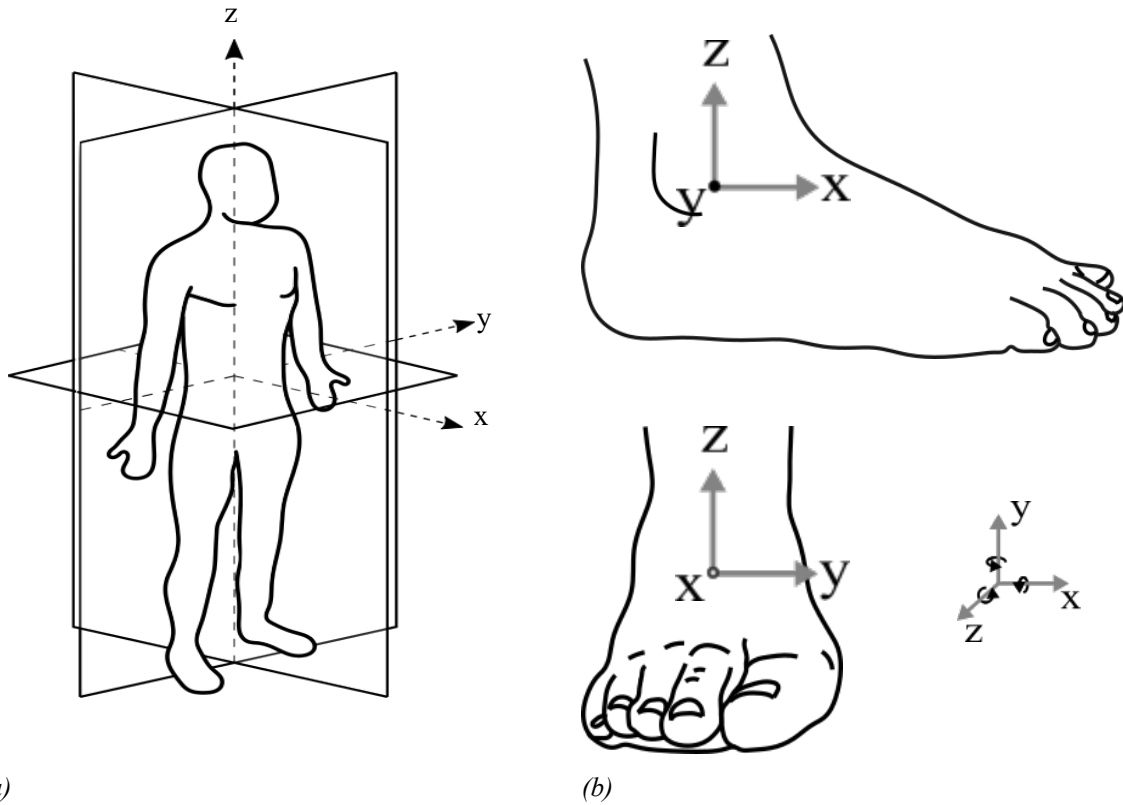


Figure 2.1.1: (a) Planes of motion (x - y plane is named transverse plane, y - z plane is named coronal plane (or frontal), x - z plane is named sagittal plane). (b) Clockwise rotation about x , in the coronal plane, is described as inversion (anticlockwise as eversion). Clockwise rotation about y , in the sagittal plane, is described as plantarflexion (anticlockwise as dorsiflexion). Clockwise rotation about z , in the transverse plane, is described as internal rotation (anticlockwise as external rotation).

2.2 COMPONENTS

2.2.1 Bones

The 26 bones of the foot are categorised as tarsals, metatarsals, and phalanges, indicated in Figure 2.2.1. The 14 most distal bones are the phalanges; each toe consists of 3 phalanges (distal, middle, and proximal) except for the great toe consisting of only two (distal and proximal). There are 5 metatarsals located between the phalanges and the tarsals. The 7 tarsal bones consist of 3 cuneiforms, the cuboid, the navicular, the calcaneus and the talus.

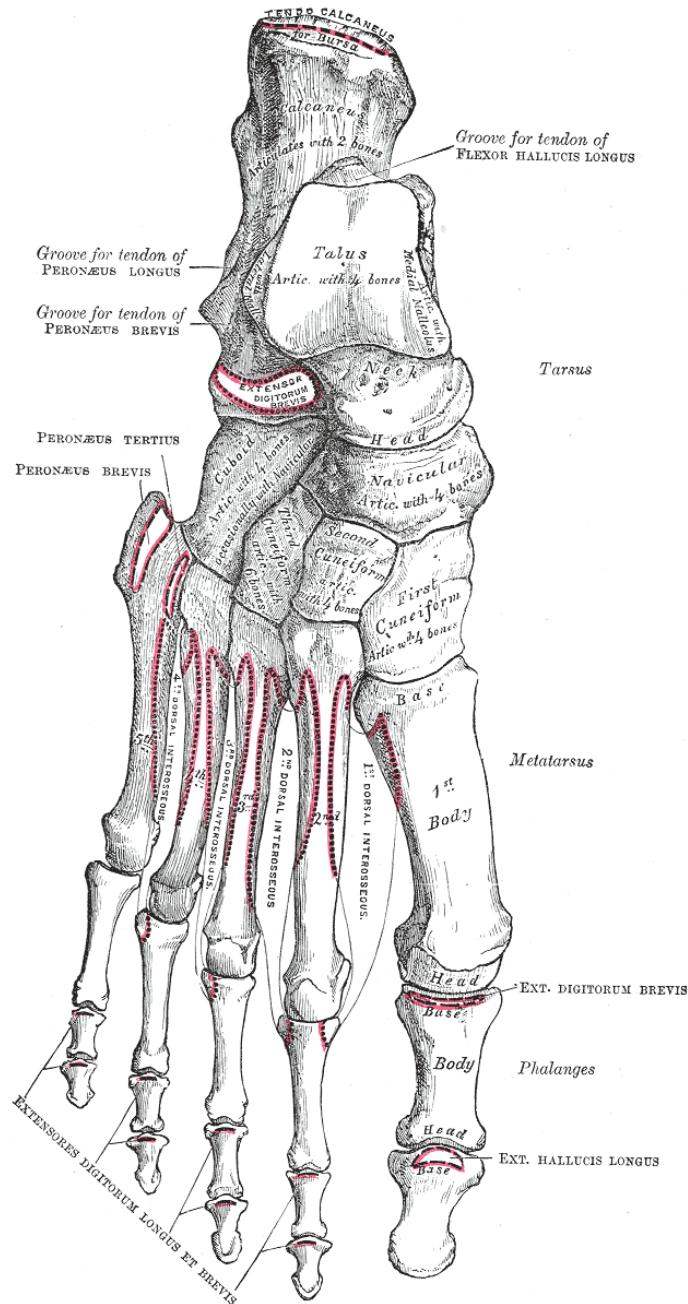
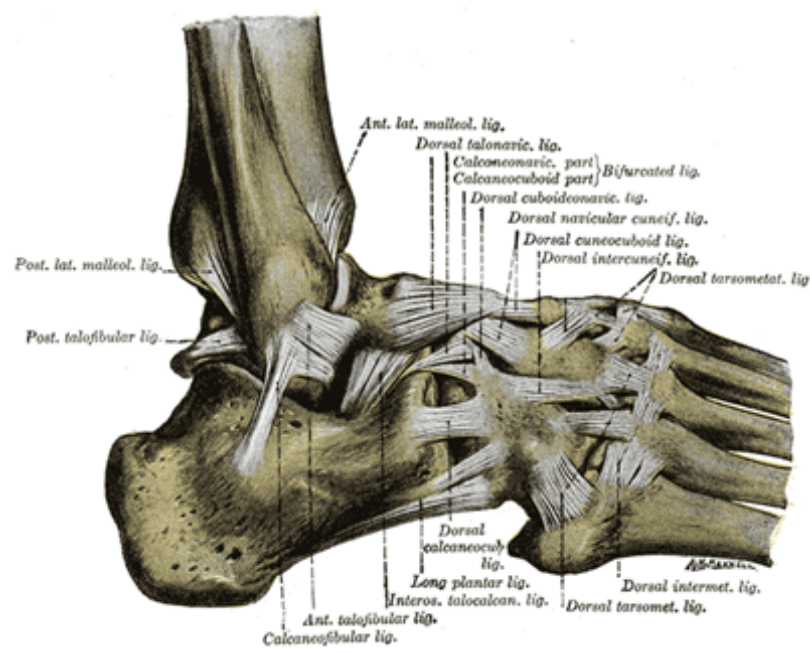


Figure 2.2.1: Bones of the foot as viewed from the dorsal surface. Image reproduced is open access [23].

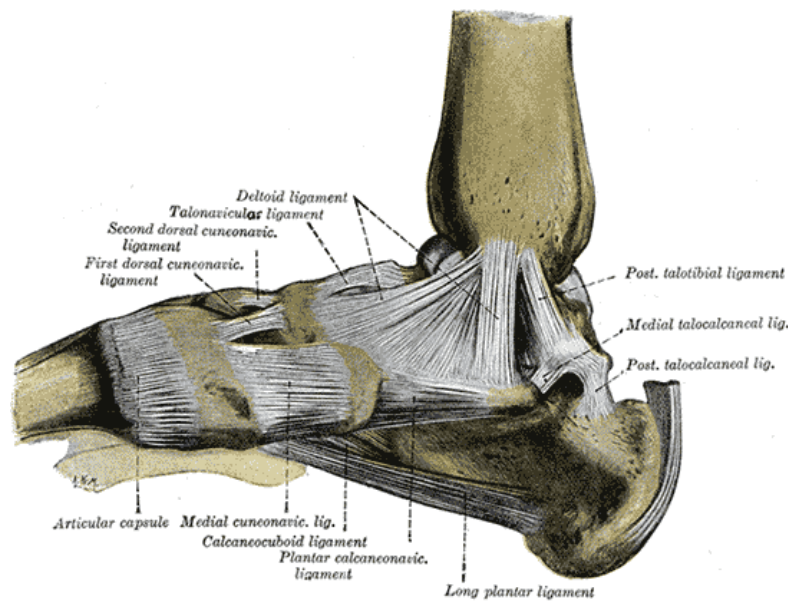
The calcaneus, the largest of the bones (forming the heel), withstands compressive loads of 300-400% body weight during gait [24, 25]. The Achilles tendon attaches to the posterior aspect of the calcaneus and connects it to the posterior compartment of muscles (see section 2.2.4 below). The talus sits superior to the calcaneus and makes contact with the tibia and fibula on its proximal surface to form the talocrural joint. The tibia and fibula are joined together by an interosseous membrane and there is a small amount of relative movement between them [24].

2.2.2 Ligaments and Plantar Fascia

The bones within the foot are connected by many ligaments (Figure 2.2.2) Two of the most complex include the medial (also known as the deltoid) and lateral ligaments, connecting the navicular, talus, calcaneus, tibia and fibula. The strongest is the long plantar ligament, joining the calcaneus to the proximal heads of the phalanges. The ligaments help to stabilise the foot, limiting degrees of freedom of movement, and relative motion between bones.



(a)



(b)

Figure 2.2.2: Ligaments in the foot, from (a) the lateral aspect and (b) the medial aspect. Images reproduced are open access [23].

The plantar fascia, also known as plantar aponeurosis, extends across most of the plantar aspect of the foot. The bulk of the plantar fascia originates from the plantar aspect of the calcaneus and extends distally to the distal end of the proximal phalanges. There are also fibres that extend transversely across the phalanges [24].

2.2.3 Cartilage

Cartilage is a tissue on the surface of bones that allows bones to articulate over one another smoothly. Due to the many joints within the foot, there are several regions of cartilage. Figure 2.2.3 shows regions of cartilage on the talus, demonstrating the complex surface geometry over which the bones move. The surfaces over which the navicular, tibia and fibula slide are convex, whilst the surfaces over which the calcaneus slides are concave.

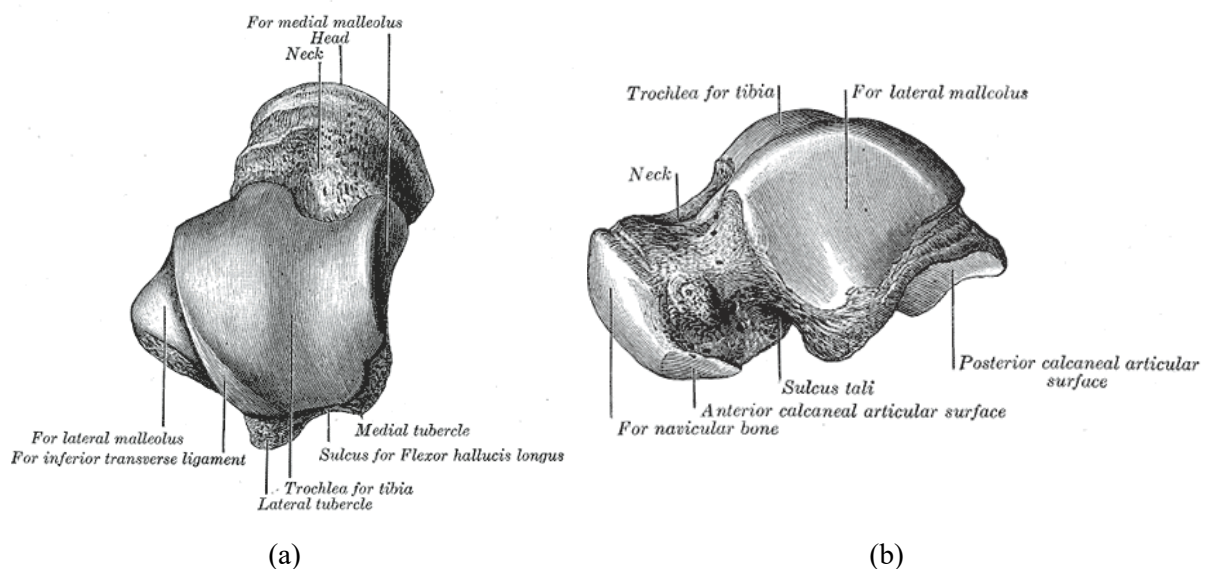


Figure 2.2.3: The cartilage on the surface of the left talus viewed from (a) a proximal aspect (b) a lateral aspect. Images reproduced are open access [23].

2.2.4 Muscles

The motion of the foot depends on extrinsic muscles. These are split into 3 compartments: the posterior, lateral and anterior.

The gastrocnemius, soleus and plantaris muscles form part the posterior compartment and contribute to plantarflexion of the foot. The gastrocnemius can be felt superficially; it forms the majority of the calf. Four further muscles are also part of the posterior compartment, of which 3 (the flexor hallucis longus, flexor digitorum longus, and tibialis posterior) influence the movement and rotation of the foot. The flexor hallucis longus and flexor digitorum longus are responsible for flexing of the toes. The tibialis posterior is responsible for inversion and further helps with plantarflexion [24].

The anterior compartment consists of 4 muscles; these are responsible for dorsiflexion, inversion and extension of the toes. The extensor hallucis longus and extensor digitorum longus are responsible for extension of the toes (as well as dorsiflexion). The peroneus tertius is responsible for both dorsiflexion and eversion, whilst the tibialis anterior is responsible for dorsiflexion and inversion. [24] The lateral compartment is responsible for eversion of the foot, consisting of the peroneus longus and the peroneus brevis. The fibularis longus, along with the tibialis posterior (posterior compartment) and tibialis anterior (anterior compartment) provide arch support during gait [24]. Intrinsic muscles provide support to the arch of the foot, particularly just before toe-off. They also help to prevent too much force from loading the extrinsic muscles [24].

2.3 MOVEMENT AND ROTATION

2.3.1.1 Overview

A person's gait is highly reliant on effective coordination and relative motion of all the bones within the foot. Tri-planar joints are those that allow rotation about all 3 axes. The extent of rotation about each axes may be different. There are two tri-planar joints within the foot (subtalar and talocrural); if one direction of motion is inhibited this causes other rotational movements to be severely limited [26]. The subtalar and talocrural joints are sometimes referred to as the ankle joint complex; provide stability and balance [27].

2.3.1.2 Talocrural Joint

The most proximal joint within the foot, the talocrural joint (also referred to as the tibiotalar) is between distal tibia, fibula and talus, and forms what is commonly called the ankle joint. The main plane of motion is the sagittal plane however due to the joint's tri-planar nature, movement in the frontal and coronal planes are common. During plantarflexion the foot also experiences inversion and internal rotation, and during dorsiflexion eversion and external rotation [26].

2.3.1.3 Subtalar Joint

Distal to the talus is the subtalar joint. The proximal surfaces of the calcaneus articulate with the talus forming this joint, which is predominantly responsible for rotation in the coronal plane, allowing inversion and eversion [24]. Similarly, to the talocrural joint, the subtalar joint's tri-planar nature results in:

- a) dorsiflexion and external rotation of the talus and inversion of the calcaneus when the subtalar joint is inverted
- b) plantarflexion and internal rotation of the talus, and eversion of the calcaneus, when the joint is everted [26].

The extent of the sagittal plane and coronal plane rotation is limited by the talocalcaneal ligament and the contact geometry between the talus and calcaneus. The calcaneus and talus make contact over 3

distinct regions of the talus. The contact surfaces on the talus are both convex and concave, creating a complex joint. The rotations in each plane are dependent on good contact between the 2 bones at each of the contact regions [26].

2.3.1.4 Mid-tarsal Joint

The mid-tarsal joint is formed between the talus and calcaneus, and the navicular and cuboid. It allows movement between the hind and mid-foot [28]. The joints between the tarsals allow, predominantly, for inversion and eversion of the foot about the longitudinal axis [24]. Within the mid-tarsal joint there is also an oblique rotational axis that allows rotation in the sagittal and transverse planes. Unlike a tri-planar joint, a rotation about one of these axes does not necessarily result in a rotation about the other. However, if the whole foot is inverted, the tarsals will invert about the longitudinal axis, and will experience plantarflexion and internal rotation about the oblique axis (and vice-versa if the foot everts) [26].

Several ligaments influence the extent of rotation of the mid-tarsal joint and provide stability. These include the bifurcate ligament, the short and long plantar ligaments and the plantar, calcaneo-navicular ligaments. The kinematics of the mid-tarsal joint are also influenced by the function of the subtalar joint [26].

2.3.1.5 Summary

The three joints described above play an important part in absorbing the force during gait [26]. Due to their interlinked, complex nature, calcaneal pathologies can have serious implications on the patient's quality of life and their ability to perform daily activities and exercise.

2.3.2 Coordinate system of the ankle joint complex

As mentioned in section 2.1, global and local coordinate systems combined are used to describe the motion of the lower limb. Wu et al. have made a recommendation defining the neutral alignment of the ankle joint complex [27]. Anatomical landmarks, shown in Figure 2.3.1, are used to determine the coronal, sagittal and transverse planes of the complex. The coronal plane passes through the inter-malleolar point (IM), the lateral tibial condyle (LC) and the medial tibial condyle (MC). The sagittal plane passes through the inter condylar point (IC) and the inter-malleolar point (IM) and is perpendicular to the coronal plane. The transverse plane is orthogonal to both the coronal and sagittal planes. From these planes the coordinate systems of the tibia-fibula and the calcaneus are defined. This allows the neutral alignment to be specified [27].

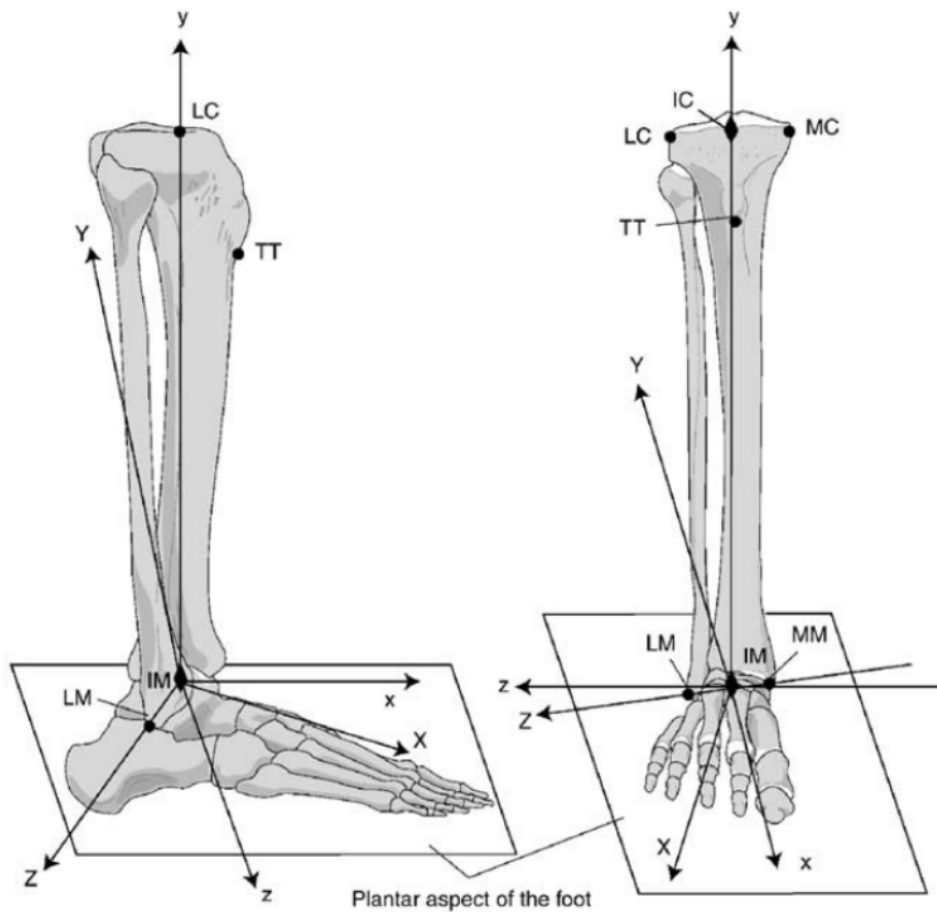


Figure 2.3.1: On the left is the lower limb, viewed from the lateral side, labelled with the anatomical landmarks used to describe the three planes of the ankle joint complex. On the right is the frontal view. The ankle joint complex is in the neutral position. MM – medial malleolus, LM – lateral malleolus, MC – medial point on border of medial tibial condyle, LC lateral point on lateral tibial condyle, TT – tibial tuberosity, IM – inter-malleolar point located at midpoint of MM and LM, IC – inter-condylar point located at midpoint of MC and LC. XYZ shows the tibia coordinate system and the xyz coordinate system shows the calcaneus coordinate system.[27] Image reproduced with permission of the rights holder, Elsevier.

The foot and ankle is a complex anatomical system; the ability of the foot to rotate is highly dependent on all constituents working together. If one is injured and inhibited in some way, particularly the talus or calcaneus, it can result in severe limitations for the patient. The tarsal and calcaneus are typically injured following high energy trauma, resulting in life changing disability with concomitant pathological alteration of gait.

2.4 GAIT

Gait is defined as the manner in which a person locomotes. An individual can have several different gaits (for example walking and running), and between individuals gait can vary, depending on factors

such as sex, age and physical ability [29]. One gait cycle is defined as the period between two heel strikes of the same limb. During normal gait the centre of mass does not vary in height significantly, minimising energy requirements [24].

Within a healthy gait cycle, each limb will undergo two distinct phases: stance phase and swing phase. The stance phase is when that limb is in contact with the ground, whilst the swing phase comprises of that limb being propelled forward. During walking, the stance phase for both limbs overlaps; this is called the double support phase. In running, the double stance phase can be very small, or non-existent depending on the speed [29]. The speed of gait is influenced by the distance between one foot entering the swing phase and the other entering the stance phase, defined as the stride length, and the speed the subject moves their limb is defined as cadence.

British ISO standards have outlined terminology that should be used when describing gait when walking. Within stance phase there are 5 sub-phases and within swing phase there are 3. These sub-phases, and the respective time at which they occur during the gait cycle are shown in Figure 2.4.1 [30]. The gait cycle is described assuming 0% is based upon the left limb striking the ground. For the purpose of this thesis, early stance is considered to be between 0-30% of the gait cycle and late stance is between 30-60% of the gait cycle.

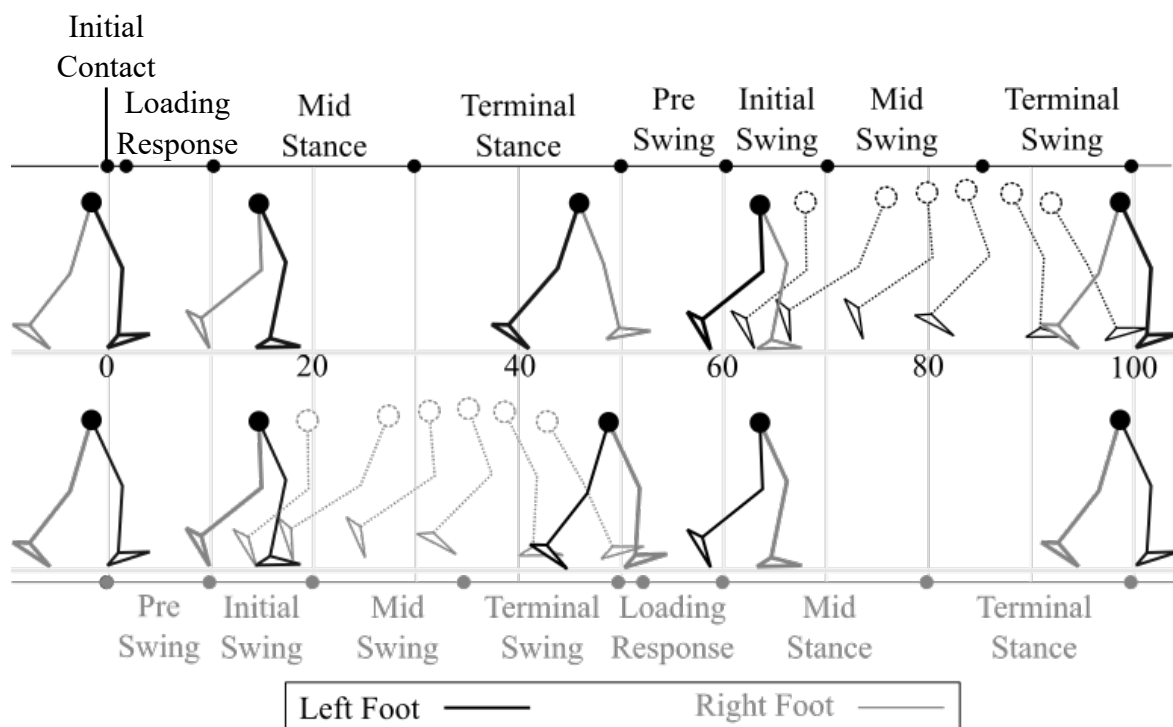


Figure 2.4.1: The sub-phases of the gait cycle for the left foot on the top row and right foot on the bottom row. 0% of the cycle, in this case, is based upon the gait cycle of the left limb. The sub-phases of the stance phase are initial contact (0-2%), loading response (2-10%), midstance (10-30%), terminal stance (30-50%) and pre-swing (50-60%). The sub-phases of swing phase are: initial swing (60-70%), mid-swing (70-85%) and terminal swing (85-100%). [30].

From 0-2% the limb makes **initial contact**. The left talocrural joint is in the neutral position in the sagittal plane as it makes contact and remains in the neutral position. The subtalar joint is slightly inverted on contact, and during the initial contact everts to become neutrally aligned.

From 2-10% the left limb is loaded (the loading response). Throughout the **loading response** the talocrural joint plantarflexes (by up to $\sim 10-15^\circ$) until the foot is flat on the floor. The subtalar joint continues to evert resulting in 5° of eversion. During this time the other limb is still in contact with the floor, in its pre-swing phase. As both limbs are in contact with the floor this is also a period of double support.

Once the foot is flat on the floor, the limb enters the **midstance** phase (between 10-30%). At this point the tibia progresses over the foot (the foot remains flat on the floor) and results in a position of 10° dorsiflexion. The subtalar joint continues to evert beyond 5° . At this point the other limb is progressing from initial swing to mid-swing.

The posterior aspect of the foot begins to rise as it enters the **terminal stance** phase. This results in the talocrural joint moving in a plantarflexed motion until it is in the neutral position. The subtalar joint inverts into a neutral position. The other limb is now in its terminal swing phase and is preparing for contact.

The talocrural joint continues to plantarflex, resulting in a plantarflexion of 20° . This is the **pre-swing** phase. The subtalar joint also continues to invert during this time (it will reach its maximum degree of inversion during this time). The other foot at this point makes initial contact and begins its loading response. This is the second double support period during the cycle.

As the foot leaves the floor, during the **initial swing** phase, the talocrural joint dorsiflexes by 10° so it remains only slightly plantarflexed. The subtalar joint everts, leaving it slightly inverted. As the foot progresses through to mid swing the talocrural joint continues to further dorsiflex, and the subtalar joint - evert, so both joints reach a neutral position. The talocrural joint remains neutral, though the subtalar joint begins to invert again (resulting in slight inversion) during **terminal swing**, as it prepares to come into contact with the ground once more.

Pathological gait is that which is considered to deviate in terms of angular motion, foot contact, or timing from the average gait characteristics of healthy subjects [31]. A pathological gait may be caused by both neurological conditions limiting limb motion control, and musculoskeletal pathology and injury restricting the functionality of musculoskeletal tissues.

2.5 GAIT ANALYSIS

Determining whether a gait is normal can be achieved through gait analysis. Gait can be analysed using a variety of parameters depending on the focus of the assessment. Functional assessments, measuring temporal parameters, such as speed and stride length, are simple but effective ways to measure gait. Other, more advanced techniques include electromyography to analyse the muscle forces used, and metabolic analysis to determine the amount of oxygen used during a set amount of activity. The range of assessment techniques used to describe and analyse gait are described below.

Temporal parameters are the simplest to measure (in terms of equipment required). Examples of such parameters include self-selected velocity and cadence. Breaking this down further, the gait can be analysed in terms of stride length of each limb, and the time spent in stance phase and swing phase of each limb.

Kinematic parameters are commonly reported in the literature. These can be calculated by placing reflective markers on the subject and recording their relative change in movement throughout gait. Gait software is then able to construct a rigid body model of the subject and produce ankle, knee and hip angles, along with their acceleration, power and moments. Clinically, this can be very useful to identify abnormal limb rotations, for example knee hyperextension, or foot drop (a lack of dorsiflexion during swing). Temporal parameters are normally calculated within any kinematic analysis software.

Kinetic measurements are also performed, often, but not always, in combination with kinematic parameters. These are achieved by using force plates embedded in the ground that can analyse the force. This allows both the direction and magnitude of the ground reaction force (GRF) to be recorded. The GRF only gives information on the stance phase (as the foot must be in contact with the floor). It has a very classical double peak shape in healthy gait as seen in Figure 2.5.1. These distinct peaks render it easy to spot deviations from the norm. For the purpose of this thesis the first peak shall be referred to as weight acceptance and the second peak as push off.

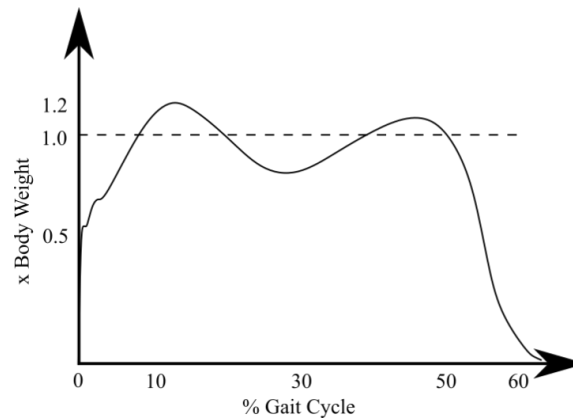


Figure 2.5.1: Standard ground reaction force (GRF) for healthy walking gait during stance phase

Analysing the pressure distribution on the plantar aspect of the foot gives a similar result to that of the GRF, but with a more detailed analysis of which region of the foot is undergoing the loading. It also allows the tracking of the centre of pressure (CoP), indicating whether the subject may walk with an altered strike pattern when compared to normal gait. Similarly to kinematic analysis, it gives no information during swing phase. Most pressure-sensing devices automatically calculate the temporal parameters.

Metabolic analysis involves the recording of amount of oxygen consumed/carbon dioxide exhaled or the heart rate, during gait. This does not give any information on the aspects of gait that may be causing a problem but clinically does allow, for example, the change in energy consumption of a patient following prescription of different types of prostheses to be analysed.

Electromyography analyses the intensity of the muscle activity within the lower limb, and the point at which each muscle activates. Similarly to metabolic analysis, this gives an indication of how much work is required for the subject to walk (higher intensity of muscles forces implies higher metabolic requirement). It also gives information on how the gait differs from the norm, and whether muscles are being used to compensate or stabilise, other weaker muscles, during gait. This muscle analysis can be performed using surface EMG or fine wire EMG. Fine wire EMG is intrusive and therefore subject to further ethical considerations.

2.6 CONCLUSION

This chapter described the complex anatomy of the foot and ankle, demonstrating how injuries to one bone within the foot can result to a serious limitation of joint movement. This limited joint movement can result in pathological gait, which can be diagnosed using gait analysis. To minimise the effect of pathological gait on a subject's day-to-day life, a patient may be prescribed an ankle-foot-orthosis (AFO). The next chapter will describe what an AFO is and how they can improve a patient's ability to walk. In particular it will focus on a specific PD-AFO that is the subject of this thesis.

3 PD-AFO LITERATURE

3.1 INTRODUCTION

Orthoses are assistive devices prescribed to patients to improve stability, aid movement, and reduce pain of the body part. For lower limbs, a variety of orthoses may be prescribed, from a simple foot insole orthotic, to a rehabilitative hip-knee-ankle-foot-orthosis that extends from waist to foot [32]. AFOs, specifically, extend from the plantar aspect of the foot up to, and around, the ankle joint, ending distally of the knee, and can be inserted into footwear.

When describing AFO use, the gait cycle, as described in Chapter 2, is sometimes described in terms of 3 ‘rocker’ stages [26]. The first rocker coincides with loading response and midstance and describes the motion of the foot as it makes contact with the ground and progresses to the end of the midstance phase, where the tibia is normal to the ground. The second rocker coincides with the start of the terminal stance phase, where the plantar aspect of the foot remains horizontal to the ground, and the tibia progresses forward, creating a dorsiflexed ankle. Finally, the third ‘rocker’ occurs during latter terminal stance phase and pre-swing phase, where the heel lifts from the ground and propulsive forces are applied.

Depending on the underlying pathology, different types of AFO are prescribed with different levels of control and assistance. An AFO may be prescribed for long term use, or as a rehabilitative aid. Most AFOs are designed to provide adequate stiffness to prevent unwanted plantarflexion during the swing phase of gait. AFOs that are more rigid, may also be designed to prevent motion in other planes.

During the stance phase AFOs may also help with stability and improve limb posture. Designs may aim to lower muscle activity or alter loading through different regions of the foot. The choice of AFO design, and its compromises, must be carefully considered for each patient; for example, solid AFOs

can decrease the soleus and gastrocnemius muscle activity but may increase the Achilles tendon force [32]. An example of some common types of AFO and their primary aims are shown in Table 3.1.1.

Table 3.1.1: Common types of AFO and their influence on lower limb movement and loads [26, 32]

Name	Primary Aim
Solid AFO	Prevent movement in all planes
Posterior Leaf Spring	Limit movement in sagittal plane and control the loading of the limb during loading response
Articulated AFO	Limit movement in coronal plane (sagittal plane if desired)
Weight-Relieving/ Patellar-Tendon Bearing AFO	Reduce axial load through the ankle and apply it to the anterior tibial surface
Supramalleolar orthosis	Limit movement of midfoot and forefoot
Carbon Fibre Spring Orthosis	Increase the power during pre-swing, the energy storage and release of spring
Ground Reaction AFO	Prevent excessive dorsiflexion (prevents buckling of the knee)

AFOs can be made from a variety of materials, most commonly polypropylene, polyethylene, and carbon fibre. The choice of material may be influenced by cost, the ease of moulding and reshaping, fatigue resistance, and stiffness. The stiffness of the AFO influences how the orthosis interacts with the lower limb. Very stiff AFOs, that aim to prevent motion in all planes, are named static AFOs. An example of such is the solid AFO. These AFOs prevent dorsiflexion (and plantar flexion), inhibiting the second rocker. This results in a staccato, shortened stance phase [26]. AFOs that allow for some in-plane motion, by reducing stiffness, are named dynamic AFOs. These include AFOs such as the posterior leaf spring and articulated AFO. These allow smooth transitions between the rocker stages. PD-AFOs are a subset of dynamic AFOs, that use passive design properties such as the material type, shape of the orthotic and subsequent stiffness to achieve a range of desired effects throughout the gait cycle. PD-AFOs not only limit the ROM, as seen in other AFOs, but also aid the gait of the patient, for example by providing energy storage and return to aid power generation [33, 34]. Within Table 3.1.1, the posterior leaf spring AFO and carbon fibre spring AFO could both be considered PD-AFOs.

3.2 PD-AFO DEVELOPMENT

This thesis focuses on a specific design PD-AFO (Figure 3.2.1) prescribed to US and UK military personnel who sustained traumatic foot and ankle injuries during the conflicts in Iraq and Afghanistan and subsequently required a limb-salvage procedure. The Military Extremity Trauma

Amputation/Limb Salvage (METALS) study found that patient reported outcome scores for those with limb salvage, were worse compared to those with an amputation [7].

Military limb-salvage patients also observed that amputees were achieving higher levels of functional outcome than themselves, thought to be due to advances in prosthetic design and structured rehabilitation [35]. The young, active, military limb-salvage patients, therefore, demanded a higher level of functional activity than had been previously attainable [35]. As a consequence, the PD-AFO, that is the subject of this thesis, was developed with the aim of permitting higher levels of functional activity and improving outcome for limb salvage patients (see Figure 3.2.1).

3.2.1 PD-AFO Design

The PD-AFO design was first prescribed in the US in December 2008, and named the Intrepid Dynamic Exoskeletal Orthosis (IDEO™) or the Exosym™ in US civilian industry [20]. The UK military followed by prescribing a nearly identical design of PD-AFO named the British Offloading Brace (B.O.B) in the UK military and the Momentum® in UK civilian industry.

It is widely accepted amongst professionals in the field, that the UK and US version achieve the same results for patients. There are, however, slight differences in the manufacturing method, as described by Bennett [36]. The US version uses wet lamination (thought to be heavier but cheaper) and the UK version manufactures with pre-impregnated resin carbon fibre (thought to lighter and slimmer, but more expensive and more difficult to alter) [36].

Figure 3.2.1 shows the PD-AFO, specifically the UK Momentum (Blatchford, UK). Briefly, the device consists of a carbon-fibre base, fitted with a sole pad, lateral ankle pad and medial ankle pad. Two posterior struts connect the base to the cuff region. The cuff is in two parts (anterior and posterior aspect) connected by a rivet and a strap. A shin pad is located on the interior side of the anterior cuff. A prescribed heel wedge is placed between the PD-AFO and the patient's shoe. Additionally an Aramid reinforcement was added to the base of the UK versions.

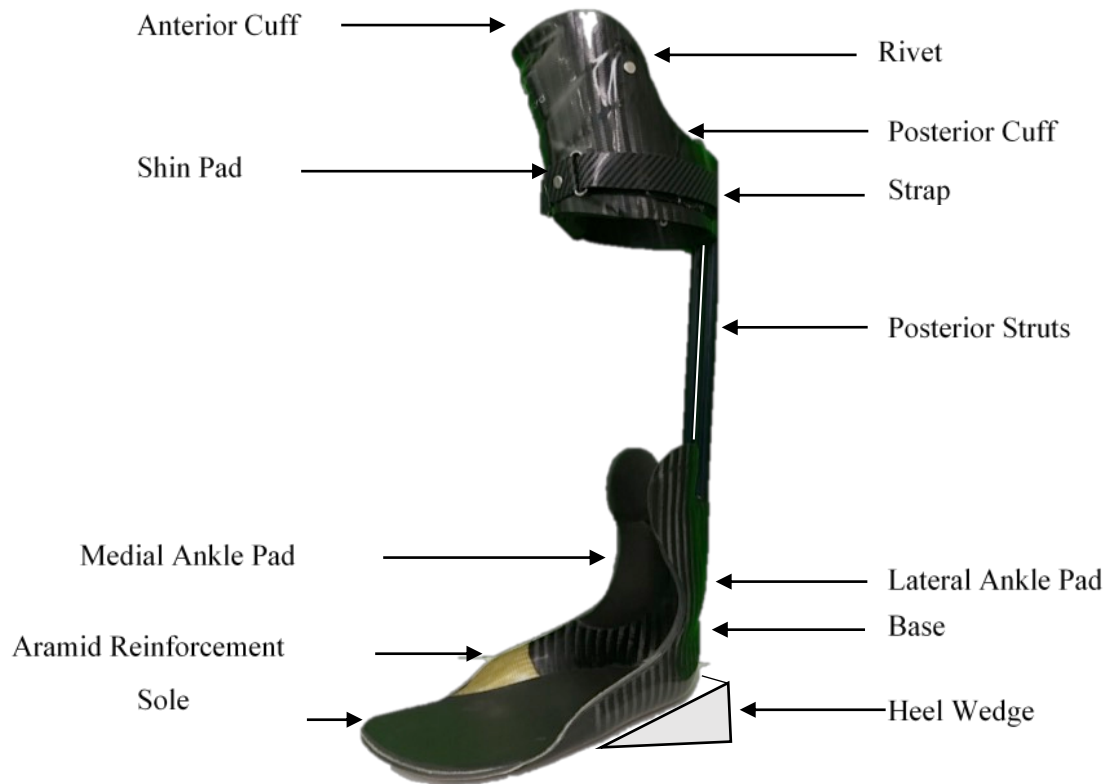


Figure 3.2.1: The PD-AFO and its components (Momentum[®] provided and manufactured by Blatchford).

The PD-AFO is custom made for each patient. The choice of carbon fibre ensures that it is stiff and strong. From personal communication, this author understands that the addition of Aramid (not seen in the US version) aims to increase the impact resistance but not alter the mechanical response during gait [36]. The base is stiff, to prevent foot drop (a plantarflexed ankle angle) during the swing phase [36].

Two, thin foam, ankle pads (lateral and medial) are glued to the base, providing padding for the patient's malleoli. The ankle region of the base is thought to help to minimise movement in the transverse and coronal planes. A foam sole sits between the base and the plantar aspect of the patient's foot to provide comfort. It also provides a higher coefficient of friction than a bare carbon fibre base, minimising slipping between the foot and PD-AFO.

The base is connected to the posterior aspect of the cuff via 2 posterior struts. The stiffness of each strut can be modified, depending on patient requirements. These struts are thought to deflect during the stance phase of the injured limb. This deflection has been hypothesised to alter the forces during loading response and provide energy storage and return [36, 37]. In the Momentum[®] these struts are cylindrical and built-in to the posterior cuff and base by bonding directly into the lay-up. Studies with the IDEO have used a modular strut system, attaching cuboidal struts to the posterior aspect of the base and cuff using bolts. However it is understood that in the US the struts are also built-in following the final prescription [38, 39].

The anterior aspect of the cuff is fixed to the posterior via 2 rivets, allowing the anterior cuff to pivot up and down to allow the patient's limb to slide in and out (seen in Figure 3.2.2 in the open position). These rivets may be removed if the patient's injury requires more flexibility when putting the PD-AFO on. Once the patient has the PD-AFO on, the anterior aspect is fixed in place to the posterior cuff using 2 Velcro straps. The posterior cuff is designed so that the proximal aspect does not contact the posterior aspect of the patient's knee joint during flexion [36]. On the interior surface of the anterior cuff there is a thick foam shin pad to distribute the contact pressure and provide comfort to the patient, where the anterior tibial surface touches the PD-AFO during gait. The anterior cuff is moulded around the patella tendon and tibial condyles,; an area that is able to take higher loads [36]. This anterior cuff is through to provide weight-bearing capabilities, reducing axial loading through the ankle joint [36, 40].



Figure 3.2.2: Cuff region of the PD-AFO (the Momentum[®] provided by Blatchford, UK)

Other designs of PD-AFO exist, however for the remainder of this thesis the term 'PD-AFO' will refer to the collective group of orthotics made by this design, namely the IDEO[™], Exosym[™], B.O.B, and Momentum[®]. Most studies investigate the US manufactured IDEO. All literature referenced has evaluated the IDEO, unless explicitly stated otherwise.

3.3 PERFORMANCE

It is common for studies to analyse the PD-AFO's efficacy in terms of functional outcome. Commonly used functional outcome measures include the return to duty rate (RTD), the number of late amputations, mental health scores (VR-12), walking and running speed, and agility tests. Gait characteristics have also been evaluated, including joint kinematics, joint kinetics and plantar pressure, to quantify the influence of the PD-AFO on the lower limb. This author could find only one

study analysing the mechanical response of the PD-AFO. Although, there is an increasing number of studies analysing the effect of the PD-AFO, many limitations are present; namely control size, heterogeneity of the cohorts and the influence of factors such as rehabilitation and injury type. Functional outcome are used to assess whether a treatment is beneficial to the patient. These outcome reflect a patient's need for further treatment, their ability to perform specified tasks, including measures such as walking a set distance, or their ability to return to work.

Bedigrew et al. found that for an initial 50 patients considering a late amputation (>90 days after injury), once prescribed the PD-AFO, 82% chose to remain with the orthotic [21]. Ladlow et al. demonstrated a lower rate of requests for a late amputation following prescription of the B.O.B, at only 9% [41]. This particular outcome is important as there are probable negative effects of late amputation compared to an immediate amputation (primary amputees) [42-46]; Melcer et al. presented evidence suggesting that late amputees suffer worse mental health scores than primary amputees or successful limb-salvage patients [42].

Late amputations are not the only functional outcome recorded; Owens et al. reported that 8/10 patients with the PD-AFO were able to run 2 miles without stopping, a metric deemed by the study to demonstrate improved functional outcome [35]. Ladlow et al. reported similar findings with the B.O.B, with 1/23 patients able to run prior to prescription of the B.O.B, and 13/23 able to run post-prescription [41]. As acknowledged by Bedigrew et al., these studies often have a small number of patients with heterogenous injuries [21]. Despite this, a review by Highsmith et al. in 2016 concluded an increased return-to-duty rate, improved agility, and decreased pain were associated with the prescription of the PD-AFO [46]. It should be noted, however, that all studies are relatively short term and, as yet, a long-term study has not been published.

In addition to demonstrating its positive effect on the functional outcome of limb-salvage patients, several studies described below have examined factors that may influence the extent of these outcomes, including the role of rehabilitation and injury type.

3.3.1 Influencing Factors

The success of the PD-AFO, in a military context, is suggested to be improved when combined with a specific rehabilitation programme launched by the US in 2009 [13, 20, 47]. It was designed specifically for limb-salvage patients prescribed the PD-AFO and named the Return to Run (RTR) programme. It mimics aspects of the successful rehabilitation regime established for amputees within the military [7]. Figure 3.3.1 shows the improvement in agility and speed tests over the 8 week programme [21].

Sheean et al. assessed patients with different injury types against validated physical performance measures to observe that all of them performed better, regardless of injury, during the RTR programme [22]. Similarly Blair et al. found an increased in RTD and a decrease in late amputations

with the RTR programme; of the 146 patients in this study, 31 chose not to complete the RTR; these patients performed poorly in comparison to those patients who underwent the rehabilitation programme, when considering outcome such as RTD [20]. The study does indicate that provision of the PD-AFO alone, with no RTR programme, results in similar rates of RTD as those seen in amputees [20]. However, it should be noted that this study also concluded that an explosive injury mechanism resulted in a lower RTD, and 30/31 patients had such an injury mechanism in the group with no rehabilitation, compared to 85/115 for the rehabilitative group [20].

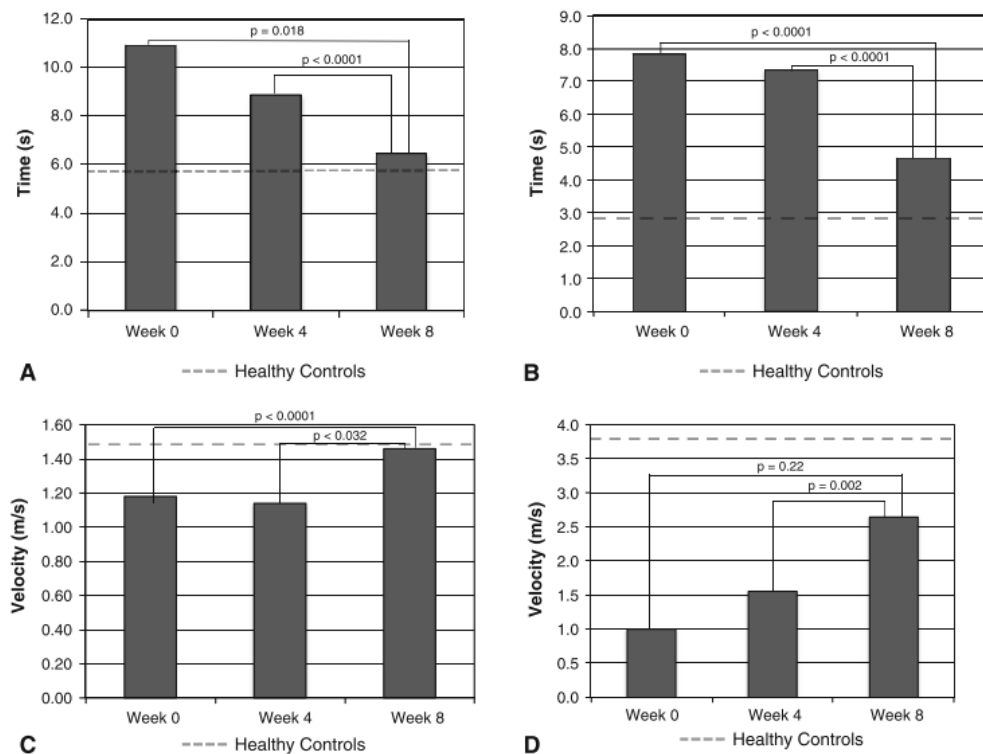


Figure 3.3.1: Data from Bedigrew et al. demonstrating improvements seen in functional outcome measures, including A) four square step test B) timed stair ascent C) self-selected walking velocity (SSV) and D) 20m shuttle run, at the start (week 0), middle (week 4) and end (week 8) of the RTR run programme [21]. Image reproduced with permission from the rightsholder Wolters Kluwer Health, Inc

Ladlow et al. demonstrated that patients prescribed with the B.O.B who undergo some rehabilitation (10/14), based on the RTR, are more likely to run independently than those who do not (3/9) [41]. However, the study also shows that all patients, regardless of rehabilitation, can walk following the prescription of the B.O.B [41]. The cohort within this study was small ($n=23$) however it indicates that, despite the necessity of a structured rehabilitation regime, outcome provision of the PD-AFO alone could provide some improvement in a patient's ability to walk.

Overall, literature is conclusive in demonstrating that the RTR programme contributes to the improved functional outcome of those patients who complete it. However, the control cohort within these studies (those who do not complete the RTR) is not randomised. The control group consists of

patients who have chosen not to complete the programme, and therefore inherent selection bias might be present [20].

Several aspects of the RTR may be responsible for the improvements in patient outcomes. Firstly, the rehabilitation programme provides patients with the opportunity to become accustomed to their device. Secondly, it can provide strength-building exercises for patients, many of whom will have undergone several operations and therefore have muscle weakness. Finally, as discussed by Potter et al. mental health is an important factor in successful outcome [37]. The group therapy and intensive programmes may provide an increase in self-efficacy amongst the patients [20]. Bedigrew et al. noted a significant improvement in the Veterans Rand 12 item health survey (VR-12), analysing mental health, at 0 and 8 weeks of the RTR programme [21]. Overall, it is predicted that the success of the RTR is due to a combination of all the above factors. It is difficult to determine which aspect may be the most significant. Further granular analysis may prove valuable, particularly when considering the more cost-sensitive civilian sector in the UK.

As mentioned above, Blair et al. found that patients with an explosive mechanism of injury had a lower RTD rate, than patients with blunt trauma [21]. This is likely due to the fact that blast-injured patients often suffer from multiple injuries, and the accumulation of these injuries may prevent RTD. Several attempts have been made to determine which injuries and injury mechanisms perform well with the PD-AFO.

Prior to development of the PD-AFO, it had been demonstrated that some injury types reported poor functional outcomes with limb salvage. For example, when comparing the sickness impact profile (SIP), a measure of degree of disability, patients with ankle fusions and free flaps performed worse than those with below-knee amputations (BKA), though it should be noted BKA amputees with skin grafts were excluded [48]. Similarly, Shawen et al. found those with free flaps may be better suited to an amputation than limb salvage [8].

The PD-AFO is recorded to have been prescribed for a range of pathologies including fracture, fusion, nerve injury, post-traumatic osteoarthritis (PTOA), foot pain, partial amputation and osteomyelitis [49]. Several studies have attempted to group patients into subgroups depending on injury type or mechanism; a summation of the groups is shown in Table 3.3.1 [20, 22, 37, 49-51].

Table 3.3.1: Categorisation of injury within the literature by type, region, and mechanism. RTD – return to Duty, LEFS – Lower Extremity Functional Scale, PPM – Physical Performance Measures, SMFA – Short Musculoskeletal Function Assessment

Author	Categorisation Type	No.	Categories	No. of Patients	Outcome Measure	Ref.
Blair et al.	Injury Mechanism	6	a) Explosion b) gunshot wound c) motor vehicle collision d) fall e) unknown f) Miscellaneous	145	RTD	[20]
Ikeda et al. 2019	Injury type	3	a) Arthritis b) nerve c) fracture	90	LEFS	[50]
Sheean et al. 2016	Treatment type	2	a) Talocrural joint is in the final fusion type ('isolated ankle fusion or ankle fusion combined with ipsilateral subtalar fusion b) subtalar fusion only	23	PPM	[22].
Patzkows ki et al. 2012	Symptom	1	a) PTOA in the talocrural or subtalar joint	16	Recreation Capability RTD, PPM	[51].
Hill et al. 2016	Region	7	a) Ankle b) tibia c) nerve injury (below knee) d) hindfoot e) soft tissue, f) midfoot/forefoot g) other (osteomyelitis, late effects of fracture, nerve injury above knee)	624	Late amputation	[49]
Potter et al.	Functional deficit	5	a) Weakness of ankle dorsi/plantar flexors, b) limited ankle dorsi/plantar flexion, c) mechanical pain with loading to hindfoot/midfoot, d) ankle or hindfoot fusion (or a candidate for), e) candidate for amputation secondary to ankle/foot impairment	81	PPM, SMFA	[37]

Following the prescription of the PD-AFO, Hill et al. analysed how the region of injury influenced the likelihood of a late amputation (Figure 3.3.2) [49]. The study found that those patients with midfoot/forefoot injuries had the highest number of requests for late amputations [49]. Conversely, ankle injuries and nerve injuries were found to have the lowest number of requests [49]. Hill et al. discuss that the small numbers within certain sub-groups (the smallest being ‘midfoot/forefoot’: n=21) limit the significance of the result. The heterogenous nature of the pathologies seen in each category (for example, the ‘ankle’ sub-group includes pilon fractures, PTOA and fusions, and the ‘midfoot/forefoot’ subgroup includes foot pain, forefoot/midfoot PTOA and toe amputation) is perhaps more of a limiting factor when considering the significance of the results; one of these injury types may result in the apparent success (or lack of) with the PD-AFO.

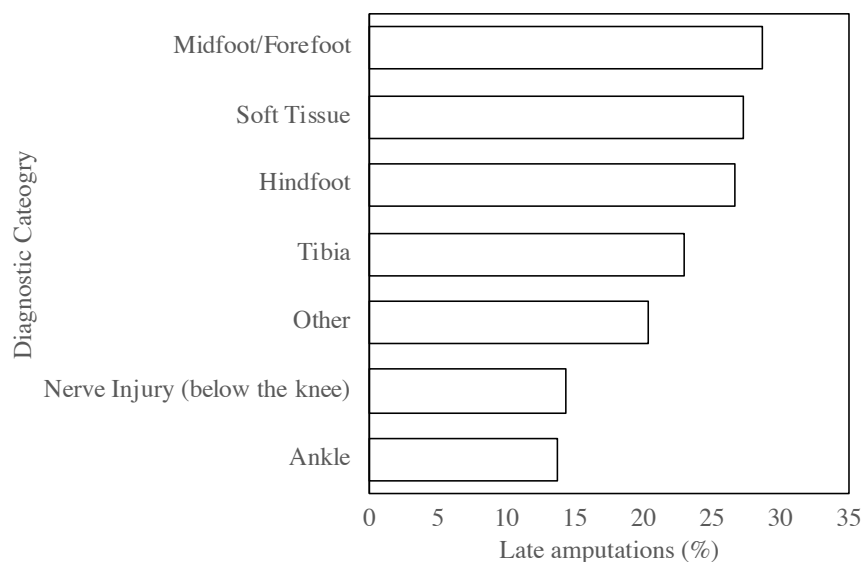


Figure 3.3.2: Adapted from Hill et al. showing the percentage of late amputations in each diagnostic category [49]

Patzkowski et al. focussed solely on the success of the PD-AFO in patients with PTOA; this is a common disease in veterans, reporting that 18% of all patients on the RTR programme had such a diagnosis [51]. The IDEO was found to ease pain in patients with PTOA; the rates of potential late amputations were reduced from 6/16 to 1/16 [51]. In the study by Hill et al. the ankle, hindfoot and midfoot/forefoot categories all encompass PTOA, with the former performing the best and the latter performing the worst [49]. Further analysis is required to understand whether PTOA is improved by the PD-AFO in all regions of the foot or just specific regions.

Ikeda et al. examined injury type, including arthritis (not specifically stated as PTOA), fracture, and nerve injury [50]. Although the study found improvements in outcomes, according to the lower

extremity functional scale (LEFS); they were unable to draw any conclusions as to the influence of injury type due to the large variety of pathologies seen [50].

Sheen et al. focussed on fusions specifically [22]. The study found that those with subtalar fusions only (compared to ankle fusions in combination with a subtalar fusion) performed better in validated physical and mental health assessments across the 8-week RTR however it should be noted that both patient cohorts improved in the physical performance scores [22].

Blair et al. analysed the mechanism of injury, rather than the injury itself; many patients who experienced an injury as a result of an explosion did not RTD [20]. The study concluded that explosive mechanisms result in a lower RTD rate than those injuries caused by blunt traumas. As discussed, this is potentially due to the comorbidities associated with high energy trauma [20]. The PD-AFO, however, still improves the functional outcome of some patients with high energy trauma. Potter et al. approached this from a different angle and grouped patients by the functional deficit resulting from their injury, rather than the injury or region of injury itself [37]. This is a more clinically minded approach; orthotics are designed and manufactured to compensate or overcome specific functional deficits rather than a specific injury type. However, the study did not compare results between the groups, and does not allow any further conclusions on the association between the success of the IDEO and the type of injury. Understanding how the PD-AFO alters the gait pattern of the injured limb, could provide insight into how it is able to compensate and overcome functional deficits discussed here.

The studies described above attempt to granulise the patient cohort to determine for whom the PD-AFO is a successful treatment. Due to the relatively recent introduction of the PD-AFO, the cohort to whom it has been prescribed is still small, with many studies being performed retrospectively with incomplete data. Therefore, it has been difficult to create subgroups from this cohort that are both homogenous in nature and with an adequate effect size.

3.3.2 Gait Analysis

Several studies have examined the impact of the PD-AFO on gait evaluating both kinematic and kinetic factors such as joint angles, moments, power, plantar pressure, and reaction forces with the aim of understanding how the PD-AFO alters gait. This section details previous studies analysing the gait of patients when wearing the PD-AFO.

3.3.3 Joint Kinetics and Kinematics

All gait analyses described have evaluated the performance of the US-built PD-AFO, the IDEO. The injured limb, when described below, is the limb that wears the PD-AFO, and the uninjured limb is the shod limb (does not wear the PD-AFO).

Several studies have demonstrated that the PD-AFO prevents plantarflexion of the foot throughout the gait cycle and limits the ankle ROM during a variety of gait patterns including, walking, running and uphill walking [52-57]. The peak dorsiflexion and plantarflexion angle, plus the ROM are significantly lower in patients walking with the PD-AFO when compared to healthy controls [56]. During up-hill walking a significant reduction in peak plantarflexion, peak dorsiflexion and ankle ROM compared to the healthy control population and the shod limb was seen [55].

Limiting ankle ROM is an important design feature of many AFOs. The PD-AFO, that is the focus of this thesis, allows patients to run, as well as walk, something not all AFOs enable. Therefore, although a significant design feature, it does not explain why the PD-AFO works for high level activity; if limiting ankle ROM was all that was required, other AFOs would be adequate. For example, the Blue Rocker also limits ankle angle [52] but resulted in worse functional outcome than the PD-AFO [18]. Studies that examined joint angles also evaluated joint moments and power; abnormal moments and power can suggest compensatory gait patterns that can lead to long term musculoskeletal problems. A greater absolute, peak dorsiflexion moment has been reported during walking in the injured limb with the PD-AFO [56, 57], along with a lower absolute peak ankle power absorption in the injured limb compared to healthy controls [56]. Lower ankle power generation has also been recorded when compared to healthy control subjects [56, 57].

Instead of comparing to healthy controls, Esposito et al. compared the injured limb of the patient to their uninjured limb when wearing the PD-AFO whilst running [54]. They found similar results to those of walking, showing a lower ankle power generation in the injured limb of patients wearing the PD-AFO compared to their uninjured limb [54]. Schmidtbauer et al. also compared the injured limb kinetics in 12 patients wearing the PD-AFO to those of their uninjured limb whilst running [53]. A higher plantarflexor moment in the ankle during toe-off and a total lower ankle power generation of their injured limb in comparison to the uninjured one was reported [53]. Haight et al. examined kinetic changes during up-hill walking, comparing the injured limb wearing a PD-AFO to healthy control joint kinetics. The study found a higher magnitude of ankle power absorption and lower peak angle power generation in the injured limb when compared to the controls [55].

To achieve lower power generation or absorption whilst undergoing higher joint moments, the angular speed of the rotation must be decreased; equation (3.3.1) shows the relationship between power and moments, where P is the power, M is the internal joint moment/torque and ω is angular velocity.

Therefore, the studies demonstrate that the ankle joint of the injured limb wearing the PD-AFO is moving at a much slower angular velocity when compared to their choice of control (healthy or uninjured limb). This is to be expected, as the PD-AFO will result in a stiffer, overall ankle joint. This is eluded to in a study by Esposito et al. examining changes in running gait, following an alteration of strut stiffness [58].

$$P_{joint} = M_{internal\ joint} \cdot \omega \quad (3.3.1)$$

To calculate the internal joint moment (the moment generated by internal structures such as muscles and ligaments) in a limb not wearing an orthotic, equation (3.3.2) is used, where M_{total} is calculated from the derivative of the joint angles, $M_{external}$ is the moment calculated by the GRF acting on the limb, and $M_{joint\ reaction}$ is calculated from segmental velocities. When wearing an orthotic the GRF is acting on both the limb and the AFO. Therefore, the internal joint moment calculated is the sum of the internal joint moment and the moment produced by an AFO. This is because it cannot be discerned which proportion of the GRF is loading the ankle joint.

$$M_{internal\ joint} = M_{total} - M_{external} - M_{joint\ reaction} \quad (3.3.2)$$

Joint Power is a function of the internal joint moment and therefore using equation (3.3.1) when wearing an AFO gives the sum of power generated/absorbed by both the ankle joint and the AFO. It is not clear whether the studies mentioned above considered this. It should be noted that the PD-AFO is a passive device and therefore power generated by the PD-AFO alone, during the late stance phase of gait, is as a result of the return of a fraction of the energy stored in the PD-AFO during early stance, when power is dissipated (i.e. no net power is generated by the PD-AFO).

Knee and hip, moments and power can be calculated correctly using equation (3.3.1) and (3.3.2) when wearing the PD-AFO as it ends distally of the knee joint and therefore all GRF is loading the joint. During walking it has been reported that peak knee power generation during early stance was lower when compared to healthy controls [57]. Contrastingly, peak hip power generation during early stance is larger than that seen in healthy controls [57].

Schmidtbauer et al. when comparing the injured limb wearing the PD-AFO to the uninjured limb during running also found lower, absolute, knee power generation along with lower peak knee extensor moment [53]. Lower absolute knee power absorption was also seen in the injured limb when compared to the uninjured limb [53]. Esposito et al. found the absolute, knee flexor moment and the absolute, hip flexor moment, to be smaller in the injured limb than the uninjured limb during running [54]. During up-hill walking the peak knee extensor moment and peak knee power generation were also reported as lower in the injured limb compared to healthy control [55]. As seen during walking, the peak hip power generation was higher in the injured limb than in the healthy controls [55].

Most studies conclude that use of the PD-AFO results in lower knee power generation in the injured limb but greater hip power generation when compared to controls including both healthy subjects or measurements from the sound limb of patients [53, 55, 57]. This suggests the hip may be

compensating for the lack of power generated in the ankle and knee. Similar patterns are seen in patients with BKAs and may be relevant when considering long-term effects of the PD-AFO [57]. The changes seen in the knee and hip joint kinetics in the injured limb wearing the PD-AFO, when compared to the uninjured limb and healthy controls, demonstrates that wearing the PD-AFO alters the gait pattern of the patient. This in turn implies that the loading of the limb would be altered too. Changes in ankle power generation/absorption in the injured limb were demonstrated. It is not known to what extent the PD-AFO contributes to the power generated and absorbed. To establish this, loading through the ankle joint alone (not the combined load through the PD-AFO and lower limb as has been done) must be established. It is important to determine whether the moments and power experienced by the ankle are altered due to the PD-AFO, or whether the changes seen are due to the injury alone. This will also allow calculation of the moment generated by the PD-AFO; understanding this could give greater ability to alter the design to make it suitable for each patient.

3.3.4 GRF and Plantar Pressure

Kinetics such as the GRF in each direction are also discussed in previous studies although not to such an extent as joint kinetics and kinematics. Esposito et al. found no significant differences in the vertical and medial/lateral GRF between patients wearing the PD-AFO and healthy controls [56]. The peak propulsive force was, however, significantly lower for the PD-AFO users, as shown in Figure 3.3.3 [56]. Haight et al. also reported significantly lower propulsive forces during uphill walking, and lower vertical GRF in the injured limb compared to the uninjured limb [55]. Bennet, however, found increased propulsive forces in the injured limb when wearing the PD-AFO, compared to walking without ($p=0.02$) in 12 patients [36]. This suggests that whilst the propulsive forces do not match that of healthy controls, the PD-AFO does increase them within the injured limb. The mediolateral GRF in the injured limb, whilst not significantly different from the uninjured limb, was significantly higher than healthy controls [55]. This can be seen in Figure 3.3.3.

The decrease in propulsive force discussed above aligns with the joint kinetic and kinematic data demonstrating lower total, ankle power generation from the combined ankle joint and PD-AFO compared to healthy controls. A mediolateral change may indicate less stability in the injured limb. The GRFs recorded are the combined load that is experienced by the lower limb and PD-AFO. Understanding how this load is split between the lower limb and the PD-AFO is vital in understanding how the PD-AFO changes the loading patterns, and ultimately functions efficiently.

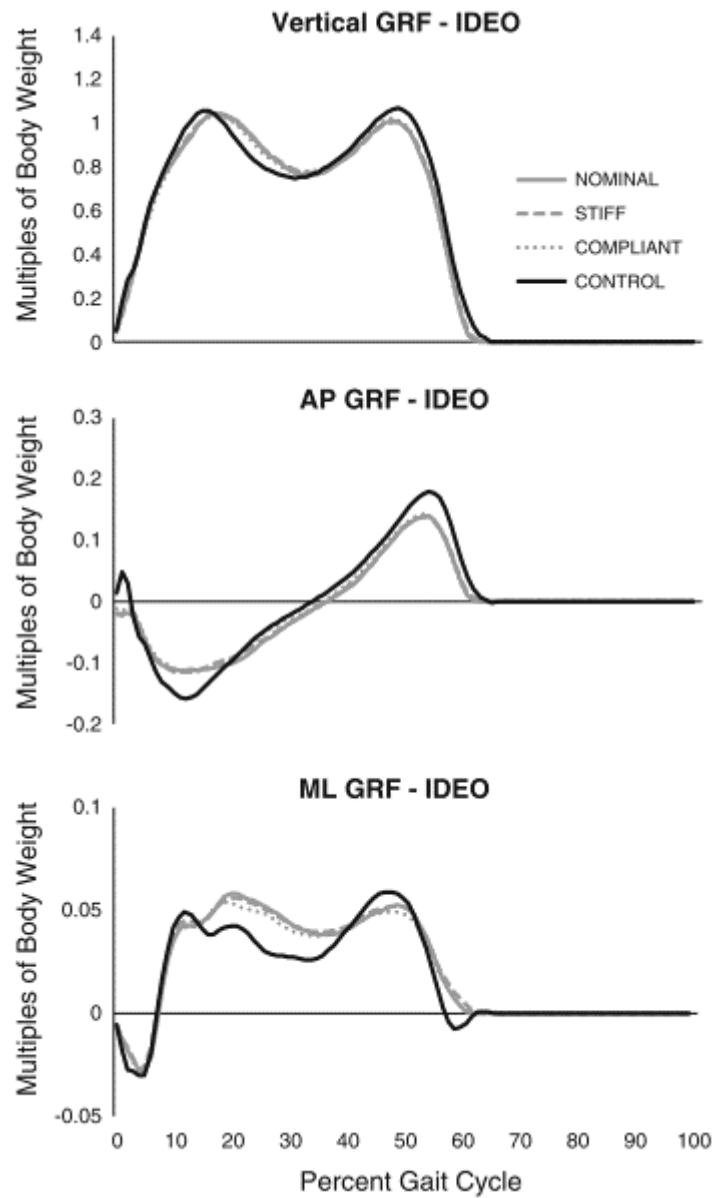


Figure 3.3.3: Data acquired by Esposito et al. demonstrating the ground reaction forces in the vertical direction, the anteroposterior (AP) direction and the mediolateral (ML) direction, (in PD-AFOs of 3 different strut stiffnesses) compared to healthy controls [56]. Image reproduced with permission from the rights holder Wolters Kluwer Health, Inc

Stewart et al. recorded the plantar pressure changes in 12 patients with varying injuries both with and without the PD-AFO, finding a significant reduction in plantar pressure in the injured limb in all regions of the foot except the medial midfoot whilst wearing the PD-AFO [59]. A reduction in pressure implies that load is being diverted through the PD-AFO instead of loading the injured limb. Stewart et al. describes this ‘offloading’ of the pressures as greatest during midstance and terminal stance. The study also observed that the CoP did not progress as anteriorly in the injured limb wearing

the PD-AFO when compared to both the uninjured limb and the injured limb when not wearing the PD-AFO.

The plantar pressure is significant in understanding how the PD-AFO may be changing the loading of the injured limb. Injuries amongst the cohort varied, though the patients selected were able to walk without the PD-AFO and therefore act as their own control. Although this gives a direct comparison of the changes that the PD-AFO caused to the injured limb loading, it introduced bias into the selection as any patients who could not walk without the PD-AFO were excluded [59].

Stewart et al. eluded to ‘offloading’ of the lower limb as a result of the PD-AFO [59]. The plantar pressure could be used to calculate the load through the plantar aspect of the foot, $F_{PLANTAR}$, allowing the loading of the lower limb to be calculated. This in turn, in combination with the GRF, would allow the loading of the PD-AFO, F_{PD-AFO} , to be calculated using equation (3.3.3).

$$F_{PD-AFO} + F_{PLANTAR} = GRF \quad (3.3.3)$$

The study above did not analyse GRF and therefore it is not possible to establish how the load is split between the PD-AFO and foot. This study has only examined walking; examining plantar pressure changes during higher impact activities such as running would be valuable, as enabling high-level activity is one of the PD-AFO’s key features compared to other AFOs [52]

3.3.5 Limitations

The literature evaluating the PD-AFO is growing, however limitations remain in the studies presented. The small cohort sizes with heterogenous injuries makes it difficult to draw significant conclusions. The retrospective studies are unable to shed light for whom the PD-AFO will be most effective, and the influence injury type may have on the success of the PD-AFO. Understanding how the PD-AFO functions will be essential in identifying potentially suitable patients and help predict the effects of long-term use [36]. The interaction between the PD-AFO and lower limb, in particular identifying the loading pathway through the foot when wearing the PD-AFO, may provide further insight into why certain regional pathologies may have better functional outcome. It will also help guide further patient studies on how to divide the cohort into sub-groups. Mechanical analyses of the PD-AFO will provide insight into how it compensates for, and overcomes, different functional deficits.

The gait analyses conducted to date demonstrate how the PD-AFO may be altering patient gait. However, the ability to provide a control variable is difficult. The ideal control would be for patients to be their own control, comparing gait before and after injury; this is clearly not possible to plan. Second preference would be to directly compare a patient’s gait with the PD-AFO and without, allowing direct understanding of how the patient’s gait is altered. Only two studies found following

this approach, due to the inherent presence of an injury, meaning patients may not be able to walk unaided [36, 40]. Several studies compared their results to healthy controls. This methodology allows understanding of how the gait with the PD-AFO is different to healthy gait, however, it does not give a direct comparison of how the PD-AFO alters the response of the patient's limbs [55-57, 60, 61]. Finally, several studies compared the injured limb wearing the PD-AFO to the uninjured limb, during the same gait trial [53-55, 58, 59, 61]. One study compared the gait kinematics of patients with a PD-AFO to those with a BKA; this is significant when discussing the treatment options, and may give indications of long-term issues (as more is understood about BKA long-term consequences) but does not give further insight into the changes in gait caused by wearing the PD-AFO [62]. Differences have been also seen in the joint kinematics and kinetics of the uninjured limb compared to healthy controls when wearing the PD-AFO [55, 57, 61].

For patient gait analyses, using the uninjured limb as a control is the most practical method, without requesting the patient walk without the PD-AFO. To do this, it is important to understand to what extent the gait of the uninjured limb is altered when wearing the PD-AFO on the injured limb. This ensures patient gait trials account for the differences in gait seen in the uninjured limb, if making comparisons between the two limbs. Previous studies only found a small number of differences between the gait pattern of the shod limb and healthy controls. One of the differences reported was that the vertical and mediolateral GRF in the shod limb was higher than controls [57].

The patient cohorts are also heterogeneous. As described in the retrospective studies, the PD-AFO was prescribed to patients with many different injury types. As such, during gait studies the patients have a variety of pathologies and injury mechanisms, though some studies did discuss that all patients had functional deficits such as plantarflexion weakness [57]. To understand how the PD-AFO alters gait, removing the heterogeneous nature of the patients would be beneficial. This could be achieved by mechanically testing the PD-AFO as seen by Wach et al. [63] (discussed below) or by analysing the influence of the PD-AFO on the gait of healthy subjects, as seen in a study on a different orthotic by Arch et al. [33].

3.4 DESIGN AND MECHANICAL RESPONSE

There are several studies examining the influence of the design components of the PD-AFO on gait [38, 39, 53-56, 58, 60, 64, 65], and one study examining the mechanical response of the PD-AFO compared to other AFOs [63]. Understanding how the mechanical behaviour of the PD-AFO changes, particularly in response to changes in the design is important in understanding how the PD-AFO may compensate for patients' functional deficits.

Wach et al. evaluated the mechanical response of the PD-AFO by mechanically testing 4 types of AFO including a solid-ankle AFO, an anterior floor reaction AFO, a Phat Brace, and an IDEO [63]. The study uses a prosthetic limb to apply a load in 3 different orientations representing midstance,

terminal stance and pre-swing. The study evaluated strut deflection and compressive stiffness, comparing between AFOs. The IDEO was consistently stiffer in all phases compared to the other AFOs (Figure 3.4.1) [63]. The IDEO also experienced a 42% increase in strut deflection in the pre-swing phase compared to the midstance phase. Similarly to the gait studies analysing ankle joint angles, this study only examined strut deflection in the sagittal plane, yet there may be deflections in the coronal plane. Deflections in this plane indicate mediolateral instability.

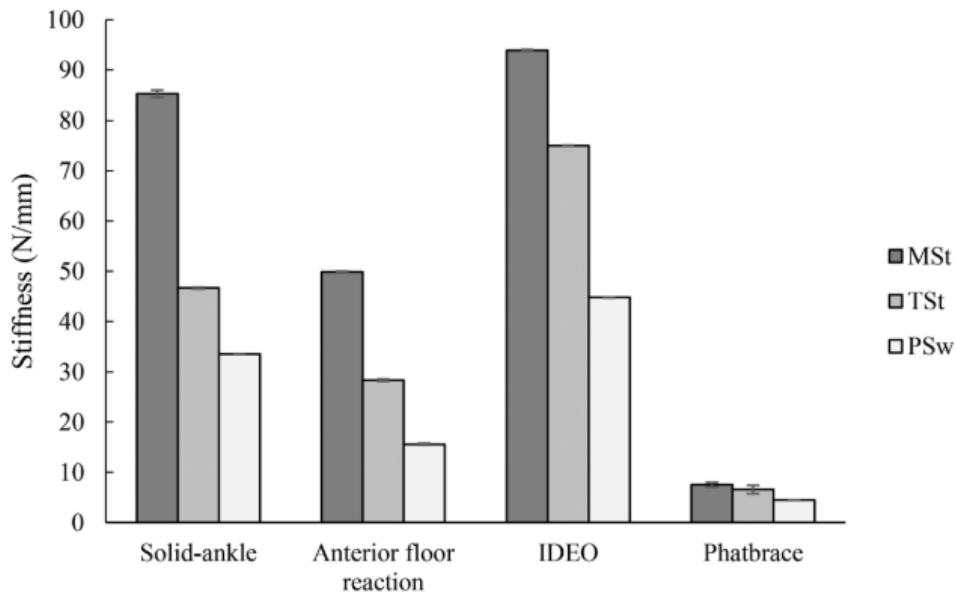


Figure 3.4.1: A study by Wach et al. evaluating the stiffness of 4 different AFOs at three points in gait: Midstance, (MSt) Terminal Stance (TSt) and Pre-swing (PSw) [63]. Image reproduced with permission from the rights holder ASME.

This study allows direct comparison between the different AFOs, helping to understand which aspects, for example the higher overall stiffness of the IDEO, may make it more suitable for patients wishing to return to high level activities [63]. Further analysis of how specific design parameters of the PD-AFO influence its mechanical response would be useful to understand how it overcomes different functional deficits.

This author found no studies analysing the influence of design parameters on mechanical response directly, but found several studies examining the changes in gait in a small cohort of injured patients, following the alteration of strut stiffness, strut alignment, strut bending axis, and heel wedge properties. These are discussed below.

3.4.1 Strut Manufacture and Stiffness

Harper et al. examined how changing the manufacturing techniques of the posterior struts may influence gait. The study used selective laser sintered (SLS) to print a single posterior strut and compared this to the original, posterior struts [64]. Each SLS strut, as shown in Figure 3.4.2 [56], was designed to be within 5% stiffness measured using a 3-point bend test [64]. This study found that the SLS struts resulted in significantly less peak ankle plantar flexion in both the injured and non-injured limb compared to the carbon fibre struts. Peak angle dorsiflexion was also lower in the SLS condition [64]. The SLS strut was described as a channel beam, meaning the second moment of area is not the same about all axes. Although the bending stiffness calculated of the strut was considered the same as the carbon fibre struts, the shape is not axisymmetric and therefore the stiffness according to a 3-point bending test would not be constant in all directions. This was not discussed by the authors, so it is not known whether this was considered. However, investigating the effect of the posterior strut second moment of area could be significant on the mechanical response of the PD-AFO.

Harper et al. also compared how different stiffnesses of the SLS strut affected gait parameters of patients during walking [65]. Other studies have also done that, evaluating both walking, running and uphill walking [55, 56, 58]. Generally, minimal kinematic and kinetic changes were seen when varying the strut stiffnesses by up to $\pm 20\%$ [55, 56, 65]. No significant vertical GRF changes in the injured limb were seen across stiffnesses [55, 56]. Although the stiffness had minimal changes on kinematic and kinetic variables for the injured limb, it did alter the GRF of the uninjured limb; a higher first peak GRF and higher peak medial/lateral GRF were seen when the injured limb wore nominal and stiff struts compared to the compliant struts in uphill walking ($p \leq 0.03$) [55]. This demonstrates the importance of evaluating the uninjured limb during gait analysis; although a design change may not alter the injured limb response, it may result in an altered gait pattern for the uninjured limb. It is generally considered best to mimic healthy gait as closely as possible, so deviations from this may be an important consideration for long term outcomes.



Figure 3.4.2: Figure reproduced from Esposito et al. showing an selective laser sintered posterior strut [56]. Image reproduced with permission from the rights holder Wolters Kluwer Health.

Although differences in joint kinematics and kinetics due to variation in strut stiffness were few, some were found. Peak knee flexion was significantly lower at initial contact for more compliant struts in uphill walking ($p \leq 0.015$) [55]. Peak knee flexion at stance was up to 26% lower for the more compliant struts in normal walking ($p < 0.003$) [56, 65]. Harper et al. also found increased degrees of dorsiflexion and plantar flexion in a compliant strut ($p \leq 0.045$) [65]. No differences were found during running [58]. It should be noted that the studies do not demonstrate that the joint kinematics and kinetics across all 3 strut stiffness were significantly different from each other.

When prescribing the PD-AFO the strut stiffness selected by the orthotist depends on weight and level of activity expected by the patient. Across these studies, the baseline stiffness was the stiffness that had been prescribed to the patient initially; it was therefore not the same range of stiffnesses tested across each patient [56, 58, 65].

3.4.2 Alignment

Brown et al. and Schmidtbauer et al. examined the influence of strut alignment on walking and running, respectively [38, 53]. Brown et al. examined the change in gait kinematics and kinetics during walking, when the strut alignment was changed by $\pm 3^\circ$ in the sagittal plane. Strut alignment was found to alter peak ankle angle, with a more plantarflexed strut alignment, resulting in a significantly more plantarflexed ankle angle during stance ($p < 0.001$) (Figure 3.4.3) [38]. This is also seen when running [53]. This result is to be expected, as an alteration in strut alignment would force the limb into a new position, altering the ankle angle.

Increasing the plantarflexed angle of the struts results in a more anterior located CoP at $\sim 15\%$ of the gait cycle during walking, resulting in the vertical GRF acting anterior of the knee joint ($p \leq 0.006$) [38]. As suggested, this may result in improved stability; 8/13 patients preferred the plantarflexed alignment which indicates that the strut alignment may significantly alter the gait pattern of injured patients [38].

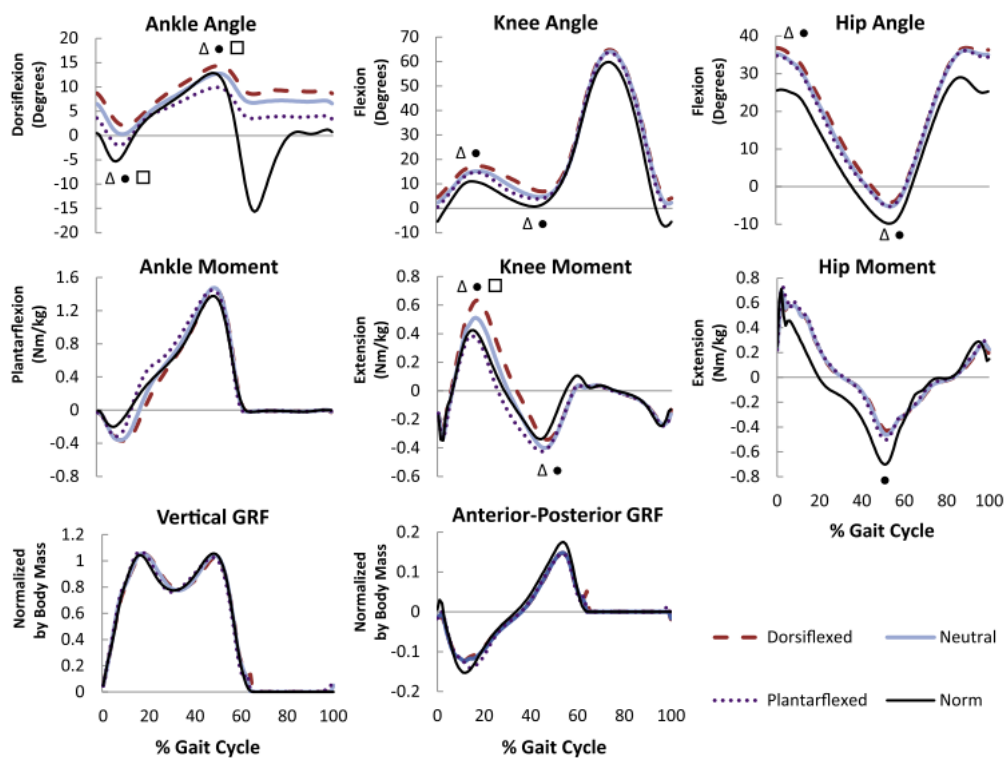


Figure 3.4.3: A study by Brown et al.; changes in joint kinematics and kinetics during walking, following changes in strut alignment. The shapes indicate a significant difference between 2 alignments: Δ -between the dorsiflexed and neutral alignment, \bullet - between the dorsiflexion and plantarflexed alignment, \square - between the neutral and plantarflexed alignment. Image reproduced with permission from the Rightsholder Elsevier [38]

During running, Schmidtbauer et al. found that the strut alignment had limited effects on the rate of change of GRF experienced [38, 53]. The more plantarflexed the alignment, however, the greater the difference in the loading rate between the injured and shod limbs. An initial impact peak was seen for the shod limb, but not for the injured limb. Again, this demonstrates that the PD-AFO alters the gait of the uninjured limb. As with the studies on stiffness, the neutral alignment was defined as that which was originally prescribed, so was not the same for all patients [38, 53].

3.4.3 Bending axis

Studies also examined the location of the bending axis, varying from a proximal to a distal location, as shown in Figure 3.4.4, in both walking and running [39, 54]. Significant differences were found in the GRF and GRF impulse experienced during both running and walking, following changes in the bending axis [39, 54]. Whilst running, a significant difference was found between the anteroposterior propulsive GRF between the neutral and distal bending axis however the absolute differences were still small [54]. During the midstance phase of walking, the peak vertical GRF impulse was found to be significantly higher at the middle bending axis than the distal and proximal location for both the injured and shod limbs ($p \leq 0.011$) [39]. However, there is no notch in the ‘middle’ bending axis and this may alter the bending stiffness of this strut compared to the other 2 notched struts evaluated. Although it is thought that strut stiffness has minimal effect on gait, it is not conclusive and therefore may be a limitation in this study. Also, without a notch located at the middle, the authors cannot be sure that the bending axis was indeed at that location; the bending axis is likely to occur at a more distal location.



Figure 3.4.4: The 3 selective laser sintered posterior struts used in studies by Ranz et al. and Esposito et al. examining the changes in gait during walking and running, as the bending axis changes [39, 54]. Image reproduced with permission from the rights holder, Elsevier [54]

Esposito et al. found that during running an increased ankle ROM was seen as the bending axis became more distally located ($p < 0.003$) [54]. This led to increased power generation and absorption seen in the most distal bending axis set-up [54], accounting for an increase in propulsive GRF mentioned above. No patterns in changes of joint kinematics and kinetics were seen when walking [39]. As suggested, by Esposito et al. this may be due to the larger impacts seen during running, and therefore larger deflection of the struts. This demonstrates the need to evaluate the PD-AFO struts during both running and walking.

Furthermore, the bending axis has been changed in the sagittal plane only. Whilst that is the most important plane of rotation during the gait, changing the bending axis may also result in changes in the rotation about the axes in other planes.

3.4.4 Heel Wedge Properties

This author found 1 study examining how heel-wedge height and stiffness alters gait; Ikeda et al. analysed 3 different heel wedge heights (1-3 cm) and 2 heel wedge stiffnesses [60]. The greatest changes were seen with changes in heel-wedge height. An increased height resulted in an increase in the time to peak CoP ($p \leq 0.003$) and a decreased peak CoP velocity ($p = 0.008$) [60]. It also resulted in an increased (absolute) peak dorsiflexion moment ($p < 0.001$) and peak knee extension moment ($p < 0.017$). The time to peak knee extension moment also increased with heel wedge height ($p \leq 0.005$) [60].

The heel wedge height influences the CoP, and it was previously discussed that strut alignment also does this [38]. Both changes may result in changes in knee extension and flexion, though heel-wedge height will not change the ankle angles. This suggests that the heel wedge may be a good method to change the gait kinematics of the knee, without altering the fixed ankle angle chosen. The effect of the heel wedge on the PD-AFO's mechanical response should be further investigated to understand its significance, particularly as the heel wedge is an easy component for the orthotists to change and tune.

3.4.5 Limitations

Several PD-AFO design parameters have been tested in the literature to evaluate their influence on gait. However, throughout the studies, small heterogenous cohorts have been used, introducing possible bias. Within each study, only 3 changes were made to each parameter, again limiting the ability to determine any significant differences resulting from the change. The nominal values for the parameters were also chosen to be that which were prescribed to the patient initially, so, although the variation was the same for all patients, the absolute values were not.

No studies have been published that analyse the effect of the different manufacturing techniques used by the US and UK designs described earlier (wet laminate and pre-impregnated carbon fibre) on the mechanical response. The principal design is the same, and amongst professionals that work within

the field, it is considered that literature relating to the US PD-AFO (the IDEO or Exosym) can be directly applied to the UK PD-AFO (the B.O.B or Momentum) [36]. Although outcomes for both manufacturing techniques are similar, it would be beneficial to confirm, that indeed, there are no significant differences in mechanical response.

These studies provide initial insight into the significant features of the PD-AFO indicating that strut alignment and heel-wedge properties may have the most significant effect on the response of the PD-AFO. An understanding of the sensitivity of the PD-AFO's mechanical behaviour to different components without the variability introduced by the patient cohort will provide further, valuable insight.

3.5 CONCLUSION

The novel PD-AFO has been shown in the literature to improve functional outcome for many limb-salvage patients. It is understood that the rehabilitation programmes improve outcome for patients regardless of injury type, though this may be due to the increased morale and self-efficacy that such a programme provides. There is still a distinct lack of understanding as to how the PD-AFO interacts with the foot and ankle and the significant design features that contribute to its success.

Understanding how the PD-AFO alters the limb kinematics and kinetics during gait could provide valuable insight into which regions of the foot and ankle the PD-AFO influences most and help indicate which patients would benefit from the PD-AFO. Additionally, understanding how the PD-AFO aids movement would enable the quantification of the implications of design changes and provide a basis to potentially widen the patient cohort and help predict long-term consequences.

Literature has previously examined how the PD-AFO, and its design, alters gait kinematics, with a minor focus on kinetics. No studies have evaluated the internal changes in loading of the foot and ankle, and limited research has been undertaken analysing external loading and the possible ESAR characteristics of the device. As such, this thesis aims to quantify how the PD-AFO alters the external and internal loading of the foot and ankle when wearing the PD-AFO, along with its ESAR characteristics. To evaluate this, the influence of injury type, behaviour, and rehabilitation must be negated. The loading of the limb when wearing the PD-AFO is also important when considering long term complications, such as bone resorption; on-going studies are currently investigating the longer-term success of the PD-AFO [66].

This chapter described the development of the PD-AFO and the literature that has demonstrated its functional improvement for limb-salvage patients. Chapter 5 evaluates how the PD-AFO alters the gait of a healthy subject, evaluating whether any off-loading of the limb occurs. Prior to this, the next chapter commences the mechanical characterisation of the PD-AFO by quantifying the material behaviour of its components, analyses used throughout the remainder of the thesis

4 MATERIAL BEHAVIOUR OF THE COMPONENTS OF THE PD-AFO

4.1 INTRODUCTION

In the previous chapter it was demonstrated that further investigation is needed to understand how the PD-AFO alters loading of the limb. Within this thesis this is achieved using a combination of experimental and computational analysis of the PD-AFO. More specifically, for the computational analysis, an FE model of the PD-AFO is developed and used. As part of this process, the material behaviour of the individual components of the PD-AFO are determined to allow the in-depth analysis of PD-AFO gait trials and to represent them accurately in the computational analysis. This chapter details the different materials used in the manufacture of the Momentum® brace produced by Blatchford, which is the PD-AFO of interest, and characterises their behaviour. The UK Momentum® is the AFO analysed throughout this thesis and will be referred to as ‘PD-AFO’ from this point forward. Table 4.1.1 details the components of the Momentum® and the materials used in its manufacture. An image of the Momentum® can be seen in Figure 3.2.1 in Chapter 3.

Table 4.1.1: The materials used to manufacture the components of the PD-AFO. CF: carbon-fibre. The foams used for the shin pad, lateral pad, medial pad and sole were unknown and therefore referred to as Foam A and Foam B.

Component	Materials	Type	Ref.
Posterior Struts	Composite with solid core	Composite	
Anterior Cuff	Carbon-twill/Unidirectional Carbon-fibre	CF Layers	
Posterior Cuff	Carbon-twill/ Unidirectional Carbon-fibre	CF Layers	
Base (Ankle Region)	Carbon-twill/ Unidirectional Carbon-fibre	CF Layers	
Base (Toe Region)	Carbon-twill/ Unidirectional Carbon-fibre/Aramid	CF Layers	
Shin Pad	Foam A	Foam	
Lateral Pad	Foam B	Foam	
Medial Pad	Foam B	Foam	
Sole	Foam B	Foam	
Heel Wedge	Polyurethane foam	Foam	[36, 60]

This chapter is divided into 3 sections, each focussing on a different material type. The first section describes the material characterisation of the carbon-fibre layers, the second the composite struts, and the third the foam materials. Within each section the method used to determine the material behaviour is described, followed by the results and their analysis.

4.2 CARBON-FIBRE LAYERS

The carbon-fibre layers are used to manufacture patient-specific regions of the PD-AFO. These include the anterior and posterior cuffs, and the base. The anterior cuff is shaped to fit to the patella tendon and tibial condyles, whilst the posterior cuff connects to the posterior struts. The cuff, as a whole, is hypothesised to be the point through which load is transferred from the PD-AFO to the limb [36, 40]. The base extends along the plantar aspect of the foot and is thought to act as rotational spring during pre-swing to aid with propulsion [36]. During gait, the two main modes of loading of the base and cuff regions are predicted to be compression and bending.

The components of the PD-AFO are made up of layers of different types of carbon-fibre: carbon-twill (CT), uni-directional carbon-fibre (UD), and aramid. The different components have different lay-ups (numbers of each layer). The lay-ups of the different components of the PD-AFO are described in Table 4.2.1 as provided by Blatchford. For the components with only CT and UD carbon-fibre, the UD carbon-fibre is sandwiched between the carbon-twill. Information regarding the layer order, following the addition of aramid was not provided. However, the aramid is visible on the component of the PD-AFO and therefore it is assumed that it sits outside the CT and UD carbon-fibre. This

author has not found any literature or data sheets on the material properties of the lay-ups described in Table 4.2.1.

Table 4.2.1: The lay-up of different components within the PD-AFO. CT is carbon twill and UD is uni-directional

Components	Lay-up
Base (Ankle Region)	4 x CT / 6 x UD
Base (Toe Region)	4 x CT / 4 x Aramid / 10 x UD
Posterior Cuff	4 x CT / 3 x UD under struts / 3 x UD over struts
Anterior Cuff	3 x CT / 3 x UD cross

4.2.1 Literature Review and Analysis

The Young's moduli in the 2 directions, E_1 , and E_2 , were provided by the manufacturer for each type of carbon-fibre as shown in Table 4.2.2. The Young's modulus, E_3 , along with the Poisson's ratios (ν_{12} , ν_{13} , ν_{23}) and shear moduli (G_{12} , G_{13} , G_{23}) of the 3 layers were not provided. The equivalent material properties of the lay-ups used for each component of the PD-AFO were also not provided. Suitable material samples were not available for experimental testing, and catastrophic testing of the PD-AFO was not an option as it was required for future experimental analysis. As a result, material properties of each component were determined from literature.

Table 4.2.2: Details of carbon-fibre layers used in manufacture of the base and cuff region of the PD-AFO as provided by the manufacturer. UD is uni-directional, E_1 and E_2 are the Young's moduli in the first two directions

	Code	E_1 (GPa)	E_2 (GPa)	Regions Used
Carbon-twill	VTC401-C280T - 4x4-40%RW-1250	50-60	50-60	All
UD Carbon-fibre	VTC401-UD300-T700-24K-37%RW-300P	110-130	40-60	All
Aramid	VTC401-A200T-46%RW-1000	24-34	24-34	Toe Region

UD carbon-fibre has been considered in the literature to be transversely isotropic ($E_2=E_3$) [67-69]. For both carbon-twill and aramid the Young's moduli in the first two directions (E_1 and E_2), as provided by the manufacturer, were the same. As such all, 3 layers were assumed to be transversely isotropic. Table 4.2.3 lists the known coefficients for each of the 3 materials, and any relationships between them after assuming transverse isotropy [69]. The grey-shaded cells indicate a coefficient that needed to be established. By convention $E_1 \geq E_2 \geq E_3$.

Table 4.2.3: Known material coefficients, and the links between them, for the carbon-twill, uni-directional carbon-fibre and aramid. The grey-shaded cells indicate values that need to be determined. E_1 , E_2 , and E_3 are the Young's moduli in each direction; ν_{12} , ν_{13} , and ν_{23} are the Poisson's ratio in each direction; and G_{12} , G_{13} , and G_{23} are the shear moduli in each direction.

	E_1 (GPa)	E_2 (GPa)	E_3 (GPa)	ν_{12}	ν_{13}	ν_{23}	G_{12} (GPa)	G_{13} (GPa)	G_{23} (GPa)
CT	55	55	$< E_1$			$= \nu_{13}$	$= \frac{E_1}{2(1 + \nu_{12})}$		$= G_{13}$
UD	120	50	$= E_2$		$= \nu_{12}$			$= G_{12}$	$= \frac{E_2}{2(1 + \nu_{23})}$
Aramid	29	29	$< E_1$			$= \nu_{13}$	$= \frac{E_1}{2(1 + \nu_{12})}$		$= G_{13}$

Studies using both computational modelling and experimental testing were used to determine suitable values for the unknown constants.

Table 4.2.4: Material properties for different types of carbon-fibre found in the literature. E_1 , E_2 , and E_3 are the Young's moduli in each direction ($E_1 > E_2 > E_3$); ν_{12} , ν_{13} , and ν_{23} are the Poisson's ratio in each direction; and G_{12} , G_{13} , and G_{23} are the shear moduli in each direction

Material	Author	Composite as described	E_1 (GPa)	E_2 (GPa)	E_3 (GPa)	ν_{12}	ν_{13}	ν_{23}	G_{12} (GPa)	G_{13} (GPa)	G_{23} (GPa)	Ref.
CT	Lomov et al.	'glass/PP woven composite'	52.2-59.2	N/A	5.0-7.8	0.37-0.38	0.24-0.25	N/A	1.8-2.8	2.2-3.4	N/A	[70]
CT	Stier et al.	'textile carbon-fibre reinforced plastics... woven tows'	45.9-46.2	N/A	7.5	0.074-0.08	0.35	N/A	2.8-3.1	2.2	N/A	[68]
CT	Foroutan et al.	'carbon/epoxy prepreg plain weave'	66.4	N/A	-	0.08		N/A	4.8		N/A	[71]
CT	Matveev et al.	'Carbon-fibre 2 x 2 twill weave'	55.4-56.0	N/A	-	0.054-0.069		N/A	-	-	N/A	[72]
CT	MatWeb	"Solvay CYCOM® 759F Epoxy – 2X2 Twill Fabric reinforced Prepreg"	57-62	N/A	-	0.13	-	N/A	4.0	-	N/A	[73]
CT	MatWeb	"Toray G-85FR Prepreg Laminate with T300B-3K-40B Fiber 2X2 TWILL AT 204 g/m2 FAW AND 42% RC"	54.9	N/A	-	0.043	-	N/A	3.5-		N/A	[74]

Mate-rial	Author	Composite as described	E₁ (GPa)	E₂ (GPa)	E₃ (GPa)	v₁₂	v₁₃	v₂₃	G₁₂ (GPa)	G₁₃ (GPa)	G₂₃ (GPa)	Ref.
CT	MatWeb	<i>“Toray G-85FR Prepreg Laminate with T700S-12K-60E Fiber 2X2 TWILL AT 665 g/m2 FAW AND 36% RC”</i>	57.5	N/A	-	0.055	-	N/A	4.3	-	N/A	[75]
UD	Sevenois et al.	<i>‘predicted homogenised properties for a UD yarn’ for V_f= 0.5-0.6</i>	113.6-135.7	7.6-9.7	N/A	0.19-0.33	N/A	0.48-0.55	3.3-5.3	N/A	2.5-3.2	[67]
UD	Stier et al.	<i>‘unidirectional carbon-fibre reinforced plastics’</i>	99.8-102.1	6.8-6.4	N/A	0.30-0.31	N/A	-	2.9-3.1	N/A	2.4	[68]
Ara mid	MatWeb	<i>“Solvay CYCOM® 950-1 Epoxy Prepreg with 52% 285 Kevlar Fabric”</i>	28.2-32.0	N/A	-	-	-	N/A	1.93	-	N/A	[76]
Ara mid	MatWeb	<i>“Arlon Electronic Materials 45NK Woven Kevlar® Reinforced Laminate and Prepreg”</i>	27.6	N/A	-	0.2	-	N/A	-	-	N/A	[77]

Table 4.2.5 shows the values for the orthotropic material constants, provided by the manufacturer, and determined from literature, for each of the 3 carbon-fibre layers. The values from literature were determined by taking the mean value of the maximum and minimum values found in Table 4.2.4. For aramid, no values were found for E_3 , ν_{13} , and G_{13} . To determine the value for these constants it was assumed that the ratio between these constants and E_1 was the same as the ratio between these constants and E_1 for carbon-twill. For those values provided by the manufacturer, the mean value was used.

Table 4.2.5: Orthotropic material constants chosen for 3 different carbon-fibre layers. E_1 , E_2 , and E_3 are the Young's moduli in each direction; ν_{12} , ν_{13} , and ν_{23} are the Poisson's ratio in each direction; and G_{12} , G_{13} , and G_{23} are the shear moduli in each direction.

	E₁ (GPa)	E₂ (GPa)	E₃ (GPa)	ν₁₂	ν₁₃	ν₂₃	G₁₂ (GPa)	G₁₃ (GPa)	G₂₃ (GPa)
CT	55	55	6.4	0.21	0.30	0.30	23	2.8	2.8
UD	120	50	50	0.26	0.26	0.48	3.9	3.9	17
Aramid	29	29	3.0	0.20	0.28	0.28	12	1.5	1.5

4.2.2 Sensitivity analyses

To determine the effect of each material constant on the behaviour of each carbon-fibre layer, several sensitivity analyses were performed using FE modelling. This process highlighted those material constants that were significant in the behaviour of the layer in the modes of loading seen during gait, namely axial compression and bending.

For each carbon-fibre layer, a sample geometry was created in FE, representative of the geometry of interest. Baseline orthotropic material properties were assigned to the sample as listed in Table 4.2.5. Linearly elastic, transversely isotropic and homogenous material behaviour was assumed. For each independent material constant, a sensitivity analysis was performed by varying the respective baseline value by $\pm 40\%$ (selected to be greater than the variation from the mean of material properties provided by the manufacturer) or to the maximum and minimum value found in the literature (whichever was greatest), without violating rules of the linearly elastic orthotropic material model. For those values provided by the manufacturer, the sensitivity was performed at the maximum, mean and minimum value. One material property was changed at a time, with all other independent material properties kept constant. All dependent relationships (Table 4.2.3 above) between the constants were, however, maintained throughout the sensitivity analysis.

The meshed sample was loaded in compression and bending. The geometry was created in MSC.Mentat and the sensitivity was performed in MSC.Marc. The sample layer was created with a

cuboid geometry ($200 \times 30 \times 4$ mm) consisting of 400 solid, hex20, quadratic elements (Figure 4.2.1). This sample was compressed between two rigid surfaces (touching, frictionless contact) by up to 1 mm in total, or failure to converge. The geometry was fixed in x , y and z at the central nodes indicated in red in Figure 4.2.1 to prevent rigid body motion. The x direction was assigned E_1 , the y direction: E_2 and the z direction: E_3 .

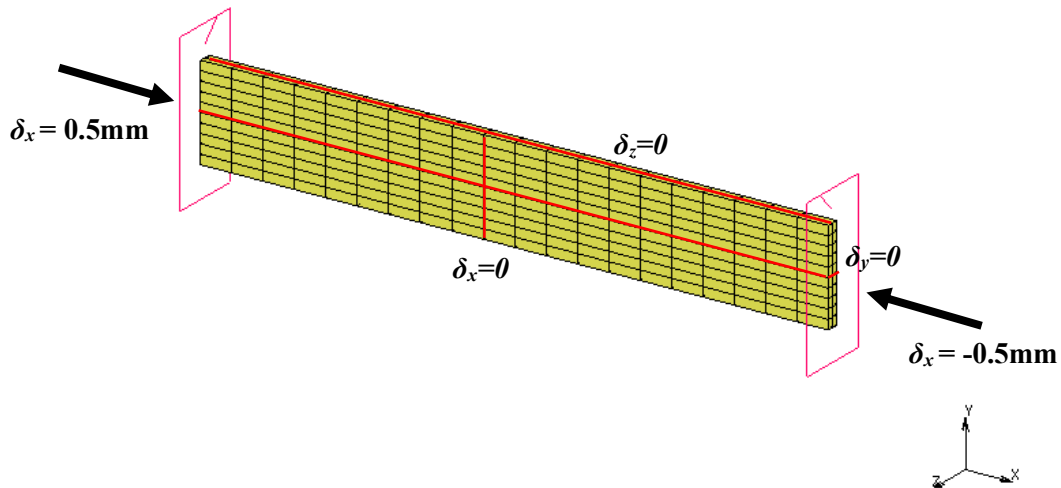


Figure 4.2.1: Carbon-fibre layers sensitivity analysis geometry and boundary conditions in compression. The red lines indicate the location where nodes were fixed in 1 degree of freedom, where δ indicates the displacement at that point. Each end of the sample was compressed 0.5mm. The primary direction of the Young's Modulus was in x .

The same geometry and mesh were used to model bending. The sample was placed between 4 cylindrical surfaces, with touching, frictionless contact, as seen in Figure 4.2.2. The central nodes indicated by the red cross in Figure 4.2.2 were fixed in translation in x and y to prevent rigid body motion. The bottom cylindrical surfaces were fixed in all degrees of freedom. The top surfaces were displaced by 1 mm in the z direction, simultaneously, to bend the meshed geometry.

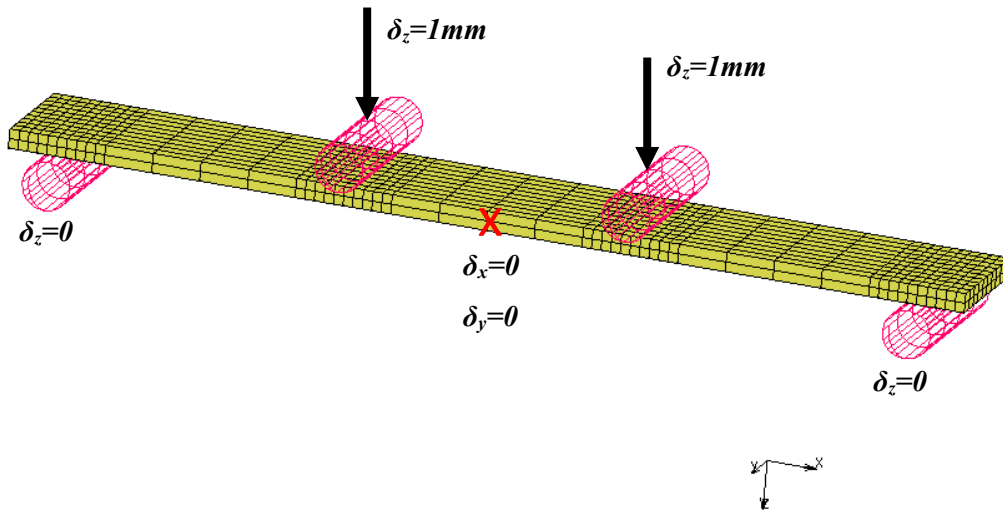


Figure 4.2.2: Carbon-fibre layers sensitivity analysis geometry and boundary conditions in bending. The red cross indicates the nodes fixed in 2 degrees of freedom, where δ indicates the displacement at that point. The top 2 cylindrical surfaces displaced the layer downwards, whilst the bottom 2 cylindrical surfaces remained fixed. The primary direction of the Young's Modulus was in x .

The simulations conducted using the baseline material property values (Table 4.2.5) provided the baseline stiffness, K_b , with one value for compression and one for bending. The stiffness was calculated using equation (4.2.1) where P represents the force that displaced the sample (either in compression or bending), and δ the displacement/deflection in the same direction.

$$K = \frac{P}{\delta} \quad (4.2.1)$$

For each change in material parameter a new simulation, i , was run. The stiffness derived for each analysis, K_i , was compared to the baseline stiffness using equation (4.2.2), to give the percentage change with respect to each baseline stiffness, ΔK .

$$\Delta K = \frac{K_i}{K_b} - 1 \quad (4.2.2)$$

4.2.3 Results

The results of the sensitivity study assessing the effect of various material parameters on each individual carbon-fibre layer are presented in this chapter, in Figure 4.2.3, if the parameter resulted in

a relative change from the baseline stiffness of >5%. The full set of results can be found in Appendix 12.1.1.

Across the range tested, the primary directions of the Young's modulus of the carbon twill had the largest influence on both its bending and compressive stiffness, changing the stiffness by $\pm 9.0\%$ and $\pm 9.2\%$ respectively. Similarly for uni-directional carbon fibre E_1 , had the greatest influence on the compressive and bending stiffness. The stiffness varied by $\pm 8.3\%$ in bending and $\pm 8.4\%$ in compression compared to the baseline value. For aramid the change in the Young's Moduli, E_1 and E_2 , resulted in a change of $\pm 17.2\%$ in the bending stiffness and $\pm 17.5\%$ in the compressive stiffness.

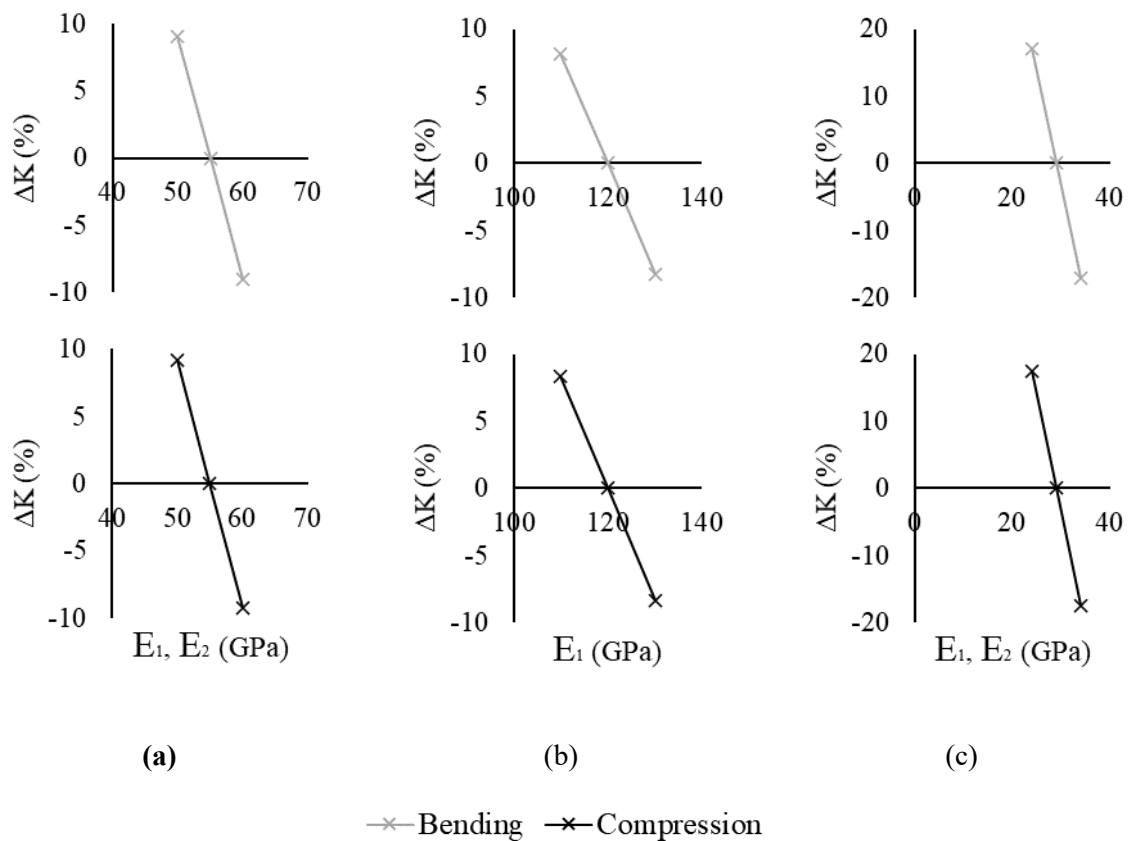


Figure 4.2.3: The sensitivity of the bending and compressive stiffness in the primary direction (s) of the Young's Modulus (E_1 , E_2) of (a) carbon-twill (b) uni-directional carbon fibre and (c) aramid. ΔK is the change with respect to the baseline stiffness.

4.3 DISCUSSION

The manufacturer provided material constants for the Young's modulus in certain directions. To determine the remaining material properties of the carbon-fibre layers literature was used. All data used to determine these material constants had a respective value of E_1 within 11% of the range provided by the manufacturer of the material layer being examined. Therefore, these baseline values were considered a reasonable approximation.

To evaluate the effect of the material properties determined from literature on the mechanical response of the carbon-fibre layer, a sensitivity analysis was performed. The baseline material properties used for each individual carbon layer were found in the literature, except for E_1 and E_2 provided by the manufacturer. The behaviour of each layer was most sensitive to the Young's modulus, E_1 . As this value was provided by the manufacturer, the range of values given was assumed correct. The FE sensitivity demonstrated that all other material properties obtained from literature, had a negligible effect on the behaviour of the material in the two main modes of loading experienced by the PD-AFO during gait (results presented in Appendix 12.1.1). As such, the baseline values were used to describe the materials and further testing was not deemed necessary.

The carbon-fibre layers were assumed to behave in a linearly elastic behaviour. The carbon-fibre is not seen to permanently deform on the PD-AFO when in use and therefore the assumption of elasticity is valid for the range of loading of interest. Literature has previously considered the assumption of linearity of carbon-fibre within the elastic range to be a valid assumption [78]. Furthermore, Yan et al. recorded a modulus in tension that was similar to that seen in compression [79]. The carbon-fibre was also assumed to be transversely isotropic. This is an assumption previously made in the literature and is acceptable when the overall behaviour of the composite is of interest, as is the case in this study [67-69].

Within this section the material properties of the individual carbon-fibre layers have been established. As the lay-up of the components is known, these material properties provide enough information on the behaviour of the carbon-fibre composite sections to replicate the overall material behaviour of the based and cuff.

4.4 STRUT COMPOSITE

The posterior struts deflect during the loading response phase of gait [36, 37]. They are thought to reduce the force through the limb by transferring the load to the anterior aspect of the tibia. Deflection of the struts is also thought to provide energy storage and return capabilities throughout the midstance phase and terminal stance phase, which is then released during pre-swing to aid the limb in propulsion [36, 37].

As discussed in Chapter 2, a limb is exposed to the greatest force in the direction vertical to the ground during gait, with the largest ankle rotations recorded in the sagittal plane. Therefore, the

posterior struts of the PD-AFO are expected to undergo two main modes of loading during gait; bending in the sagittal plane and compression in the direction vertical to the ground.

The specific posterior struts used in the manufacture of the PD-AFO used in this thesis, named Clever Bones (Össur, UK), are made from a carbon-composite with a solid core. No studies were found in the literature investigating the complete material behaviour of Clever Bones. In 2 relevant studies found, the behaviour of an SLS-printed posterior strut and the original posterior struts of an IDEO were assessed by comparing the bending stiffness derived from 3-point bending tests [56, 64]. Due to this literature gap, and since suitable samples of the composite strut were available from the manufacturer, experimental testing was used to determine the material behaviour of the struts.

4.4.1 Experimental protocol

Three samples of the composite strut (Clever Bone) were supplied by Blatchford. The samples were flattened at each end, to produce ends normal to the long axis of the cylinder. The diameter and length of each sample were measured 3 times with vernier callipers and a ruler, respectively.

Each sample was tested in compression and bending using a materials testing machine (5866 series, Instron, High Wycombe, UK) with a sample rate of 50Hz. This was to ensure that the material properties determined were representative of both relevant modes of loading. A 10kN loadcell was used to record the force in the direction of loading. The compliance of the machine was recorded (with a 10kN loadcell at 50Hz) with no fixtures attached and accounted for in all future measurements (see Appendix 12.1.2). The strain gauges shown in Figure 4.4.1 and Figure 4.4.2 were not used for the material characterisation of the sample but for evaluation of accuracy of strain gauge attachment as explained in Chapter 6.

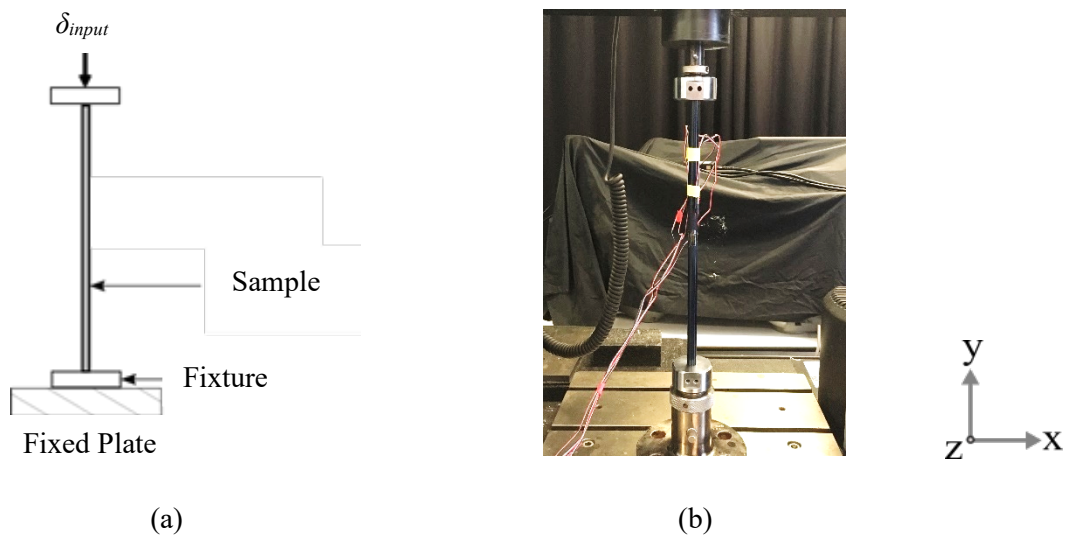


Figure 4.4.1 (a) Schematic showing experimental set-up for compression where δ_{input} was the applied displacement; the fixture consisted of two flat surfaces between which the sample was placed unconstrained (b) Image showing same experimental set-up, with strain gauges

The three samples underwent compression at a strain rate of 0.119/s. This rate was chosen following preliminary tests examining the sensitivity of the posterior struts to a range of strain rates expected to be experienced during gait. The preliminary results found no statistical difference in the predicted Young's modulus calculated in compression for a strain rate of 0.059/s, 0.119/s and 0.234/s. The preliminary results are described in Appendix 12.1.4. 12 repeats were performed on each sample, rotating the sample by 90° about the long axis, every 3 tests. The samples were pre-loaded to 50N before being displaced to 0.5mm.

Assuming a linear, elastic, isotropic material the Young's modulus, E_c , was calculated from the compression force-displacement curve using equations (4.4.1)-(4.4.3). l and A were the length and area of each respective sample.

$$\sigma = \frac{P}{A} \quad (4.4.1)$$

$$\varepsilon = \frac{\Delta l}{l} \quad (4.4.2)$$

$$E_c = \frac{\sigma}{\varepsilon} = \frac{P}{\delta} \cdot \frac{l}{A}; \text{ where } \delta \equiv \Delta l \quad (4.4.3)$$

To calculate the Young's modulus from bending, a 4-point bend test was performed on the same 3 samples at a displacement rate of 0.38mm/s. The samples were manually loaded to a small compressive force of <3N to remove slack. At this point δ_{input} was set to zero. The sample was then loaded to 1mm, and the force recorded. 12 repeats were performed on each sample; they were completely removed between each test and rotated 90° about the long axis every 3 tests. To calculate the Young's modulus from bending, E_b , Macauley's Beam Theory was utilised (see Appendix 12.1.3)

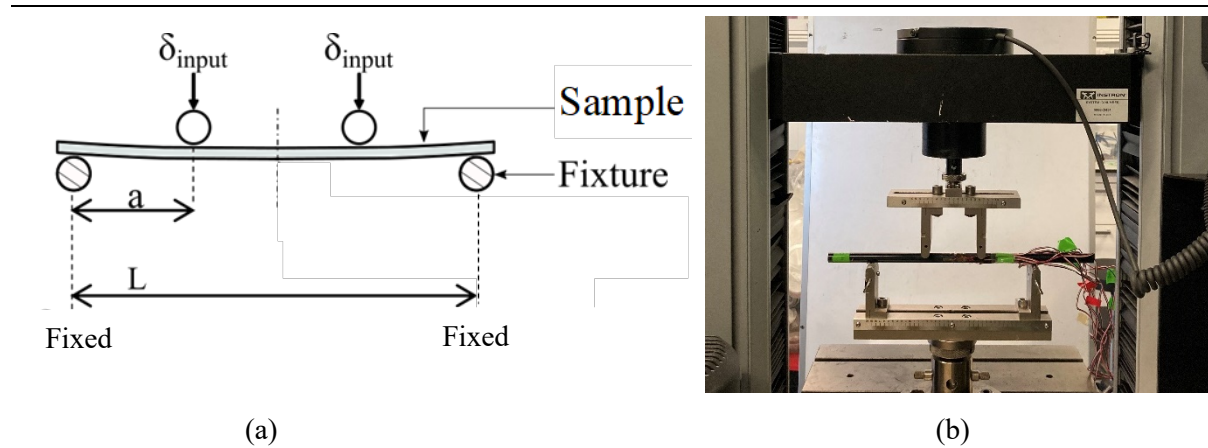
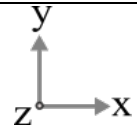
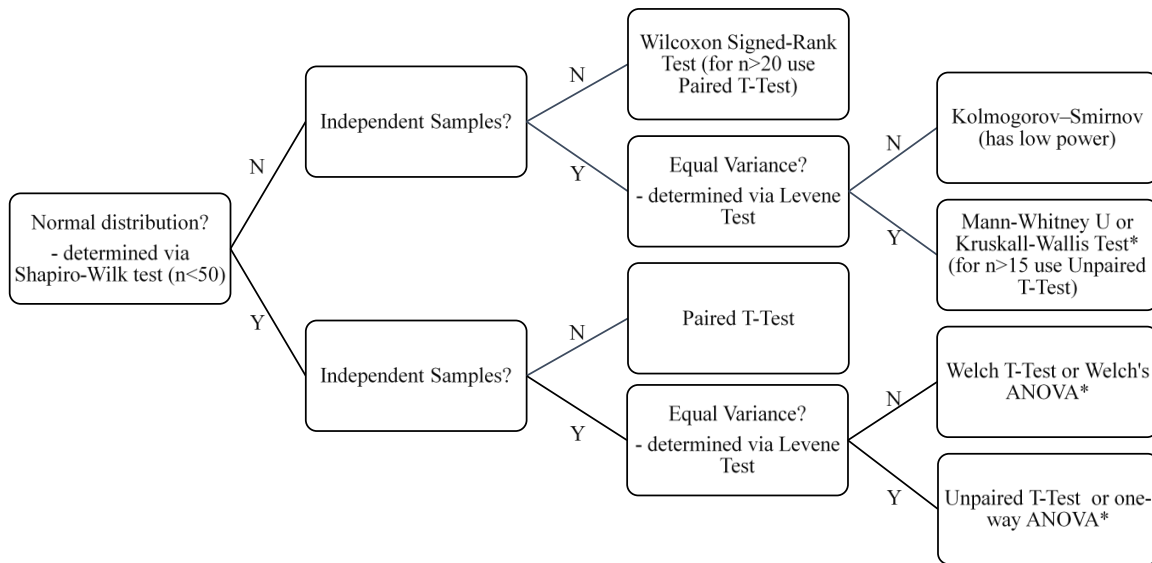


Figure 4.4.2: Schematic showing experimental set-up for 4-point bend test (bending), the fixture consisted of 4 rounded surfaces constrained relative to one another; $a = 6\text{mm}$, $L = 18\text{mm}$ (b) Image showing same experimental set-up. δ_{input} was the applied displacement.



The Young's modulus calculated from bending and the Young's modulus calculated from compression across all samples were compared to evaluate if there was a statistical difference between the 2 methods of calculation. The significance level was set to $\alpha = 0.05$. The tests were assumed paired, and the appropriate statistical test was established by following the protocol shown in Figure 4.4.3. Where linear regression was performed, the R^2 value is denoted.



*for 2 or more independent groups; further analysis required

Figure 4.4.3: Process to determine the appropriate statistical test for each comparison coded in Python

To characterise the composite strut, the Poisson's ratio is also required. This was not determined experimentally as it would require a very detailed, independent study, with strain gauges that are fixed on the sample with an attachment of known properties. Due to the nature of the surface of the strut composite, this is very difficult, and it would have been attempted only if sensitivity analyses would have revealed a strong correlation between the Poisson's ratio and the stiffness of the strut in compression and bending. As the posterior struts are composites, the baseline value of Poisson's ratio (ν_{13}/ν_{23}) established for carbon twill from literature above, was used as a preliminary baseline value. A sensitivity analysis was then performed to evaluate how sensitive the posterior struts were to the value of Poisson's ratio selected, to determine whether further testing was required.

4.4.2 Experimental results

In this section the results for the materials testing on the composite strut samples are described. The samples had a mean length of 304 mm and a mean cross-sectional area of 105 mm² (Appendix 12.1.5). Figure 4.4.4 shows the values of Young's modulus calculated across all 3 samples in both compression and bending. The values were found to have a non-normal distribution, and were found to be statistically different. The mean Young's modulus calculated from the bending test was 8.4% higher than that calculated from the compression test. The interquartile range for the values of Young's modulus calculated during compression was 5.92GPa, whilst for bending it was 2.38GPa. The minimum value of Young's modulus calculated was 28.30GPa and the maximum value was 38.27GPa across both bending and compression. The mean value of Young's modulus ± 1 standard

deviation (SD) calculated across all 3 samples from both compression and bending was 35.23 ± 2.66 GPa.

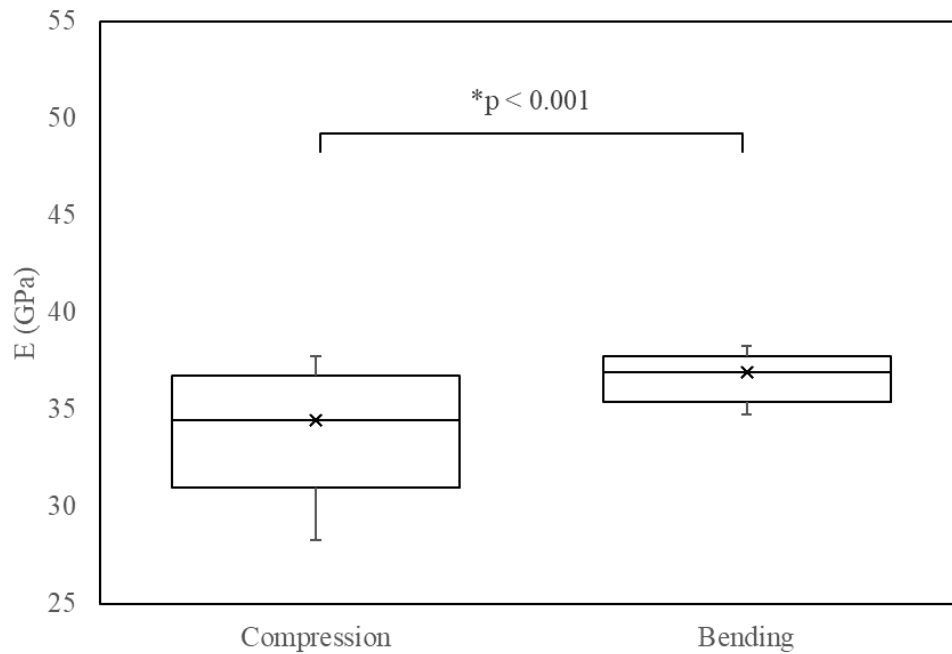


Figure 4.4.4: The Young's modulus (E) calculated across all 3 samples for both compression and bending ($n = 36$). The median Young's modulus in compression was calculated to be 34.45 GPa and in bending 36.92 GPa. The mean Young's modulus \pm 1SD in compression was 33.77 ± 2.96 GPa, and 36.65 ± 1.18 GPa. in bending. *indicates a statistical difference for $p < 0.05$, using a Wilcoxon signed rank test.

The final material properties, determined from experimental testing and from literature, for the composite struts are shown in Table 4.4.1.

Table 4.4.1: Material properties of the composite struts. Experimental values shown as the mean \pm 1 SD. E is the Young's modulus and ν is the Poisson's ratio.

	E (GPa)	ν
Strut Composite	35.23 ± 2.66	0.16

4.4.3 Sensitivity analyses

The material properties of the composite struts were fully defined using experimental testing and literature. An FE model was used to perform sensitivity analyses on the assumption of isotropy and the value of Poisson's ratio selected from literature to evaluate whether further testing was required. The FE model was developed to mimic the experimental tests (compression and bending) performed on the strut samples as described above. A cylindrical geometry was constructed (radius = 5.76 mm, length = 198 mm) using MSC.Mentat (v2020, MSC.Software, Santa Ana, CA, USA) to represent the

samples. The geometry was meshed and consisted of 3248 solid, hexahedral, 20-node quadratic elements.

For simulating the compression tests, the meshed sample was compressed between two rigid surfaces by 1mm, with touching frictionless contact, allowing the cylinder to expand in diameter. The cylinder was constrained at its long axis in both the y and z direction, to prevent rigid body motion.

For simulating the bending tests, the meshed sample was compressed between 4 circular surfaces. The bottom 2 surfaces were fixed in space, and to the top a 1 mm displacement was applied. The cylinder was constrained at its central long axis in the z direction, and at the midpoint of its length in the x direction to prevent rigid body motion.

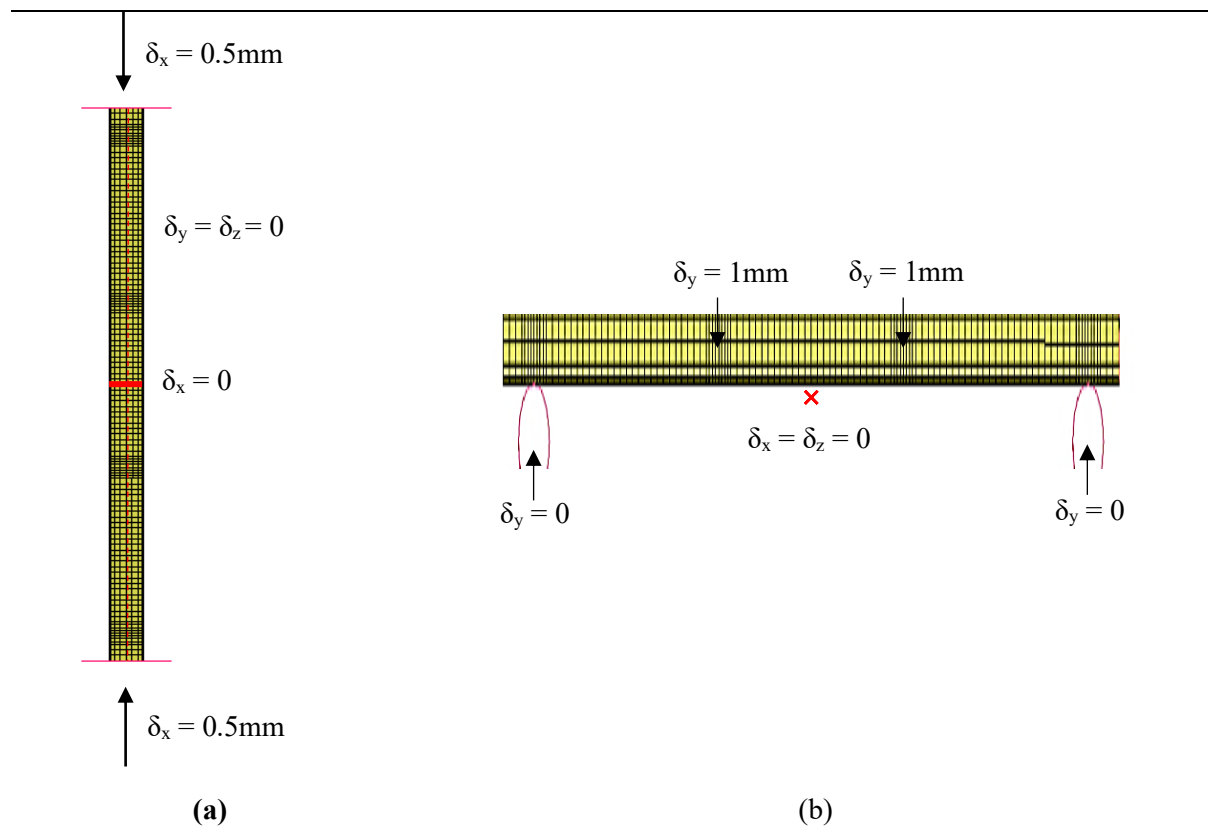


Figure 4.4.5: The FE model used to analyse the sensitivity of Poisson's ratio and assumption of isotropy on the posterior strut in (a) compression and (b) bending. (a) The sample is compressed between two rigid surfaces. The red dashed line indicates the long axis; this was fixed in x and z , where δ indicates the displacement at that point. The centre of the sample, indicated by the solid red line was fixed in y to prevent rigid body motion. (b) The top 2 cylindrical surfaces displaced the sample downwards, whilst the bottom 2 cylindrical surfaces remained fixed. The red cross indicates a boundary condition preventing motion in x and z directions.

To assess the assumption of isotropy, the model was assigned orthotropic material properties. E_1 was assigned to the long axis of the cylinder. The samples were axisymmetric and therefore transversely isotropic: the Young's Moduli in the other 2 directions, E_2 and E_3 , were the same. The baseline values

were assigned to assume isotropy: $E_1 = E_2 = E_3$. The Young's modulus was determined from the experimental tests (Table 4.4.1). The Poisson's ratio was assigned to be the same in all directions. The respective shear moduli were determined from equation (4.4.4). Due to the transverse isotropy $G_{12} = G_{13}$ remained constant as they are dependent on the unchanged E_1 . The final shear modulus, $G_{23} = f(E_2)$, is a function of E_2 and was therefore changed as the value of E_2 was changed to maintain the material relationship. The simulation was run in bending and compression to determine the respective baseline stiffnesses.

$$G_{ij} = \frac{E_i}{2(1 + \nu_{ij})} \quad (4.4.4)$$

To evaluate the assumption of isotropy 4 simulations were run, in compression and bending, varying the values of E_2 and E_3 by $\pm 20\%$ and $\pm 40\%$. The compressive and bending stiffnesses were obtained and compared to baseline stiffness that was calculated using the baseline, isotropic properties. Additionally, the sensitivity of the mechanical response of the strut to the Poisson's ratio was investigated. The same baseline stiffness was used when assessing the influence of isotropy. Four simulations were run, in bending and compression, varying the baseline Poisson's ratio by $\pm 20\%$, and $\pm 40\%$. The compressive and bending stiffness were recorded from each simulation and compared to the baseline values to calculate the relative stiffness change.

4.4.4 Sensitivity analyses results

The results for the sensitivity analyses examining the influence of isotropy are shown in Figure 4.4.6a. A change in these constants resulted in no change in the compressive stiffness, and a change of $\pm 0.5\%$ in the bending stiffness.

Figure 4.4.6b shows the results analysing the influence of Poisson's ratio on the bending and compressive stiffness. A change in Poisson's ratio of $\pm 40\%$ resulted in a change of compressive and bending stiffness of $\pm 0.1\%$ compared to the baseline value.

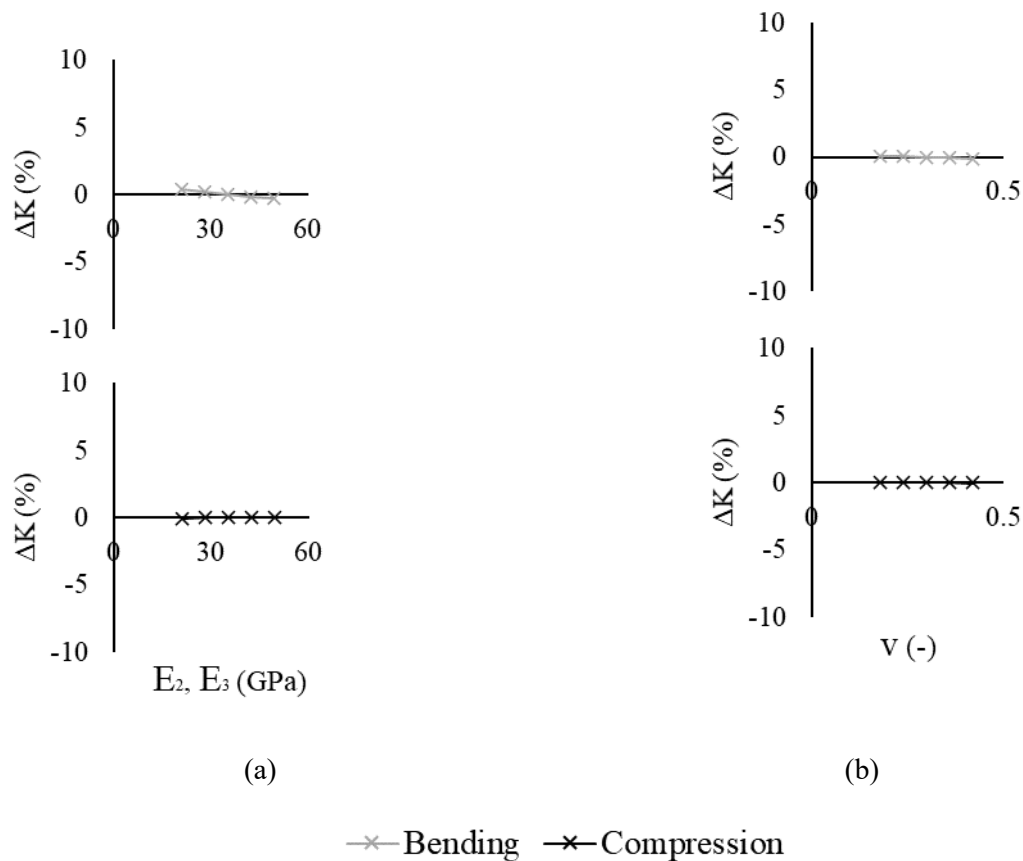


Figure 4.4.6: Sensitivity of (a) orthotropy of the Young's Modulus (E_2 , E_3) and (b) the Poisson's ratio (ν) on the bending and compressive stiffness relative to the baseline stiffness. ΔK is the change with respect to the baseline stiffness.

4.4.5 Discussion

The material properties of the composite struts used in the manufacture of the Momentum® PD-AFO were quantified in this study. Within this study the bending stiffness calculated during the 4-point bend test across the 3 samples was $271 \pm 8 \text{ N/mm}$. The PD-AFO is made up of 2 posterior struts, thus giving a total bending stiffness of $542 \pm 16 \text{ N/mm}$. This is within the range of bending stiffnesses recorded for struts used by Harper et al. ($466\text{-}981 \text{ N/mm}$) using a 3 point bend test set up [64], and Esposito et al. ($490\text{-}1029 \text{ N/mm}$) [56].

Variability in the calculated Young's modulus was seen between and within samples in both bending and compression. The standard deviation and interquartile range were greater in compression. It is thought that these variations are due to inherent variability within the compression test set up due to non-normal contact surfaces between the sample and the fixture on the material testing machine (due to the tolerance when cutting the sample). Steps were taken to minimise repeat bias, by rotating samples within the testing machine. Variability is also likely due to manufacturing differences, demonstrated by the small differences in diameter between samples. To improve this, additional

samples could be tested. However, for the purpose of this study the accuracy of the results was deemed acceptable and further testing was not carried out.

Within the experiments, the strut composites were subjected to the 2 main modes of loading that are experienced by the posterior struts during gait. To calculate the Young's modulus, the strut composite was assumed to behave in a linear manner. However, the Young's moduli were statistically different when calculated from the compression and bending tests. This could be explained by the non-linear behaviour of the strut composite; the non-linearly elastic composite material has a higher resistance in tension, which is present in the bending tests, than compression. However, although statistically different, the Young's modulus calculated from the bending tests was only 8.4% higher than that calculated in the compression tests and the mean values calculated from each test were also within $\pm 1SD$ of each other. This would result in a small percentage error in calculation when using the mean Young's modulus calculated from both tests, resulting in a slight under prediction of stresses in compression, and a slight over prediction of stresses in bending. Since the Young's modulus derived is suitable for the modes of loading of interest and within the range of accuracy required for the application within this study, it was deemed an acceptable assumption to model the strut composite as a linear material with an average Young's modulus derived from compression and bending tests. The plasticity, failure and fatigue behaviour of the strut composite were not investigated, though a brief check was undertaken to confirm no buckling would occur during compression at the loads applied (see Appendix 12.1.7). During gait, it is thought that the struts do not plastically deform over the long periods of use by patients. Therefore, the assumption of elasticity is valid within the range of the loading of interest. The struts did not reach their plastic limit or fail under the experimental loading cases tested within this study.

The posterior struts were assumed isotropic. The sensitivity analysis evaluated the influence of this assumption on the 2 main modes of loading seen during gait. The change in stiffness was $<0.5\%$ in bending, with no change in compression. Therefore, the assumption of isotropy was deemed acceptable for the range and modes of loading that are applied during gait.

Within this section, the material properties of the composite struts were determined. A linearly elastic and isotropic material behaviour was deemed acceptable for the range and modes of loading experienced by the PD-AFO during gait.

4.5 HEEL WEDGE AND FOAMS

Three non-linearly elastic materials are used in the manufacture of the PD-AFO: a polyurethane foam, and 2 unknown foams labelled *Foam A* and *Foam B*. The polyurethane has been previously described in the literature as the material used to manufacture the heel wedge [36, 60]. The heel wedge is thought to deform during loading response, reducing the peak load through the limb, mimicking the action of plantarflexion during normal gait [60]. The 2 other foams of unknown material are used in

the shin pad, sole and ankle pads. These foams form the contact areas between the limb and PD-AFO, providing comfort to the user. They are expected to have minimal effect on the overall deformation and mechanical response of the PD-AFO due to their high compliance relative to the other components. Within the gait cycle the main mode of loading for all foams is compression. A thicker layer of foam that forms the shinpad is labelled *Foam A* for the purposes of this study. The thinner layer of foam that forms the other contact components (sole, medial ankle pad and lateral ankle pad) is labelled *Foam B*. Visual examination suggested that these two foams are the same material, however, both were experimentally tested to evaluate this.

4.5.1 Experimental protocol

Foams are hyperelastic materials and can be characterised by their non-linearly elastic stress-strain behaviour. To determine the stress-strain curve, an experimental compression test was carried out. Samples of each foam were provided by Blatchford. A punch biopsy pen, 8 mm in diameter, was used to prepare 3 samples of *Foam A* and *Foam B*. A 12 mm punch was used to cut the samples of polyurethane. The diameter and thickness of each sample were measured 3 times using Vernier callipers. The samples of the polyurethane were less consistent in size and therefore 2 additional samples were cut (totalling 5 samples).

Compression tests were performed in a material testing machine (5866 series, Instron, High Wycombe, UK) using a load cell with a maximum capacity of 500N; the data-capture frequency was 50Hz. The test set-up is shown in Figure 4.5.1. Before placement of each test sample on the machine, the surface of the compressive platens was greased to prevent the sample from sticking. The materials testing machine top jog was manually lowered and the displacement was manually zeroed when the force reading reached 2N (tare load).

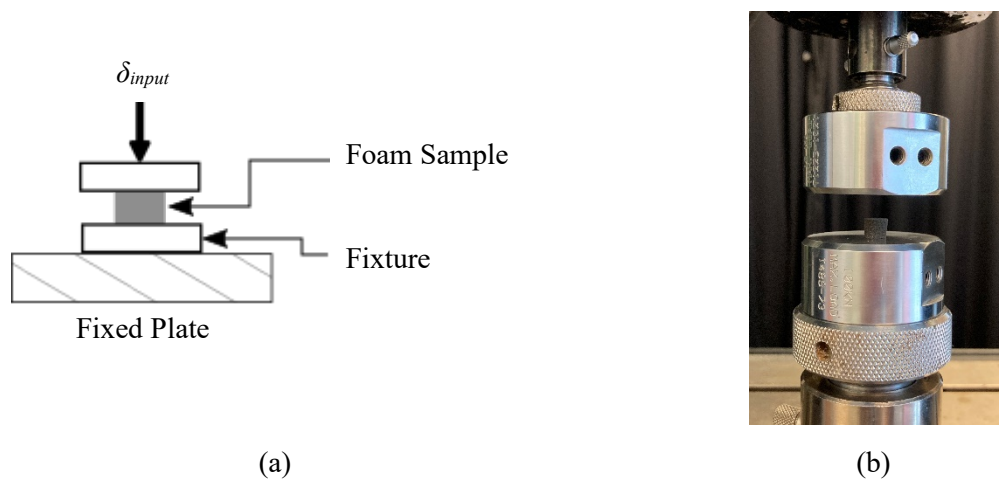


Figure 4.5.1: (a) A schematic of the experimental test set-up showing the applied displacement, δ_{input} , and (b) an image of the fixtures and a thick foam sample set up in the uniaxial materials testing machine

Each test compressed the sample from 0-80% strain for 25 cycles, with the last 5 cycles analysed. This was to mimic the cyclical compression the foam would experience during gait. The maximum strain was set to 60% for the polyurethane samples, as their larger size meant that the force limit of 500 N load cell was reached.

A strain rate of 0.1s^{-1} was used for all foams. Both *Foam A* and *Foam B* were not expected to experience strain rates higher than 0.1s^{-1} during gait due to their function and their location.

The cyclical force-displacement curve was recorded. The last 5 cycles of each test used to determine a stress-strain curve for each sample. An average stress-strain curve was then taken across samples to derive a representative mean mechanical response of each foam. For *Foam A* and *Foam B* the stress-strain curves recorded for both were compared to determine whether one material formulation would be suitable for both foams.

For each foam, the experimental, engineering stress was calculated using equation (4.4.1) and the experimental, engineering strain was calculated using (4.4.2). Each stress-strain curve was imported into Mentat. Using the experimental data-fit function, the stress-strain curves for each foam were fitted to an Ogden material formulation, shown in equation (4.5.1), the full formulation can be seen in Appendix 12.1.8 [80]. W is the strain energy, λ is the true strain, and μ and α are material constants to be derived. For a second order material model, with $N=2$ terms, 4, independent material constants for each foam were calculated.

$$W = \sum_{n=1}^N \frac{\mu_n}{\alpha_n} \left(\lambda^{\alpha_n} + 2\lambda^{-\frac{\alpha_n}{2}} - 3 \right) \quad (4.5.1)$$

To confirm the material formulation for each foam, 3 axisymmetric FE models were produced, an example of which is shown in Figure 4.5.2. The model was compressed between two surfaces, undergoing a compression of up to 60% strain for the polyurethane foam, and 80% strain for *Foam A* and *Foam B* were applied to the model from the applied displacement, δ . The symmetry constrained the model in all directions except that of the applied displacement. Each model was assigned the mean diameter and mean thickness of each foam type, respectively. Following completion of the simulation the reaction force was obtained from the same point as the applied displacement. The force-displacement curve from the FE model was compared to the experimental force-displacement curves.

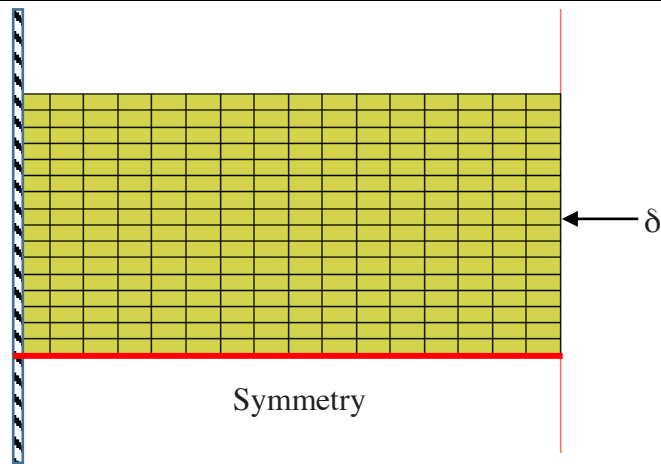


Figure 4.5.2: An axi-symmetric FE model of the polyurethane foam sample. The horizontal red line indicates symmetry. δ is the displacement applied to the rigid line (orange vertical line), compressing the foam.

4.5.2 Results

The heel wedge samples had a mean cross-section of $100.79 \pm 3.00 \text{mm}^2$ and a mean thickness of $11.89 \pm 0.23 \text{mm}$. The samples of *Foam A* had a mean area of $48.11 \pm 2.24 \text{mm}^2$ and a mean thickness of $6.63 \pm 0.05 \text{mm}$. The samples of *Foam B* had a mean area of $49.60 \pm 1.93 \text{mm}^2$ and a mean thickness of $3.19 \pm 0.07 \text{mm}$.

4.5.2.1 Material Formulation

4.5.2.1.1 Heel-wedge

The constants determined for the Ogden material model are shown in Table 4.5.1. The computed error by Mentat is the relative error between the two curves determined by the method of least squares. The stress-strain curve fitted with the Ogden material model can be seen in Appendix 12.1.9.

Table 4.5.1: Material coefficients of the heel wedge represented with an Ogden material model. μ_1 , α_1 , μ_2 , and α_2 are all material constants used in the material formulation and K is the bulk modulus.

μ_1 (MPa)	α_1	μ_2 (MPa)	α_2	K (MPa)	Computed Error
-7.44e-07	-0.0536	0.231	1.56	899	0.00243

4.5.2.1.2 Foam A and Foam B

Figure 4.5.3 shows the stress-strain curves calculated during the experimental testing of *Foam A* and *Foam B*. Both foams had very similar stress-strain curves and were within 1 SD of each other. This strongly suggests they were of the same material and for the remainder of this chapter will be referred to as *Foam AB*.

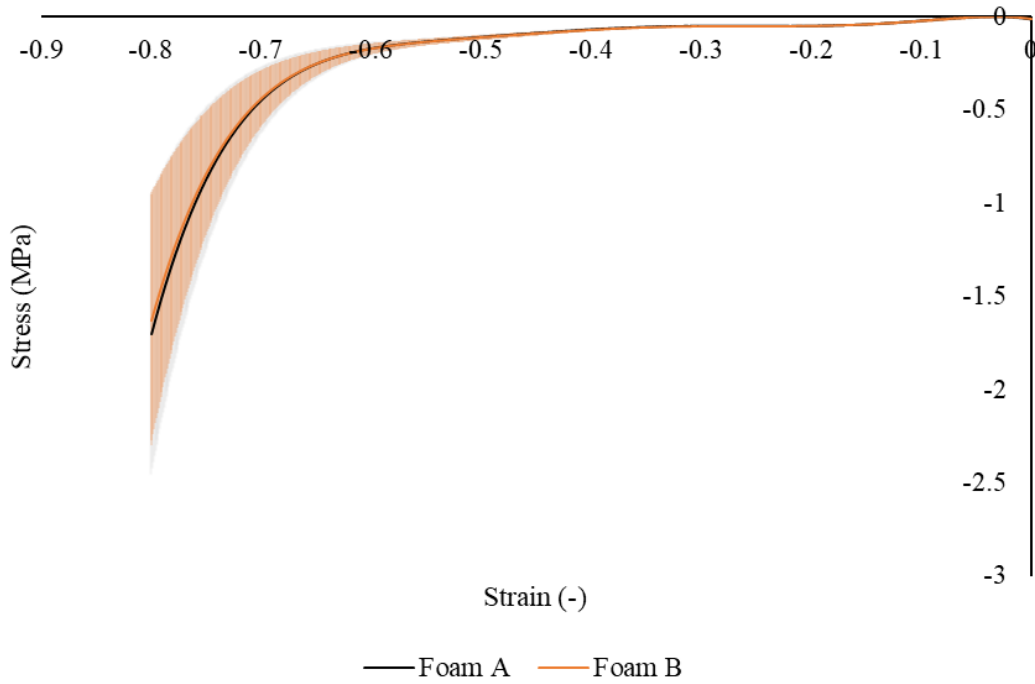


Figure 4.5.3: Experimental stress-strain curve for Foam A and Foam B. The shaded area denotes 1 SD..

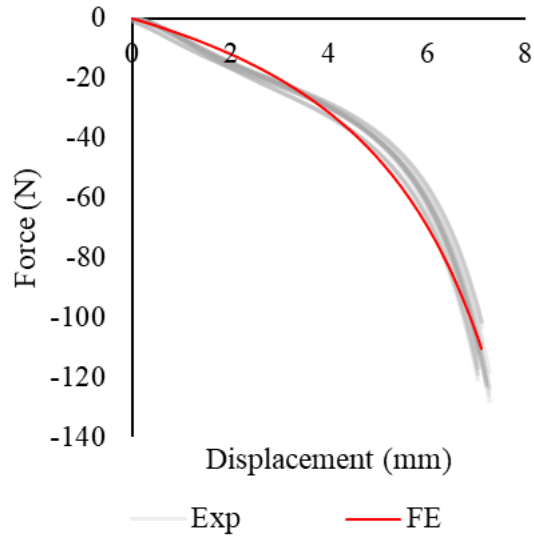
The material coefficients of the fitted Ogden material model of *Foam AB*, along with the computed error (method of least squares) in these calculations, are shown in Table 4.5.2. The stress-strain curve fitted with the Ogden material model can be seen in Appendix 12.1.9.

Table 4.5.2: Material Coefficients of Foam AB represented with an Ogden material model. μ_1 , α_1 , μ_2 , and α_2 are all material constants used in the material formulation. K is the bulk modulus.

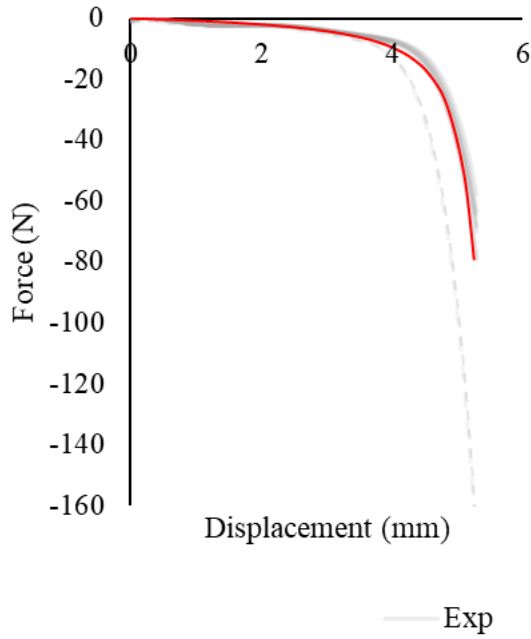
μ_1 (MPa)	α_1 (-)	μ_2 (MPa)	α_2 (-)	K (MPa)	Computed Error
-0.000107	-4.78	0.0365	1.61	149	0.00137

4.5.2.2 Comparison of force-displacement curves

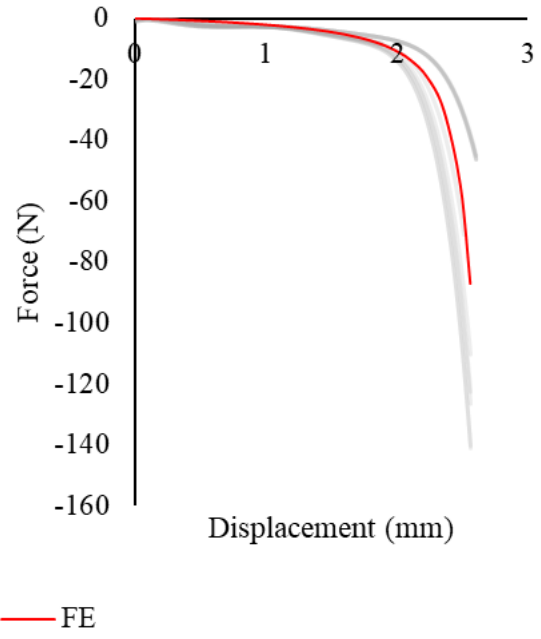
The force-displacement curves obtained from the experimental compression tests, and the FE compression test, for all foam samples are shown in Figure 4.5.4. It can be seen that for all foams the FE model is in good agreement to the force-displacement curves.



(a)



(b)



(c)

Figure 4.5.4: The force-displacement curves recorded during the experimental compression tests of the foams samples and obtained via the FE simulation for (a) the polyurethane foam (b) Foam A and (c) Foam B

4.5.3 Discussion

The stress-strain curves for *Foam A* and *Foam B* were similar. As such it was deemed acceptable to assume that they were manufactured from the same material. Both the polyurethane foam, and *Foam AB*, used in the remaining components, were characterised using the Ogden material formulation. The material constants established resulted in a computational force-displacement curve in agreement with the experimental data. The maximum absolute errors between the material model and experimental data were small, at $< 0.08\text{MPa}$. These were considered to have negligible effect on the overall mechanical response of the PD-AFO that consists of much stiffer materials, and the accuracy obtained was enough for the required function within the FE model.

During gait there may be a small amount of shear force applied to the sole. However, this is predicted to be very small compared to the normal force experienced in these regions; during gait the normal vertical ground reaction forces are much greater than the shear mediolateral and anteroposterior forces. Therefore, it was deemed not to require further investigation. Additional shear force may be applied to the shin pad, however this thesis does not focus on the contact between the shinpad and the leg.

The heel wedge had previously been tested using a durometer by Ikeda et al. [60]. The study examined two stiffnesses and these had durometer readings of 50.0-78.0 on the OO scale [60]. This gives a crudely estimated Young's modulus of 0.1-1MPa [81]. Approximating a linear curve to the stress-strain curve ($R^2 = 0.945$) of the polyurethane results of this study would give a Young's modulus of 1.16 MPa. This is close to the estimations using the durometer tests.

Within this section, it has been confirmed that *Foam A* and *Foam B* are the same material. The behaviour of *Foam AB* and the heel wedge have been modelled using an Ogden material model. The most significant foam, in terms of mechanical response of the PD-AFO, is the heel wedge, and this has been demonstrated to be close to values previously recorded [60].

4.6 CONCLUSION

The material behaviour for each of the components used in the manufacture of the PD-AFO have been determined in this chapter. This is the first study to characterise these components fully and will allow for the accurate development of an FE model. Experimental tests were performed when samples of the material were available. Literature was used to ascertain suitable material constants where samples were not available. In the cases where literature values were adopted, a detailed sensitivity study was performed to determine the influence of the respective material constant on the overall material behaviour to determine whether further investigation into that property was required. These material properties are utilised in the following chapters for experimental analyses and development of an FE model of the PD-AFO. In the next chapter gait analysis of a healthy subject will be performed to quantify the changes in lower limb loading when wearing the PD-AFO.

5 LIMB LOADING DURING GAIT

Chapter 3 highlighted limitations of previous studies analysing the gait of injured cohorts when wearing the PD-AFO. Most notably, within the methodology, there was a difficulty in providing a strong control variable. Additionally, a lack of understanding remains with respect to how the PD-AFO alters forces experienced by the limb. To address this, gait analysis was carried out on a healthy subject, with and without a PD-AFO, allowing a direct comparison between the two gaits. The load and pressures experienced by the limb are evaluated to improve understanding of how the PD-AFO alters external loading.

5.1 INTRODUCTION

As described in Chapter 3, AFOs are designed to augment gait and improve the functional outcome for patients. Many different designs of AFOs exist. When prescribing an AFO, one aim is to mimic a healthy gait, restoring function. The PD-AFO was developed using design features seen in a variety of AFOs [17]. This is thought to be the reason for its success across a broad spectrum of patients, all with different injury types, locations, and mechanisms.

Different components of the PD-AFO are hypothesised to provide different alterations to gait. These alterations may limit movement, reduce loading, or provide additional power, all with the aim of augmenting gait or reducing pain. These hypothesised alterations have not, however, been fully evaluated in the literature, so it cannot be conclusively stated what effects the PD-AFO have on gait. Table 5.1.1 shows the hypothesised gait alterations as a result of wearing the PD-AFO, and the design aspects of the PD-AFO thought to be responsible for them [36, 37, 82]. Also listed are possible gait-analysis metrics (described in Chapter 2) that could be relevant to evaluate each hypothesis.

Understanding how the PD-AFO alters gait is an important consideration for the patient, both in the immediate and long term. In the short term, it may provide insight into which functional deficits or regional injuries may perform well with the PD-AFO. It may also highlight unintentional and potentially detrimental alterations in gait, providing additional information to clinicians. In the long term, it may highlight possible, long term effects of usage, such as excessive offloading, allowing pre-emptive physiotherapy and usage limits to be implemented to minimise risks if required.

Table 5.1.1: Design components and their alterations to gait. ML is mediolateral, AP is anteroposterior, CoP is centre of pressure, GRF is ground reaction force. Adapted from Bennet, Potter et al. and understanding of previous AFOs. [36, 37, 82]

Hypothesised Alteration of Gait	Design Aspects of the PD-AFO	Gait Metrics to Evaluate
Prevent plantarflexed ankle angle during the swing phase (and inadvertently during early stance)	Stiff base plate inhibits rotation of the foot in the sagittal plane	Ankle angles in sagittal plane
Reduction in the peak force experienced by the PD-AFO and limb during loading response (due to inadvertent limitation of plantarflexion during this phase)	-Deflection of posterior struts -Deformation of the heel wedge	-Plantar force -GRFs
Reduction in peak dorsiflexion moment about the ankle joint during late stance phase	Anterior cuff (fixed relative to the posterior struts) limits anterior tibial progression and anterior progression of CoP	- Joint ankle, moment, power and work -AP CoP -Plantar pressure distribution
Aid with propulsion during late terminal stance phase and pre-swing	-Relaxation of posterior struts during pre-swing after deflection in terminal stance -Relaxation of base plate during pre-swing acting as a lever arm	-Joint ankle, moment, power, and work -AP GRF -Plantar force -Plantar pressure distribution
Reduction in loading through the ankle joint	Anterior cuff acts as a patellar-tendon bearing cuff, allowing force to be diverted through the PD-AFO and not load the limb	-Plantar Force -GRFs
Reduction in peak stress/pressure to the plantar aspect of the foot. Achieved by decreasing peak forces and/or increasing plantar area over which it acts	-Deflection of the posterior struts -Deformation of the heel wedge -Patella-tendon bearing cuff reduces load through the limb -Anterior cuff limits anterior progression of CoP	Plantar Pressure

The limb and PD-AFO can be modelled as a simple system, consisting of 2 springs in parallel of unknown stiffness, shown in Figure 5.1.1. When considering alterations in gait, it is important to understand whether the metric being measured evaluates the overall, combined limb-PD-AFO system, or whether it provides information on changes seen in the limb alone or the PD-AFO alone. For example, it is hypothesised that the load through the ankle joint is reduced. This would be evaluated by investigating the force through the lower limb only, by measuring the plantar force. In Figure 5.1.1 the points of measurement of GRF (blue line) and plantar force (green line) are shown. Whilst for a limb with no PD-AFO (Figure 5.1.1a) the GRF and plantar force are measured at the same point and therefore are predicted to be the same, when a limb is wearing the PD-AFO (Figure 5.1.1b) the point of measurement is different. The plantar force is measured between the lower limb and the PD-AFO and is therefore representative of the force through the lower limb only. The GRF is the sum of the force through the lower limb (plantar force) and the force through the PD-AFO. For each hypothesis it is important to ensure the gait analysis metric, measures the desired output.

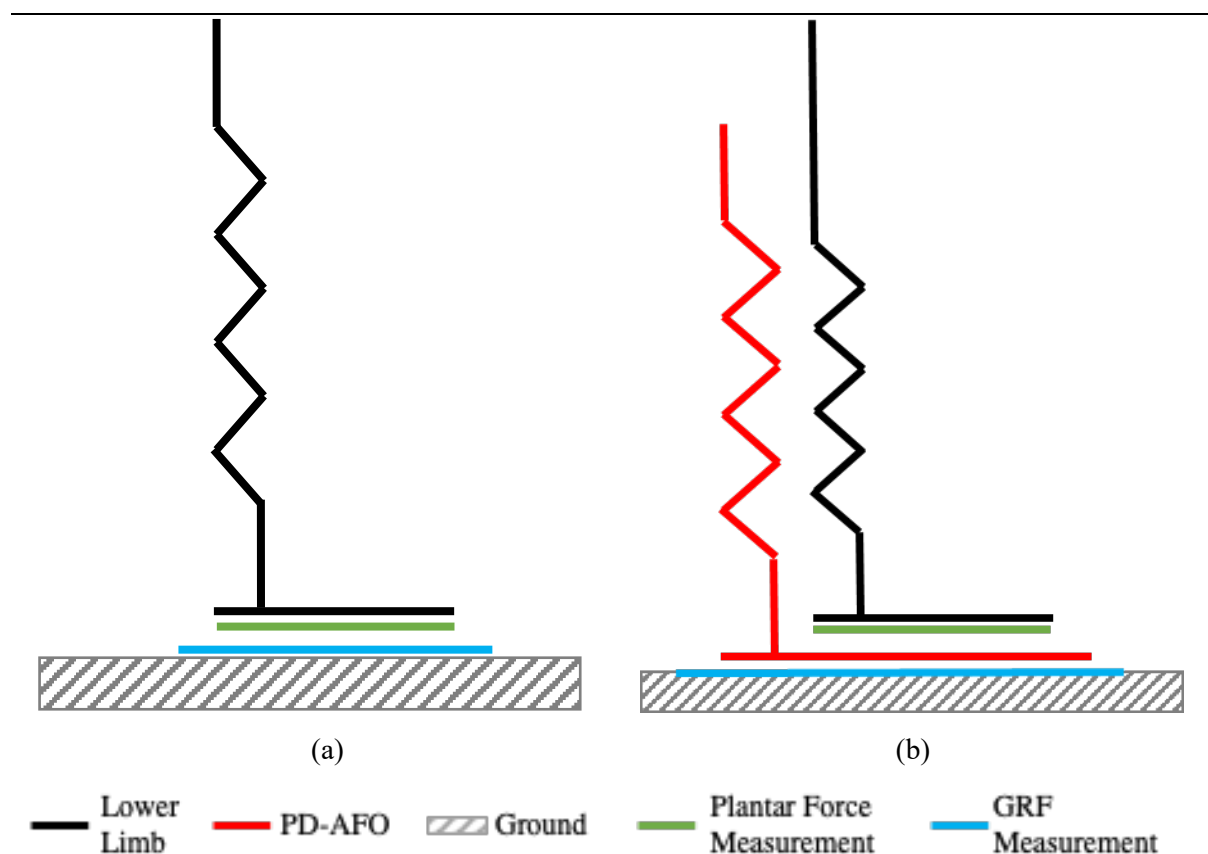


Figure 5.1.1: Location of where plantar force and ground reaction force (GRF) would be recorded, modelling the limb and PD-AFO as springs

5.2 LITERATURE

Within this section, previous studies are evaluated against the hypothesised gait alterations described in Table 5.1.1, distinguishing between those hypotheses that have been sufficiently researched and those that require further investigation. Previous published studies have predominantly focussed on joint kinematics and kinetics to establish the PD-AFO's influence on gait [52-57]. Metrics, including GRF, CoP, and plantar pressure, have all been analysed, but not extensively or simultaneously [38, 56, 59]. To date, no studies have investigated, specifically, the effect that wearing the PD-AFO has on the forces experienced by the lower limb only.

5.2.1 Plantarflexion and Peak Forces

Of the hypothesised alterations in gait described in Table 5.1.1, the limitation in the range of the ankle angle is the most researched [52-57]. Literature has demonstrated that during the swing phase of gait the ankle is prevented from entering a plantarflexed angle [52-57]. This is beneficial to prevent unwanted footdrop (the inability to prevent plantarflexion). The stiff base is thought to be responsible for this gait alteration. Whilst the influence of the base stiffness on the plantarflexion angle has not been directly evaluated, it is acceptable to assume that the base causes this alterations, as prevention of plantarflexion is a feature of many AFOs [26].

Literature, however, has also demonstrated that the plantarflexed angle is minimised during loading response [52-57]. Plantarflexing of the foot during this phase in normal gait, due to loading of the limb at a point to the posterior of the foot and tibia, reduces the rapid loading of the limb, by converting the force into a rotational moment [60]. Removal of this ability to plantarflex when wearing the PD-AFO theoretically increases peak forces during early stance. Peak vertical GRFs were, however, found to be unchanged by the PD-AFO, compared to healthy controls [57]. This supports the hypothesis that another mechanism of action of the PD-AFO reduces the peak GRF, compensating for the inability to plantarflex [60]. It is thought that the posterior struts and/or heel wedge deflect/deform, increasing the time over which the force acts, thereby reducing the peak load for the same change in momentum [60].

CoP velocity was evaluated by Ikeda et al. in relation to the change in heel wedge height and firmness [60]. A softer, shallower heel wedge resulted in greater CoP velocities (with the differences being statistically significant between the shallowest and deepest heel wedge) [60]. Theoretically, an increase in velocity magnitude would result in an increase in momentum, and therefore in an overall change in momentum. These data, however, suggest that a deeper heel wedge results in a smaller change in momentum. This supports the hypothesis that deformation of the heel wedge alters the peak forces, increasing the time over which the force is absorbed for the same impulse. Further research is needed to understand whether the posterior struts contribute to the reduction in peak GRF in early stance.

5.2.2 Dorsiflexion Moment

It is hypothesised that the dorsiflexion moment about the ankle joint is reduced during terminal stance. This hypothesis requires evaluation of the moments experienced by the lower limb only, not the combined limb-PD-AFO system. As discussed in Chapter 3, although studies were able to measure ankle angle, and determine a limited degree of plantarflexion, the ankle moment, work, and power calculated were for the combined limb-PD-AFO system, as the GRF was used to calculate them [52-57]. Therefore, these cannot be used to determine the dorsiflexion moment experienced by the limb alone during terminal stance phase.

Stewart et al. found limited anterior progression of the CoP in the injured limb when wearing the PD-AFO compared to the uninjured limb during the same gait trial and compared to the injured limb when not wearing the PD-AFO (Figure 5.2.1) [59]. A more anterior CoP supports the hypothesis of a reduced dorsiflexion moment in the ankle joint due to a reduced moment arm. The study also demonstrated that the PD-AFO reduced the peak plantar pressure by ~64% in the forefoot of the patients' injured limbs (n=42) compared to walking without the PD-AFO [59]. The reduction in forefoot pressure occurred during terminal stance, again supporting a reduction in dorsiflexion moment [59].

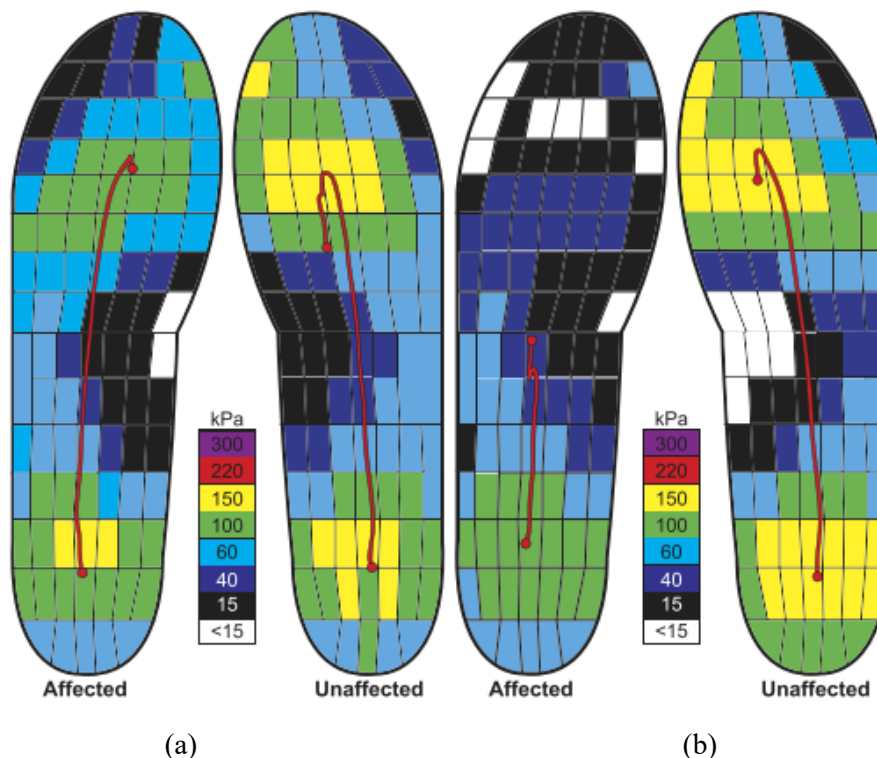


Figure 5.2.1: Results from Stewart et al. showing the averaged peak plantar pressures (coloured patches) and the CoP progression line in red, in the affected (injured) and unaffected foot when (a) not wearing the PD-AFO on the affected foot and (b) wearing the PD-AFO on the affected foot [59]. Image reproduced with permission from the copyright holder Wolters Kluwer Health

Strut alignment has also been found to influence the CoP location, and therefore, the dorsiflexion moment [38]. Setting the strut alignment to be 3° more dorsiflexed, resulted in an increased peak dorsiflexion ankle angle by 1.62° [38]. It is logical that the peak dorsiflexion ankle angle is correlated to the extent of tibial progression. These findings, therefore, suggest that it is the anterior cuff, fixed relative to the posterior struts, that contributes to a reduction in the dorsiflexion moment.

5.2.3 Propulsive Forces

Whilst the dorsiflexion moment is hypothesised to be reduced within the lower-limb, the propulsive forces, exerted by the combined limb-PD-AFO system, are thought to be increased compared to the injured limb alone. Propulsive forces of the combined limb-PD-AFO system ($0.15\pm 0.02\text{BW}$) were shown to be lower than those recorded on the uninjured side ($0.19\pm 0.03\text{BW}$), and lower than those seen in healthy controls ($0.18\pm 0.02\text{BW}$) [57]. Harper et al. also demonstrated a lower propulsive impulse when compared to the uninjured limb [65]. Bennet indicated¹, however, that propulsive forces of the combined limb-PD-AFO system increased compared to those seen in the injured limb alone (when not wearing the PD-AFO) [36]. These findings suggest that, although the PD-AFO does not restore propulsive forces to levels seen in healthy subjects, it does improve them. The PD-AFO may not need to restore propulsive forces to a healthy level to provide a clinical benefit; improvement may be adequate. Further research on the gait of injured patients, without the PD-AFO, would provide evaluation on whether the PD-AFO aids propulsion, however this is outside the scope of this thesis. The ESAR characteristics of the posterior struts is thought to be responsible for aiding propulsion. No studies have yet evaluated the behaviour of the posterior struts during gait, which would allow analysis of whether the posterior struts do provide propulsive power.

5.2.4 Loading of the Limb

This author could find no studies to date that evaluated any change in loading of the limb when wearing the PD-AFO. Although peak vertical GRFs were found unchanged in patients wearing the PD-AFO compared to healthy controls, limb forces may still be altered [57]. Whilst Stewart et al. did not analyse the force through the limb, they did analyse the peak plantar pressures in the injured limb when wearing and not wearing the PD-AFO [59]. They found a reduction in total peak pressure by 26.4% when wearing the PD-AFO, suggesting ‘offloading’ of the injured limb [59]. The study did not, however, present the change in pressure distribution throughout the gait cycle. Analysing the plantar pressure throughout gait, combined with evaluation of the force, would allow analysis of the mechanism by which the pressure is reduced, and whether this reduction is due to a reduction in peak forces, or a change in plantar area over which the force is applied. This may provide insight into why the PD-AFO is successful for certain regional injuries.

¹ Study carried out with the B.O.B

Stewart et al. suggested that the PD-AFO offloads the limb, and Blatchford advertise the PD-AFO as the '*Momentum Offloading Brace*' [59, 83]. AFOs are not often designed to offload the limb; other design features, such as those that limit the plantar flexion ankle angle are more common. If indeed the PD-AFO offloads the limb, then it is plausible to hypothesise that its success in improving functional outcomes for high activity patients is in some part attributed to this design feature. Analysis of the force through the limb, in combination with measuring the GRF, could allow the quantification of the ratio of loading between the PD-AFO and the lower limb. This would provide information for clinicians, as well as allow further fine tuning of the PD-AFO to achieve a target loading ratio should this be desired by the clinician in certain cases. It is also important to help evaluate long term effects, for example excessively reducing the force through the limb may result in muscle shortening or bone loss.

5.2.5 Limitations

It should be noted that within the studies mentioned above, only 2 directly compared the same patients' gait with and without the PD-AFO [36, 59]. This is due to the inherent injury present if prescribed the PD-AFO, often meaning patients are unable to walk unaided and therefore the gait cannot be directly compared. Selecting only a cohort who are able to walk without the PD-AFO also introduces bias into a study. As most studies were unable to use the patients as their own control without the PD-AFO, they compared the gait of the injured limb wearing the PD-AFO to a healthy control cohort, and/or to the patient's uninjured limb (whilst wearing the PD-AFO on the injured limb). Research into how the PD-AFO changes the gait of the uninjured limb is limited, though some studies compared this limb to the healthy control group demonstrating that the PD-AFO changed the GRF and peak pressure of the uninjured limb [55, 57, 59]. Gait analysis using a healthy subject allows for direct comparison of gait with and without the PD-AFO, ensuring a strong control. It also allows analysis of how the PD-AFO alters the limb not wearing the PD-AFO. This will provide information for future trials with patient cohorts to use the uninjured limb as a control, whilst accounting for the changes in the uninjured limb.

Of the hypothesised alterations in gait shown in Table 5.1.1, previous literature has focussed on the ability of the PD-AFO to reduce the plantarflexion ankle during swing phase and loading response, and to reduce the peak dorsiflexion moment experienced by the limb during terminal stance, compared to healthy controls and the uninjured limb. To date, no studies have examined the force through the limb alone, when wearing the PD-AFO, or presented how the plantar pressure varies through the gait cycle. Evaluating the force through the limb, allows the following hypotheses to be evaluated:

1. The PD-AFO reduces the peak forces within the lower limb.

2. The PD-AFO reduces peak plantar pressures in the limb due to the reduction in peak forces through the limb.
3. The PD-AFO reduces peak plantar pressures by increasing the plantar area in contact.

These hypotheses can be evaluated experimentally, by examining the plantar force, GRF, CoP and plantar pressure during gait. The use of computational modelling would be very time intensive for metrics that can more easily be measured experimentally. This study will evaluate these hypotheses using a healthy subject, representative of the normative population. This is the first study to use a healthy subject to analyse the changes in the left and right limb when walking with and without the PD-AFO, removing the influence of injury and providing a strong control variable.

5.3 METHODS AND MATERIALS

5.3.1 Manufacture

A 38 year old male with no known, current, lower limb injuries or diseases (height 1.79m, mass 74kg) was fitted for a PD-AFO, the Momentum® brace, by Blatchford (copy of consent form in Appendix 12.2.1). To produce the PD-AFO, the lead clinical orthotist at the UK military Rehabilitation Centre fitted a cast on the subject's left leg, following the standard fitting protocol used in the Centre (Figure 5.3.1a). A clear mould was manufactured and fitted against the subject's leg to confirm the fit, which was then altered as required (Figure 5.3.1b).



Figure 5.3.1: (a) Initial fitting using plaster cast (b) Assessment of fit by orthotist

The PD-AFO was fabricated in carbon fibre, from the geometry of a clear mould and plaster cast, with the choice of posterior struts based on the subject's weight and activity level (high), as per standard protocol. The materials used to manufacture the PD-AFO have been described and characterised in Chapter 4. Following production, the orthotist confirmed the appropriate fit of the PD-AFO and made

the final trimmings of any excess material that may cause discomfort during use. The final PD-AFO, the Momentum, as worn by the subject without a knee-high sock, is shown in Figure 5.3.2.



Figure 5.3.2 PD-AFO as worn by the subject (a) without and (b) with trainers

5.3.2 Gait Trials

To understand how the PD-AFO alters the forces in the lower-limb, gait trials were performed on the healthy subject allowing a direct comparison of the subject walking with and without the PD-AFO.

The gait trials in which no orthotic was worn are referred to as *control gait* with the right limb referred to as the right control and left limb referred to as the left control. The gait trials in which the PD-AFO was worn are referred to as *PD-AFO gait* with the right limb referred to as the *shod limb* and the left foot referred to as the *PD-AFO limb*.

A gait lab with a 10 m long, raised walkway, instrumented with 2 force plates (Kistler, Advanced Mechanical Technology Inc, MA, USA) was used to analyse both the control gait and PD-AFO gait. The force plates recorded forces in all 3 directions at a frequency of 1200 Hz. The GRF data were collected using Vicon (Vicon Motion Systems Ltd, Oxford, UK).

The subject, for whom the PD-AFO was manufactured in section 5.3.1, was fitted with a PEDAR sensor in each shoe (Novel, Munich, Germany), used for measuring the plantar pressure distribution in 99 discrete areas on the sole of each foot. The PEDAR also returned the total force experienced by the plantar aspect of the foot (the plantar force) and the CoP. The PEDAR recorded at a minimum frequency of 50Hz.

During control gait the subject wore their own trainers. During PD-AFO gait the subject wore their own trainer on their shod foot and wore a different style trainer, one size larger on their PD-AFO foot,

to accommodate the orthotic. The subject had a heel wedge inserted between the PD-AFO and shoe to give a shank-to-vertical-angle of 10° , as recommended by the orthotist [84].

During control gait the PEDAR sensors were placed between the plantar aspect of the foot and the shoe. During PD-AFO gait the PEDAR sensors were placed between the PD-AFO and the plantar aspect of the foot, within the shoe. The sensors were zeroed each time the subject put on their shoes. The PEDAR sensors were set to record and the subject was asked to stamp 3 times to help align data. After the stamps, recording of the GRF was started. The subject was asked to walk from one end of the walkway to the other, at a self-selected velocity. This was repeated 10 times.

To evaluate whether increased use altered the subject's gait, their gait was additionally analysed on 3 separate occasions over a 4-day period with the same set-up described above. On each day the subject used the PD-AFO for at least 60 minutes before undergoing gait analysis on day 1, day 2 and day 4. 10 trials were performed with the PD-AFO on each day. The GRF and plantar force for each limb were analysed across the days. The results for these gait trials were analysed separately and not included in the main body of analysis.

5.3.3 Post-Processing

5.3.3.1 Data Alignment

Python was used to align and window the data from the PEDAR sensors and the force plates, demonstrated in Figure 5.3.3. Within 1 gait trial, several gait cycles were observed. The PEDAR sensors recorded all gait cycles within a gait trial, whilst the force plates only recorded one gait cycle. The PEDAR data were aligned with the GRF data using the changes in PEDAR force caused by the 3 stamps undertaken before the gait trial. The 3 stamps resulted in unique changes in the PEDAR force, different to those changes seen during normal gait. The period over which the stamps occurred was used as the initial time offset between the 2 data sets ('1.' in Figure 5.3.3). This was used to match the steps recorded by the PEDAR sensor with the steps recorded by the force plates. The steps from each data set were aligned, by manually adjusting the offset further ('2.' in Figure 5.3.3)

The data was windowed to select 1 gait cycle from each limb, from each gait trial ('3.' in Figure 5.3.3). This gait cycle was selected to include 2 clean force plate hits (one for each foot). A clean force-plate hit was where 1 limb wholly struck a force plate and no other part of the walkway. If 2 clean force-plate hits were not achieved within a trial, then the trial was excluded from analysis. One full gait cycle was established using the aligned GRF and PEDAR data, where 0% was when one foot impacted the floor (indicated by subscript 0 for the left and right limb Figure 5.3.3), and 100% was the same foot impacting the floor at its next step (indicated by subscript 100 in Figure 5.3.3). For each gait cycle the time was normalised to percentage of the cycle, from 0% to 100%. All data were linearly interpolated to give the respective values at 0.5% increments. To analyse the data against

time, the mean value of each metric at each percentage of the gait cycle was found, ± 1 standard deviation (SD). This was carried out for both control gait and PD-AFO gait.

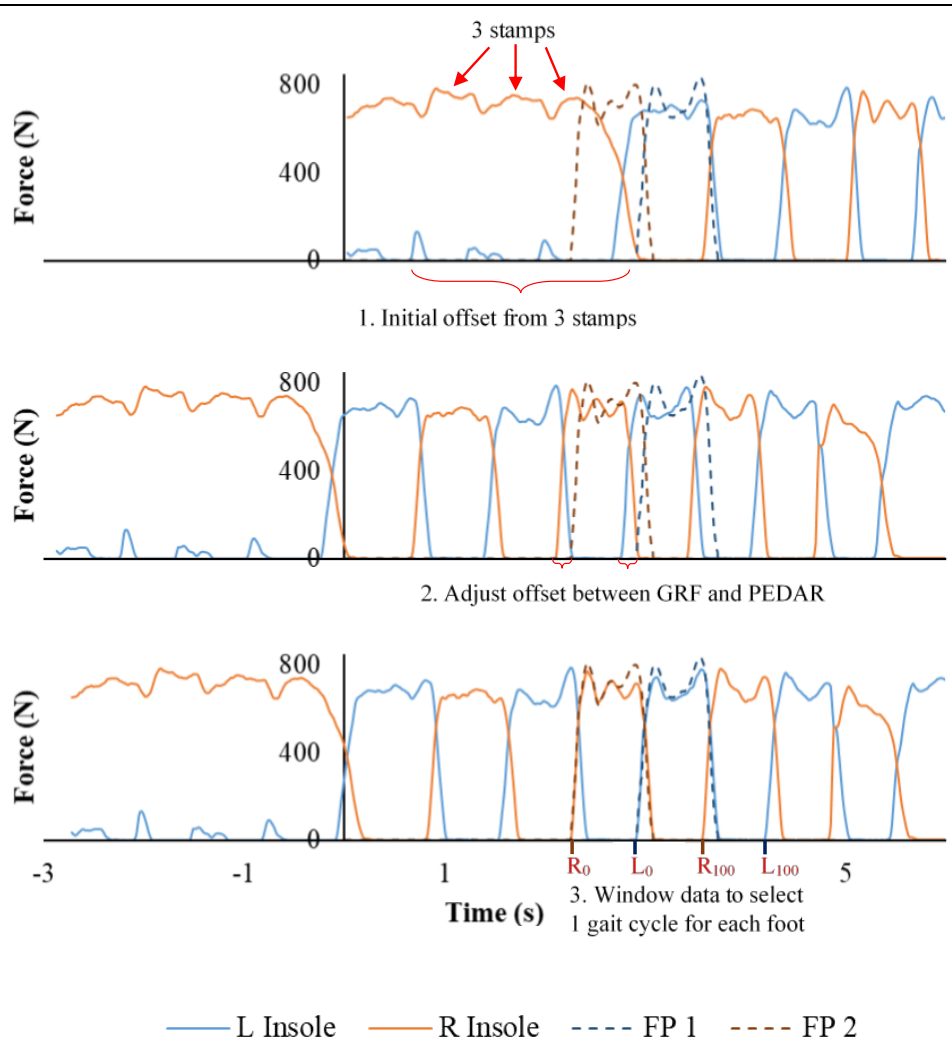


Figure 5.3.3: Alignment and windowing of PEDAR and force plate data. ‘L’ indicates a measurement for the left foot and ‘R’ indicates a measurement for the right foot. ‘insole’ is the plantar force recorded by the PEDAR sensors. FP 1 and FP 2 are the ground reaction forces recorded by the force plates. A subscript 0 indicates the start (0%) of the gait cycle chosen for that limb and a subscript 100 indicates the end (100%) of the gait cycle chosen.

5.3.3.2 Ground Reaction Force and Plantar Force

The GRF, recorded by VICON, was recorded in the anteroposterior direction (GRF_x), the mediolateral direction (GRF_y) and the vertical direction (GRF_z). The total GRF was calculated from the force readings supplied by the force plates using equation (5.3.1). To determine which limb contacted the force plate both video and the timing of the PEDAR sensors was used.

$$GRF = \sqrt{GRF_x^2 + GRF_y^2 + GRF_z^2} \quad (5.3.1)$$

The plantar force, as recorded by the PEDAR sensor, was automatically post-processed by the Novel software (Novel, Munich, Germany) and outputted, for each limb in each gait type. During some gait trails PEDAR data were dropped resulting in all measurements reading zero. These measurements were calculated by linearly interpolating between the previous and next non-zero number (this was also done for plantar pressure and CoP). The GRF and plantar force were normalised for the subject's body weight.

To calculate the load through the PD-AFO equation (5.3.2) was used. The ratio of loading between the PD-AFO and lower limb could then be calculated.

$$F_{PD-AFO} = GRF - F_{plantar} \quad (5.3.2)$$

5.3.3.3 *Plantar Pressure*

The 99 discrete measurements of pressure, recorded by the PEDAR were categorised into 8 sections to closely match the regions analysed by Stewart et al. [40]: *Lesser Toe, Greater Toe, Lateral Forefoot, Medial Forefoot, Lateral Midfoot, Medial Midfoot, Lateral Hindfoot, Medial Midfoot* (Figure 5.3.4). The toe region covered 17% of the total area of the foot, the forefoot covered 28%, the midfoot covered 28% and the hind foot covered 26%. Within each section the discrete measurements were averaged to give the mean pressure value in that region. The mean pressure value was normalised for the subject's body weight to give a unit of kPa/N.

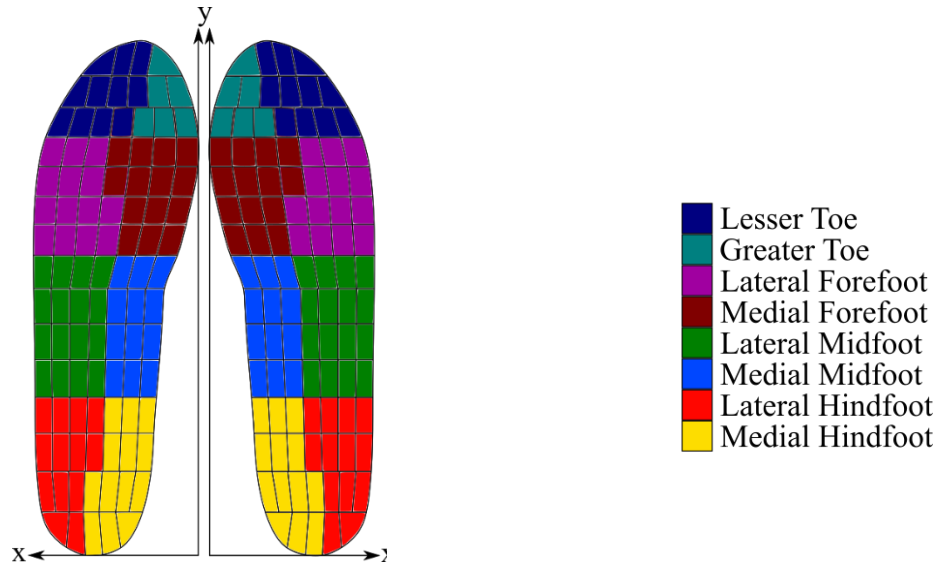


Figure 5.3.4: Map of 99 discrete pressure sensors in the PEDAR, divided into 8 regions.

5.3.3.4 Centre of Pressure

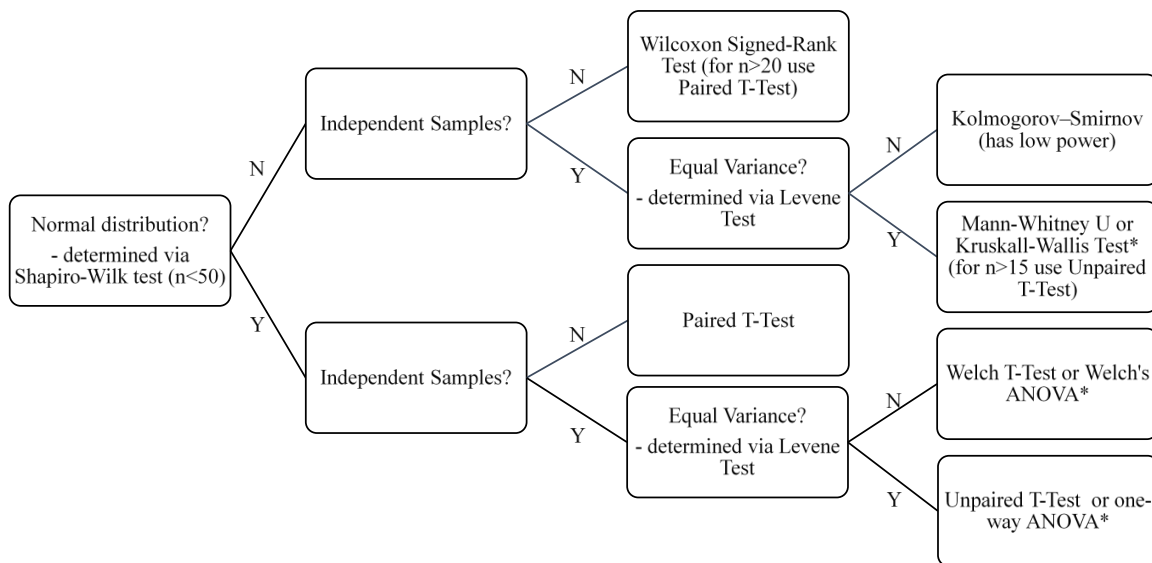
Novel software automatically post-processed the data to output the CoP throughout the gait cycle. The measurements were described by x and y in the co-ordinate system of the PEDAR sensors, as seen in Figure 5.3.4. An increase in x indicated a movement of the CoP in the lateral direction and an increase in y indicated a movement in the anterior direction.

5.3.3.5 Analysis between points in gait

Analyses between limbs were performed for the peak value of each metric that occurred during the loading response and early midstance phase (between 2-20% of the gait cycle), and the peak value that occurred during the late terminal stance phase and pre-swing phase (between 40-70% of the gait cycle), unless otherwise stated. All statistical analyses were assumed paired (i.e. not independent samples) and calculated in Python following the process shown in Figure 5.3.5.

For the total GRF and plantar force these peak values reference the time points in gait named weight acceptance, T_{WA} , and push off, T_{PO} . For clarification, for all metrics (except mediolateral GRF) the peak value occurring during the loading response and the early midstance phase is referred to as the peak at weight acceptance. The peak in data that occurs during the late terminal stance and pre-swing phase is referred to as the peak at push off.

Additionally, the transition between the midstance phase and the terminal stance phase was defined as the time at which midstance occurred, T_{MS} . This was calculated as the midpoint between the time at which weight acceptance, T_{WA} , and push off, T_{PO} , occurred. The value of each metric at midstance was taken as a mean of all the values that occurred across the time range, denoted by $T_{MS} \pm 5\%$. For each limb and metric the value of T_{WA} , T_{MS} , and T_{PO} could be different.



*for 2 or more independent groups; further analysis required

Figure 5.3.5: Process to determine the appropriate statistical test for each comparison coded in Python

5.4 RESULTS

During control gait, 2 clean force plate hits were seen in all trials (n=10), whilst during PD-AFO-assisted gait 4 trials were excluded (n=6). All figures in this section are presented referencing each limb to start its own gait cycle at 0%. This allows for direct comparison, through the gait cycle, for each limb both within the control gait and PD-AFO gait. The results are split into three sections. The first section describes the results for the overall load within the limb, the second describes the region of application or distribution of the load and the third section describes the changes seen in overall loading during PD-AFO gait across 4 days. During the gait trials the subject was asked to walk at a self-selected velocity.

5.4.1 Overall Limb Loading

5.4.1.1 Resolved Ground Reaction Force

The normalised, mean GRF for each limb was calculated during control gait and PD-AFO gait. Figure 5.4.1 shows mediolateral, anteroposterior, and vertical GRF throughout the gait cycle. The x-axis shows the time in terms of percentage gait cycle for each limb. The y-axis shows the GRF, normalised to BW.

The mediolateral GRF for the control limbs and shod limb were seen to have 1 lateral peak during loading response, followed by 2 medial peaks. The PD-AFO limb had an additional medial peak during early stance before reaching its maximum peak medial GRF at a later point in the cycle (20%) compared to the other limbs (10-12.5%). Control limbs remain within ± 1 SD of each other through the midstance phase and terminal stance phase.

A positive anteroposterior GRF demonstrates that the subject is braking and a negative GRF indicates that the subject is accelerating. All 4 limbs experienced a peak braking force during early stance and a peak propulsive force during late stance. The PD-AFO limb experienced the peak braking force later, at 20% of the gait cycle, compared to the other limbs at 10-11.5% of the gait cycle.

The vertical GRF for the right limb, left limb and shod limb were within ± 1 SD through the terminal stance phase and pre-swing. The peak vertical GRF experienced by the shod limb at weight acceptance was greater than the other limbs and occurred earlier during the gait cycle (11.5% compared to 15-17%). The PD-AFO limb experienced a distinct impact peak at 5% of the gait cycle, an occurrence not seen during the control gait. The PD-AFO limb experienced a larger, absolute vertical GRF during the midstance phase compared to the other limbs. This then reduced entering the terminal stance phase compared to the other limbs.

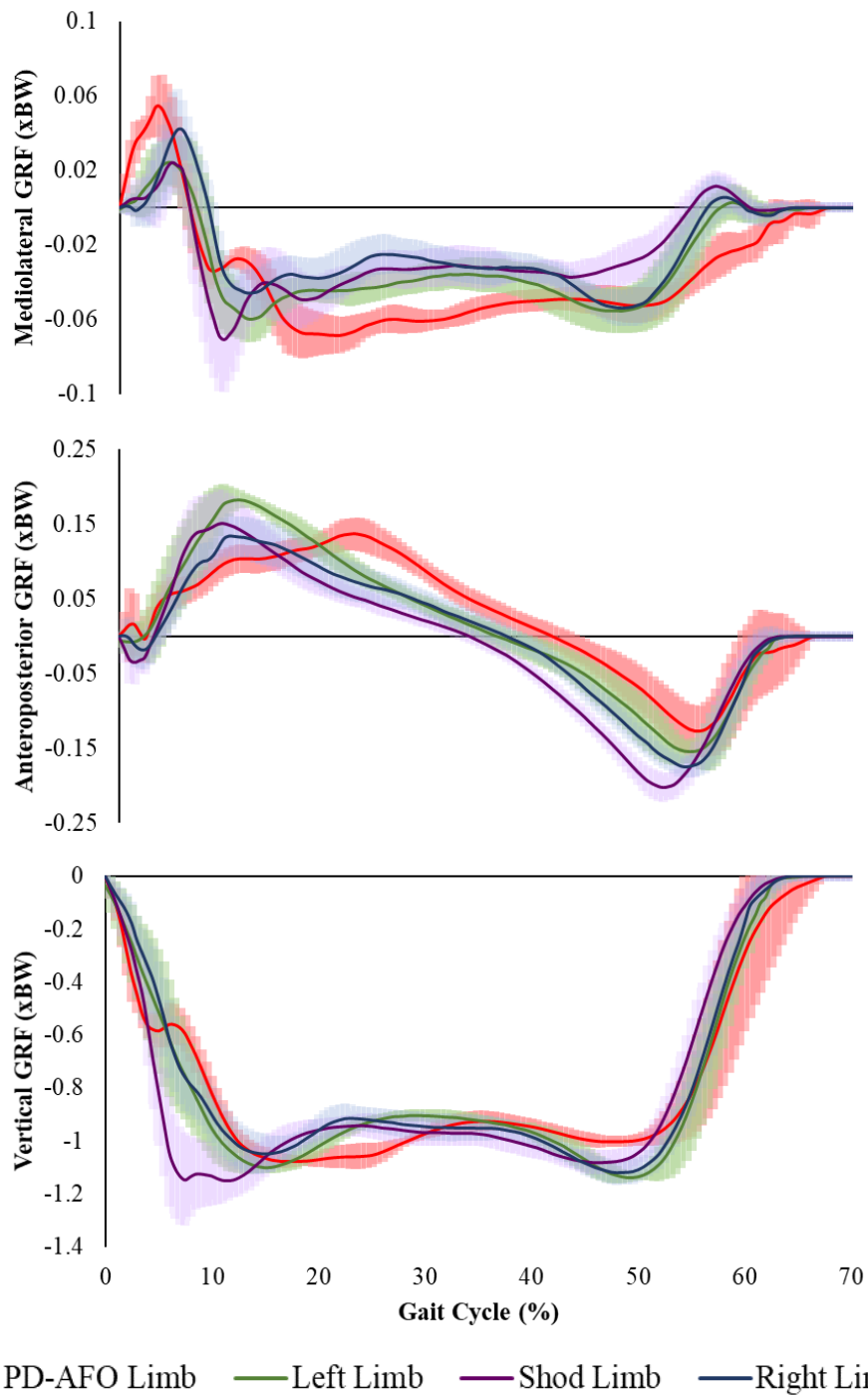


Figure 5.4.1: The mean, normalised, ground reaction force (GRF) normalised to body weight (BW), as recorded by the force plates, for the left and right limbs during the control gait and the PD-AFO and shod limb during PD-AFO gait in each direction. The shaded area around the mean value denotes one standard deviation. For the mediolateral GRF, a positive value indicates a laterally directed force and a negative value indicates a medially directed force. For the anteroposterior GRF, a positive value indicates a braking force and a negative value indicates a propulsive force.

The peak medial GRF occurring during terminal stance and pre-swing, for each limb, is shown in Figure 5.4.2. The median, medial peak was similar between the PD-AFO limb and the left control limb (within 2.5%). The shod limb experienced a smaller median, medial GRF compared to both the right limb (31%) and the PD-AFO limb (31%, $p < 0.001$).

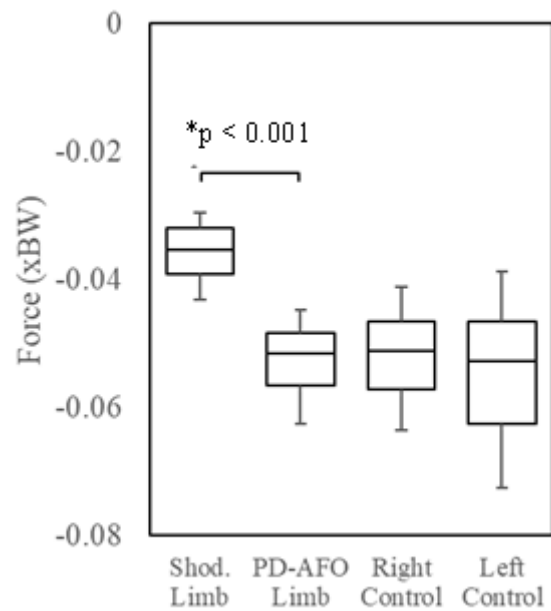


Figure 5.4.2: The peak medial GRF, normalised to body weight (BW), recorded during terminal stance and pre-swing, in each of the 4 limbs. * indicates a statistical difference for $p < 0.05$ using a paired t-test

Figure 5.4.3 shows the statistical analyses performed to compare the peak braking force (Figure 5.4.3a) and the peak propulsive forces (Figure 5.4.3b) for each limb. During PD-AFO gait, the limbs experienced similar magnitudes of peak braking GRF. The GRF experienced by the left limb was significantly higher than that experienced by the right control or the PD-AFO limb ($p < 0.001$). The median, propulsive GRF was lower in magnitude for the PD-AFO limb when compared to the shod limb (30%, $p = 0.001$) and the left control (14%). The shod limb experienced a greater, median propulsive force, when compared to the right (19%).

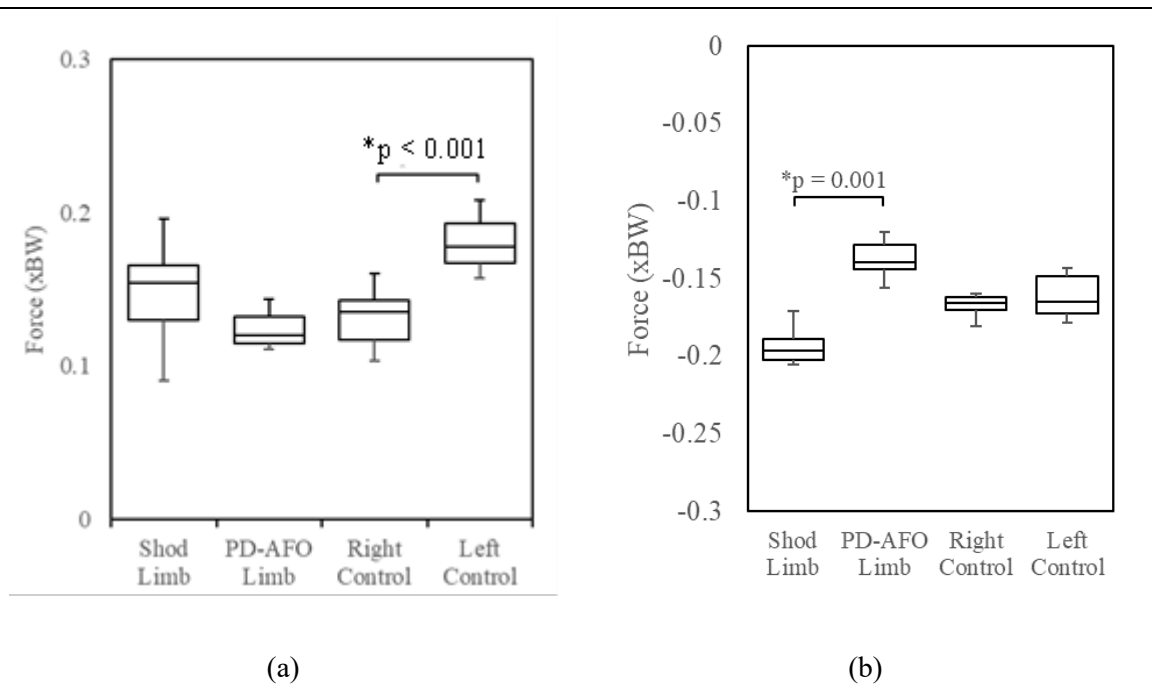


Figure 5.4.3: (a) The peak, braking GRF, normalised to body weight (BW), and (b) the peak propulsive GRF seen in all limbs. *indicates a statistical difference for $p < 0.05$ using a paired *t*-test.

Statistical analyses were performed comparing the peak, vertical GRF at weight acceptance, and at push off (Figure 5.4.4). The peak (absolute) median value of the shod limb was greater than that of the PD-AFO limb and the right control at both weight acceptance and push off, by between 4-11%. The peak, median GRF experienced by the PD-AFO at weight acceptance was also smaller in magnitude than the left control (3%). The peak (absolute) median GRF exerted by the PD-AFO limb at push off was lower than the shod limb (6%, $p=0.0049$) and left control (11%).

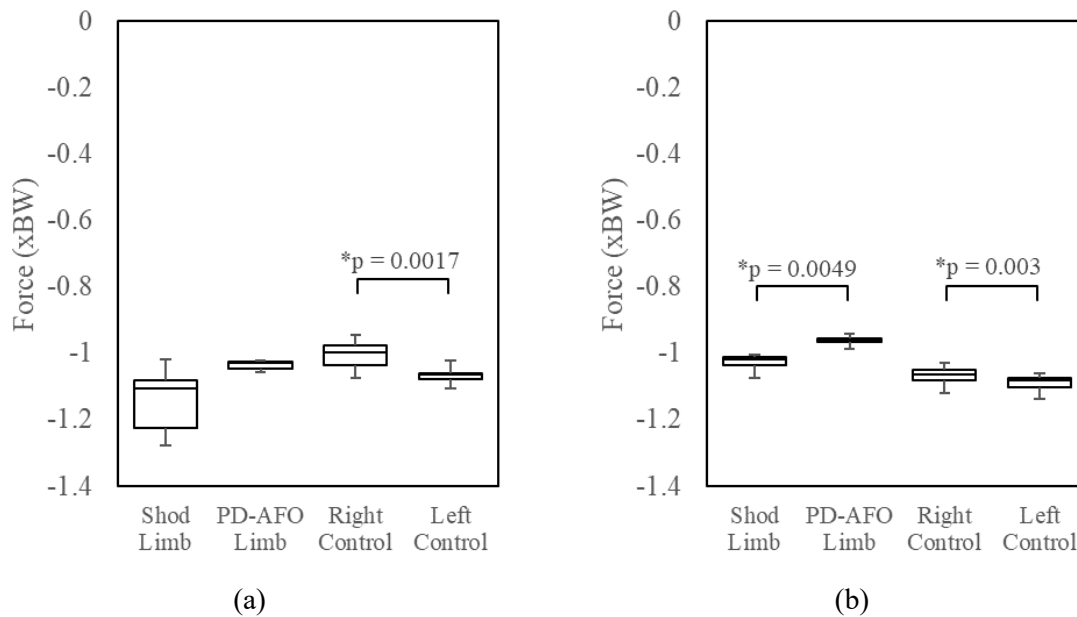


Figure 5.4.4: The peak vertical GRF, normalised to body weight (BW), recorded by all limbs during (a) weight acceptance and (b) push off. * indicates a statistical difference for $p < 0.05$ using a paired t-test.

5.4.1.2 Ratio of loading of the Lower Limb

The total GRF was calculated using equation (5.3.1). The total, normalised GRF and the normalised plantar force for each limb, throughout the gait cycle is shown in Figure 5.4.5. Both the total GRF and the plantar force of the left and right control were similar throughout the gait cycle remaining within $\pm 1SD$ of each other. The plantar force experienced by the PD-AFO limb was smaller than the shod limb and left control limb in all phases except for the pre-swing phase. Presentation of the total GRF and the plantar force for each limb, throughout the gait cycle, are also shown in Appendix 12.2.1. Total GRF was used, instead of vertical GRF alone, as the PEDAR sensor does not remain parallel to the ground throughout gait and may have antero-posterior and medio-lateral force components.

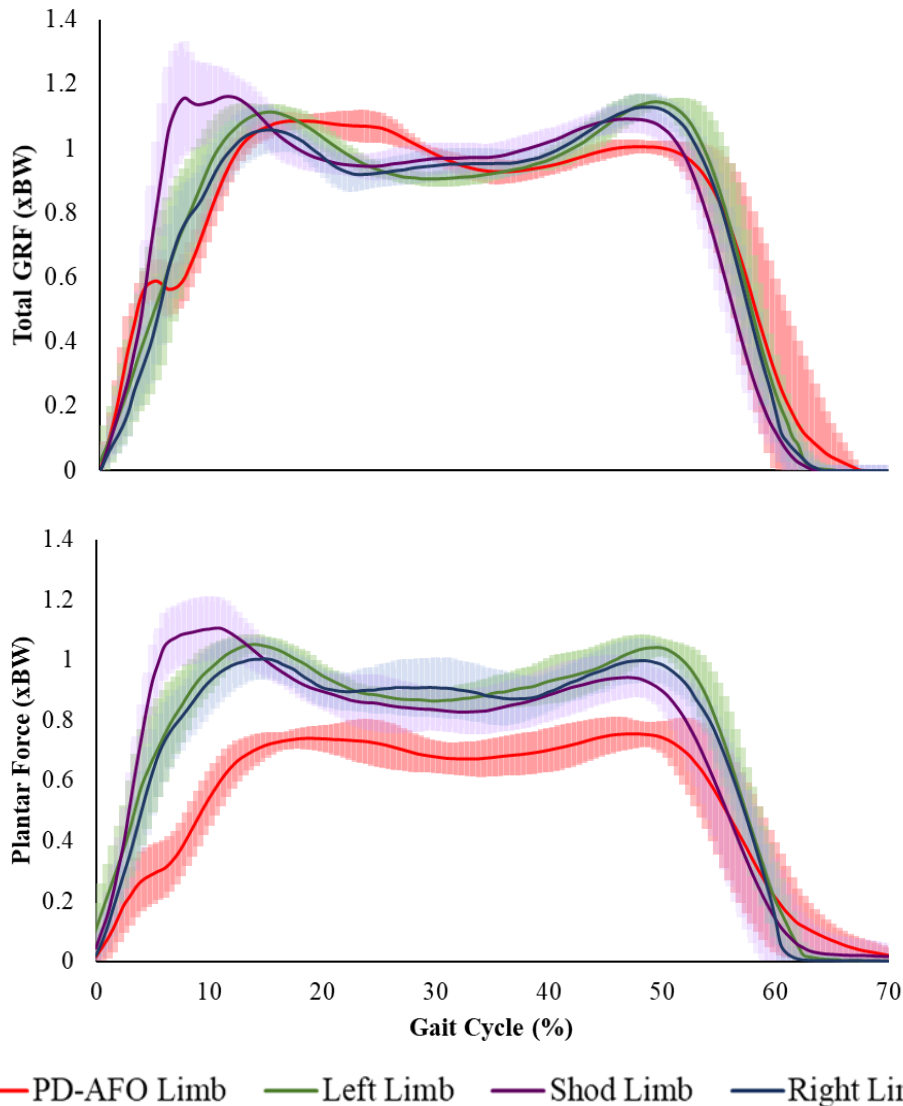


Figure 5.4.5: Total (a) GRF and (b) plantar force, both normalised to body weight (BW), for all limbs through the gait cycle

Figure 5.4.6 shows statistical analyses performed to compare relative values of the 2 measurements at weight acceptance, midstance and push off for each limb. A value of 100% of the total GRF would indicate that the plantar force and the total GRF were the same. This is shown in Figure 5.4.6 by a grey dotted line. At all points in gait, the mean plantar force was recorded as less than the mean total GRF. The plantar force and total GRF were within ± 1 SD of each other for the shod limb and control limbs, up until terminal stance. The mean percentage difference, across 5-55% of the gait cycle, between the plantar force measurement and the total GRF measurement was 4% for the left control limb, 5% for the right control limb and 12% for the shod limb, The difference between the plantar force measurement and the total GRF were greater in the PD-AFO limb than in the shod limb at weight acceptance, midstance and push off ($p < 0.001$, $p < 0.001$, $p = 0.0172$ respectively). The median ratio of plantar force to GRF of the PD-AFO limb was also lower

than that observed in the left control at weight acceptance, midstance and push off (37%, 35%, 18%, , respectively).

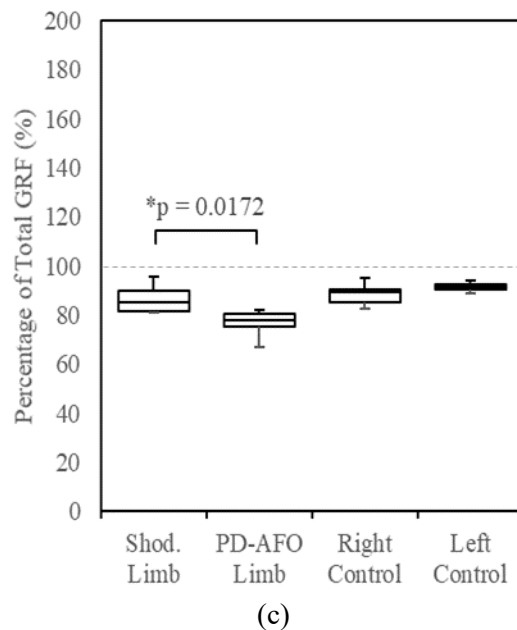
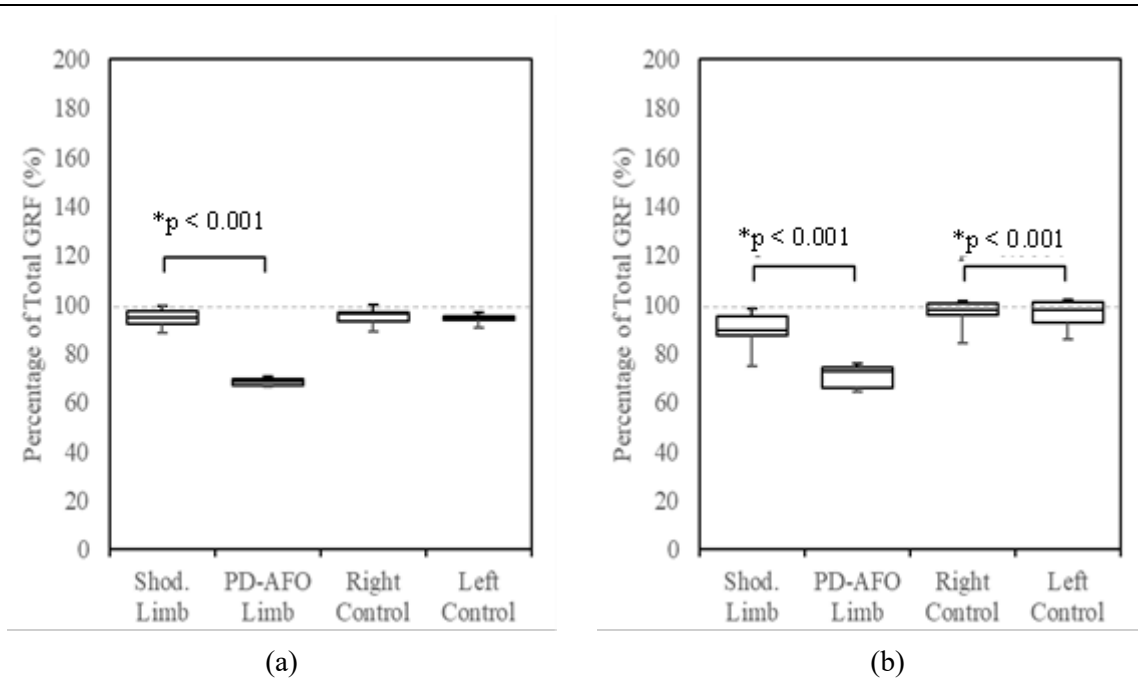


Figure 5.4.6: The plantar force at (a) weight acceptance (b) midstance and (c) push off as a percentage of the total GRF recorded for each limb. * indicates a statistical difference for $p < 0.05$ using a paired t-test.

The ratio of load, as split between the PD-AFO limb and the PD-AFO itself was determined using equation (5.3.2) by directly comparing the plantar force and total GRF. Figure 5.4.7 shows the total GRF presented as the sum of load experienced by the PD-AFO limb (the plantar force) and by the PD-AFO. The arrows indicate the percentage of the total load that passes the limb and the PD-AFO

respectively at weight acceptance, midstance and push off. The calculated errors for these measurements are shown in brackets, accounting for differences in plantar force and total GRF in the shod limb and control limbs discussed above. Appendix 12.2.3 describes the method to determine the value of this error.

At weight acceptance the total load taken by the PD-AFO was between 27.5-32.2%. This was an absolute load of between 0.30-0.35 BW. At 33% of the gait cycle, the PD-AFO took between 22.0-28.4% of the load, an absolute load of 0.21-0.27 BW. At push off the PD-AFO took 15.5-24.8% of the load; this was between 0.16-0.25 BW.

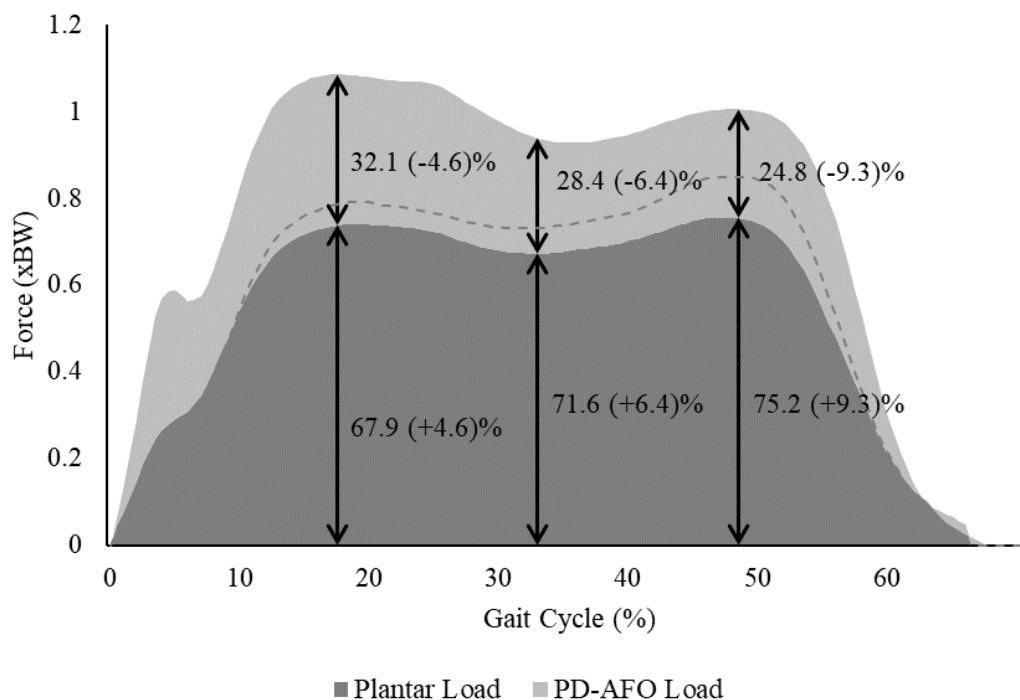


Figure 5.4.7: The dark grey region shows the loading experienced by the PD-AFO limb (the plantar force normalised to body weight (BW)). The light grey region indicates the loading experienced by the PD-AFO. The summation of both areas gives the total GRF. The dotted line indicates the calculated error, used to account for the measurement techniques from the PEDAR sensors and force plates. The data labels indicate the percentage of total load +/- calculated error, at weight acceptance, midstance and push off.

5.4.2 Regional Loading of the Lower Limb

The plantar force and GRF have been analysed, evaluating the changes in overall load of the lower limb. The ratio of loading between the lower limb and PD-AFO has also been established. This section of results presents the metrics that describe which regions of the foot are loaded throughout gait.

5.4.2.1 Centre of Pressure

The CoP, in Figure 5.4.8, shows the progression of the point of application of load in the foot throughout the gait cycle for all limbs. The time at which this CoP was recorded in relation to the gait cycle, is shown by the percentages, with 0% being the limb entering the stance phase and 60% when the limb would be expected to leave the stance phase.

The variation of the CoP in the mediolateral direction was similar for all limbs and within $\pm 1SD$.

Through the terminal stance phase the shod limb and control limbs saw their CoP move medially, whilst in the PD-AFO limb this was not seen. The range of mediolateral motion between 10-50% of the gait cycles was 17 ± 11 mm for the left limb, and 23 ± 4 mm for the right limb. The range of mediolateral motion for the shod limb was similar to the controls, at 19 ± 7 mm, whereas the range for the PD-AFO limb was smaller at 6 ± 6 mm (indicating a small change in mediolateral CoP).

The maximum anterior location of the CoP (between 10-50% of the gait cycle) was similar for the shod limb, 217 ± 4 mm, and the right and left limbs, 213 ± 5 mm and 206 ± 4 mm, respectively. For the PD-AFO limb the most anterior point of CoP was located more posteriorly than the other limbs, at 174 ± 15 mm. At $\sim 40\%$ of the gait cycle, indicated by the 40% label in Figure 5.4.8, the CoP of the PD-AFO limb was seen to move in the lateral direction in a ‘jerk’ like movement.

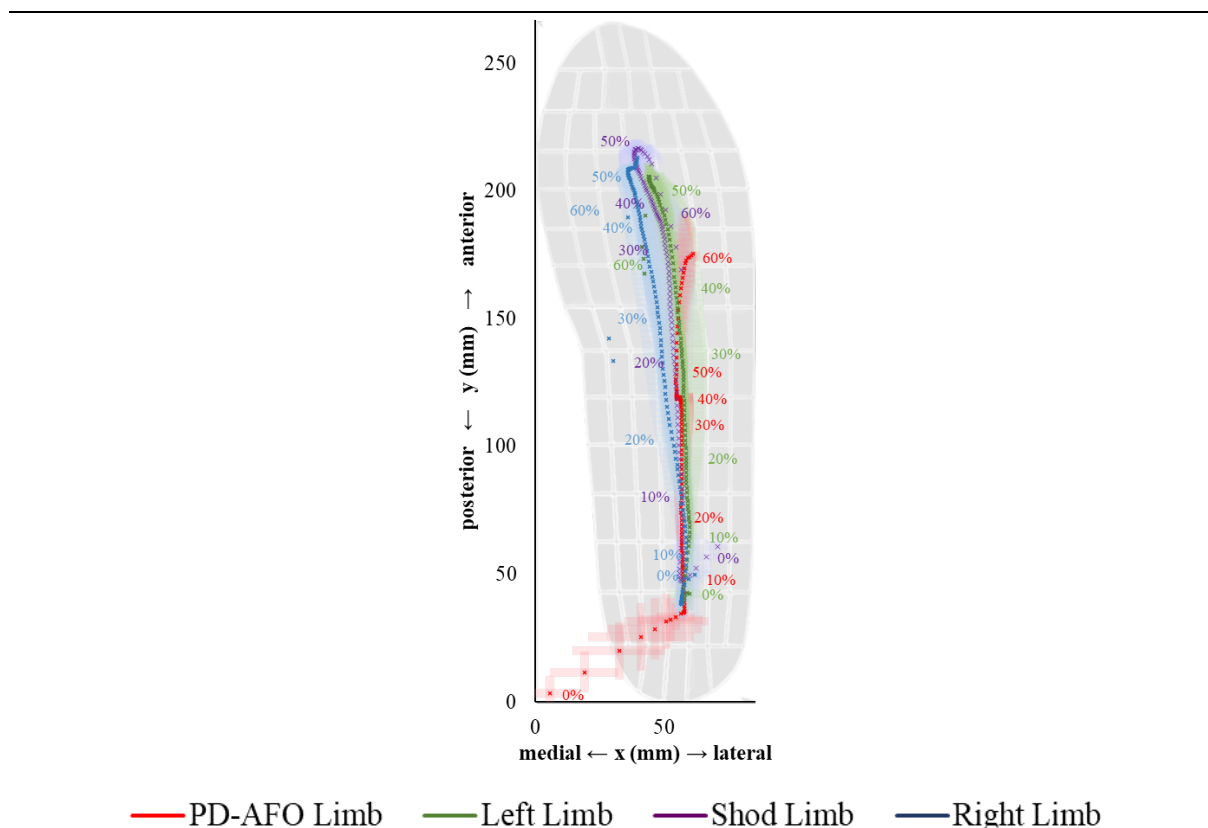


Figure 5.4.8: The centre of pressure (CoP) for each limb throughout the gait cycle. The percentages indicate the point of the gait cycle at which this CoP was reached. The CoP readings not located on the insole are erroneous as the foot strikes the ground.

5.4.2.2 Plantar Pressure

Figure 5.4.9 shows the peak plantar pressure within the foot evaluated from the PEDAR data, across all regions, throughout the gait cycle. The values are normalised for body weight. The shod limb and controls limbs experienced 2 peaks in total plantar pressure, one during loading response and one during terminal stance. The PD-AFO limb experienced 1 peak during the early stance phase. The peak pressures during loading response occurred earlier in the gait cycle than the peak plantar force for all limbs. The peak plantar pressure during the early stance phase, experienced by the PD-AFO limb, was 0.250 ± 0.012 kPa/N occurring at 15% of the gait cycle. The peak plantar pressure experienced by the shod limb occurred at 51.5% of the gait cycle, and was 0.309 ± 0.032 kPa/N. The peak plantar pressure during loading response for the shod limb, at 6% of the gait cycle, was 0.308 ± 0.079 kPa/N. The left and right control limbs both experienced a similar maximum plantar pressure during loading response, at 9% of the gait cycle, with values of 0.309 ± 0.032 kPa/N and 0.300 ± 0.033 kPa/N respectively.

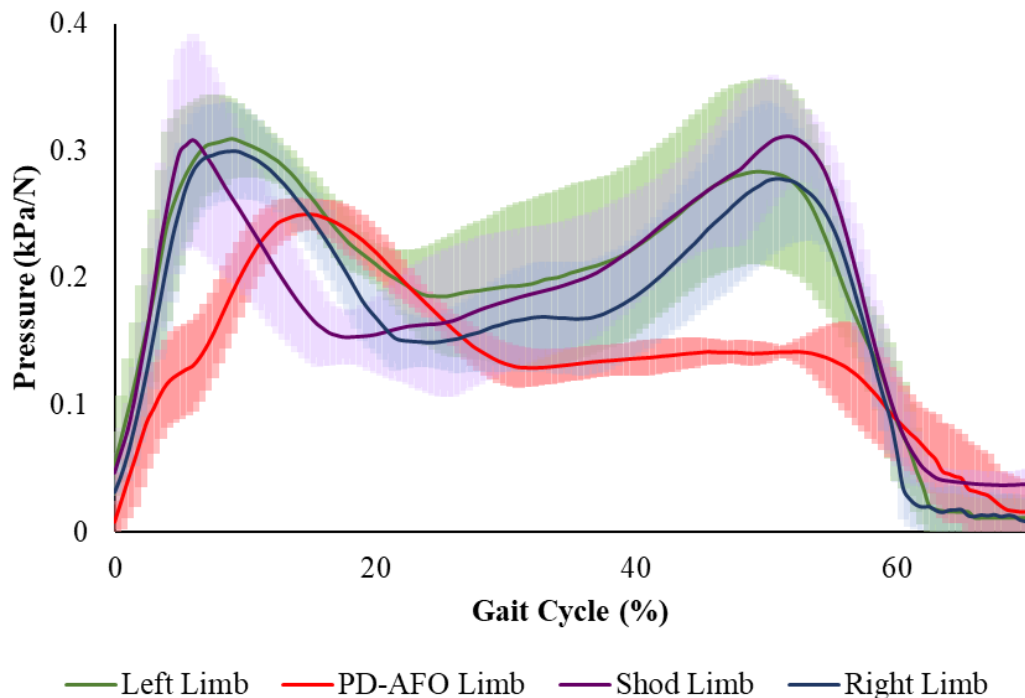


Figure 5.4.9: Peak Plantar Pressure in each limb, normalised for body weight, throughout the gait cycle

Figure 5.4.10 shows the plantar pressure recorded during gait for each limb, in each of the 8 regions. Figure 5.4.10a and Figure 5.4.10b demonstrate an increase in the plantar pressure experienced by the toe regions, by the control limbs and shod limb as the gait cycle progressed to terminal stance. The mean values experienced by right limb and shod limb were within ± 1 SD of each other. The plantar pressure experienced by the PD-AFO limb was lower than both the shod limb and left control limb. An increase in the pressure in the toe region as the gait cycle progressed to terminal stance was seen

but at a lower rate than all other limbs. This resulted in a significantly lower peak plantar pressure in the toe region of the PD-AFO limb, during terminal stance, compared to all other limbs.

Figure 5.4.10c and Figure 5.4.10d shows the plantar pressure experienced in the medial and lateral forefoot regions, respectively. This pressure, again, increased as the cycle progressed to terminal stance. The increase in pressure in this region occurred at a similar rate for all limbs however it was notably lower in the PD-AFO limb in the medial forefoot region.

Figure 5.4.10e and Figure 5.4.10f show the change in plantar pressure in the medial and lateral midfoot regions. The peak pressures experienced in this region were lower than those experienced in other regions of the foot, with no pressure recorded for the PD-AFO limb in the medial midfoot region. In the lateral midfoot region, the shod limb experienced a greater peak during loading response than the right control limb. The PD-AFO limb experienced a consistently lower lateral midfoot pressure, until the end of the gait cycle, where an additional peak was seen before the end of the stance phase. This was within $\pm 1SD$ of the plantar pressure recorded in the other limbs at that point in the gait cycle.

Figure 5.4.10g and Figure 5.4.10h show the medial and lateral hindfoot plantar pressures experienced by each limb. The plantar pressure in the hind foot regions, experienced by each limb, peaked during the loading response and midstance phase and decreased throughout terminal stance phase to pre-swing. This occurred at a similar rate for the right and left control limb and the shod limb. The PD-AFO limb experienced a second, smaller peak during the latter stance phase, not seen in any other limb. The initial peak, during loading response, was smallest for the PD-AFO limb, in both regions. The shod limb experienced the greatest peak in the medial hindfoot region. The right and left limb experienced a hindfoot plantar pressure within $\pm 1SD$ of each other.

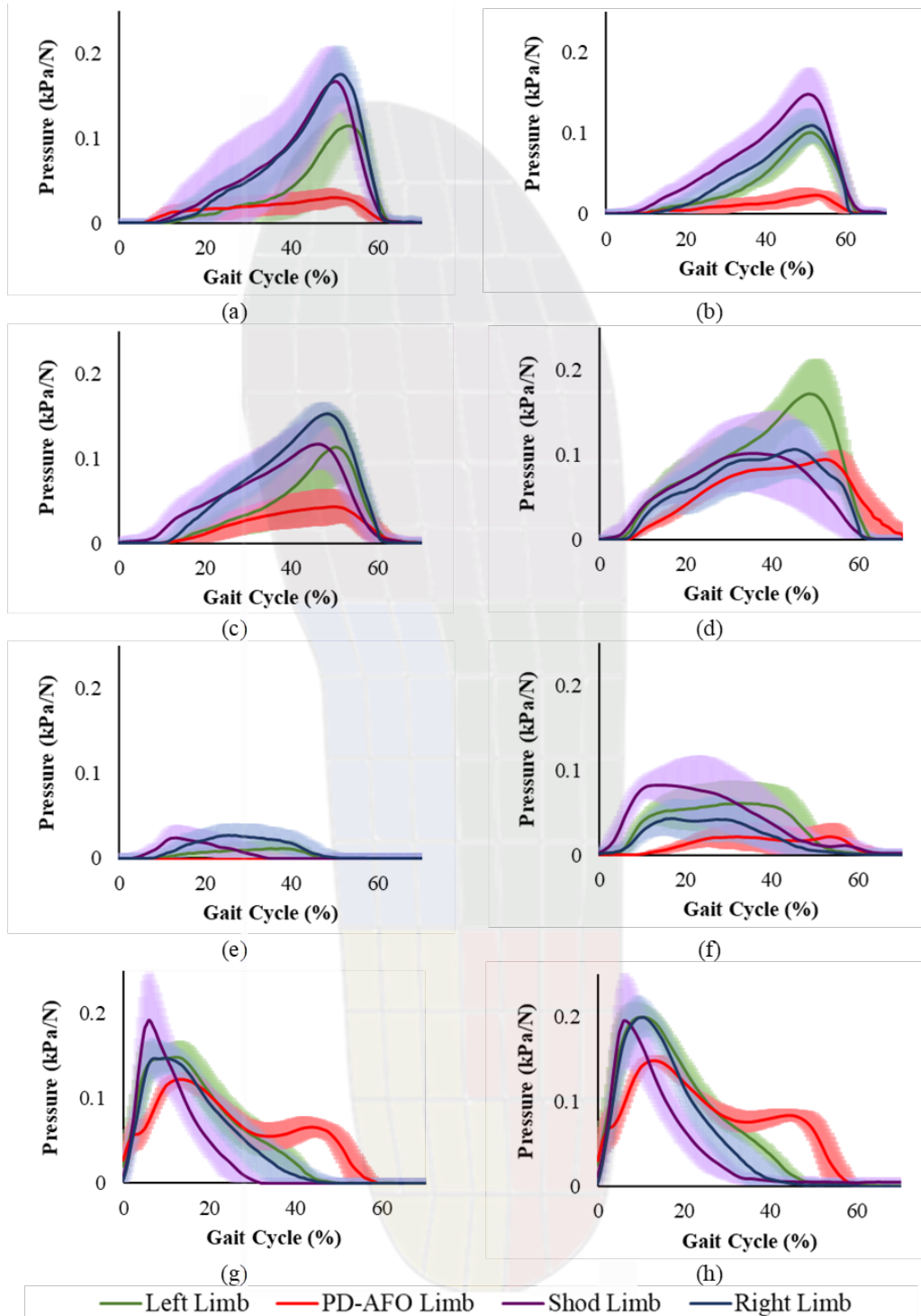


Figure 5.4.10: The normalised, plantar pressure in (a) the greater toe (b) the lesser toe (c) the medial forefoot (d) the lateral forefoot (e) the medial midfoot (f) the lateral midfoot (g) the medial hindfoot (h) the lateral hindfoot, throughout the stance phase of the gait cycle, for both the control gait and PD-AFO gait. As viewed the figures are presented in the respective regions of a right footprint, with the medial regions demonstrated on the left hand side of the page, and the lateral regions to the right hand side. The toe regions are represented in at the top of the page, and the hindfoot regions at the bottom.

For the data shown in Figure 5.4.10 statistical analyses of the peaks in plantar pressure at weight acceptance and push off, and the mean value of plantar pressure at midstance, were performed in the 8 regions between the shod limb and PD-AFO limb during PD-AFO gait, between the left and right control limb during control gait, between the shod limb and the right control limb, and between the left control limb and PD-AFO limb. All analyses are presented on the same scale axis to allow for comparison. All analyses are presented in Appendix 12.2.4 for completeness; those of particular interest are presented below.

The plantar pressures observed at weight acceptance for the hindfoot regions are shown in Figure 5.4.11. The PD-AFO limb experienced a lower, peak, median, hindfoot plantar pressure at weight acceptance in both the medial and lateral regions compared to the left control by 27% and 34%, respectively. The shod limb also experienced a higher, median plantar pressure within the medial hindfoot regions compared to the PD-AFO limb (38%, $p = 0.0039$) and the right control (25%).

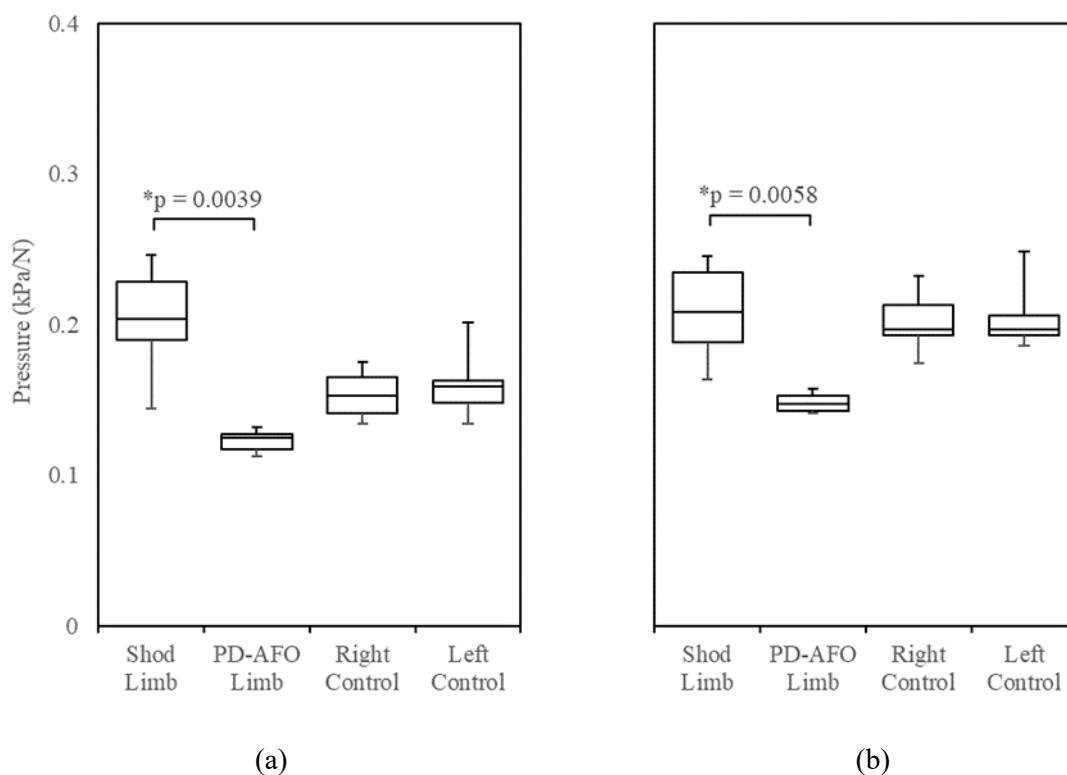


Figure 5.4.11: The peak plantar pressure, normalised for body weight, at weight acceptance in the (a) medial and (b) lateral hindfoot region. * indicates a statistical difference for $p < 0.05$ using a paired t-test.

Figure 5.4.12 shows the mean plantar pressures experienced in the medial and lateral regions of the midfoot during midstance. No pressure was recorded in the medial region at midstance in the PD-AFO limb. The PD-AFO limb experienced a lower plantar pressure in both regions compared to both the shod limb (medial $p = 0.0167$, lateral $p = 0.0018$) and the left control. The shod limb experienced a higher pressure in the lateral region, by 43%, and lower pressure in the medial region, by 196%, compared to the right control limb. The left control also experienced a lower pressure than the right control in the medial region ($p = 0.0051$).

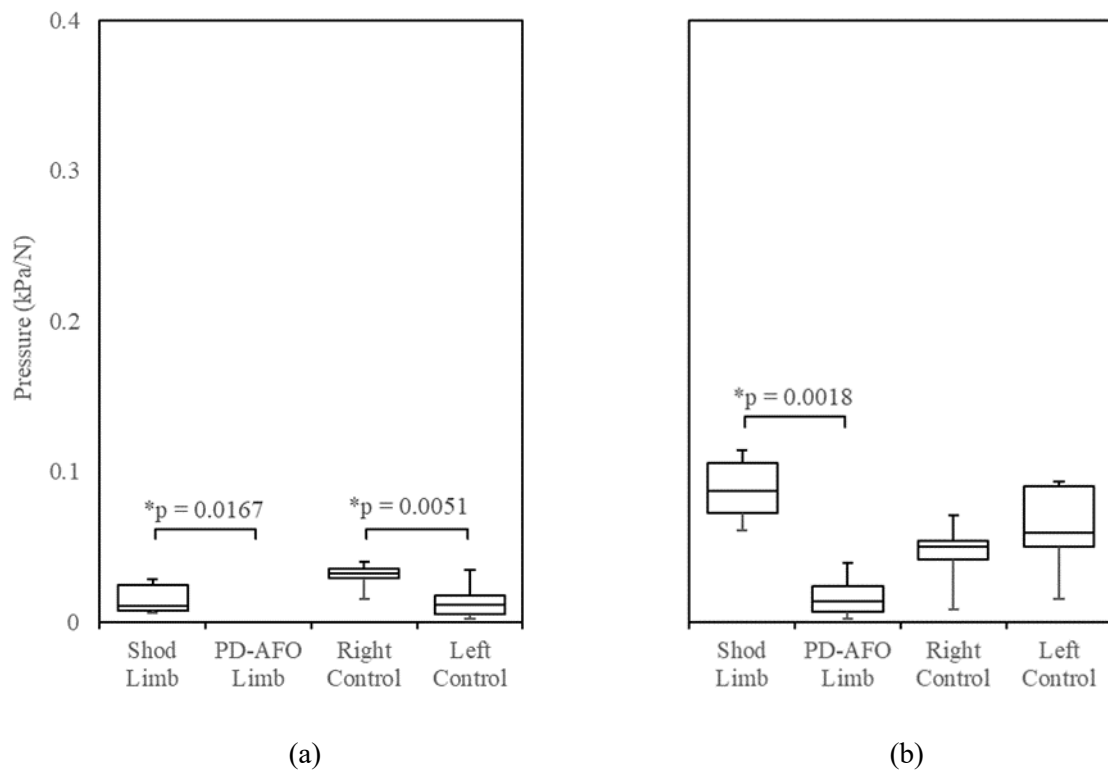


Figure 5.4.12: The mean plantar pressure at midstance, normalised for body weight, in (a) the medial and (b) the lateral midfoot. * indicates a statistical difference for $p < 0.05$, using a paired t -test between the shod limb and PD-AFO limb and a Wilcoxon signed rank test between the left control and right control.

Figure 5.4.13 shows the peak plantar pressure in the hind foot regions at push off. The plantar pressure experienced by the PD-AFO limb in the hindfoot regions was higher than both the shod (medial $p < 0.001$, lateral $p < 0.001$). The median peak plantar pressure experienced by the PD-AFO limb was 242% greater in the medial hindfoot compared to the left control, and 137% greater in the lateral hindfoot region. The pressures experienced in the hindfoot region in the shod limb and the right control limb were very small and tended to zero.

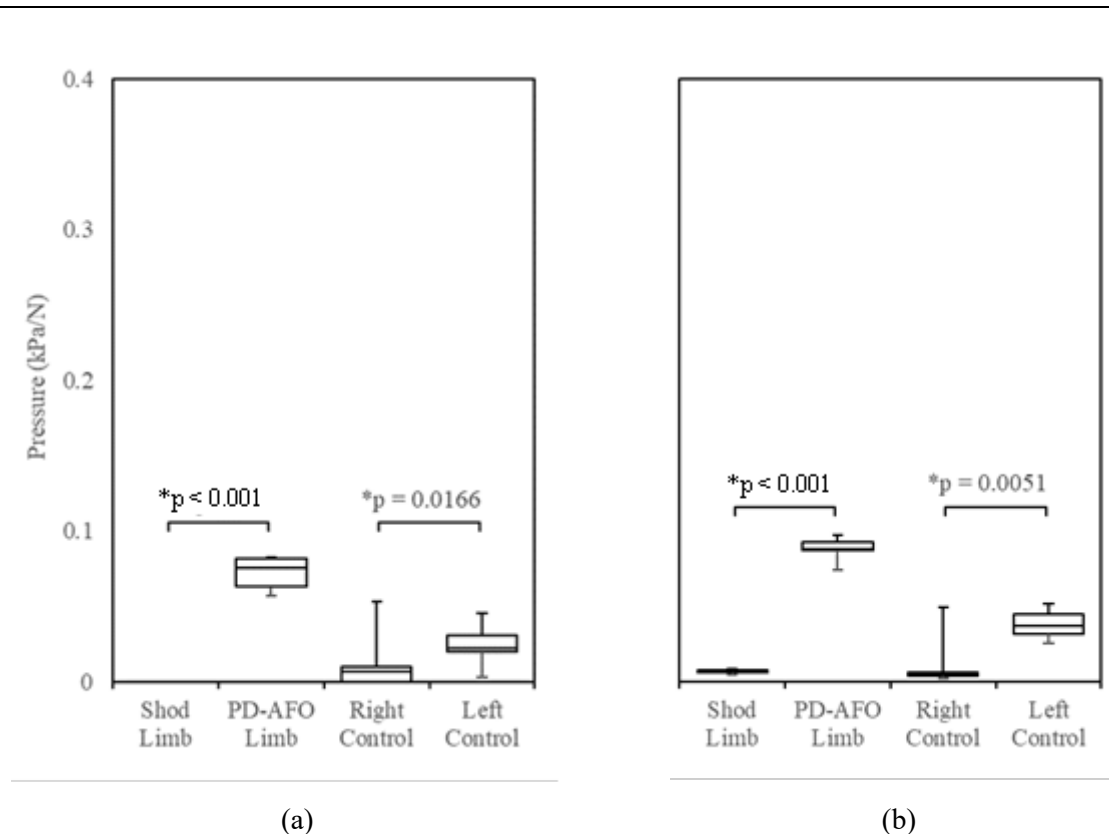


Figure 5.4.13: The peak plantar pressure, normalised for body weight, at push off in the (a) medial and (b) the lateral hindfoot region. * indicates a statistical difference for $p < 0.05$ using a paired t-test between the PD-AFO limb and the shod limb, and using a Wilcoxin signed rank test between the left control and the right control.

Figure 5.4.14 shows the peak plantar pressures experienced at push off within the forefoot and toe regions. No medial pressure was recorded at push off in the shod limb. The PD-AFO experienced lower peak plantar pressures in the medial forefoot, and both the greater toe and lesser toe regions, compared to the shod limb ($p = 0.0013$, $p < 0.001$, $p < 0.001$ respectively). The PD-AFO also experienced lower median peak plantar pressures compared to the left control, in the medial forefoot region (64%), lateral forefoot region (43%), greater toes (74%) and lesser toes (72%). Differences were also seen between the right and left control in the forefoot regions (medial $p = 0.0024$, lateral $p < 0.001$) and the greater toe ($p = 0.0038$).

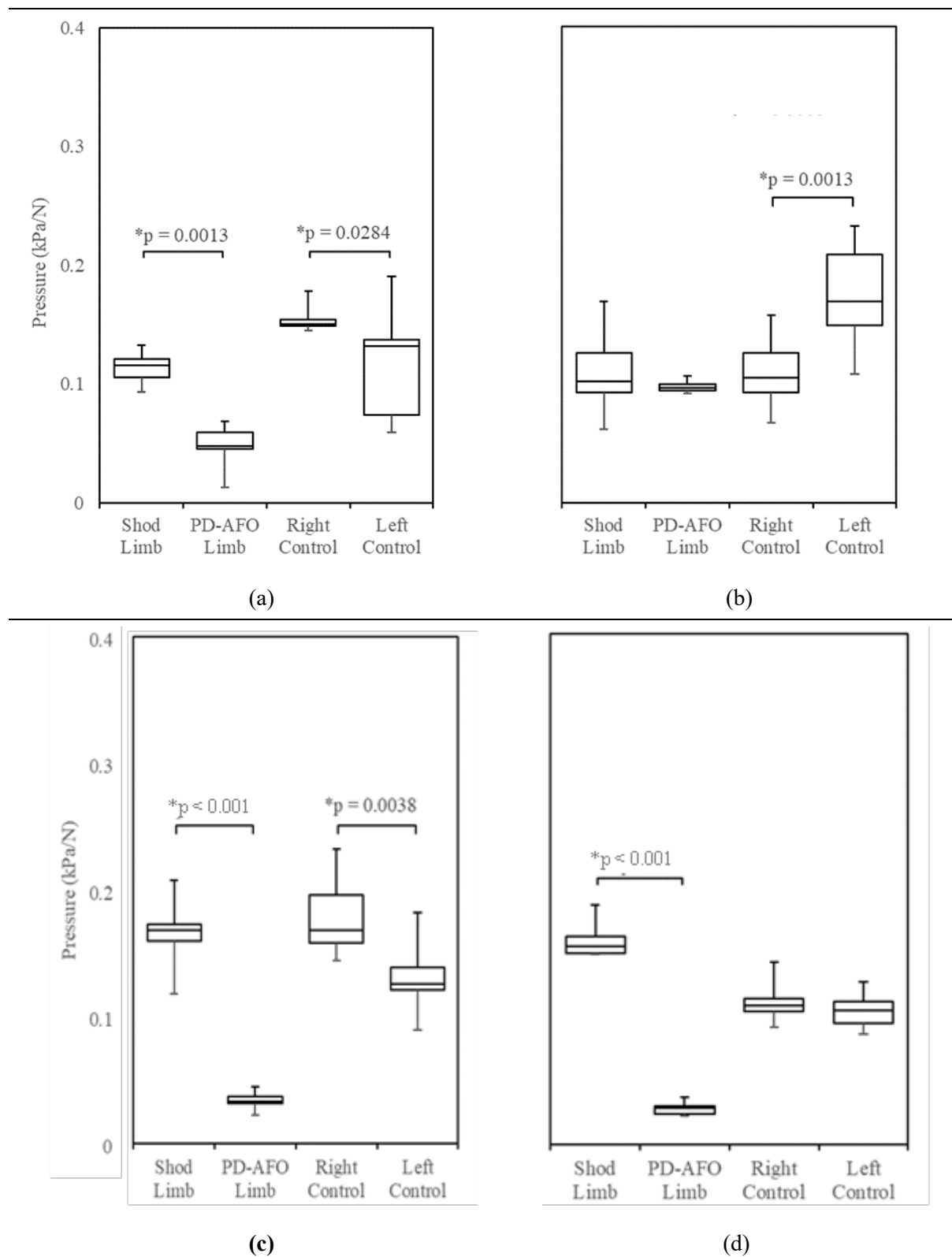


Figure 5.4.14: The peak plantar pressures experienced at push off in each limb, normalised for body weight, in the (a) medial forefoot region, (b) the lateral forefoot region, (c) the greater toe and (d) the lesser toes. * indicates a statistical difference for $p < 0.05$ using a paired t-test in all cases except between plantar pressure in the medial forefoot region between the left control and right control where a Wilcoxon signed rank test was used.

5.4.3 PD-AFO gait across 4 days

The additional gait trials performed to analyse whether the gait of the subject changed with further use of the PD-AFO are described in this section. Figure 5.4.15 shows the peak, total GRF and plantar force at weight acceptance, recorded across 4 days. The peak GRF and plantar force at weight acceptance, recorded on day 1 for the PD-AFO limb, were statistically lower than that recorded on day 2 ($p=0.0076$, $p < 0.001$ respectively) for the PD-AFO limb.

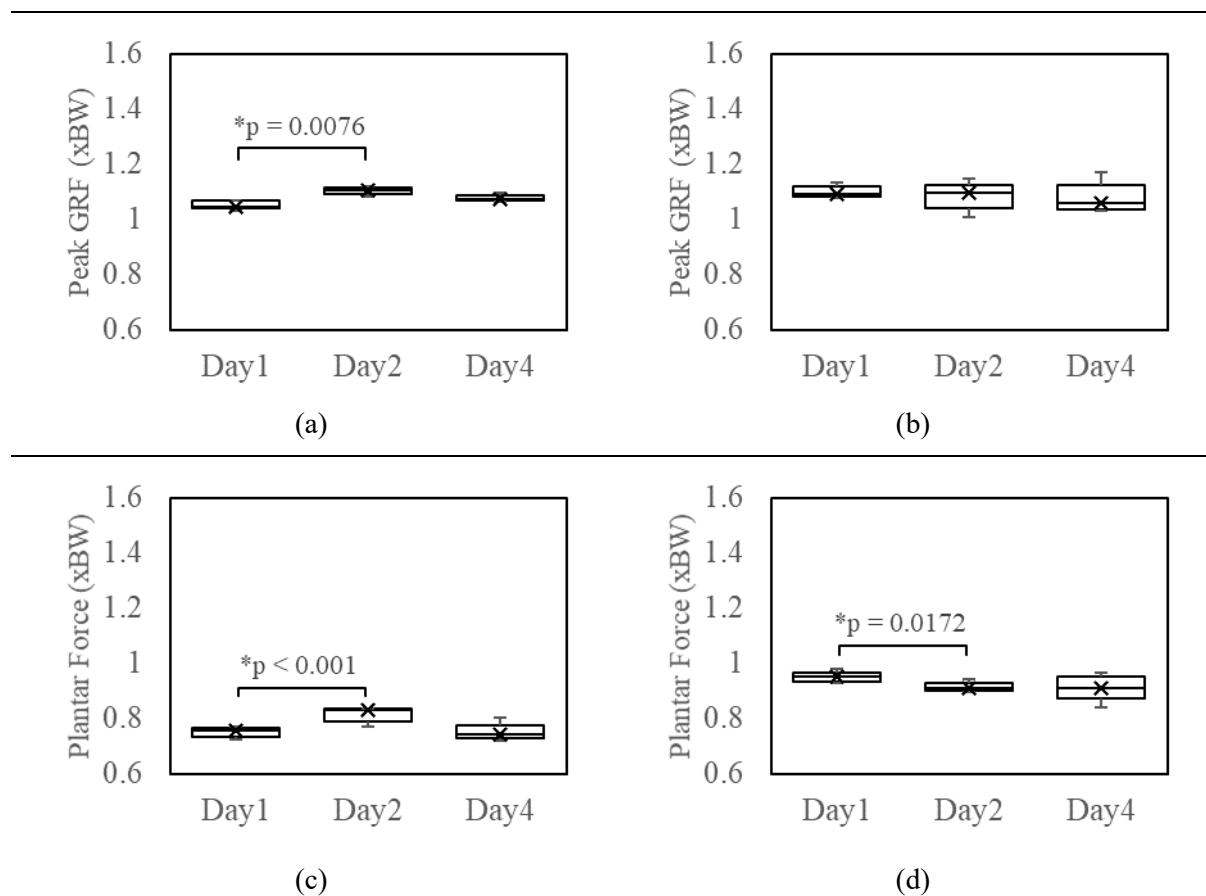


Figure 5.4.15: The peak GRF in the (a) PD-AFO limb and (b) shod limb and the peak plantar force in (c) PD-AFO limb and (d) shod limb at weight acceptance ($n=5$). * indicates a statistical difference for $p < 0.05$, using a paired t -test.

Figure 5.4.16 shows the changes across days in the peak GRF and plantar force at push off. No statistically significant differences were observed in the PD-AFO limb or shod limb at push off.

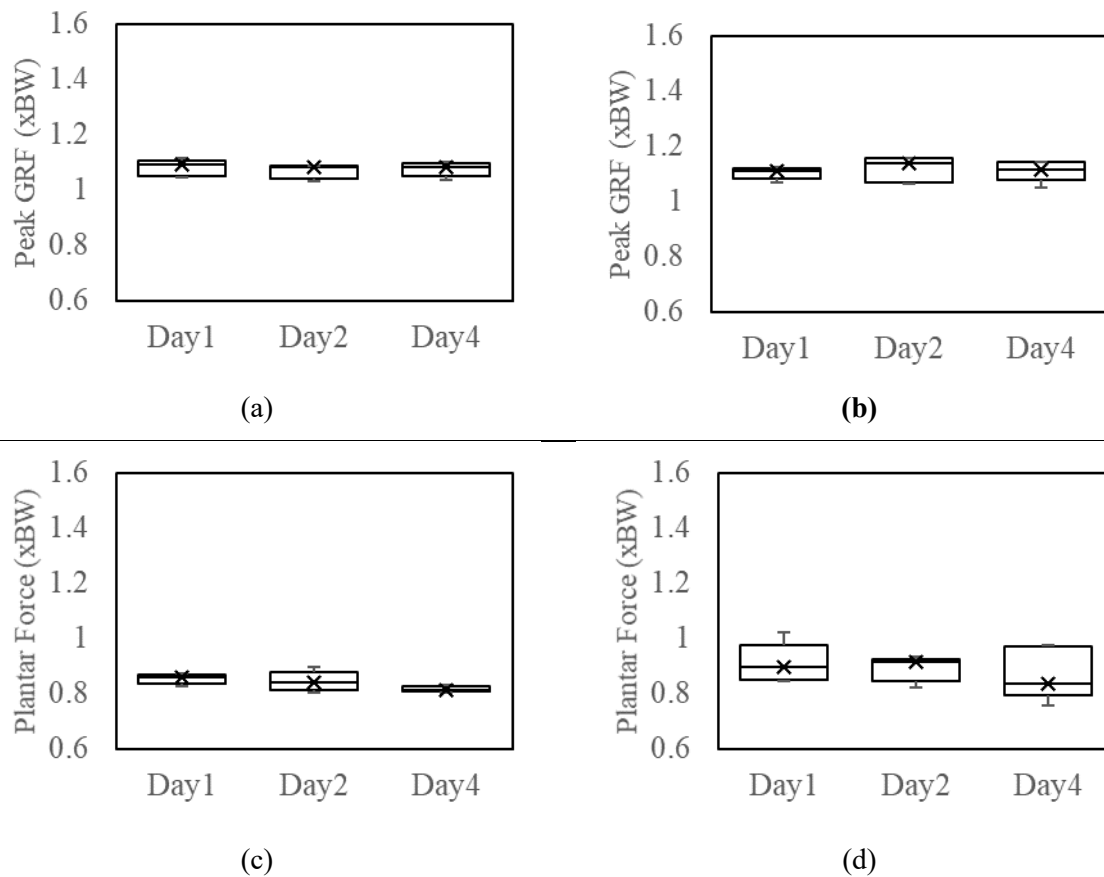


Figure 5.4.16: The peak GRF in the (a) PD-AFO limb and (b) the shod limb and the peak plantar force in (c) PD-AFO limb and (d) shod limb at push off ($n=5$). * indicates a statistical difference for $p < 0.05$ using a paired t -test.

5.5 DISCUSSION

This is the first study to quantify the extent of offloading of the lower limb during gait when wearing this novel PD-AFO. The study also analysed the plantar pressure and CoP, demonstrating how the PD-AFO alters the loading in different regions of the foot. All values from literature discussed in this section are taken to be absolute (due to varying coordinate systems during gait trials) and the direction is provided.

5.5.1 Combined Peak Loads

The values of peak vertical GRF recorded for the control limbs, PD-AFO limb and shod limb at during early stance (weight acceptance) and late stance (push off) were found to be within ± 1 SD of those recorded in previous studies analysing injured cohorts and healthy controls [57, 62]. Similar results were also seen for the peak anteroposterior GRFs for all limbs in injured patients with the PD-AFO and healthy patients [57]. Similarly the peak medial directed force was within ± 1 SD of those reported in literature [57].

Although similarities were seen between the data obtained here and literature, an impact peak at loading response was exhibited by the PD-AFO limb in this study. This is the peak force recorded during initial contact (0-2% of the gait cycle) with the floor. This has not been seen with previous injured cohorts however is exhibited during normal gait by some people, particularly if wearing firmer-soled shoes [29]. The substantially stiffer base of the PD-AFO compared to a regular shoe is likely to be the reason why the impact peak occurs. The lack of presence of an impact peak in previous data evaluating patient gait may be due to averaging of data across patients; if only a small number of patients exhibited an impact peak this would not be visible when the mean value is presented. The remainder of the GRF throughout the gait cycle is similar to that reported in literature, and therefore is considered similar to how the PD-AFO acts with a patient cohort.

The peak vertical GRF was not lower for the PD-AFO limb compared to the left control. However, the shod limb vertical GRF did increase relative to control. This is thought to be due to instability of the PD-AFO limb when wearing the PD-AFO. This instability is indicated by the jerk of the CoP in the mediolateral direction at terminal stance. It is thought that this resulted in a higher vertical GRF in the shod limb, as the subject was unable to place the shod limb down as smoothly. This jerk movement was also seen in the study by Stewart et al. [40]. The subject in this study had undergone training on how to correctly walk with the PD-AFO, though did not wear it regularly as it was not required. Changes in gait over a 4-day period were also, analysed to determine any progressive change in gait when the subject used the PD-AFO more regularly; no consistent changes were seen (discussed below). The cohort in the study by Stewart et al. had also not undergone the formal rehabilitation programme, and had been using the PD-AFO for less than 2 weeks [40]. As such it is difficult to say whether the mediolateral instability is due to lack of use of the PD-AFO or whether it is a characteristic that will affect all people wearing the orthotic. The presence of an increase in vertical GRF of the shod limb in injured cohorts who have undergone the full rehabilitation programme suggests that the instability is present in all users of the PD-AFO [57, 62].

The peak braking force and propulsive forces in the PD-AFO limb were lower than that of the left control. Variation was also seen within the 2 control limbs. More significantly, the rate of braking force seen in the PD-AFO limb was slower, with the peak force occurring later in the gait cycle, compared to all other limbs. Previous studies of an injured cohort demonstrated a reduction in peak braking force and a less distinct peak braking force, though it is not clear if there was a shift in the time to peak braking force [38, 56]. This reduction suggests that the struts and/or heel wedge are deflecting/deforming to reduce the peak load. At the time of the peak braking force the CoP of the PD-AFO limb is in a similar anteroposterior position to the shod limb and left control, despite the peak braking force of the PD-AFO limb occurring later in the gait cycle compared to the other limbs. This is likely due to the heel wedge acting as an energy absorber where, during normal gait, plantarflexion of the foot would allow for energy absorption. The former does not result in forward

progression of the CoP whereas the latter does. Therefore, the PD-AFO limb remains with a more posterior CoP for longer during the gait cycle.

Whilst alterations in gait of the PD-AFO limb are the most important clinically, the changes in the gait of the shod limb may provide insight for future patient studies. The shod limb in previous studies has been used as a control to compare the changes in gait in the PD-AFO limb. Within this study it has been demonstrated that the shod limb experienced an increased vertical GRF and propulsive GRF compared to the right control. The peak medially directed GRF was also higher when compared to the control. The CoP was similar for the shod limb and the right control, as were the plantar pressures. The exception to this was the peak pressure during early stance where the shod limb experienced slightly higher pressures in the hindfoot and midfoot region, due to the increased GRF. Use of a healthy control allowed direct comparison of the shod limb when the PD-AFO is and is not worn. This provides information for future patient cohort studies who use the shod limb as a control.

5.5.2 Lower Limb Peak Loads and Peak Pressures

The GRF indicates whether the response of the PD-AFO alters the overall loading of the PD-AFO limb system. Very small changes were seen and therefore further investigation was needed to understand the loading within the limb alone. This is the first study to quantify the plantar force of a subject wearing the PD-AFO.

The plantar force in the PD-AFO limb was reduced by 30% relative to the left control during loading response and early midstance, demonstrating that the PD-AFO reduces peak loads in the limb. This is hypothesised to be the load being diverted through the struts to the anterior cuff which acts as a patellar tendon-bearing cuff. A reduction in peak pressure in early stance, by 19%, was also observed in the PD-AFO limb relative to the left control. Stewart et al. observed a similar reduction of 26% when comparing injured patients walking with and without their PD-AFO [40]. The values were within ± 1 SD between the studies.

The extent of reduction in pressure between the PD-AFO limb and left control was less than the extent of reduction in plantar force between the PD-AFO limb and the left control; during the late stance phase the reduction in peak plantar pressure relative to the left control was 51% and the reduction in peak force of the PD-AFO limb relative to the left control was less, at 12%. This suggests that the region of plantar loading changes in the PD-AFO limb compared to the left control. This may be due to the stiff base, which, although a foam sole is present, does not deform as much as a shoe and insole, which allows for an increased contact region.

The difference in extent of reductions in peak pressure compared to the reduction in force suggests that the contact region over which the force was distributed is greater. The CoP during the late stance phase of gait was more posterior than that seen in the left control limb, suggesting that the loading had not been fully shifted to the forefoot region. This is further supported by the regional analysis of the

plantar pressures demonstrating hindfoot pressure was still present at during the late stance phase in the PD-AFO limb, not seen in any other limbs. The toe region and forefoot pressures were also reduced in the PD-AFO limb compared to the control by between 45-76%. Similar reductions were seen by Stewart et al. [40]. Overall, this suggests that the PD-AFO reduced the peak pressures during late stance by shifting the CoP more posteriorly. This increased the contact area, reducing pressures. It also reduced the moment arm about the ankle joint complex, as previously described in literature [40]. Lower torque provided by the foot accounts for the lower propulsive force seen compared to the left control. Further research is needed to understand to what extent the PD-AFO provides additional power during terminal stance and pre-swing. This will be evaluated in chapter 6.

Additionally, the minimal pressure within the toe regions indicates that the PD-AFO prevented the user from progressing onto the ball of their foot as they entered the pre-swing phase. This is likely due to the stiffness of the base and the anterior cuff preventing plantarflexion. The reduction in forefoot pressure and increase in hindfoot pressure is also seen in a previous study evaluating a rigid-bottom AFO, that limits both plantar and dorsiflexion [85].

5.5.3 Loading ratio

It was predicted that for a limb without the PD-AFO that the plantar force and total GRF would be the same. Differences, however, were observed between the plantar force and total GRF force recorded in the control limbs and shod limb. These differences are thought to be due to the PEDAR sensors' ability to only record normal force (not shear), compared to the force plates that are able to record forces in all 3 directions. Therefore, it is thought that the PEDAR sensors under predict slightly. This is supported by the fact that the difference between the two readings increases during terminal stance, a phase in gait where the shank-to-vertical angle is increased therefore the foot is more likely to be exerting a shear force on the PEDAR sensor. This difference was accounted for in the analysis of the plantar force.

The PD-AFO was found to alter the amount of load experienced by the limb throughout the gait cycle. The amounts of offloading are presented as a range, to account for discrepancies between the PEDAR sensors and force plate readings. The amount of load through the PD-AFO reduced from midstance through to pre-swing. The peak offloading occurred during the early stance phase, between 27-34%, suggesting the PD-AFO helps to reduce the impact when the limb make contact with the ground.

The offloading reduced to 16-25% of the total load during terminal stance. The peak plantar force at this point was however, only 3% more than the peak observed during early stance. This suggests that the PD-AFO limits the peak forces experienced within the limb, rather than providing a constant reduction in load. The relative increase in load through the limb at push off is thought to be due to the need for the limb to exert a torque to provide a propulsive force, with the posterior struts recovering to their initial undeformed configuration and providing additional propulsion. Analysis of the posterior

struts would provide further insight into the mechanisms occurring at these points and whether they perform as hypothesised. This is evaluated in chapter 6.

5.6 LIMITATIONS

When calculating the loading ratio 2 different recording systems were used: GRF and plantar force. Due to the high rate at which the GRF and plantar force change during the initial and latter stance phases (~0-5% and ~55-60%) a small error in the alignment (by 0.5% of the gait cycle) would result in a large change in the loading ratio. Therefore, these results were addressed with caution. It would be preferred to sync the GRF and PEDAR sensors to minimise any error in alignment. However, due to visible peaks within both recordings, the accuracy was still adequate to allow the ratio of loading to be determined for the remainder of the gait cycle.

During the PD-AFO gait it was necessary for the subject to wear a different, larger shoe on the PD-AFO limb to accommodate the orthotic; with a heel wedge used to ensure the correct shank-to-vertical alignment. This is common practice amongst PD-AFO users and was therefore deemed acceptable. The type of shoe worn on the PD-AFO limb was also of a different type to that used on all other limbs. Shoe type has previously been shown to influence the CoP [86]. However, the results seen in this study were in good agreement with previous studies and therefore suggests the shoe type did not influence the results [40, 60].

Use of a healthy subject could be argued to limit the clinical relevance. However, the results in GRF and plantar pressure were similar to those observed in an injured cohort; this suggests that the offloading found within this study may also be similar to the injured cohort. When aiming to understand how the PD-AFO alters gait, use of a healthy subject, increased the strength of the control and reduced unknown variables associated with the severity and type of injury. Some variability between limbs is common, as seen between the right and left control limbs in this study; this is likely due to dominance of one limb. Using a healthy subject, and therefore a direct control rather than a normative data set, allows the influence of limb dominance to be accounted for. Using a healthy subject also removes the variability in patient pathologies and the influence these may play.

As the healthy subject does not require the PD-AFO they did not undergo the full rehabilitation programme described in Chapter 3. However, as discussed, it is not fully understood which aspects of the programme provide the most benefit; the training to use the PD-AFO, the muscle strengthening following injury, or the benefits in self-efficacy. The latter two benefits are not relevant to a healthy subject who has not experienced lower limb trauma. To mitigate the first benefit, the subject underwent training with the PD-AFO upon fitting and used it several times before the gait trials. Some changes were seen in the total GRF and plantar force of the PD-AFO limb across 4 days, when the subject wore the PD-AFO for a minimum of 60 minutes before each session. However, the changes were not consistent across measurement techniques and did not suggest a trend across the days. The

differences between the mean values between days did not exceed 5%. This level of accuracy was deemed acceptable.

The study is limited to the use of only 1 participant. Developing the PD-AFO is expensive in both time and cost. However, for those metrics which have been previously measured in the literature the values obtained were in good agreement during PD-AFO gait [57, 62]. The subject was also found to have similar results to literature during walking, when not wearing the PD-AFO [57, 87]. The extrapolation of the results to a wider cohort can be considered with caution, and therefore the additional time and cost of further gait trials was not considered necessary.

Running has been used as one of the functional outcomes, that has hailed this PD-AFO as a success [35]. The 2 force plates within the gait set up were too close to achieve clean force-plate hits for both limbs during running. Due to the length of the raised platform, it was difficult to alter which limb made contact with the force plate in each cycle without altering the running gait. A new gait lab set up and calibration would have been required to analyse the running gait. Additionally, running biomechanics during healthy gait are known to vary amongst the normative population more so than healthy walking biomechanics, with people running with forefoot, midfoot and heel strike patterns and so the limitation of using a single subject could have biased the results [88, 89]. Whilst the PD-AFO rehabilitation programmes encourage mid-foot strike [35] and it is therefore likely that the biomechanics of gait during running do not vary greatly between patients when wearing the PD-AFO, more than 1 subject would have been required to ensure the range of healthy running techniques is compared to the biomechanics seen during PD-AFO gait. As such alterations of gait whilst running compared to control gait were not considered, due to the combination of new gait set up and the deemed importance of a larger cohort to analyse normal running to ensure meaningful results.

5.7 CONCLUSION

The study was able to quantify the offloading offered by the PD-AFO. The greatest alterations to loading were seen in the lower limb during early stance. Peak plantar forces and peak plantar pressures were also reduced. During loading response and early stance, the reduction in pressure was likely to be mainly due to the reduction in peak load. During later stance the reduction was likely due to a combination of reduction in load and an increase in the contact region. The mechanism by which the PD-AFO reduces the peak loads is hypothesised to be different at different points in gait. In particular, during loading response and early midstance, a combination of heel wedge deformation and posterior strut loading are thought to reduce the peak load. During terminal stance and pre-swing, the peak load is thought to reduce due to the more anterior CoP resulting in decreased propulsive force seen from the foot, compensated for by the PD-AFO's energy storage and return characteristics. In the next chapter, the deflection of the posterior struts during gait will be examined to explore further the energy storage and return characteristics of the PD-AFO.

6 ENERGY STORAGE CHARACTERISTICS

Chapter 5 highlighted changes in gait, when wearing the PD-AFO. These changes in gait have, in part, been hypothesised to be due to the mechanical function of the posterior struts, by process of energy storage and return (ESAR). In particular, it is thought the posterior struts provide propulsive power at push-off. Using an instrumented PD-AFO, this chapter aims to demonstrate whether the PD-AFO possesses ESAR characteristics and, if so, quantify the power dissipation and generation during walking and running. Reliability and accuracy tests of the instrumentation of the posterior struts using bending and compression experiments is also presented.

6.1 INTRODUCTION

In chapter 5 the hypothesised alterations to gait were discussed, along with which components of the PD-AFO were thought to be responsible for these changes. Literature has demonstrated that the PD-AFO limits the plantarflexion angle and reduces the dorsiflexion moment of the ankle. Chapter 5 also addressed the offloading capabilities of the device. This chapter aims to investigate the ESAR characteristics of the posterior struts, and quantify the propulsive power, if any, generated.

Specifically, it is hypothesised that the posterior struts deflect during midstance and terminal stance to store energy, and this energy is returned, generating propulsive power during pre-swing. It is also thought that the strut deflection during loading, together with deformation of the heel-wedge, act as a damper to reduce the peak load experienced by the combined limb-PD-AFO system, by increasing the time over which the impulse occurs. Therefore, an additional aim is to quantify how the struts deflect in the sagittal plane throughout gait, to provide further information for studies that wish to examine different possible manufacturing techniques for the component, such as the use of SLS [64]. In

particular, for the PD-AFO that is the focus of this thesis, part of its considered success is the ability to enable patients to return to high-level activities such as running. Therefore, both walking and running are evaluated to quantify the energy stored and power generated by the PD-AFO.

The posterior struts have been considered an important aspect of the PD-AFO's success, with 9 out of the 10 design analyses of the PD-AFO focussing on the influence of the posterior strut component on gait [38, 39, 53-56, 64, 65]. ESAR characteristics of the PD-AFO's posterior struts, whilst alluded to in the literature, have not been directly evaluated [18, 37, 58, 63]. As discussed by Patzkowski et al. previous AFOs that have claimed ESAR properties have, upon evaluation, been shown to exhibit very little energy return [17]. This is due to hysteresis.

Within healthy gait the ankle joint complex produces more energy than it absorbs; this is why walking expends energy [90]. This is not possible to replicate using a passive device. In an ideal world, if a passive device behaves perfectly elastically, it returns the same amount of energy as it stores. In reality, it exhibits inelastic behaviour, where, due to energy losses through heat, sound and friction, the energy returned is less than that stored [91]. This is known as hysteresis and means that the work done on an AFO during braking is greater than the work done by an AFO during propulsion. The difference between these energy transfers is the inefficiency. Therefore, despite visible deflection of the posterior struts during gait, it is not possible to assume that the posterior struts provide propulsive power. To evaluate the energy generated by the struts the efficiency must be quantified. This is addressed in this chapter.

The derivative of energy with respect to time is power. Calculation of the energy stored and returned within the struts, accounting for hysteresis, allows the power dissipated and generated to be calculated. Ankle power of the combined-PD-AFO-limb system has been examined in the literature but not the power of the PD-AFO alone [54, 56]. The power characteristics of the combined limb-PD-AFO system during walking and running, as recorded in literature, are shown in Figure 6.1.1 [54, 56]. It is hypothesised that the PD-AFO will follow the same pattern of power dissipation and generation as the combined limb-PD-AFO system but will provide a fraction of the total power seen.

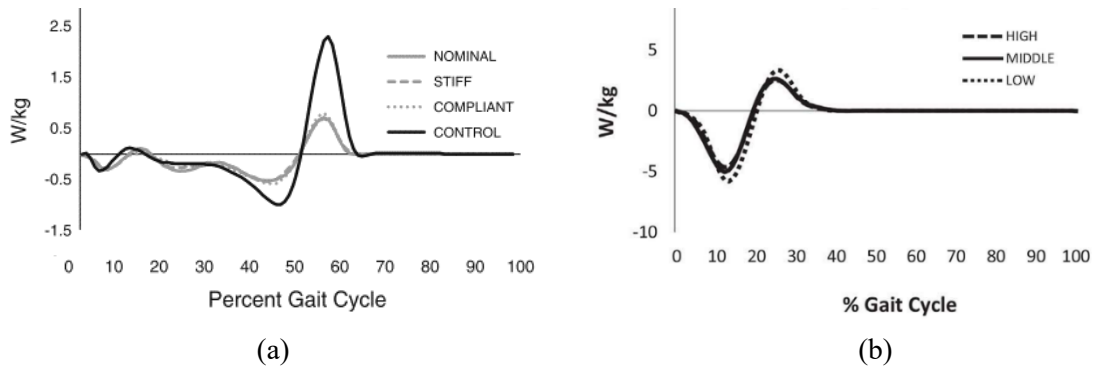


Figure 6.1.1: The ankle power (W) of the combined limb-PD-AFO system, normalised to body weight, during (a) walking with 3 different posterior strut stiffnesses and a healthy control [56] and during (b) running with 3 prescribed bending axis location of the posterior struts [54]. Images reproduced with permission from the rights holder [(a) Wolter Hu (b) Elsevier].

Although the ESAR characteristics of the posterior struts have not been evaluated, Wach et al. directly examined the deflection of the struts [63]. Using mechanical testing to mimic discrete points in gait, Wach et al. analysed both stiffness and strut deflection of the IDEO in the sagittal plane, comparing it to 3 other AFOs. The deflection of the PD-AFO posterior struts was found to be much greater than that seen by the posterior aspect of the other AFOs, shown in Figure 6.1.2 [63]. This suggests that more energy is stored within the IDEO than in the other AFOs tested by Wach et al. supporting the notion that the posterior struts contribute to the uniqueness of the PD-AFO that is the subject of this thesis and the successful outcomes for patients wishing to return to high level activity.

Evaluating the concept of ESAR characteristics of other AFOs in literature is also limited [92-94]. AFOs are designed to accommodate a variety of functional deficits, and not all require ESAR to meet patient needs. Many AFOs are made of thermoplastics, for example, which are designed to limit ROM, but do not possess the material properties to accommodate large elastic strains and energy storage [94]. There are a lot more data on the evaluation of ESAR in prosthetics, as this has been a design feature of prosthetics since the early 1980s [90, 91, 95-99]. This prevalence of studies is due to the necessity of an effective prosthetic to store and return energy. Within lower limb prosthetics, ESAR is theorised to replicate muscle forces, applied through the Achilles tendon, allowing for storage of energy during loading response and propulsion during terminal stance [98]. This is similar to the mechanism of action thought to occur within the PD-AFO.

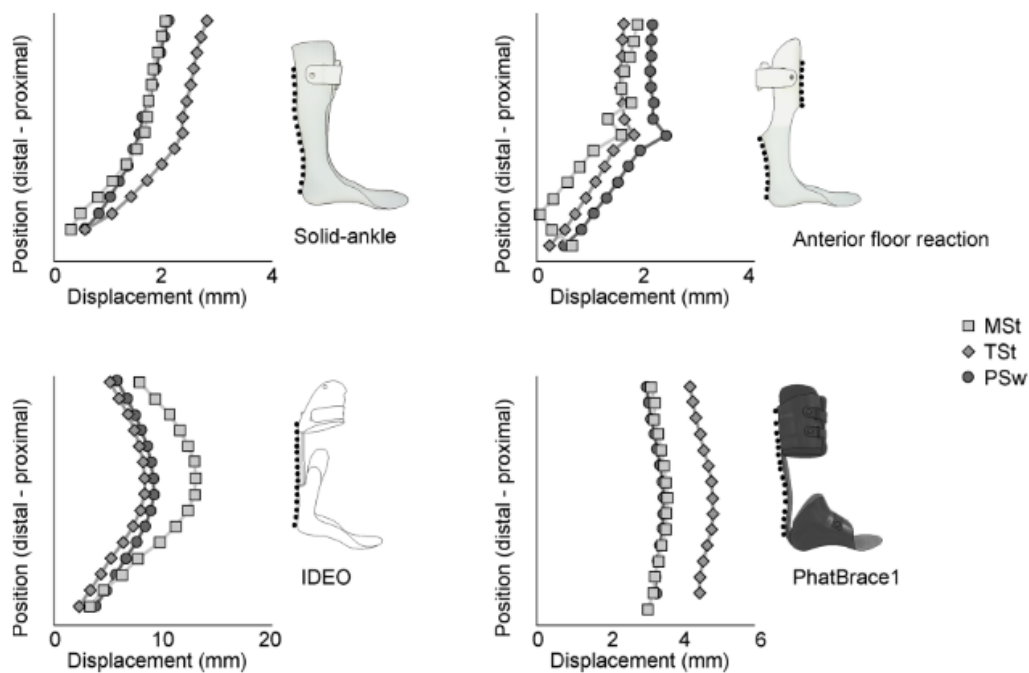


Figure 6.1.2: Strut deflections in the sagittal plane seen during mechanical testing of 4 different AFOs, including the US military version of the PD-AFO, the IDEO, at 3 points in gait: Midstance (MSt), Terminal Stance (Tst) and Pre-swing (PSw) [63]. Image reproduced with permission from the rights holder ASME.

Studies examining ESAR characteristics of orthotics and prosthetics, highlight the importance of quantifying efficiency [99]. Previously mechanical tests using a materials testing machine have been used to calculate the efficiency of running prosthetics [91, 95, 99]. This method provides accurate measurements of the force-displacement curves allowing the efficiency to be calculated. It should be noted that the mode of loading in which the component is tested should be realistic to the mode of loading seen during gait. For this study, only the ESAR characteristics of the posterior struts are to be examined, and therefore only the efficiency of these components needs to be quantified.

To quantify the energy stored, the deflection of the struts needs to be established. It is hypothesised that the strut deflections are greatest in the sagittal plane, and minimal in the coronal plane. To track this deflection during gait, reflective markers [99] or strain gauges [100, 101] can be used. The geometry of the PD-AFO and the dynamic activity itself may limit placement of the reflective markers. Comparatively, strain gauges are small and can be adhered to the struts rigidly, and therefore can be placed in more locations. Strain gauges can be used to quantify the deflection in the sagittal plane and also confirm that bending of the posterior struts in the coronal plane is negligible.

6.2 METHODOLOGY

6.2.1 Strain Gauge Reliability and Accuracy

Due to the surface coating on the posterior struts, it was deemed necessary to confirm the reliability and accuracy of the strain gauges when adherent to the surface. A validation experiment was conducted on 3 samples of the posterior strut. The samples of the posterior struts were the same as those used to characterise the material properties in chapter 4, provided by Blatchford. On each sample, 2 sets of 4 strain gauges, as shown Figure 6.2.1, were attached at 90° from one another, with their axis parallel to the long axis of the strut.

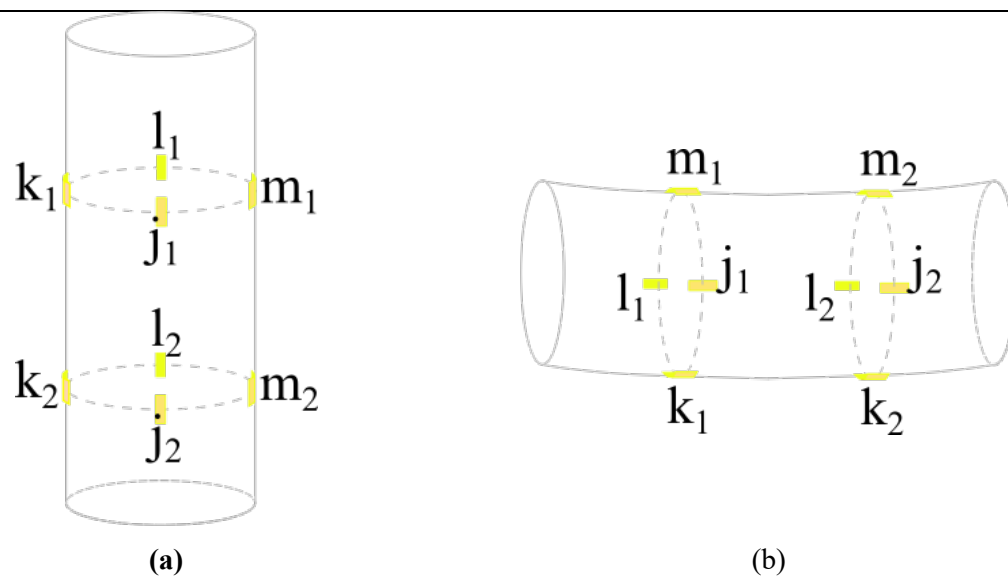


Figure 6.2.1 Schematic showing strain gauges on samples at 2 sites (1 and 2), located at 90° to one another (at locations j , k , l , m) in the; (a) orientation for compression tests (b) orientation for bending tests

The samples were sanded before attaching the strain gauges, and a small custom-made tool was manufactured to help ensure the correct location and orientation of the gauges (Figure 6.2.2). To remove any systematic error, a baseline reading was taken with the struts unloaded to quantify the output signal at zero load (see Appendix 12.3.1).



Figure 6.2.2: A custom made strain gauge attachment to help ensure consistent strain-gauge placement. This attachment fitted around the sample of each posterior strut to indicate the location and orientation for each strain gauge.

The samples underwent a compression test and 4-point bend test, as shown in Figure 6.2.3, on a uniaxial material testing machine (model 5866, Instron). These were the same tests used to characterise the material properties of the samples in Chapter 4; full details of the set-up is described in chapter 4. The samples were rotated 90° (about the long axis) every 3 tests to ensure the same strain gauge did not always record the same location relative to the axis of loading. In total 12 tests were performed on each sample. The values of strain were recorded at a sample rate of 1000Hz, using a data acquisition system (National Instruments, cDAQ-9174 with module NI 9236) and processed with LabView (National Instruments, v2018). During post processing this was reduced to an effective sampling frequency of 250Hz.

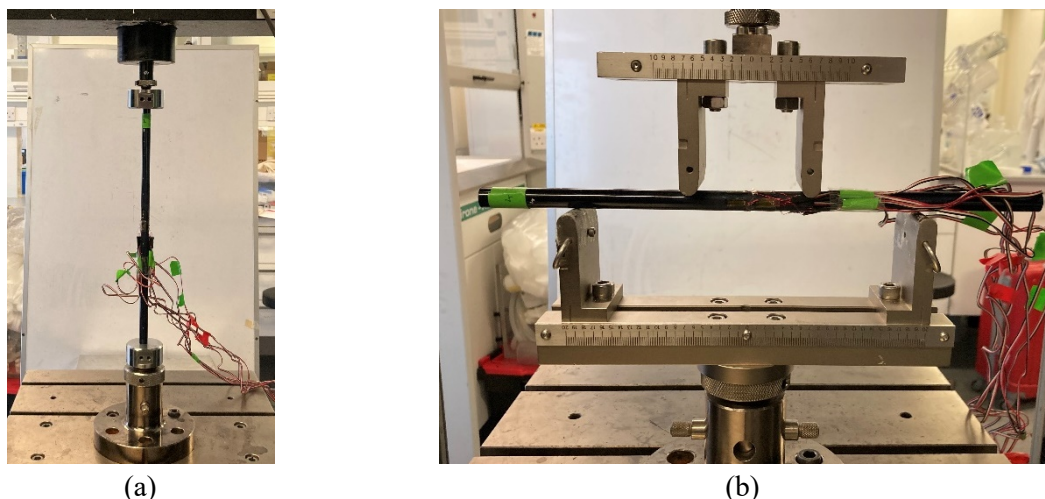


Figure 6.2.3: Experimental test set-ups used to validate the strain gauge attachments in (a) compression and (b) 4-point bending

During the compression and bending tests, $\delta_{input} = \delta_{input}(t)$ was logged by the material testing machine, where δ_{input} was the displacement applied by the materials testing machine as a function of time. The strain, ε , was recorded by the strain gauges as a function of time: $\varepsilon = \varepsilon(t)$. The displacement-time plots recorded by the materials testing machine and the strain-time plots recorded by the strain gauges, were fitted with a linear regression model for both bending and compression.

The applied displacement rate from the materials testing machine over the respective length of each sample gave the predicted strain rate. Comparison of this predicted strain rate and the strain rate as recorded by the strain gauges, was used to determine the accuracy of the strain reading. It was predicted that all strains as a function of time, $\dot{\varepsilon}_i$, at each site, i , were equal to the applied displacement rate $\dot{\delta}_{input}$ over the respective length of each sample, l , as shown in equation (6.2.1):

$$\dot{\varepsilon}_j = \dot{\varepsilon}_k = \dot{\varepsilon}_l = \dot{\varepsilon}_m = \frac{\dot{\delta}_{input}}{l} \quad (6.2.1)$$

Comparison of the strain rates from the bending tests were used to establish the reliability of the attachment. During bending it was hypothesised that the strain gauges on the sides of the samples would record $\sim 0 \text{ s}^{-1}$ strain rate, and the absolute values of the strain rates recorded on the top and bottom of the samples would be the same. These relationships are shown in equations (6.2.2) and (6.2.3), where locations j , k , l and m are as indicated in Figure 6.2.1b with bending occurring about the axis normal to the page.

$$\dot{\varepsilon}_j = \dot{\varepsilon}_l = 0 \quad (6.2.2)$$

$$|\dot{\varepsilon}_k| = |\dot{\varepsilon}_m| \quad (6.2.3)$$

6.2.2 Efficiency

To determine the extent of energy return of the posterior struts the efficiency was established. This was achieved by performing a 4 point-bend test, the main mode of loading contributing to energy storage during gait, on the 3 samples. All 4-point bend test parameters were the same as used as in chapter 4, with the exception that the struts were loaded up to a maximum of 500N and unloaded at the same rate. For each sample, the force-displacement curve during loading and unloading was recorded. The force displacement curves were fitted with a linear regression model, excluding values of displacement $< 0.2\text{mm}$.

The PD-AFO was instrumented with 16 strain gauges; 4 strain gauges were added to 2 sites on each strut (see Figure 6.2.4), in a 90° orientation as described in section 6.2.1 for the strain gauge validation. The diameter of the struts at each of these 4 sites was recorded using Vernier Callipers. The strains were recorded using the same data acquisition system described in section 6.2.1. Before the gait trials, the strain-gauge values were recorded with the PD-AFO unloaded to provide a zero-reading to be subtracted from all trial values.

The work done to deform the strut was calculated, using equation (6.2.4), where $P(\delta)$ is the force recorded by the materials testing machine as a function of the displacement, δ [94]. For loading, the limits, a and b , were set as 0.2 mm and the maximum displacement, respectively. For unloading, the limits, a and b , were set as the maximum displacement and 0.2mm, respectively.

$$\mathit{work\ done} = \int_b^a P(\delta) d\delta \quad (6.2.4)$$

The efficiency, η , was calculated using equation (6.2.5), where E_S is the work done on the sample during loading and E_R is the work done by the sample during unloading. The mean efficiency across all repeats (n=12) and all samples (n=3) was calculated.

$$\eta = \frac{E_S}{E_R} \quad (6.2.5)$$

6.2.3 Instrumented Gait Trials

The strain gauge locations were named using the following naming pattern: “XS_Y_Z”.

- Where X indicates the strut on which the strain gauge is attached:
 - M for medial strut
 - L for lateral strut
- Y is the site on that strut
 - P for proximal site
 - D for distal site
- and Z is the side of the strut on which the strain gauge is attached
 - A for anterior
 - P for posterior
 - M for medial
 - L for material

For example, “*MS_D_A*” indicates the strain gauge on the medial strut, at the distal site on the anterior side, and “*LS_P_L*” indicates the strain gauge on the lateral strut, at the posterior site on the lateral side. Note that when referring to medial or lateral locations, this is in reference to the lower limb and not the relative location in terms of the struts.

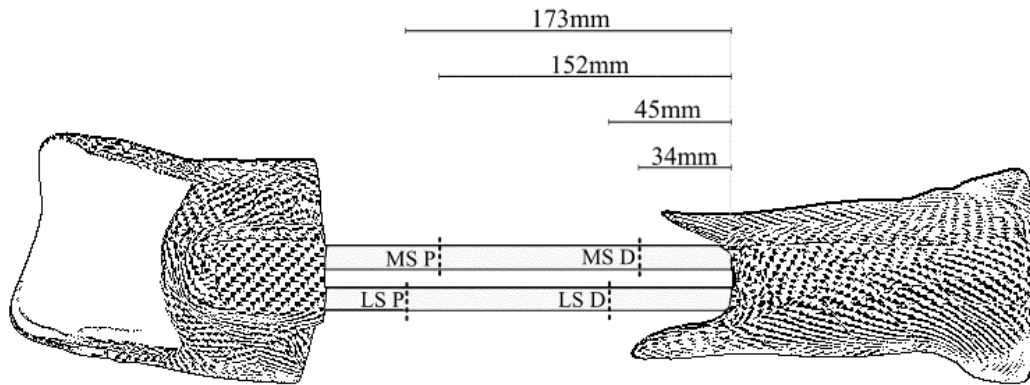


Figure 6.2.4: Schematic showing the location of the 4 sites where strain gauges were attached as measured from the posterior, proximal surface of the base of the struts. It is a rear view of the orthotic. At each site there are 4 strain gauges. ‘MS’ indicates the site on the medial strut, and ‘LS’ indicates the site on the lateral strut. ‘P’ and ‘D’ indicate whether it is a proximal or a distal site.

The subject donned the instrumented PD-AFO. Care was taken to ensure minimal tension was within the cables connecting the strain gauges with the data acquisition system. The subject was asked to walk across the platform 10 times. These 10 walking trials were the same as those analysed in Chapter 5. On a different occasion, the subject was also asked to run across the platform 10 times whilst wearing the instrumented PD-AFO. The same shoes were used in all trials.

During each trial, the GRF was recorded by Vicon and the plantar force was recorded by the PEDAR sensors to allow one gait cycle to be established. The strain gauges were synchronised with the Vicon system, so that the strain gauges and force plates began recording at the same time. The GRF and plantar force data were used to determine one gait cycle within each gait trial. The GRF data were aligned with the plantar force data as described in chapter 5 for both running and walking. These data were then windowed and normalised to 100%. The syncing of the strain gauge data with the GRF allowed the same windowing and normalisation to be directly applied to the strain gauge data to give one full gait cycle.

6.2.3.1 Strains

Using simple beam-bending theory, the strains were resolved in one plane, to represent strain due to bending, ϵ_b , in that plane and the strain due to axial load, ϵ_a , shown in Figure 6.2.5. To achieve this bending was considered separately in 2 planes (the sagittal plane and the coronal plane). It was

assumed torsion of the struts is negligible. Additionally, it was assumed that the neutral axis did not move. It was also assumed that the posterior struts were ‘built-in’ to the posterior cuff and base, so these regions did not bend.

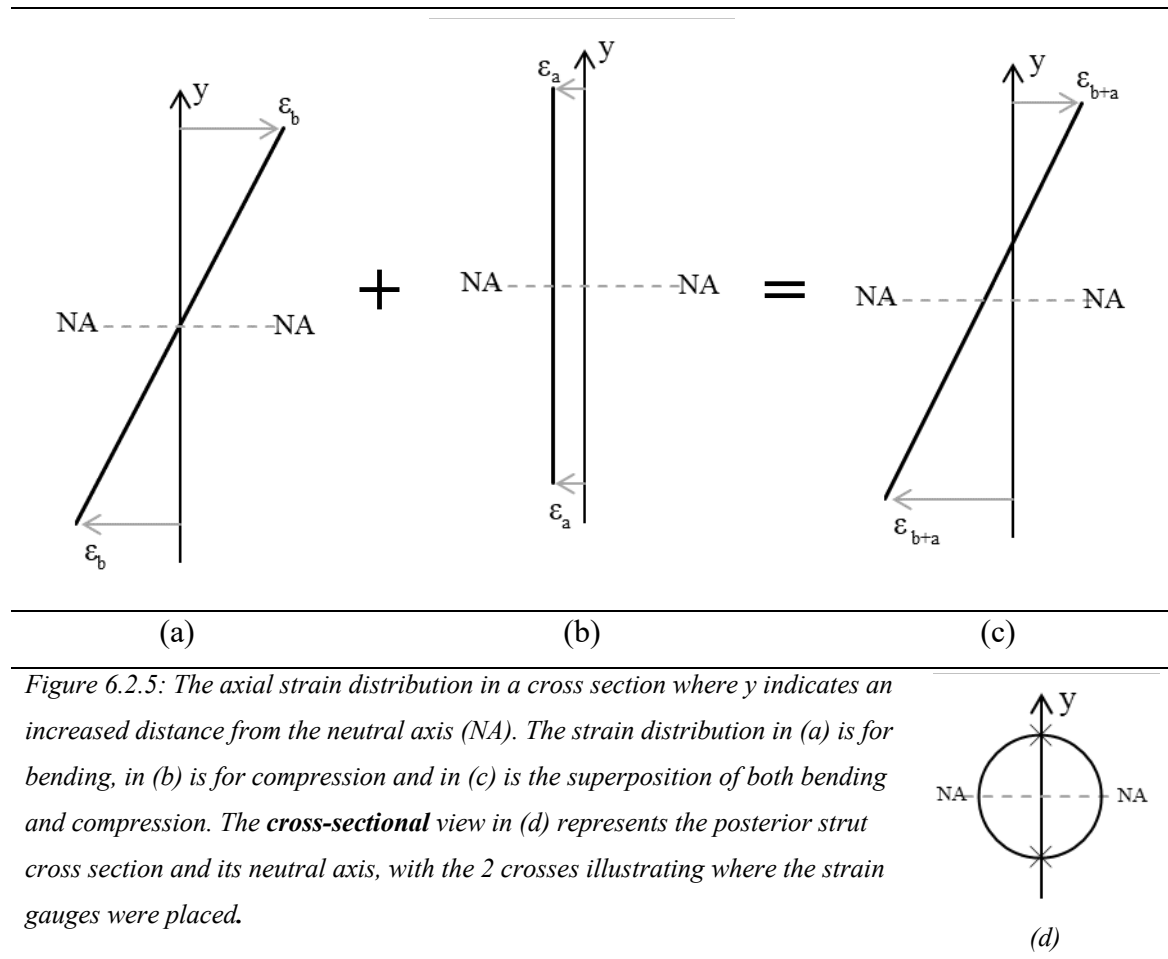


Figure 6.2.5: The axial strain distribution in a cross section where y indicates an increased distance from the neutral axis (NA). The strain distribution in (a) is for bending, in (b) is for compression and in (c) is the superposition of both bending and compression. The **cross-sectional** view in (d) represents the posterior strut cross section and its neutral axis, with the 2 crosses illustrating where the strain gauges were placed.

The strain recorded by the strain gauges were those values illustrated in Figure 6.2.5c. A negative strain indicates compression, and a positive strain indicates tension. To find the axial strain due to bending alone, shown in Figure 6.2.5a, the difference between the maximum recorded strain, ϵ_{b+a} , and minimum recorded strain was found and then divided by 2. This is shown in equation (6.2.6).

$$\epsilon_b = \frac{\epsilon_{b+a}^{max} - \epsilon_{b+a}^{min}}{2} \quad (6.2.6)$$

The axial strain due to the compression alone was calculated by taking the mean value of the maximum recorded strain and minimum recorded strain, shown in equation (6.2.7).

$$\varepsilon_a = \frac{\varepsilon_{b+a}^{max} + \varepsilon_{b+a}^{min}}{2} \quad (6.2.7)$$

To calculate the strain energy stored due to axial compression, U_A , equation (6.2.8) was used. E is the Young's modulus calculated in Chapter 4, with a value of 35.23 ± 2.66 GPa. A is the mean cross-sectional area of the strut. The length, L , of each strut, was assumed to be the region visible on the PD-AFO (it did not include the region built-in to the posterior cuff or base).

$$U_A = E \int_0^L \frac{\varepsilon_a^2 A}{2} dx \quad (6.2.8)$$

To calculate the strain energy stored due to bending, equation (6.2.9) was used. I is the second moment of area of the strut at distance, x , along the strut, and y is the distance from the neutral axis at which the bending strain, $\varepsilon_b(x)$, was measured. In this case $y \equiv R$ and $I = \frac{\pi R^4}{4}$, where $R=f(x)$ was the mean radius of the strut. Again, the length, L , of each strut, was assumed to be the region visible (did not include the region built-in to the posterior cuff or base).

$$U_B = E \int_0^L \frac{\varepsilon_b^2 I}{2y^2} dx \quad (6.2.9)$$

The bending strain and compressive strains were used to calculate the strain energy stored, U , within the struts throughout the gait cycle using (6.2.10). The energy stored is always a positive value.

$$U = U_A + U_B \quad (6.2.10)$$

The error in the calculation of the energy was determined using propagation of errors. For measurements with $n > 5$ readings, the error of the measurement was assumed to be the standard error. For all other measurements, the absolute error was used.

The power dissipated and generated by the posterior struts, not accounting for efficiency, was given by equation (6.2.11). P_{SG} is the power, which is the derivative of energy, U , with respect to time, t . A

positive power indicates that the PD-AFO is storing energy; work is being done on the PD-AFO. A negative power indicates that energy is being returned; the PD-AFO is doing work.

$$P_{SG} = \frac{dU}{dt} \quad (6.2.11)$$

Equation (6.2.11) details the calculation for power, not accounting for inefficiencies.; the energy stored by the struts, as calculated by the strain gauges, is less than the energy put into the struts to cause the deflection. Similarly, the energy returned by the struts, as calculated by the strain gauges, is greater than the true work done by the PD-AFO, as some energy is lost due to inefficiencies. The true power, P_t , can be calculated by multiplying the recorded power, P_{SG} , by a constant $C(\eta)$ as shown in equation (6.2.12), where η is the efficiency calculated in equation (6.2.5) above.

$$P = P_{SG} \cdot C$$

$$C(\eta) = \begin{cases} \eta & P_{SG} < 0 \\ 1/\eta & P_{SG} \geq 0 \end{cases} \quad (6.2.12)$$

6.3 RESULTS

6.3.1 Strain Gauge Reliability and Accuracy

During the compression tests described in Chapter 4, values of strain over time were recorded by 8 strain gauges on each sample. These were compared to the rate of strain predicted by the materials testing machine as calculated from the displacement rate over the length of the respective sample.

Figure 6.3.1 shows the rates of strain recorded over time by the strain gauges on 3 samples and the rate of strain predicted by the recordings of the tests with the materials testing machine ($R^2 > 0.98$). Two outliers were seen in sample 1, 1 outlier was seen in sample 3 and 1 outlier seen by the materials testing machine. One test repeat was recorded incorrectly on sample 1 and was therefore disregarded. On sample 3, two strain gauges were damaged and therefore not used. A statistical difference was found between the data from sample 2 and those from the materials testing machine calculation, and between the data from sample 3 and the materials testing machine calculation. The median strain rate of sample 1 was 3.5% higher than that of the materials testing machine calculation, of sample 2 was 19.8% lower and of sample 3, 13.6% lower than that of the materials testing machine calculation.

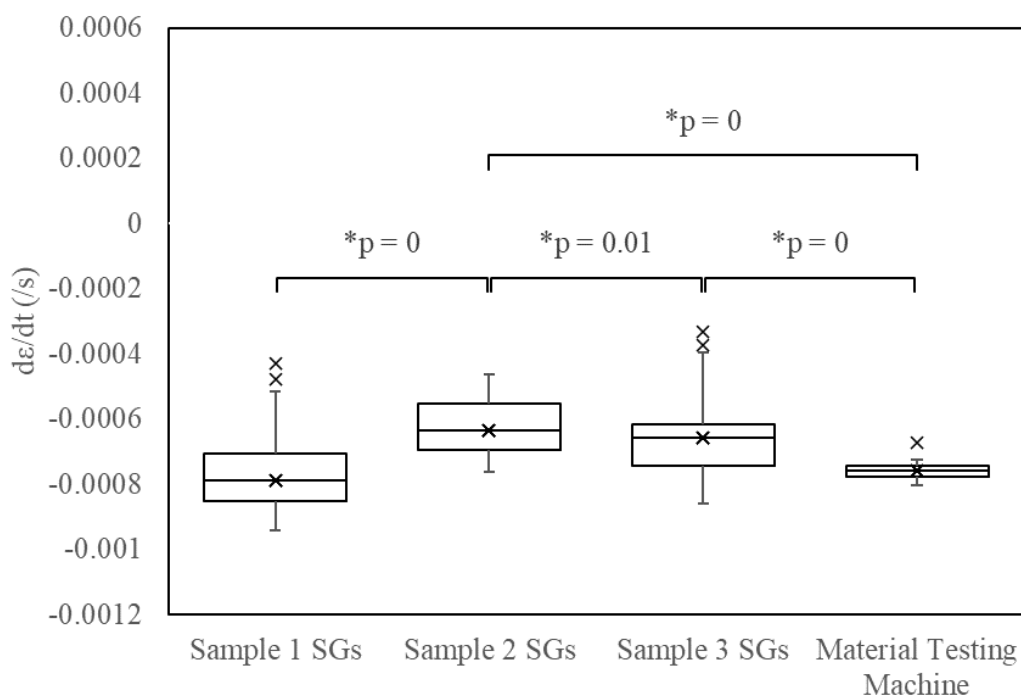


Figure 6.3.1: Change in strain over time (strain rate) during compression as recorded by 8 strain gauges (SGs) on 3 samples, and as calculated by the force-displacement curve recorded by the materials testing machine. The median strain rate for samples 1, 2, and 3 was $-0.0007863 \text{ s}^{-1}$, $-0.0006332 \text{ s}^{-1}$, and $-0.0006560 \text{ s}^{-1}$ respectively. The median strain rate, as calculated by the materials testing machine readings was $-0.0007586 \text{ s}^{-1}$. *p indicates the p value calculated using an unpaired t-test with the significance level set at $\alpha=0.05$.

Figure 6.3.2 shows the change in absolute strain over time, across the 3 samples, during 4 point-bending. These values were recorded at the bottom and top of the sample (sites k and m in Figure 6.2.1b respectively). Two outliers were recorded by the strain gauges when positioned at site k and 3 at site m . The median values were within 1.00% of each other.

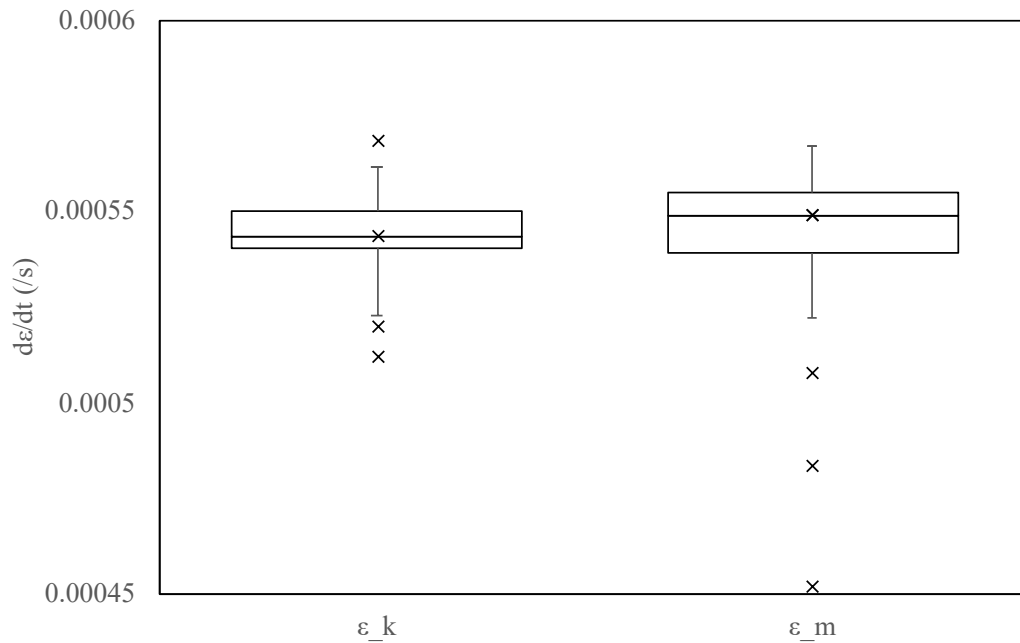


Figure 6.3.2: Change in absolute strain over time, across 3 samples during 4-point-bending. The strain was recorded by 2 strain gauges (SGs) on 2 sides (where ϵ_k and ϵ_m are the strain gauges top and bottom as indicated in Figure 6.2.1b) of the sample. The median absolute value of strain over time for the bottom strain gauges was $0.0005435 s^{-1}$, and for the top strain gauges was $0.0005490 s^{-1}$.

Figure 6.3.3 shows the values of strain over time recorded by strain gauges on the sides of each sample, during 4-point-bending. The values recorded by the strain gauges were all <1% of the values of strain rate recorded at the top and bottom locations on the samples.

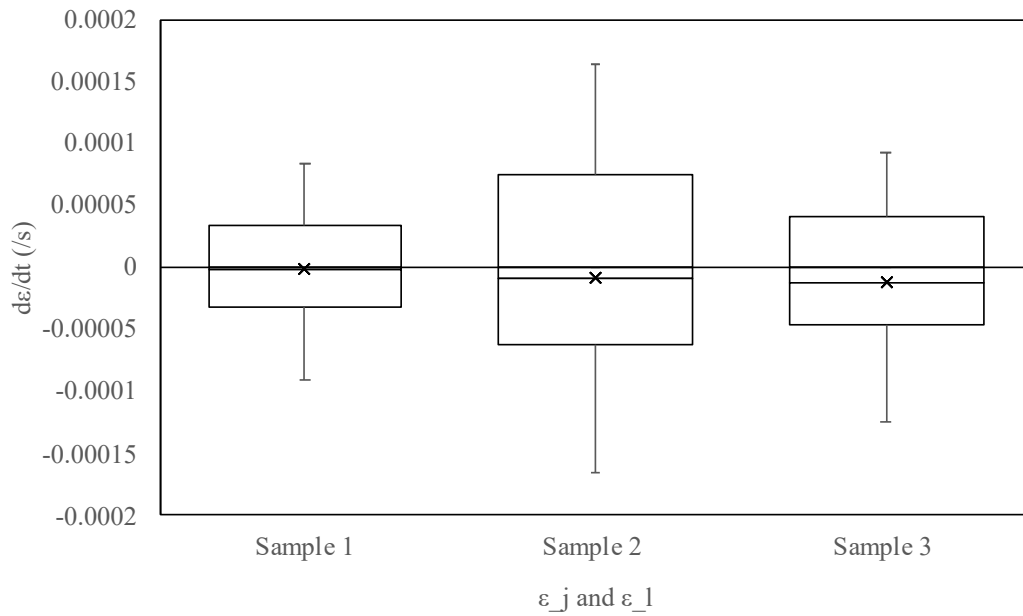


Figure 6.3.3: Change in the absolute value of strain over time during bending, as recorded by 4 strain gauges (those located on the side of the samples during the 4-point-bend test: ε_j and ε_l) on 3 samples, and the maximum change in strain over time as calculated by the force displacement curve recorded by the materials testing machine. The median strain rate for samples 1, 2, and 3 was $3.112 \times 10^{-6} \text{ s}^{-1}$, $1.991 \times 10^{-6} \text{ s}^{-1}$, $1.089 \times 10^{-5} \text{ s}^{-1}$ respectively.

6.3.2 Efficiency

Figure 6.3.4 shows the force-displacement curve, recorded by the materials testing machine, for 1 repeat on sample 2. The loading and unloading curves for all repeats on all samples (n=15) were fitted with a linear regression model ($R^2 > 0.99$). Raw data for sample 1 are shown in Appendix 12.3.2.

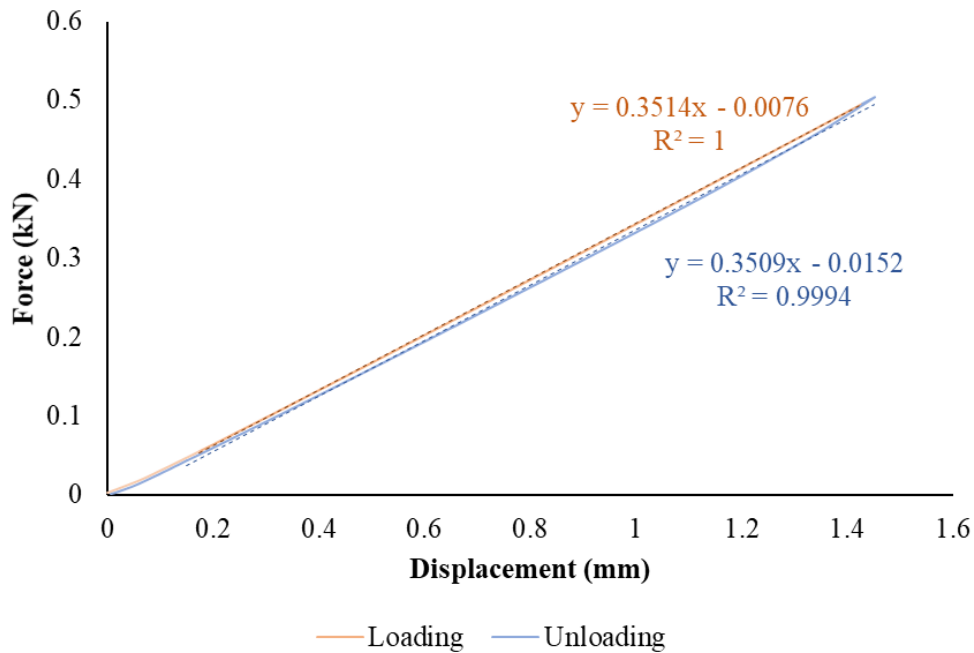


Figure 6.3.4: The force-displacement curve recorded during 4 point-bending for 1 sample during loading and unloading. The linear regression models fitted to the loading and unloading curve between 0.2 mm and the maximum displacement are shown.

Figure 6.3.5 shows the efficiency calculated for each strut during 4-point bending. A statistical difference was seen between the efficiency calculated for samples 1 and 2. The maximum difference of efficiency between samples was less than 0.5%. The mean value \pm 1SD of efficiency was calculated as $96.9 \pm 0.3\%$.

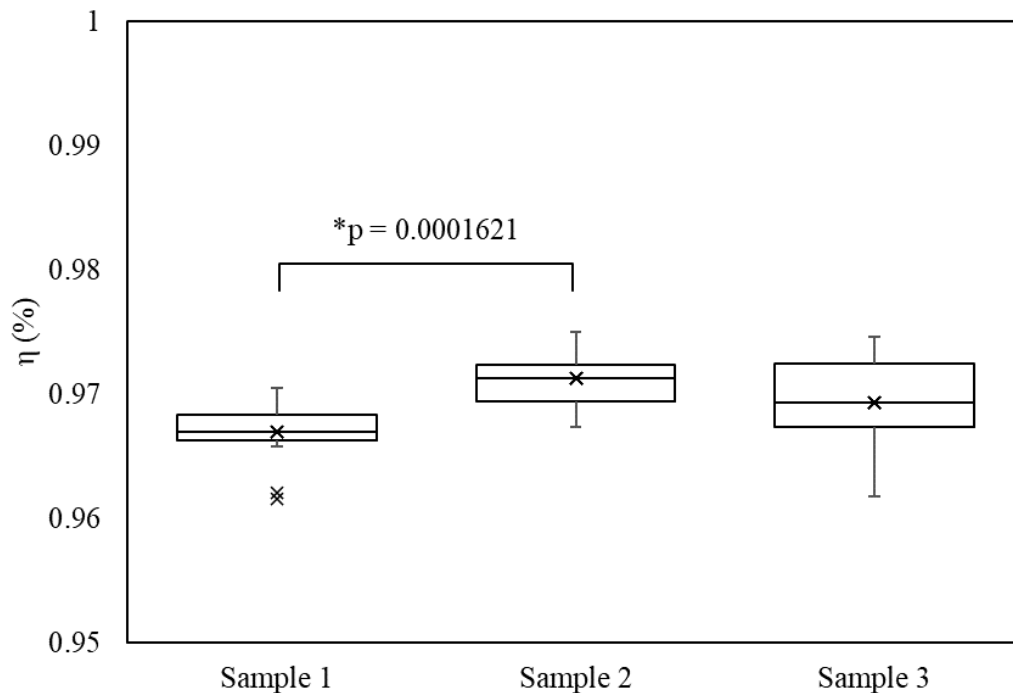


Figure 6.3.5: The efficiency, η , calculated from each sample ($n=12$) from 4-point bending. The median efficiency recorded by sample 1 was 0.967, by sample 2 was 0.971 and by sample 3 was 0.969. * p indicates the p value calculated using an unpaired t -test with $\alpha=0.05$

6.3.3 Instrumented Gait Trials

Eight strain gauges were attached to each posterior strut of the PD-AFO and recorded during both walking and running gait. The medial strut had a mean diameter of 11.84 ± 0.11 mm. The lateral strut had a mean diameter of 11.71 ± 0.09 mm. For walking gait 6 trials were analysed, and for running 10 trials were analysed.

6.3.3.1 Walking Gait

The mean values of strain, recorded at the posterior and anterior sides of the struts ($n=8$), during the 6 PD-AFO walking gait trials, are shown in Figure 6.3.6 on page 153. A negative strain shows compression, and a positive strain shows tension. The anteroposterior strain gauges represent a movement of the struts largely within the sagittal plane.

The values of strain recorded on the medial and lateral sides indicates a movement of the struts in approximately the coronal plane. The values of strain recorded on the medial and lateral sides, during

walking are shown in Appendix 12.3.3. The values of strain at these sides were an order of magnitude smaller than those seen in the anteroposterior direction and therefore considered negligible.

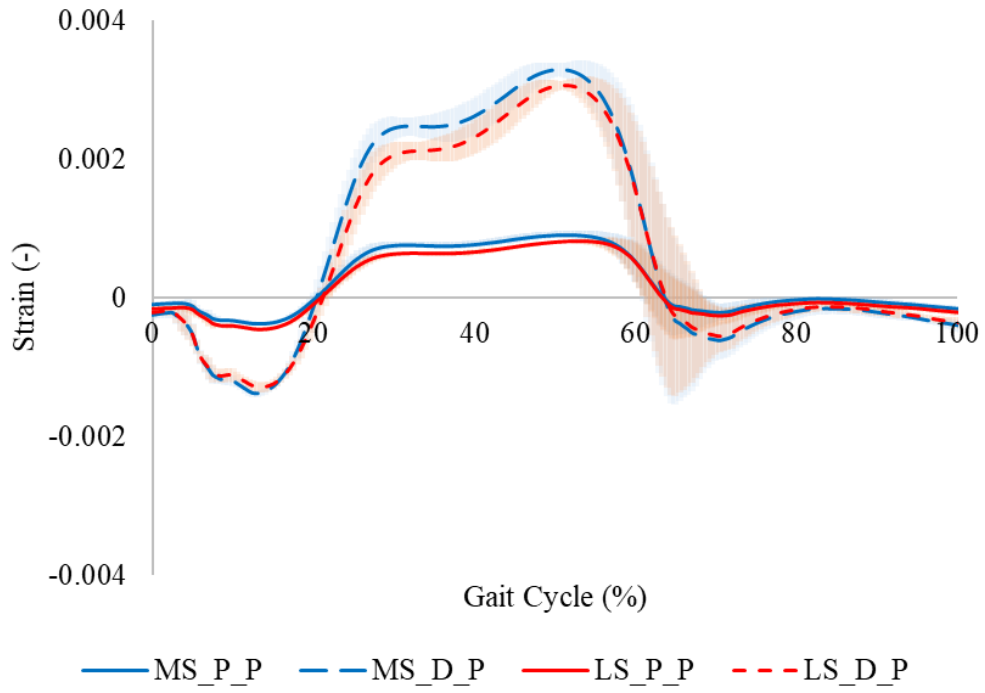
Figure 6.3.6a shows the strain recorded on the posterior side of the struts. The strains on the posterior sides at the proximal sites on both struts (MS_D_P and LS_D_P) experienced compression as the PD-AFO limb entered stance phase. They continued to be compressed until ~15% of the gait cycle, at which point they relaxed. At ~20% of the gait cycle the posterior strain gauges transitioned into tension. Tension increased until ~50% and then reduced until ~60% of the gait cycle. Between 60-70% of the gait cycle, during the swing phase of the PD-AFO limb, the posterior strain gauges entered compression. The posterior sides at the proximal sites on both struts (MS_P_P and LS_P_P) experienced the same directions of strain (compressive and tensile) at the same points in gait, however at a lesser magnitude.

Figure 6.3.6b shows the strains experienced on the anterior sides of the struts. This side experienced approximately equal and opposite strains to those recorded on the posterior side. As the posterior strains became tensile, the anterior strains became compressive and vice versa.

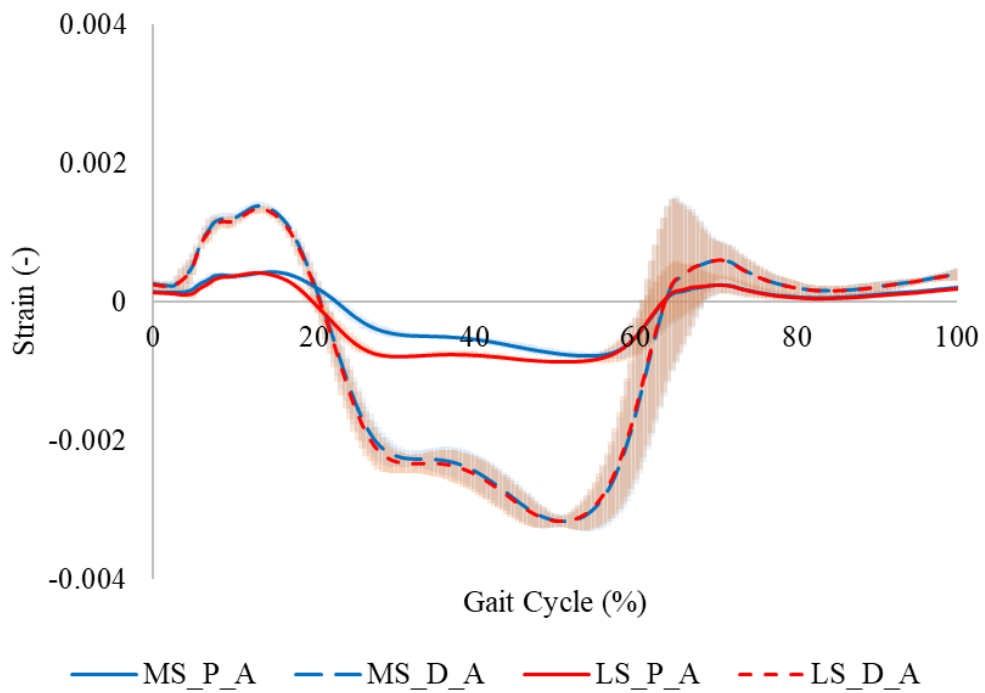
6.3.3.2 Running Gait

Figure 6.3.7, on page 154, shows the strains recorded on the anterior and posterior sides of the struts during running. The strain gauges on the posterior side, Figure 6.3.7a, experienced compression during the first ~15% of the gait cycle. This became tensile, peaking at ~20% of the gait cycle. At 40% of the gait cycle, the PD-AFO limb entered the swing phase during which the posterior strain gauges experienced further compression.

Similarly, to that seen in walking, the proximal sites recorded smaller values of strain compared to the distal sites. Additionally, the anterior sides recorded approximately equal and opposite values of strain to the posterior sides. The peak values of strain (both tensile and compressive) recorded during the stance phase of running were 220-223% greater than those recorded during the stance phase of walking.

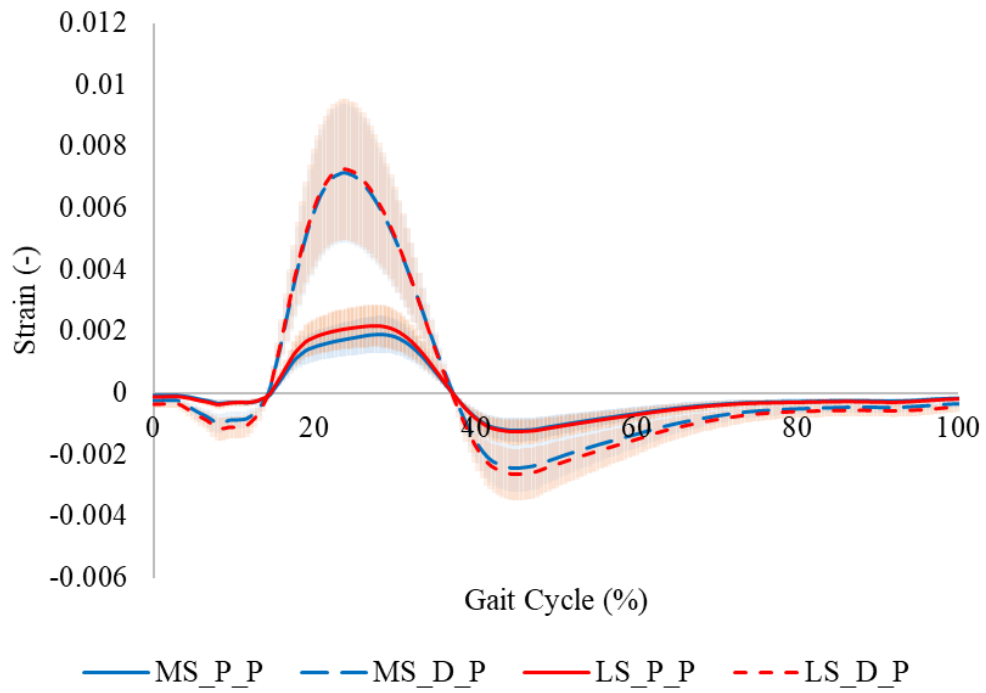


(a)

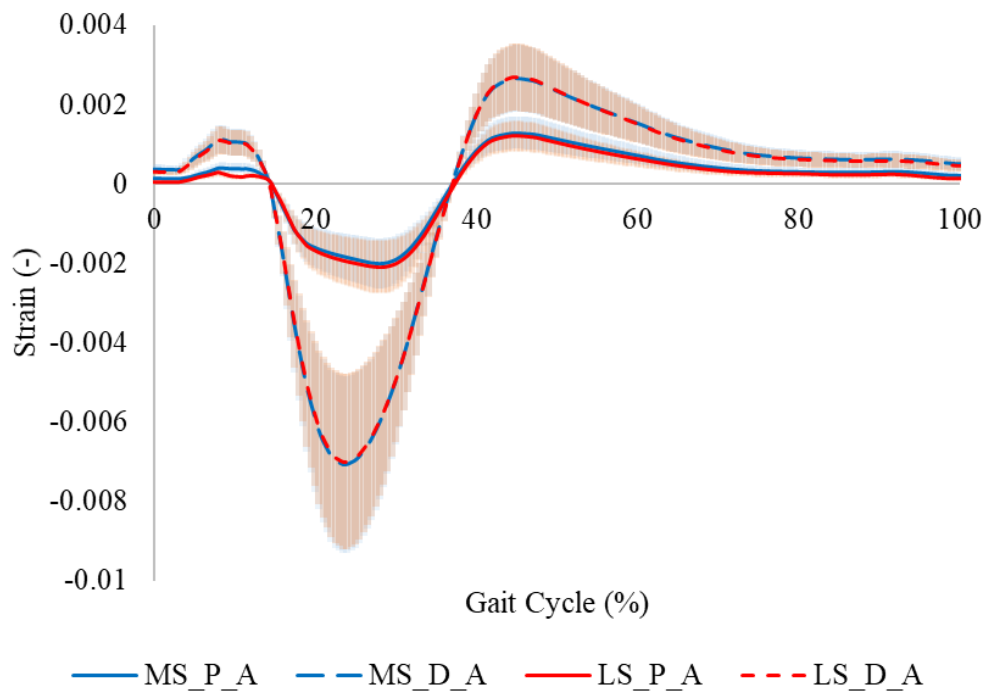


(b)

Figure 6.3.6: The mean strain values during walking on (a) the posterior side of the struts and (b) the anterior side of the struts: on the medial strut, at the proximal (MS_P) and distal sites (MS_D); and on the lateral strut, at the proximal (LS_P) and distal sites (LS_D). The shaded areas show 1 standard deviation.



(a)



(b)

Figure 6.3.7: The mean strain values recorded during running on (a) the posterior side of the struts and (b) the anterior side of the struts: on the medial strut, at the proximal (MS_P) and distal site (MS_D); and on the lateral strut, at the proximal (LS_P) and distal site (LS_D). The shaded area shows 1 standard deviation.

6.3.4 Energy and Power

The strain energy was calculated using equations (6.2.10)-(6.2.9) and the true power was calculated using equation (6.2.11) in the sagittal plane for both running and walking.

6.3.4.1 Walking Gait

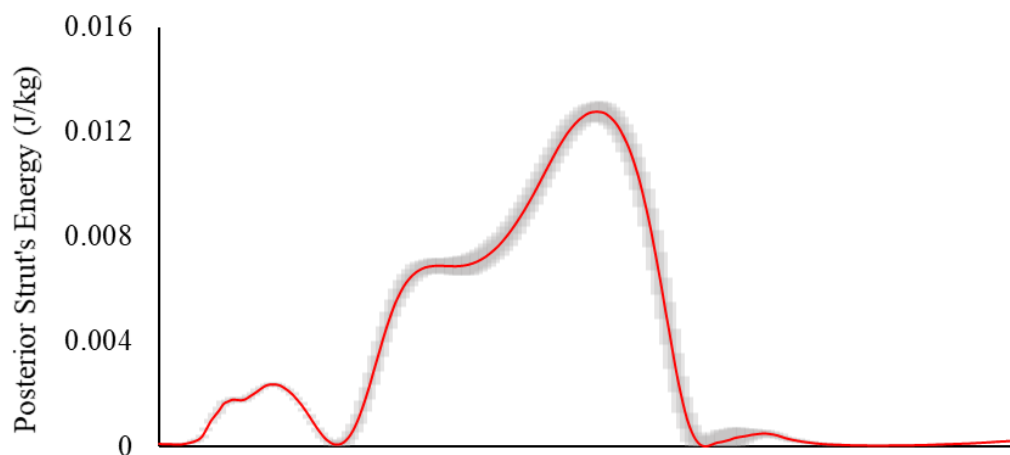
The combined strain energy of both posterior struts, and their power throughout the walking gait cycle is shown in Figure 6.3.8 on page 156. At 13% of the gait cycle the strain energy stored in the posterior struts peaked at 0.00237 ± 0.00008 J/kg. Another peak was observed at 51% of the gait cycle, with 0.0128 ± 0.0004 J/kg of energy stored.

For power a positive value indicates that the struts are generating power (strut relaxation), and a negative value indicates power dissipation (strut deflection). During loading response the posterior struts dissipated power with a peak of 0.0469 ± 0.0001 W/kg at 5.5% of the gait cycle. Power was generated through loading response and early midstance phase, with a peak of 0.0383 ± 0.0013 W/kg at 17.5% of the gait cycle. During the remainder of the midstance phase the struts dissipated more power with a peak of 0.0915 ± 0.0042 W/kg at 25% of the gait cycle. During terminal stance the struts, again, dissipated power with a peak of 0.0510 ± 0.0001 W/kg at 44.5% of the gait cycle. During the pre-swing phase the posterior struts generated power with a peak of 0.1422 ± 0.0003 W/kg at 59% of the gait cycle.

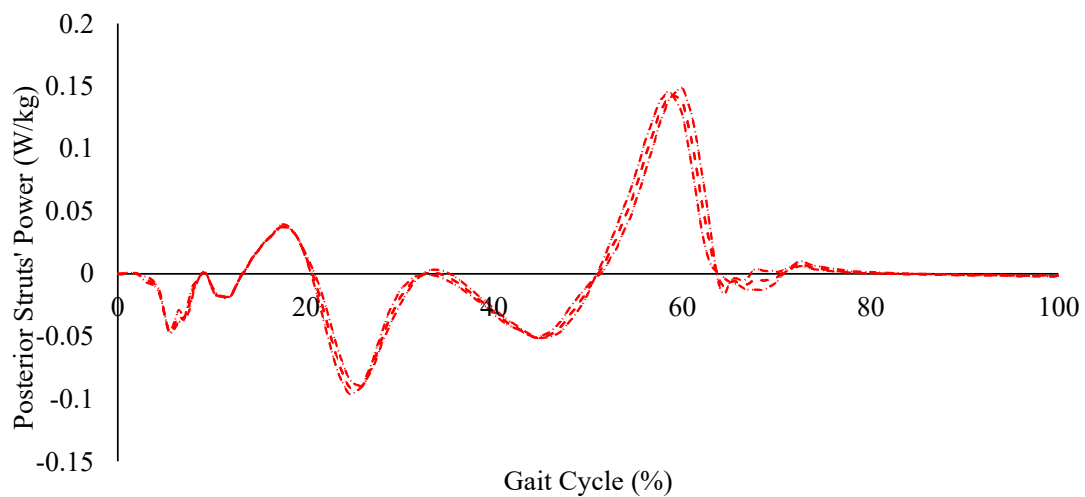
6.3.4.2 Running Gait

Figure 6.3.9 on page 157 shows the energy stored within the posterior struts and the power throughout the gait cycle during running. The first small peak in energy stored occurred at 8% of gait cycle at 0.0016 ± 0.0008 J/kg. The maximum energy stored occurred at 24% of the gait cycle with a value of 0.0642 ± 0.0306 J/kg. An additional peak of 0.0101 ± 0.0043 J/kg was seen during the swing phase of the PD-AFO limb, at 45% of the gait cycle.

During the loading response at 7.5% of the gait cycle, peak power absorption of 0.0409 ± 0.0196 W/kg was seen. Slightly after this, at 13% of the gait cycle, power generation of 0.0454 ± 0.0242 W/kg was observed. The maximum power absorption occurred at 18.5% of the gait cycle at 0.915 ± 0.448 W/kg. The peak power generation occurred at 30.5% of the gait cycle at 0.587 ± 0.270 W/kg. Additional peak absorption at 40% of the gait cycle was seen with a value of 0.183 ± 0.074 W/kg. The peak power dissipated by the struts during running was 10 times greater than that dissipated during walking. The peak power generated during running was 4.3 times greater than that generated during walking.

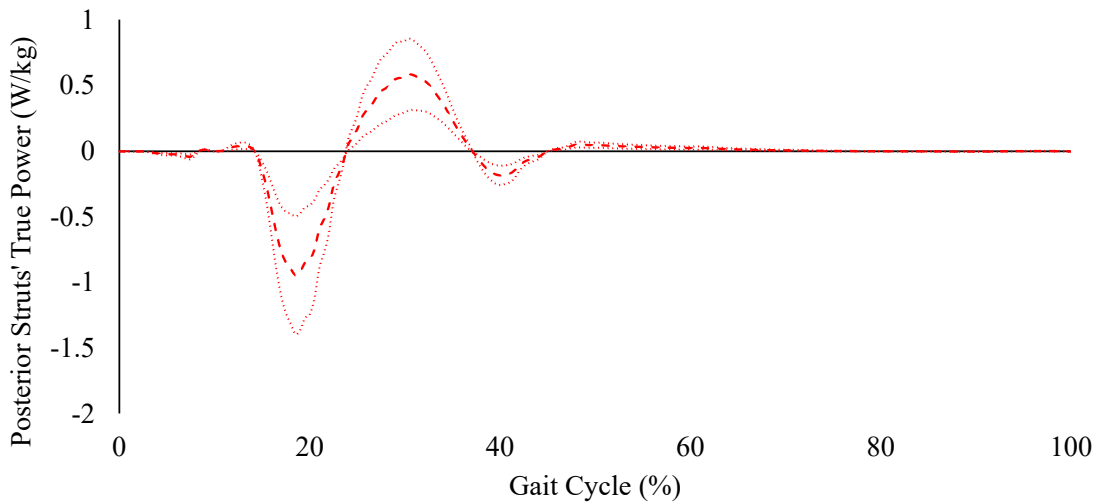
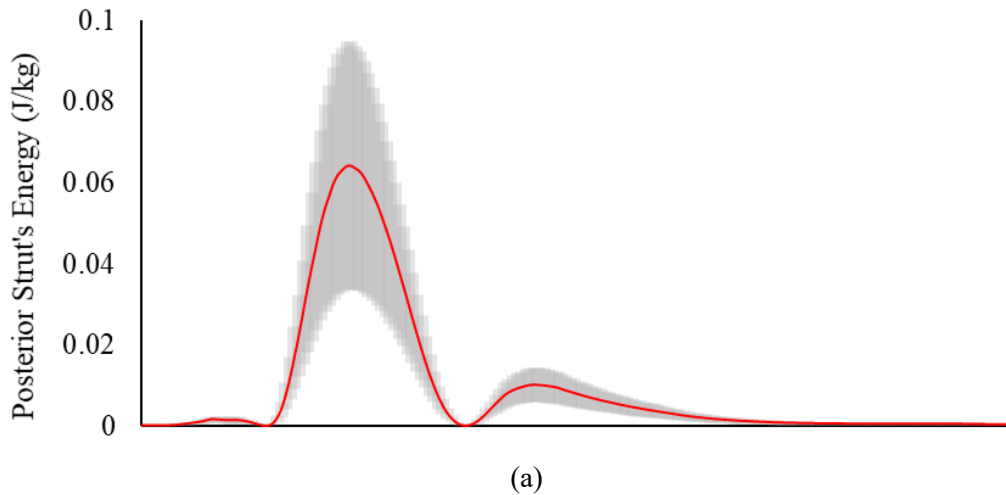


(a)



(b)

Figure 6.3.8: (a) Strain energy stored within the posterior struts during walking gait. The shaded region is the propagated error from all measurements used to calculate the energy. (b) Power consumed and generated by the posterior struts. The efficiency of the posterior struts was accounted for to give the true values of power. The small, dotted lines indicate the true power when calculated with the values of energy \pm propagated error.



(b)

Figure 6.3.9: (a) Strain energy stored within the posterior struts during running gait. The shaded region is the propagated error from all measurements used to calculate the energy. (b) Power dissipated and generated by the posterior struts. The efficiency was accounted to give true values of power of posterior struts. The small, dotted lines indicate the true power when calculated with the values of energy \pm propagated error.

6.4 DISCUSSION

This is the first study to evaluate the mechanical ESAR characteristics of the PD-AFO that is the subject of this thesis. A novel technique was also presented to quantify the power dissipated and generated by the posterior struts during walking and running gait using strain gauges.

6.4.1 Strain Gauge Reliability and Accuracy

The reliability and accuracy of the values of strain obtained from the strain gauges when attached to the posterior struts were evaluated. The compression tests were used to establish the accuracy and the bending tests were used to establish the reliability.

Across the compression tests the strain calculated from the force-displacement sensors of the materials testing machine was, on average, 10% higher than that recorded by the strain gauges. This is thought to be due to the surface coating on the posterior struts affecting adhesion of the strain gauges. Although every effort was made to sand and smooth the surfaces, imperfect contact between the strain gauge and the sample may have remained. Additionally, the strain gauges may not have been perfectly aligned with the long axis of the posterior struts and therefore only recorded a portion of the axial strain. However, a small misalignment of 5° would result in $<0.5\%$ of the strain reading being 'lost' and therefore is unlikely to significantly change the values of strains recorded. Overall, the inclusion of these small errors should be considered when drawing conclusions from the absolute values of energy.

During 4-point bending, rotating the samples between each test allowed comparison of the consistency of the attachment of each strain gauge. The median, absolute values of strain recorded at these locations across samples were within 1% of each other, with no statistical differences found, demonstrating the reliability of the attachment method. The strain gauges located on the neutral axis of the samples (site j and site l) experienced $\sim 0\%$ strain during bending, a value $<1\%$ of the strain recorded by the gauges at the top and bottom locations (site k and site m). This behaviour was as theorised for 4-point bending, demonstrating that the strain gauges were attached in a consistent manner and behaved in similarly across samples.

6.4.2 Efficiency

The efficiency of the posterior struts was calculated to be $>96\%$. This is the first study, known to this author, that quantifies the efficiency of these posterior struts used in the Momentum. The efficiency was similar to that recorded by Beck et al. for running prosthetics [99]. This demonstrates that the PD-AFO's posterior struts, have the ability to provide energy return, with a high proportion of energy stored within the struts being returned. Any future materials used to manufacture the struts should exhibit a similar efficiency in bending to maintain the ESAR characteristics.

The efficiency was only analysed for the posterior struts in bending. Beck et al. demonstrated that for a prosthetic limb the ESAR characteristics may change as direction of loading changed [99].

However, the strains recorded during gait demonstrated that the energy stored from bending was on average 234 times greater than that stored from compression. Therefore, it was reasonable to consider the efficiency in this mode of loading only.

6.4.3 Strain gauges

The strain gauge readings provided descriptive characteristics of how the struts deflect throughout gait in both walking and running. Figure 6.4.1 shows a representation of strut deflections in the sagittal plane seen during walking gait throughout the stance phase of the gait cycle (not to scale).

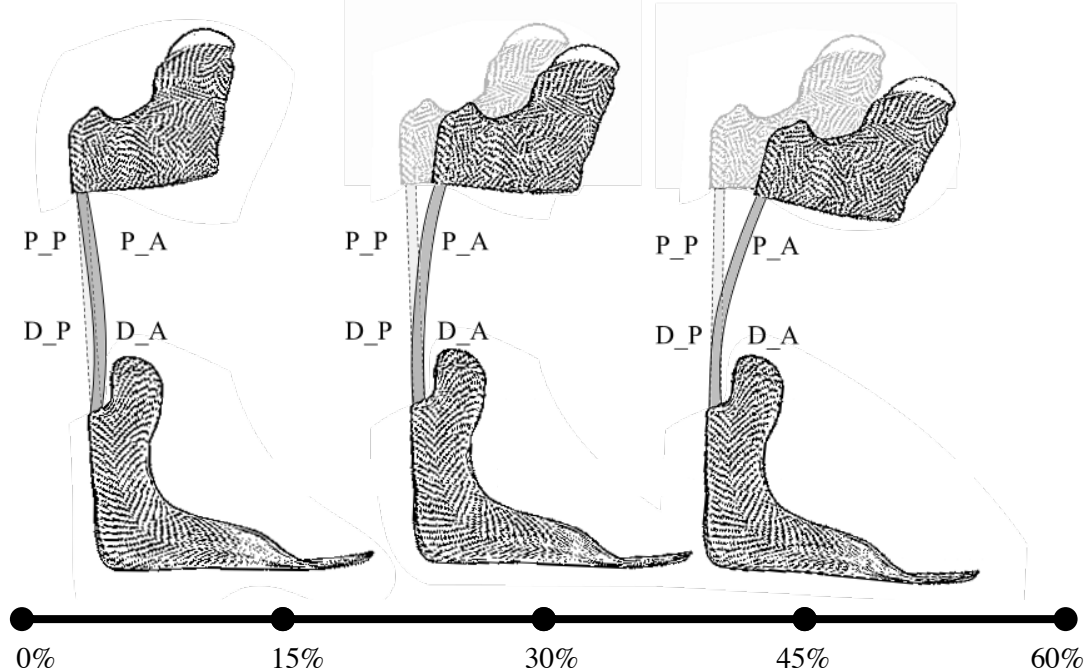


Figure 6.4.1 Diagram showing the changes in the shape of the struts throughout the gait cycle. The magnitudes of displacement are not to scale, and timings within the gait cycle are approximate. The first letter described the proximal (P) /distal (D) location of the strain gauge, and the second letter, describes the posterior (P) /anterior(A) location.

During loading response and early midstance the struts inverted, bending outwards in the anterior direction. This suggests the calf is making contact with the posterior cuff of the PD-AFO. This was also seen during running gait. The ‘inverted’ bending may explain the distinct impact peak seen in GRF at this point in PD-AFO gait in chapter 5, also replicated in Figure 6.4.2 here. At this point in gait the foot is unable to plantarflex, due to the base of the PD-AFO and this increases the effective stiffness resulting in a shorter, more staccato, contact with the ground [57].

Whilst the struts were inverted at the start of the gait cycle, the direction of deflection changed, at ~20% of the gait cycle. This change in direction of deflection coincided with the end of the first peak in total GRF of the PD-AFO limb during walking. This may explain why the first total GRF peak of the PD-AFO limb is prolonged and less distinct than that seen in the control limbs; the deflection and relaxation of the struts at this point in gait act as a damper and smoothen out the changes in GRF.

The increased strains at the distal sites of the struts suggest that during midstance phase and terminal stance phase they deform in a cantilever manner. This is also seen during running gait. This implies that the bending axis is located at the distal end of the PD-AFO, not in the middle of the struts as assumed in previous studies [39, 54]. This supports the hypothesis that posterior struts are loaded by the forward progression of the anterior tibial surface making contact with the anterior cuff during terminal stance. If the cause of bending of the struts is contact with the anterior cuff, then the moment arm would be greater at the distal sites of the struts compared to the proximal sites; this explains why larger strains were seen at the distal sites.

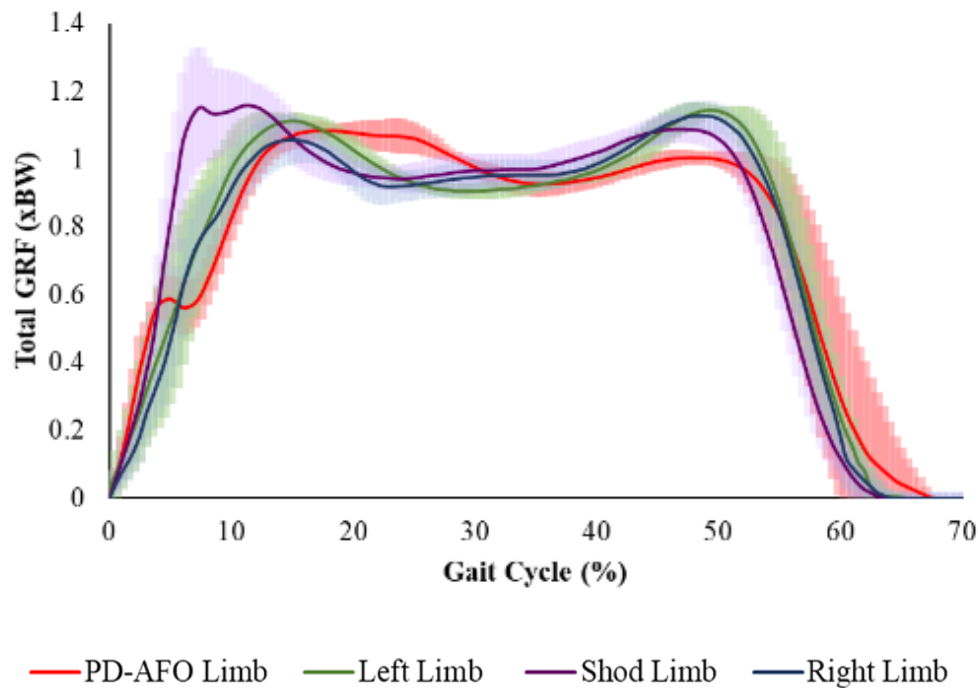


Figure 6.4.2: Total ground reaction force, normalised for body weight, during walking gait, as described in Chapter 5.

6.4.4 Energy and Power

For both walking and running the energy storage during loading response and early midstance was low comparative to that which occurred during the latter stance phases. This may be due to the angle of the posterior struts at this point in gait and the loading direction. During the latter stance phases, the absolute posterior-strut-to-vertical-angle would be greater than during early stance. The greatest force through the combined limb-PD-AFO system is in the vertical direction. Therefore, as the angle to the vertical increases, so does the effective moment arm. As the bending stiffness of the posterior struts is lower than the compressive stiffness, more energy is stored with increased moment.

During loading response, it was hypothesised that the posterior struts deflected, along with deformation of the heel wedge, to reduce the peak impulse and peak forces experienced by the combined limb-PD-AFO system. During walking, the energy stored by the struts during loading

response and early midstance was ~7-9% of the peak work done to the combined limb-PD-AFO system as recorded by Harper et al. when considering the possible error in the strain gauge readings [65]. Comparatively, during terminal stance and pre-swing the posterior struts stored ~20-24% of the peak work done on the combined limb-PD-AFO system [65]. The low energy stored during early stance implies that the posterior struts are not a significant component during this phase, suggesting the heel wedge plays a more significant part in reducing the peak combined limb-PD-AFO load by increasing the time over which the force is applied. This effect has been seen in heel wedges of prosthetics [91]. The offloading of the limb is greatest during this phase, suggesting that during the early stance phase the main influence of the posterior struts on gait is to divert force through the PD-AFO, thus reducing the load through the limb, by altering the ratio of loading between the PD-AFO and limb.

The power dissipated and generated by the posterior struts throughout the gait cycle is, for the most part, similar in pattern (not magnitude) to the combined limb-PD-AFO ankle power recorded in the literature during both types of gait, shown in Figure 6.1.1 above [54, 56]. In both running and walking, small amounts of power dissipation and generation are seen in the early stages of the swing phase of the PD-AFO limb; this has not been reported before in the literature. This is thought to be due to the dynamic response and overshooting of the struts as they return to their undeflected position. If this response generates too much power, then this may cause unwanted gait patterns or discomfort, such as a 'pinging' sensation, like that of an elastic band being released, due to work being done by the PD-AFO onto the limb as this energy is released.

Throughout the gait cycle it was observed that the PD-AFO dissipated and generated a varying fraction of the total combined limb-PD-AFO power. During walking the power dissipated by the PD-AFO experienced two peaks during the midstance and terminal stance phases, with the first of greater magnitude. Comparatively, in literature, although 2 peaks are seen in the power dissipated for the combined-limb-PD-AFO system, the second appears to be greater [56]. This suggests that during the midstance phase the PD-AFO dissipated a higher proportion of power relative to the lower limb. during the terminal stance phase the PD-AFO dissipated a lower proportion of power relative to the lower limb. This agrees with the finding in Chapter 5, that the PD-AFO experiences a higher ratio of the total loading during the earlier phases of gait.

As mentioned above, although the power generated and dissipated follows a similar pattern to that seen in the combined limb-PD-AFO, as with energy stored, the magnitude of power seen in the struts is smaller. During walking the peak power found within this study was ~13-17% of those values seen in literature of the combined limb-PD-AFO during early stance [56, 57]. The peak power generation during late stance was 16-19% of those recorded for the combined limb-PD-AFO in literature [56, 57]. During running the peak power dissipation recorded by the posterior struts was 13-18% of that recorded for the combined limb-PD-AFO system in literature [53, 57]. At peak power generation the values were 14-19% of those recorded for the limb-PD-AFO system [53, 57]. For both walking and

running the ratios of peak values of power dissipation and generation to the combined-limb-PD-AFO powers as recorded in literature were similar. The power generation seen in this study, supports the hypothesis that the PD-AFO aids propulsion, by providing up to 14-19% of the total power generation of the combined limb-PD-AFO system during both running and walking.

6.5 LIMITATIONS

To calculate the energy stored, the moment within the posterior struts was considered to be that seen within a cantilever, neglecting the effects of torsion. The second moment of area about the long axis is greater and therefore it is very stiff, so comparatively a negligible angle of twist would be seen. The strains within the coronal plane were an order of magnitude lower and were therefore considered negligible in all calculations. These assumptions were deemed to give acceptable accuracy, without requiring a computational solution to quantify the energy and power.

The study analysed the power dissipated and generated by the posterior struts and no other component of the PD-AFO. Other components, such as the base may provide some power generation. However, the high Young's moduli of the carbon fibre layers relative to the posterior struts, would increase the stiffness of the components; therefore the energy stored in these components would likely be much smaller than that seen in the posterior struts. Additionally, due to the geometry of the base, such calculation would have required a computational solution. As such, the focus of this thesis was the posterior struts, considered to be the most significant ESAR component of the PD-AFO. The FE modelling in the next chapter is used to analyse the energy stored within the base to ascertain the implication of the simplification made here.

The overall ankle power of the combined limb-PD-AFO system was not analysed here, and the values were compared to literature. Further evaluation of the combined limb-PD-AFO ankle power of the subject, during an instrumented gait cycle would provide a more accurate estimation of the fraction of power dissipated and generated by the posterior struts.

All trials here were done using one subject. It is known, that for walking, the subject walks with a similar PD-AFO gait to injured patients, as discussed in chapter 5. Additionally, the energy and power values calculated were the correct order of magnitude when compared to values of combined limb-PD-AFO energy and power in the literature. Therefore, one subject was considered adequate to study the ESAR characteristics of the PD-AFO.

6.6 CONCLUSION

A novel method was presented with which to quantify the ESAR characteristics of the PD-AFO. It was demonstrated that the posterior struts used in the manufacture had a high efficiency, at 97%, and contributed between 0.14 W/kg of power generation during walking and between 0.61 W/kg of power generation during running. This suggests that the ESAR characteristics of the PD-AFO aid with

propulsion in the latter stance phases in walking and in running. In the next chapter, a design sensitivity conducted computationally evaluates how changes in the strut geometric and material properties, along with alterations in other PD-AFO components, affects the mechanical response and energy storage properties of the PD-AFO.

7 FE MODEL OF PD-AFO

Chapter 6 described how the posterior struts of the PD-AFO have ESAR characteristics. Previously, as discussed in chapter 3, studies have researched the influence of the posterior struts, along with other design components, on gait; the associations between the mechanics of the PD-AFO and the characteristics of its components still remains, ill understood. Better knowledge of this would facilitate the prescription process and the development of improved designs. Particularly, it may guide options to reduce costs of manufacture; this is particularly relevant if the PD-AFO is to be used by civilian cohorts. The aim of this chapter is to understand which design components most influence the mechanical response of the PD-AFO by performing a computational design sensitivity on the PD-AFO. This chapter describes the development of an FE model of the PD-AFO and the experiments conducted to calibrate it. The model is then used to describe the mechanical response of the PD-AFO and a design sensitivity analysis performed.

7.1 INTRODUCTION

Previous studies have analysed the influence of some design parameters of the PD-AFO, namely strut alignment, strut stiffness, strut bending axis, heel wedge height and heel wedge stiffness on the response of the PD-AFO, by evaluating gait in injured patients [38, 39, 53-56, 58, 60, 64, 65]. These were discussed in chapter 3. To summarise, the results of these studies suggested that strut alignment and heel height had the most significant influence on joint kinematics and kinetics [38, 53, 60]. Strut stiffness was found to have little effect, though this was not conclusive [55, 56, 58, 64, 65]. Whilst bending axis of the posterior strut was found to have some effect, the methodology to prescribe the location of the bending axis was flawed [39, 54].

During these studies gait was subject to variability across patients due to the different pathologies within the cohort. It is not possible to isolate the effect of the chosen design parameter from the effect of injury on gait. For relevant design parameters, such as strut stiffness, studies used the patients' personal PD-AFO as the baseline design, from which a variation of $\pm 20\%$ of a chosen parameter, was selected to analyse. This resulted in different, absolute change for each patient, though ensured they all experience the same relative change. The baseline parameters should be fully described to allow comparisons across studies. Additionally, using patients who have already been prescribed the PD-AFO, may introduce bias to the analyses as they are likely accustomed to their own specific design of PD-AFO.

One method to overcome the issues seen in the literature is to use mechanical bench testing to analyse design changes; in other words, eliminate the variables associated with the patient. Such tests were performed by Wach et al. on 4 different AFOs, discussed in chapter 6 [63]. However, there is a high cost of manufacture and a lengthy fitting process associated with the PD-AFO [36]. Therefore, it is not practical to create multiple, physical PD-AFOs to test multiple design variations.

To remove the manufacturing limitation, a sensitivity study can be performed using FE to determine the influence of the different components on the mechanical response of the PD-AFO. Computational models of AFOs are emerging as a novel way to test and adjust design parameters, minimising both cost and manufacturing time [102]. This is particularly relevant as carbon fibre, a material more difficult to adjust and more expensive than traditional thermoplastics, is fast becoming a popular material for manufacturing AFOs due to its superior properties.

7.2 PREVIOUS FE MODELS OF AFOs

Within this section FE analyses of AFOs are discussed with a focus on validation protocols and controllable boundary conditions. Ielapi et al. highlight the importance of validation within their comprehensive literature review analysing computational and experimental methods to determine the mechanical behaviour of AFOs [102]. FE models of the specific design and materials of the PD-AFO that is the subject of this thesis were not found in the literature. The most comparable model available is that developed by Ielapi et al.; the FE model developed is geometrically similar to that used in this thesis but used Polyamide for the base and cuff regions [103].

Kobayashi et al. performed a review of the literature, investigating the different experimental methodologies with which to test AFO stiffness [104]. These methods were split into two categories: bench testing analyses and functional analyses. Functional analyses use gait trials to evaluate the mechanical response of the AFO, whilst bench testing applies fixed loads or displacements.

Kobayashi et al. suggested that bench testing gives better control over the experimental conditions [104] and has been used in previous studies validating FE models [103, 105]. For the purpose of validating an FE model the boundary conditions must be well controlled and therefore all

experimental set-ups, and FE validation methodologies discussed below are bench tests. Applying boundary conditions to mimic functional analyses would be more suitable for a design sensitivity, though this may compromise computational efficiency.

Schrank et al. virtually developed a PD-AFO of a different design to the one that is the subject of this thesis and produced it using additive manufacturing, aiming to demonstrate that the manufactured AFO closely matched the mechanical response predicted in the virtual design process [105]. They compared the numerical results with those from an experimental set-up designed to test the bending stiffness. To evaluate the bending stiffness half of a surrogate calf, with a surrogate tibia inserted through it, was placed within the AFO and restrained at the ‘ankle joint centre’ (assumed to be the talocrural joint) allowing movement in the sagittal plane only. During the experiment a force was manually applied perpendicular to the long axis of the tibia and measured using a force plate to result in a PD-AFO dorsiflexed angle of at least 20° [105]. The FE simulation and boundary conditions to mimic this set up is shown in Figure 7.2.1. Fixing of the tibia at the centre of the talocrural joint provides clinical relevance to the rotational stiffness determined, as it models the effective stiffness of the joint when wearing the AFO. Although there was a good comparison between the numerical and experimental bending stiffness, 11.7% once optimised, the AFO was completely clamped at the foot plate, meaning that region of the AFO was not analysed [105].

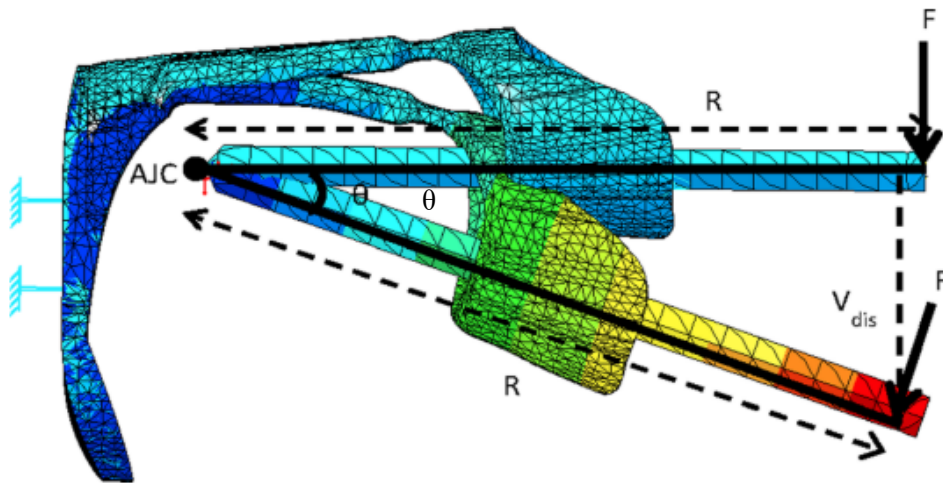


Figure 7.2.1: An FE model of a PD-AFO by Schrank et al. with a surrogate tibia, of length R , fixed at the ‘ankle joint centre’ (AJC) demonstrating how the model simulated an experimental testing set-up. A force, F , was applied to the proximal end of the surrogate tibia and the rotational stiffness determined by the change in angle, θ , of the tibia [105]. The plot shows vertical displacement with blue indicating minimal displacement and red indicating the greatest displacement. Image reproduced with permission from the rights holder the American Society of Mechanical Engineers ASME

Contrastingly, Amerinatanzi et al. developed an FE model based on a hinge-AFO, with a simple, replicable validation protocol that evaluated the footplate region of the AFO [106]. The AFO was positioned vertically, and weights were hung from the distal end of the footplate. The angle between the plantar aspect of the footplate and the posterior aspect of the ‘strut’ was then measured [106]. However, this method resulted in a plantarflexed angle; the majority of AFOs limit plantarflexion motion and therefore validation using this rotation may be clinically less relevant for other AFO types [57].

Ielapi et al. used a surrogate limb to apply a displacement in the anterior direction at the proximal cuff region of the AFO as seen in Figure 7.2.2 [107]. Similar boundary conditions were applied to the FE model, developed from a scanned geometry [103]. The rotation and torque applied were obtained to give the rotational stiffness, achieving accuracy of 8.5-10.4% when compared to the experimental set-up. Use of a surrogate limb allowed the point of rotation to be about the ankle joint complex, which is a clinically relevant point about which to measure the stiffness [103]. The surrogate limb also allowed limitations in the rotation to be prescribed, which is beneficial for controlling boundary conditions. However, the surrogate limb completely fixed the footplate, and therefore this region of the AFO was not validated in the experiment. Furthermore, addition of a surrogate limb in an FE model could be computationally expensive, and therefore not suitable for a design sensitivity where multiple simulations are needed.

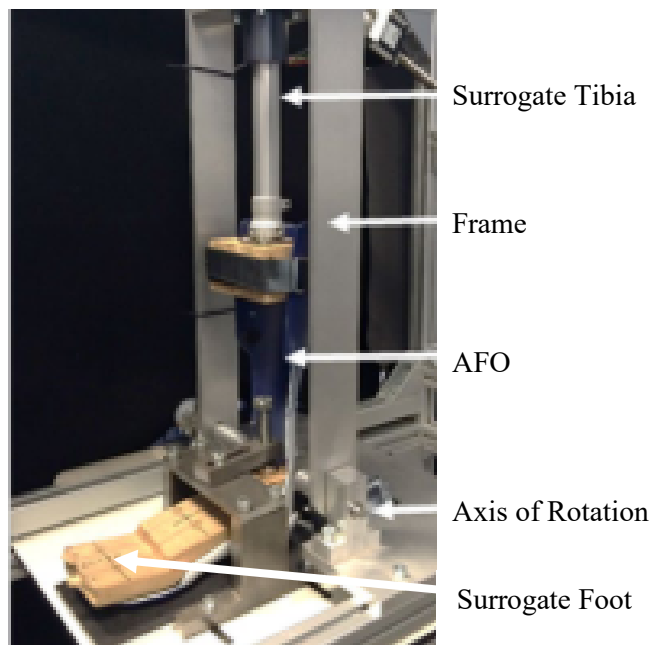


Figure 7.2.2: Experimental set-up, with surrogate limb, used by Ielapi et al. to test the rotational stiffness of an AFO. A linear motor drives the surrogate tibia in the anteroposterior direction [107]. Image reproduced is Open Access.

During the experiment shown in Figure 7.2.2 above, the force applied, was recorded using a load cell and the change in dorsiflexion of the AFO was recorded using a digital goniometer, accounting for the stiffness within the set-up of the surrogate limb, with good reliability in measurements [107]. The surrogate tibia was free to move distally and proximally, to prevent overloading of the AFO. Additional movement, although resulting in improvements in clinical relevance, introduces complications to the boundary conditions and is therefore not ideal for validation. It is, however, a consideration for a design sensitivity.

Stier et al. also clamped the footplate region of the AFO and applied a displacement at the cuff in the anterior direction (resulting in dorsiflexion) at a rate of 2mm/min [68]. The force-displacement curve was compared between the experimental set-up and the FE simulation. Although it appeared to be in good agreement, no value was given to indicate the error.

Zou et al. did not use a surrogate limb, nor did they completely restrain the footplate [94]. The AFO was positioned vertically, and upside down (Figure 7.2.3). The posterior aspect of the cuff was clamped and loaded with a force applied at 8mm/s downwards to the midfoot region of the foot plate and then unloaded. This resulted in a dorsiflexed rotation in the loaded position. An FE simulation was produced with boundary conditions to mimic this set-up. The force-displacement curves were derived both experimentally and computationally, and were used to calculate the elastic energy return ratio between loading and unloading. The point of rotation was unknown. The comparison of the FE and experimental energy return ratio resulted in differences of 0.02-2.7% for the 2 carbon fibre AFOs. Although the footplate was not clamped, the cuff was, therefore this region was not loaded. However, it is argued that the posterior cuff is likely to be less significant in the AFO's mechanical response than the footplate, and therefore inaccuracies in its behaviour less important than that of the footplate. Therefore, the footplate should be prioritised for validation.

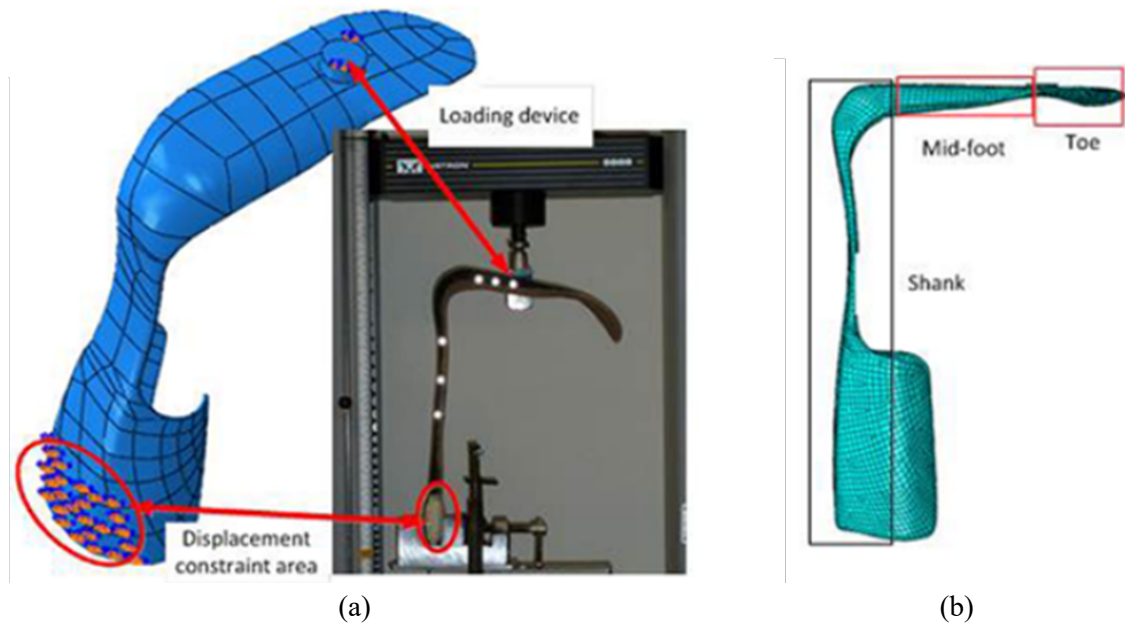


Figure 7.2.3: (a) An AFO loaded at the plantar aspect of its footplate in an experimental set-up with the boundary conditions shown in the FE model. (b) The different regions of the AFO shown in the FE model. Images reproduced from Zou et al. [94] are open access.

Zou et al. also compared the point of contact between the AFO and the applied force, during the experimental set-up and FE simulation. This was required as the design of the experiment resulted in the point of application of the force moving distally down the foot plate due to the non-spherical puck resulting in a change in point of contact between the puck and AFO as the angle of the footplate changed [94]. It would be preferable to have no slipping both to control boundary conditions and to ensure computational efficiency; however, if slipping does occur, quantification is needed as seen in this study [94].

Of those FE validation studies discussed, most compare compressive or rotational stiffness [34, 101, 103, 108-111]. The commonality of this evaluation metric is likely due to the relative ease at which force and displacement can be measured. The majority of studies performing purely experimental tests on AFOs also use rotational stiffness as an evaluation metric; some studies focused on the sagittal plane alone (plantarflexion and dorsiflexion are the largest foot motions during gait) [112-116], some in the sagittal and coronal [117-119] and others in all 3 planes [120, 121]. For validation purposes, rotations should be fixed in a plane if the rotation in that plane is not to be measured. Zou et al. examined energy storage instead of stiffness in their experimental work, as did Ielapi et al. [107]. The work by Novacheck et al. suggests that this is a less popular evaluation metric than stiffness due to a more complex set-up required to ensure repeatability [114]. This lack of repeatability means that it is less appropriate for a validation metric. However, due to its clinical relevance, it would make a suitable metric to evaluate the influence of design changes.

As seen, there is no standard procedure to validate an FE model of an AFO. Of those FE studies that provide comprehensive FE validation experiments, several fail to analyse the experimental response of the footplate region; a component of the PDAFO that is hypothesised to deflect and therefore may have a significant effect on the mechanical response of the PD-AFO. Therefore, it is particularly important that this region is included in the validation procedure. Additionally, the accuracy of the application of a force or displacement is important, for controlled boundary conditions; a materials testing machine, if available, is both accurate and versatile.

7.3 METHODOLOGY

This section describes the methodology used to develop an FE model of the PD-AFO, the manufacture of which is described in chapter 5, and the experiments used to test the FE model for validity. Additionally, the boundary conditions used to evaluate the mechanical response and the selection of design parameters chosen to alter are described.

7.3.1 Geometry

The process to create the meshed geometry of the PD-AFO is summarised in Figure 7.3.1. A CT scan of the PD-AFO was taken (Siemens Somatom Definition AS 64, Erlangen, Germany) with a slice thickness of 0.6mm. These images were imported into MIMICS (v20.0, Materialise, Leuven, Belgium). Segmentation of these images was performed, using automatic features of the software, including ‘Thresholding’, ‘Split Mask’ and ‘Region Growing’ and a smoothing filter was applied upon creation of the 3D surfaces. In total the PD-AFO was split into 9 components: base, sole, lateral pad, medial pad, lateral strut, medial strut, anterior cuff, posterior cuff and shin pad.

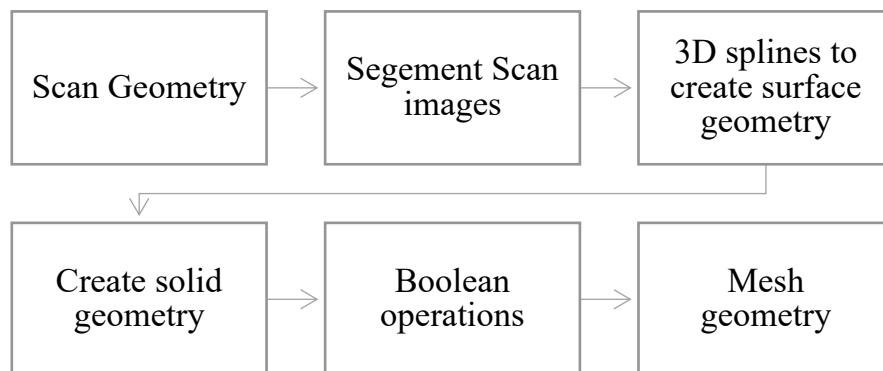


Figure 7.3.1: Process to develop the geometry of FE model of the PD-AFO

The surface geometries of each component (excluding the two struts) were imported into Geomagic (v2013, Geomagic Inc., Morrisville, NC, USA). Using the ‘Autosurface’ feature, 3D splines were

produced to fit patches to the geometries, allowing solids of each component to be generated. The solids of the posterior and anterior cuff were orientated to mimic a closed position, as when worn. These were separated using a spline to ensure good contact between the two aspects of the cuff. All components had Boolean operations applied to ensure good contact between meshes. To ensure good mesh quality of the struts, it was decided to generate the strut geometry in CAD rather than segmenting an image. The CT scans of the struts were used to identify the total length of the struts (the struts of the PD-AFO were built into the cuff and base and therefore not possible to measure without damaging the PD-AFO). The strut diameters were measured from the visible sections of the struts that made up the PD-AFO using vernier callipers. The struts were then drawn up in Inventor (v2018, Autodesk Inc., San Rafael, CA, USA) as cylinders and their ends tapered using the dimensions from the segmented CT scans.

7.3.2 Mesh and model set up

Nine solids were imported into Hypermesh (v13.0.110, Troy, MI, USA) to mesh. To establish the appropriate size of mesh, a mesh convergence study was performed in MSC.Marc (v2020.0.0, MSC.Software, Santa Ana, CA, USA), analysing meshes with a target element size 1.2 mm 1.5mm, 1.75mm, 2 mm and 3mm. The toe region of the PD-AFO was fixed in all degrees of freedom and an anterior displacement of 10 mm applied to the anterior cuff. The reaction force and the peak equivalent Von Mises stress was outputted for each mesh size.

The results are shown in Figure 7.4.1 in the result section 7.4 on page 187. The final choice of mesh had ~720,000 tetrahedral, strain smoothing elements, with a target element size of 1.75mm. Foam components of the PD-AFO were meshed using full and Hermann formulation tetrahedral elements. Contact was modelled by assigning 'glued' interaction (no relative motion or separation allowed) between all neighbouring components. The boundary conditions were load-case dependent and are discussed later.

7.3.3 Material Properties

All except for the carbon fibre components were assigned the mean material properties determined in chapter 4. The carbon fibre components were assigned a mixture model. Within each mixture the appropriate fraction of each carbon-fibre layer in the appropriate order was added, with the properties of each layer determined in chapter 4. The base was split into 5 regions with local coordinate systems prescribed to each region to ensure that the principal Young's modulus, E_1 , followed the curve of the base (Figure 7.3.2).

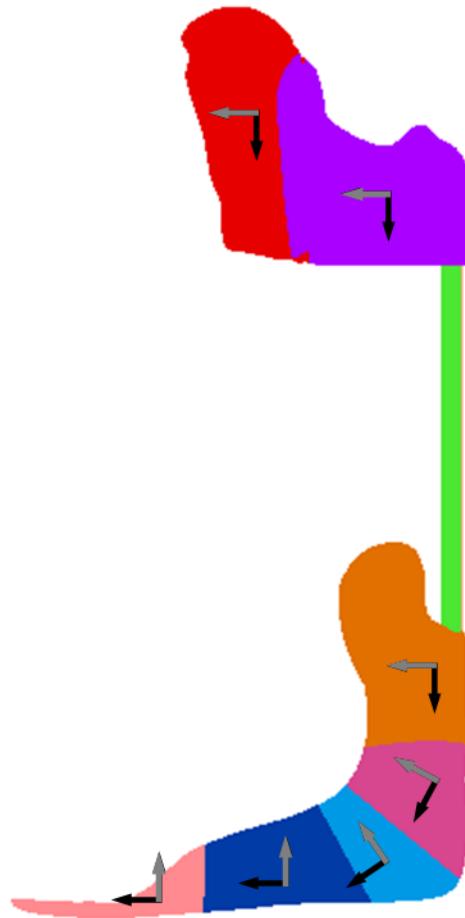


Figure 7.3.2: The local coordinate systems assigned to the carbon fibre regions. The black arrow indicates the prescribed direction of E_1 , normal to the page (for all components) prescribes the direction of E_2 and the grey arrow indicates the direction of E_3 .

7.3.4 Model Calibration and Validation

An experimental set-up was devised to compare to the PD-AFO FE simulation and provide the opportunity to make minor adjustments to the model to improve its accuracy. This section describes the experimental set-up and the boundary conditions used to mimic this set-up in the FE model. Kobayashi et al. noted bench tests were performed using various equipment including muscle training machines, force plates, tensiometers, dial gauges and mechanical testing machines [104]. The use of muscle training machines may be more representative of normal gait conditions, however the complex device results in difficult boundary conditions to implement accurately in FE, and is therefore not suitable as an FE validation method. The use of force plates, with reflective markers allows good understanding of the deformation of the AFO; however, a custom rig would need to be manufactured to perform repeatable experiments and control the boundary conditions; this time and cost investment is not justified for the validation procedure, when other, simpler set-ups have similarly controllable

boundary conditions. Both tensiometers and dial gauges are possible methods for validation, however a materials testing machine provides more options in terms of loading rate, ROM, and accuracy [104]. Therefore, it was decided to test the PD-AFO with an experimental set-up utilising a material testing machine.

7.3.4.1 Experimental Methodology

A surrogate calf, made from plaster, with a surrogate tibia, made from aluminium, was produced using the original cast used to produce the PD-AFO. The posterior cuff of the PD-AFO was screwed into the surrogate calf, using the holes that usually connect the anterior and posterior cuff, to minimise alterations to the PD-AFO. The anterior cuff and shin pad were removed from the experimental set-up to enable this attachment.

Using a surrogate calf allows application of a displacement to the proximal cuff, that would not otherwise be possible due to the thin geometry of this region. Once screwed to the surrogate calf, the posterior cuff was limited to only 2 degrees of freedom (in relation to the surrogate tibia); translation in the z axis and rotation about the x axis (Figure 7.3.3). No surrogate foot was used due to the boundary conditions that would be introduced between this surrogate foot and the PD-AFO and the restrictions it would place on movement of the base.

The surrogate tibia was directly attached to the materials testing machine (model 5866, Instron, High Wycombe, UK). The machine was fitted with a 10kN load cell. The compliance of the materials testing machine combined with the surrogate tibia was measured, and used to adjust all future measurements (see Appendix 12.4.1).

The forefoot region of the base of the PD-AFO made contact with the aluminium fixture, set at an angle of 20°; this angle was also used by Wach et al. to mimic pre-swing (though they altered limb angle to the vertical) [63]. The fixture does not prohibit any degrees of freedom of the PD-AFO or decrease control of the boundary conditions, but does result in a more clinically relevant set-up than a horizontal fixture, resulting in a dorsiflexed motion of the PD-AFO under loading.

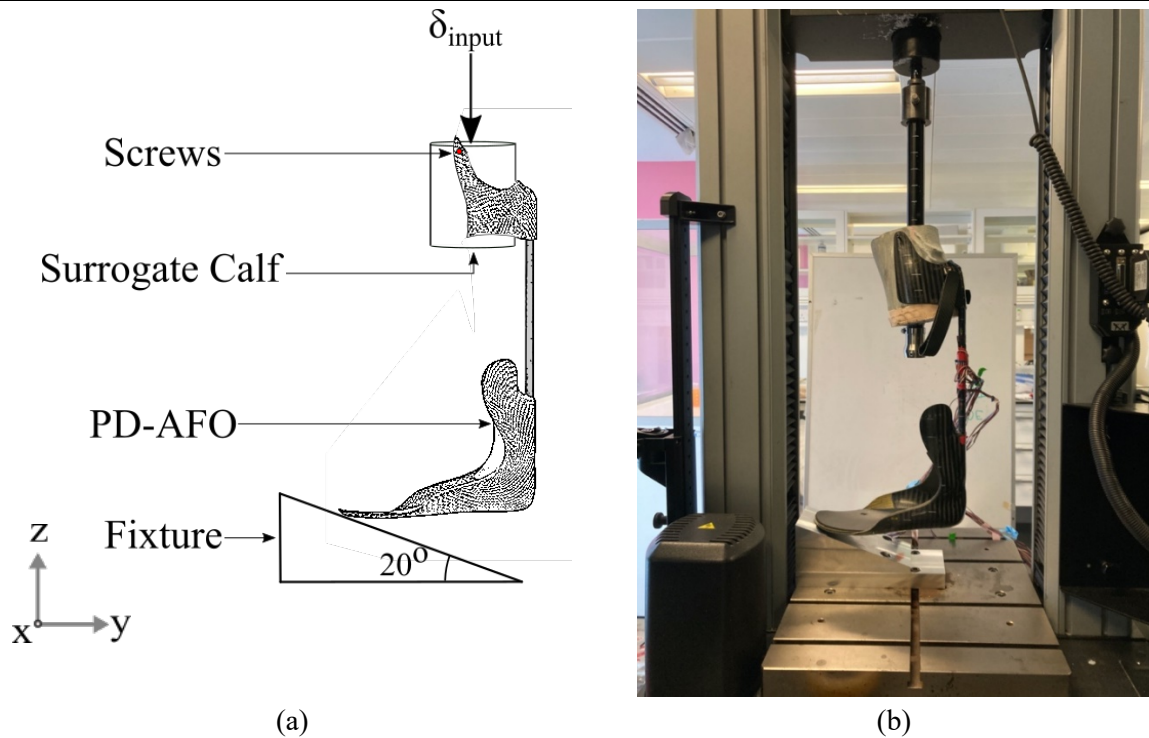


Figure 7.3.3: The (a) schematic and (b) experimental set-up used to test for validation the PD-AFO FE model. The schematic demonstrates the 0° orientation of the PD-AFO, with posterior struts sitting within the x - z plane and normal to the ground (parallel to z). The force was measured at the same point as δ_{input} .

Figure 7.3.3a shows the PD-AFO at 0° orientation; the PD-AFO was considered to be at 0° orientation when the posterior struts were normal to the ground (their long axis parallel to the z axis) and the two posterior struts were aligned in the z - x plane. An inclinometer (model Laserliner, UMAREX GmbH & Co, Arnsberg, Germany) was used to confirm the orientation of the PD-AFO, in the set up as shown in Figure 7.3.3b, and record any deviations from the assumed 0° orientation set-up. These values are shown in Table 7.3.1.

Table 7.3.1: Relative rotations to the prescribed 0° orientation shown in Figure 7.3.3.

Set-up	rot x ($^\circ$)	rot y ($^\circ$)	rot z ($^\circ$)
Late stance	-0.4	-1.6	-6.3

A small displacement in z (proximal to distal) was applied manually to the surrogate tibia at the point δ_{input} , until the materials testing machine recorded a force of between 0-3N. At this point the displacement reading was zeroed. A displacement was then applied at a rate of 0.38mm/s chosen to mimic the rate used in the material tests of the carbon strut specimens tested in chapter 4. The PD-AFO was loaded to a displacement resulting in peak compressive force of 400N.

The stiffness of the PD-AFO was determined as a function of displacement: $K = f(\delta)$. The stiffness was calculated from the derivative of the force-displacement curve, across 16 displacement increments. To calculate the mean stiffness, a linear regression was fitted to the curve, and the derivative calculated. Using strain gauges or optical markers to measure the deflection of the base was not deemed necessary, as it was hypothesised that the posterior struts have a greater influence on the mechanical response of the PD-AFO than the base does.

7.3.4.2 FE Boundary Conditions

The meshed geometry of the PD-AFO, described above, was imported into Mentat in the 0° rotation. The geometries of the anterior cuff and shin pad were removed from the model as they were not included in the experimental set-up. The FE geometry was positioned to match those rotations measured during the experimental set-up, as shown in Table 7.3.1.

Boundary conditions were then applied to the FE model of the PD-AFO to replicate the experimental set-up as described in section 7.3.4.1. Two small surfaces were created and glued (no relative movement allowed) to the posterior cuff at the point of contact of the screws; surfaces are rigid bodies, and their translation and rotation is considered about one *control* node (Figure 7.3.4). The two surfaces representing the point of contact of the screws were assigned the same control node located at the point of δ_{input} (between the centre of the 2 surfaces representing the screws). The control node was fixed in 4 degrees of freedom, only allowing translation in z and rotation about x .

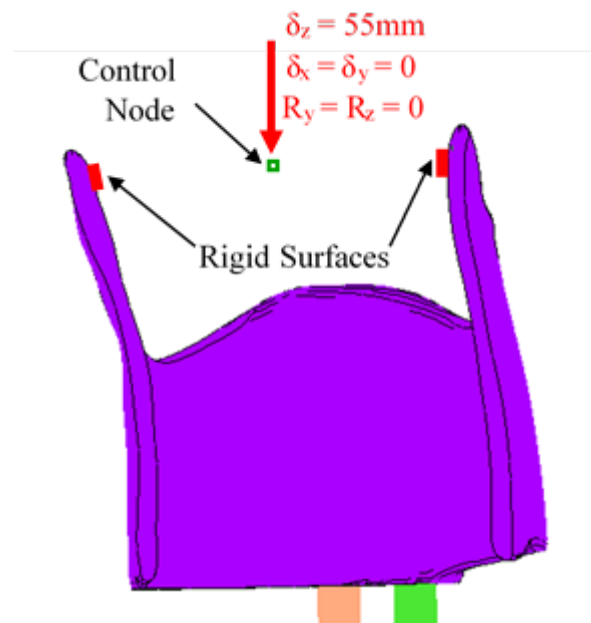


Figure 7.3.4: The boundary conditions, in red, applied to the control node of the cuff contact body during the FE validation, where δ indicates displacement in that direction, and R indicates rotation about that axis. The location of the two surfaces, representing the point of contact of the screws, is shown, and the control node is located centrally between them.

To replicate the aluminium fixture used in the experimental set-up, a surface was created normal to the struts, when in the 0° rotation, (in the plane x - y in Figure 7.3.3). This was then rotated about x by 20° and fixed in all 6 degrees of freedom. A coefficient of 0.68 was used between the surface and the base of the PD-AFO (aluminium and carbon fibre) [122].

To load the FE model, a displacement of up to 55 mm was applied in z to the control node linked to the screws and surrogate calf. The reaction force in the z -direction at the control node was obtained from the simulation results. The resulting force-displacement curve was fitted using linear regression, and the derivative of the curve used to calculate the mean stiffness.

Due to the sensitivity of the carbon fibre layer response to E_1 and the small non-linearity exhibited by the posterior struts in chapter 4, 2 further simulations were run assigning the material properties as the maximum and minimum values of the ranges investigated in chapter 4. The stiffnesses of these simulations were also obtained.

All stiffnesses from the FE simulations were compared to the those obtained experimentally to allow for minor adjustments with the aim of matching the FE model to the experiment as best as possible. Baseline material properties were assigned to the PD-AFO as determined from the comparison with the experiment, the results of which are presented in section 0.

7.3.5 Mechanical Response

Only 1 study has previously analysed the mechanical response of the PD-AFO (the IDEO), evaluating strut deflection and stiffness [63]. The FE model provides a tool to further analyse the mechanical response, including peak stresses and energy stored. Within chapters 5 and 6 it was shown that the peak loading of the PD-AFO occurred during loading response and the maximum energy stored within the struts was during terminal stance and pre-swing. As such it was decided to model the response of the PD-AFO during both early and late stance, at 10% of the gait cycle (between loading response and midstance) and at 50% of the gait cycle (between terminal stance and pre-swing). This section describes the boundary conditions applied to the FE baseline model with material properties of the PD-AFO, as determined in chapter 4, to evaluate the mechanical response in these 2 loading conditions, separately.

7.3.5.1 Boundary Conditions

In chapter 5 the ratio of loading between the PD-AFO and lower limb was calculated. As calculated in chapter 5 during gait, a force, P , was considered to load the PD-AFO. This was applied as a boundary condition to the FE baseline model to evaluate the mechanical response. The direction of the force, P , was resolved such that it acted in the same ratio as the GRF recorded during gait. When simulating 10% of the gait cycle, a total force, P_{ES} , was applied across a region on the posterior cuff, shown in

Figure 7.3.5a, with a value of $\sim 0.3\text{BW}$. For 50% of the gait cycle, a total force, P_{LS} , was applied across a region on the anterior cuff, shown in Figure 7.3.5b with a value of $\sim 0.151\text{BW}$.

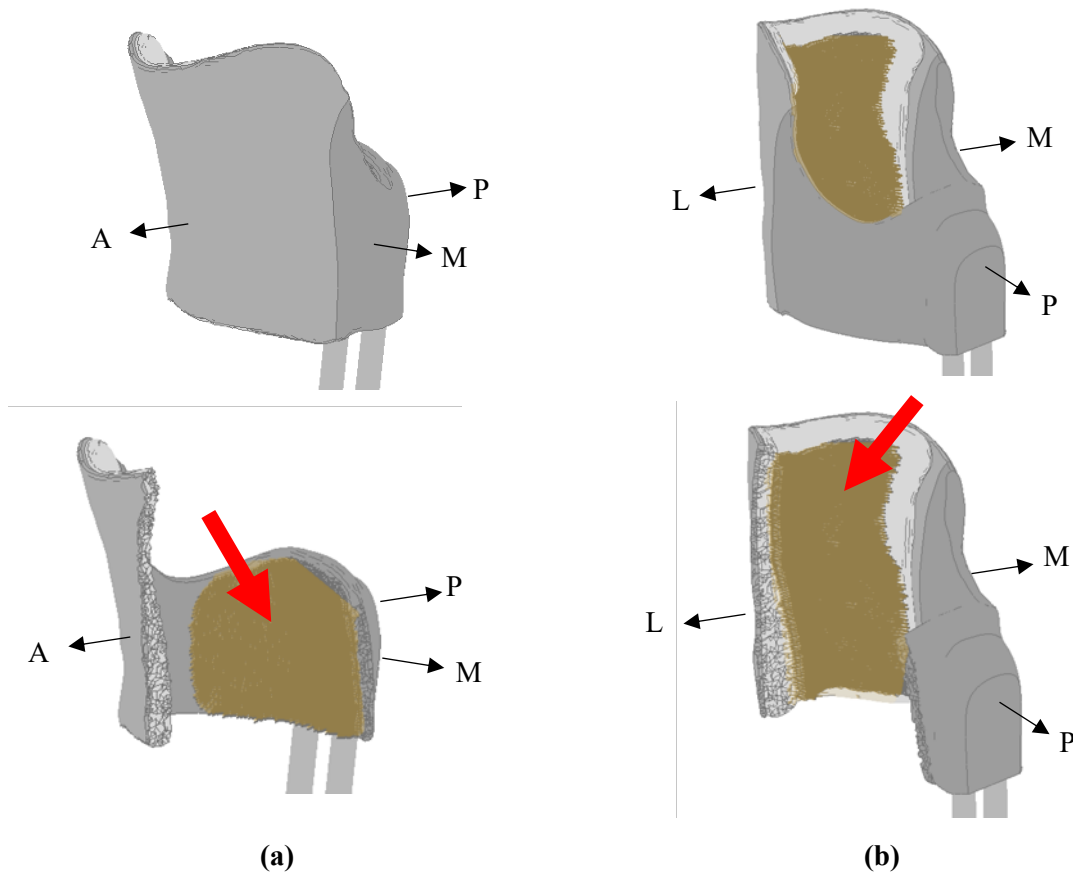


Figure 7.3.5: The top figures show the whole PD-AFO, and the bottom illustrate a region of the PD-AFO partly invisible to show the area, in yellow, over which the total force was applied at (a) early stance - 10% of the gait cycle and (b) late stance - 50% of the gait cycle. 'A' indicates the anterior direction, 'P', the posterior direction, 'M', the medial direction and 'L', the lateral direction .

To orientate the PD-AFO to the appropriate angle relative to the floor for each point in gait, the long-axis of the tibia was described within the PD-AFO, using a spring of negligible stiffness, shown in Figure 7.3.6. The distal end was fixed at the location where the centre of the ankle joint complex would sit when the subject wears the PD-AFO. The centre of the ankle joint complex was also assigned to be the origin of the coordinate system. The tibia was free to rotate about this point, but unable to translate. It was aligned $\sim 10^\circ$ to the long axis of the posterior struts in the sagittal plane, the same as described for fitting in chapter 5. The proximal end of the tibia was rigidly linked to the posterior cuff, so all displacements experienced by this point of the posterior cuff were experienced by the proximal end of the tibia (not vice-versa). This is shown by the red cross in Figure 7.3.6. For each point in gait the region of the PD-AFO that first contacts the ground was fixed in all degrees of freedom. The PD-AFO was rotated in the sagittal plane to give an initial angle, θ_i , between the tibia and the vertical axis. The determination of this angle is described below.

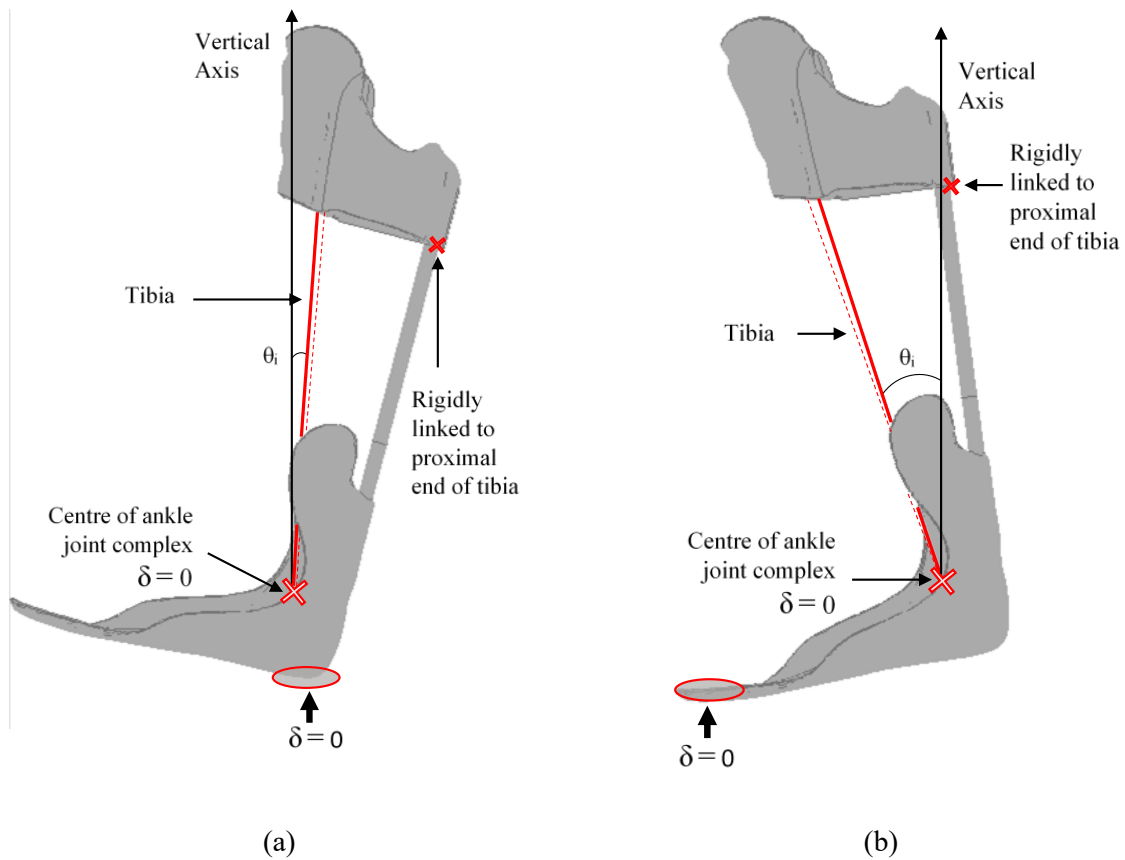


Figure 7.3.6: The boundary conditions applied to the PD-AFO model, for both (a) early stance (10% of the gait cycle) and (b) late stance (50% of the gait cycle). The red, solid line represents the angle of the long axis of the tibia compared to the vertical at the start of the analysis (the initial shank-to-vertical angle, θ_i) and the red, dotted line indicates the final position of the tibia compared to the vertical (the final shank-to-vertical angle described as θ_f). $\delta=0$ indicates that region is fixed in all directions.

7.3.5.2 Orientation

To mimic each point in gait, the final shank-to-vertical angle, θ_f , (the angle between the tibia and the vertical axis in the sagittal plane at the end of the simulation) upon application of the force, P , was determined from literature. This is seen in Figure 7.3.7, where the angle was taken at 10% and 50% of the gait cycle, respectively [123]. A final shank-to-vertical angle of $-5 \pm 0.5^\circ$ was defined for 10% of the gait cycle and a final shank-to-vertical angle of $20 \pm 0.5^\circ$ at 50% of the gait cycle. A negative angle indicates the proximal end of the tibia is more posterior than the distal end.

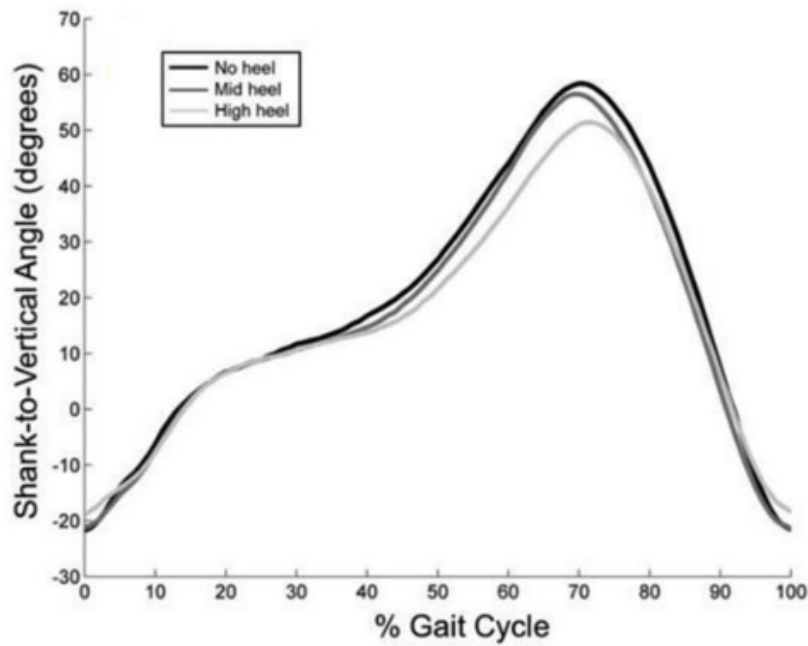


Figure 7.3.7: Shank-to-vertical angle throughout the gait cycle when wearing 3 different heel heights according to a study by Owens et al. [123]. Image reproduced with permission from the rights holder Sage Publications, Open Access.

An iterative process was used to determine the initial shank-to-vertical angle, θ_i , that resulted in the desired final angle, θ_f , upon application of the force, P . The initial shank-to-vertical angles, in the sagittal plane, used for each point in gait are shown in Table 7.3.2.

Table 7.3.2: The initial shank-to-vertical angle, θ_i , at early stance and late stance, as shown in Figure 7.3.6.

	Early stance (10%)	Late Stance (50%)
θ_i (°)	4.02	-18.13

7.3.5.3 Outputs

Each model was run, and several metrics were analysed including the peak Von Mises stresses, strain energy stored and rotational stiffness. Von Mises stress and strain energy within each component were direct outputs from the software. The rotational stiffness was calculated about the ‘ankle joint complex’ similar to that seen by Schrank et al. [105]; the calculation is described below.

The displacement of the proximal end of the tibia, in each direction, was obtained and used to calculate the resultant change in the tibia angle. Additionally, the force input in each direction was known. The resultant applied moment, \vec{M} , about the distal end of the tibia (centre of the ankle joint complex) was derived using (7.3.1), where \vec{r} was the distance from the centre of the ankle joint

complex, to the proximal end of the tibia and \vec{F} was the force experienced at the proximal end of the tibia.

$$\vec{M} = \vec{r} \times \vec{F} \quad (7.3.1)$$

Using equation (7.3.2) the resultant rotational stiffness, K , was calculated, where M was the applied moment, and θ was the resultant rotation.

$$K = \frac{M}{\theta} \quad (7.3.2)$$

7.3.6 Sensitivity analysis on device-design parameters

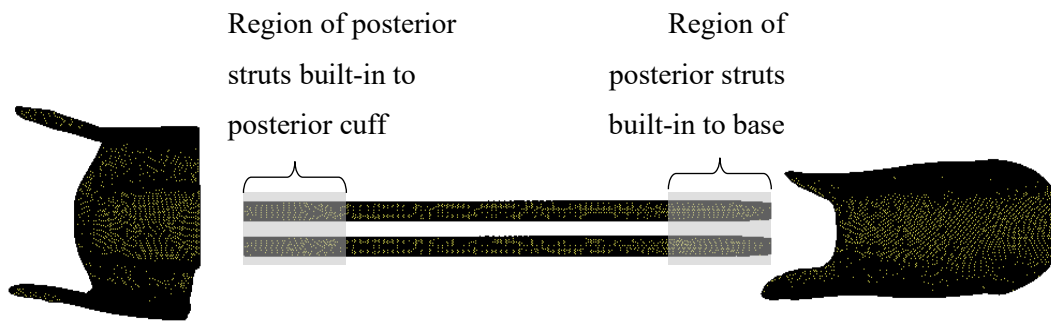
To capture the influence of different components on the mechanical response of the PD-AFO, a sensitivity analysis was performed. This section describes the design parameters analysed and the metrics chosen to study their influence on the response.

The 2 simulations, as described above in section 7.3.5, were used as the baseline results, and considered to be the *baseline* model. When possible, only one parameter was changed at a time; all other parameters remained constant. The exception to this was when altering the geometry of the posterior struts. During these analyses an altered *strut* model was used to run each simulation, and the final result adjusted to account for any changes introduced by the altered geometry and not by the change in parameter. This methodology is described below in 7.3.6.1.

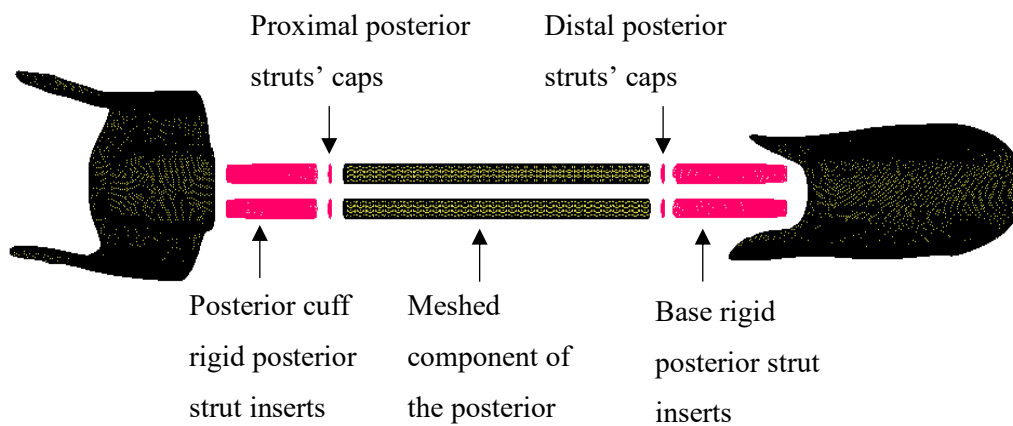
7.3.6.1 Altered Strut Model

To allow alterations of the posterior struts, the connection between the posterior struts, base and posterior cuff was altered. The built-in regions of the posterior struts were removed and replaced with rigid surface inserts, shown in Figure 7.3.8. These rigid surfaces were glued to the posterior cuff and base. Additionally, 4 surface caps were glued to each end of the new, shortened, posterior struts.

These surfaces and the built-in surfaces were considered to rotate and translate about the same control node located at the central axis at each end of the posterior struts.



(a)



(b)

Figure 7.3.8: The expanded view baseline model is shown in (a) with the region that is considered built-in to the posterior cuff and the base. The strut model is shown in (b) with the alterations made to the posterior struts, replacing the built-in region with rigid strut inserts. These rigid inserts were glued to the posterior cuff and base. The strut caps were glued to the posterior struts and had the same control node as the rigid inserts, so did not move relative to one another during the simulation.

7.3.6.2 Output Metrics

To analyse the PD-AFO's sensitivity to the different design components, energy storage and rotational stiffness were chosen as output metrics as they were found to be clinically important metrics in the literature [17, 112, 113, 124]. The strain energy, U , was considered to be the strain energy stored in the posterior struts only and was directly calculated by the FE software. In a dynamic FE model, the change in strain energy could be representative of the energy return capacity of the device, however this was not possible to calculate in a static model such as the one developed here. The rotational stiffness, K , was determined using the methodology described in section 7.3.5.3. The baseline rotational stiffness, K_b , and baseline strain energy, U_b , are denoted with a subscript 'b'. For each change in parameter during the sensitivity analysis, the PD-AFO was rotated to the same initial shank-to-vertical angle and the same force was applied at each point in gait. The sensitivity of each parameter on rotational stiffness, K , and strain energy, U , was calculated using equations (7.3.3) and (7.3.4), respectively.

$$S_K = \frac{K - K_b}{K_b} \quad (7.3.3)$$

$$S_U = \frac{U - U_b}{U_b} \quad (7.3.4)$$

The results from the *strut* model were compared to the *baseline* model using these output metrics, to observe any discrepancies within the results. Parameters analysed using the *strut* model were adjusted to account for differences due to the changes introduced by the strut model using equation (7.3.5), where C is the difference in stiffness, C_K , or energy stored, C_U , between the *baseline model* and the *strut* model.

$$S_K = \frac{K - K_b + C_K}{K_b} \quad (7.3.5)$$

$$S_U = \frac{U - U_b + C_U}{U_b} \quad (7.3.6)$$

7.3.6.3 Parameters

Within this section the parameters analysed during the sensitivity are described. Briefly, those parameters varied and analysed using the *baseline* model included the material properties of the struts and base, the addition of aramid to the base and the geometry of the base. Those parameters varied and analysed using the *strut* model included the alignment of the struts relative to the base, the alignment of the cuff relative to the struts, the struts' second moment of area and the ratio of the

struts' cross-sectional areas. For physiological parameters, limits on the extent of imposed variation were based on feasibility of clinical use. All other parameters were varied by $\pm 40\%$. All baseline values are fully described to allow for comparisons with future studies.

Material properties of the posterior struts and the carbon fibre regions were varied. These simulations were run in the *baseline* model. For the carbon fibre regions, the Young's Moduli in each direction, of each carbon fibre layer, were varied by $\pm 40\%$; all dependent constants were changed accordingly considering orthotropic properties. Additionally, the Young's Moduli of the carbon twill layer and of the uni-directional carbon fibre layer were adjusted by $\pm 40\%$ keeping all other material properties constant. To analyse the influence of the aramid, originally modelled within the toe region of the base only, a sensitivity was performed analysing the response when all regions of the base contained aramid and when no regions contained aramid.

Table 7.3.3: Material Properties changed for the design sensitivity

Parameter	Simulations	Baseline values (MPa)
Strut Young's modulus	$\pm 40\%$	32,570 (as determined in Chapter 4)
Base Young's modulus	$\pm 40\%$	Minimum values of the range as defined in Chapter 4
Base Aramid	All regions of the base with, all regions without	Within toe region only
Carbon Twill (in all regions)	$\pm 40\%$	Minimum values of the range as defined in Chapter 4
UD (in all regions)	$\pm 40\%$	Minimum values of the range as defined in Chapter 4

The angle of base alignment and toe region alignment were examined in the *baseline* model. Figure 7.3.9 shows the maximum changes in the rotations of the base regions within, approximately, sagittal plane. Figure 7.3.9a-c shows the rotations of the toe region $\pm 4^\circ$, to give a more dorsiflexed toe position and more plantarflexed toe position. Figure 7.3.9d-f shows the distal base rotated by $\pm 4^\circ$. This fixes the foot in a relatively dorsiflexed alignment or a plantarflexed alignment.

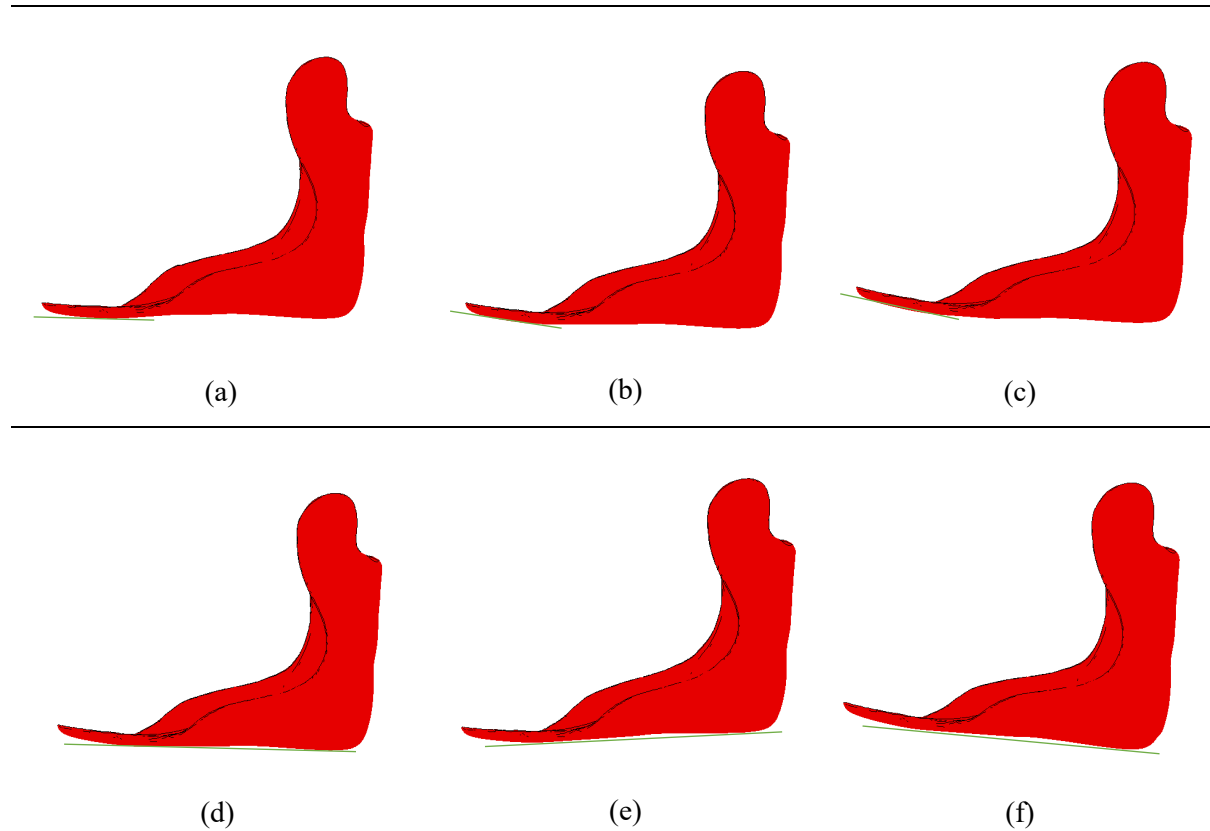


Figure 7.3.9: Rotation of the toe region in the sagittal plane relative to the long axis of the posterior struts to give (a) dorsiflexed angle of 4° relative to baseline (b) neutral toe position as prescribed of 2° dorsiflexed relative to the long axis of the posterior struts and (c) plantarflexed angle of 4° relative to baseline and rotation of the distal base portion to give (d) dorsiflexed position of 4° relative to baseline (e) baseline position as prescribed as prescribed at 3° plantar flexion relative to the long axis of the posterior struts (f) plantarflexed by 4° relative to baseline

Using the *strut* model, the alignment of the struts, was varied by $\pm 4^\circ$ in the sagittal plane, shown in Figure 7.3.10a-c. Additionally, the alignment of the cuff relative to the struts was altered by $\pm 4^\circ$ in the sagittal plane, shown in Figure 7.3.10d-f.

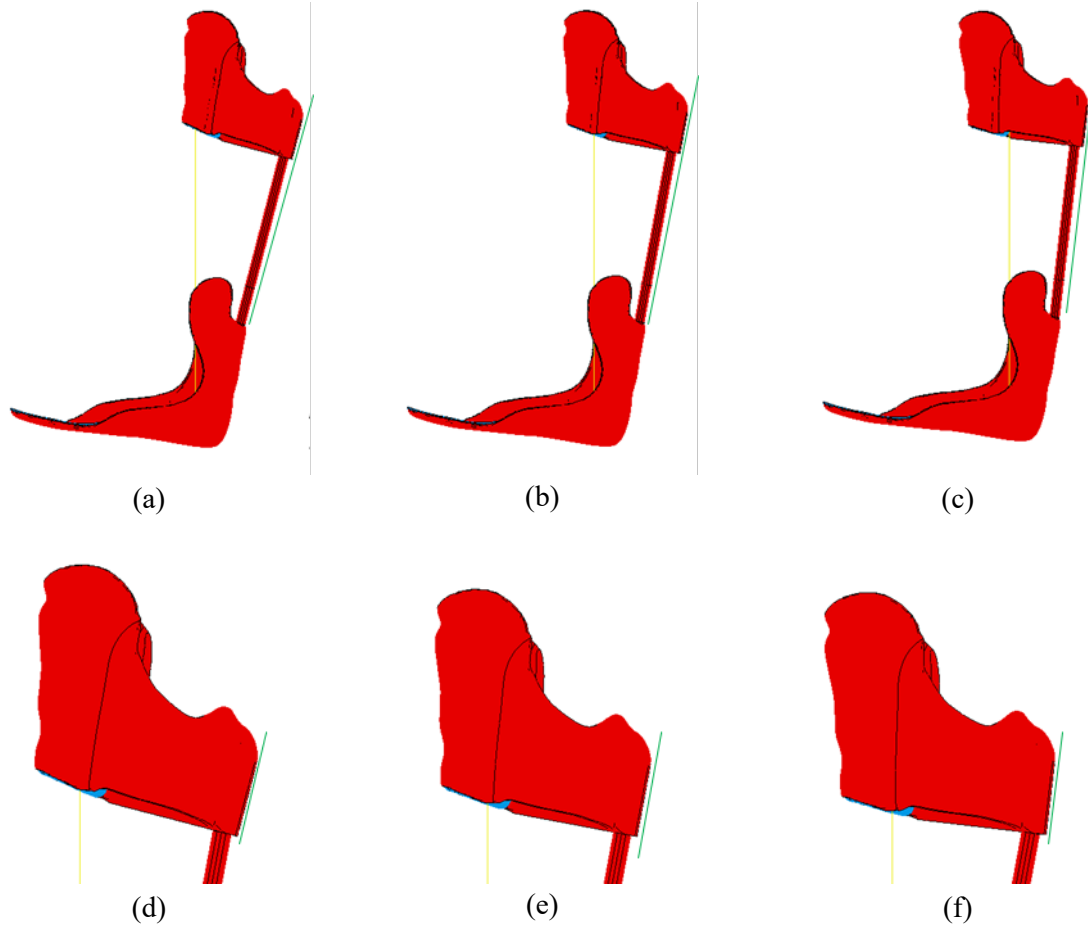


Figure 7.3.10: Rotation of the posterior struts to (a) plantarflexed position of 4° relative to baseline (b) baseline position as prescribed with posterior aspect of base and long axis of posterior struts in plane (c) dorsiflexed by 4° relative to baseline and rotation of the cuff to (d) plantarflexed position of 4° relative to baseline (e) baseline position as prescribed with posterior aspect of cuff and long axis of posterior struts in plane (f) dorsiflexed by 4° relative to baseline

Figure 7.3.11 shows the parameters altered using the *strut* model. Figure 7.3.11a-c illustrates the variation in strut cross-section by $\pm 40\%$, with a small diameter of 9.12 mm and a larger diameter of 13.93mm. The cross-section of the strut was also altered to change the second moment of area in the sagittal plane by 40%, shown in Figure 7.3.11d-f. Figure 7.3.11g-i shows the variation in individual strut diameters, increasing one strut by 40% relative to the baseline diameter whilst decreasing the other by 40%.

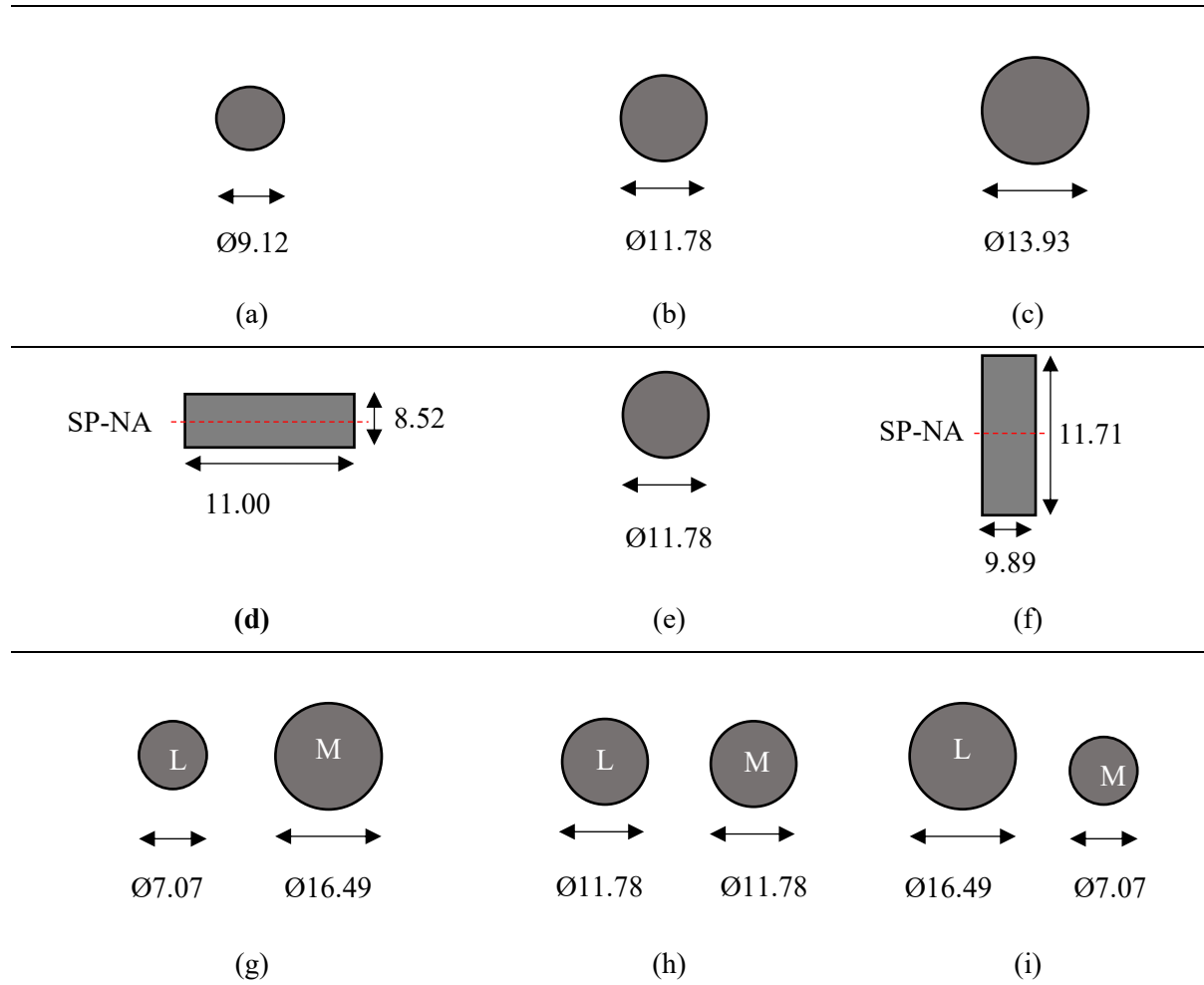


Figure 7.3.11: Changing the cross sectional areas of the struts by (a) -40% of the base line area (b) baseline value and (c) +40% of the baseline area. Altering the second moment of area - in the sagittal plane - of the struts, whilst maintaining the cross-sectional area, to give a second moment of area of (d) 567mm^4 (e) 944mm^4 and (f) 1323mm^4 about the sagittal plane neutral axis, SP-NA. Altering the diameter of the lateral (L) and medial (M) posterior struts to give (g) an increase in 40% diameter of the medial strut and 40% reduction of the lateral strut diameter, (h) the baseline diameters, and (i) an increase in lateral strut diameter by 40% and a decrease in medial strut diameter by 40%. All dimensions are in mm.

7.4 RESULTS

Prior to calibration of the model, a mesh convergence was performed to determine the appropriate size of mesh. The results are shown in Figure 7.4.1. The mesh converged at ~70,000 elements, where the values of reaction force and peak equivalent Von Mises stress recorded by the FE model were within 10% of those values obtained with over 2,000,000 elements. The peak equivalent Von Mises Stress was seen in the same location for all models.

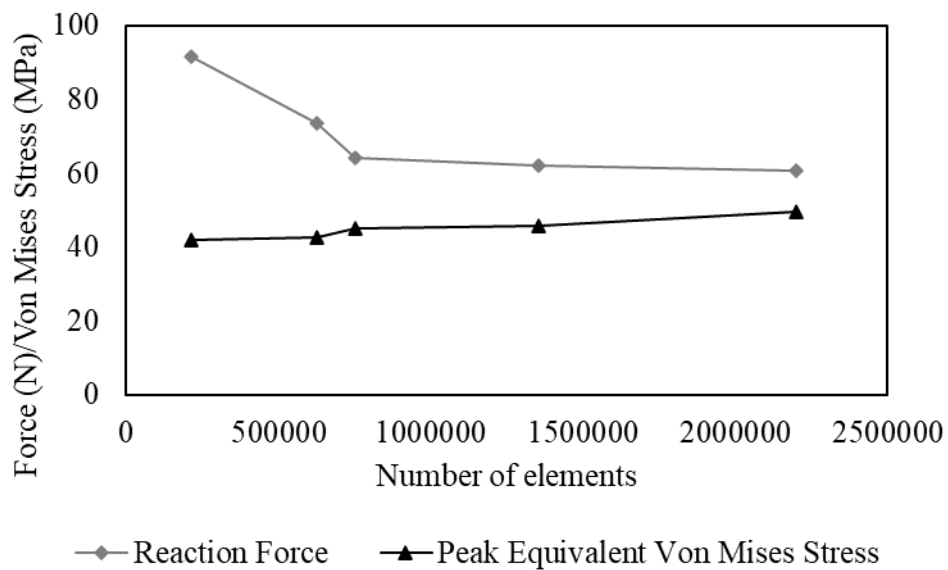


Figure 7.4.1: Mesh convergence analysis on the PD-AFO FE model. The model reaction force and peak equivalent Von Mises Stress.

7.4.1 Model Calibration and Validation

Figure 7.4.2 shows the force-displacement curves measured during the experimental validation test set-up for 5 repeat tests (T1-T5). No slipping was observed during the test. The maximum displacement applied was 53.8 mm and the maximum force recorded was 400N.

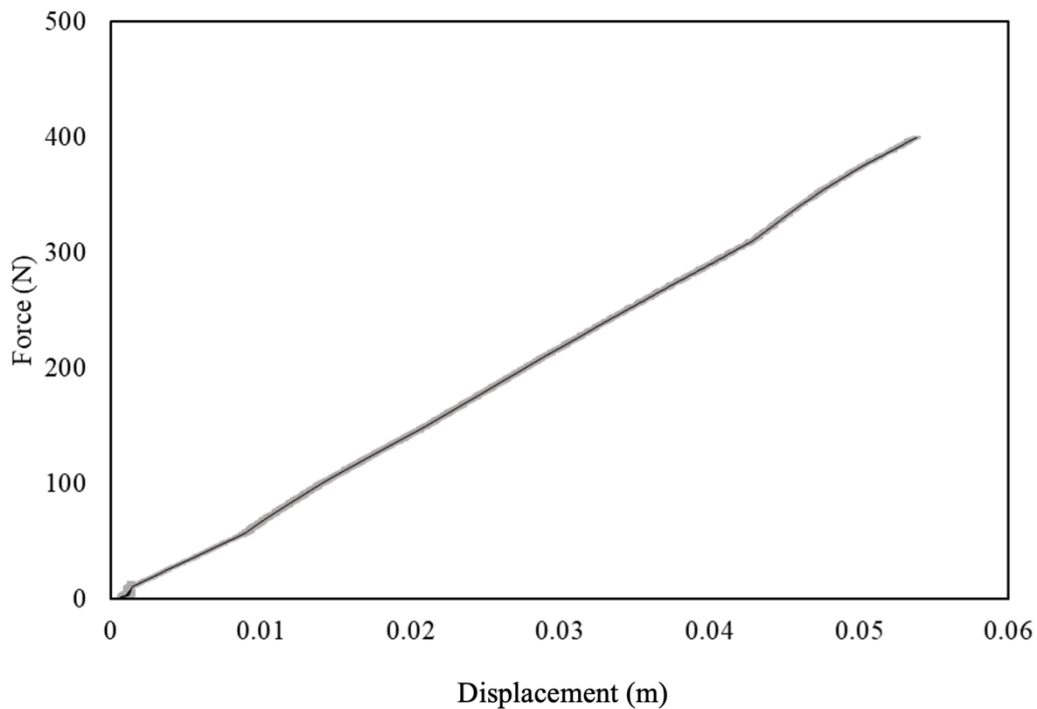


Figure 7.4.2: Mean force-displacement curve, ± 1 SD, for 5 tests for the experimental, validation set-up.

Figure 7.4.3 shows (a) the experimental set-up and (b) the corresponding FE simulation used to compare the model to the experiment. In both cases the PD-AFO was vertically compressed. The locations of maximum Von Mises stress in each component, obtained from the FE simulation, are indicated. On the lateral strut (i) the Von Mises stress was 287MPa and on the medial strut (ii) it was 285MPa. On the posterior cuff, at the site of the medial rivet (iii) the stress was 181MPa. Site (iv) recorded 141MPa where the base and lateral strut are attached, on the interior, anterior surface. Site (v) is located on the medial side of the base and recorded a Von Mises stress of 130MPa.

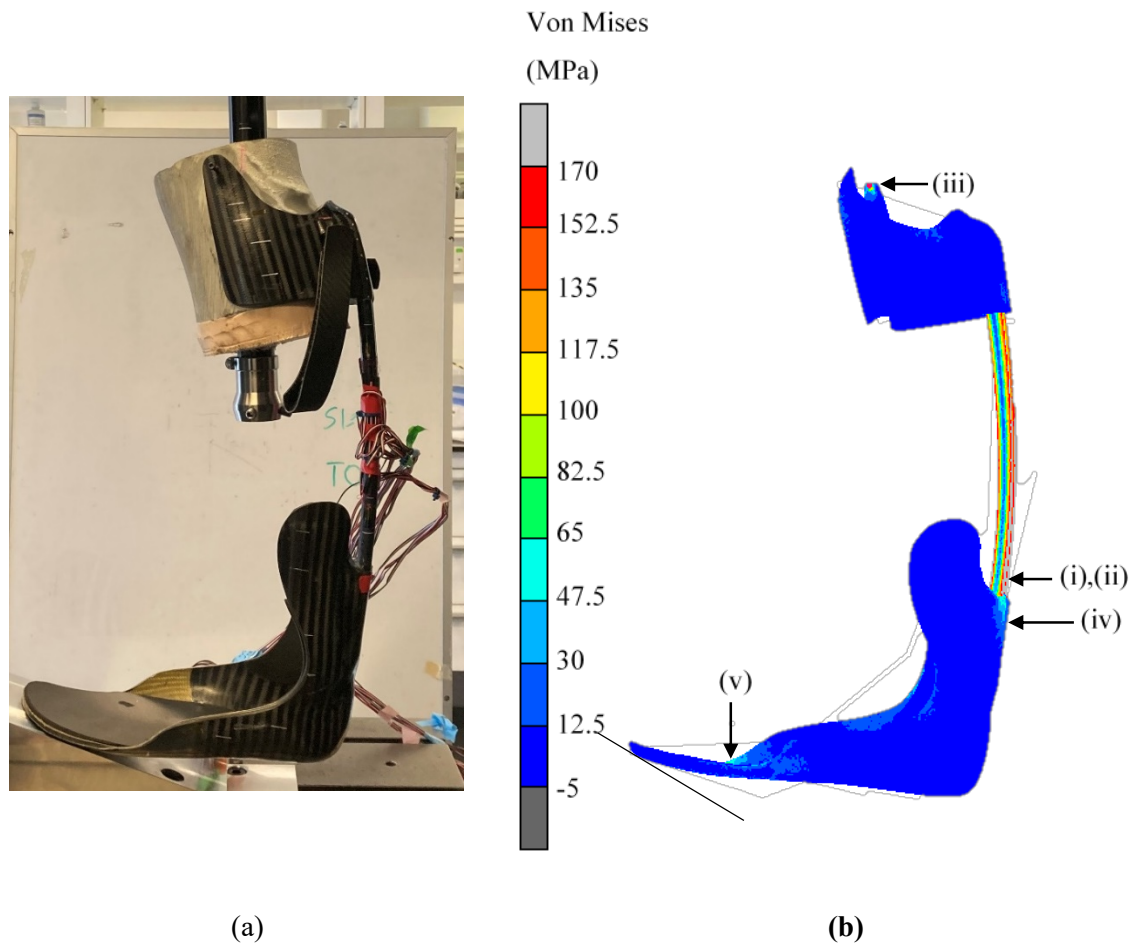


Figure 7.4.3: The (a) experimental and (b) computational compression testing of the PD-AFO showing the device at full compression with 400 N. The location of the maximum value of Von Mises stress recorded in each component during the FE simulation is shown in (i) the lateral strut (ii) the medial strut (iii) the posterior cuff and, (iv) the proximal region of the base (v) the distal region of the base.

The experimental force-displacement curve was adjusted to have zero force at 0.0015mm, to remove initial slack. The minimum experimental stiffness, as calculated by the derivative of the force-displacement curve was 5914N/m, calculated between 2.2-3.3 mm of displacement. The maximum experimental stiffness was 9891N/m calculated at 42.7-43.8 mm of displacement. The experimental force-displacement loading curve, was adequately represented by linear regression ($R^2 > 0.99$), to give a mean, linear stiffness of 7307N/m.

The results for the stiffness of the PD-AFO recorded during the FE simulation were within the range of stiffnesses calculated from the experiment. When fitted with a linear regression ($R^2 > 0.99$) the stiffness of the PD-AFO in the FE simulation was calculated to be 8223N/m, 8883N/m and 9540N/m when using the minimum, mean and maximum material properties established in chapter 4 (Figure 7.4.4). The FE simulation recorded a higher mean linear stiffness than the mean linear experimental stiffness by between 13 - 31%.

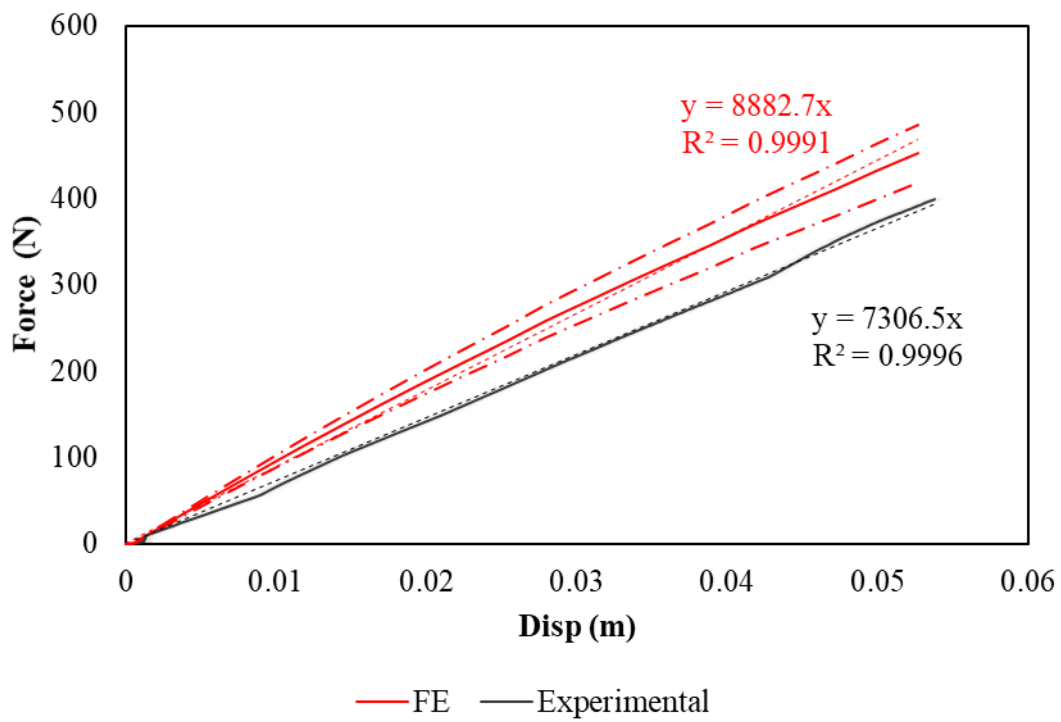


Figure 7.4.4: The force-displacement (disp) curve recorded during the experimental set-up and the force-displacement curves calculated by the FE simulation. The solid red line indicates the force-displacement curve obtained using the mean material properties. The steeper and shallower dotted red lines indicate the force-displacement curves obtained using the maximum and minimum material properties, respectively.

7.4.2 Mechanical Response

Figure 7.4.5 shows the ratio of strain energy within each component as calculated within the FE simulations during early and late stance. The sum of strain energy within the posterior struts at 10% of the gait cycle (183mJ) made up 83% of the total strain energy within the PD-AFO (220mJ). At 50% of the gait cycle the total strain energy within the posterior struts (635mJ) was 82% of the total strain energy within the whole PD-AFO (779mJ). Comparatively, the base made up only 17% and 5% of the total strain energy within the PD-AFO during early stance and late stance respectively.

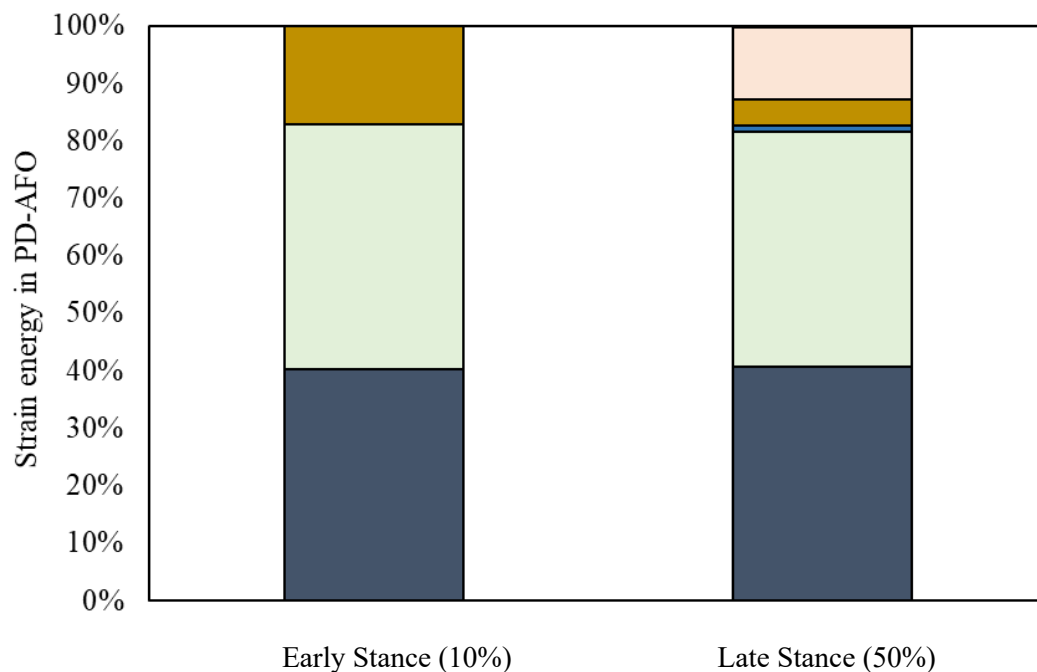


Figure 7.4.5: Ratio of strain energy recorded by the FE model within each component of the PD-AFO upon completion of both the early stance and late stance simulation.

The equivalent Von Mises stress distributions for both points in gait are shown in Figure 7.4.6. The maximum Von Mises stress during early stance was observed at the point of loading in the base shown in Figure 7.4.6c (i). The maximum Von Mises stress at late stance was observed at the insert of the base. The bending axis for both points in gait occurred at the distal end of the struts. The rotational stiffness, calculated using equations (7.3.1)-(7.3.2), was found to be $6.745\text{Nm}/^\circ$ at early stance and $8.108\text{Nm}/^\circ$ at late stance.

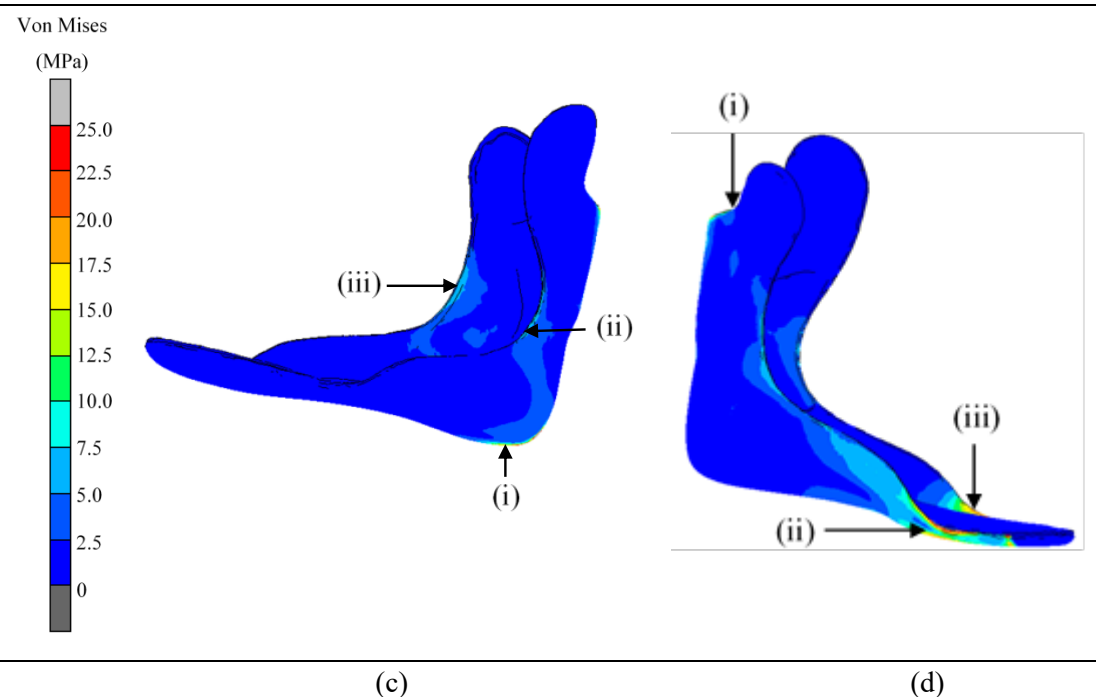
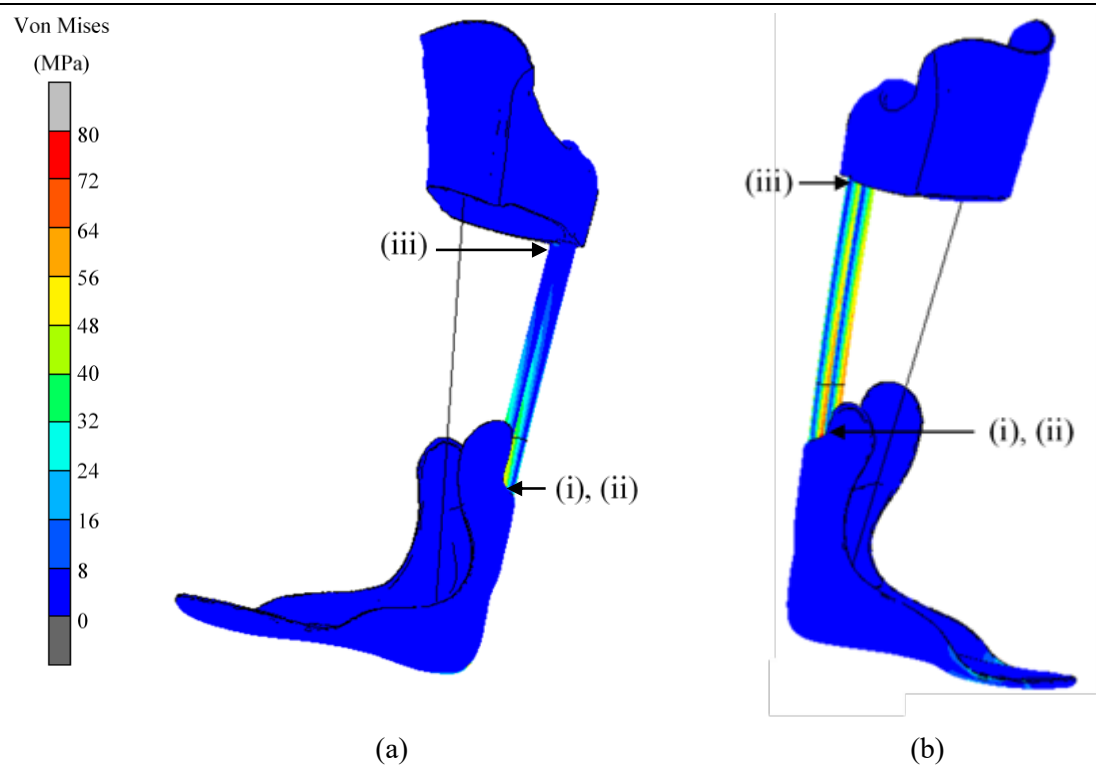


Figure 7.4.6: The equivalent Von Mises stress in the PD-AFO at (a) early stance with (i) 59MPa on the lateral strut, (ii) 58MPa on the medial strut and (iii) 8 MPa on the insert for the medial strut in the posterior cuff and (b) late stance with (i) 82MPa on the medial strut (ii) 75MPa on the medial strut and (iii) 47MPa on the insert for the medial strut in the posterior cuff, and within the base alone at (c) early stance with (i) 86MPa (ii) 10MPa and (iii) 7MPa and (d) late stance with (i) 107MPa on the insert for the lateral strut in the base (ii) 38MPa and (iii) 22MPa.

7.4.3 Design Sensitivity

7.4.3.1 Baseline model and Strut Model

Table 7.4.1 shows the change in the rotational stiffness and energy stored within the *strut* model when compared to the *baseline* model. A negative value indicates that the *strut* model gave a value greater than the *baseline* model. At early stance, the *strut* model calculated a rotational stiffness 13.2% higher than the *baseline* model, with 10.6% less strain energy stored in the posterior struts. At late stance the *strut* model recorded a rotational stiffness 8.8% higher than the *baseline* model and 9.2% less strain energy in the posterior struts. The absolute differences were used to adjust the results of parameters analysed using the *strut* model, using equations (7.3.5)-(7.3.6) above.

Table 7.4.1: Absolute difference between the baseline model and the strut model, calculated by subtracting the output metric from the strut model, from the baseline model.

Difference in Rotational Stiffness (Nmm/°)		Difference in Strain Energy (mJ)	
Early stance	Late stance	Early stance	Late stance
-890	716	19	58

7.4.3.2 Parameter Analysis

This section described the results of the sensitivity analysis comparing the change in strain energy stored in the posterior struts and the rotational stiffness of the PD-AFO, to the baseline model. The full results are listed in Table 12.4.1 in Appendix 12.4.2.

Figure 7.4.7 shows the influence of the posterior strut Young's modulus on the mechanical response of the PD-AFO at early stance, 10% of the gait cycle - shown by ES, and late stance, 50% of the gait cycle - shown by LS. The green bar indicates the change in resultant, rotational stiffness, and the red bar indicates the change in strain energy in the posterior struts. A positive value indicates that the output metric was greater than that of the baseline model and a negative value indicates that the output metric was less than the value obtained from the *baseline* model. The greatest changes were observed in the energy stored at both early stance and late stance, with a change of +89% and +75%, respectively, following a decrease in the Young's modulus. Where an increase in energy stored was observed, the rotational stiffness was seen to decrease, and vice versa. The maximum change in rotational stiffness, of -44%, was observed at early stance, following a decrease in the parameter.

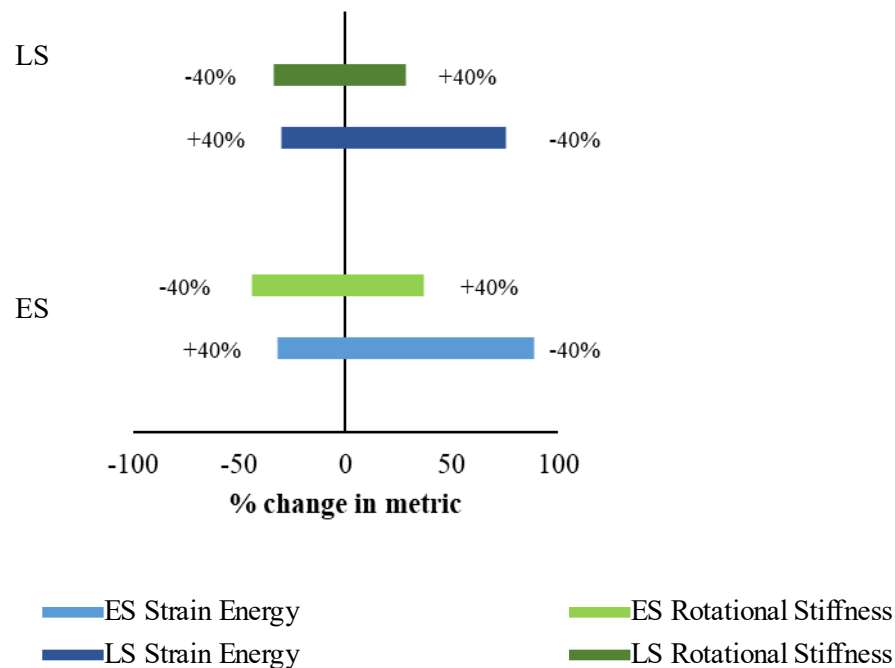
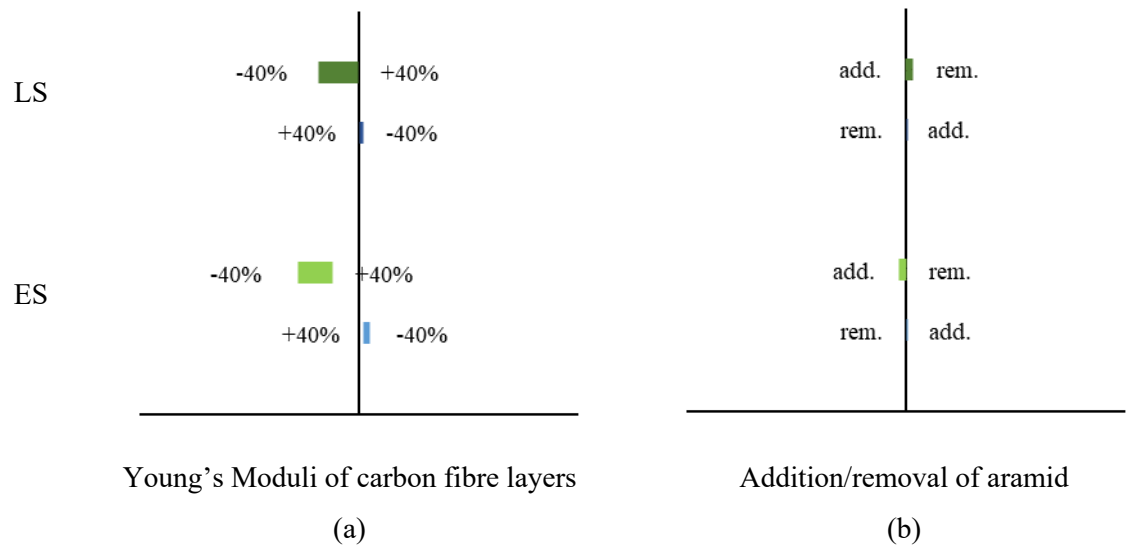


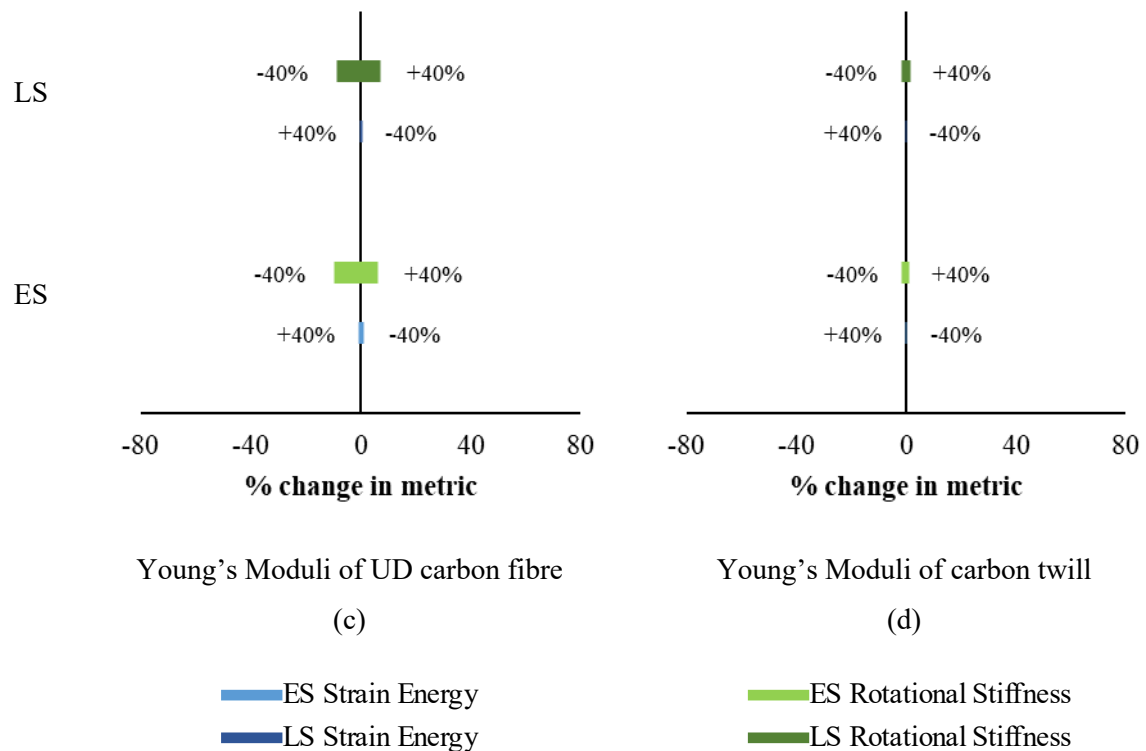
Figure 7.4.7: Influence of the Young's modulus of the posterior struts, when varied by $\pm 40\%$, on the rotational stiffness and strain energy stored in the posterior struts, when compared to the baseline model. ES: early stance, simulation 10% of the gait cycle; LS: late stance, simulation 50% of the gait cycle

Altering the Young's Moduli of all carbon fibre layers, had $<5\%$ change on the energy stored within the posterior struts (Figure 7.4.8a). Following both a decrease and increase in the Young's Moduli, the rotational stiffness was observed to decrease by between 10-23% at early stance and 0-15% at late stance. Similarly minimal changes ($<5\%$) in the energy stored were observed when altering the Young's Moduli of the UD carbon fibre (Figure 7.4.8c). At both points in gait an increase in the Young's Moduli resulted in a 7% increase in the rotational stiffness. A decrease in the Young's Moduli gave a change of -10% and -9% at early stance and late stance respectively. The PD-AFO's mechanical response was found not to be sensitive to additional aramid (Figure 7.4.8b) or the Young's Moduli of the carbon twill (Figure 7.4.8d) at either points in gait.



Young's Moduli of carbon fibre layers
(a)

Addition/removal of aramid
(b)



Young's Moduli of UD carbon fibre
(c)

Young's Moduli of carbon twill
(d)

ES Strain Energy
LS Strain Energy

ES Rotational Stiffness
LS Rotational Stiffness

Figure 7.4.8: Influence of the carbon fibre material properties on the rotational stiffness and strain energy stored in the posterior struts, when compared to the baseline model. The parameters changed were (a) the Young's Moduli of all carbon fibre layers used in the base and the cuff by $\pm 40\%$ (b) the addition (add.) and removal (rem.) of aramid from all areas within the base (c) the Young's Moduli of the uni-directional carbon fibre in the base and cuff by $\pm 40\%$ and (d) the Young's Moduli of the carbon twill carbon fibre in the base and the cuff by $\pm 40\%$. ES: early stance, simulation 10% of the gait cycle; LS: late stance, simulation 50% of the gait cycle.

The response of the PD-AFO was found not to be sensitive to the plantar alignment of the toe region (Figure 7.4.9a). Similarly, the rotation of the whole base resulted in <1% change in energy stored across all gait conditions (Figure 7.4.9b). The rotational stiffness increased by 6% with the whole base in a more dorsiflexed position at early stance, but all other changes in the stiffness were <5%.

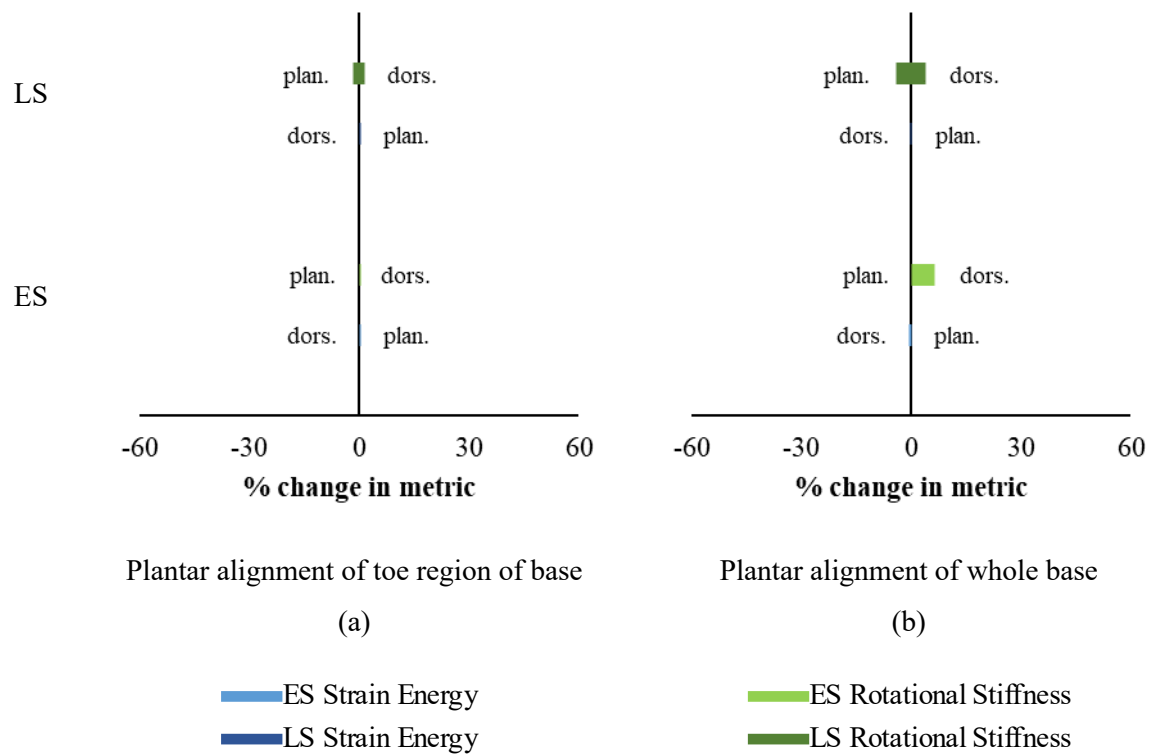


Figure 7.4.9: Influence of the base alignment on the rotational stiffness and strain energy stored in the posterior struts, when compared to the baseline model. The parameters changed were (a) the alignment of plantar region of the toe region relative to the posterior struts by $\pm 4^\circ$ (b) the alignment of plantar region of the whole base relative to the posterior struts $\pm 4^\circ$. (Plan. indicates the mode plantarflexed alignment and dors. indicates the more dorsiflexed alignment.) ES: early stance, simulation 10% of the gait cycle; LS: late stance, simulation 50% of the gait cycle.

Figure 7.4.10 and Figure 7.4.11 shows the relative change in output metric to the *baseline* model, of those parameters analysed using the *strut* model, and adjusted to account for those differences, as described in section 7.4.3.1.

The alignment of the struts and cuff were altered in the sagittal plane. A greater change in energy stored and rotational stiffness was observed at early stance than late stance (Figure 7.4.10a), with a maximum change in the energy stored of +50% in a more plantarflexed alignment. At push of the maximum change in energy stored, -11%, was also in a more plantarflexed alignment. Overall, the maximum change in rotational stiffness at early stance was +39%, and at late stance was +14%.

Alignment of the cuff alone (relative to the posterior struts) had a smaller influence on the mechanical response of the PD-AFO, than the alignment of the struts and cuff combined. At late stance all changes seen were <5%. The greatest change observed at early stance was the energy stored, +12%, in a more plantarflexed alignment. The maximum change in rotational stiffness was +8%.

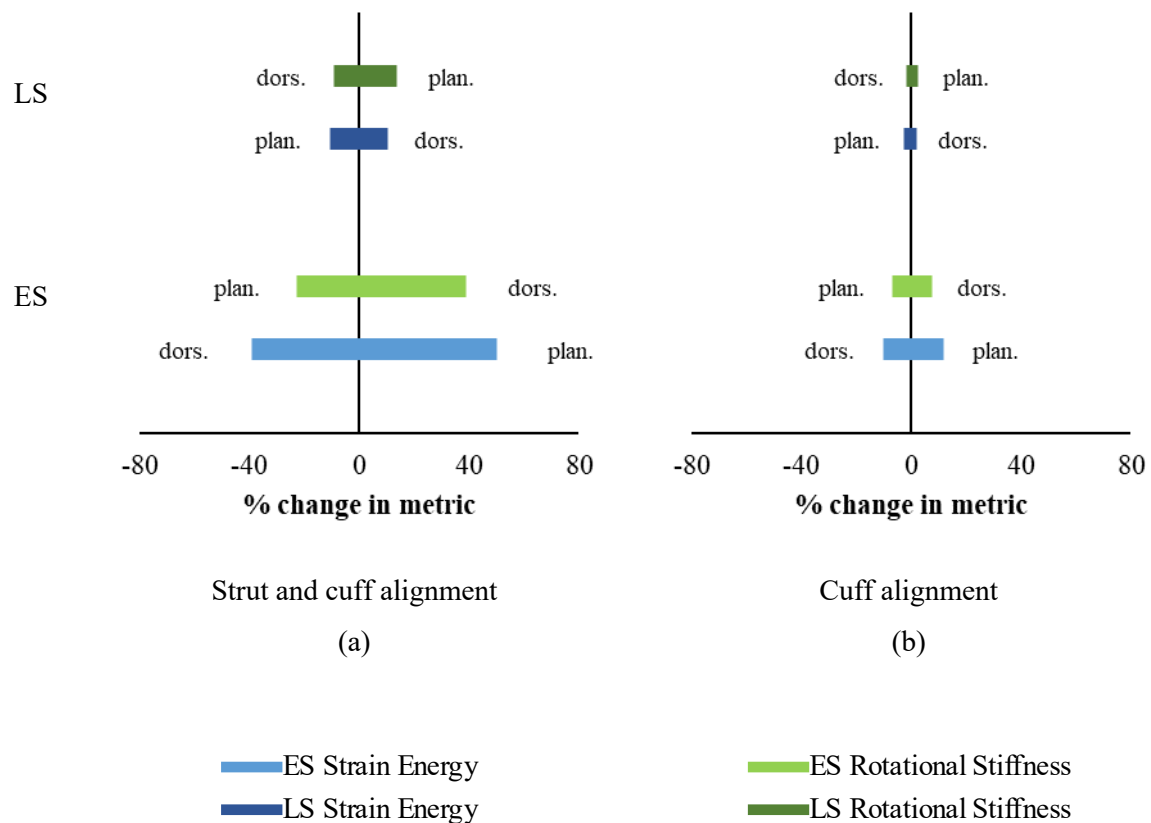


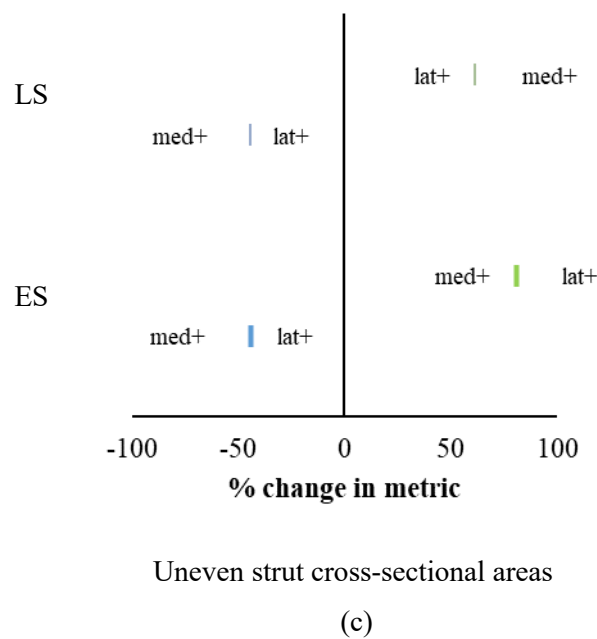
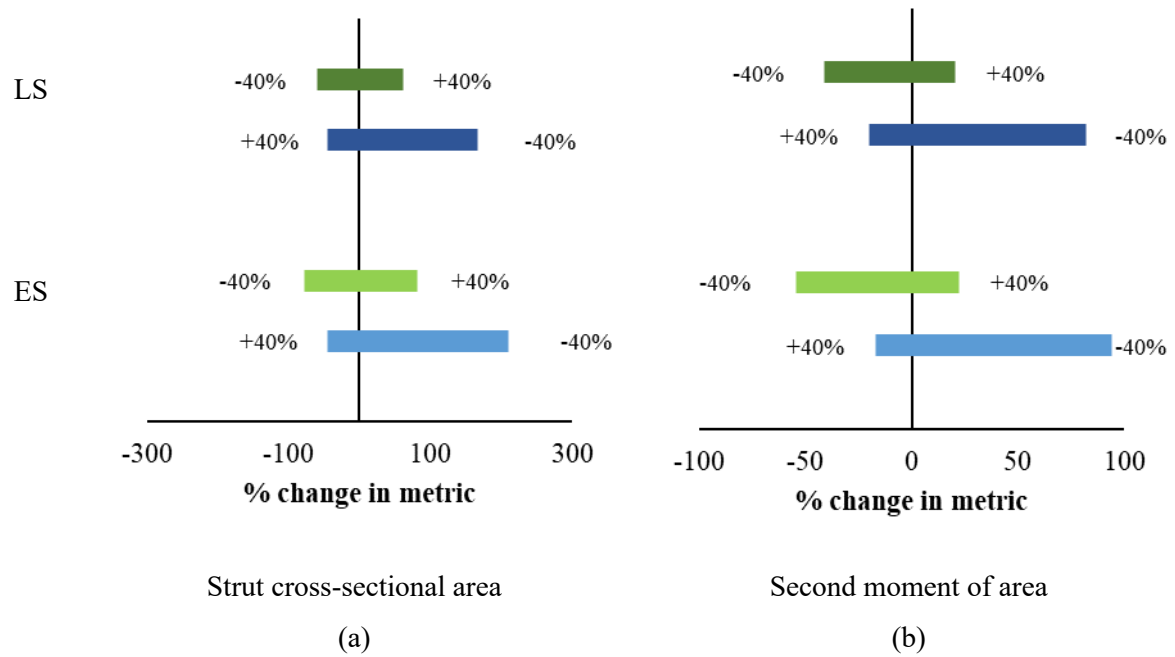
Figure 7.4.10: Influence of the strut and cuff alignment on the rotational stiffness and strain energy stored in the posterior struts, when compared to the baseline model. The parameters changed were (a) the relative alignment of the struts and cuff to the ground by $\pm 4^\circ$ (b) the relative alignment of the cuff to the posterior struts by $\pm 4^\circ$. (Plan. indicates the plantarflexed alignment, and dors. the dorsiflexed alignment.). ES: early stance, simulation 10% of the gait cycle; LS: late stance, simulation 50% of the gait cycle.

Of all parameters changed, those related to the cross-sectional area of the posterior struts influenced the mechanical response of the PD-AFO the most. When altering the strut cross-sectional area, the energy stored changed by a greater amount than the rotational stiffness at both points in gait (Figure 7.3.11a). The maximum change in energy stored at early stance was +210% and at late stance was +168%, when decreasing the diameter of the posterior struts. Comparatively, the maximum change in rotational stiffness was only +82% and +61%.

A change in the second moment of area also resulted in a greater change in energy stored than change in rotational stiffness (Figure 7.3.11b). The energy stored changed by +82 to +94% following a

reduction in the second moment of area, and by -17 to -20% following an increase. The changes in rotational stiffness, whilst smaller, were still between +21 to +22% and -41 to -54%.

The assignment of different cross-sectional areas for each strut, shown in Figure 7.4.11c, had a large change in output metrics relative to the baseline, between -44 to -46% change in energy stored and +61 to +82% change in rotational stiffness, though the direction of the changes were both the same regardless of whether the medial or lateral strut had the larger cross-sectional area. The changes observed in both energy stored and rotational stiffness, when decreasing the cross-sectional area, were within 2% of those observed when increasing the cross-sectional area.



■ ES Strain Energy ■ ES Rotational Stiffness
■ LS Strain Energy ■ LS Rotational Stiffness

Figure 7.4.11: Influence of the strut cross-sectional area on the rotational stiffness and strain energy stored in the posterior struts, when compared to the baseline model. The parameters changed were (a) the strut cross-sectional area by $\pm 40\%$ (b) the second moment of area by $\pm 40\%$ in the sagittal plane (c) uneven strut cross-sectional areas (with med+ indicating the medial strut had a larger cross-sectional area and lat+ indicating the lateral strut had a larger cross-sectional area). ES: early stance, simulation 10% of the gait cycle; LS: late stance, simulation 50% of the gait cycle.

7.5 DISCUSSION

7.5.1 Model Calibration and Validation

This chapter presents the development of the first FE model of the specific PD-AFO that is the subject of this thesis. Before using the model for analysis, boundary conditions were applied to mimic that of an experimental set-up and the results compared. The FE model was run 3 times with the minimum, mean and maximum material properties for the range of values determined in chapter 4.

Whilst the stiffnesses measured experimentally could be approximated well as linear ($R^2 > 0.99$), the rate of change in stiffness was not smooth. Qualitatively, 3 distinct, approximately linear, sections of the experimental force-displacement curve were seen. This is thought to be due to slack between the surrogate tibia and the materials testing machine; as slack is taken up the fixture becomes stiffer.

Taking the mean, linear stiffness for all displacements greater than 45.3mm, assuming most slack is removed from within the set up at this point, gives a linear stiffness of 7448N/m ($R^2 > 0.99$). The FE model gives a stiffness within 10% of this value when using the minimum material properties within the range determined in chapter 4, and is within the minimum and maximum stiffness calculated experimentally. This demonstrates good agreement between the FE model and experimental set-up.

The lowest values of the material properties were therefore assigned to the baseline model.

During the experiment, the anterior cuff and shin pad were not included in the experimental set-up and therefore not compared to the computational output. It was deemed important to control the boundary conditions and fixed contact between the loading points during the experimental set-up was required to do this. The most appropriate place for this was the pre-existing holes for rivets on the posterior cuff as this did not change the PD-AFO in any way. This made the anterior cuff redundant. This was deemed an acceptable compromise, particularly as the anterior cuff is not thought to deform significantly during gait.

7.5.2 Mechanical Response

To analyse the mechanical response of the PD-AFO, boundary conditions were applied to mimic those experienced during gait. Upon application of these boundary conditions, the FE model deflected in a similar manner as that reported in chapter 6 and in the literature. The sagittal plane rotational stiffness was of the same order, but slightly higher in value than those observed when Schrank et al. analysed a different PD-AFO by [105]. Wach et al. however, did report that the IDEO had a higher compressive stiffness than other AFOs so it is not unlikely for the PD-AFO that is the focus of this study to have a higher stiffness than other AFOs [63].

When simulating early stance, the posterior struts inverted as seen during gait in chapter 6. During both the early stance and late stance simulations, greater strains were observed at the distal end of the

posterior struts, again, as observed experimentally within chapter 6. This supports the assumption made in chapter 6, that the struts act as a cantilever.

The peak Von Mises stresses observed in the base were located in the toe region at 50% of the gait cycle. In a personal discussion with the Blatchford Orthotist in February 2018, it was discussed that aramid was introduced to the carbon fibre lay-up of this region of the base, as several failures had been observed at this location. This indicates that the toe region of the base was an area of peak stress, which matches the stress distribution observed in the FE simulation, thus providing qualitative confidence in the result.

The values of strain energy calculated from the FE model were an order higher at early stance than those recorded experimentally. At late stance, the FE model recorded strain energy of the same order but lower than the experimental calculation. The results from the model were deemed close enough to the behaviour of the experimental response for the PD-AFO for the boundary conditions chosen to be considered clinically relevant. Whilst further refinement of the boundary conditions could be achieved with further experimental testing, the model was suitable to provide comparative results within different regions of the PD-AFO.

Within chapter 5, one hypothesised mechanism of action of the PD-AFO was that the base may deflect and act as a lever arm during the late terminal stance phase. However, the strain energy within the base at late stance was less than 6% of that seen within both posterior struts. This suggests that is unlikely to have a significant effect on additional propulsive power during late stance, relative to the posterior struts.

7.5.3 Design Sensitivity

A design sensitivity was performed to evaluate the effect of individual design aspects of the PD-AFO on its mechanical response. Specifically, the influence of the parameters on the energy stored within the posterior struts and the rotational stiffness were compared. The change in energy stored was only evaluated within the posterior struts; this was acceptable due to the relatively low strain energy observed within the other components when analysing the mechanical response as discussed in section 7.5.2.

Within the design sensitivity, it was shown that, at both points in gait, changes in the strength of the carbon fibre used, along with the addition of aramid had limited influence on the energy stored within the posterior struts. Changing the Young's Moduli of the uni-directional carbon fibre had some influence on the rotational stiffness and this is thought to be due to the stiffening in one direction only. Additionally, the shaping of the base was found to have very little effect on both rotational stiffness and energy stored in the struts. The influence of the base strength and shape on the mechanical response is valuable when considering the accuracy required during fitting and manufacturing, and the

cost implications of this. The minimal influence of the base shape on the ability to store and return energy also suggests that comfort and alignment most suited to the patient should be the priority. In addition to this, different manufacturing methods have been used for different PD-AFOs. The PD-AFO described within this thesis is the Momentum®. Within the US military a similar PD-AFO named the IDEO is used, as described in chapter 3. It is generally assumed that the IDEO and Momentum alter gait in the same way, though no study has directly compared the mechanical response of US and UK manufacturing methods. The difference in the manufacturing is mainly the type of carbon fibre used within the cuff and base. The limited influence of the carbon fibre material properties on the energy stored and rotational stiffness, therefore supports the current assumption that the IDEO and Momentum are likely to alter gait in a similar manner.

Significant changes in rotational stiffness and energy stored were observed when altering the strut Young's modulus. Similar results were also seen when changing the cross section of the struts. Schrank et al. when analysing a different PD-AFO, found virtual bending stiffness to be most sensitive to strut dimensions and Young's modulus [105]. However, previous gait analysis studies using the PD-AFO, found that altering the bending stiffness had a limited effect on gait biomechanics; it was suggested that this may be due to compensatory measures from the patient [56]. The alteration in energy storage, theoretically alters the ability of the PD-AFO to provide propulsive power. It may be possible that patients are able to compensate for this change for a short period, but over a longer period of time this may influence the patients' fatigue.

Alternatively, the lack of change seen in gait biomechanics could be due to the relative change in stiffness and energy stored at early stance. When altering the Young's modulus and strut cross-section the relative changes observed at early stance and late stance were similar. Comparatively, the extent of change in rotational stiffness and energy stored when altering the strut alignment were much greater at early stance than late stance, a parameter which, when altered in previous gait studies, indeed resulted in differences in gait biomechanics and muscle response [38]. This could suggest that patients are sensitive to changes in the ratio of rotational stiffness to energy stored when walking. Additional gait studies would need to be conducted to elucidate this further.

As mentioned, when altering the strut alignment, a large increase in energy stored was observed at early stance. This is thought to be due to shank-to-vertical angle at these points in gait, where, at early stance, the angle change in strut alignment was 80% of the shank-to-vertical angle, whereas it was only 20% of the late stance shank-to-vertical angle. A change in shank-to-vertical angle alters the moment about the ankle joint and therefore the rotational stiffness for the same GRFs. The increase in energy stored at early stance in the plantarflexed alignment may suggest that a more plantarflexed alignment allows the PD-AFO to dissipate more power, mimicking plantarflexion during normal gait. Overall, the base geometry and properties had limited influence on the mechanical response of the PD-AFO in terms of energy stored and rotational stiffness and therefore other factors such as durability and comfort should be the focus in its design. Comparatively the alignment and bending

properties of the posterior struts were found to have a large influence on the energy stored and rotational stiffness of the PD-AFO. Therefore special care must be given to the selection of the struts used for each patient, and the alignment of the posterior struts.

7.5.3.1 Limitations

To allow alteration of the posterior struts, the built-in regions of the posterior struts were replaced with rigid bodies. This altered the mechanical response of the PD-AFO, with an increase in rotational stiffness by between 9-13%, and a decrease in strain energy stored within the posterior struts by between 9-11%. A more accurate method may have been to alter the strut geometric properties using a different software and re-mesh them. However, this would have been significantly more time consuming and introduce additional, uncontrolled changes. The strut model was deemed an acceptable compromise, allowing further parameter changes to be analysed, whilst still adjusting for changes made to the model.

The heel-wedge was not analysed as part of the design sensitivity. The study by Ikeda et al. demonstrated that several of the significant changes observed when altering the heel wedge were time based [60]. These would therefore be not possible to see in a static simulation. Additionally, the heel wedge is easy to replace, being low cost and separate from the rest of the PD-AFO. Therefore, it is possible to analyse this experimentally. It could be possible to develop the model to analyse time-based changes, and this could also be used for future work.

The model, whilst designed to mimic the loading during gait, does not include the lower limb. To understand how a design change alters the lower limb loading a combined model would need to be developed, however this requires significantly more computational power and therefore is not as suitable for a sensitivity analysis.

7.6 CONCLUSION

This is the first FE model developed of the PD-AFO with which this thesis is concerned, analysing its mechanical response. The model was calibrated and compared to the experimental behaviour of the PD-AFO. It was then used to examine the influence of design parameters on rotational stiffness, an output metric deemed significant for AFOs in the literature, and energy stored, an important metric for this particular PD-AFO due to its ESAR characteristics as discussed in chapter 6. The posterior struts were the most significant component with regards to energy storage, and their change in material properties or shape had the greatest influence on the mechanical response of the PD-AFO compared to all other design parameters analysed. Additionally, the base strength and shape were found to have limited influence on the mechanical response of the PD-AFO, suggesting that comfort should be a priority when fitting. In the next chapter the development of a lower limb model, which is then used in conjunction with the model of the PD-AFO described here, is presented and discussed.

8 LOWER LIMB FE MODEL

8.1 INTRODUCTION

The gait analysis in chapter 5 demonstrated reduced loading through the limb when wearing the PD-AFO. To further investigate the influence of the PD-AFO on the lower limb, an FE model of the lower limb is developed and combined with the PD-AFO model developed in chapter 7. This chapter describes the development process of the lower limb model along with assumptions and simplifications adopted. The combining of the lower limb and PD-AFO models is described in chapter 9.

Success in use of the PD-AFO is hypothesised to be due to a combination of reduction in loading, limitation of movement and provision of propulsive power. Whilst chapters 5 and 6 demonstrated that the PD-AFO reduces external loading through the limb and the posterior struts provide power absorption and generation throughout the gait cycle, it is not understood how the PD-AFO alters internal loading through the joints. Understanding the changes in joint loading when wearing the PD-AFO may help to predict whether certain regional pathologies would perform well with the PD-AFO. Additionally, previous studies have linked contact stresses above a threshold with the development of PTOA [125-127]. This is a pathology common in patients with traumatic foot and ankle injuries, such as the cohort who use the PD-AFO. The aim of this chapter is to develop an FE model of the lower limb that allows for relative changes in joint loading, specifically the contact stresses, to be quantified when the PD-AFO is, and is not, worn.

8.2 PREVIOUS FE MODELS OF THE LOWER LIMB

Previous FE models of the lower limb were reviewed to evaluate methodologies to develop this model. Whilst reviewing the literature, the focus remained on appropriate development procedures for a subject-specific model based on the geometry of a living subject.

8.2.1 Geometry

To generate the geometry in FE and determine the posture of the lower limb, an understanding of the shape and orientation of the individual components needs to be established. Imaging techniques may be used, such as MRI and CT, to scan the geometry. Although CT scans facilitate the automatic, segmenting process of osseous structures accurately, MRI is used for live subjects due to the high radiation dosage of a CT scan. Therefore, most recent studies basing geometry on live subjects, performed an MRI scan [128-133]. Due to the fact that MRI scans are neither time nor cost effective; it is common for 1 scan to be taken in 1 position. The position scanned may not be correct for all the required simulations. Therefore, it is important to evaluate the position in which the lower limb is scanned to allow adjustment of the lower limb to the desired orientation using computer software if needed. The volunteer participating in a study is typically scanned in a supine position in an MRI scanner. In the literature, when in this position, the lower limb is often described as at a 'neutral' angle and/or 'unloaded' [130, 134-137].

Several authors described the lower limb position as 'neutral' when the tibia was 90° to the plantar surface of the foot [131, 138, 139]. The determination of the tibia angle depends on the measuring equipment and methodology to locate the long axis of the tibia and identify bony landmarks. These studies only considered the 'neutral' angle in the sagittal plane. Although this is the most significant plane of motion in terms of absolute rotation, the 'neutral' angle in the other 2 planes may influence the relative location of the bones that play a part in inversion/eversion, such as the subtalar and talocrural joints.

Wu et al. proposed a standard definition for the ankle joint coordinate system and from this described the neutral angle in all 3 planes and how to determine these angles using surface landmarks [27]. Several models adopted this definition and used a specially designed orthosis to ensure the lower limb was scanned in the neutral kinematic position [140-142]. Although more repeatable, such an orthosis would have to be subject specific due to anatomical variation and is therefore impractical. However, quantification of the deviations from the neutral angle in all 3 planes should be evaluated.

Whilst the lower limb is often said to be scanned 'unloaded' no details in the literature could be found as to how the 'unloaded' configuration was determined (when using MRI scans) [138]. This is an important point for consideration as maintaining a neutral angle by fixing the ankle joint during the MRI scan, may cause loading to the joint. Ideally, a force plate would be installed in the scanner to

quantify the load, albeit this is not feasible in an MRI scanner as metal components cannot be inserted in the scanning area.

Overall, when scanning the limb, the neutral angle in all planes should be considered. This can be achieved using the coordinate system prescribed by Wu et al. [27]. Once scanned, the orientation can be evaluated and if it deviates significantly from neutral, then post-processing of the geometry can account for this [27]. Any restraints or equipment used to maintain the neutral position should apply as little force as possible and should be considered when further developing the FE model.

8.2.2 Tissue components

The term ‘tissues’ encompasses all components of the foot, including osseous tissue (bone), skin, cartilage, ligaments, and muscles. To increase computational efficiency, it is necessary to exclude some tissues from the model, or to simplify the method with which to model them. These decisions should be made considering the application of the model and how the simplification may impact the accuracy of the desired application. In the next section previous FE lower limb models are explored to determine the tissue components that were included and excluded, along with any simplifications made to achieve increased computational efficiency whilst still ensuring meaningful results.

8.2.2.1 Osseous tissues

Bones provide structural stability to the foot, and are the bodies through which load is transferred to the tibia. Most of the load experienced is compressive. The bones can move relative to one another to allow movement of the foot during activity. The bones themselves do not make contact within one another; cartilage is located between them. Due to the importance of the shape of the bones in their function, all previous studies found modelled them as 3D bodies, aiming to represent the realistic geometry. Some studies used meshed (deformable) 3D bodies and others used rigid (not deformable) 3D bodies, depending on the application [143].

When evaluating the contact stresses between the tibia and talus, Anderson et al. modelled the bones as rigid and the cartilage as a deformable body. [144]. It was validated by comparing the contact stresses at the joint to those seen in two cadaveric ankles. The maximum FE contact stress was within 1.5-6.2% of the experimentally recorded values and the mean FE contact stress within 3.2-18.3% [144]. Other studies used deformable bodies to evaluate the stresses within the bones [132, 145]. The simulations were compared against experimental plantar pressures; the FE models exhibited pressures of 64-130% and 5-14% higher than the experimental data respectively [132, 145]. The comparisons to experimental data, both joint contact stresses and plantar pressures, demonstrate that both rigid bodies and meshed bodies can provide good agreement between experimental and simulated outputs.

Chen et al. also used 3D rigid bodies, with tension only shell elements to provide the insertion points for ligaments to evaluate loading of the plantar fascia [146]. The study compared the results from the 3D rigid body model, to a 3D meshed model under static loading. The results of the 3D rigid body

were deemed to result in no significant difference in the plantar fascia tension (though this was not quantified). The final 3D rigid body with shell elements was validated using both plantar fascia tension and GRF recorded in the literature, shown in Figure 8.2.1. The comparison of the meshed model and rigid body model demonstrated that, depending on the application, the increase in efficiency by modelling bones as rigid bodies is an acceptable compromise.

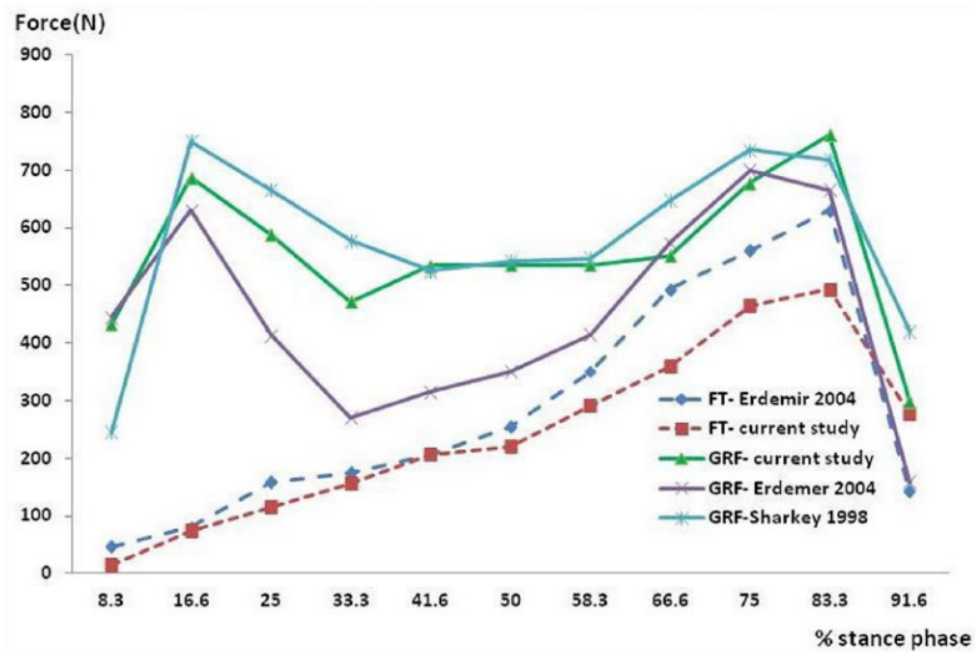


Figure 8.2.1: Validation results reported by Chen et al. (noted as 'current study'), comparing the ground reaction force (GRF) and the plantar-fascia tension (FT) to 2 cadaveric studies (Erdemer 2004 and Sharkey 1998) in literature, throughout different instances of the gait cycle [146]. Image reproduced with permission from Sage Publications, Open Access.

Beaugonin et al. developed 2 dynamic models, 1 using meshed bones and 1 using rigid bones, to analyse impact loading, shown in Figure 8.2.2 [147]. Both models were within the range of experimental values recorded, though the meshed model recorded a slightly increased dorsiflexion making the result closer to the experimental mean [147]. However, the rigid model ran in $1/8$ of the simulation time required to run the meshed body, demonstrating the compromise between accuracy, output and simulation time.

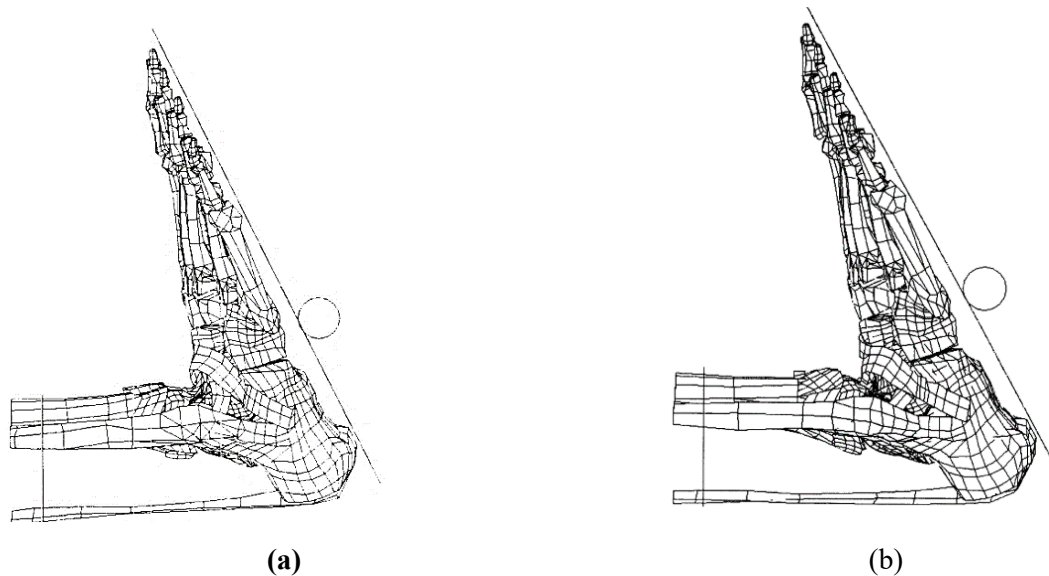


Figure 8.2.2: The maximum dorsiflexion experienced in the (a) rigid model and (b) deformable model [147]. Images reproduced with permission from the rights holder Society of Automotive Engineers.

Previous studies used 3D geometry of the bones to allow the appropriate contact to be modelled between them. Rigid bodies and meshed components have been used, both demonstrating good agreement with experimental results. Whilst 3D meshed components allow thorough investigation of the bone response, with the ability to evaluate stress and strain, they are computationally expensive. If the application of the model does not require extensive analysis on the bones, it is a suitable compromise to model the bones as rigid bodies.

8.2.2.2 Cartilage

Cartilage plays an important role allowing smooth, painless movement of bones, and transmission of load from one bone to the next. Previously, cartilage has been modelled as a meshed 3D body or simplified and modelled as a set of constraints.

Several models developed a single meshed layer of cartilage to represent each contact pair [130, 134, 136, 139, 145, 148]. Generally the mesh was said to be developed between the space in the bones, though a full explanation was often limited [134, 136, 148]. Both Li et al. and Guiotto et al. developed the mesh by segmenting the scans [130, 139]. Meshing 1 layer of cartilage per contact pair (i.e., adding cartilage to one bone only, resulting in a cartilage-bone contact) allows a larger element size (and therefore fewer elements) to be used compared to meshing two regions. Having fewer elements helps to improve the run time of a model. However, due to the irregular shapes, particularly of the tarsals, bones that play a major part in the foot's largest rotations, using a single meshed layer would result in cartilage moving over bone during rotation, potentially resulting in unrealistic movements. Contrastingly Anderson et al. and Akrami et al. developed two meshed layers of cartilage for each contact pair modelled [131, 144]. Developing an accurate 3D mesh of 2, thin layers of cartilage that

are in contact, via segmentation, would require a powerful, expensive MRI scanner with adequate resolution to be able to differentiate between the 2 geometries. Instead Anderson et al. developed the mesh by extruding a surface up to 1.7 mm distance normal to the bone surface (based on values from literature due to the inability to see in the scans) [144]. The study had good agreement in values for contact stresses - within 1-15% - between simulation and those measured experimentally, though the study only focussed on the talocrural joint [144]. Modelling 2 layers of cartilage requires a large number of elements and therefore is more computationally inefficient than using 1 layer. However, using 2 layers of cartilage allowed the contact stresses to be visualised. Depending on the model application this may be important. In particular if there is large rotation expected within the simulation it may be suitable to compromise on computational efficiency and model 2 layers to improve the accuracy of this aspect of the model.

Other methods have included modelling the cartilage as a set of constraints between each contact pair [142]. However, determining the set of constraints is challenging, and it was not clear how the properties were determined. Also, using a set of constraints to represent the cartilage does not allow the contact stresses between the cartilage pairs to be quantified.

Overall, if larger rotations are expected, or contact stresses are the primary output of the model, it may be beneficial to model the cartilage as 2 layers to improve the accuracy of the geometry. Otherwise it would be suitable to model the cartilage pairs as one, single meshed layer.

8.2.2.3 *Soft Tissue*

Soft tissue is a term used here for all other components within the lower limb, including skin, muscles, fat and ligaments. The skin encompasses the bones, cartilage muscle and ligaments. It is the aspect of the lower limb that contacts exterior surfaces. Skin consists of different layers, including the epidermis, dermis, and subcutaneous layers. The skin layer that forms the fat pad, on the plantar aspect of the foot, is different to that which encompasses the rest of the lower limb. This fat pad region makes contact with the floor during gait and is critical in distributing and transferring the load protecting the lower limb for high stresses [149]. The exterior geometry is visible on MRI scans, and can be computed automatically using threshold values. The interface between the skin and bones, whilst visible, requires manual processing.

Due to its volume, modelling the skin as a 3D meshed body can be computationally expensive. Akrami et al. modelled skin with 3D elements around all bones, as shown in Figure 8.2.3. The proximal surface of the soft tissue was fixed representing all tissue proximal of the foot, along with the tibia and fibula to constrain the model [131]. The contact between the bones and the tissue was not clearly described, nor was how the skin tissue geometry was determined. The model by Akrami et al. was validated using plantar pressure and therefore the contact between the skin tissues and floor was important, and deemed a necessary compromise in simulation time [131]. However, whilst modelling skin tissues on the dorsal surface may provide resistance to movement between bones, this may be

adequately represented by the inclusion of ligaments and therefore may not need to be modelled. Gefen et al. took this approach and only modelled skin tissue on the plantar aspect of the foot, though the description of the development of its geometry is limited [145].

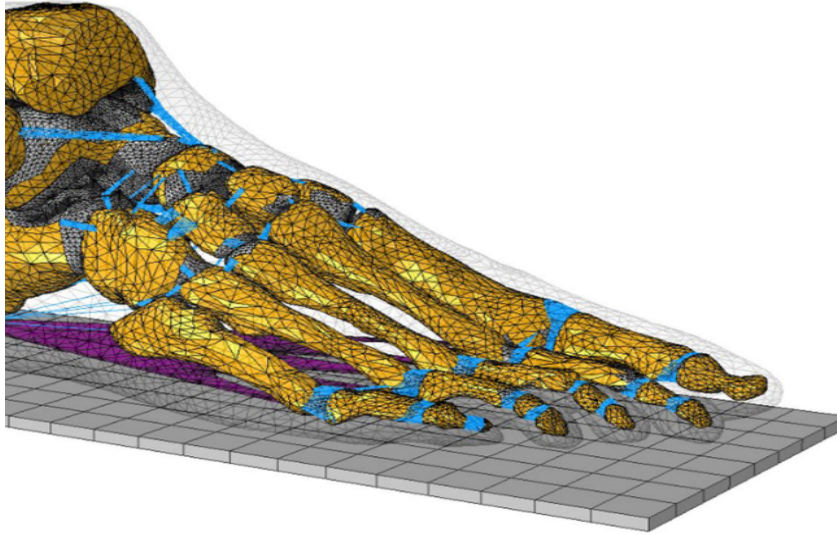


Figure 8.2.3: FE model developed by Akrami et al. showing the soft tissue (transparent), along with a meshed plantar fascia, 30 bones, 1814 line elements representing 85 ligaments and 74 cartilage layers [131]. Image reproduced with Open-Access.

Other methods to avoid including a 3D representation of skin have been attempted, such as modelling the plantar skin tissues as a series of contact springs [147] or using shell elements [140]. However, these simplifications require thorough investigation prior to being implemented and extensive sensitivity analyses as the accurate representation of a complex 3D behaviour with a 1D or 2D structure is not a trivial process. Since this thorough process was not presented in the studies above, it is impossible to determine whether these simplifications are acceptable.

Finally, there is the option not to model any skin tissue, as seen in a study by Chen et al. [146]. Within this study the calcaneus made direct contact with floor. The validation methods used focussed on plantar fascia tension, particularly relevant for the study, and GRF. If the output of interest is irrelevant to the contact characteristics of the foot and the external boundary, removing the skin tissue could be considered as an acceptable compromise. However, given the crucial role of the fat pad to distribute loads on the calcaneus, incorporating its behaviour into the model is likely necessary for most applications.

The skin tissue forms an important role in providing contact with exterior surfaces, with the fat pad distributing the loads through the limb. As such, inclusion of this component within the model is important for most applications. Modelling of the skin can increase simulation time due to the large volume that is meshed, therefore only regions required for the application should be included.

8.2.2.4 Ligaments and Plantar Fascia

Ligaments are passive stabilisers that control the ROM of the joints within the lower limb. Therefore, they are important elements to allow lower limb joint motion to be modelled accurately. A review by Behforootan et al. demonstrated this importance with an overwhelming majority of studies incorporating them within their FE models [143].

Tension only elements, commonly truss elements or springs, were used to model the ligaments in most studies [129-132, 136, 137, 140-142, 146, 148, 150]. Chen et al. and Akrami et al. developed a 3D mesh to model the plantar fascia [131, 146]. This is a particularly significant component and has been linked to common pathologies [151]. Chen et al. directly examined the stresses within the plantar fascia, and therefore a 3D mesh was required [146]. The remainder of the FE models reviewed used tension only elements to model the ligaments [129, 130, 132, 135, 137, 140-142, 148, 150].

Commonly, 5 connectors were used to represent the plantar fascia, connecting the calcaneus to the distal heads of the phalanges [129, 132, 141, 142, 145, 150]. When the application of the model does not require detailed stress analysis of the ligaments themselves, then tension-only elements are an acceptable representation.

Models featured a varying number of ligaments: from 38 [145] to 85 [131]. The number used was dependent on the rigour of the model produced, along with simplifications of relative bone movements, for example fusing of bones, which may negate the need for the ligaments. More ligaments are required with increased expected rotations; they are needed to maintain stability, as is the case in real life.

Determining the insertion point of both the ligaments and plantar fascia is challenging from MRI scans and therefore previous studies relied on anatomical landmarks and used anatomy books [146, 150] and other literature to locate them [143].

8.2.2.5 Muscle Forces and the Achilles Tendon

Within the foot and ankle, the intrinsic muscle forces are small comparative to the extrinsic muscle forces, and mainly provide stability to the foot [152]. The larger, extrinsic muscle forces, originating in the calf of the lower limb, are responsible for the rotations of the foot. They are predominantly applied to the foot through the Achilles tendon [153].

Whilst several models found in literature make no mention of the muscle forces in their methodology [87, 134, 139, 144, 154], the majority did [129, 130, 132, 135, 136, 141, 142, 146, 148, 150, 155]. Of these studies, none modelled the intrinsic muscle forces. This was suggested to be due to the fact that if enough ligaments were modelled this would stabilise the foot adequately and therefore the intrinsic muscle forces would have limited effect [155]. Assuming the influence of the intrinsic muscle forces as negligible is a reasonable assumption due to their relatively small influence on bone movement. Additionally, quantification of these intrinsic forces is challenging [156].

The majority of FE studies reviewed used a methodology proposed by Simkin [157] and applied the extrinsic muscle forces through the Achilles tendon [129, 130, 132, 135, 136, 141, 142, 146, 148, 150]. The method proposed uses 5 or 6 force vectors attached to the posterior surface of the calcaneus. No additional mesh is created ensuring computational efficiency. The loading applied through the force vectors was 50% of the GRF applied during balanced standing (25% of total BW) [129, 130, 132, 135, 136, 141, 142, 146, 148, 150]. Cheung et al. performed a sensitivity on the Achilles tendon, finding 75% of the GRF of a balanced foot (37.5% of BW) resulted in the correct CoP according to the experimental plantar pressure distribution [142]. Comparatively Spyrou et al. meshed the Achilles tendon, to develop a 3D body [137]; however, the study focussed on stress and strain within the Achilles tendon and therefore it was necessary to mesh the component.

Gefen et al. focused heavily on extrinsic muscles; connecting the triceps surae through the Achilles tendon, applying a different force depending on the chosen phase in gait [145]. The study varied the Achilles force as follows from 0N during the early stance phases, increasing to 100% of BW during the latter stance phases. It highlights how the forces through the Achilles tendon change depending on the phase of gait. This is an important consideration when developing the lower limb model and how the choice should be based on the point of gait modelled.

Whilst intrinsic muscles are small and have limited effect on bone movements, extrinsic muscles influence the movement of the lower limb throughout gait [158]. It is therefore important to include them within the model and choose forces that are relevant to the time point modelled. Previous studies have modelled the Achilles tendon as a point force at the insertion point, and as a 3D meshed body. The former allows extrinsic muscle forces to be applied within the model, whilst maintaining computational efficiency with no increase in contact parameters. Comparatively, a meshed body is computationally expensive, but allows analysis of the Achilles tendon, including stresses and strains. If the focus of the study is examining the response of the Achilles tendon, a meshed body should be used, otherwise application using point loads is acceptable.

8.2.3 Material Properties

For those components that are not assumed to be rigid, material properties must be determined. It may be suitable to approximate the material behaviour of the components, in order to improve computational efficiency. Behforootan et al. summarise well previous material properties used within FE models [143].

8.2.3.1 Bone

Bone consists of different types of osseous tissue; in a healthy adult, this is cortical bone tissue and trabecular bone tissue. The tissue types have different material properties. Most FE lower limb models using a homogenous material model based on the ratio of cortical to trabecular bone, producing a weighted average value for the Young's modulus accordingly [130, 132, 135-137, 139, 145, 154].

Florio et al. performed a sensitivity analysing on the Young’s modulus of cortical bone (between 8-14GPa) and found the results to be within 3.2%, suggesting it likely has limited influence on the model accuracy, and therefore it is acceptable to simplify the material behaviour of bone.

Table 8.2.1 summaries some of the material properties for bone, when not modelled as rigid bodies, used in previous studies found in the literature. All studies reviewed use isotropic linearly elastic properties.

Table 8.2.1: Material Properties for Osseous Tissue used in the literature of lower limb FE models

Study	Trabecular and Cortical	Young’s modulus (MPa)	Poisson’s ratio (-)	Ref.
Beaugonin et al. 1997	Discrete	Calcaneus, talus, navicular, cuboid: 15000 Cortical fibular: 18900 Cortical tibia: 18400 Trabecular: 531	Calcaneus, talus, navicular, cuboid: 0.29 Cortical fibula: 0.29 Cortical tibia: 0.29 Trabecular: 0.3	[147]
Antunes et al. 2008; Spyrou et al. 2012; Guiotto et al. 2014; Gefen et al. 2000; Li et al. 2017; Cheung et al. 2005; Qiu et al. 2011	Homogenous	7300	0.3	[130, 132, 135-137, 139, 145]
Florio et al. 2011	Discrete	Cortical: 16350 Trabecular: 8000- 14000	Cortical: 0.34 Trabecular: 0.3	[159]
Taha et al. 2016	Homogenous	10000	0.34	[154]

8.2.3.2 Cartilage

A list of the material properties of cartilage used in previous lower limb FE models, including the coefficient of friction for cartilage-on-cartilage contact, were examined and are shown in Table 8.2.2. All studies listed below modelled cartilage as an isotropic, linearly elastic material. Whilst the material properties used varied throughout models, Anderson et al. specifically achieved similar contact stresses at the talocrural joint when compared to experimental data, using the properties described [144].

Table 8.2.2: Material properties of cartilage that have been used in previous lower limb FE models.

*indicates that the information was not provided in the study

Study	Isotropic Linearly Elastic	Young's modulus (MPa)	Poisson's ratio (-)	Cartilage-on- Cartilage Friction Coefficient (-)	Ref.
Akrami et al. 2014; Brilakis et al. 2012; Cheung et al. 2005; Qiu et al. 2011	Yes	1	0.4	Frictionless	[131, 132, 136, 148]
Anderson et al. 2007	Yes	12	0.42	*	[144]
Beaugonin et al. 1997	*	*	*	0.01	[147]
Antunes et al. 2008	Yes	10	0.4	*	[135]
Gefen et al. 2000	Yes	1	0.1	*	[145]
Wang et al. 2014	Yes	0.98	0.4	*	[141]
Chen et al. 2014	Yes	50	0.1	Frictionless	[146]

8.2.3.3 Fat pad

Material properties for the heel fat pad vary greatly across FE studies. Behforootan et al. recorded that 65% modelled the skin, fat and muscle as one homogenous geometry [143]. Several studies found the fat pad can influence, unsurprisingly, the simulated plantar pressure [131, 160, 161]. Akrami et al. recorded a lower peak plantar pressure when the Young's modulus was reduced [131]. Behforootan et al. surmised that, should the model application focus on soft tissue, a non-linear material model would be most suitable, though a linear material model may suffice should the study focus on other aspects such as ligament tension [143].

Non-linear properties will provide a more accurate representation of strains and stresses within the fat pad. Non-linear properties will increase the simulation time marginally, though if the fat pad contains a large number of elements this could be significant. As such, it is important to consider the accuracy of the fat pad's deformation required.

Table 8.2.3: Fat pad material properties as found in the literature. α and μ are constants used to describe the Ogden material model.

Study	Linear/ Non-Linear	Young's modulus / Material Model	Poisson's ratio	Ref.
Tao et al. 2009	Linear	0.45±0.3 MPa	0.45	[160]
Akrami et al. 2017	Linear	1.15 MPa	0.49	[131]
Erdemir et al. 2006	Ogden 1st order	$\alpha = 6.82$, $\mu = 16.45\text{kPa}$		[161]
Chokhandre et al. 2012	Ogden 1st order	$\alpha = 9.78$, $\mu = 1.084\text{k Pa}$		[162]
Isvilanonda et al. 2016	Ogden 1st order and 2nd order	1st: $\alpha = 12.01$, $\mu = 0.0235\text{kPa}$ 2nd: $\alpha_1 = 16.829$, $\mu_1 = -4.629 \times 10^{-6}$ kPa, $\alpha_2 = -1.043$, $\mu_2 = -1.613$ kPa		[163]

8.2.3.4 Ligaments and Plantar Fascia

Some of the major ligaments (most commonly those more proximal) have been analysed experimentally within the literature to determine the material behaviour. Table 8.2.4 details the experimentally determined material behaviour found in the literature for various foot and ankle ligaments.

Table 8.2.4: Ligament material behaviour as found in the literature

Study	Assumptions	Linear Stiffness (N/mm)	Ligaments measured	Ref.
Hofstede et al. 1999	Linear	61-127	11 x Dorsal ligaments proximal first tarsometatarsal ligament and distal of the anterior tibiofibular ligament	[164]
Funk et al. 1999	Non-linear	-	8 x medial and lateral ligaments connecting the tarsals, the tibia and fibula	[165]
Kitaoka et al. 1994	Non-linear		Plantar Fascia	[166]
Corazza et al. 2003			8 x medial and lateral ligaments connecting the tarsals, the tibia and fibula	[167]

The majority of lower limb FE studies assumed the ligaments to be linearly elastic [129-132, 134, 136, 137, 139-141, 143, 146, 148, 150]. Grigoriadis and Shin et al. described some ligaments using non-linear properties [168, 169]. Grigoriadis' model was designed for high loading rates, and therefore also included failure loads for the ligaments; this is not needed at the low rates applied in this model [168]. The use of non-linear properties for ligaments, where available, increases the accuracy of the model without any penalty on computational time.

Shin et al. described a scaling technique, based on the cross sectional area of the ligaments, to predict their stiffness when there is no direct material behaviour data [169]. Here, for ligaments with unknown stiffness, their cross-sectional area was established and compared to the area of the anterior tibiofibular ligament to give a ratio of areas between the 2. The stiffness of the ligament was then defined by the same ratio, relative to the known stiffness of the anterior tibiofibular ligament.

8.2.4 Comparison to Experimental Data

For this study, the model is based on a living subject and therefore any experimental methodology must not harm the subject. The most common method to evaluate the results of FE lower limb models of live subjects is to compare the pressure interface between the plantar aspect of the foot and simulated floor to experimental data. This has been performed in several studies, comparing peak values of plantar pressure [131, 132, 136, 154, 160] and mean values of plantar pressure [131] to both literature and their own experimental data. Plantar pressures were often reported on a regional basis, split into a forefoot, midfoot and hindfoot region. This allows for a more granular comparison between the FE model and experimental data. Depth of analysis between the experimental data and FE results varies wildly between studies. Differences between simulation results and experimental data are to be expected, and quantification of these differences is vital to understand the limitations of the model.

Several of the studies evaluated the difference between the lower limb model and experimental data during balanced standing [132, 136, 154, 160]. It has been demonstrated that the difference between experimental and FE results using the same geometry and material properties can vary throughout gait [130]. In some cases, where additional validation measures were used, such as the use of radiographs by Tao et al. to measure plantar displacement [160], balanced standing was required in order to perform the experiment. However, as plantar pressure can be measured during gait, it would be better to compare the model to experimental values at the chosen point in gait (if gait is to be modelled) rather than balanced standing, on the condition that the boundary conditions, for example the GRF, can be recorded accurately.

Similarities of FE models with experimental data was varied, with some studies achieving a discrepancy of <15% [131] and others of >60% [132]. Cheung et al. argued that the resolution of the

FE pressures was higher than that of the plantar pressure sensor and therefore the FE output was lower due to localised regions of higher pressure being recorded [132].

When using plantar pressure as a validation tool the material properties assigned to the fat pad may influence the model results significantly. In the review of FE models by Behforootan et al. it was reported that peak plantar pressures changed by up to 7% when using average material properties compared to subject specific material properties [143]. Akrami et al. demonstrated that the peak plantar pressures change by up to 41% when altering the fat pad Young's modulus by $\pm 20\%$, whilst the average pressures changed up to 29% when altering the fat pad Young's modulus by $\pm 20\%$ [131]. Defining the material characteristics of the fat pad is not trivial and should be considered if using plantar pressure as a validation method.

Depending on the output of the model, inaccuracies in the deformation of the fat pad may not be relevant to the desired application. However, these inaccuracies still prevent plantar pressure from being a useful metric to evaluate the model. Beaugonin et al. took a different approach and analysed the peak dorsiflexion angle after impact loading, with FE results lying within an experimental corridor [147]. Analysing the joint angles is only possible in the sagittal plane as these are the angles measured during gait. However, this is the major plane of motion. This method relies on improved accuracy of geometry rather than accuracy of material properties, and therefore may be a suitable method if assumptions are made regarding the material properties.

Gefen et al. used CT to examine the *in vivo* response of the cartilage during gait; this was then used to estimate loads [145]. A similar method could be used to examine the deformation of the plantar soft tissue during gait. However, the resolution of segmentation of such medical images means the deformation of the tissue being examined must be great enough in order to be observed; this is unlikely in the case of cartilage during normal gait. For the plantar soft tissue of live subjects, it would be preferable to use external plantar pressure mapping instead of high radiation imaging such as CT. Overall, a validation method should capture the important motions or features used in the application of the model. It should avoid focussing on regions of the model that are of less interest where possible, as these inaccuracies may be an acceptable compromise in the overall use of the model, though it is understood that comparing to a live subject has limited options. Finally, the model should be compared to the phase of gait it is simulating, if the protocol allows.

8.2.5 Summary

Within this section previous methodologies used to develop FE models of lower limbs have been reviewed. The literature highlighted a few key points that should be factored in when developing a model. Firstly, the scanned orientation should be quantified to understand whether post processing is required to alter the geometry location. Secondly, depending on model application, simplification of the tissue components is acceptable, and indeed necessary; these include modelling ligaments using

truss only elements, representing muscles as a force acting through the Achilles tendon (represented by point forces), and modelling only regions of skin that are considered important. Finally, the comparison to experimental data should be evaluated to understand where discrepancies occur.

8.3 METHODOLOGY

This section describes the development of the lower limb FE model based on the lower limb geometry of the subject for whom the custom PD-AFO was produced as explained in chapter 5. To ensure computational efficiency, assumptions and simplifications are made when developing a complex model, such as that of the lower limb. These decisions were made by taking into consideration the application of the lower limb model, and the desired output. The following criteria were established to guide the development of the model, and were evaluated within the results:

1. Contact stresses between bones (cartilage surfaces) can be quantified
2. Lower limb movement and loading simulating that of the selected point in gait
3. Lower limb is able to fit within the PD-AFO model developed in chapter 7
4. Ability to compare the FE model outputs to experimental data acquired through a non-invasive protocol described in chapter 5.

8.3.1 Geometry generation

The subject was scanned in a non-weight bearing, supine position, with a foot plate fixing the plantar aspect of the foot at $\sim 90^\circ$ to the bed of the scanner as seen in Figure 8.3.1, to keep the ankle joint complex neutral. The rotations in the coronal and frontal planes were kept small visually. The extent of loading through the lower limb was not controlled, however it was deemed to be significantly less than BW and therefore a small fraction of the load to be applied within the simulation. The scan posture was evaluated and compared to the neutral position described by Wu et al. after surface generation of the bones was completed, to ascertain whether any manipulation was required [27].

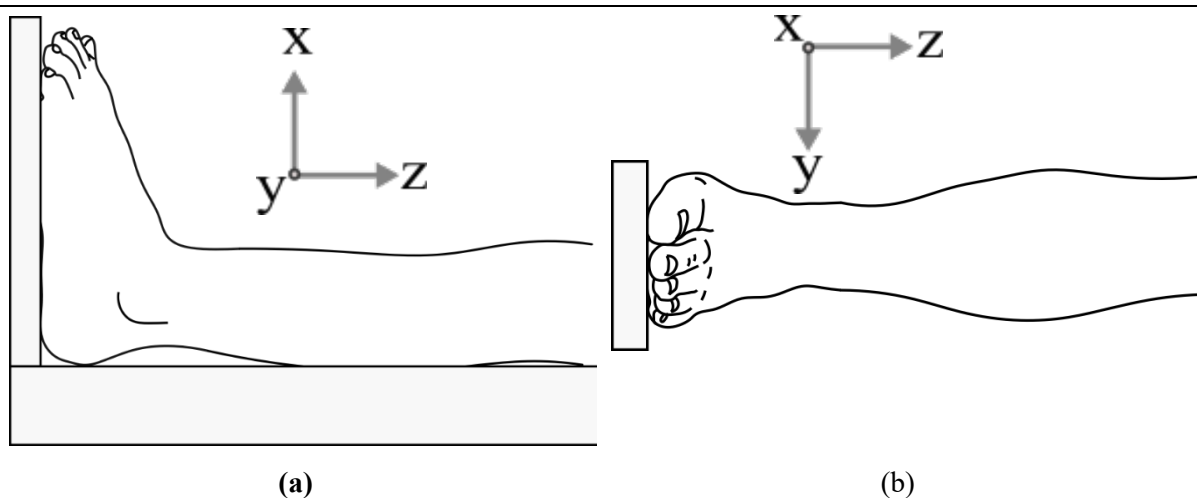


Figure 8.3.1: Schematic showing foot as scanned using MRI

The scans were acquired in two sets on a long-bore 1.5T MRI (Siemens) using a T1 weighted, 1.5 mm thickness, 3D echo Dixon sequence at St Thomas' Hospital (London, UK). The first scan consisted of the foot and ankle to a location approximately 200 mm proximal of the most distal point of the tibia. The second scan continued proximal from this location encompassing the rest of the tibia and distal end of the femur.

8.3.1.1 Surface generation

Segmentation of the osseous tissues and skin was performed in Mimics (v20.0, Materialise, Leuven, Belgium) as seen in Figure 8.3.2. Trabecular and cortical regions of the bone were segmented as one body. Segmentation was performed using automatic threshold values along with manual processing. In total 28 surface geometries of the bones, including the tibia and fibula, were produced. The skin was segmented as 1 component.

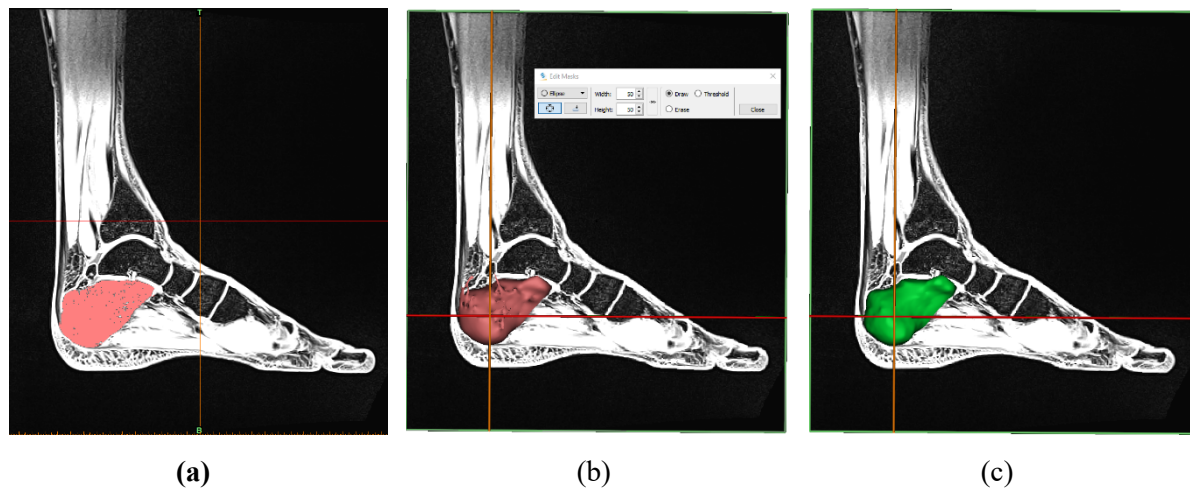


Figure 8.3.2: Segmentation process of the MRI scans for the calcaneus with (a) 2D slice (b) Region Growing tool to create 3D geometry (c) final smoothed 3D volume

Two distinct layers of cartilage between the bones were not clearly visible on the MRI scans. Therefore, the cartilage was produced by creating a 3D surface between the two bones, automatically generated by the Mimics software as an average of the respective external areas of the contacting bones. This surface was located at the mid-point between the 2 exterior surfaces of the bones of interest, demonstrated in 2D in Figure 8.3.3. This surface became the contact interface between the two layers of cartilage. The 3D cartilage surface was created by extruding from the bone surface up to this interface. The thickness of cartilage was not uniform. This methodology was used to produce all contact pairs of cartilage except for those between the metatarsals.

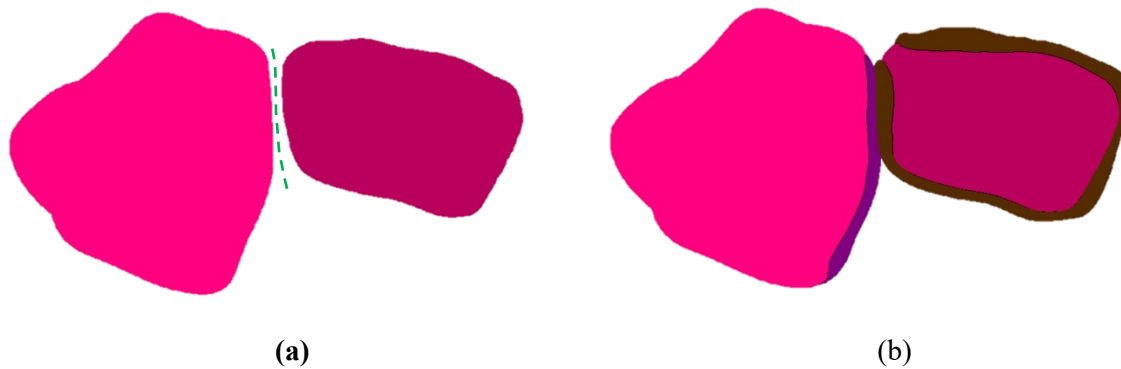


Figure 8.3.3: The methodology to create cartilage surfaces. First a surface was created at the midpoint between the 2 exterior surfaces of the bones, demonstrated by the green dashed line in 2D in (a). The cartilage was then extended to this surface from both bones to form two layers of cartilage. This is shown in 2D in (b).

Between the metatarsals the cartilage geometry was produced by segmenting the region between the bones creating a single body. This was due to the small thickness of the cartilage in this region, which would result in a very fine mesh size if meshed as 2 separate bodies, along with the more standard ball-and-joint geometry observed here.

In total 25 individual cartilage geometries were produced, for the hind foot and mid foot region, including the tibia and fibula. 5 geometries were created for the metatarsals. The thickness of the talocrural cartilage was compared to values in literature at randomised points, to confirm appropriate values.

8.3.1.2 Solid geometry generation

3D surfaces of the cartilage, osseous tissues and skin were imported into Geomagic (v2013, Geomagic Inc., Morrisville, NC, USA). The cartilage was smoothed to ensure a good mesh. Cartilage layers that were associated with the same bone were combined, using a Boolean operation, to generate one cartilage layer for each bone. 3D splines were fitted to the cartilage and bone geometries and solids were generated. The bone geometry was subtracted from the respective cartilage geometry, using a Boolean operation, to create the final cartilage layer. Cartilage layers in contact with each other were also subtracted from one another to ensure good contact, accounting for geometry discrepancies when generating the solids.

The skin geometry was cut using 3D splines to leave only the fat pad region. The fat pad region was minimally enhanced, to produce a rounder ball and heel removing the small flattening that had occurred during the MRI scan due to the contact of the plantar foot to the MRI scanner. 3D splines were fitted to the surface geometry, and solids were generated. Gaps and penetration regions between contacting bodies were eliminated using Boolean operations.

8.3.1.3 Scanned Position

The 3D solid geometries were imported into Autodesk Inventor (v2018, Autodesk Inc., San Rafael, CA, USA). The tibia-fibula coordinate system was determined using anatomical landmarks according to the ISB recommendations [27]; the respective anatomical landmarks were selected and confirmed by a lower limb orthopaedic surgeon.

Figure 8.3.4 shows the orientation of the lower limb as scanned, compared to the defined neutral orientation in each of the 3 planes. The lower limb was scanned in 0.2° of external rotation, 1.8° of inversion and 3.3° of dorsiflexion. The deviations from the neutral axis that were measured post geometry generation, in the frontal and sagittal planes, were 5% and 5% of the total ROM of the foot, respectively [30, 170]. Therefore, it was acceptable to assume that the small difference between the scanned position and neutral position would have a negligible effect on bone loading and contact stresses; the position scanned was assumed to be approximately neutral and so no preliminary computational adjustments were performed.

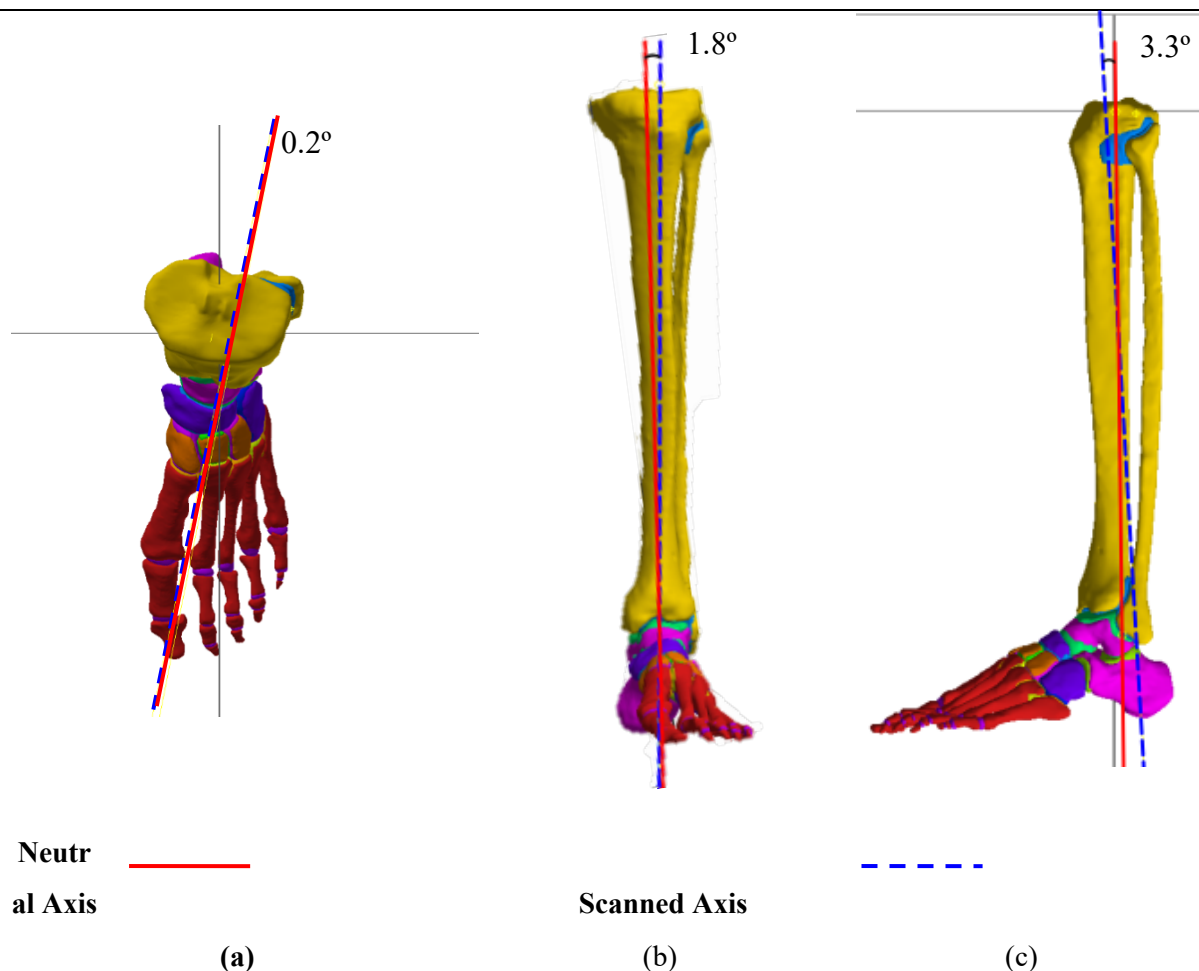


Figure 8.3.4 The orientation of the lower limb as scanned compared to the neutral orientation as defined by Wu et al. [27] in the (a) transverse, (b) frontal and (c) sagittal planes

8.3.1.4 Modelling of Tissue Components

Hypermesh (v13.0.110, Troy, MI, USA) was used to mesh the cartilage and bone geometries, providing a matching surface mesh between each bone and its respective cartilage. The same methodology as described in chapter 7 was adopted. Cartilage was meshed to an element size of 0.5mm. The cartilage and bone geometries were imported into MSC.Mentat (v2020.0.0, MSC.Software, Santa Ana, CA, USA). In MSC.Mentat the bone geometries were converted to rigid bodies, consisting of rigid surface elements. The rigid surfaces were assigned a ‘control node’ at their centre of mass, a point about which they were set to rotate. The tibia and fibula were assigned a control node at the origin of the tibia-fibular coordinate system determined using the recommendations by Wu et al. [27].

Insertion points for ligaments were modelled as 2D shell elements to allow attachment of spring elements (described below) on to the rigid bones. The shell elements were glued to the rigid bone surfaces. A thickness of 0.1 mm was assigned. The location of the insertion points was determined from a combination of anatomy websites and text books [24, 171].

The surface geometry of the fat pad was imported into MSC.Marc and meshed. The posterior rim of the proximal surface of the fat pad, was glued to a thin, rigid surface that prevented relative movement between these regions, indicated in Figure 8.3.5. This represented the effect of the soft tissues proximal to the fat pad.

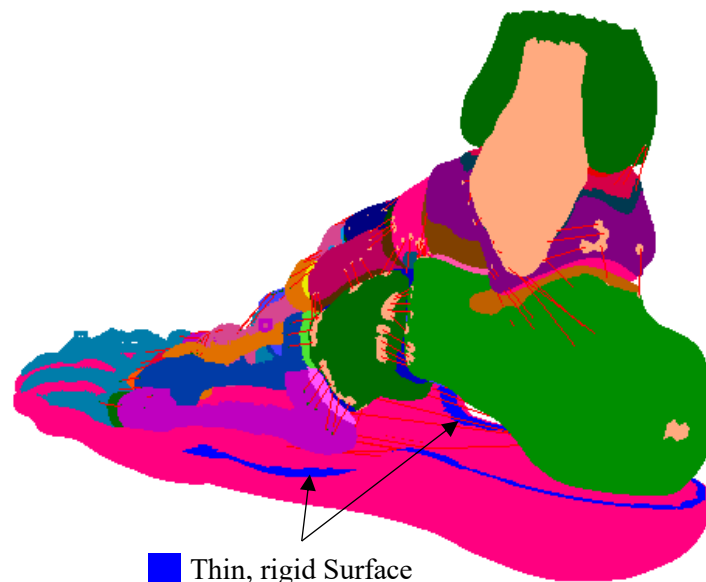
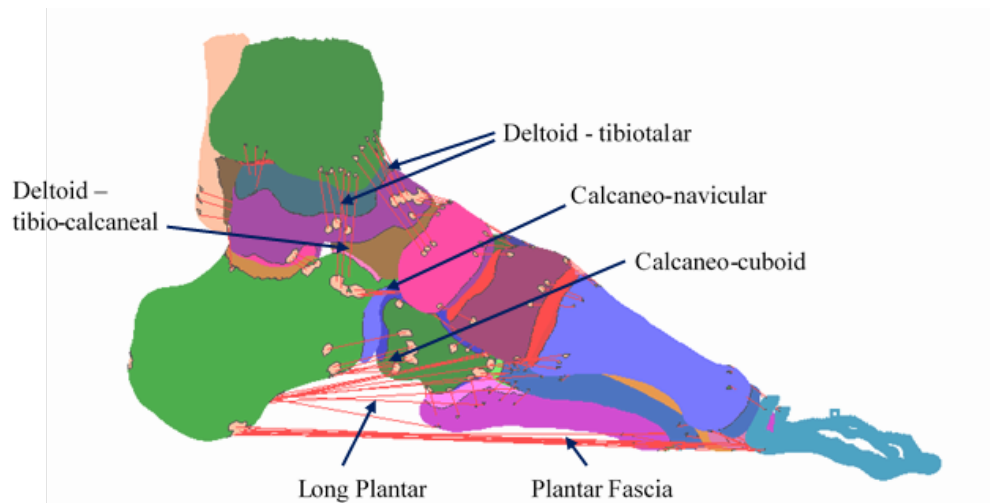


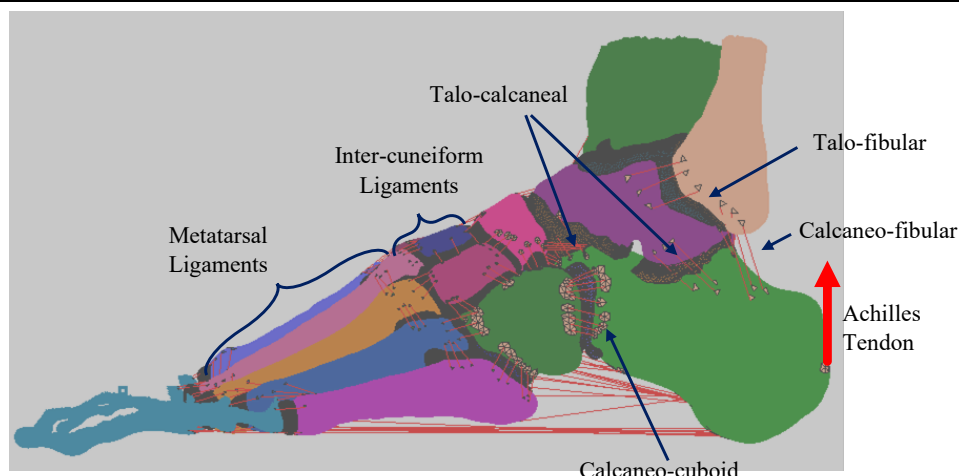
Figure 8.3.5: The blue region, as indicated, is the location of a thin, rigid surface to represent the constraining effect of the skin tissue proximal the fat pad. All points in contact with the surface were fixed relative to one another but otherwise free to translate and rotate.

Some simplifications were made regarding the geometry and relative movement between the geometries. The tibia and fibula were assumed fixed relative to one another, with the distal ends modelled by a rigid surface. The 3 cuneiforms were assigned one control node, and fixed relative to one another, as were 3 of the metatarsals (III-V). The distal phalanges were also assigned one control node. All remaining bodies were able to move freely.

Ligaments, including the plantar fascia, were represented by tension only spring elements. The ligaments included were determined from anatomy websites and text books [24, 171]. For each ligament, between 3-5 spring elements were used to represent it. Figure 8.3.6 shows some of the major ligaments and their insertion points within the FE model. In total 78 ligaments were included in the model represented using 235 tension only, spring elements; the full list can be found in Appendix 12.5.1.



(a)



(b)

Figure 8.3.6: Ligaments modelled as springs (shown by red lines) within the FE model and their insertion points viewed from the (a) medial side and (b) the lateral side. The lateral side, (b), also shows the point at which the Achilles Tendon was considered to act.

All significant, extrinsic muscles were considered to act through the Achilles tendon. The Achilles tendon was not meshed as a geometry and was instead applied as a boundary condition described below. The intrinsic muscles, and the forces they generated, were assumed negligible.

The final model had ~962,250 meshed elements and ~280,000 rigid surfaces. The summation of the meshed elements within the model are shown in Table 8.3.1. The element types were chosen due to their efficiency and ability to perform well in compression.

Table 8.3.1: Elements used for each tissue type in the FE model

Tissue	Element Type	Number of Elements
Osseous – ligament insertion points	Thin shell	~1850
Cartilage	Tetrahedral	~720,400
Fat Pad	Tetrahedral - strain smoothing	~240,000

8.3.2 Material Behaviour

Following the generation of the tissue geometry, material properties were assigned. Material properties for the osseous tissue, skin tissue and cartilage, along with the material behaviour of ligaments, were established where needed. Within this section the final values used within the model are described.

8.3.2.1 Osseous tissues

As mentioned previously, this study modelled the majority of osseous tissue as rigid bodies [144, 146]. This geometry type assumes infinite stiffness and therefore does not require assignment of material properties. The material properties of the ligament insertion points are negligible due to their attachment to a rigid body

8.3.2.2 Cartilage

The material properties chosen for the cartilage were those used by Anderson et al. [144]. These values were selected due to the detailed contact stresses at the talocrural joint that were validated within the study; modelling contact stresses was one of the applications of this model. The contact between 2 cartilage surfaces was assumed frictionless.

8.3.2.3 Plantar foot

The plantar foot comprises ~17% of the total elements within the model. The whole of the plantar foot was assumed to have the same material properties as the fat pad region, located beneath the calcaneus. Previous models have used both linearly and non-linearly elastic material properties to model the fat pad. Non-linear elasticity may produce a more realistic output but is more computationally expensive. As the focus of the model is contact stresses in joints it was deemed acceptable to compromise and so

linearly elastic properties were assigned, with a Young's modulus of 1.15 MPa and a Poisson's ratio of 0.49 [131]. A small region beneath the metatarsals was defined to have a Poisson's ratio of 0.4 to prevent excessive deformation at this contact point.

8.3.2.4 Ligaments

The mechanical behaviour of the ligaments was defined by their stiffness. Experimentally determined material properties were found for some ligaments, though studies normally focussed on ligaments located proximal to the metatarsals. Ligament properties were taken from literature where available, with both linear and non-linear stiffness. For those for which no structural properties were found in the literature, the method to estimate the stiffness, described by Shin et al. [169] was used, with cross-section area data from several studies [169, 172-174]. Ligaments with no literature data about their stiffness or cross-section area were assumed to be similar to nearby ligaments.

8.3.3 Contact

The contact between bone and cartilage was defined as glued, which constrains movement relative to one another. Between cartilage pairs, the contact was set to touching and frictionless. For the bones in contact with the fat pad at the start of the simulation, the calcaneus, and the distal phalanges the contact was set as glued. The contact between the metatarsals and the fat pad was set as touching, should the foot deform to result in contact between the bodies. Finally, the contact between the fat pad and the floor was defined as glued.

8.3.4 Initial Position and Boundary Conditions

The point in gait chosen to model was 10% of the gait cycle, between loading response and midstance. This point in gait experienced relatively high offloading (compared to the rest of the gait cycle); as calculated in chapter 5. The initial position of the lower limb and the boundary conditions applied to mimic the selected point in gait are described in this section and shown in Figure 8.3.7. The lower limb was imported into Mentat in the assumed neutral position. To mimic the selected point in gait, the whole model was rotated to result in the correct shank-to-vertical angle, taken as that between the long axis of the tibia and the sagittal plane, estimated from literature to be $\sim 5^\circ$ of reclination [123]. This rotation gave the initial position of the model shown in Figure 8.3.7.

No other changes in relative bone position were made, and instead it was assumed that the model would find its own equilibrium upon application of an appropriate force using a similar methodology to that presented by Chen et al. and Cheung et al. allowing relative movement between bones. This ensured that stresses in the bones and tensions within the ligaments were not ignored, as they would be if the model was moved pre-simulation [132, 150].

Once rotated to be in the initial position, boundary conditions were applied at the floor, whilst fixing the tibia and fibula section of the FE model. The GRF, recorded in chapter 5, was applied to the floor.

The mediolateral force was not modelled as it was small relative to the vertical GRF, with values <6%, and was expected not to influence the contact joint stresses.

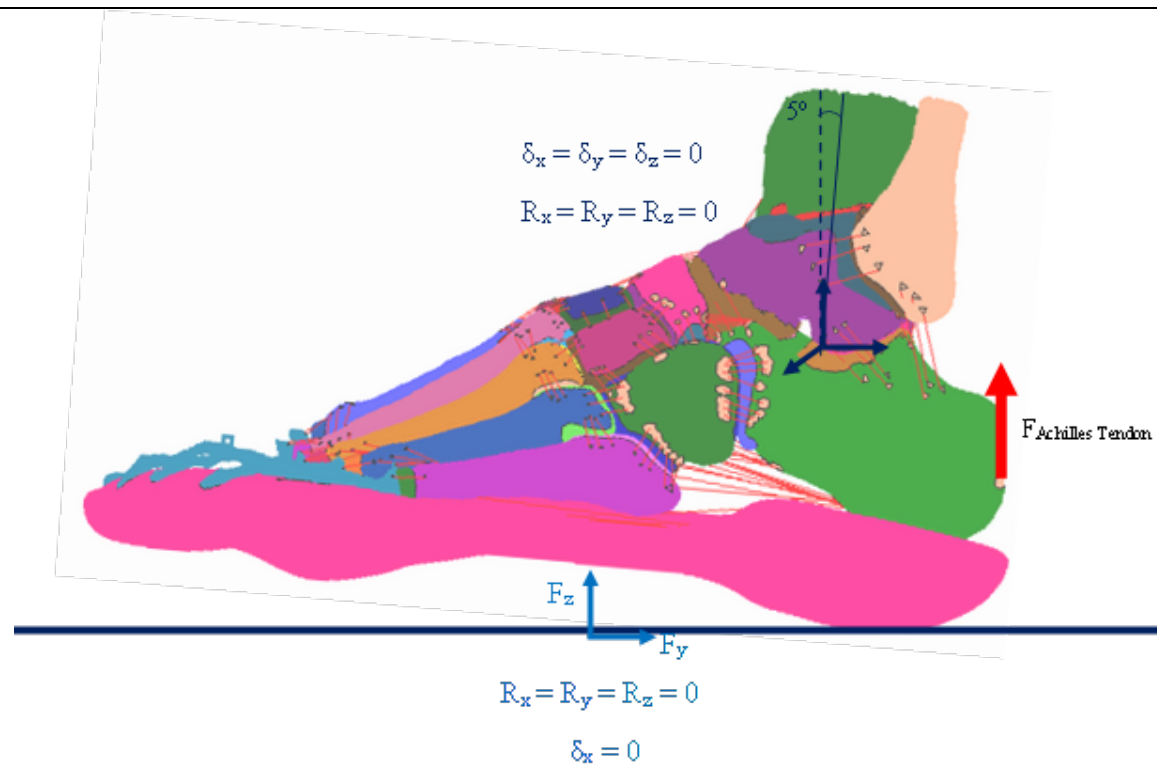


Figure 8.3.7: The rotation of the model to the initial position, to give the desired shank-to-vertical angle, and the boundary conditions imposed on the simulation. F indicates a force in that direction, δ indicates the displacement in that direction, and R indicates the rotation about that axis.

8.3.4.1 Muscle Forces through the Achilles Tendon

The significant, extrinsic muscles were not assigned a geometry and, instead, were all assumed to act through the Achilles tendon. The Achilles tendon was modelled by 5 vertical force vectors acting on the most posterior surface of the calcaneus. The point of application is shown in Figure 8.3.7. During gait the value of the Achilles-tendon force changes as the muscle use varies. Previous gait studies have predicted Achilles tendon loading experimentally during gait using shear wave tension meters [175, 176]. Ebrahimi evaluated the peak Achilles force, in 2 different aged cohorts: young and old, at a range of walking speeds [175]. The force was calculated from the stresses shown in Figure 8.3.8 with a peak force calculated as $3.01(\pm 0.75)$ BW for the younger cohort and (2.44 ± 0.91) BW for the older cohort [175]. Keuler et al. reported similar results for a young cohort with a peak force of (3.73 ± 1.14) BW at a walking speed of 1.5m/s and (3.86 ± 1.25) BW at 1.75m/s [176]. Whilst the point in gait modelled will have the greatest influence on the size of the Achilles Tendon force, speed of gait and age of subject were also considered.

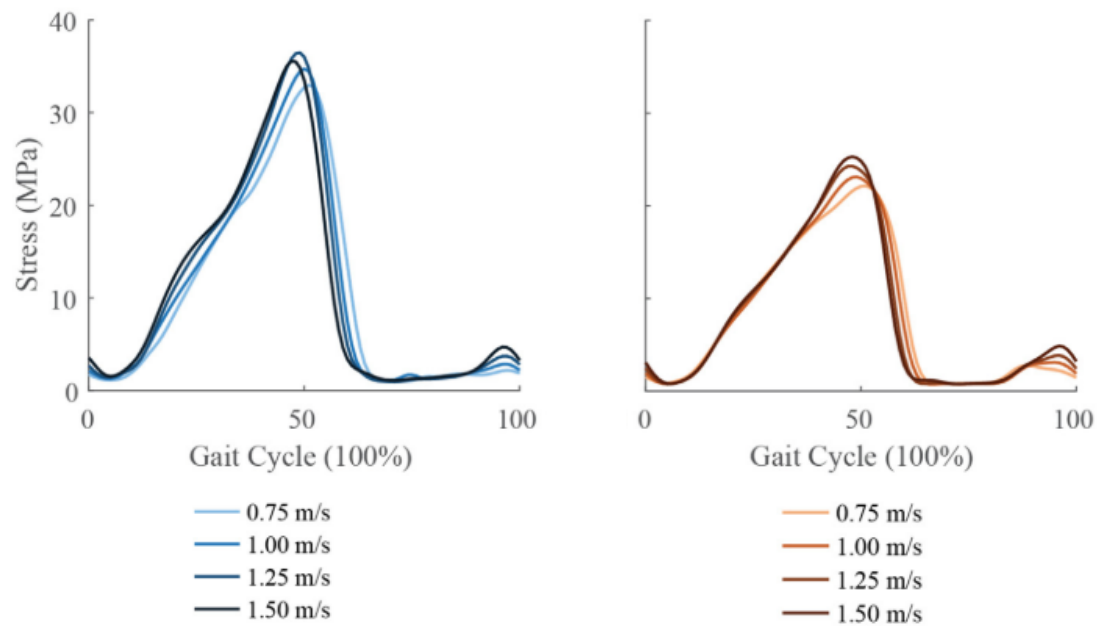


Figure 8.3.8: The stress within the Achilles tendon throughout gait at different walking speeds [175]. The stresses seen in the Achilles tendon of the younger cohort are shown on the left and of the older cohort are shown in the right. Image reproduced with permission from the rights holder Elsevier.

The force through the Achilles tendon was assumed to be that recorded during gait studies by Ebrahimi et al. with averaging of the two different age cohorts over the 4 speeds [175]. To calculate the Achilles-tendon force, the stress was estimated from Figure 8.3.8 and the normalised force calculated using the mean body weight and mean tendon cross-section area of the 2 cohorts as reported, to give a value of 0.18 BW [175].

8.3.5 Comparison to experimental data

The mean contact normal stress obtained from the FE simulation, between the plantar aspect of the foot and the floor, was compared to the plantar pressure obtained during the gait analysis in chapter 5. The peak pressures and mean pressures observed were compared. Additionally, the relative ratio between the pressure in the hindfoot region and the pressure in the midfoot and forefoot regions was compared. The non-zero plantar pressure sensors and nodal values that fell within the most posterior 26% of the length of the foot were considered to be in the hindfoot region.

8.3.6 Sensitivity Analysis

A sensitivity analysis was run to evaluate the influence of several parameters on the output of the FE model. The parameters altered were those predicted to have an influence on the plantar pressure and contact stress and are summarised in Table 8.3.2. Each parameter was altered by $\pm 20\%$ from the baseline value, apart from the floor material. For the floor, the baseline value was rigid, and this was altered to leather and aluminium to evaluate the influence on a meshed contact surface and a contact point of similar material properties of those used in a shoe. When altering a parameter all other variables were kept the same. In total 8 additional simulations were run.

Table 8.3.2: Parameters altered during the sensitivity analysis. F is the force, normalised to body weight (BW), E is the Young's modulus and ν is the Poisson's ratio. LL indicates the use of the lower limb model.

Parameter	Variable	Minimum	Baseline	Maximum	Model	Ref.
Achilles Tendon	F (\times BW)	0.14	0.18	0.22	LL model	
Cartilage	E (MPa)	9.6	12	14.4	LL model	
Fat pad	E (MPa)	0.92	1.15	1.38	Fat pad only	
Floor Material	E (MPa)	172	Rigid	68000	Fat pad only	[177, 178]
	ν (-)	0.4	-	0.36		

When altering the material properties of the fat pad and the floor material, a supplementary model was developed (described below) consisting of the fat pad alone, in order to achieve workable computational times. When altering the Achilles tendon force and the cartilage Young's modulus, the whole model of the lower limb was used.

For both models (fat pad only model and whole model) a baseline run was performed with the baseline material properties as listed in Table 1.3.2. For both baseline models, the mean plantar pressures in the hind foot region, and in the midfoot and forefoot region were obtained. These were compared to the altered model. For those sensitivity changes evaluated using the whole model, a comparison of mean contact stress at the talocrural joint was also analysed.

8.3.6.1 Supplementary Simulation – Fat-pad only

Whilst the sensitivity analysis for cartilage material properties and Achilles tendon force required the whole model, analysis of the floor properties on plantar pressure could be carried out with a simplified, fat pad only model. This model consisted of only the floor, fat pad, distal phalanges and calcaneus. The distal phalanges and the calcaneus were rigid bodies that were considered to rotate about the centre of the ankle joint at origin, O, shown in Figure 8.3.9. The floor was meshed using

hexahedral elements with reduced integration and Hermann formulation, and assigned the material properties shown in Table 1.3.2.

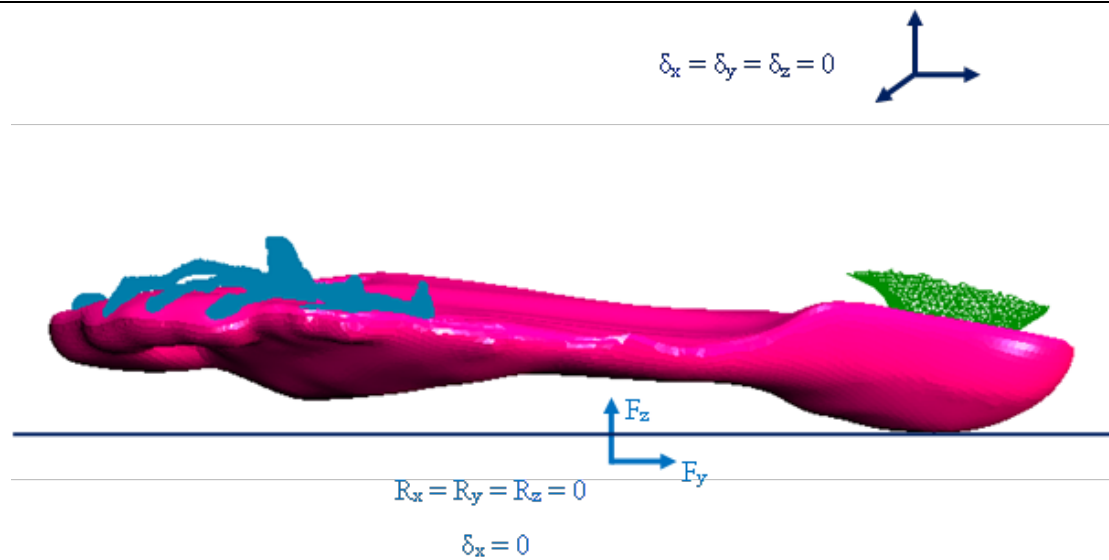
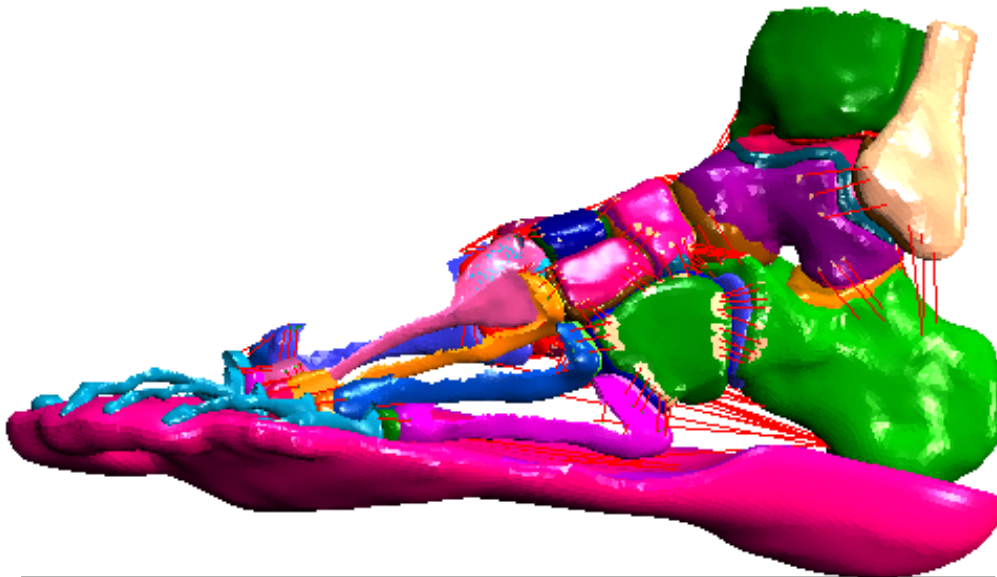


Figure 8.3.9: Simplified, fat pad only, model to evaluate the sensitivity of the floor material properties and fat pad properties on the plantar pressure. The distal phalanges (light blue) and the calcaneus (green) were considered to rotate about the ankle joint, indicated as the origin, O . F indicates a force in that direction, δ indicates the displacement in that direction, and R indicates the rotation about that axis.

8.4 RESULTS

The initial prescribed angle of 5° to simulate 10% of the gait cycle, shown in Figure 8.4.1a, resulted in the final position of the foot shown in Figure 8.4.1b. With the foot in the final position, contact was observed between the floor and fat pad in both the hindfoot and forefoot region and the foot was in a plantarflexed position. Further views can be seen in Appendix 12.5.2



(a)



(b)

Figure 8.4.1: The lower limb FE model viewed from the medial side in (a) the initial position and (b) its final position after application of boundary conditions to mimic 10% of the gait cycle, between loading response and midstance.

8.4.1 Comparison to Experimental data

The plantar pressure recorded during the experimental gait trials (described in chapter 5) and simulated during the FE study are shown in Figure 8.4.2. The peak experimental plantar pressure, shown in Figure 8.4.2a, recorded was 220kPa and this was located in the hindfoot region. The maximum plantar pressure recorded in the midfoot and forefoot region was 70kPa located on the lateral side. The mean, experimental plantar pressure within the hindfoot region was 130kPa (values <10kPa were considered to be 0 and not included) and within the forefoot and midfoot region, the mean, experimental pressure was 40kPa.

The maximum, contact normal stress (normal to the floor) obtained from the FE simulation was 990kPa located the hindfoot region and the peak normal stress observed in the midfoot and forefoot region was 320kPa (Figure 8.4.2b). The mean pressure in the hindfoot region was 430kPa and the mean pressure within the midfoot and forefoot region was 150kPa.

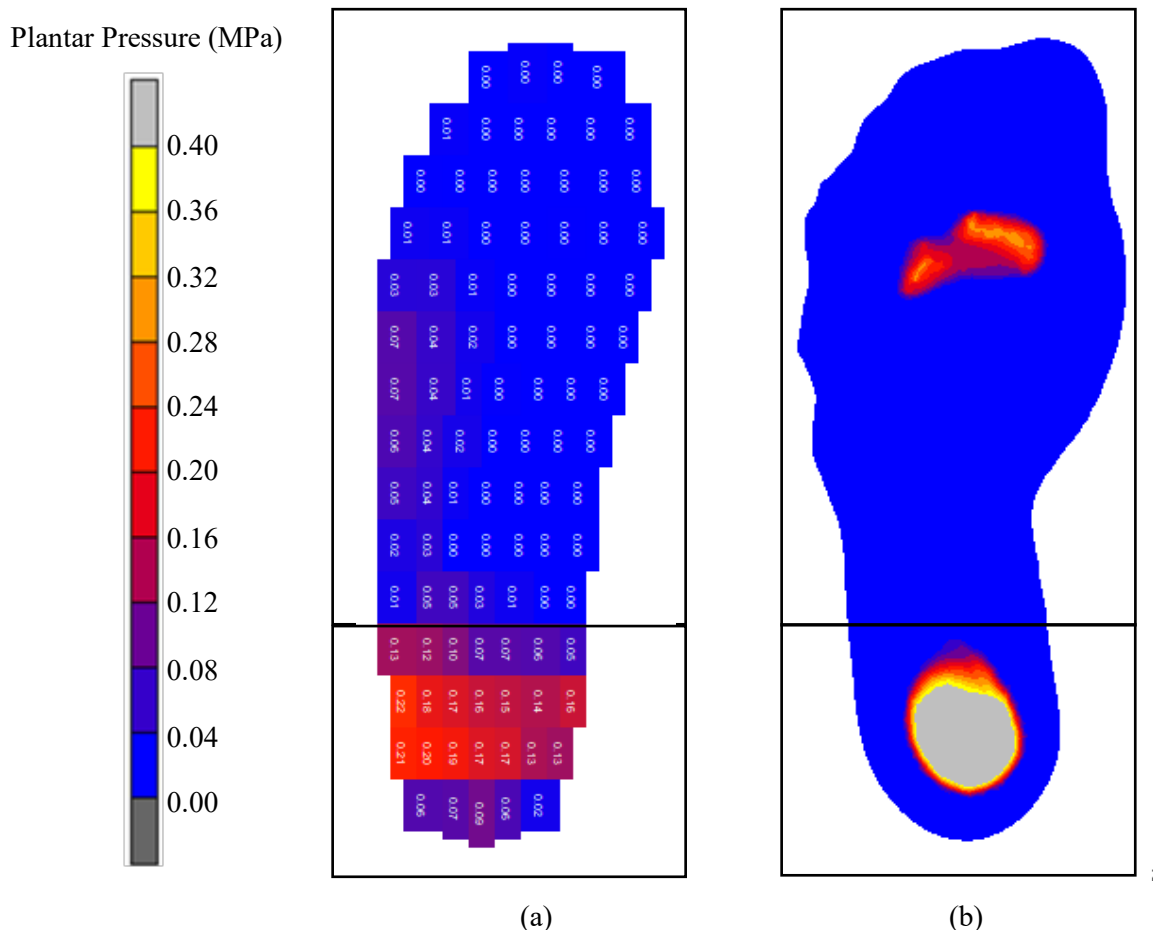


Figure 8.4.2: The plantar pressure in the left foot at the selected point in gait, as recorded during (a) the gait analysis described in Chapter 5 and (b) the FE simulation. The foot is split into 2 regions, the hindfoot region, and the midfoot and forefoot region. The light grey region indicates the value of plantar pressure is off of the scale.

Figure 8.4.3 shows the ratio of mean plantar pressure between the hindfoot region of the foot, and the remainder of the foot. From the experimental analysis, the ratio of mean plantar pressure recorded in the hindfoot region, compared to the midfoot and forefoot region was 3:1. The mean plantar pressures obtained from the FE simulation, gave a ratio of ~2.9:1 between the hindfoot and the remainder of the foot.

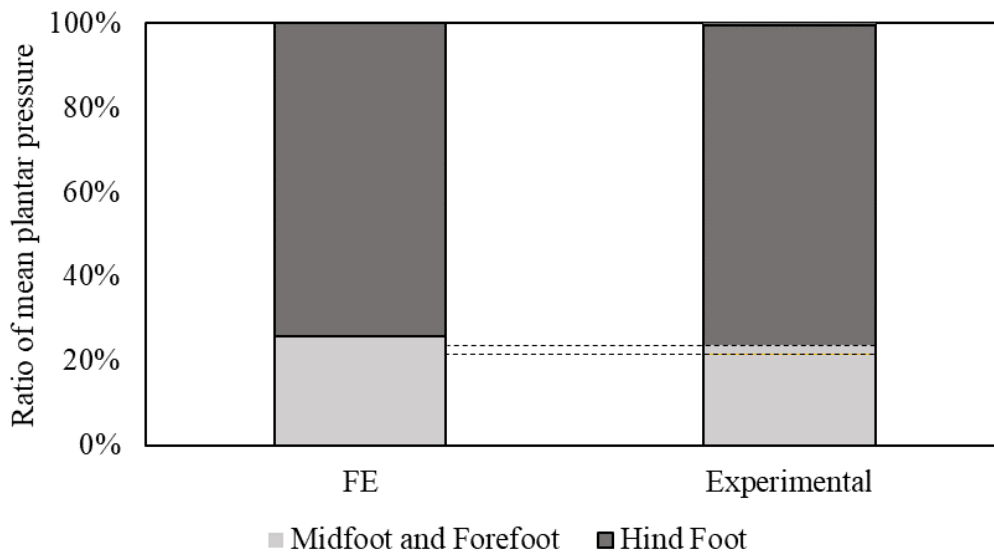


Figure 8.4.3: The relative magnitude of mean plantar pressures $\pm 1SD$ (indicated by the dashed line) recorded experimentally and simulated computationally, in the hindfoot region, and in the midfoot and forefoot regions.

8.4.2 Contact Stresses

Figure 8.4.4 shows the normal contact stresses at the talocrural joint, between the talus cartilage and the tibia and fibular cartilages and at the subtalar joint. The peak normal, contact stress at the talocrural joint was 4.12MPa between the tibial cartilage and the talar cartilage. The mean, normal contact stress observed at the talocrural joint was 1.8MPa.

The peak normal contact stress observed at the subtalar joint was 6.26MPa. The mean contact stress observed was 2.3MPa. Further views of the cartilage contact stresses are shown in Appendix 12.5.3.

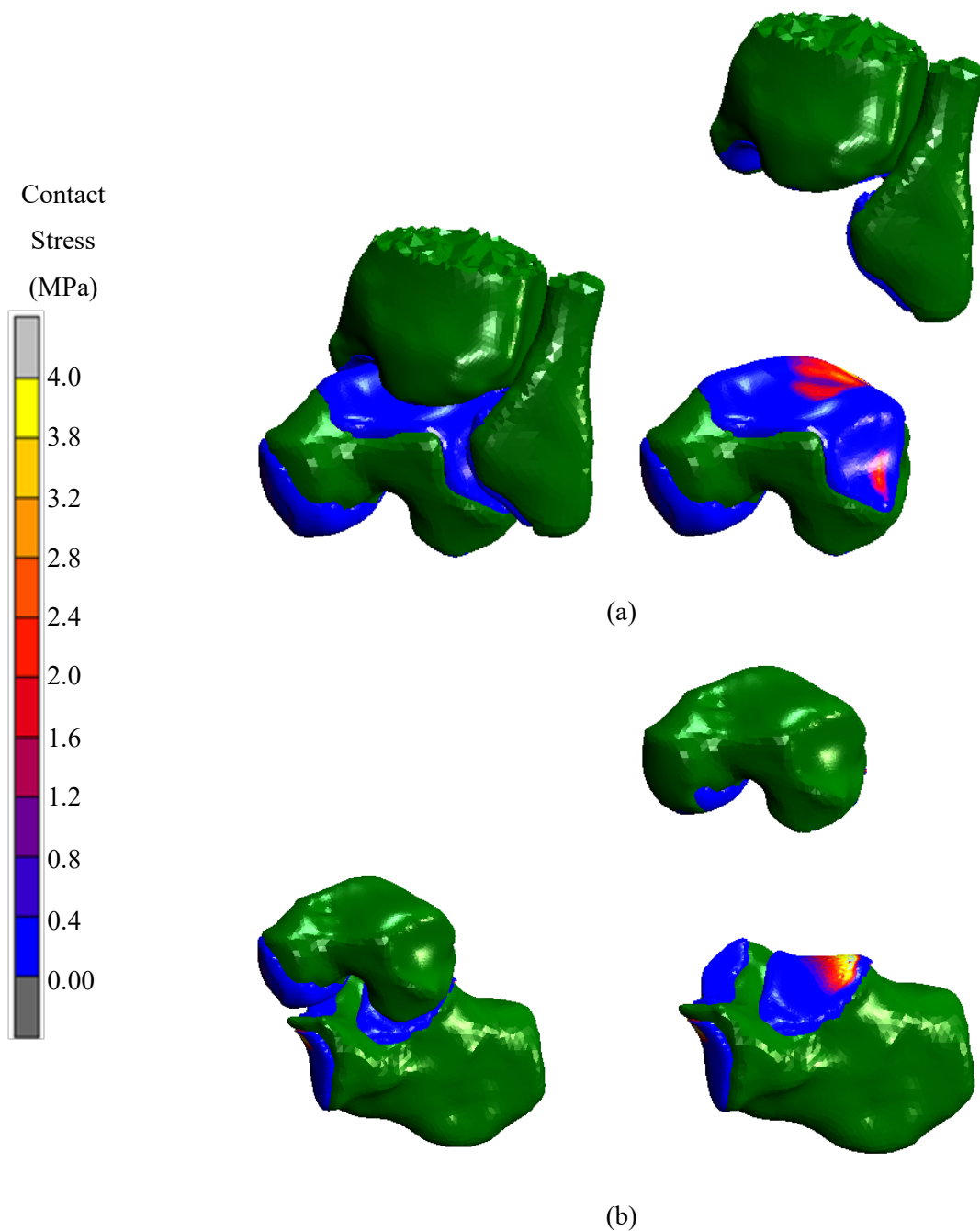


Figure 8.4.4: Contact normal stress at (a) the talocrural joint and (b) the subtalar joint when simulating 10% of the gait cycle

8.4.3 Sensitivity Analysis

Figure 8.3.9 shows the plantar pressure distribution between the whole model, baseline simulation and that with altered cartilage Young's modulus and altered Achilles tendon force. Altering the Young's modulus of the cartilage resulted in a change of $<1\%$ in both the peak and mean plantar pressure. Altering the Achilles tendon force resulted in a change of $< \pm 1.4\%$ in the peak and mean values of plantar pressure.

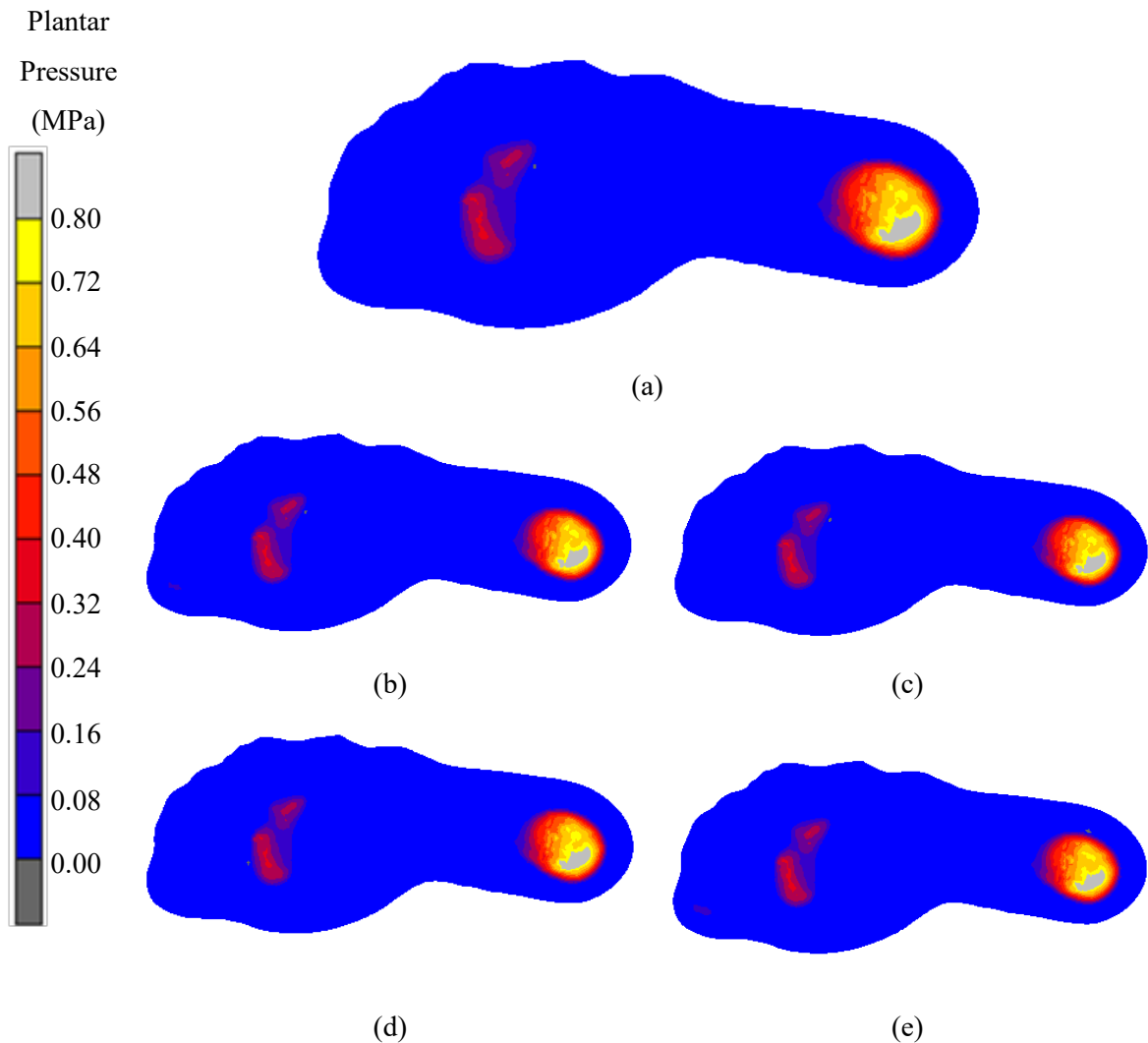


Figure 8.4.5: The plantar pressure distribution obtained from the FE whole model with (a) the baseline properties and boundary conditions (b) the baseline Young's modulus of cartilage altered by -20% (c) the baseline Young's modulus of cartilage altered by +20% (d) the baseline Achilles tendon force altered by -20% and (e) the baseline Achilles tendon force altered by +20%

Figure 8.4.6 shows how the changes in cartilage Young's modulus and Achilles tendon force altered the peak talocrural contact stress. The change in Young's modulus of the cartilage resulted in a change in peak talocrural contact stress from the baseline by $\pm 7.0\%$. The change in Achilles tendon force resulted in a change in peak talocrural contact stress from the baseline by $\pm 3.7\%$.

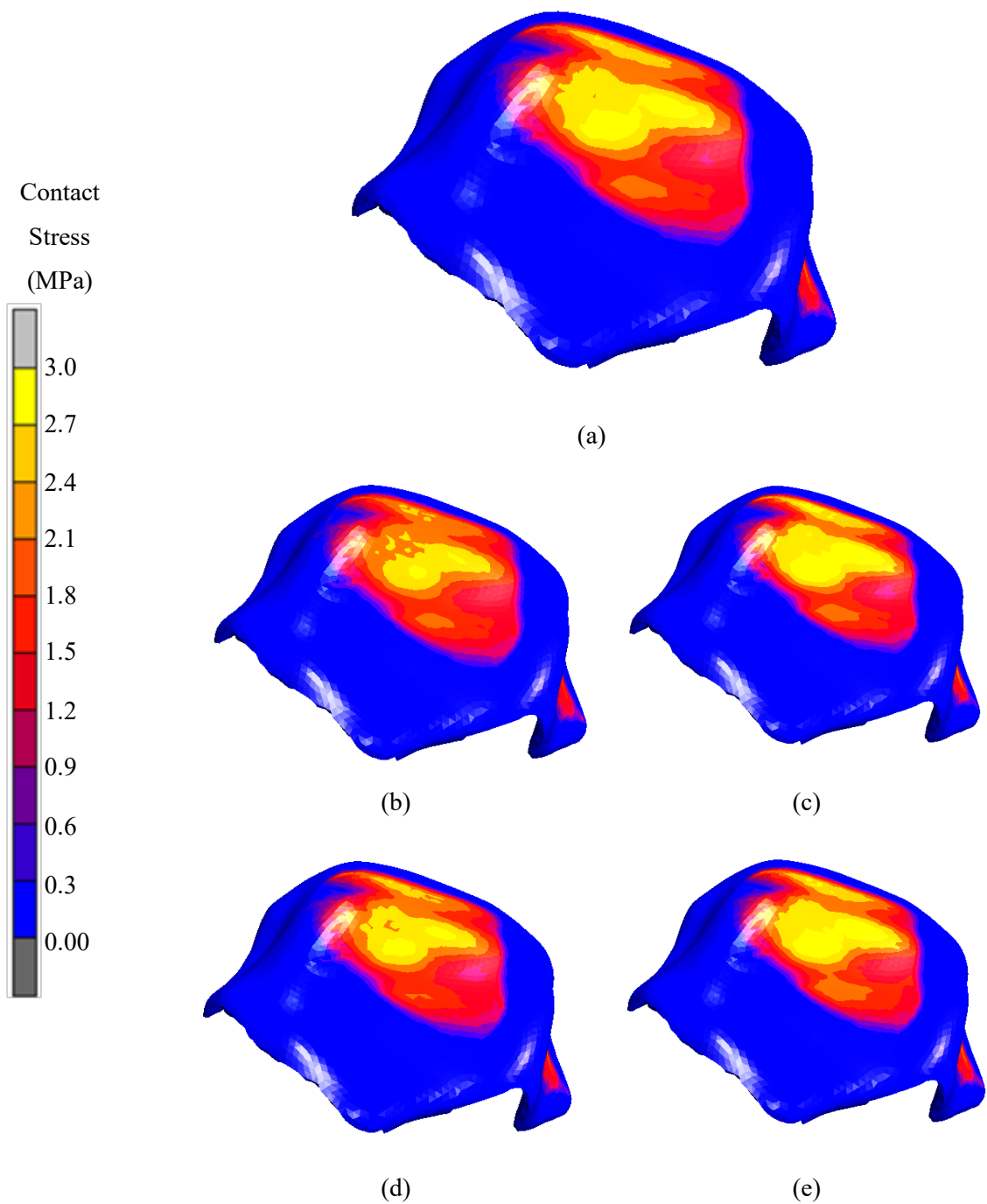


Figure 8.4.6: The contact stress at the talocrural joint (on the talus' cartilage) from the FE whole model with (a) the baseline properties and boundary conditions (b) the baseline Young's modulus of cartilage altered by -20% (c) the baseline Young's modulus of cartilage altered by +20% (d) the baseline Achilles tendon force altered by -20% and (e) the baseline Achilles tendon force altered by +20%

Figure 8.4.7 shows the plantar pressure distribution observed in those models run with the simplified fat pad only model. Running the model with a deformable base resulted in changes to the peak contact stress, in the direction normal to the ground, of $\pm 0.6\%$, and resulted in a reduction in the mean contact normal stress by up to 2%. The changes to the material properties resulted in an increase in peak contact normal stress by up to $\pm 9.3\%$ and the mean contact normal stress by 19.2%.

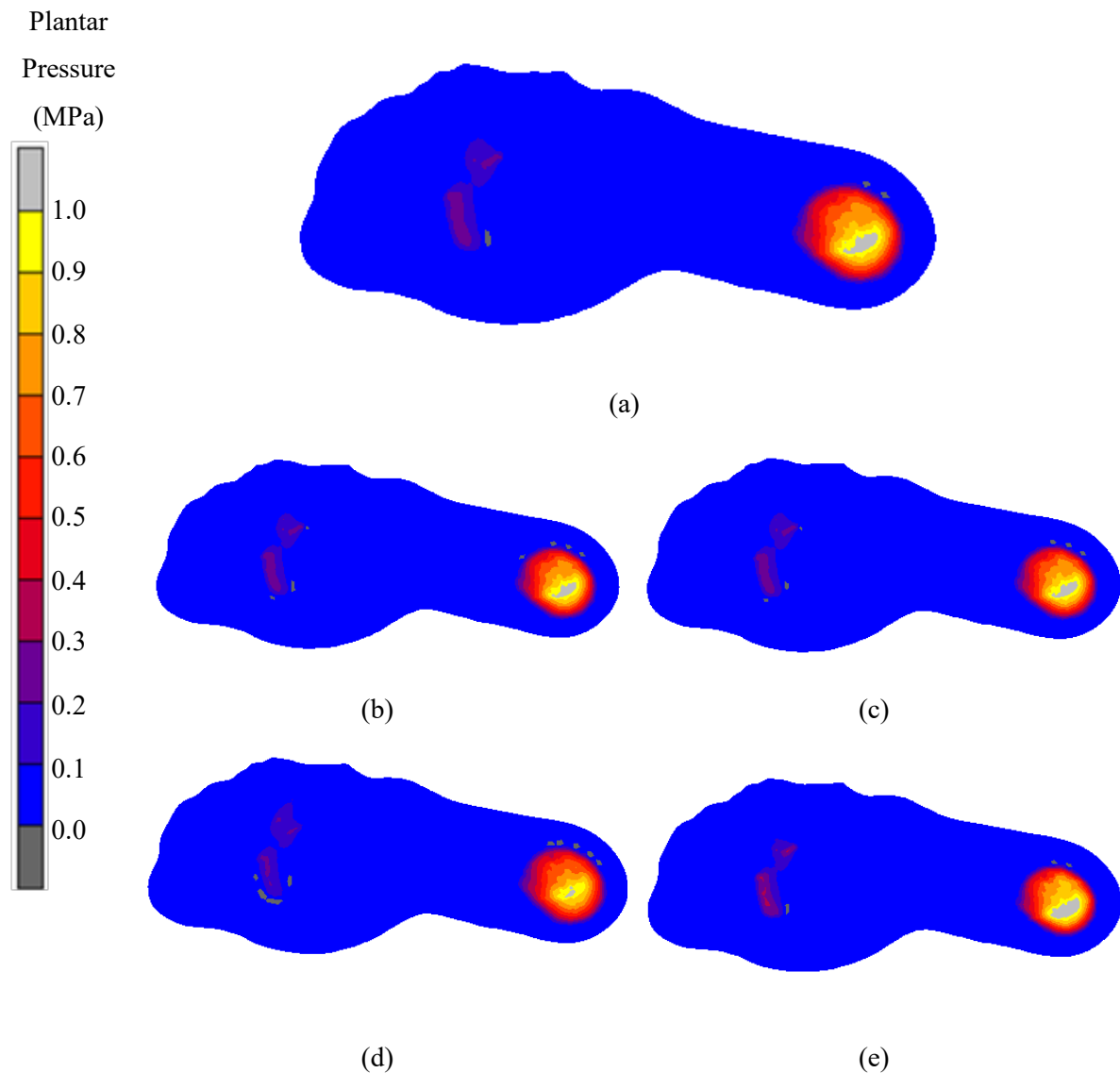


Figure 8.4.7: The plantar pressure distribution obtained from the fat pad only, FE model with (a) the baseline properties and boundary conditions (b) the addition of a deformable floor with leather properties (c) the addition of a deformable floor with aluminium properties (d) the fat pad Young's modulus decreased by 20%, and (e) with the fat pad Young's modulus increased by 20%

8.5 DISCUSSION

8.5.1 Calibration and comparison to experimental data

The lower limb model was compared with experimental data obtained using a non-invasive protocol presented in Chapter 5. The initial angle chosen resulted in a simulation with expected rotations; with a final plantarflexed position. This was observed in the early stages of gait in chapter 5.

Experimental plantar pressures during gait were compared to the FE simulation. The mean plantar pressures recorded in the hindfoot from the FE simulation were of the same order as those recorded experimentally. Plantar pressures are reliant on accurate representation of the floor and fat pad contact and properties. However, the floor-fat pad interface was simplified due to the lesser importance in the model application. The pressures recorded by the FE simulation were higher than that recorded experimentally likely due to the rigid surface used to represent the floor and the assumption of fully bonded ('glued') contact with the fat pad. Additionally, during the experimental testing the subject wore a shoe, whilst the model was simulated barefoot. The softer surface of the shoe would likely increase the contact region with the foot, thereby reducing the peak pressures seen, though the sensitivity suggested this could be by a small amount. The insole of a shoe was also moulded with an arch, possibly explaining why lateral midfoot pressure was observed experimentally, but not within the FE model. This may also explain why forefoot pressure was seen in the FE model at the selected point in gait, as the presence of an arch in the sole may inhibit further plantarflexion of the foot. The sensitivity evaluating the effect of the fat pad material properties on plantar pressure, was shown to have a more significant influence than the other properties evaluated. However, the baseline material properties resulted in a similar ratio of the mean plantar pressures recorded in the hindfoot region and the remainder of the foot observed in the experimental values and FE outputs. As such the baseline material properties were deemed acceptable for the model application, namely the relative comparison of contact stresses between the lower limb model, and the combined PD-AFO lower limb model.

The cartilage was developed using a novel method, by extruding a surface up to a midpoint interface due to the lack of definitive line visible between 2 cartilage surfaces on the MRI scans. The resulting range of thicknesses of the cartilage at the talocrural joint from this method (1.29-1.88 mm for the tibial surface and 1.32-1.63 mm for the talar surface) was deemed to be similar to previously recorded values in the literature [126, 128, 179]. Additionally, the contact stresses between the cartilage surfaces were quantified. The contact stresses observed were of the same order as those observed in previous FE models and invasive experimental data obtained using cadaveric models at the talocrural joint [144, 180].

A lower limb model was developed which met the 4 criteria laid out in the methodology. The model followed a comprehensive methodology, ensuring that each simplification was carefully justified. The final lower limb model resulted in expected rotations of the foot, and plantar pressures of the same

order as those observed experimentally. Additionally, the contact loads and contact stresses between the cartilage surfaces were able to be quantified. The lower limb model produced can be used in 2 scenarios; on its own and, as it was based on the subject, for whom the PD-AFO was fitted as described in chapter 7, it can also be modelled within the PD-AFO.

One point in gait was simulated. With different boundary conditions the model could be used to evaluate other points in gait, including points during midstance and terminal stance. The logical methodology described in this chapter, provides the basis to begin assessing the requirements for simulating these alternative points in gait. It should be noted that for those points in gait with greater rotation (late stance phase) the influence of the fat pad and plantar fascia may be greater, and therefore further analysis of this should be considered. Further simplifications may also be required in the tarsals to allow the simulation to converge to a solution, given the greater rotations expected.

8.5.2 Limitations

When developing the model of the lower limb assumptions and simplifications were made. Combining of the lower limb FE model and PD-AFO FE model requires a large number of elements and contact interactions, rendering it highly inefficient computationally. As such simplifications were made to ensure improved computational efficiency. One simplification was to run a static simulation, rather than a significantly more computationally expensive dynamic solution, to model the instance of gait of interest. Additionally the bones were assumed rigid, some bones were unable to move relative to one another, and both the cartilage and fat pad assumed linearly elastic. As the application of this model was to compare contact stresses, it was considered important to focus on accurate, meshed contact between cartilage, prioritising computational resources on this aspect of the model. Rigid representation of bone have been previously used and found to have limited influence on the overall results in terms of contact stresses on cartilage surfaces compared to meshed representations of bone. Assignment of linear material properties to the fat pad was deemed acceptable for this application [143] due to the large number of elements of the fat pad. The linear material properties selected for the cartilage and fat pad were also obtained from literature. Whilst the sensitivity analyses performed suggested the fat pad does influence the plantar pressure, the main output of interest is the joint loads and cartilage stresses. The cartilage material properties were found to have a very limited effect on the contact stresses and therefore considered acceptable.

Whilst the model did not constrain motion to one plane; some restraints, however, were in place to ensure that the model was able to converge to a solution. The tibia and fibula were unable to move relatively to one another. During gait, only a very small movement was seen between the two bones and therefore this was considered acceptable. The second to fifth metatarsals were considered to be one body rotating about one point, as were the 3 cuneiforms. Finally, the distal phalanges were all merged together and glued to the fat pad surface. Again, the relative motion between these bones is

minimal compared to the overall rotations exhibited by the foot during the point in gait simulated [145]. These simplifications were deemed acceptable to ensure computational efficiency with minimal loss in accuracy in terms of hindfoot contact stresses.

Intrinsic muscle forces were considered negligible, however due to the large number of ligaments used this was thought not to alter the stability of the foot. The spring elements used to model the ligaments allowed for all ligaments to be modelled without a penalty on computational efficiency. This allowed accurate free rotations and translations of the bones. Comparatively, extrinsic muscles were considered to have an important effect on the limb during gait. Modelling 3D meshed muscles was considered computationally inefficient as the muscle forces were not the focus of the study, therefore, the extrinsic muscles were simplified and considered to act through the Achilles tendon. This technique has been used in several previous FE models with good success. Within this study the value of force applied through the Achilles tendon was taken from experimental literature analysing the Achilles-tendon force during gait, instead of using the value for balanced standing seen in previous studies. The sensitivity demonstrated that the extent of Achilles tendon force had a limited influence on the contact stresses at the talocrural joint, and therefore the values taken from literature were considered adequate.

8.6 CONCLUSION

In this chapter an FE model of the lower limb simulating 10% of the gait cycle (between loading response and midstance) was developed and compared to the same instance in experimental gait. Whilst some assumptions had to be made to ensure computational efficiency, the model is able to quantify the contact stresses at the cartilage surfaces at the selected point in gait with good accuracy; the focus of this model. The plantar pressure obtained from the model was in adequate agreement with experimental data to allow relative comparisons when run in combination with the PD-AFO model and without. In the next chapter the methodology to combine the lower limb model and PD-AFO model is described, and the applications of the model presented.

9 COMBINED MODEL

9.1 INTRODUCTION

Chapters 5 and 6 examined the alterations in external loading of the lower limb when wearing the PD-AFO, and the mechanical response and ESAR characteristics of the posterior struts throughout the gait cycle. This chapter describes the development of a combined FE model of the PD-AFO developed in chapter 7 and the lower limb developed in chapter 8 which is then used to evaluate changes in the internal mechanics at major joints with and without the PD-AFO.

Combining an FE model of a lower limb with a model of an orthotic provides the opportunity to evaluate internal loading of the foot, without using invasive measures. However, combining such models is a challenge due to the overall model size and the ability to define the contact between the 2 geometries to constrain the model (but not over-constrain it) to ensure it converges to a solution. In particular, for the PD-AFO that is the focus of this thesis, there are 2 areas of contact with the lower limb, as shown in Figure 9.1.1: (a) the proximal tibia and calf with the cuff; and (b) the plantar aspect of the foot and sole of the PD-AFO. Defining these 2 areas of contact is not trivial in terms of both model complexity and accuracy.

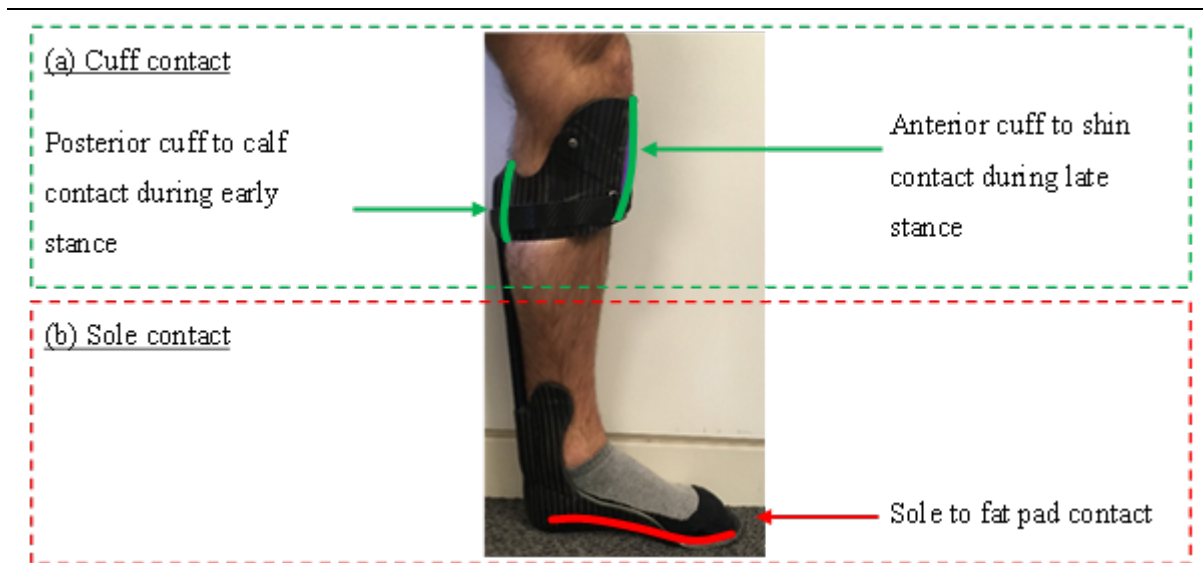


Figure 9.1.1: The areas of contact between the lower limb and the PD-AFO and how these can change at different points in gait. This includes the (a) cuff-tibia contact shown in green, which varies between contact between the posterior cuff and posterior calf during early stance and the anterior cuff and anterior aspect of the tibia during late stance. Additionally, there is (b) contact between the sole and fat pad shown in red.

The cuff-calf contact varies throughout the gait cycle, with the posterior cuff in contact with the calf during early stance, and the anterior cuff and shin pad in contact with the shin during late stance. Therefore, the contact defined must be appropriate for the point of gait to be evaluated. Due to the already challenging nature of developing an FE model of the lower limb, few studies have combined these models with wearables such as a shoe or an orthotic. Only a small percentage of the models of lower limbs reviewed included (or planned to include) a lower limb in combination with some form of orthotic [111, 181-184]. As such, models including a wearable device of some kind (e.g., a foot insole) were also considered; these studies were reviewed with a particular focus on the definitions of contact between the 2 geometries [132, 136, 185].

9.1.1 Previous FE models

To improve contact between the orthotic and lower limb, previous models developed the geometry of the orthotic/wearable computationally, from the geometry of the lower limb, one of such as those shown in **Figure 9.1.2** and Figure 9.1.3 [111, 132, 136, 183]. This method of model development allows improved computational efficiency from improved contact. If, such as Cheung et al. the focus of the model is to evaluate the changes in plantar pressure upon variation of material properties, this may provide adequate accuracy to quantify the differences seen [132]. However, it is a method more suited to analysing and selecting design prototypes, instead of evaluating the behaviour of existing designs.

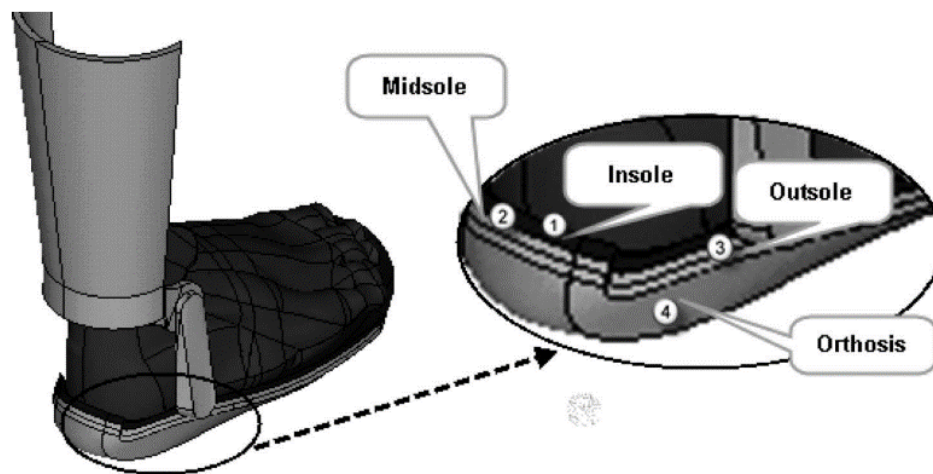


Figure 9.1.2: A solid model of an AFO combined with an AFO and insole [183]. Reproduced with permission from the rightsholder Taylor and Francis.

The main point of contact, considered in all models reviewed, was that between the orthotic and plantar surface of the foot. The models reviewed of lower limbs with AFOs did not choose to include the geometry of a shoe, which would generally be required to be worn with most AFOs [182]. When wearing an AFO, the shoe maintains the relative position of the AFO to the limb, preventing extensive slip between the 2. Therefore, if the shoe is not to be modelled it is important to mimic the role of the shoe during gait. As observed by Chu et al. modelling a non-slip contact (glued) represents the shoe's role and prevents relative movement in a computationally efficient way, without introducing computationally expensive features such as friction [182]. Other studies modelled the interface as touching with a coefficient of friction set to be 0.6 [132]. If the outcome of the study is to focus on the contact interface, then it would be more suitable to model a touching, friction contact, assuming relatively small movements are modelled. If the plantar interface is not the main focus of the study, then the introduction of friction is an unnecessary complexity.

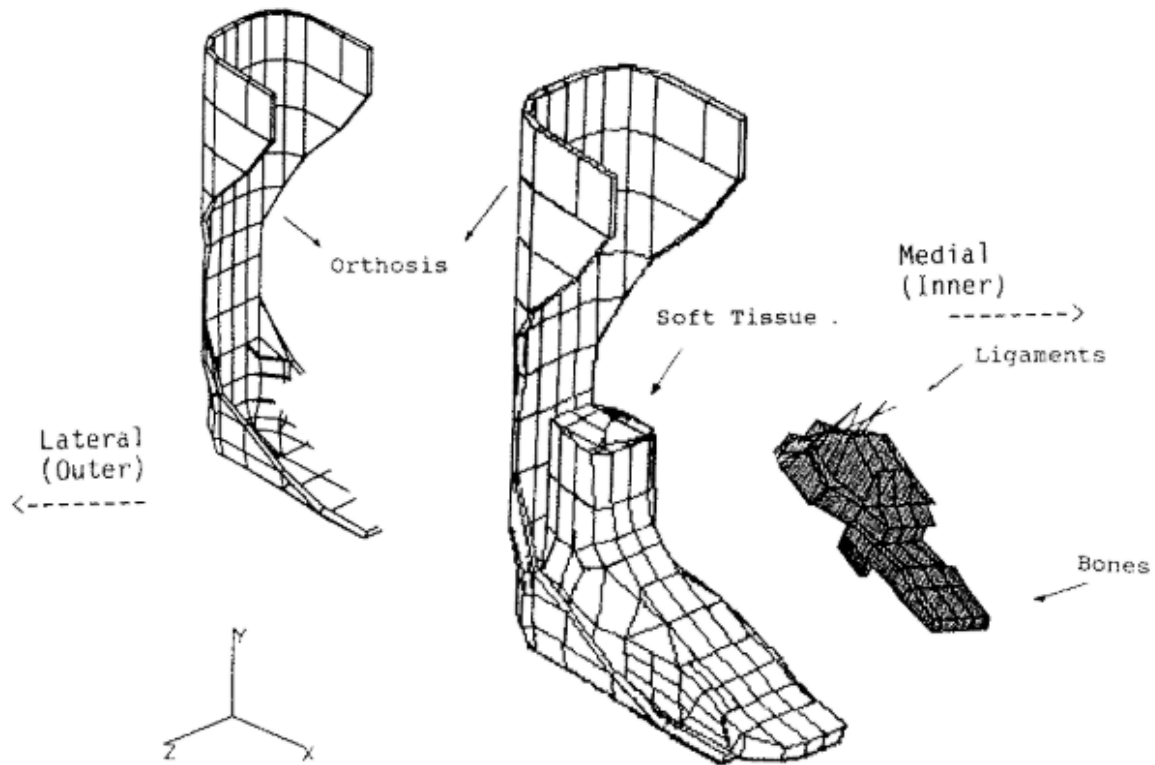


Figure 9.1.3: FE model of a lower limb in an AFO [183]. Image reproduced is in the public domain.

Of the studies mentioned above, only 1 had modelled 2 areas of contact [182]; all others considered contact at the plantar region of the foot only; effectively an insole only. As mentioned above, Chu et al. modelled the plantar aspect of the foot and AFO as glued relative to one another. For the proximal contact region, the proximal tibia and proximal AFO were fixed in all planes, with no motion between the 2. However, modelling the contact between the AFO and limb as glued may not be a suitable method for all points in gait as it does not account for deformation of the skin and calf muscle around the proximal tibia. To improve on the assumption of glued contact, the mechanical properties of the region of contact must be understood; this is discussed below.

9.1.2 Calf Mechanical Properties

During the early stance phase of gait, the posterior region of the calf makes contact with the PD-AFO. This posterior contact region involves mostly muscles and fat, and so is less stiff than the anterior contact region – which is mostly bone – that would occur later in gait. The stiffness of the calf muscle and skin will likely effect the predicted mechanics of the combined model, and therefore must be considered.

A limited number of studies have analysed calf muscle properties, most analysing compression sleeves using inverse FE methodologies to calculate the material behaviour. The material properties defined within some of the studies are summarised in Table 9.1.1. Whilst Dai et al. modelled the calf

region as linearly elastic and isotropic [186], others modelled the calf with a neo-Hookean material model [187]. Lima et al. also reviewed studies that had used shear wave propagation to calculate the Young's modulus of muscle, presenting a range of values dependent on age, stretching and flexion of the knee joint [188].

Overall, the level of detail into which the different components of the calf are broken down, and their material properties evaluated, varies between studies. Some considered the calf region to be a homogenous body, whilst others considered its constitutive microstructure of veins, skin, and muscle. The level of detail required is dependent on application; if only the overall mechanical response of the calf is desired, a homogenous material model is acceptable.

Interestingly, Dai et al. measured a Young's modulus of 12kPa using their experimental set-up but half this, 6kPa, for subjects older than a certain age range. It is not understood how a value of 6 kPa was determined, although it should be considered for which ages these material properties were calculated.

Table 9.1.1: Calf material properties as found in the literature. E is the Young's modulus, ν is the Poisson's ratio, K is the Bulk Modulus, and C_{10} is a material parameter used to describe a neo-Hookean material and is a function of the shear Modulus.

Study		Material Properties Assigned	Ref.
Avril et al. 2010	Neo-	Muscle: $C_{10} = 11.2\text{kPa}$ and $K = 69.5\text{kPa}$.	[187]
	Hookean	Skin: $C_{10} = 4.5\text{kPa}$ and $K = 106\text{kPa}$	
Dai et al. 1999	Linear	Skin: $E = 2\text{MPa}$ and $\nu = 0.5$	[186]
	Isotropic (with assumed Poisson's ratio)	Fascia: $E = 340\text{MPa}$ and $\nu = 0.5$	
		Vein: $E = 0.133\text{MPa}$ and $\nu = 0.5$	
		Calf Region: $E = 6\text{-}12\text{kPa}$ and $\nu = 0.5$	
Lima et al. 2018	Linear	Gastrocnemius: $E = 17 - 225 \text{ kPa}$	[188]
	Isotropic	Soleus: $E = 15 - 55 \text{ kPa}$	

9.2 METHODOLOGY

9.2.1 Orientating the PD-AFO and lower limb models

The FE models of the PD-AFO and the lower limb as described in Chapters 7 and 8 were imported into one model to create the combined limb-PD-AFO model. The PD-AFO was rotated to align the sole of the PD-AFO to the fat pad. This achieved the final relative position as seen in Figure 9.2.4. The combined model was rotated to give a reclined shank-to-vertical angle of 5° , which is the same as that used for the FE model of the lower limb to evaluate gait during early stance, at 10% of the ait cycle.

9.2.2 Geometry and Contact

Two points of contact were to be modelled; the contact between the sole and the fat pad, and the contact between the calf and cuff. As such the tibia was extended up to meet the proximal cuff of the PD-AFO. The distal head of the tibia and fibula were modelled using surface geometries as in chapter 8. The remainder of the tibia/fibula was modelled using a truss element, with a diameter of 36 mm, estimated from the volume of the tibia and length of the long axis of the tibia (Appendix 12.6.2). The distal end was assigned to be the contact node of the tibia and fibula. The truss element was assigned material properties, as discussed in Chapter 8, with a Young's modulus of 7300 MPa and a Poisson's ratio of 0.3 [130, 132, 135, 137, 139, 145].

A rigid floor was created, parallel to the transverse plane. The contact between the base of the PD-AFO and the floor was defined as glued, as was the plantar aspect of the foot with the sole of the PD-AFO. The anterior cuff and shin pad were removed from the model, as contact was not made with this region during early stance. The proximal region of contact between the tibia and the posterior calf was modelled using spring elements, to represent the calf muscle, similar to the truss elements used previously in the literature [186]. Thirty springs were connected to the proximal end of the tibia and fixed to 30 points on the posterior cuff, on the interior side, shown in Figure 9.2.1.

Of the 30 springs 15 were defined to provide stiffness in the vertical direction only and 15 were defined to provide stiffness in the anteroposterior direction only. The springs were prescribed to act in compression only. The stiffness of these springs was determined from a simulation described below, the results of which are described in Section 9.3.1.

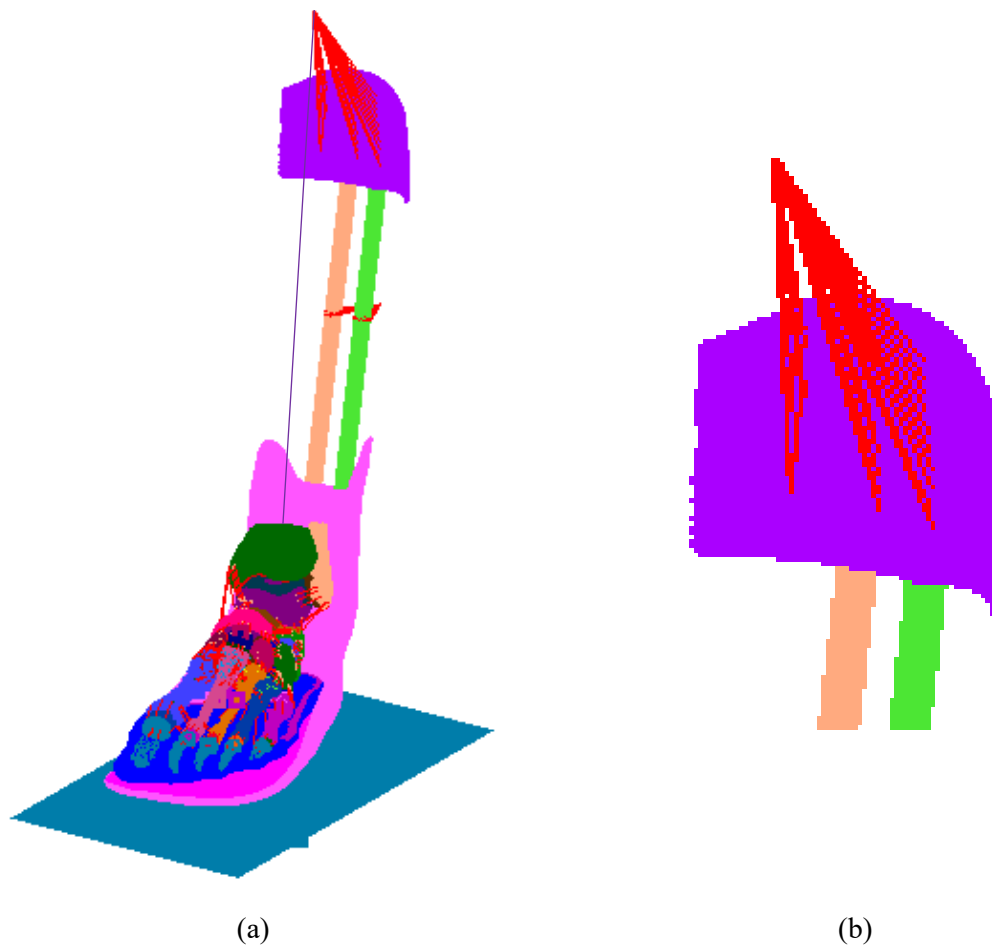


Figure 9.2.1: The connection of the tibia to the posterior cuff shown with (a) the whole model and (b) the posterior cuff with 30 springs, shown in red, used to model the calf muscle. 15 of the springs act in the vertical direction only, and 15 in the anteroposterior direction only.

9.2.2.1 Calf muscle Stiffness

The section of calf was generated from an idealised geometry, with a diameter of 110 mm, and a tibia diameter of 30 mm. A solid mesh was generated, and an idealised cuff created, with an internal diameter of 110 mm, and an external diameter of 113 mm. The calf was considered as one homogenous body, including the adipose tissue, veins and muscle. The region representing the tibia was fixed in all degrees of freedom as shown by the orange cross in Figure 9.2.2a. The proximal and distal surface of the meshed calf were fixed in z . A rigid surface was created and glued to the exterior of the cuff and assigned a control node to allow a displacement to be applied to the exterior of the cuff. The cuff was glued to the calf. An overall displacement of up to 20 mm was applied. This displacement was resolved into the anterior and proximal directions, to give the same ratio of displacement as observed in each direction, between the peak anteroposterior and vertical GRF observed during early stance phase of gait. The cuff was unable to rotate and translate in x .

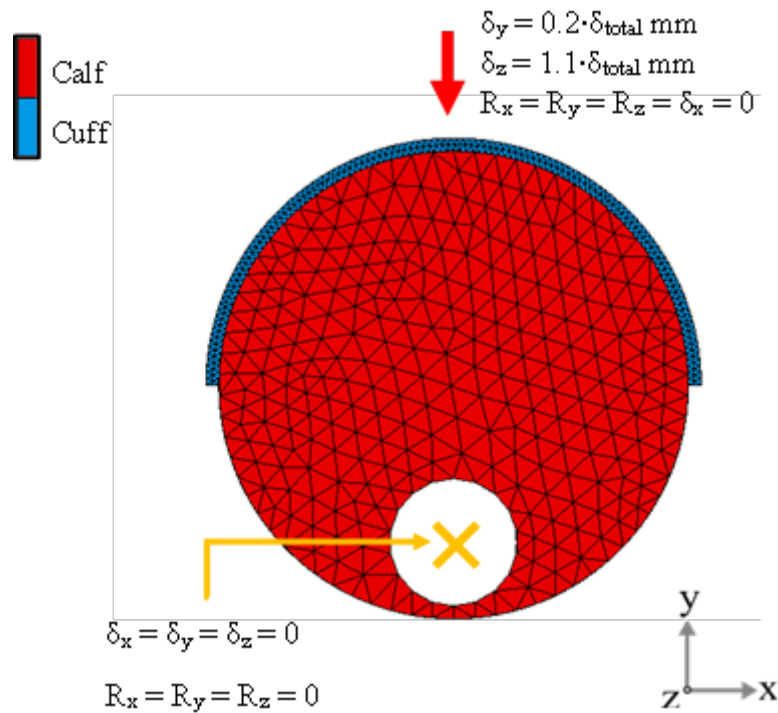


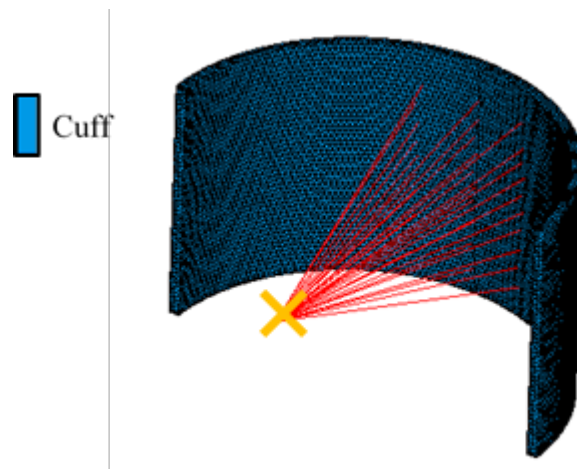
Figure 9.2.2: FE model boundary conditions used to determine the suitable stiffness for the springs to represent the contact between the calf and the PD-AFO. The tibia was fixed in all degrees of freedom. The contact region was a rigid surface, in contact with the calf, and positioned in 3 locations, distal (left), central (middle) and proximal (right). A total displacement, δ_{total} of up to 20 mm was applied to the control node. x : lateral direction, y : posterior direction, z : proximal direction. δ indicates the displacement in that direction, and R indicates the rotation about that axis.

The calf was assigned 4 different sets of material properties as determined from literature [186-188]. No Poisson's ratio was defined by Lima et al. and therefore the Poisson's ratio of ~ 0.5 as defined by Dai et al. was used. For each simulation the force-displacement curve, in y , was used to calculate the effective stiffness of the calf muscle of the contact region.

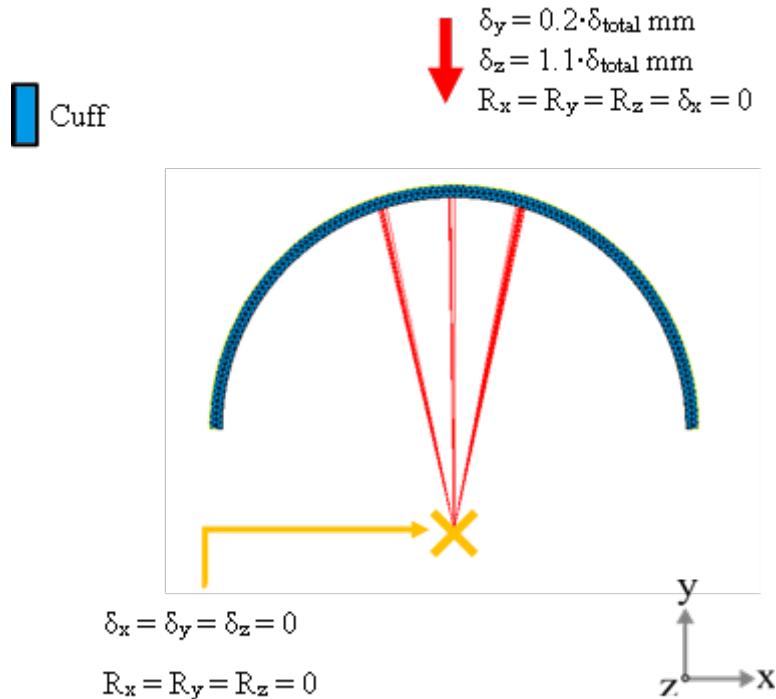
To mimic this contact a second model was created with 30 springs (15 with stiffness in the proximal direction only and 15 with stiffness in the anteroposterior direction only) connecting the central point of the tibia to the interior surface of the cuff, shown in Figure 9.2.3. These springs were assigned a force-displacement curve based on that calculated from the meshed model. Each spring was assigned a fraction of the total force-displacement curve, to give the same ratio in the anteroposterior and vertical directions as observed between the GRF as mentioned above.

A displacement of up to 20 mm was again applied in the same direction as described in Figure 9.2.2. The force-displacement curve from the control node of the cuff was obtained. This was compared to the force displacement curve obtained from the meshed model. The input curve for the springs was adjusted in an iterative process to obtain a good match between the meshed model and the spring model. The results can be seen in section 9.3.1. This stiffness was used to define the properties of the

spring in the combined PD-AFO and lower limb model. The final overall stiffness used in the combined model was 22 N/ mm split between the 30 springs; the mean value established.



(a)



(b)

Figure 9.2.3: The spring model, with (a) the contact points between the 30 springs and the interior surface of the cuff and (b) the boundary conditions applied, where δ_{total} was the resultant displacement of up to 20mm. δ indicates the displacement in that direction, and R indicates the rotation about that axis.

9.2.3 Boundary Conditions

The boundary conditions applied to the model are shown in Figure 9.2.4. The vertical and anteroposterior components of the GRF observed during PD-AFO gait in chapter 5, at 10% of the gait cycle, were applied to the control node of the rigid floor, with the mediolateral component assumed negligible as in chapter 8. An Achilles Tendon force was also applied, assumed to be the same as that applied for the lower limb only. The mediolateral displacement of the floor and all rotations were set to 0. The mediolateral displacement of the cuff of the PD-AFO was also set to 0. The proximal end of the tibia truss was fixed in all degrees of freedom. The distal end of the tibia truss was unable to rotate and fixed in translation in x and y .

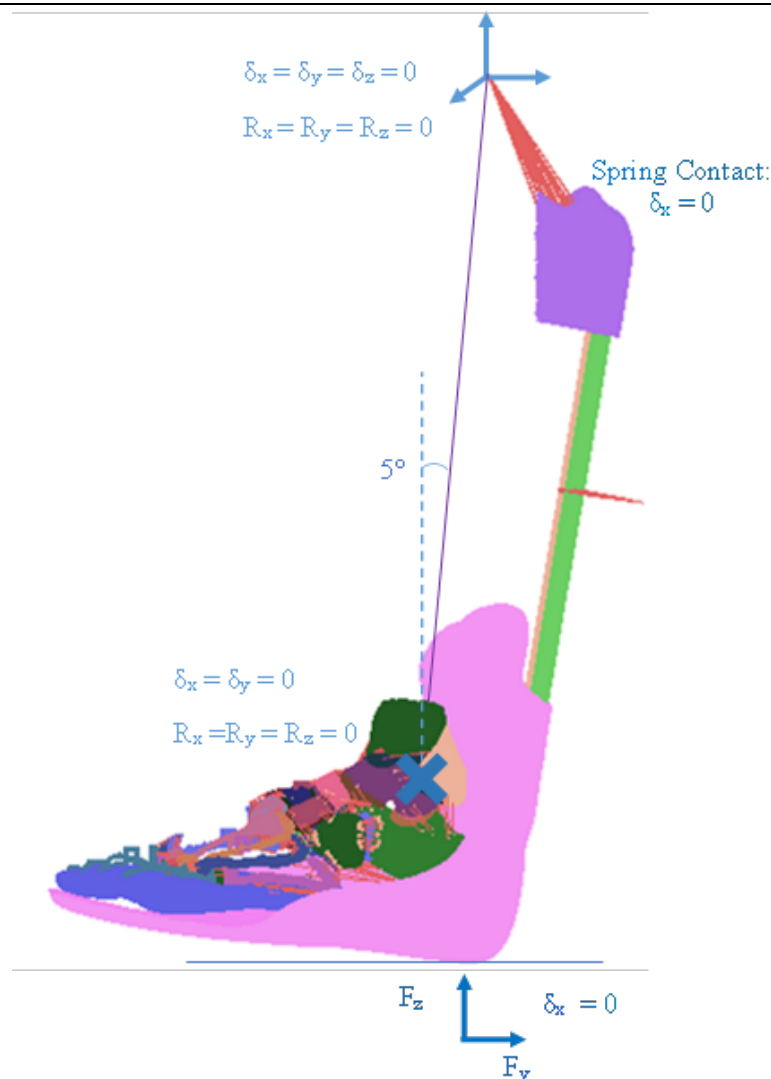


Figure 9.2.4: The initial position of the combined limb-PD-AFO model and the boundary conditions applied to mimic 10% of the gait cycle. F indicates a force in that direction, δ indicates the displacement in that direction, and R indicates the rotation about that axis.

9.2.4 Model Outputs

The contact normal force between the sole of the PD-AFO and the plantar aspect of the fat pad was obtained and the force through the posterior struts was calculated, using matching boundaries, a feature within MSC.Mentat. These values were used to calculate the ratio of loading between the limb and PD-AFO and this was compared to the value obtained experimentally. The plantar pressure recorded experimentally in chapter 5 was also compared to that obtained from the simulation.

For the major joints, the mean contact normal stress between each cartilage pair was obtained and normalised to the total force applied in each simulation (Achilles tendon and GRF). Additionally, the loads through the joints were calculated and normalised to the total force applied, by summing up the contact normal forces between all cartilage pairs for a particular joint. The normalised joint contact stresses and joint loads were compared between the simulation with the PD-AFO and without.

9.3 RESULTS

9.3.1 Calf Properties

Figure 9.3.1 shows the force-displacement curves obtained from the FE simulation compressing the meshed calf (Appendix 12.6.3) when assigned with material properties defined by Avril et al.[187], Dai et al. [186], and Lima et al. [188]; and the force-displacement curves obtained from the spring-replacement model. The simulation run with material properties assigned by Dai et al. and Lima et al. reached a maximum displacement of ~10 mm. The spring model representing the meshed calf with properties from Avril et al. used an overall spring stiffness of 15.8 N/mm and the model representing the meshed calf with properties from Dai et al. used an overall spring stiffness of 3.4 N/mm. The spring model representing the meshed calf with a range of properties from Lima et al. used an overall spring stiffness of 3.9 N/mm and 63.6N/mm (Appendix 12.6.3). The mean of all the stiffness values was 22 N/mm.

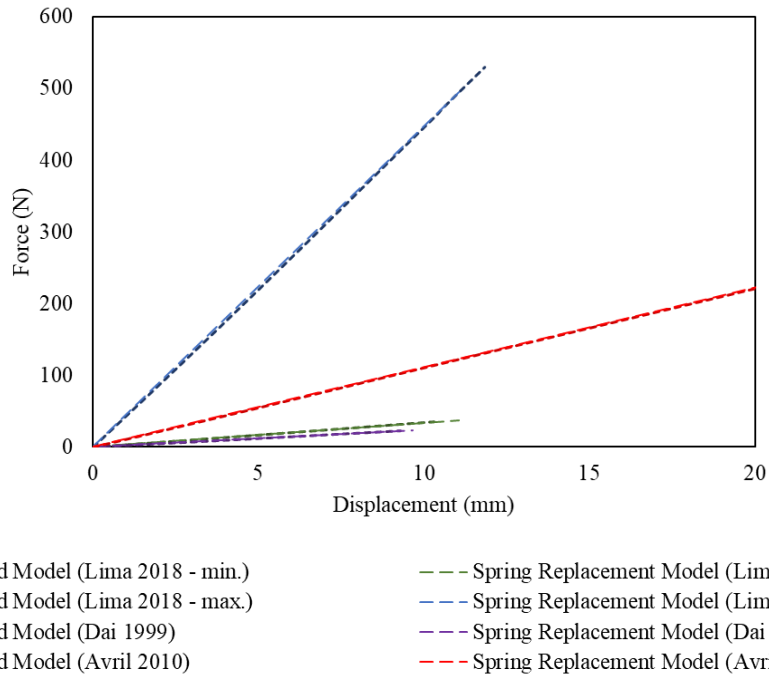


Figure 9.3.1: The force-displacement curves as recorded from compression of the meshed calf and the spring replacement model when run with 4 sets of material properties.

9.3.2 Comparison of the FE combined models to experimental data

Figure 9.3.2 shows the initial and final (loaded) position of the lower limb in the PD-AFO. The PD-AFO experiences a small rotation forward in the sagittal plane. Further views can be seen in Appendix 12.6.1.

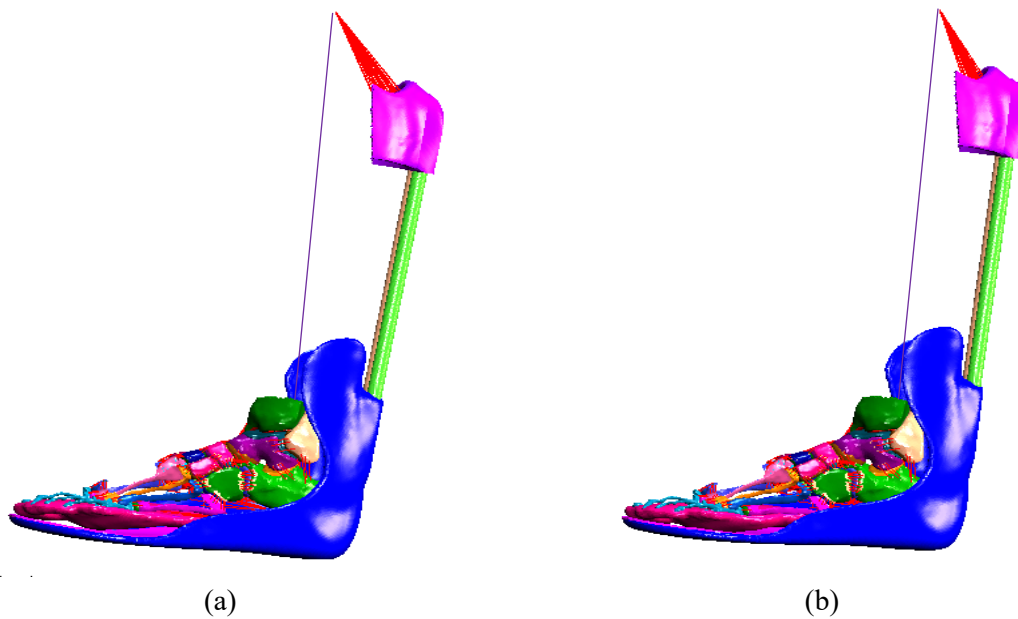


Figure 9.3.2: FE model of the limb and PD-AFO in (a) the initial position and (b) upon completion of the simulation at 10% of the gait cycle.

9.3.2.1 PD-AFO and Limb Loading

Figure 9.3.3 shows the loading experienced by the plantar aspect of the fat pad and by the PD-AFO struts for both the FE simulation and experimental analyses. As calculated in chapter 5, the experimental loading predicted through the PD-AFO was 28-34% of the total GRF applied. Within the FE simulation, the ratio of loading was 30% of the (same) total GRF applied.

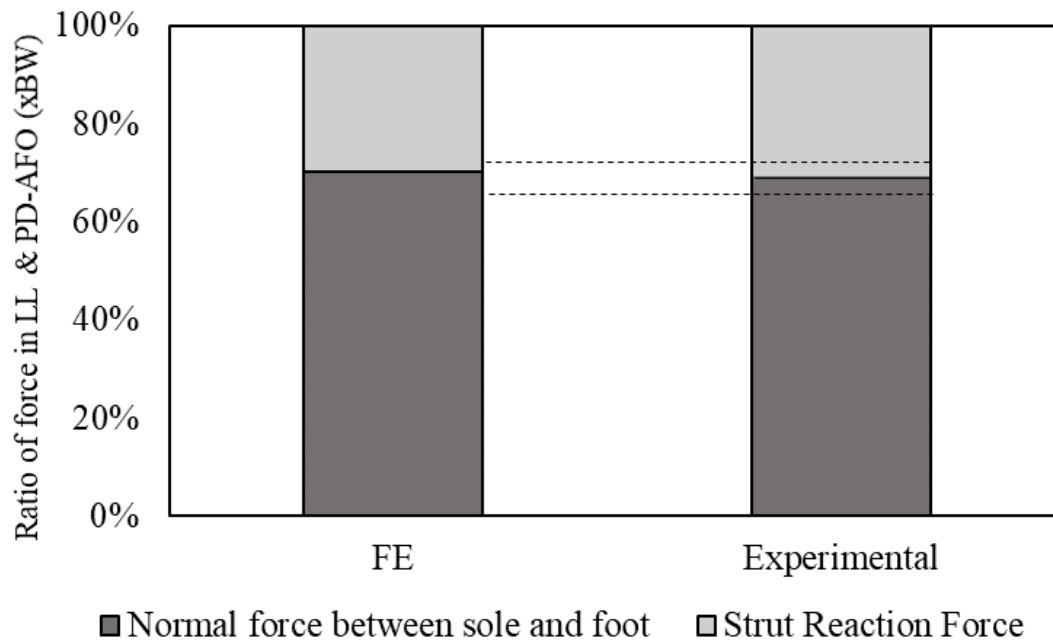


Figure 9.3.3: The ratio of load between the limb and PD-AFO as calculated by the FE simulation and during the experimental gait analysis. The dotted lines represent the experimental corridor, accounting for difference in measurement between the PEDAR sensors and force plates.

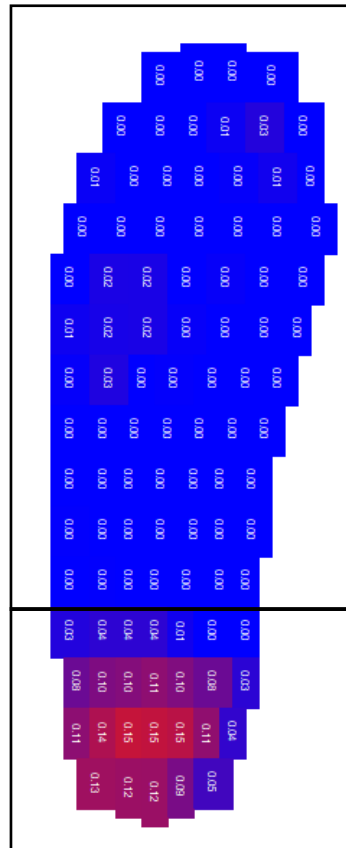
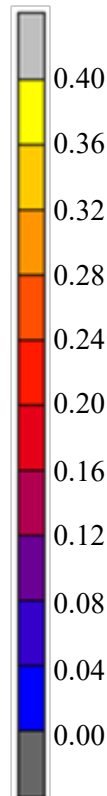
9.3.2.2 Plantar Pressure

The experimental plantar pressure recorded during PD-AFO gait is shown in Figure 9.3.4a. The peak pressure in the hindfoot region was 150 kPa and the peak pressure in the midfoot and forefoot region was 30 kPa. The mean pressure in the hindfoot region was 90 kPa and the mean pressure in the forefoot and midfoot region was 20 kPa.

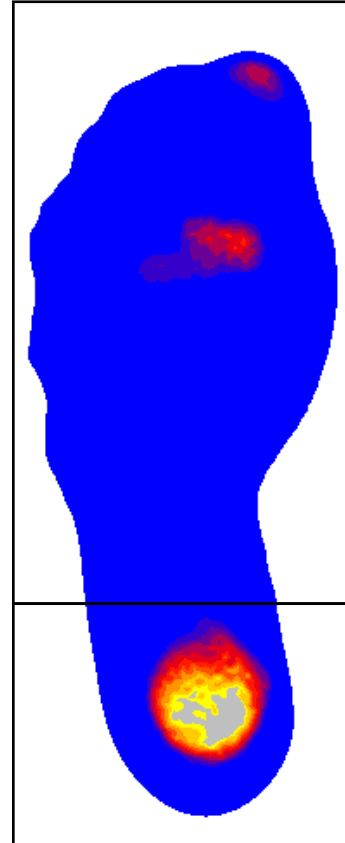
The contact normal stress obtained from the FE simulation, is shown in Figure 9.3.4b. The peak contact normal pressure observed during the FE simulation was 590 kPa in the hindfoot. In the forefoot and midfoot region, the peak contact normal stress was 240 kPa. The mean contact normal stress observed in the hindfoot region was 220 kPa; in the forefoot and midfoot region the mean contact normal pressure was 70 kPa.

Plantar Pressure

(MPa)



(a)



(b)

Figure 9.3.4: The plantar pressure obtained (a) experimentally in the PD-AFO gait analysis described in chapter 5 and (b) from the FE simulation of the limb when wearing the PD-AFO. The foot is split into 2 regions, the hindfoot region, and the midfoot and forefoot region. The light grey region indicates the value of plantar pressure is off the scale.

Between mean plantar pressures in the hind foot region, and forefoot and midfoot region, a ratio of $\sim 1:4.5$ was obtained experimentally, and from the FE analysis, a ratio of $\sim 1:3$ was calculated (Figure 9.3.5). During the FE simulation the ratio of the mean plantar pressure in the hindfoot region relative to the forefoot and midfoot regions was similar, though slightly higher, when compared to the experimental ratio.

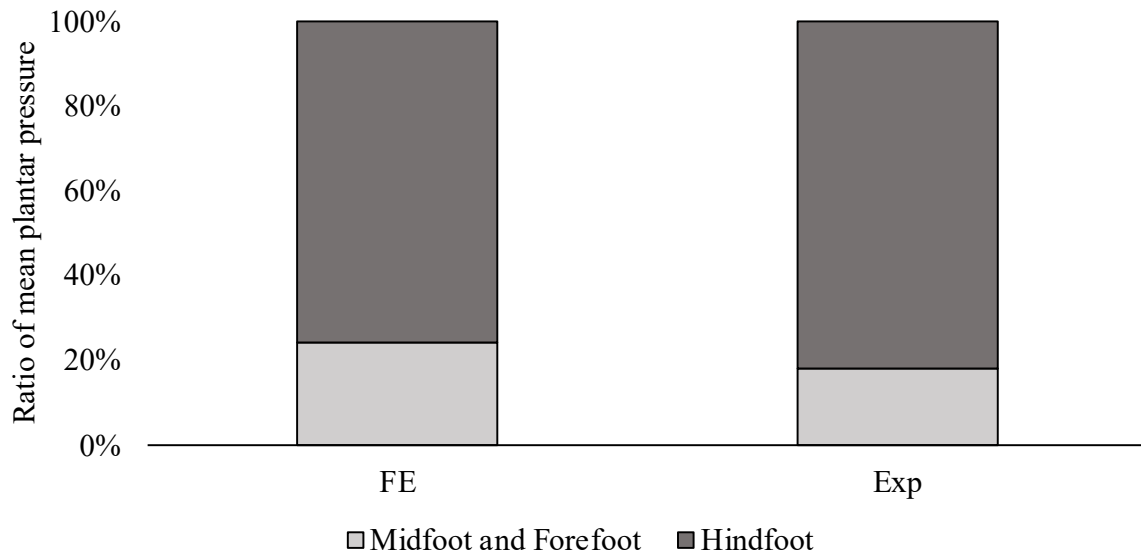


Figure 9.3.5: The relative magnitude of mean plantar pressures recorded, both experimentally and computationally, in the hindfoot region of the foot, and the midfoot and forefoot region of the foot, during PD-AFO gait.

9.3.3 Comparison of lower limb loading with and without the PD-AFO

9.3.3.1 Joint Loads

Figure 9.3.6 shows the joint loads, normalised to the total force applied, evaluated in the lower limb simulations, with and without the PD-AFO. All joints experienced a lower normalised load with the PD-AFO than without. On average the normalised loads experienced by the joints when wearing the PD-AFO were $23\pm 6\%$ lower than for the lower limb alone. The greatest reduction was observed at the talonavicular joint, with a normalised load 30% less when wearing the PD-AFO compared to without. The smallest reduction was observed at the midfoot joint, with a reduction of 17% of the normalised joint load when wearing the PD-AFO. At the talocrural joint a reduction of 23% in the normalised load was observed when wearing the PD-AFO compared to without, and at the subtalar joint a reduction of 22% in the normalised load was observed.

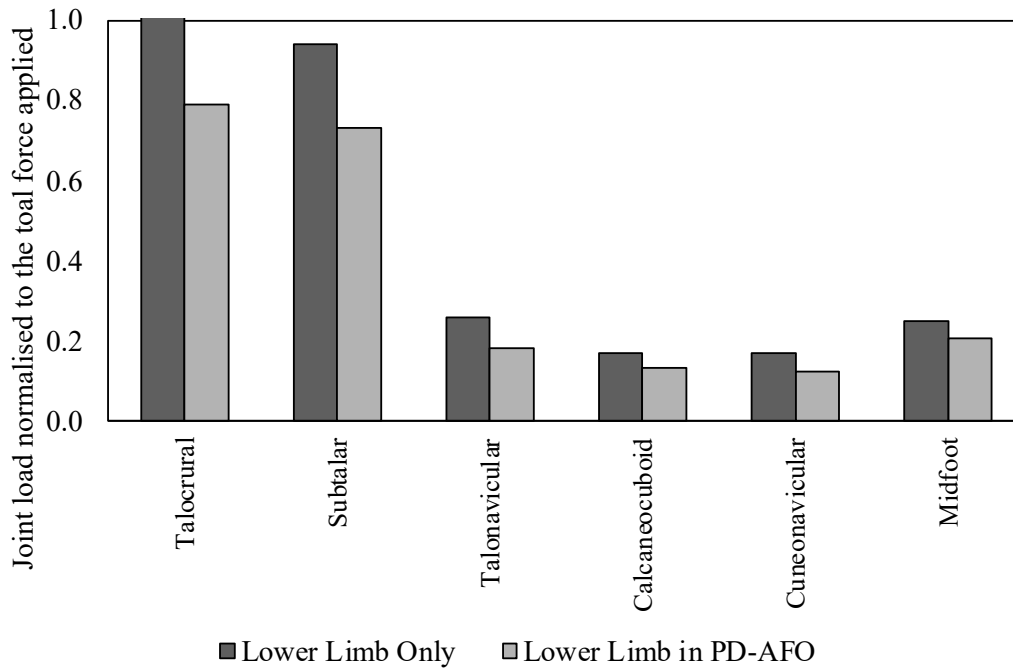


Figure 9.3.6: The joint loads when the lower limb is simulated with and without the PD-AFO, normalised for the total force applied in each model.

9.3.3.2 Contact Stresses

Figure 9.3.7 shows the contact normal stresses observed in the talocrural and subtalar joints when wearing the PD-AFO as modelled at the selected point in gait. Further views of the joints are shown in Appendix 12.6.4. The peak contact normal stresses in the talocrural joint was 2.53MPa and the mean contact normal stress was 1.1 MPa. At the subtalar joint, the peak contact normal stress was 4.2 MPa and the mean contact normal stress was 1.2 MPa.

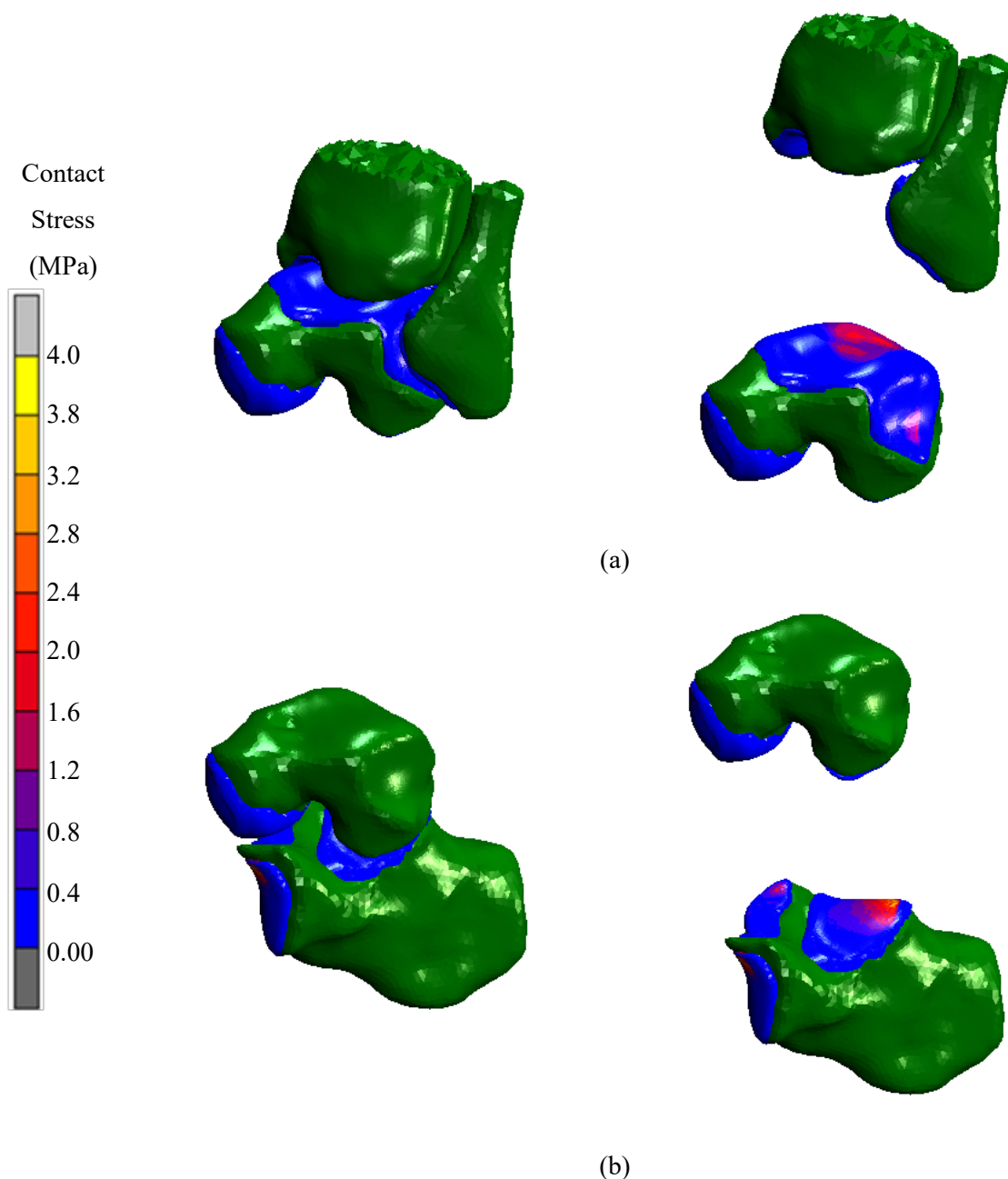


Figure 9.3.7: Contact normal stresses at the (a) talocrural joint and (b) subtalar joint at 10% of the gait cycle with the limb in the PD-AFO

Figure 9.3.8 shows the mean contact normal stresses observed at each joint, normalised for the total applied force in each model. The mean normalised contact stresses observed without the PD-AFO were greater than with the PD-AFO for all joint contact stresses evaluated. On average the normalised mean contact joint stresses were $27 \pm 14\%$ lower when wearing the PD-AFO. For the talocrural joint, when wearing the PD-AFO the normalised mean contacts stress was 29% lower, whilst the subtalar joint experienced a normalised mean contact joint stress 42% lower. At the midfoot joints a reduction

of 22% in the normalised joint contact stress was observed when wearing the PD-AFO, compared to without. The smallest changes were observed at the talonavicular joint, with a reduction of 19% in the normalised joint contact stress.

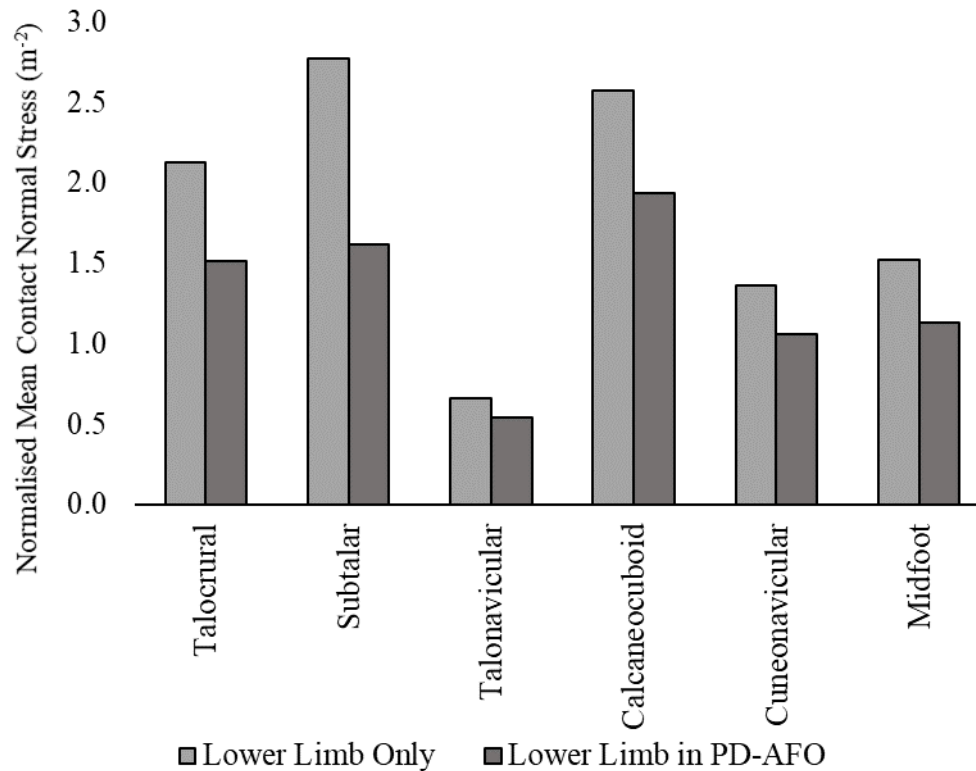


Figure 9.3.8: The mean contact normal stress at the major joints, evaluated in the lower limb only model and the combined limb-PD-AFO model. The contact stresses are normalised for the total force applied in each model.

9.4 DISCUSSION

9.4.1 Comparison to Experimental Data

The combined lower limb-PD-AFO model was compared to experimental results obtained in Chapter 5 and 6 of this thesis. The plantar pressure between the foot and the PD-AFO, obtained from the FE simulation, was compared to the plantar pressures recorded in Chapter 5. Whilst higher pressures were observed in the FE simulations, the ratio of pressures in the hind foot and midfoot area was similar to that observed experimentally.

The distal end of the struts of the PD-AFO deflected in a posterior direction, similar to that observed in Chapter 6. The proximal ends of the struts simulated compressive strains on the anterior side of the struts, unlike those recorded in Chapter 6. This difference is thought to be due the boundary conditions applied at the proximal end; the tibia was fixed and with a linear stiffness prescribed across

the region of the calf, assuming a cylindrical geometry. The ratio of load sharing between the limb and PD-AFO was also compared. The value of load recorded through the PD-AFO in the FE simulation was within the range observed during the experimental analysis. Overall, the model was deemed to mimic well PD-AFO gait at 10% of the gait cycle, between the loading response and midstance phases, and therefore could be used to evaluate the joint loads and contact stresses. The calf region of the cuff was modelled using springs, the stiffness of which was derived from a preliminary simulation using an idealised model of the calf and cuff. There was good agreement in the result obtained from the simulation using the idealised meshed calf and its representation using 30 springs. Whilst using a meshed calf would provide further insight into the contact region, the representation of the calf using the springs was considered an adequate compromise given the decrease in computational time it offered (Appendix 12.6.3).

9.4.2 Comparison with and without the PD-AFO

The normalised loading of the bones was reduced when wearing the PD-AFO, compared to without. This reduction in load is due to the offloading of the PD-AFO thereby bypassing the loading of the limb itself. This demonstrated that the overall offloading observed during chapter 5 results in some form of reduced load across all the joints evaluated. It should, however, be noted that a reduction in bone loading may result in bone mineral density loss and has been linked to osteopenia [189]. Therefore, the extent of use of the PD-AFO and the potential long-term effects of the offloading it offered, should be considered

Whilst the normalised loading of bones is reduced when wearing the PD-AFO, the reduction is fairly uniform (all within 6% of the average reduction) across all joints, suggesting that the PD-AFO does not alter the loading pathway greatly at the point of gait modelled. This could suggest that it is the reduction in load across all joints as a result of wearing the PD-AFO that is aiding patients, rather than a redirection of load away from one specific joint. It may be possible to tailor the design of the PD-AFO to achieve a target reduction in load suitable for the patient, whilst preventing excessive offloading to minimise the possibility of long-term effects.

Additionally, the normalised joint contact normal stresses were evaluated and compared. When wearing the PD-AFO the contact stresses at all joints were less than those observed without the PD-AFO. Links between elevated contact stresses due to altered cartilage geometry and the development of PTOA have been suggested previously [125, 127]. The reduction in normalised contact stresses observed at the joints could imply that the PD-AFO helps prevent further degeneration of cartilage, helping to slow the progression of PTOA. It has previously been reported that patients with PTOA reported reduced requested for late amputations upon prescription of the PD-AFO, though the cohort was small (n=6) [51].

Whilst the reduction of loading of the joints was similar when comparing healthy and PD-AFO gait, the extent of reduction of the normalised joint contact stresses were more varied. In particular at the subtalar joint, a reduction in normalised mean contact stress of 42% was observed, compared to the average reduction in stress, of 27%, across all joints. The variation in reduction of joint contact stresses but not joint loading suggests that the contact region between cartilage pairs changed when wearing the PD-AFO. The contact region would be altered by different ankle joint angles, therefore suggesting that the limitation of the rotation of the foot is reducing the contact stresses observed at the subtalar joint relative to the other joints. In chapter 7 it was demonstrated that the base alignment had limited influence on the rotational stiffness or energy storage properties of the PD-AFO. The alignment would, however, affect the ankle joint angle that occurs at the point in gait modelled. This therefore suggests that alignment of the base could play a role in reducing stresses in the subtalar joint.

Interestingly, one study observed that those with subtalar fusions (only) performed better than those with ankle fusions when prescribed the PD-AFO [22]. Assuming the region of fusion is indicative of the injury location, this could support the findings that the subtalar joint experiences the greatest change in normalised contact stresses with the PD-AFO. Previously, it was also suggested that midfoot/forefoot injuries had a higher rate of requests for late amputations, though the cohort was limited in numbers [49]. The contact stresses in that region, whilst reduced, were one of the smallest reductions observed across all the joints evaluated. This may explain why patients with these regional injuries were poor performers relative to patients with other regional injuries.

9.4.3 Limitations

The combined model was rotated to give a shank-to-vertical angle of 5° reclination; this was the same initial angle used for the lower limb alone, as determined from literature, described in chapter 8.

Owen et al. suggested that shank-to-vertical angles remained unchanged when varying the heel height by a small amount; as such it was considered acceptable to approximate the shank-to-vertical angle as being the same with and without the PD-AFO [123].

The combined models were created by aligning the meshed geometry of the PD-AFO with the meshed geometry of the lower limb. This alignment was performed manually, as the geometries were not scanned at the same time and therefore had different coordinate systems. Additionally, it was not possible to identify 2 clear, single, relative reference points on the computational geometry with which to calculate a rotational matrix. However, due to the custom moulding of the PD-AFO to the subject's lower limb, the alignment of the 2 geometries were guided by the shape and arch of the base of the PD-AFO with the fat pad. With the tibia in the neutral position, the manual alignment gives good visual comparison with video footage during gait.

The lower limb and PD-AFO have 2 points in contact. The point of contact between the fat pad and sole was modelled in both simulations, with glued contact. Whilst some relative movement may be observed between the foot and PD-AFO during gait, the movement was expected to be small compared to the overall movement of the limb and PD-AFO as the user would wear a shoe; therefore, considering this negligible was deemed an acceptable compromise. Additionally, when wearing the PD-AFO the user would have a heel wedge inserted between the PD-AFO and shore; this was not modelled. As mentioned in chapter 7, previous literature analysing the heel wedge, suggests that it has the greatest influence on time-based metrics, for example velocity. By increasing the time over which the load is applied, the heel wedge is also thought to reduce peak loads. As such the effect of the heel wedge was considered to be accounted for by using the experimental PD-AFO gait GRF as the boundary condition.

The second point of contact is between the proximal tibia and calf region, and the PD-AFO cuff. This contact was simplified and modelled by spring elements to reduce computational time. Literature was used to estimate the material properties of the calf, though differences between studies were seen. As such the mean set of properties was used. Additionally, the literature used only considered the material properties when applying a normal force to the calf and not a tangential force. To define the properties for the springs, an additional simulation of the idealised calf was run. Whilst the use of properties from literature and the idealised simulation was approximate, the stiffness used resulted in good agreement for the ratio of loading between the PD-AFO and lower limb when compared to the experimental analysis. This suggests that the methodology used was adequate.

9.5 CONCLUSION

This chapter describes the development of a combined limb-PD-AFO model. The ratio of load between the PD-AFO and lower limb obtained from the model was compared to results from chapter 5 and was found to be within the experimental corridor. The model allowed for evaluation of joint loads and joint contact stresses in the limb with and without the PD-AFO. The normalised joint loads were reduced by, on average, 23% when wearing the PD-AFO compared to without, and the normalised joint contact stresses by 27%. Whilst the reduction in normalised loads, when wearing the PD-AFO compared to without, was fairly consistent across joints, the reduction in contact stresses varied more greatly. The normalised contact stresses at the subtalar joint were reduced by 42% with compared to without the PD-AFO. This suggests that the limitation of the ankle joint angle when wearing the PD-AFO may play an important role in reducing contact stresses, which have been linked to PTOA.

This model can now be used to study the influence of orthotic design on the internal loads of the foot, potentially fine tuning the device to achieve desired joint loads or contact stresses. The next chapter summarises the work undertaken in this thesis and offers possibilities for future work.

10 SUMMARY AND FUTURE WORK

This chapter summarises the work undertaken for this thesis. Future strategies to progress the research are also discussed. Finally, the chapter presents the major conclusions reached from this piece of work.

10.1 SUMMARY

The aim of this work was to characterise the mechanical response of the PD-AFO and understand how the PD-AFO alters the internal and external loading of the lower limb during gait. This was achieved using a combination of experimental analysis and FE modelling.

Following the prescription of the PD-AFO, literature has shown that the functional outcome of limb salvage patients had improved [20]. Studies have demonstrated the capability of the PD-AFO in preventing unwanted plantarflexion during the swing phase. Other hypothesised mechanisms of action, such as ESAR capabilities and offloading, whilst referred to in previous studies, were not directly evaluated.

Here, following the review of literature, the material behaviour of each component of the PD-AFO (specifically the Momentum) was established. Through both 4-point bending tests and axial compression tests, it was determined that the posterior struts could be approximated as isotropic, and linearly elastic with a Young's modulus of 35.2 ± 2.7 GPa. FE analysis was used to assess the assumption of transverse isotropy on the bending stiffness of the struts and carbon fibre layers; it was found to be negligible. Additionally, experimental compression tests were used to establish a material model for the foams used on the surfaces of the PD-AFO that make contact with the lower limb.

Finally, the material properties of the carbon fibre regions were established from the manufacturer and literature as no adequate samples were available. Again, FE analysis was used to assess the sensitivity of each material property value on the behaviour of the carbon fibre, and, where necessary, a range of material constants was defined. This is the first study, known to this author, to quantify the material behaviour of each component of this type of PD-AFO.

Following the establishment of the material properties of the components of the PD-AFO, the impact of the orthosis on gait was investigated. Using experimental gait analysis of a healthy subject allowed for a direct comparison of walking with and without the PD-AFO. This is the first body of work to evaluate how the PD-AFO changes the plantar force experienced by the lower limb during gait. It was shown that the PD-AFO reduced the load through the limb by up to 34%. The extent of offloading changed throughout the gait cycle, peaking during the early stance phase of the gait cycle and reducing as a percentage of total GRF throughout the remainder of the stance phase.

Additionally, this analysis supported previous findings that, when wearing the PD-AFO, the load was distributed across the plantar area of the foot in a different manner to gait when not wearing the PD-AFO, with the centre of pressure remaining more posterior [40]. This suggested that not only does the PD-AFO reduce the loading, but it also redirects which regions of the foot experienced load during the latter stance phase.

The ESAR characteristics of the posterior struts were also analysed, using an experimental 4-point bending test, demonstrating that the posterior struts had an efficiency of 97%. This is the first study to show that the posterior struts are capable of ESAR. A novel methodology was presented to quantify the power generated and dissipated by the PD-AFO's posterior struts, by analysing the strains throughout the gait cycle. By assuming the posterior struts acted, approximately, as a cantilever, the amount of energy stored within them at any one point in gait was calculated. The derivative of this with respect to time allowed the power to be calculated. During walking the maximum power generated by the PD-AFO was during late stance. The value recorded was 0.14 W/kg which was approximately 13-17% of the combined limb-PD-AFO propulsive power reported in literature. During running this increased to 0.59 W/kg; this was 14-19% of that recorded in literature. Additionally, the deflection of the struts during gait was quantified, providing detail of the mechanical response of the PD-AFO struts during gait.

Following on from the experimental analyses, the development of an FE model of the PD-AFO was described, with the material properties determined earlier within the thesis assigned to each component. The results from an experimental test on the PD-AFO and a simulation to mimic this test were compared and the FE simulation was considered to represent the behaviour of the PD-AFO well. The model was then used to simulate the mechanical response of the PD-AFO during early stance (at 10% of the gait cycle) and late stance (at 50% of the gait cycle). It was found that the posterior struts held the greatest proportion of the strain energy stored, indicating that the base of the PD-AFO has

very limited effect on the ESAR characteristics of the whole PD-AFO and does not act as a rotational spring as hypothesised.

The FE model was also used to perform a sensitivity study on design aspects of the PD-AFO. This provided insight into the small effect that the base material properties or shape have on the energy stored or rotational stiffness of the PD-AFO. This suggested that the general assumption that the IDEO and the Momentum behave in a similar manner is correct. The design aspects with the most significant influence on the rotational stiffness and energy stored in the posterior struts were the alignment and the stiffness of posterior struts.

The FE model of the PD-AFO was then combined with the model of the lower limb, but prior to this the development of the lower limb FE model was described. Previous FE models of lower limbs were reviewed to establish the most suitable simplifications for the desired model output whilst keeping computational cost to a minimum. The plantar pressure from the model when simulating gait analysis was compared to experimental values obtained during gait analyses and the ratio of mean plantar pressure observed in the hind foot region, and the midfoot and forefoot region, was found to be similar.

The lower limb model was then combined with the FE model of the PD-AFO. This is the first study, known to this author, to develop a combined model of a lower limb and AFO with 2 areas of contact where both are not glued. The model developed allowed changes in loading within the foot, specifically the loading path between bones and the contact stresses at joints, to be evaluated. The joint loads and mean contact normal stresses, normalised to the total force applied in the simulation, were compared with the lower limb when situated within the PD-AFO and when on its own. The reduction of normalised load in the joints was found to be similar across all joints, and was, on average, 23% lower when wearing the PD-AFO. The joint contact stresses were reduced by an average of 27% when not wearing the PD-AFO. Whilst the percentage reduction in normalised load across each joint was similar, the extent of reduction of the normalised joint contact stresses varied; the smallest reduction in contact stress, of 19%, was observed at the talonavicular joint and the greatest reduction, of 42%, was observed at the subtalar joint. The finding indicated that limitation in ankle joint angle may be an important design feature that influences contact stresses.

Overall, this thesis has characterised the mechanical response of the PD-AFO, both in terms of the behaviour of individual components and the mechanical behaviour of the PD-AFO, analysing strut deflection during gait and using FE analysis to quantify the rotational stiffness. Using the FE model of the PD-AFO, those design aspects most likely to alter the mechanical response of the PD-AFO were established. The experimental gait analysis demonstrated external changes in loading to the lower limb when walking with and without the PD-AFO, and determined the extent of off-loading that occurs. Additionally, the quantification of the ESAR characteristics, and the power generated and dissipated by the posterior struts during running and walking, provided understanding as to the extent of propulsive power that the PD-AFO provides. Finally, the comparison of the contact stresses and

loading pathways between the combined PD-AFO limb FE model and that of the lower limb model alone, allowed for quantification of how the PD-AFO changes the internal loading of the limb during early stance, at 10% of the gait cycle.

10.2 DISCUSSION AND FUTURE WORK

In this section the work undertaken in this thesis is discussed with suggestions made as to how to progress the work further.

The type of posterior strut characterised in chapter 4, were those used in the PD-AFO that is evaluated throughout this thesis. However, the same type of strut is not used for all prescriptions; orthotists have the option of assigning one of 3 strut types, based on patient weight and activity level at time of prescription. As such, other struts that are prescribed will have different behaviour and likely result in a different response of the PD-AFO. The computational design sensitivity of the PD-AFO suggested that the posterior struts had a large effect on the rotational stiffness and energy stored. By characterising each strut available for prescription, possible changes in the ESAR characteristics, along with the changes in the rotational stiffness of the PD-AFO, could be calculated. Additionally, an alternative design, such as the cuboidal struts used for gait analysis with the IDEO could be evaluated. Quantifying these differences in the struts will provide additional information for orthotists when prescribing the PD-AFO. For example, gait analysis of a patient may demonstrate a certain power deficit, and therefore a strut could be selected to account for this deficit.

Whilst the computational design sensitivity evaluated which components of the PD-AFO had the greatest impact on the mechanical response of the PD-AFO (specifically the energy stored within the posterior struts and on the rotational stiffness), the analysis did not evaluate how these changes altered the loading within the limb. The combined model developed later in the thesis could be utilised further, by altering the geometry and properties of the PD-AFO, guided by those changes identified in the sensitivity to have the greatest impact. This would allow one to determine how changes in the designs directly affect the internal loading. This process could be used as a tool to help the development of alternate PD-AFO designs, with the aim of increasing the cohort suitable for the prescription of the PD-AFO or help fine tune the design to set a specific patient target for a desired level of offloading or rotation of the limb. The ability to control the loading in the limb, could also provide wider benefits; the PD-AFO could be used as a recovery aid for patients, with medics able to set a desired loading range for bone healing.

The main body of the experimental gait analyses undertaken here was on a single subject walking with and without the PD-AFO. Running is one of the high-level activities that has been noted in the literature as part of the success of the PD-AFO. However, the use of one subject limited the analysis without the PD-AFO to walking gait only, as healthy subjects can have varied running gaits meaning it was not possible to establish a healthy running gait from one subject only. With offloading

demonstrated during walking with the PD-AFO, it would be beneficial to understand the offloading, if any, that occurs during running. To provide a comparison between running gait with and without the PD-AFO, a further study would need to be undertaken with additional healthy subjects to ensure that the variability in normal running gait is accounted for.

The use of a single, healthy subject for gait analysis, whilst allowing for a direct comparison of gait with and without the PD-AFO by removing variability introduced by using an injured cohort, does not provide the variability of the changes in gait observed when wearing the PD-AFO. It would be beneficial to undertake further gait studies to quantify the offloading that occurs during the gait of other subjects with the PD-AFO (either injured or healthy) using the method laid out in this thesis. This would allow evaluation of the variance of offloading observed across a cohort to understand whether it is consistent for all users and injury types. Evaluating the offloading experienced, in combination with the time a specific patient may spend wearing the PD-AFO could also provide insight into long term effects of use, for example the possibility of bone mineral density loss. Understanding the influence of the PD-AFO on long-term bone health would be important to the clinical and rehabilitation team, allowing them to adjust the PD-AFO prescription to minimise the negative effects of the offloading.

As mentioned above, due to the variance in healthy running gait, direct comparisons were not made between the healthy subject's normal running gait and PD-AFO running gait. However, as the PD-AFO running gait has been recorded to be fairly similar for all patients, in part due to the similar training received by patients, and in part due to the mechanical limitations imposed by the PD-AFO. As such, evaluation of the power generation and dissipation of the PD-AFO was quantified during both running and walking gait. The power of the PD-AFO alone was compared to the combined power of the PD-AFO and lower limb that was recorded in literature; using subject specific analysis of the combined limb-PD-AFO ankle power rather than using average values from literature (using reflective markers to measure joint angles and their derivatives), whilst also calculating the power generation of the posterior struts, would provide a more accurate relative contribution of the PD-AFO to gait. When analysed in more subjects this would allow the variation in relative propulsive power to be quantified. By analysing the propulsive power in combination with pathology and success of the PD-AFO, the variability could provide insight as to whether the extent of power generation by the PD-AFO is a possible reason some patients do not benefit from the PD-AFO. This is important in order to ensure that patients are directed to the most suitable treatment options as early as possible during their recovery.

The FE models developed here used the geometry of the same healthy subject whose gait was analysed experimentally. Whilst this provided the opportunity to compare results from the simulations to experimental data, the results may not be directly applicable across patients, in terms of both anthropometry and injury. To allow evaluation of loading for specific patients, one option would be to develop an averaged model of the lower limb and PD-AFO and scale it to represent the patient in

question [190]; this reduces the segmentation time and model development. The averaged model could be compared to gait using experimental corridors.

However, a generalised FE model would likely not allow comparison across patients, due to the large range of pathologies observed in patients prescribed the PD-AFO. Further development of the FE model could be undertaken to account for generalised pathologies observed in the cohort who were prescribed the PD-AFO. This could be used to evaluate differences in internal loading for different patient cohorts or functional deficits, including comparisons between cohorts for whom the PD-AFO does, and does not work.

To help progress towards the possibility of developing multiple patient specific models, further studies examining specific aspects of model development are needed. One example is the alignment of the PD-AFO and lower limb that was performed manually, preventing scalability to a wider patient cohort. It is not possible to scan both the lower limb and PD-AFO together, as the PD-AFO must be scanned using CT and the lower limb with MRI. Further work could develop a novel set-up within a gait laboratory to allow the movement of both the foot and the PD-AFO to be tracked. This could be used to define a relative rotation matrix allowing automation of the combination process, overcoming one of the hurdles to developing patient specific models. These data would also improve the accuracy of the current manual alignment process.

Alternatively, the combined PD-AFO-lower limb model developed in this thesis could be used to guide the boundary conditions of a new, smaller-scale model, similar to that developed by Anderson et al. that focusses on one major joint at a time (e.g. the talocrural and subtalar) [144]. The specific joint rotations and loads can be established from the combined limb-PD-AFO presented in this thesis and used as boundary conditions for smaller models. Whilst not patient specific, more representative geometry could be developed for different cohorts of patients due to the smaller model size.

Additionally, a smaller, single joint focussed model, with a faster run time, could allow a variety of injuries to be accounted for and the contact stresses established, though further research is needed to understand how injuries within the foot may result in changes such as alterations in bone geometry, cartilage thickness, ligament laxity, scarring and material properties.

Development of the FE model has allowed the changes in internal loading to be evaluated, and comparisons between the lower limb loads with and without the PD-AFO were made. However, FE modelling does not perfectly represent the real world, as demonstrated by the presence of discrepancies between the plantar pressures recorded experimentally during the gait analysis and those obtained from the FE simulation. One such example of this, was the pressure observed in the lateral region of the foot experimentally. Within the FE model this was not observed; the tibia was only considered to deviate from normal to the ground in the sagittal plane, which would not allow for the medio-lateral rotations causing lateral pressure. The floor within the FE simulation was rigid and flat, unlike the shoe worn during gait analysis. The compliance and shape of the shoe would result in different contact areas between the plantar aspect of the foot and the shoe. Additionally, the FE model

did not include all muscle forces, including those above the knee; these forces would likely change the contact area and therefore contact pressure between the foot and floor. However, the models were used to compare the normalised contact stresses of the lower limb with and without the PD-AFO. The relative, rather than absolute, comparison in values between the models, minimises the effect of FE simplifications and assumptions on the conclusions drawn.

Few studies have previously created such a detailed model of a PD-AFO and lower limb, and none that were found by this author created a combined model with 2 areas of contact that were not both glued. The computational analyses in this thesis were run as static simulations, to reduce the computational cost and complexity where possible. Therefore, only a single time point was modelled. In this thesis the point between the loading response and midstance phase, at 10% of the gait cycle, was chosen to be modelled; during the experimental gait analysis this was a point that experienced high offloading when wearing the PD-AFO. It would be beneficial to evaluate the changes in internal loading at other points in gait. The combined FE model, and the model of the lower limb alone, could be developed further to allow simulation of these points and compare the response to loading at these time points. This would allow understanding of the changes in internal loading throughout the gait cycle.

Additionally, as mentioned above, the ability to run with the PD-AFO is an important functional outcome, and so evaluating the changes to cartilage loading during running would be of interest. Further work could be undertaken to run simulations with the increased forces and rotations experienced during running; further simplifications of the model may need to be made such simulations possible. Understanding how the PD-AFO alters the internal loading during running may provide understanding as to why many patients were able to return to such a high-level activity, and why some were not.

To simplify the combined model, one of the areas of contact, between the calf and cuff, was modelled using springs. The simplification of the calf-to-cuff contact resulted in a similar split of loading between the limb and PD-AFO as seen during gait and expected deflections of the struts at the distal end; as such, it was considered suitable to evaluate the joint loads and contact stresses. However, the contact between the 2 bodies itself could be of interest. Due to the nature of traumatic injuries, patients often suffer comorbidities; the skin around the calf area may be of poor quality. Patients are advised to wear a long compression sock underneath the PD-AFO (so that the PD-AFO and skin do not make direct contact), and, anecdotally, this can be a point of irritation for the user. A combination of experimental analysis, evaluation of the pressures at the contact interface, and development of a new FE 3D meshed model of the calf and cuff region only, could provide understanding of the loading of the calf region at different points in gait. This could highlight comfort issues with the PD-AFO and provide a tool with which to guide the shape and design to suit specific patient's needs, similar to previous work seen with amputee stumps [191, 192].

During the FE simulations no medio-lateral forces were considered, and no transverse or coronal plane rotations were applied. It is common for gait studies to examine sagittal plane angles only, as the rotations in this plane are the greatest. It is thought, however, that the regions of the base of the PD-AFO that surround the ankle may limit rotations in all directions, so investigation into this could be of interest [36]. This would be difficult to achieve using visual gait kinematics, due to marker positioning and interference from the PD-AFO, along with not being able to resolve the relative change in angle (small rotations are seen in these planes) to give meaningful results [193]. The model created in this thesis could be developed further, by adjusting the simplified contact area between the exterior surfaces of the tibia and fibula, to allow evaluation of the non-sagittal plane angles.

Throughout the computational analyses undertaken in this thesis, neither the heel wedge nor the shoe were included. The actions of these components were considered to be adequately represented by simple computational elements, including glued contact and initial rotation. However, previous studies have demonstrated that the heel wedge has an effect on time-based gait metrics, such as time to peak centre of pressure velocity [60]. Whilst development of the FE model to perform dynamic simulations would allow for analysis of this component, experimental analyses may be easier as they are stand alone components and not integrated within the PD-AFO.

Throughout this thesis, the focus has been on one specific type of PD-AFO and its mechanisms of action. It could be beneficial to compare the energy stored and rotational stiffness of the PD-AFO that is the focus of this thesis, to other AFOs available on the market. This could be achieved by developing FE models of these products. Comparisons between the AFOs and the PD-AFO, when also viewed with outcome data, may provide opportunities to understand how the ESAR characteristics and rotational stiffness play important roles for different patient pathologies. It may also provide design insights, guiding alterations to the PD-AFO that would better suit certain pathologies. Additionally, the methods described to develop a combined FE model of the foot and ankle with the PD-AFO could be used to evaluate the internal joint loading introduced to the foot ankle when wearing other devices, such as sports shoes, air cast boot and exoskeletons.

10.3 CONCLUSIONS

This body of work developed computational models of a lower limb and PD-AFO, as well as performed experimental gait analysis on a healthy subject with and without the PD-AFO. The experimental studies demonstrated that the PD-AFO offloaded the foot throughout the gait cycle, with a reduction of up to 34%. Additionally, it was demonstrated that the PD-AFO's posterior struts provided propulsive power during both running and walking gait, accounting for between 14-19% of the combined limb-PD-AFO propulsive power.

The computational simulations were used to evaluate the difference in the relative joints loads of the lower limb during the early stance phase of gait, with and without the PD-AFO, finding an average

reduction of 23% across the joints when wearing the PD-AFO. Additionally, the greatest reduction in contact joint stress, of 42%, was observed at the subtalar joint when wearing the PD-AFO.

The methodology presented here can be used to study other instances of walking gait, running gait, and pathological gait. The combined model of the lower limb and PD-AFO can be used as a tool to evaluate lower limb loading for different pathologies or PD-AFO designs, and help in describing or fine tuning characteristics of orthotics to meet patients' needs.

11 REFERENCES

1. M.o.D, *Improvised Explosive Device (IED) events involving UK personnel on Op HERRICK in Helmand Province, Afghanistan 1 April 2009 to 30 November 2014*. 2016.
2. M.o.D, *Types of Injuries Sustained by UK Service Personnel on Op HERRICK in Afghanistan, 1 April 2006 to 30 November 2014*. 2016.
3. Ramasamy, A., et al., *The Modern "Deck-Slap" Injury- Calcaneal Blast Fractures From Vehicle Explosions*. J Trauma, 2011. **71**(6): p. 1694-1698.
4. Bennett, P.M., et al., *Salvage of Combat Hindfoot Fractures in 2003-2014 UK Military*. Foot & Ankle International, 2017. **38**(7): p. 745-751.
5. Ramasamy, M.A.M.A.M.D.R., et al., *Outcomes of IED Foot and Ankle Blast Injuries*. Journal of Bone & Joint Surgery - American Volume, 2013. **95**(5): p. e25.
6. Bosse , M.J., et al., *An Analysis of Outcomes of Reconstruction or Amputation after Leg-Threatening Injuries*. New England Journal of Medicine, 2002. **347**(24): p. 1924-1931.
7. Doukas, C.O.L.W.C.M.D., et al., *The Military Extremity Trauma Amputation/Limb Salvage (METALS) Study: Outcomes of Amputation Versus Limb Salvage Following Major Lower-Extremity Trauma*. Journal of Bone & Joint Surgery - American Volume, 2013. **95**(2): p. 138-145.
8. Shawen, S.B., et al., *The Mangled Foot and Leg: Salvage Versus Amputation*. Foot and Ankle Clinics, 2010. **15**(1): p. 63-75.
9. Dagum, A., et al., *Salvage after Severe Lower-Extremity Trauma: Are the Outcomes Worth the Means?* Plast Reconstr Surg, 1999. **103**(4): p. 1212-1220.
10. Georgiadis, G., et al., *Open tibial fractures with severe soft-tissue loss. Limb salvage compared with below-the-knee amputation*. J Bone Joint Surg Am, 1993. **75**(10): p. 1431-1441.
11. Hertel, R., N. Strebel, and R. Ganz, *Amputation Versus Reconstruction in Traumatic Defects of the Leg: Outcome and Costs*. J Orthop Trauma, 1996. **10**(4): p. 223-229.
12. Penn-Barwell, J.G., *Outcomes in lower limb amputation following trauma: A systematic review and meta-analysis*. Injury, 2011. **42**(12): p. 1474-1479.
13. MacKenzie, E. and M. Bosse, *Factors Influencing Outcome Following Limb-Threatening Lower Limb Trauma: Lessons Learned From the Lower Extremity Assessment Project (LEAP)*. J Am Acad Orthop Surg, 2006. **14**(10): p. S205-S210.

14. MacKenzie, E.J.P., et al., *Long-Term Persistence of Disability Following Severe Lower-Limb Trauma: Results of a Seven-Year Follow-up*. Journal of Bone & Joint Surgery - American Volume, 2005. **87**(8): p. 1801-1809.
15. Sheean, A., C. Krueger, and J. Hsu, *Return to Duty and Disability After Combat-Related Hindfoot Injury*. J Orthop Trauma, 2014. **28**(11): p. e258-e262.
16. MacKenzie, E., et al., *Health-Care Costs Associated with Amputation or Reconstruction of a Limb-Threatening Injury*. J Bone Joint Surg Am, 2007. **89**(8): p. 1685-1692.
17. Patzkowski, J., et al., *Can an ankle-foot orthosis change hearts and minds?* Vol. 20. 2011. 8-18.
18. Patzkowski, J., et al., *Comparative Effect of Orthosis Design on Functional Performance*. J Bone Joint Surg Am, 2012. **94**(6): p. 507-515.
19. Stinner, D., et al., *Prevalence of Late Amputations During the Current Conflicts in Afghanistan and Iraq*. Vol. 175. 2010. 1027-9.
20. Blair, J., et al., *Return to Duty After Integrated Orthotic and Rehabilitation Initiative*. J Orthop Trauma, 2014. **28**(4): p. e70-e74.
21. Bedigrew, K.M., et al., *Can an Integrated Orthotic and Rehabilitation Program Decrease Pain and Improve Function After Lower Extremity Trauma?* Clinical Orthopaedics and Related Research®, 2014. **472**(10): p. 3017-3025.
22. Sheean, A.J., et al., *Effect of Custom Orthosis and Rehabilitation Program on Outcomes Following Ankle and Subtalar Fusions*. Foot & Ankle International, 2016. **37**(11): p. 1205-1210.
23. Gray, H., *Gray's Anatomy of the Human Body*. 1918.
24. Richard L. Drake, A.W.V., Adam W.M. Mitchell *Gray's Anatomy for Students*. 2014.
25. Balazs, G.C., et al., *High seas to high explosives: the evolution of calcaneus fracture management in the military*. Mil Med, 2014. **179**(11): p. 1228-35.
26. Lusardi, M.M., M. Jorge, and C.C. Nielsen, *Orthotics and Prosthetics in Rehabilitation*. 2012: Elsevier Health Sciences.
27. Wu, G., et al., *ISB recommendation on definitions of joint coordinate system of various joints for the reporting of human joint motion—part I: ankle, hip, and spine*. Journal of Biomechanics, 2002. **35**(4): p. 543-548.
28. Tweed, J.L., et al., *The function of the midtarsal joint: A review of the literature*. The Foot, 2008. **18**(2): p. 106-112.
29. Whittle, M.W., *Gait analysis : an introduction* 2007.
30. Standards, B., *BS ISO 29783-1:2008: Prosthetics and orthotics. Vocabulary. Normal gait*. 2009.
31. Standards, B., *BS ISO 29783-3:2016: Prosthetics and orthotics. Vocabulary. Pathological gait (excluding prosthetic gait)*. 2016.
32. Edelstein, J. and A. Moroz, *Lower-Limb Prosthetics and Orthotics: Clinical Concepts*. 2010, Thorofare.
33. Arch, E.S., S.J. Stanhope, and J.S. Higginson, *Passive-dynamic ankle-foot orthosis replicates soleus but not gastrocnemius muscle function during stance in gait: Insights for orthosis prescription*. Prosthetics and Orthotics International, 2015. **40**(5): p. 606-616.
34. Faustini, M.C., et al., *Manufacture of Passive Dynamic Ankle-Foot Orthoses Using Selective Laser Sintering*. IEEE Transactions on Biomedical Engineering, 2008. **55**(2): p. 784-790.
35. Owens, J., et al., *Return to Running and Sports Participation After Limb Salvage*. J Trauma, 2011. **71**(1): p. S120-S124.
36. Bennett, N., *Measuring the functional and clinical effectiveness of a passive dynamic ankle foot orthosis when used to rehabilitate complex limb salvage post lower limb blast trauma, in School of Health and Society*. 2020, University of Salford.
37. Potter, B.K., et al., *Multisite Evaluation of a Custom Energy-Storing Carbon Fiber Orthosis for Patients with Residual Disability After Lower-Limb Trauma*. JBJS, 2018. **100**(20): p. 1781-1789.
38. Brown, S.E., E. Russell Esposito, and J.M. Wilken, *The effect of ankle foot orthosis alignment on walking in individuals treated for traumatic lower extremity injuries*. Journal of Biomechanics, 2017. **61**(Supplement C): p. 51-57.

39. Ranz, E.C., et al., *The influence of passive-dynamic ankle-foot orthosis bending axis location on gait performance in individuals with lower-limb impairments*. *Clinical Biomechanics*, 2016. **37**: p. 13-21.
40. Stewart, J.P.T.D.P.T., et al., *Plantar Pressure Changes with Use of an Intrepid Dynamic Exoskeletal Orthosis*. *JPO Journal of Prosthetics & Orthotics*, 2020. **32**(1): p. 59-64.
41. Ladlow, P., et al., *Passive-dynamic ankle-foot orthosis improves medium-term clinical outcomes after severe lower extremity trauma*. *Journal of the Royal Army Medical Corps*, 2019. **165**(5): p. 330-337.
42. Melcer, T., et al., *A Comparison of Four-Year Health Outcomes following Combat Amputation and Limb Salvage*. *PLOS ONE*, 2017. **12**(1): p. e0170569.
43. Covey, D.C., *Conversion From Limb Salvage to Late Amputation: Lessons Learned From Recent Battlefields With Application to Civilian Trauma*. *J Surg Orthop Adv*, 2015. **24**(3): p. 170-3.
44. van der Merwe, L., et al., *Functional and psychological outcomes of delayed lower limb amputation following failed lower limb reconstruction*. *Injury*. **47**(8): p. 1756-1760.
45. Krueger, C.A., et al., *Late amputation may not reduce complications or improve mental health in combat-related, lower extremity limb salvage patients*. *Injury*, 2015. **46**(8): p. 1527-1532.
46. Jason Highsmith, M., et al., *Outcomes Associated With the Intrepid Dynamic Exoskeletal Orthosis (IDEO): A Systematic Review of the Literature*. Vol. 181. 2016. 69-76.
47. Claydon, J.H., L. Robinson, and S.E. Aldridge, *Patients' perceptions of repair, rehabilitation and recovery after major orthopaedic trauma: a qualitative study*. *Physiotherapy*, 2017. **103**(3): p. 322-329.
48. Ellington, J.K.M.D.M.S., et al., *The Mangled Foot and Ankle: Results From a 2-Year Prospective Study*. *Journal of Orthopaedic Trauma*, 2013. **27**(1): p. 43-48.
49. Hill, O., et al., *Descriptive Characteristics and Amputation Rates With Use of Intrepid Dynamic Exoskeleton Orthosis*. Vol. 181. 2016. 77-80.
50. Ikeda, A.J., J.R. Ferguson, and J.M. Wilken, *Clinical Outcomes with the Intrepid Dynamic Exoskeletal Orthosis: A Retrospective Analysis*. *Military Medicine*, 2019.
51. Patzkowski, J., et al., *Management of Posttraumatic Osteoarthritis With an Integrated Orthotic and Rehabilitation Initiative*. *J Am Acad Orthop Surg*, 2012. **20**: p. S48-S53.
52. Russell Esposito, E., K.A. Schmidbauer, and J.M. Wilken, *Experimental comparisons of passive and powered ankle-foot orthoses in individuals with limb reconstruction*. *J Neuroeng Rehabil*, 2018. **15**(1): p. 111.
53. Schmidbauer, K.A., E. Russell Esposito, and J.M. Wilken, *Ankle-foot orthosis alignment affects running mechanics in individuals with lower limb injuries*. *Prosthetics and Orthotics International*, 2019. **43**(3): p. 316-324.
54. Russell Esposito, E., et al., *Ankle-foot orthosis bending axis influences running mechanics*. *Gait & Posture*, 2017. **56**(Supplement C): p. 147-152.
55. Haight, D.J., E. Russell Esposito, and J.M. Wilken, *Biomechanics of uphill walking using custom ankle-foot orthoses of three different stiffnesses*. *Gait & Posture*, 2015. **41**(3): p. 750-756.
56. Russell Esposito, E., et al., *How Does Ankle-foot Orthosis Stiffness Affect Gait in Patients With Lower Limb Salvage?* *Clinical Orthopaedics and Related Research®*, 2014. **472**(10): p. 3026-3035.
57. Russell Esposito, E., et al., *Gait biomechanics following lower extremity trauma: Amputation vs. reconstruction*. *Gait & Posture*, 2017. **54**(Supplement C): p. 167-173.
58. Russell Esposito, E., et al., *Biomechanical response to ankle-foot orthosis stiffness during running*. *Clinical Biomechanics*, 2015. **30**(10): p. 1125-1132.
59. Stewart, J., et al., *Plantar Pressure Changes with Use of an Intrepid Dynamic Exoskeletal Orthosis*. *JPO*, 2019.
60. Ikeda, A.J., J.R. Ferguson, and J.M. Wilken, *Effects of altering heel wedge properties on gait with the Intrepid Dynamic Exoskeletal Orthosis*. *Prosthetics and Orthotics International*, 2017: p. 0309364617728116.

61. Aldridge Whitehead, J.M., E. Russell Esposito, and J.M. Wilken, *Stair ascent and descent biomechanical adaptations while using a custom ankle-foot orthosis*. Journal of Biomechanics, 2016. **49**(13): p. 2899-2908.
62. Mangan, K.I., et al., *Limb Salvage With Intrepid Dynamic Exoskeletal Orthosis Versus Transtibial Amputation: A Comparison of Functional Gait Outcomes*. Journal of Orthopaedic Trauma, 2016. **30**(12): p. e390-e395.
63. Wach, A., et al., *Assessment of Mechanical Characteristics of Ankle-Foot Orthoses*. Journal of Biomechanical Engineering, 2018. **140**(7).
64. Harper, N.G., et al., *Selective Laser Sintered Versus Carbon Fiber Passive-Dynamic Ankle-Foot Orthoses: A Comparison of Patient Walking Performance*. Journal of Biomechanical Engineering, 2014. **136**(9): p. 091001-091001-7.
65. Harper, N.G., et al., *The influence of ankle-foot orthosis stiffness on walking performance in individuals with lower-limb impairments*. Clinical Biomechanics, 2014. **29**(8): p. 877-884.
66. Hsu, J., et al., *Patient Response to an Integrated Orthotic and Rehabilitation Initiative for Traumatic Injuries: The PRIORITI-MTF Study*. J Orthop Trauma, 2017. **31**: p. S56-S62.
67. Sevenois, R.D.B., et al., *Multiscale approach for identification of transverse isotropic carbon fibre properties and prediction of woven elastic properties using ultrasonic identification*. Composites Science and Technology, 2018. **168**: p. 160-169.
68. Stier, B., J.-W. Simon, and S. Reese, *Numerical and experimental investigation of the structural behavior of a carbon fiber reinforced ankle-foot orthosis*. Medical Engineering & Physics, 2015. **37**(5): p. 505-511.
69. *Displacements, Strains, and Stresses*, in *Mechanics of Composite Structures*, G.S. Springer and L.P. Kollár, Editors. 2003, Cambridge University Press: Cambridge. p. 3-62.
70. Lomov, S.V., et al., *Full-field strain measurements for validation of meso-FE analysis of textile composites*. Composites Part A: Applied Science and Manufacturing, 2008. **39**(8): p. 1218-1231.
71. Foroutan, R., et al., *Experimental investigation of high strain-rate behaviour of fabric composites*. Composite Structures, 2013. **106**: p. 264-269.
72. Matveev, M.Y., et al., *Effects of layer shift and yarn path variability on mechanical properties of a twill weave composite*. Journal of Composite Materials, 2016. **51**(7): p. 913-925.
73. MatWeb. *Solvay CYCOM® 759F Epoxy - 2X2 Twill Fabric Reinforced Prepreg Datasheet*. [cited 2020 27/11]; Available from: <http://www.matweb.com/search/DataSheet.aspx?MatGUID=df019b4bea0344b18f29b0fd27524978>.
74. MatWeb. *Toray G-85FR Prepreg Laminate with T300B-3K-40B Fiber 2X2 TWILL AT 204 g/m2 FAW AND 42% RC Datasheet*. [cited 2020 27/11]; Available from: <http://www.matweb.com/search/DataSheet.aspx?MatGUID=7fe388a0b03e497b8d95773b3ad90a14>.
75. MatWeb. *Toray G-85FR Prepreg Laminate with T700S-12K-60E Fiber 2X2 TWILL AT 665 g/m2 FAW AND 36% RC Datasheet*. [cited 2020 27/11]; Available from: <http://www.matweb.com/search/DataSheet.aspx?MatGUID=e4b3023b23fe46afb5a843ed6c5c2786>.
76. MatWeb. *Solvay CYCOM® 950-1 Epoxy Prepreg with 52% 285 Kevlar Fabric Datasheet*. [cited 2020 27/11]; Available from: <http://www.matweb.com/search/DataSheet.aspx?MatGUID=9f211bd60c6644a5bd449239ffdb a443>.
77. MatWeb. *Arlon Electronic Materials 45NK Woven Kevlar® Reinforced Laminate and Prepreg Datasheet*. [cited 2020 27/11]; Available from: <http://www.matweb.com/search/DataSheet.aspx?MatGUID=accc6aafb7cf435a8a50ebfeb7a29c88&ckck=1>.
78. Wu, W., Q. Wang, and W. Li, *Comparison of Tensile and Compressive Properties of Carbon/Glass Interlayer and Intralayer Hybrid Composites*. Materials, 2018. **11**(7): p. 1105.
79. Yan, X., et al., *A study of energy dissipating mechanisms in orthogonal cutting of UD-CFRP composites*. Composite Structures, 2019. **220**: p. 460-472.

80. MSC.Software. <https://www.mscsoftware.com/resources-white-papers/nonlinear-finite-element-analysis-elastomers>. 2020 [cited 2020 08/09/2020].
81. Larson, K., *Can You Estimate Modulus From Durometer Hardness for Silicones?*, T.D.C. Company, Editor. 2019.
82. Folmar, E., H. Jennings, and M.M. Lusardi, *9 - Principles of Lower Extremity Orthoses, in Orthotics and Prosthetics in Rehabilitation (Fourth Edition)*, K.K. Chui, et al., Editors. 2020, Elsevier: St. Louis (MO). p. 220-258.
83. Limited, B. *Momentum Offload Brace*. 2020 [cited 2021 18/05]; Available from: <https://www.blatchford.co.uk/products/momentum-offloading-brace/>.
84. Owen, E., *The importance of being earnest about shank and thigh kinematics especially when using ankle-foot orthoses*. Prosthet Orthot Int, 2010. **34**(3): p. 254-69.
85. Kearney, R.S., et al., *In-Shoe Plantar Pressures Within Ankle-Foot Orthoses: Implications for the Management of Achilles Tendon Ruptures*. The American Journal of Sports Medicine, 2011. **39**(12): p. 2679-2685.
86. Khoury, M., et al., *Foot Center of Pressure Trajectory Alteration by Biomechanical Manipulation of Shoe Design*. Foot & Ankle International, 2013. **34**(4): p. 593-598.
87. Aerts, W., et al., *Validation of plantar pressure simulations using finite and discrete element modelling in healthy and diabetic subjects*. Computer Methods in Biomechanics and Biomedical Engineering, 2017. **20**(13): p. 1442-1452.
88. Almeida, M.O., I.S. Davis, and A.D. Lopes, *Biomechanical Differences of Foot-Strike Patterns During Running: A Systematic Review With Meta-analysis*. The journal of orthopaedic and sports physical therapy, 2015. **45**(10): p. 738-755.
89. Estep, A., et al., *Differences in pattern of variability for lower extremity kinematics between walking and running*. Gait & Posture, 2018. **60**: p. 111-115.
90. Takahashi, K.Z. and S.J. Stanhope, *Mechanical energy profiles of the combined ankle-foot system in normal gait: Insights for prosthetic designs*. Gait & Posture, 2013. **38**(4): p. 818-823.
91. Hafner, B.J., et al., *Trans tibial energy-storage-and-return prosthetic devices: a review of energy concepts and a proposed nomenclature*. J Rehabil Res Dev, 2002. **39**(1): p. 1-11.
92. Bregman, D.J.J., et al., *The effect of ankle foot orthosis stiffness on the energy cost of walking: A simulation study*. Clinical Biomechanics, 2011. **26**(9): p. 955-961.
93. Wiggin, M.B., G.S. Sawicki, and S.H. Collins. *An exoskeleton using controlled energy storage and release to aid ankle propulsion*. in *2011 IEEE International Conference on Rehabilitation Robotics*. 2011.
94. Zou, D., et al., *Experimental and computational analysis of composite ankle-foot orthosis*. Journal of rehabilitation research and development, 2014. **51**(10): p. 1525-1536.
95. Rigney, S.M., A. Simmons, and L. Kark, *Mechanical characterization and comparison of energy storage and return prostheses*. Medical Engineering & Physics, 2017. **41**: p. 90-96.
96. Rigney, S., A. Simmons, and L. Kark, *Energy Storage and Return Prostheses: A Review of Mechanical Models*. Crit Rev Biomed Eng, 2016. **44**(4): p. 269-292.
97. Nolan, L., *Carbon fibre prostheses and running in amputees: A review*. Foot and Ankle Surgery, 2008. **14**(3): p. 125-129.
98. Gardiner, J., et al., *Trans tibial amputee gait efficiency: Energy storage and return versus solid ankle cushioned heel prosthetic feet*. J Rehabil Res Dev, 2016. **53**(6): p. 1133-1138.
99. Beck, O.N., P. Taboga, and A.M. Grabowski, *Characterizing the Mechanical Properties of Running-Specific Prostheses*. PloS one, 2016. **11**(12): p. e0168298-e0168298.
100. Dufek, J.S., et al., *Functional and dynamic response characteristics of a custom composite ankle foot orthosis for Charcot-Marie-Tooth patients*. Gait & Posture, 2014. **39**(1): p. 308-313.
101. Chen, R.K., et al., *Additive manufacturing of personalized ankle-foot orthosis*. Transactions of the North American Manufacturing Research Institution of SME, 2014. **42**: p. 381-389.
102. Ielapi, A., M. Forward, and M. De Beule, *Computational and experimental evaluation of the mechanical properties of ankle foot orthoses: A literature review*. Prosthetics and Orthotics International, 2019: p. 0309364618824452.

103. Ielapi, A., et al., *A validated computational framework to evaluate the stiffness of 3D printed ankle foot orthoses*. Computer Methods in Biomechanics and Biomedical Engineering, 2019. **22**(8): p. 880-887.
104. Kobayashi, T., A.K. Leung, and S.W. Hutchins, *Techniques to measure rigidity of ankle-foot orthosis: a review*. J Rehabil Res Dev, 2011. **48**(5): p. 565-76.
105. Schrank, E.S., et al., *Assessment of a Virtual Functional Prototyping Process for the Rapid Manufacture of Passive-Dynamic Ankle-Foot Orthoses*. Journal of Biomechanical Engineering, 2013. **135**(10).
106. Amerinatanzi, A., et al., *Application of the Superelastic NiTi Spring in Ankle Foot Orthosis (AFO) to Create Normal Ankle Joint Behavior*. Bioengineering (Basel, Switzerland), 2017. **4**(4): p. 95.
107. Ielapi, A., et al., *A novel experimental setup for evaluating the stiffness of ankle foot orthoses*. BMC Research Notes, 2018. **11**(1): p. 649.
108. Lee, Y.-S., et al., *A STUDY ON THE STRUCTURAL STRESS ANALYSIS OF PLASTIC ANKLE FOOT ORTHOSIS (AFO) UNDER DORSIFLEXION AND PLANTARFLEXION CONDITIONS*. International Journal of Modern Physics B, 2006. **20**(25n27): p. 4559-4564.
109. Syngellakis, S. and M. Arnold, *Modelling considerations in finite element analyses of ankle foot orthoses*. Vol. 160. 2012. 183-194.
110. Syngellakis, S., M.A. Arnold, and H. Rassoulian, *Assessment of the non-linear behaviour of plastic ankle foot orthoses by the finite element method*. Proceedings of the Institution of Mechanical Engineers, Part H (Journal of Engineering in Medicine), 2000. **214**(H5): p. 527-39.
111. Darwich, A., et al., *Ankle-foot orthosis design between the tradition and the computerized perspectives*. The International Journal of Artificial Organs, 2019. **43**(5): p. 354-361.
112. Kobayashi, T., et al., *Design of an automated device to measure sagittal plane stiffness of an articulated ankle-foot orthosis*. Prosthet Orthot Int, 2010. **34**(4): p. 439-48.
113. DeToro, W., *Plantarflexion Resistance of Selected Ankle-Foot Orthoses: A Pilot Study of Commonly Prescribed Prefabricated and Custom-Molded Alternatives*. JPO, 2001. **13**(2): p. 39-44.
114. Novacheck, T., et al., *Quantifying the Spring-Like Properties of Ankle-Foot Orthoses (AFOs)*. JPO, 2007. **19**(4): p. 98-103.
115. Bregman, D.J.J., et al., *A new method for evaluating ankle foot orthosis characteristics: BRUCE*. Gait & Posture, 2009. **30**(2): p. 144-149.
116. Nagaya, M., *Shoehorn-type ankle-foot orthoses: Prediction of flexibility*. Archives of Physical Medicine and Rehabilitation, 1997. **78**(1): p. 82-84.
117. Ringleb, S., et al., *Stiffness of the Arizona Ankle-Foot Orthosis Before and After Modification for Gait Analysis*. JPO, 2009. **21**(4): p. 204-207.
118. Cappa, P., F. Patanè, and M.M. Pierro, *A Novel Device to Evaluate the Stiffness of Ankle-Foot Orthosis Devices*. Journal of Biomechanical Engineering, 2004. **125**(6): p. 913-917.
119. Cappa, P., F. Patanè, and G. Di Rosa, *A Continuous Loading Apparatus for Measuring Three-dimensional Stiffness of Ankle-Foot Orthoses*. Journal of Biomechanical Engineering, 2005. **127**(6): p. 1025-1029.
120. Bielby, S., et al., *Trimline Severity Significantly Affects Rotational Stiffness of Ankle-Foot Orthosis*. JPO, 2010. **22**(4): p. 204-210.
121. Klasson, B., P. Convery, and S. Raschke, *Test apparatus for the measurement of the flexibility of ankle-foot orthoses in planes other than the loaded plane*. Prosthetics and Orthotics International, 1998. **22**(1): p. 45-53.
122. Schön, J., *Coefficient of friction for aluminum in contact with a carbon fiber epoxy composite*. Tribology International, 2004. **37**(5): p. 395-404.
123. Owen, E., S. Fatone, and A. Hansen, *Effect of walking in footwear with varying heel sole differentials on shank and foot segment kinematics*. Prosthetics and Orthotics International, 2017. **42**(4): p. 394-401.
124. Totah, D., et al., *The impact of ankle-foot orthosis stiffness on gait: A systematic literature review*. Gait Posture, 2019. **69**: p. 101-111.

125. Anderson, D.D., et al., *Is elevated contact stress predictive of post-traumatic osteoarthritis for imprecisely reduced tibial plafond fractures?* J Orthop Res, 2011. **29**(1): p. 33-9.
126. Kraeutler, M.J., et al., *Peculiarities in Ankle Cartilage*. CARTILAGE, 2016. **8**(1): p. 12-18.
127. Martin, J.A., et al., *Complementary models reveal cellular responses to contact stresses that contribute to post-traumatic osteoarthritis*. J Orthop Res, 2017. **35**(3): p. 515-523.
128. Wan, L., et al., *In vivo cartilage contact deformation of human ankle joints under full body weight*. J Orthop Res, 2008. **26**(8): p. 1081-1089.
129. Cheung, J.T.-M., et al., *Three-dimensional finite element analysis of the foot during standing—a material sensitivity study*. Journal of Biomechanics, 2005. **38**(5): p. 1045-1054.
130. Guiotto, A., et al., *3D finite element model of the diabetic neuropathic foot: A gait analysis driven approach*. Journal of Biomechanics, 2014. **47**(12): p. 3064-3071.
131. Akrami, M.Q., Zhihui ; Zou, Zhenmin ; Howard, David; Nester, Christopher J. ; Ren, Lei, *Subject-Specific Finite Element Modelling of the Human Foot Complex during Walking: Sensitivity Analysis of Material Properties, Boundary and Loading Conditions*. biomechanics and modeling in mechanobiology, 2017. **17**: p. 559-576.
132. Cheung, J.T.-M. and M. Zhang, *A 3-dimensional finite element model of the human foot and ankle for insole design*. Archives of Physical Medicine and Rehabilitation, 2005. **86**(2): p. 353-358.
133. Wang, Y., et al., *Finite element analysis of biomechanical effects of total ankle arthroplasty on the foot*. Journal of Orthopaedic Translation, 2018. **12**: p. 55-65.
134. Chen, W.-P., F.-T. Tang, and C.-W. Ju, *Stress distribution of the foot during mid-stance to push-off in barefoot gait: a 3-D finite element analysis*. Clinical Biomechanics, 2001. **16**(7): p. 614-620.
135. Antunes, P., et al., *Non-Linear Finite Element Modelling of Anatomically Detailed 3D Foot Model*. 2008.
136. Qiu, T.-X., et al., *Finite element modeling of a 3D coupled foot–boot model*. Medical Engineering & Physics, 2011. **33**(10): p. 1228-1233.
137. Spyrou, L.A. and N. Aravas, *Muscle-driven finite element simulation of human foot movements*. Computer Methods in Biomechanics and Biomedical Engineering, 2012. **15**(9): p. 925-934.
138. Beimers, L., et al., *In-vivo range of motion of the subtalar joint using computed tomography*. Journal of Biomechanics, 2008. **41**(7): p. 1390-1397.
139. Li, S., et al., *Stress distribution of metatarsals during forefoot strike versus rearfoot strike: A finite element study*. Computers in Biology and Medicine, 2017. **91**: p. 38-46.
140. Chen, T.L.-W., et al., *Foot arch deformation and plantar fascia loading during running with rearfoot strike and forefoot strike: A dynamic finite element analysis*. Journal of Biomechanics, 2019. **83**: p. 260-272.
141. Wang, Y., Z. Li, and M. Zhang, *Biomechanical study of tarsometatarsal joint fusion using finite element analysis*. Medical Engineering & Physics, 2014. **36**(11): p. 1394-1400.
142. Cheung, J.T.-M., M. Zhang, and K.-N. An, *Effect of Achilles tendon loading on plantar fascia tension in the standing foot*. Clinical Biomechanics, 2006. **21**(2): p. 194-203.
143. Behforootan, S., et al., *Finite element modelling of the foot for clinical application: A systematic review*. Medical Engineering & Physics, 2017. **39**: p. 1-11.
144. Anderson, D.D., et al., *Physical validation of a patient-specific contact finite element model of the ankle*. Journal of Biomechanics, 2007. **40**(8): p. 1662-1669.
145. Gefen, A., et al., *Biomechanical Analysis of the Three-Dimensional Foot Structure During Gait: A Basic Tool for Clinical Applications*. Journal of Biomechanical Engineering, 2000. **122**(6): p. 630-639.
146. Chen, Y.-N., et al., *Finite Element Analysis of Plantar Fascia During Walking*. Foot & Ankle International, 2014. **36**(1): p. 90-97.
147. Beaugonin, M., E. Haug, and D. Cesari, *Improvement of Numerical Ankle/Foot Model: Modeling of Deformable Bone*. 1997, SAE International. p. 3742-3754.
148. Brilakis, E., et al., *Effects of Foot Posture on Fifth Metatarsal Fracture Healing: A Finite Element Study*. The Journal of Foot and Ankle Surgery, 2012. **51**(6): p. 720-728.

149. Campanelli, V., et al., *Three-dimensional morphology of heel fat pad: an in vivo computed tomography study*. Journal of anatomy, 2011. **219**(5): p. 622-631.
150. Chen, W.-M., et al., *Effects of internal stress concentrations in plantar soft-tissue—A preliminary three-dimensional finite element analysis*. Medical Engineering & Physics, 2010. **32**(4): p. 324-331.
151. Goff, J.D. and R. Crawford, *Diagnosis and treatment of plantar fasciitis*. Am Fam Physician, 2011. **84**(6): p. 676-82.
152. McKeon, P.O., et al., *The foot core system: a new paradigm for understanding intrinsic foot muscle function*. British Journal of Sports Medicine, 2015. **49**(5): p. 290.
153. O'Brien, M., *The Anatomy of the Achilles Tendon*. Foot and Ankle Clinics, 2005. **10**(2): p. 225-238.
154. Taha, Z., et al., *A Finite Element Analysis of a Human Foot Model to Simulate Neutral Standing on Ground*. Procedia Engineering, 2016. **147**(Supplement C): p. 240-245.
155. Chen, W.-M., et al., *Role of gastrocnemius–soleus muscle in forefoot force transmission at heel rise — A 3D finite element analysis*. Journal of Biomechanics, 2012. **45**(10): p. 1783-1789.
156. Soysa, A., et al., *Importance and challenges of measuring intrinsic foot muscle strength*. Journal of Foot and Ankle Research, 2012. **5**(1): p. 29.
157. Simkin, A., *Structural analysis of the human foot in standing posture*. 1980.
158. Wibawa, A.D., et al., *Musculoskeletal modeling of human lower limb during normal walking, one-legged forward hopping and side jumping: Comparison of measured EMG and predicted muscle activity patterns*. Journal of Biomechanics, 2016. **49**(15): p. 3660-3666.
159. S. Florio, C. and K. A. Narh, *Development of a modeling technique for the investigation of muscle activity and its effect on bone stresses in the human leg during an isometric exercise*. SIMULATION, 2011. **87**(4): p. 313-333.
160. Tao, K., et al., *An In Vivo Experimental Validation of a Computational Model of Human Foot*. Journal of Bionic Engineering, 2009. **6**(4): p. 387-397.
161. Erdemir, A., et al., *An inverse finite-element model of heel-pad indentation*. Journal of Biomechanics, 2006. **39**(7): p. 1279-1286.
162. Chokhandre, S., et al., *A three-dimensional inverse finite element analysis of the heel pad*. Journal of biomechanical engineering, 2012. **134**(3): p. 031002-031002.
163. Isvilanonda, V., et al., *Hyperelastic compressive mechanical properties of the subcalcaneal soft tissue: An inverse finite element analysis*. Journal of Biomechanics, 2016. **49**(7): p. 1186-1191.
164. Hofstede, D.J., M.J.P.F. Ritt, and K.E. Bos, *Tarsal autografts for reconstruction of the scapholunate interosseous ligament: A biomechanical study*. The Journal of Hand Surgery, 1999. **24**(5): p. 968-976.
165. Funk, J.R., et al., *Linear and Quasi-Linear Viscoelastic Characterization of Ankle Ligaments*. Journal of Biomechanical Engineering, 1999. **122**(1): p. 15-22.
166. Kitaoka, H.B., et al., *Material Properties of the Plantar Aponeurosis*. Foot & Ankle International, 1994. **15**(10): p. 557-560.
167. Corazza, F., et al., *Ligament fibre recruitment and forces for the anterior drawer test at the human ankle joint*. Journal of Biomechanics, 2003. **36**(3): p. 363-372.
168. Grigoriadis, G., *Heel Biomechanics Under Blast Conditions*, in Department of Bioengineering. 2016, Imperial College London.
169. Shin, J., N. Yue, and C.D. Untaroiu, *A Finite Element Model of the Foot and Ankle for Automotive Impact Applications*. Annals of Biomedical Engineering, 2012. **40**(12): p. 2519-2531.
170. Brockett, C.L. and G.J. Chapman, *Biomechanics of the ankle*. Orthopaedics and Trauma, 2016. **30**(3): p. 232-238.
171. Pictures, P. *Anatomy.tv*. 2021 [09/03/2021]; Available from: https://www.anatomy.tv/anatomytv/html5ui_2018/#/product/har_foot_2014/type/Text%20articles/id/39344/layer/5/angle/26/structureID/571420.
172. Mkandawire, C., et al., *Foot and ankle ligament morphometry*. J Rehabil Res Dev, 2005. **42**(6): p. 809-20.

173. Imhauser, C.W., *The development and evaluation of a three-dimensional, image-based, patient-specific, dynamic model of the hindfoot*. 2004, Drexel University: Ann Arbor. p. 217.
174. Mkandawire, C., W. R. Ledroux, B. J. Sangeorzan, and R. P. Ching., *Hierarchical cluster analysis of area and length of foot and ankle ligaments*, in *American Society of Biomechanics (ASB) Conference*. 2003: San Diego, CA, USA.
175. Ebrahimi, A., et al., *Achilles tendon loading is lower in older adults than young adults across a broad range of walking speeds*. *Experimental Gerontology*, 2020. **137**: p. 110966.
176. Keuler, E.M., et al., *Shear Wave Predictions of Achilles Tendon Loading during Human Walking*. *Scientific reports*, 2019. **9**(1): p. 13419-9.
177. Lewis, G., *Finite element analysis of a model of a therapeutic shoe: effect of material selection for the outsole*. *Bio-Medical Materials and Engineering*, 2003. **13**: p. 75-81.
178. MatWeb. *Aluminium*. [cited 2021 10/07]; Available from: <http://www.matweb.com/search/datasheet.aspx?bassnum=AMEAL00&ckck=1>.
179. Cher, W.L., et al., *An analysis of changes in in vivo cartilage thickness of the healthy ankle following dynamic activity*. *Journal of biomechanics*, 2016. **49**(13): p. 3026-3030.
180. Haraguchi, N., et al., *Prediction of Three-Dimensional Contact Stress and Ligament Tension in the Ankle During Stance Determined from Computational Modeling*. *Foot & Ankle International*, 2009. **30**(2): p. 177-185.
181. Chu, T. and N. Reddy, *Stress Distribution in the Ankle-Foot Orthosis Used To Correct Pathological Gait*. *Journal of rehabilitation research and development*, 1995. **32**: p. 349-60.
182. Chu, T.M., N.P. Reddy, and J. Padovan, *Three-dimensional finite element stress analysis of the polypropylene, ankle-foot orthosis: static analysis*. *Medical Engineering & Physics*, 1995. **17**(5): p. 372-379.
183. Jamshidi, N., et al., *Modelling the interaction of ankle-foot orthosis and foot by finite element methods to design an optimized sole in stepgait*. *Journal of Medical Engineering & Technology*, 2010. **34**(2): p. 116-123.
184. Uning, R., N.A. Abu Osman, and R.B. Abdul Rahim. *3D Finite Element Analysis of Ankle-Foot Orthosis on Patients with Unilateral Foot Drop: A Preliminary Study*. 2008. Berlin, Heidelberg: Springer Berlin Heidelberg.
185. Gu, Y.D., et al., *Image-based midsole insert design and the material effects on heel plantar pressure distribution during simulated walking loads*. *Computer Methods in Biomechanics and Biomedical Engineering*, 2011. **14**(8): p. 747-753.
186. Dai, G., J.P. Gertler, and R.D. Kamm, *The Effects of External Compression on Venous Blood Flow and Tissue Deformation in the Lower Leg*. *Journal of Biomechanical Engineering*, 1999. **121**(6): p. 557-564.
187. Avril, S., et al., *Mixed Experimental and Numerical Approach for Characterizing the Biomechanical Response of the Human Leg Under Elastic Compression*. *Journal of Biomechanical Engineering*, 2010. **132**(3).
188. Lima, K.M.M.E., et al., *Assessment of the mechanical properties of the muscle-tendon unit by supersonic shear wave imaging elastography: a review*. *Ultrasonography (Seoul, Korea)*, 2018. **37**(1): p. 3-15.
189. Teichtahl, A.J., et al., *Wolff's law in action: a mechanism for early knee osteoarthritis*. *Arthritis research & therapy*, 2015. **17**(1): p. 207-207.
190. Project, P. *PIPER Project*. 2021 16/10/2021]; Available from: <http://www.piper-project.eu/child>.
191. Lee, W.C.C. and M. Zhang, *Using computational simulation to aid in the prediction of socket fit: A preliminary study*. *Medical Engineering & Physics*, 2007. **29**(8): p. 923-929.
192. Portnoy, S., et al., *Real-Time Patient-Specific Finite Element Analysis of Internal Stresses in the Soft Tissues of a Residual Limb: A New Tool for Prosthetic Fitting*. *Annals of Biomedical Engineering*, 2007. **35**(1): p. 120-135.
193. Wilken, J.M., et al., *Reliability and minimal detectable change values for gait kinematics and kinetics in healthy adults*. *Gait & Posture*, 2012. **35**(2): p. 301-307.
194. Pachi, A. and T. Ji, *Frequency and velocity of people walking*. *Structural Engineer*, 2005. **83**(3): p. 36-40.

195. Formula, E.V.-E.; Available from: https://www.engineeringtoolbox.com/euler-column-formula-d_1813.html.
196. Ogden, R.W., *Large Deformation Isotropic Elasticity - On the Correlation of Theory and Experiment for Incompressible Rubberlike Solids*. Proceedings of the Royal Society of London. A. Mathematical and Physical Sciences, 1972. **326**(1567): p. 565.
197. Mkandawire, C., et al., *Foot and ankle ligament morphometry*. Journal of rehabilitation research and development, 2005. **42**: p. 809-20.
198. Solan, M.C., et al., *Ligamentous Restraints of the Second Tarsometatarsal Joint: A Biomechanical Evaluation*. Foot & Ankle International, 2001. **22**(8): p. 637-641.

12 APPENDICES

12.1 APPENDIX A

This section is supplementary to Chapter 4.

12.1.1 Carbon fibre sensitivity analyses

The full set of results (for completeness) from the sensitivity analyses are shown in Figure 12.1.1- Figure 12.1.3.

12.1.1.1 Carbon-twill

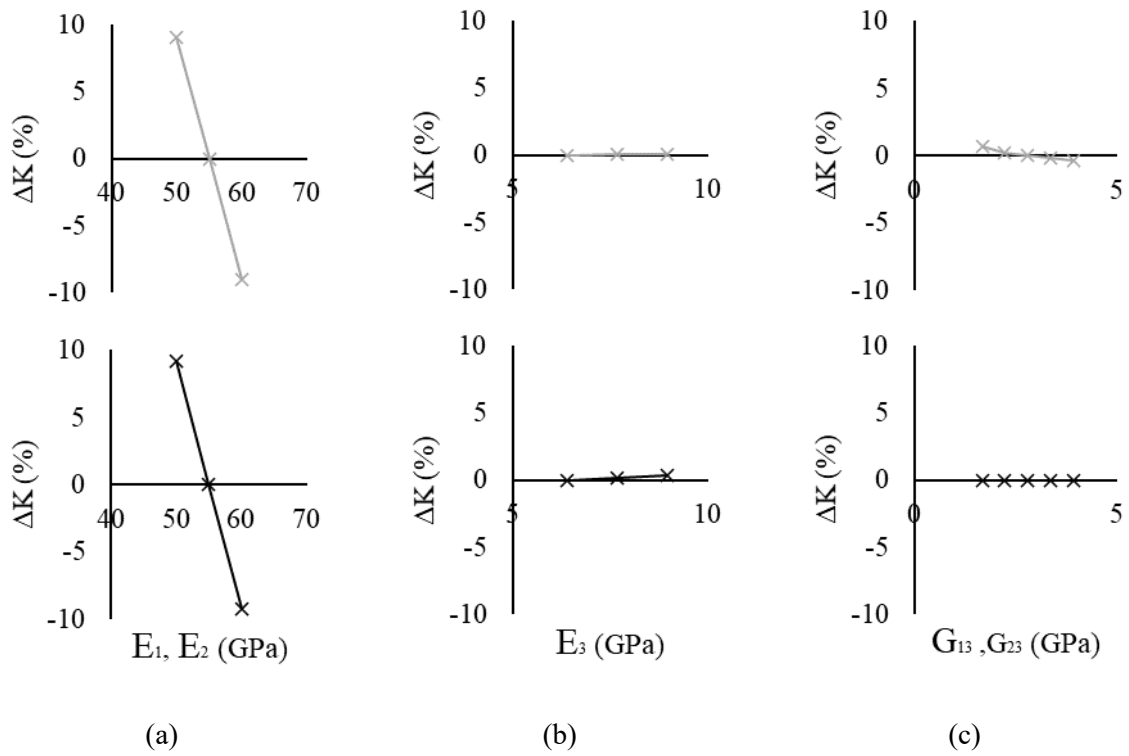
The results from the FE sensitivity analysis, examining the change in the compressive stiffness and bending stiffness of the carbon-twill, after varying the material parameters, are shown in Figure 12.1.1 on page 282. Across the range tested, the Young's modulus, E_1 , had the largest influence on both bending and compressive stiffness, changing the stiffness by $\pm 9.0\%$ and $\pm 9.2\%$ respectively. Changing the shear moduli, G_{13} and G_{23} , by $\pm 40\%$ had no effect on the compressive stiffness but changed the bending stiffness by $\pm 0.73\%$. An increase in the Young's modulus, E_3 , by 40% resulted in a slight increase of the bending stiffness by 0.06% and the compressive stiffness by 0.33%. A change in Poisson's ratio, ν_{12} , by $\pm 80\%$ altered the bending stiffness by $\pm 0.5\%$ and the compressive stiffness by $\pm 0.08\%$. Reducing the Poisson's ratios, ν_{23} and ν_{13} , by -40% reduced the bending stiffness by 0.11% and the compressive stiffness by 0.5%.

12.1.1.2 UD Carbon-fibre

The results of the sensitivity analysis examining the influence of independent material constants on the stiffness of unidirectional carbon-fibre are shown in Figure 12.1.2 on page 283. The Young's modulus, E_1 , as seen in Figure 12.1.2a, had the greatest influence on the compressive and bending stiffness. The stiffness varied by $\pm 8.3\%$ in bending and $\pm 8.4\%$ in compression compared to the baseline value. Changing the Young's Moduli E_2 and E_3 , resulted in a change of $\pm 0.1\%$ in bending stiffness and $\pm 0.07\%$ in compressive stiffness. Changing G_{12} and G_{13} by $\pm 40\%$ resulted in a change of $\pm 1.0\%$ in bending stiffness and no change in compressive stiffness. Altering Poisson's ratio, ν_{23} , by $\pm 40\%$ resulted in a change of $\pm 0.005\%$ in bending stiffness, and, again, no change in compressive stiffness. Altering Poisson's ratio, ν_{12} and ν_{13} , by $\pm 40\%$ resulted in a small change of $\pm 0.3\%$ in bending stiffness and $\pm 0.2\%$ in compressive stiffness.

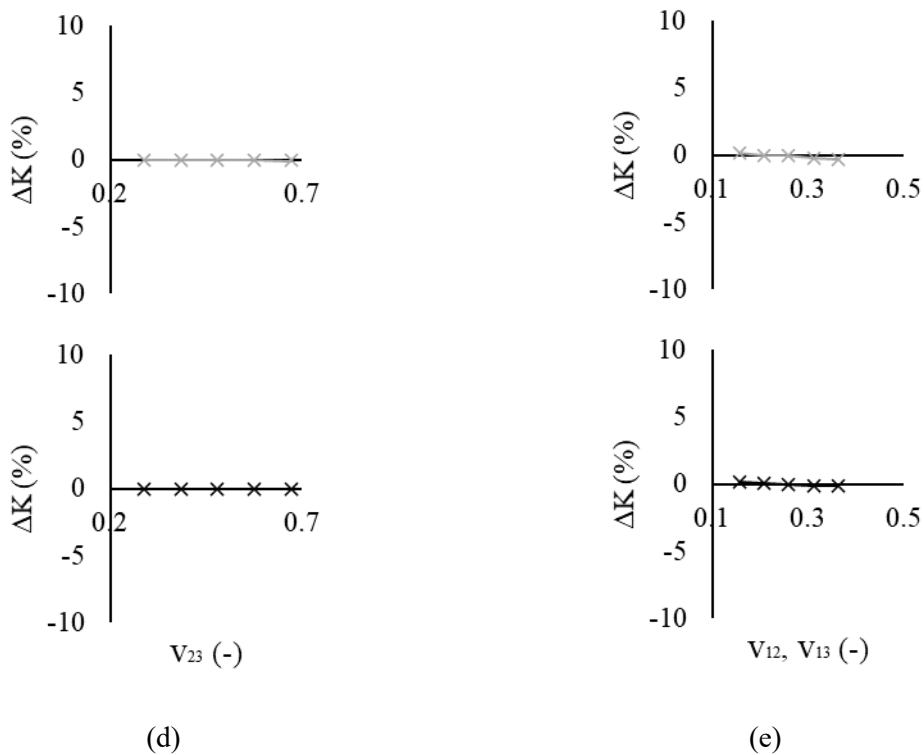
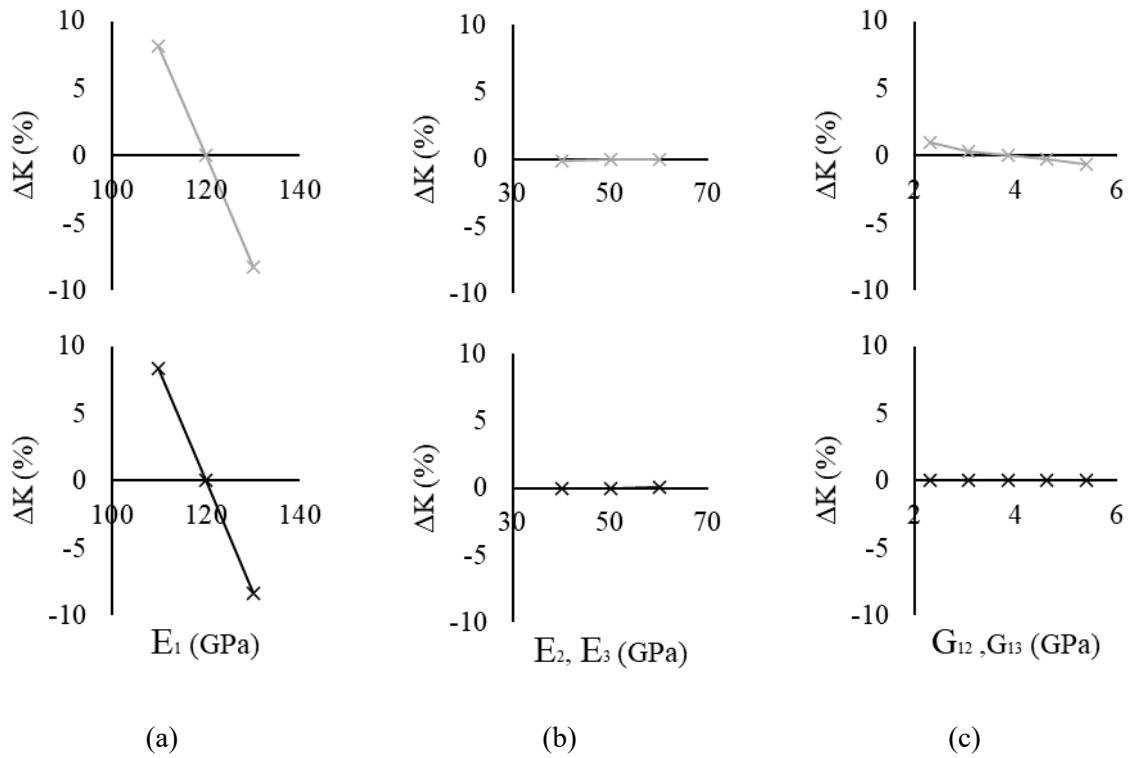
12.1.1.3 Aramid

The influence of the material parameters on the response of the aramid layer is shown in Figure 12.1.3 on page 284. Changing the Young's Moduli, E_1 and E_2 , resulted in a change of $\pm 17.2\%$ in the bending stiffness and $\pm 17.5\%$ in the compressive stiffness. Comparatively, an increase of $+40\%$ of the Young's modulus, E_3 , resulted in increase of 0.65% in bending stiffness and 0.34% in compressive stiffness. A change in the shear moduli, G_{13} and G_{23} , by $\pm 40\%$ resulted in a change of $\pm 0.73\%$ in the bending stiffness, and no change in the compressive stiffness. Altering Poisson's ratio, ν_{12} , by $\pm 40\%$ changed the bending stiffness by $\pm 0.23\%$ and the compressive stiffness by $\pm 0.04\%$. Changing Poisson's ratios, ν_{13} and ν_{23} , by $\pm 40\%$ changed the bending stiffness by 0.85% and the compressive stiffness by 0.48% .



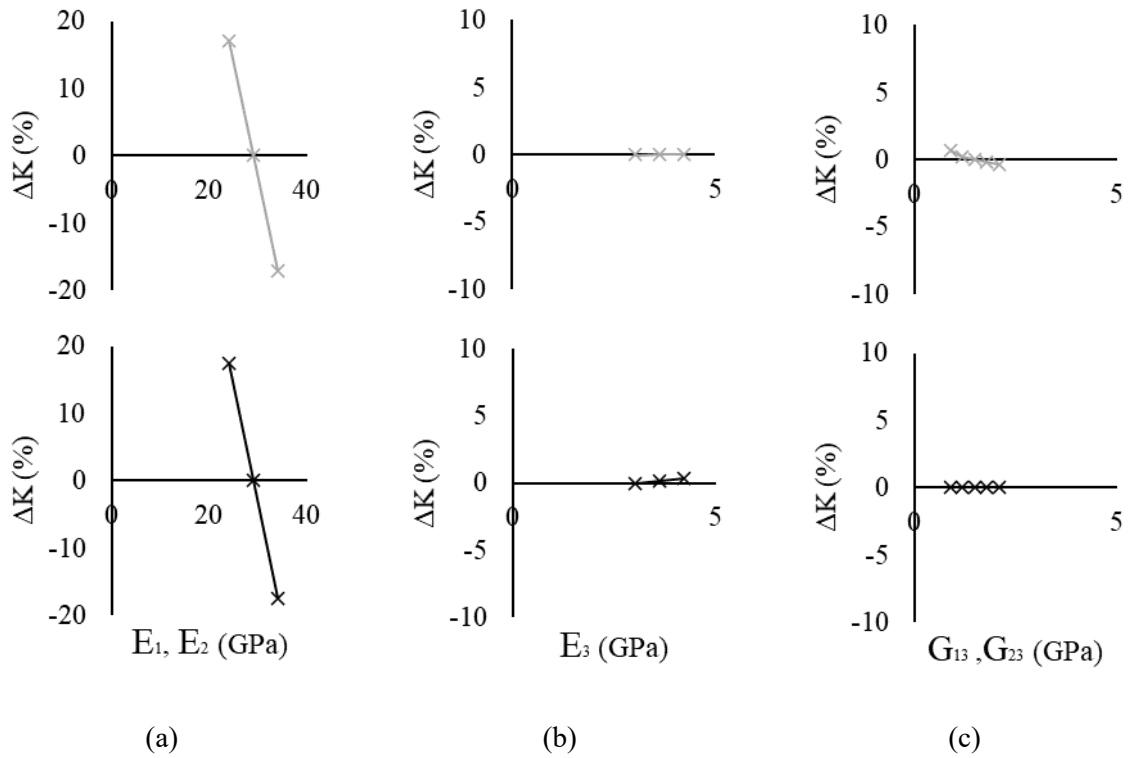
—x— Bending —x— Compression

Figure 12.1.1: The sensitivity of the compressive stiffness in the primary direction of carbon-twill to (a) Young's modulus, E_1 , (b) Young's modulus, E_3 , (c) shear moduli, G_{13} and G_{23} , (d) Poisson's ratio, ν_{12} , and (e) the Poisson's ratio, ν_{13} and ν_{23} .



—x— Bending —x— Compression

Figure 12.1.2: The sensitivity of the compressive stiffness in the primary direction of uni-directional carbon-fibre to (a) Young's modulus, E_1 , (b) Young's modulus, E_2 , (c) shear moduli, G_{13} and G_{23} , (d) Poisson's ratio, ν_{23} , and (e) the Poisson's ratio, ν_{12} and ν_{13} .



—x— Bending —o— Compression

Figure 12.1.3: The sensitivity of the compressive stiffness in the primary direction of aramid to (a) Young's modulus, E_1 , (b) Young's modulus, E_3 , (c) shear moduli, G_{13} and G_{23} , (d) Poisson's ratio, ν_{12} , and (e) the Poisson's ratio, ν_{13} and ν_{23} .

12.1.2 Compliance

To determine the compliance on the materials testing machine, a compression test was performed between the 2 fixtures, used in the compression tests in chapter 4. The compliance was assumed to be similar for all fixtures. A displacement was applied up to a maximum force of 7kN. The force was recorded with a 10kN loadcell at 50Hz. From the recorded force-displacement curve, the compliance, C , was found to be 26×10^6 m/N using linear regression ($R^2=0.988$). To account for the machine's compliance in the experimental tests, equation (12.1.1) was used where δ is the displacement, and P is the force at time i .

$$\delta_i^{corrected} = \delta_i^{raw} - P_i C \quad (12.1.1)$$

12.1.3 Macauley's Beam Theory

Macauley's theory is shown in equation (12.1.2). P was the force recorded by the materials testing machine, following the displacement, δ_{input} . I was the second moment of area, calculated with each samples' respective diameter. x was distance along the sample, and y was the displacement (deflection) of the samples, as a function of x (see Figure 12.1.4).

$$\frac{d^2y}{dx^2} = \frac{M(x)}{E_b I} = \frac{1}{E_b I} \left[\frac{P}{2} \langle x \rangle - \frac{P}{2} \langle x - a \rangle - \frac{P}{2} \langle x - L + a \rangle + \frac{P}{2} \langle x - L \rangle \right]$$

$$\frac{dy}{dx} = \frac{1}{EE_b I} \left[\frac{P}{4} \langle x \rangle^2 - \frac{P}{4} \langle x - a \rangle^2 - \frac{P}{4} \langle x - L + a \rangle^2 + \frac{P}{4} \langle x - L \rangle^2 + C_1 \right]$$

$$y(x) = \frac{1}{E_b I} \left[\frac{P}{12} \langle x \rangle^3 - \frac{P}{12} \langle x - a \rangle^3 - \frac{P}{12} \langle x - L + a \rangle^3 + \frac{P}{12} \langle x - L \rangle^3 + C_1 x + C_2 \right] \quad (12.1.2)$$

where:

$$y(0) = 0 \therefore C_2 = 0$$

$$y(L) = 0 \therefore C_1 = \frac{P}{4} (a^2 - aL)$$

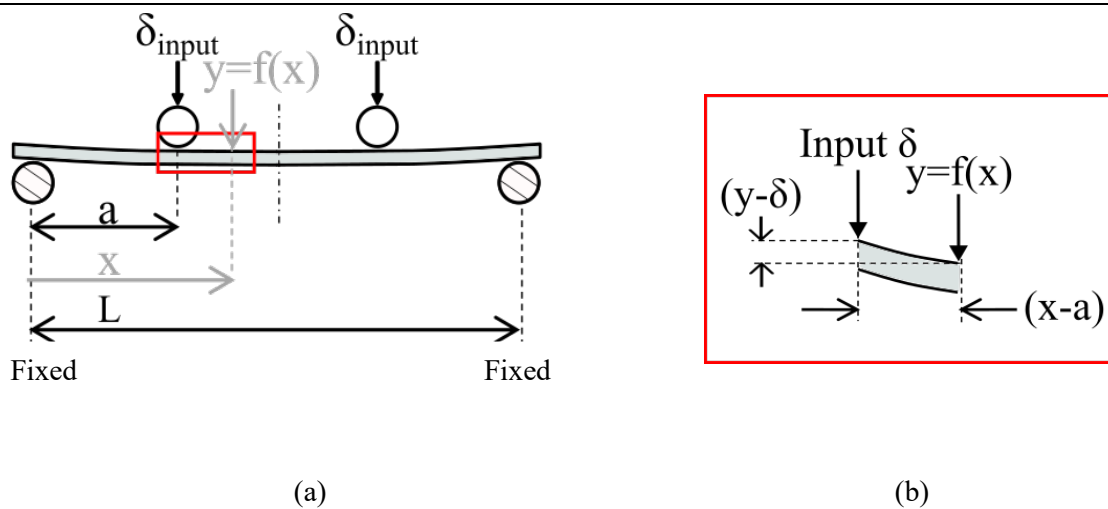


Figure 12.1.4 (a) Schematic of set up showing that the displacement y , is a function of the distance x as prescribed by figure (b) showing a close-up of the bending comparing the displacement δ_{input} and y

As the distance x tends to a , the displacement y will tend to δ_{input} ; as such, the Young's modulus was calculated by using the force displacement curve $\left(\frac{P}{\delta}\right)$, established by the 4-point bend test, to give equation (12.1.3).

$$\lim_{x \rightarrow a} y(x) = \delta; \text{ where } y = f(x)$$

(12.1.3)

$$\lim_{x \rightarrow a} E_b = \frac{P}{\delta} \cdot \frac{[4a^3 - 3a^2L]}{12I}$$

12.1.4 Strain Rate Sensitivity of the Struts

Preliminary compression tests were performed on one sample strut to determine the rate sensitivity. A baseline loading rate of 0.119s^{-1} was selected, based on a 2Hz walking frequency and the application of body weight of $\sim 1200\text{N}$ over 0.5s [194]. Compression tests (as described in Chapter 4) were performed at the baseline rate, at double this rate (0.234s^{-1}), 5 at half (0.059s^{-1}) and 5 at a quarter (0.030s^{-1}) of the baseline rate. The Young's modulus was calculated. Additionally, 4-point bend test were also performed, at the same displacement rates as used in the preliminary compression tests (0.095mm/s , 0.19mm/s , 0.38mm/s , 0.75mm/s), and again the Young's modulus calculated.

The results for the preliminary compression tests are shown in Figure 12.1.5. A statistical difference was found between the slowest strain rate and all other strain rates. No other statistical differences were observed.

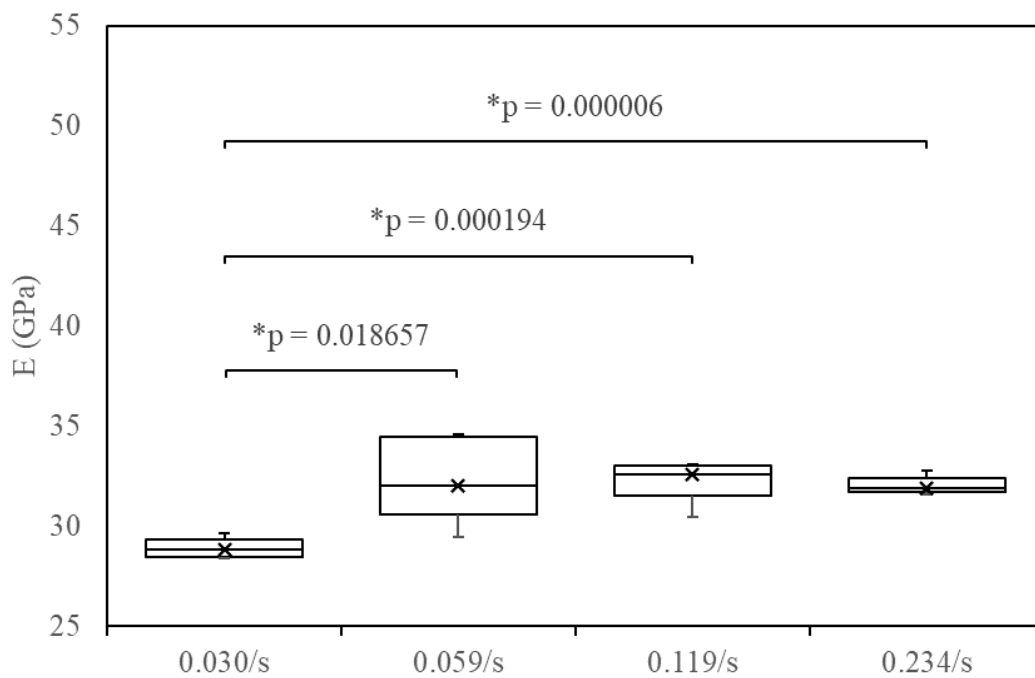


Figure 12.1.5: Young's modulus calculated in compression, of 1 sample ($n=5$) at 4 different strain rates, For each rate respectively (0.030/s, 0.059/s, 0.119/s, 0.234/s) the median Young's modulus calculated is 28.84GPa, 32.02GPa, 32.60GPa, 31.91GPa. * p indicates a statistical difference calculated from an unpaired t -test

Figure 12.1.6 shows the Young's modulus calculate from bending at the 4 displacement rates. A statistical difference was found between the 2 slowest displacement rates. No other statistical differences were observed in the calculated value of Young's modulus.

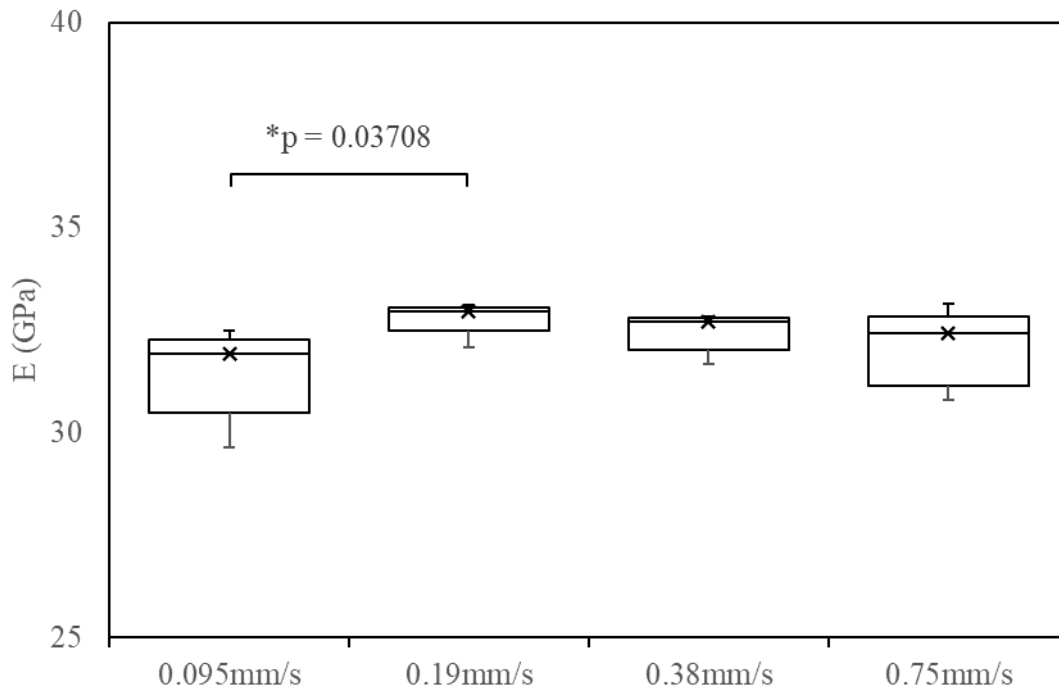


Figure 12.1.6: Young's modulus calculated in bending, of 1 sample (n=5) at 4 different displacement rates, For each rate respectively (0.095mm/s, 0.19mm/s, 0.38mm/s, 0.75mm/s) the median Young's modulus calculated is 31.93GPa, 32.95GPa, 32.69GPa, and 32.42GPa. *p indicates a statistical difference calculated from an unpaired t-test

12.1.5 Sample Strut Measurements

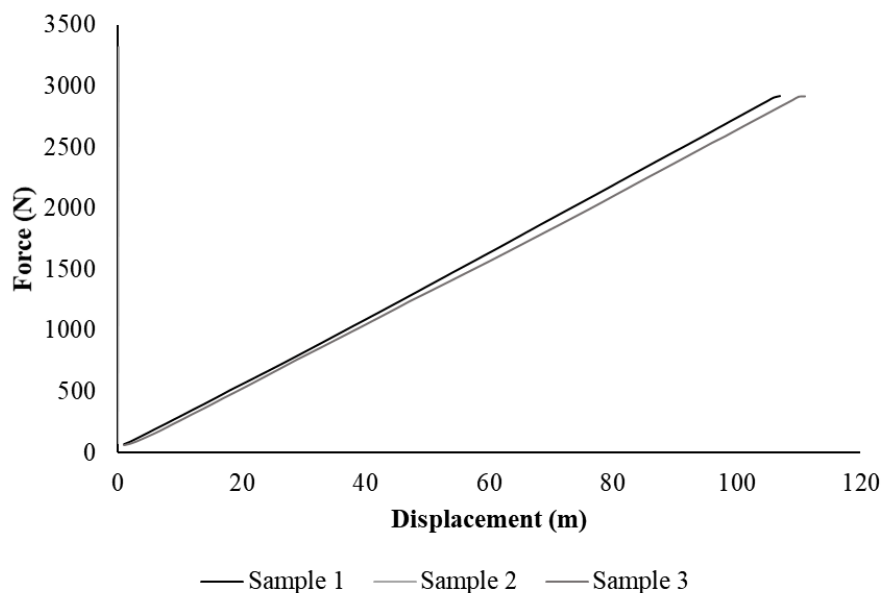
Table 12.1.1 shows the measurements of geometry taken for each sample and the mean area and length calculated.

Table 12.1.1: Measurements of geometry of sample struts

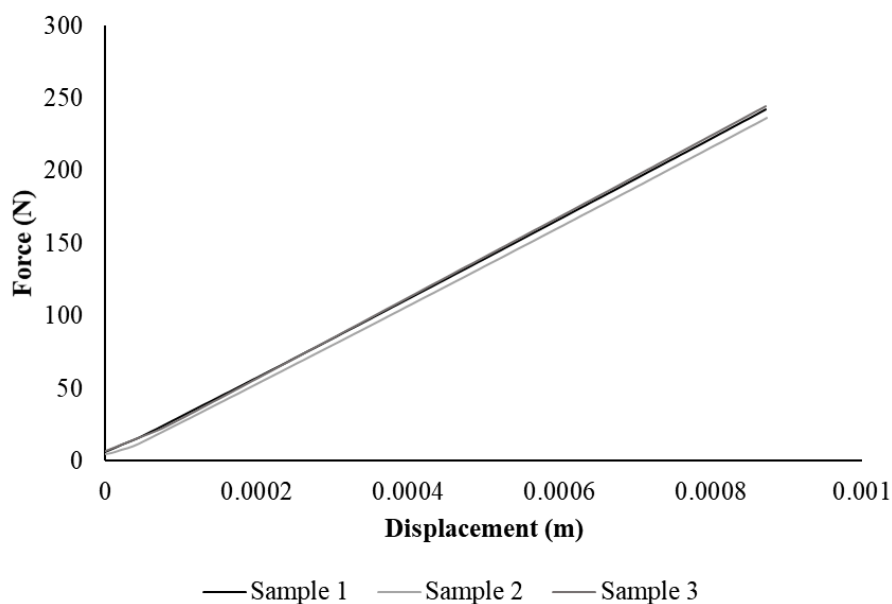
	Diameter (mm)			Length (mm)			Area	Length
	1	2	3	1	2	3	(mm ²)	(mm)
Sample 1	11.72	11.68	11.66	320	320	320	107.27	320
Sample 2	11.54	11.54	11.52	297	298	298	104.47	297
Sample 3	11.53	11.54	11.55	298	298	298	104.59	297

12.1.6 Composite Strut Force-Displacement Curves

Figure 12.1.7 shows the force-displacement curves recorded during compression and bending across the 3 samples of composite strut.



(a)



(b)

Figure 12.1.7: 1 Force-displacement curves for each of the 3 samples of composite strut in (a) compression and (b) bending

12.1.7 Buckling

A brief check was performed, using equation (12.1.4) to confirm that the critical buckling force, F , was not met when performing the compression tests [195]. In equation (12.1.4), E is the Young's modulus of the strut as calculated, I is the second moment of area, L is the length of the strut and k is the buckling factor depending on the type of buckling that would be experienced. Assuming that the struts act with either built-in ends or pivoted ends, the buckling factor varies between 0.5 and 1. Using a buckling factor of 1 gave a critical force of 3,320N and a buckling factor of 0.5 gave a critical force of 13,300N. Both values are above the maximum force applied during the compression tests.

$$F = \frac{\pi^2 EI}{kL} \quad (12.1.4)$$

12.1.8 Ogden Material Formulation

Ogden developed a strain energy function, in order to model the behaviour of non-linear, large strain materials. [196]. The FE software used (MSC.Marc) models this strain energy function, in its most general form, as shown in (12.1.5), where W is the strain energy [80]. The stretch, λ , is defined as the instantaneous length over the initial length. The dilatancy, J , is the determinant of the deformation gradient (engineering strain at large deformations) $\frac{\partial X}{\partial x}$, where x is the instantaneous coordinate, and X is the original coordinate. The variables μ and α are to be material constants to be determined, with N is the chosen number of terms.

$$W = \sum_{n=1}^N \frac{\mu_n}{\alpha_n} J^{-\frac{\alpha_n}{3}} (\lambda_1^{\alpha_n} + \lambda_2^{\alpha_n} + \lambda_3^{\alpha_n} - 3) + 4.5K(J^{-\frac{1}{3}} - 1)^2$$

where stretch in i , $\lambda_i = \frac{L_i}{L_{i0}}$ (12.1.5)

where dilatancy, $J = \det \left| \frac{\partial X}{\partial x} \right|$

The three general strain invariants, are shown in equations (12.1.6), (12.1.7), and (12.1.8). These are scalar quantities, and relate the orthogonal stretch values.

$$I_1 = \lambda_1^2 + \lambda_2^2 + \lambda_3^2 \quad (12.1.6)$$

$$I_2 = \lambda_1^2 \lambda_2^2 + \lambda_2^2 \lambda_3^2 + \lambda_1^2 \lambda_3^2 \quad (12.1.7)$$

$$I_3 = \lambda_1^2 \lambda_2^2 \lambda_3^2 \quad (12.1.8)$$

When the material is considered incompressible $I_3 = 1$. This results in equation (12.1.7) being re-written as equation (12.1.9). The dilatancy is also equal to 1, when the material is incompressible (12.1.10).

$$I_2 = \frac{1}{\lambda_3^2} + \frac{1}{\lambda_1^2} + \frac{1}{\lambda_2^2} \quad (12.1.9)$$

$$J = \mathbf{det} \left| \frac{\partial \mathbf{X}}{\partial \mathbf{x}} \right| = 1 \quad (12.1.10)$$

When a material is under uniaxial tension or compression, $\lambda_2 = \lambda_3$, this means the stretch in these directions is the same. Assuming incompressibility, equation (12.1.8) can allow the following relationship to be established between the stretch values, shown in equation (12.1.11).

$$\lambda_2 = \lambda_3 = \lambda_1^{-\frac{1}{2}} \quad (12.1.11)$$

Finally, for an incompressible material in uniaxial tension or compression, equations (12.1.9), (12.1.10) and (12.1.11) can be used to simplify (12.1.5) to equation (12.1.12), where $\lambda_1 \equiv \lambda$ for simplicity.

$$W = \sum_{n=1}^N \frac{\mu_n}{\alpha_n} \left(\lambda^{\alpha_n} + 2\lambda^{\frac{-\alpha_n}{2}} - 3 \right) \quad (12.1.12)$$

12.1.9 Foam Stress Strain Curves

Figure 12.1.8 shows the mean stress-strain curve from the experimental compression test as determined from the last 5 cycles for each of the 5 samples of for the polyurethane heel wedge, along with the Ogden material formulation generated to model it. The Ogden material stress-strain curve did not remain within $\pm 1SD$ of the mean experimental stress-strain curve. Between ~ 0 -30% strain the material under predicted stress by up to 24% of the experimental value. Between ~ 30 -60% strain the Ogden material over predicted the value of stress, by up to 13% of the experimental value.

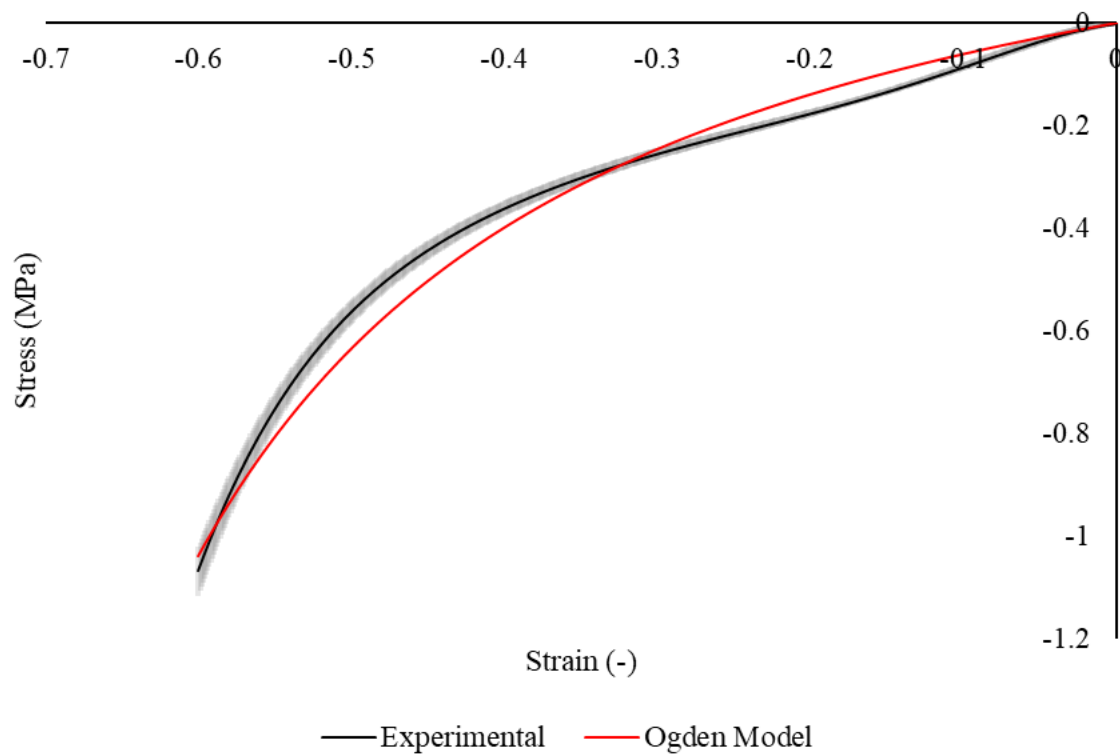


Figure 12.1.8: Stress-strain curve recorded during compression of samples of polyurethane used in manufacture of the heel wedge and fitted 2-term Ogden model. The shaded area denotes 1 SD.

Figure 12.1.9 shows the mean experimental stress-strain curve for *Foam AB* (n=30), with the stress-strain curve generated by the Ogden material model.

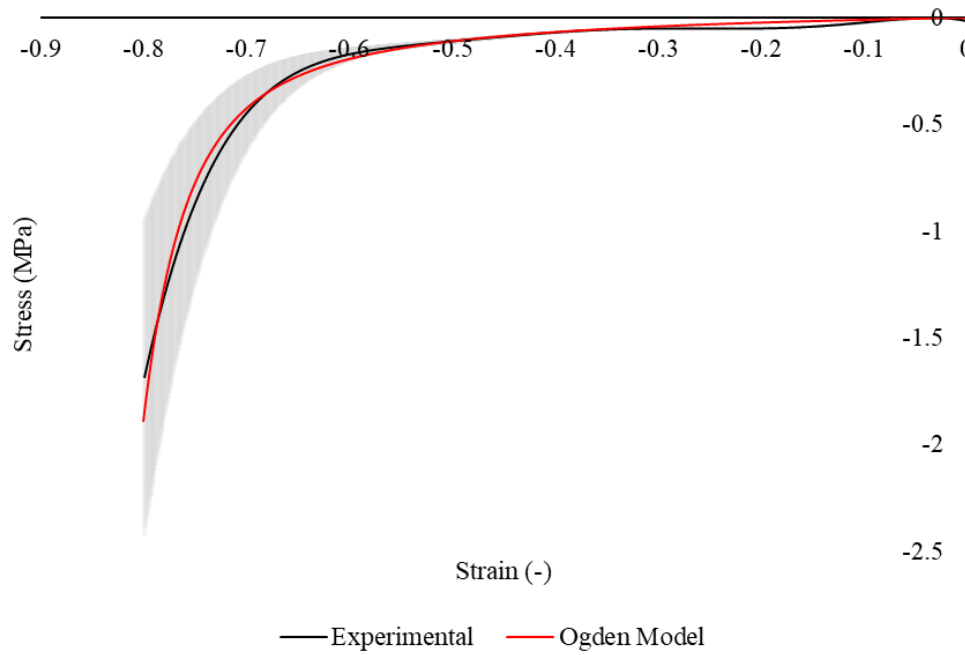


Figure 12.1.9: Mean experimental stress-strain curve for Foam A and Foam B, as calculated from the recorded force-displacement curves and Ogden model fitted to the combined dataset. The shaded area denotes 1 SD.

12.2 APPENDIX B

This section is supplementary to chapter 5.

12.2.1 Copy of Consent Form

**Imperial College
London**

Biomechanics Laboratory
5th Floor
Sir Michael Uren Hub
White City Campus
Imperial College London
London W12 0BZ

Consent Form for Participants Able to Give Consent

Full Title of Project: The mechanical response of a passive-dynamic ankle-foot orthosis and its interaction with the lower limb during gait

Investigators: Dr Spyros Masouros, Dr Arul Ramasamy, Kirstie Edwards, Louise McMenemy

Please initial box

1. I confirm that the aims of this study have been explained to me, and I understand the nature of the research and the extent of my participation. I understand the potential risks involved and have been informed about the laboratory procedures. I was given the opportunity to ask questions which have been answered fully.	
2. I understand that my participation is voluntary, and that I am free to withdraw at any time, without giving any reason and without my legal rights being affected.	
3. I give permission for Imperial College London to access my research records that are relevant to this research.	
4. I agree to my anonymised data being stored on password protected Imperial College London computer systems and that they will be treated as strictly confidential.	
5. I consent to take part in this study. This consent does not imply consent to participate in any further studies or further development of this study beyond what has been described to me.	

Name of participant Signature Date

Name of person taking consent
(if different from Principal Investigator) Signature Date

Principal Investigator Signature Date

1 copy for participant; 1 copy for Principal Investigator

12.2.2 Total Ground Reaction Force and Plantar Force

Figure 12.2.1 shows the total GRF and the plantar force throughout the gait cycle, during both control gait and PD-AFO gait.

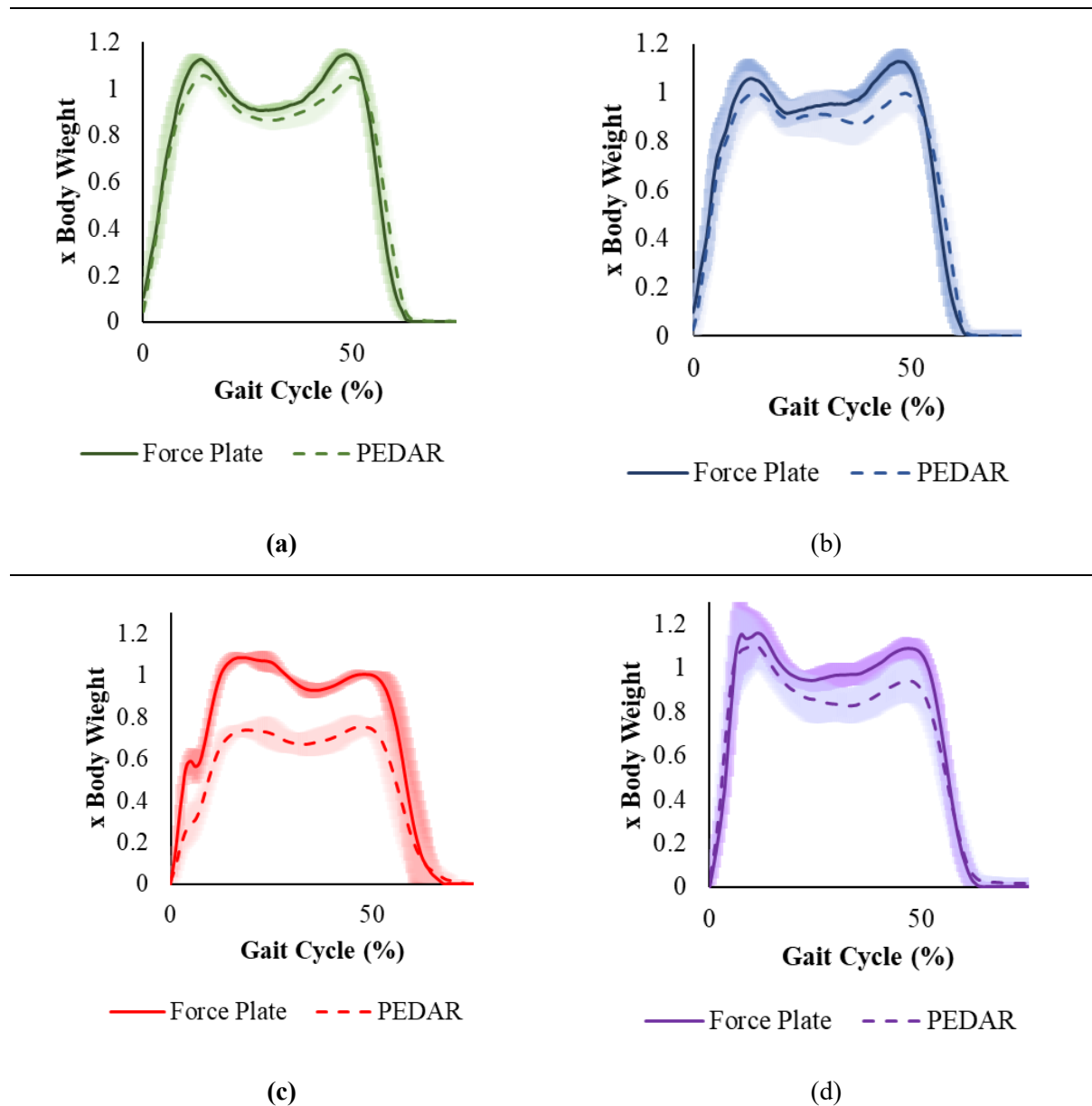


Figure 12.2.1: The mean, normalised plantar force \pm 1SD as calculated by the PEDAR sensor and the total ground reaction force as calculated by the force plates for (a) the left limb and (b) the right limb during control gait, and (c) the PD-AFO limb and (d) the shod limb for the PD-AFO gait.

Figure 12.2.2 shows the statistical analyses of the peak values of total GRF and plantar force at weight acceptance within each limb. Statistical differences between the value of GRF and plantar force recorded were observed within the left limb ($p < 0.001$), right limb ($p < 0.001$) and PD-AFO limb ($p < 0.001$).

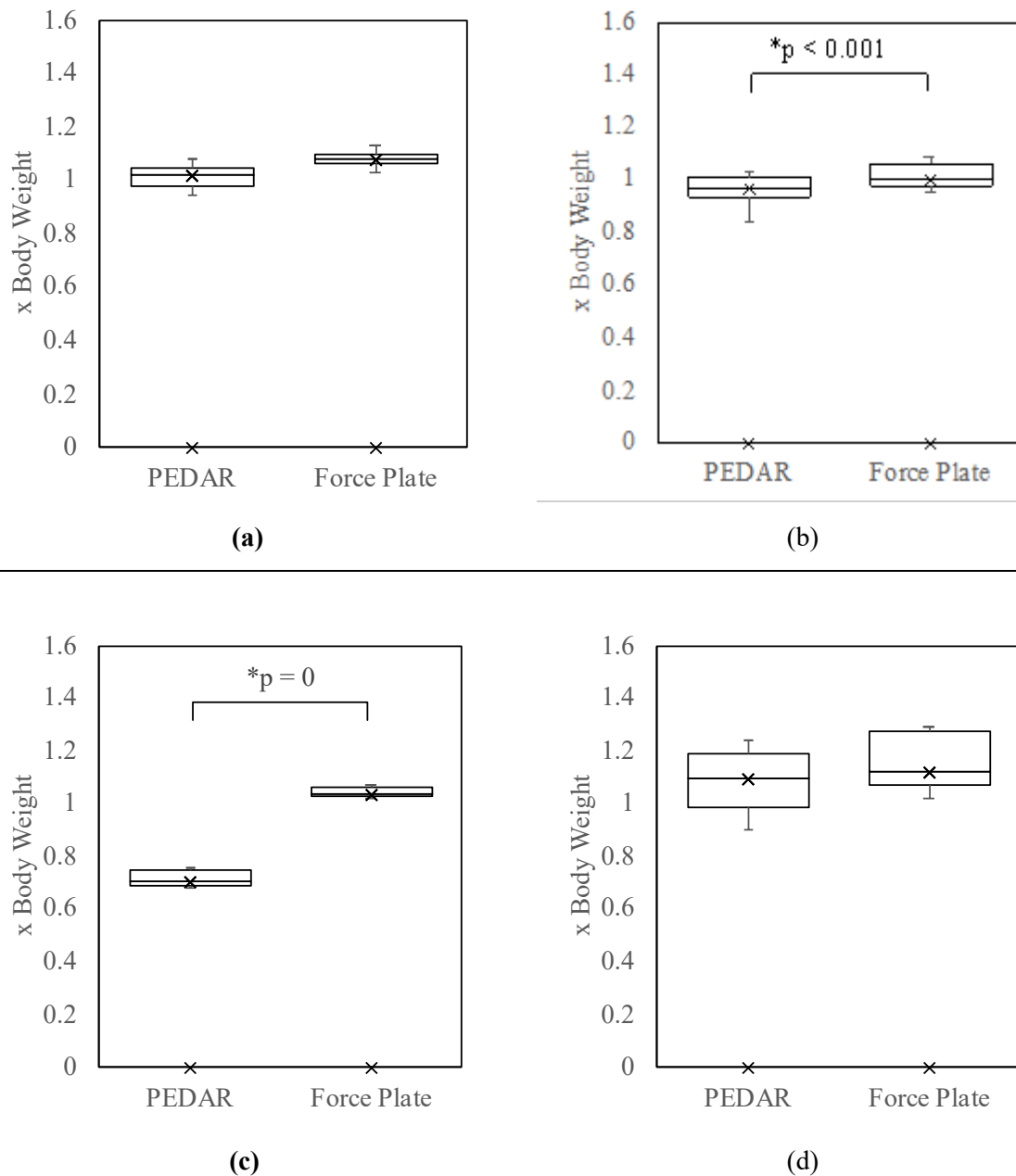


Figure 12.2.2: The plantar force, as measured by the PEDAR sensors and the total GRF as measured by the force plates at weight acceptance in (a) the left limb (b) the right limb (c) the PD-AFO limb and (d) the shod limb. * indicates a statistical difference for $p < 0.05$ for paired T-Test

Figure 12.2.3 shows the difference between the total GRF and plantar force at midstance. The difference was statistically different for the left limb during control gait ($p=0.0403$), and both the shod ($p = 0.0284$) and PD-AFO limb ($p < 0.001$) during PD-AFO gait. The mean GRF was 4.0% and 4.4% higher than the plantar force for the left and right limb, respectively. The GRF was 12.3% higher than the plantar force for the shod limb and 41.5% higher for the PD-AFO limb.

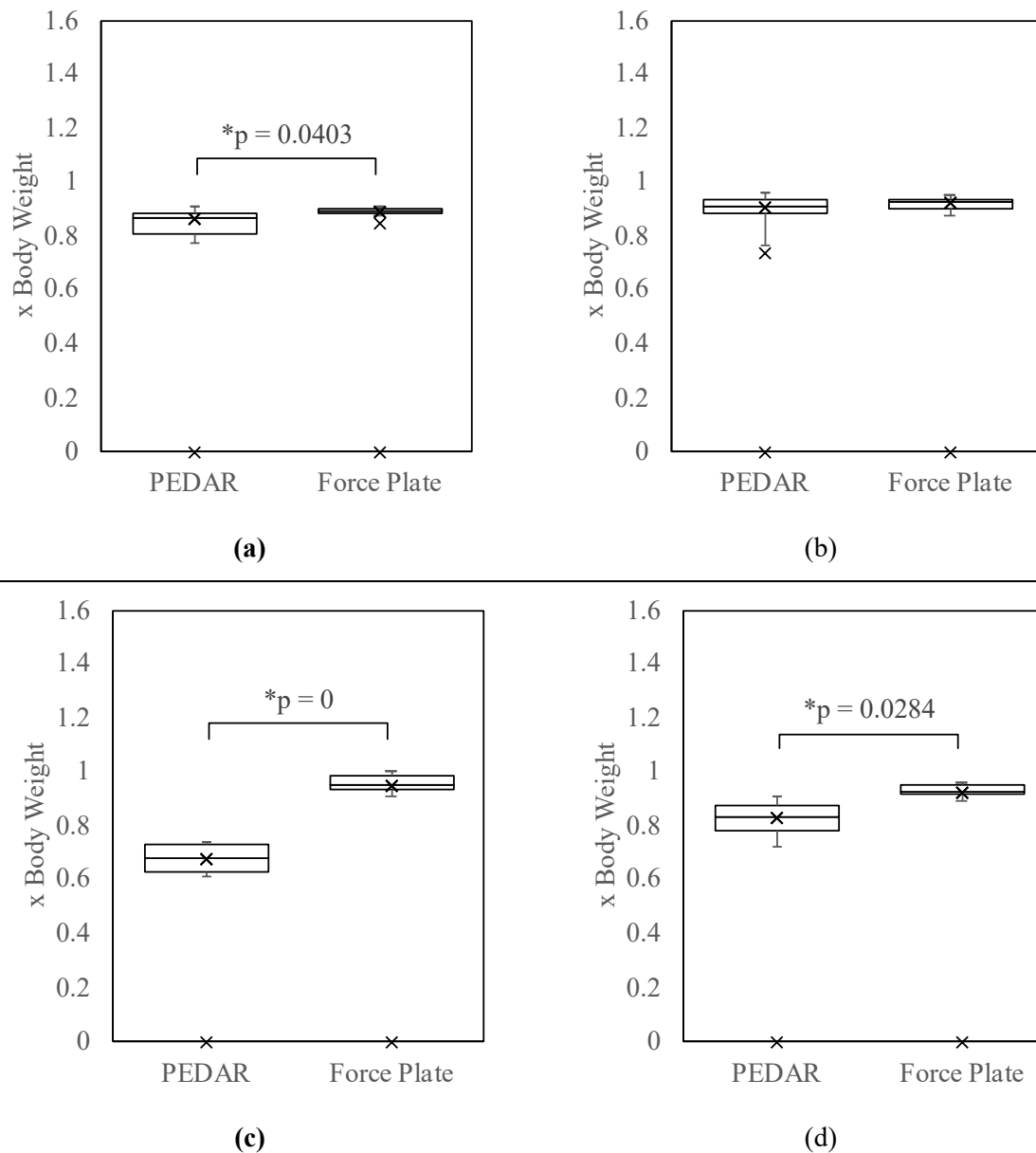


Figure 12.2.3: The plantar force, as measured by the PEDAR sensors and the total GRF as measured by the force plates at midstance in (a) the left limb (b) the right limb (c) the PD-AFO limb and (d) the shod limb. * indicates a statistical difference for $p < 0.05$ for paired T-Test

Figure 12.2.4 shows the statistical analyses performed between the total GRF and peak plantar force at push off. The total GRF and plantar force were significantly different for all 4 limbs. The GRF was 9.3% and 12.9% higher than the plantar force, for the left and right limb respectively. The GRF was 15.5% higher than the plantar force for the shod limb and 30.1% higher for the PD-AFO limb.

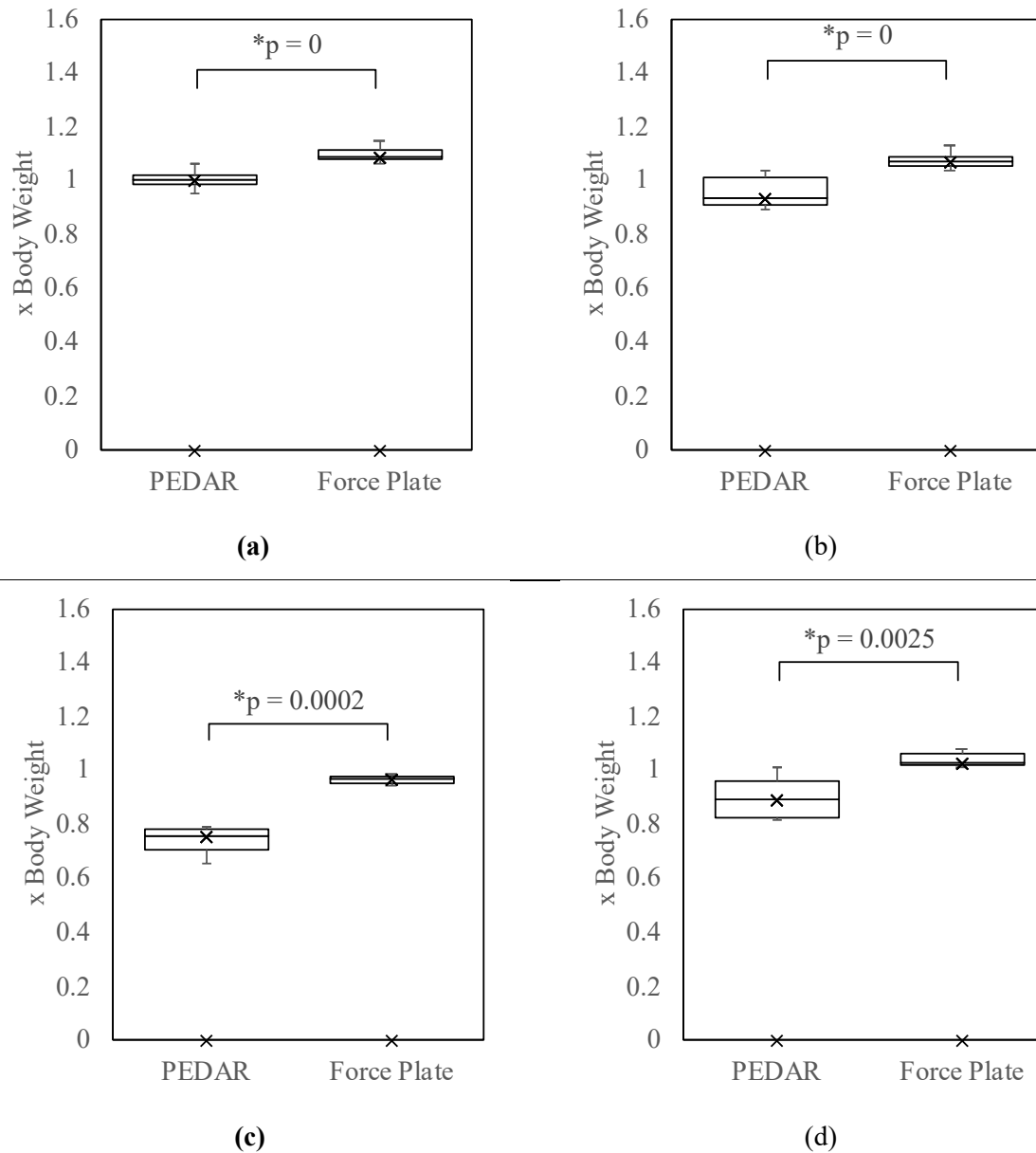


Figure 12.2.4: The plantar force, as measured by the PEDAR sensors and the total GRF as measured by the force plates at push off in (a) the left limb (b) the right limb (c) the PD-AFO limb and (d) the shod limb. * indicates a statistical difference for $p < 0.05$ for paired T-Test

12.2.3 Loading Ratio Error

The error between the value of force recorded using the force plates (the GRF) and the value of force recorded using the PEDAR sensors (plantar force) was calculated using (12.2.1) for each point in gait. The plantar force error, recorded for the PD-AFO limb was calculated by multiplying the value by the respective, $Error_{F_{plantar}}$, for that point in the gait cycle

$$Error_{F_{plantar}} = \frac{GRF}{F_{plantar}} - 1 \quad (12.2.1)$$

The underestimation of the plantar force in the shod limb and control limbs, as a percentage of the GRF at that point in the gait cycle is shown in Figure 12.2.5. The errors are greater at towards the start and end of the gait cycle.

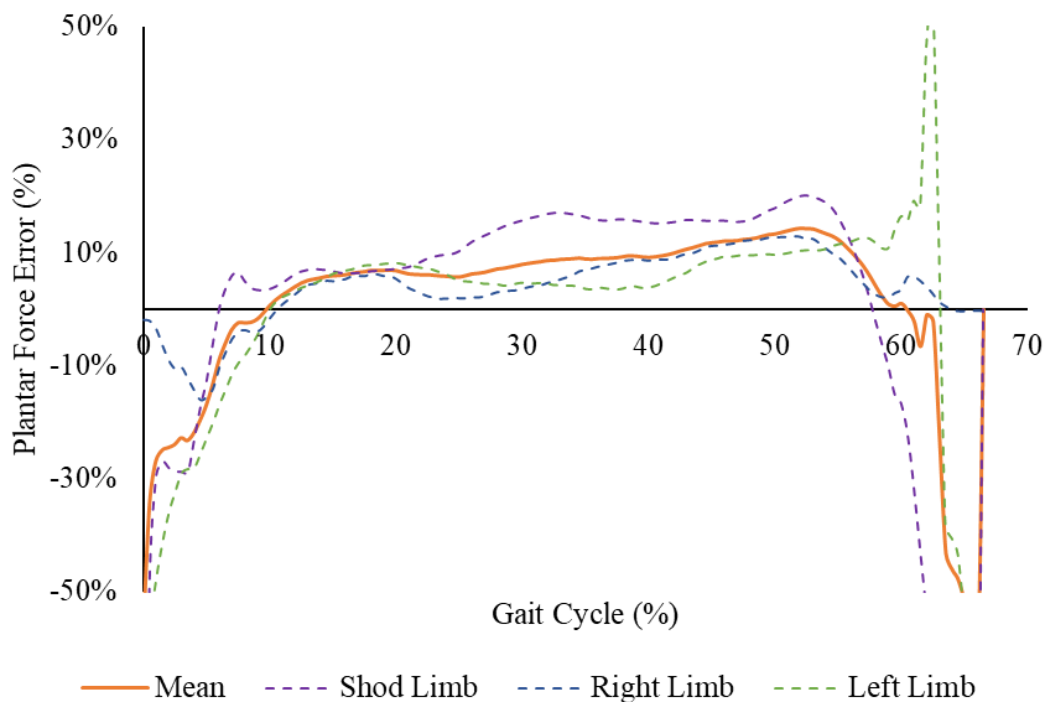


Figure 12.2.5: Underestimation of the plantar force compared to the GRF in the shod limb, left limb and right limb, and the mean values of these errors throughout gait.

The total GRF at weight acceptance and push off exhibited by each limb are shown in Figure 12.2.6. The peak total GRF at weight acceptance, was greater for the shod limb compared to the right control, shown in Figure 12.2.6a. The greatest difference at push off was seen between the PD-AFO limb and the left control, where the PD-AFO limb has a smaller peak total GRF.

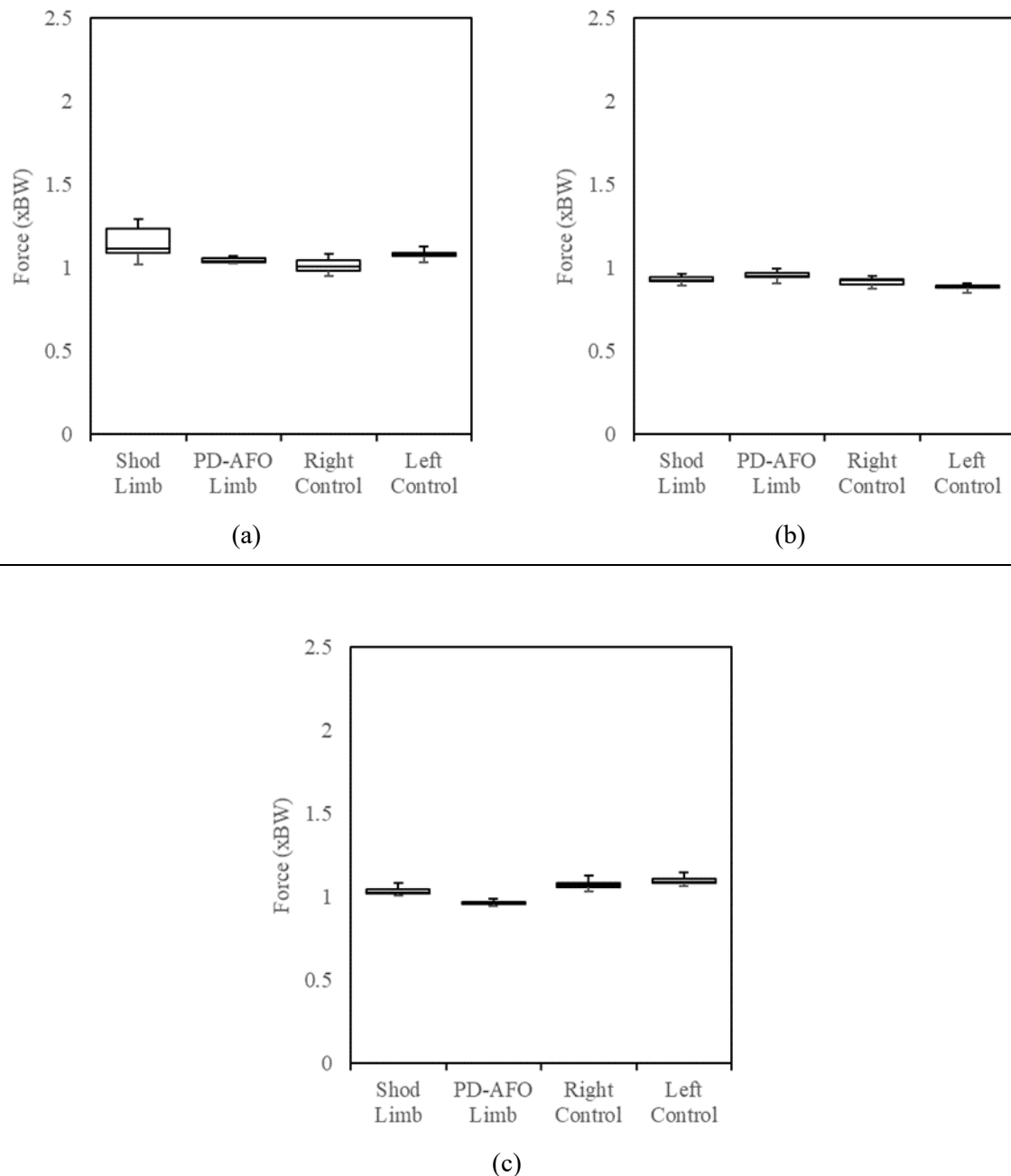


Figure 12.2.6: The total GRF recorded by all limbs during (a) weight acceptance (b) midstance (c) push-off.

Figure 12.2.7 shows the plantar force at weight acceptance (Figure 12.2.7a), midstance (Figure 12.2.7b) and push off (Figure 12.2.7c), experienced by all 4 limbs. The absolute plantar force through the PD-AFO was lower than both the shod limb and the left control limb at all 3 points in gait. A reduction of 29% was seen in the PD-AFO limb at weight acceptance relative to the left control, 21% at midstance and 12% at push off.

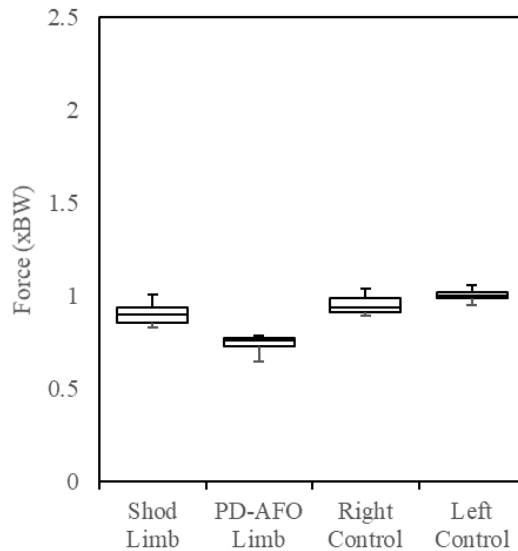
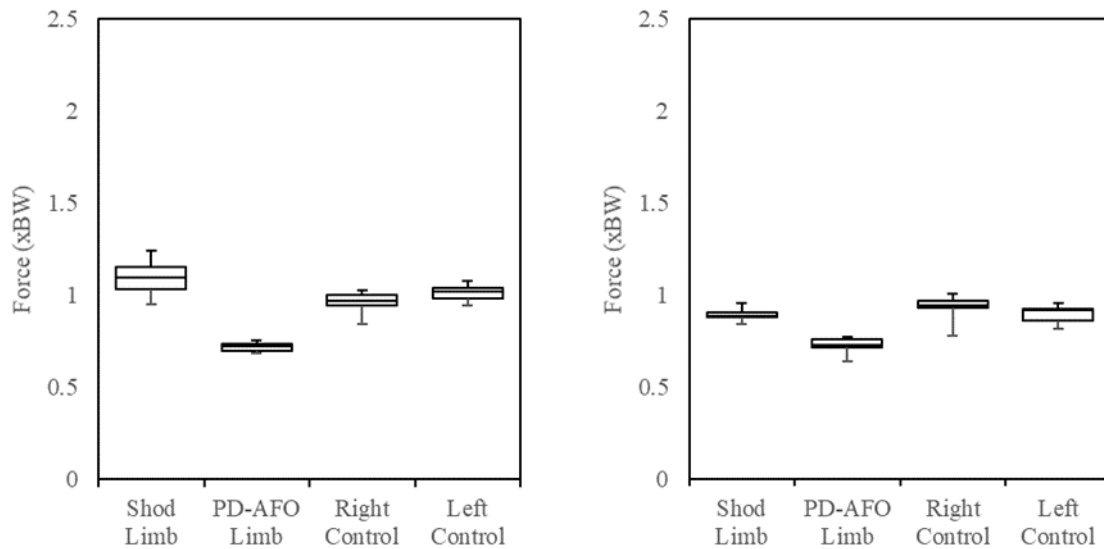


Figure 12.2.7: The peak plantar force recorded by all limbs during (a) weight acceptance (b) midstance and (c) push off.

12.2.4 Plantar Pressures

Figure 12.2.8 to Figure 12.2.14 shows the plantar pressure in each of the 8 chosen plantar regions, at weight acceptance, midstance and push off.

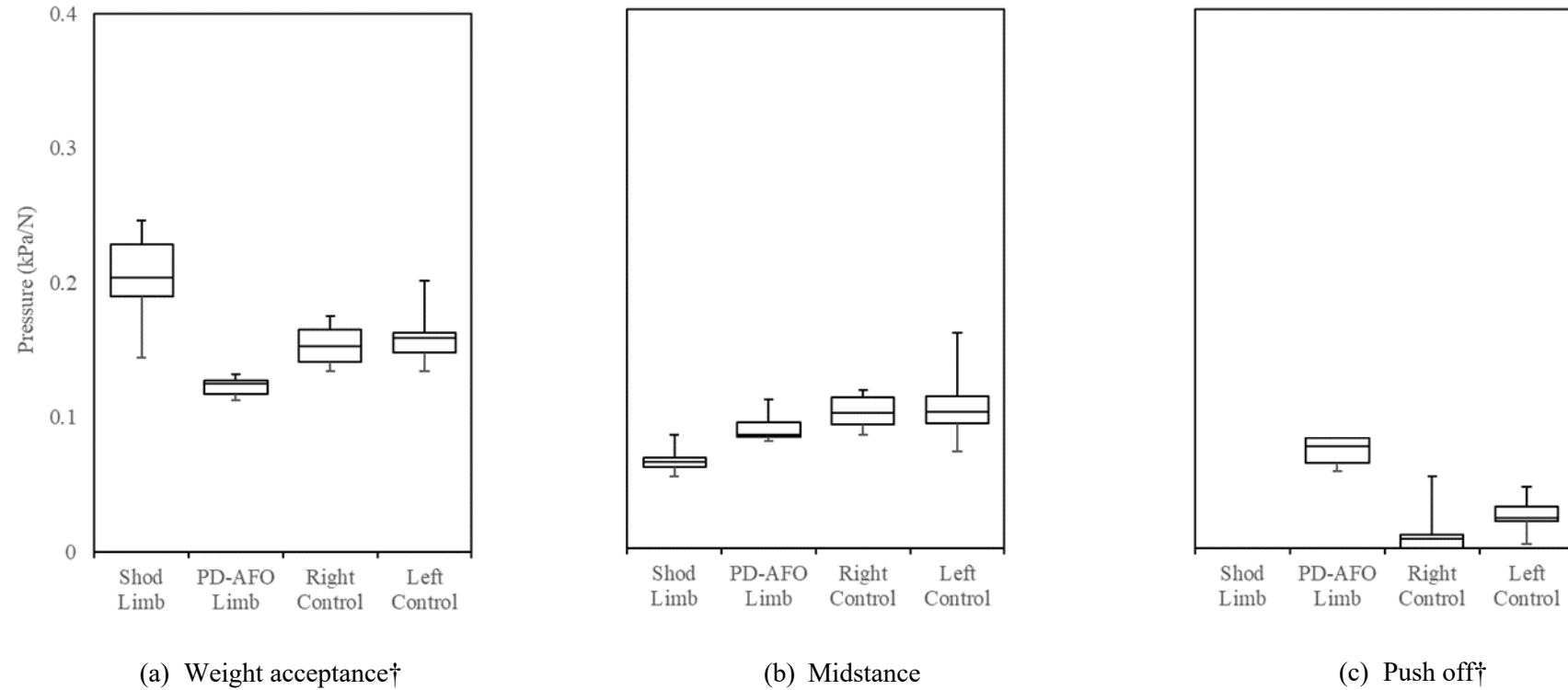


Figure 12.2.8: The plantar pressure in the medial hindfoot at (a) weight acceptance (b) midstance (c) push off. † indicates the figure is shown in the main text.

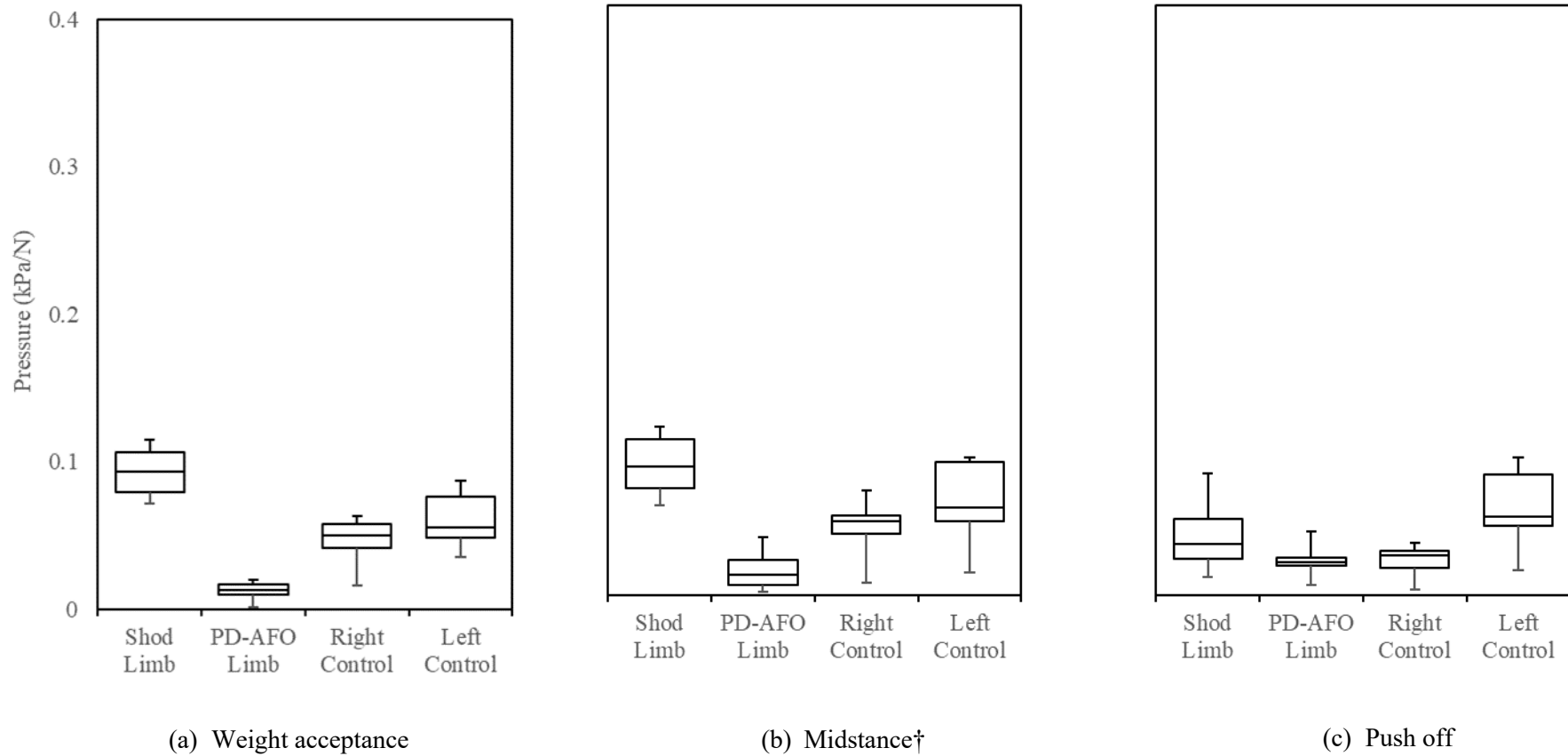


Figure 12.2.9: The plantar pressure in the lateral midfoot at (a) weight acceptance (b) midstance (c) push off. † indicates the figure is shown in the main text.

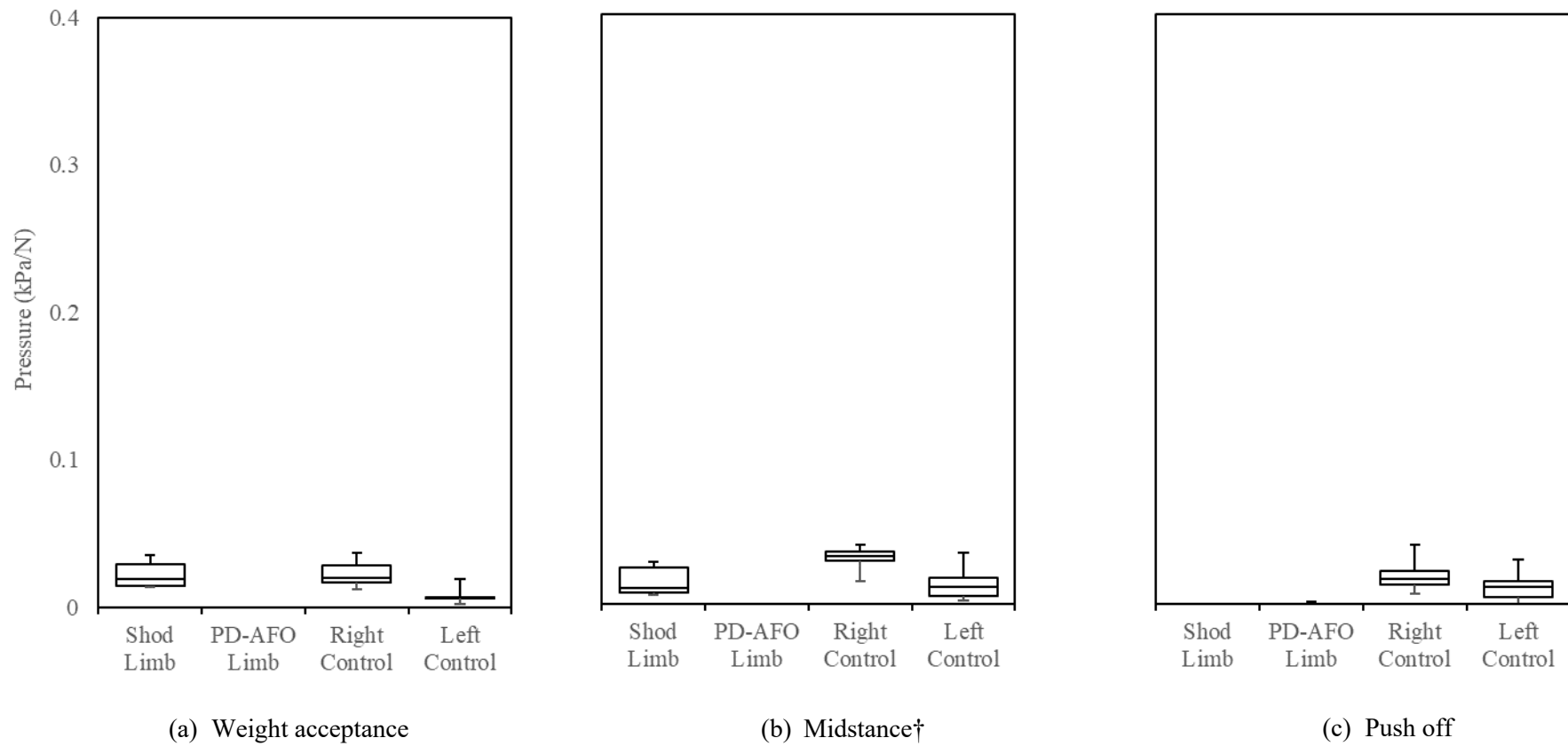
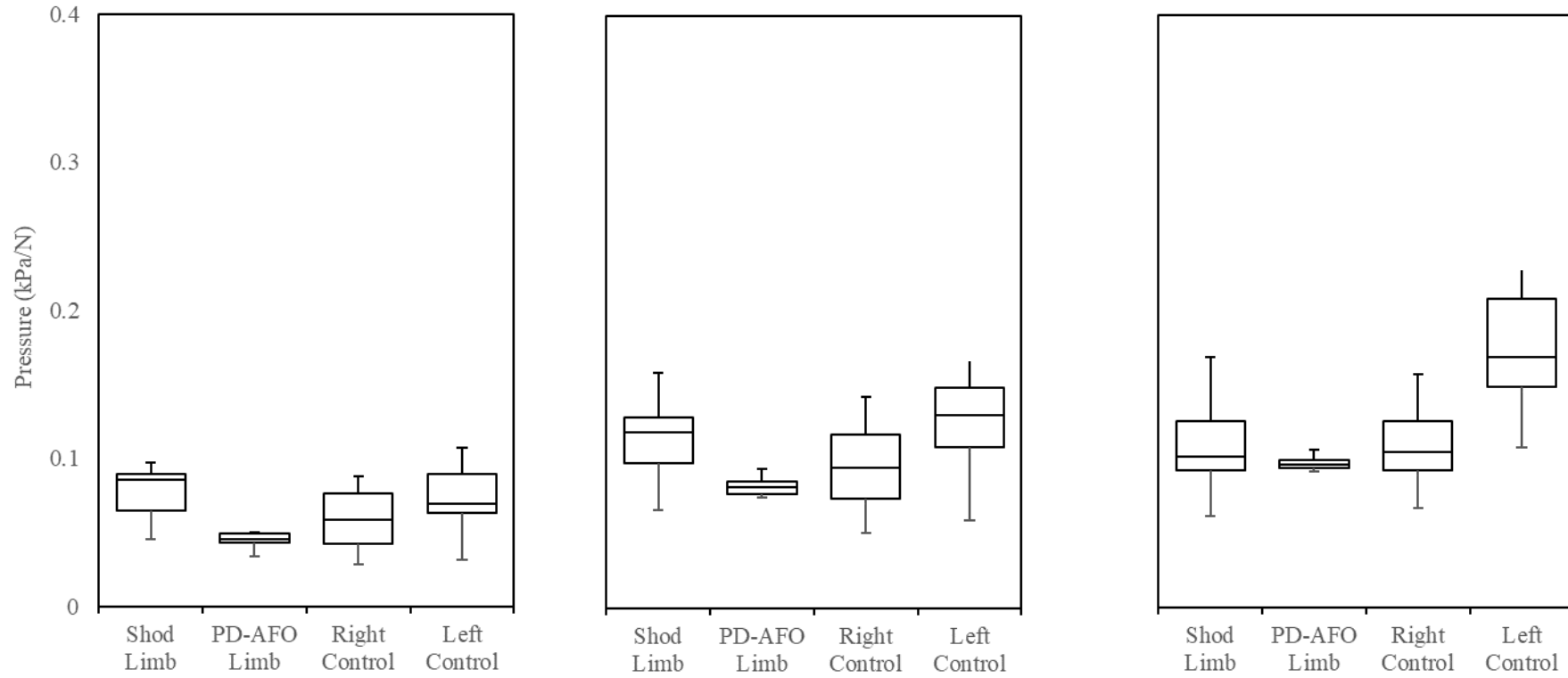


Figure 12.2.10: The plantar pressure in the medial midfoot at (a) weight acceptance (b) midstance (c) push off. † indicates the figure is shown in the main text.



(a) Weight acceptance

(b) Midstance

(c) Push off†

Figure 12.2.11: The plantar pressure in the lateral forefoot at (a) weight acceptance (b) midstance (c) push off. † indicates the figure is shown in the main text.

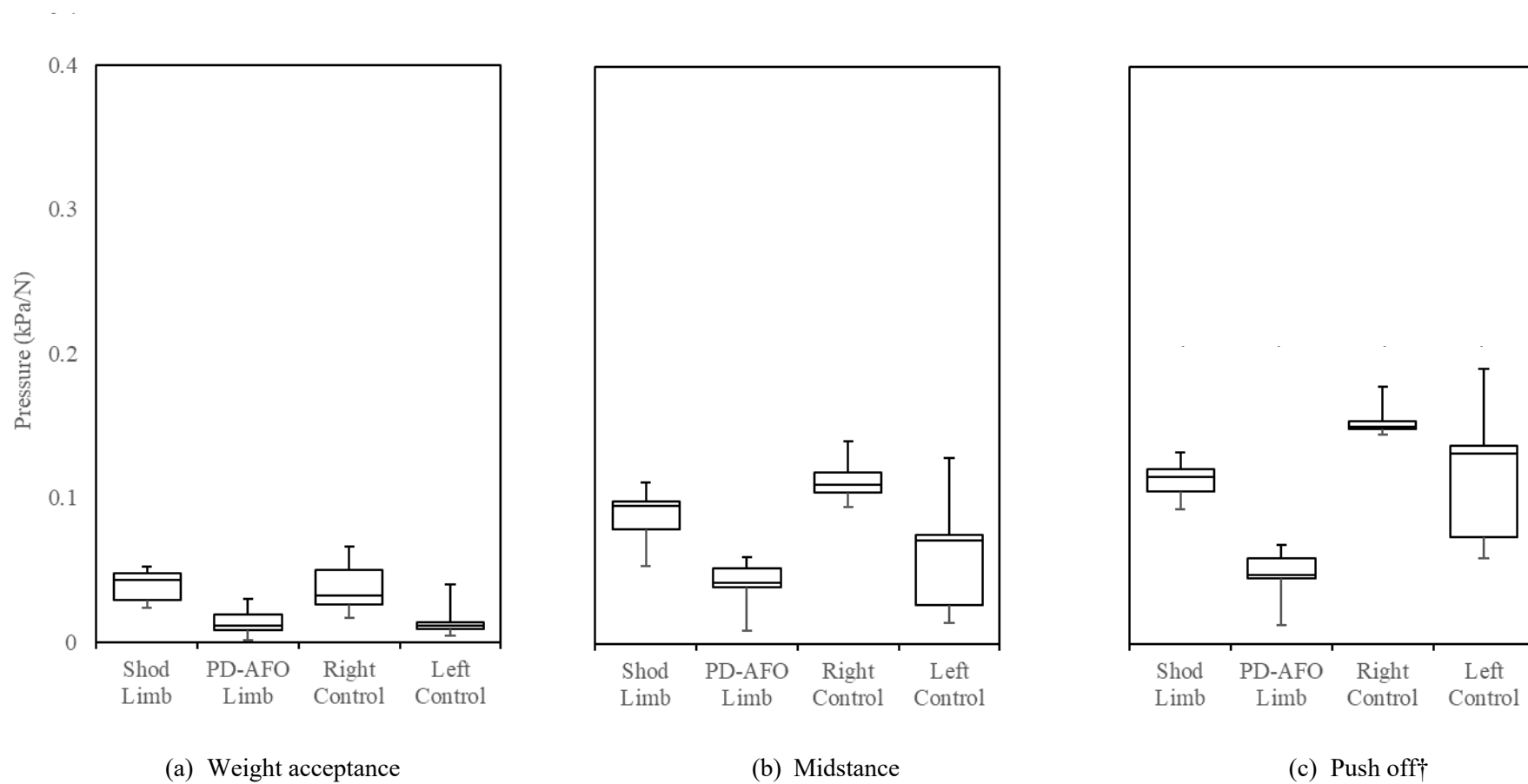


Figure 12.2.12: The plantar pressure in the medial forefoot at (a) weight acceptance (b) midstance (c) push off. † indicates the figure is shown in the main text.

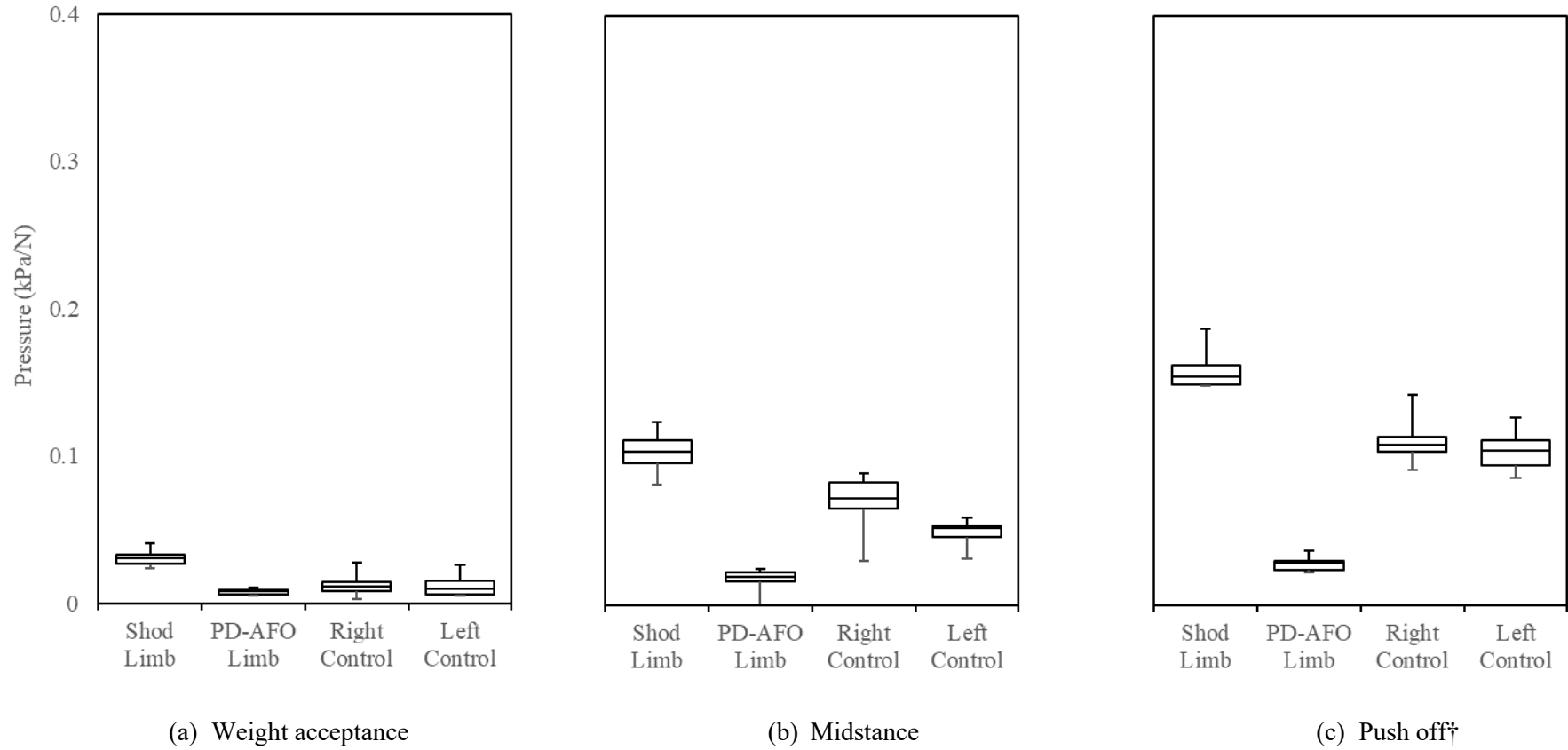


Figure 12.2.13: The plantar pressure in the lesser toe (lateral) at (a) weight acceptance (b) midstance (c) push off. † indicates the figure is shown in the main text.

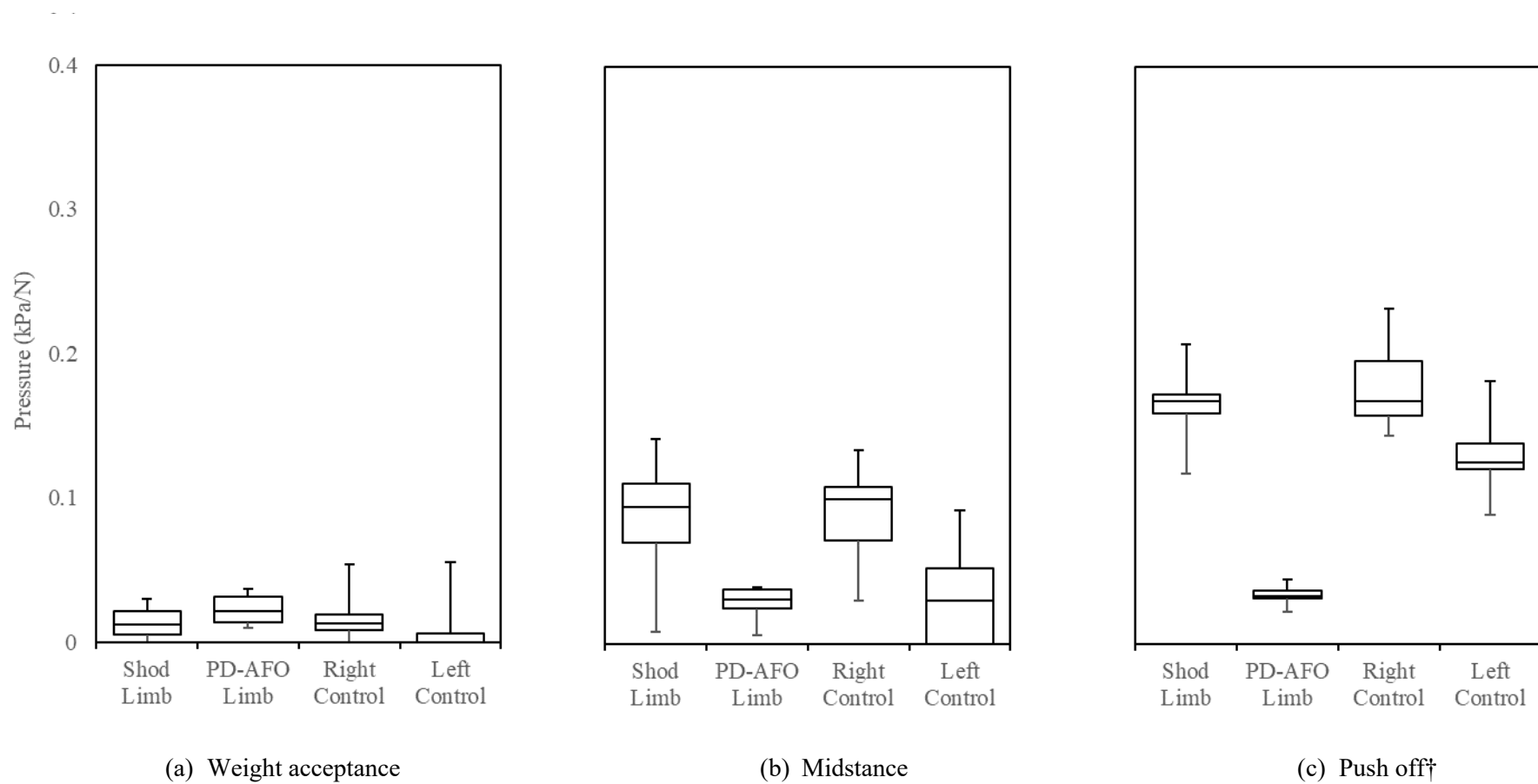


Figure 12.2.14: The plantar pressure in the greater toe (medial) at (a) weight acceptance (b) midstance (c) push off. † indicates the figure is shown in the main text.

12.3 APPENDIX C

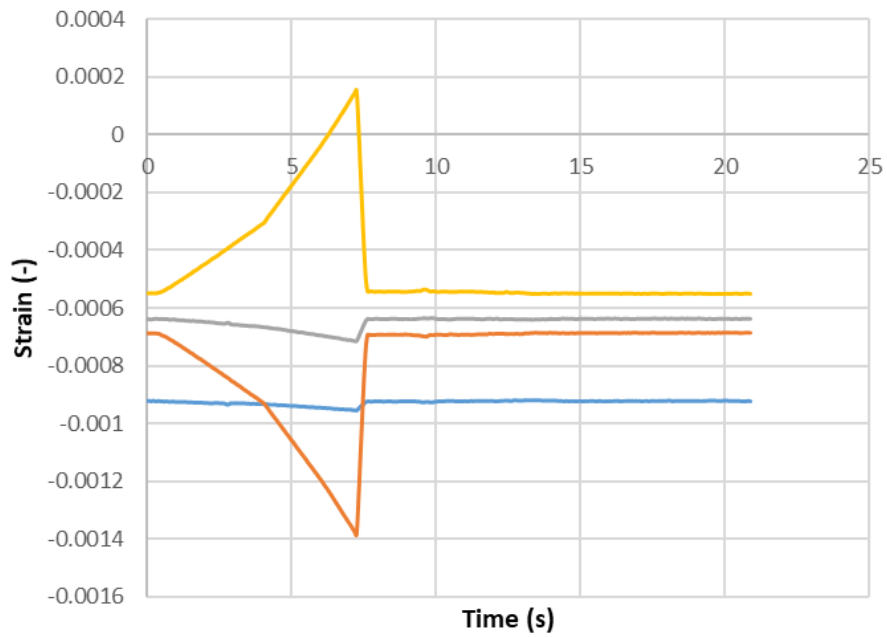
This section of the Appendix is supplementary to Chapter 6.

12.3.1 Zero strain gauge error

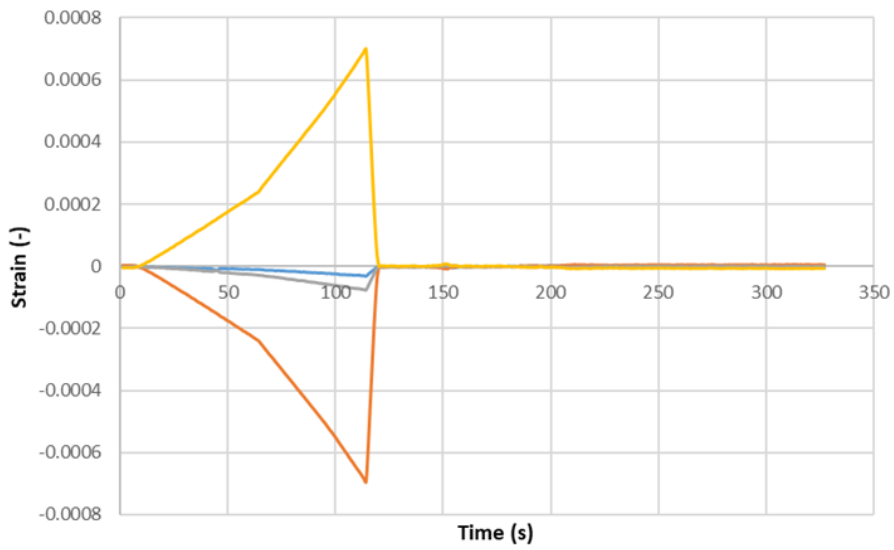
To adjust the strain gauge readings for zero error equation (12.3.1) was used. To find the zero error an average of the reading for each gauge between two chosen time points, m and n , when the sample was under no applied load. For each raw value of strain at each point in time, ε_i^{raw} , the zero error value was subtracted to give a new correct value of strain, $\varepsilon_i^{corrected}$.

$$\varepsilon_i^{corrected} = \varepsilon_i^{raw} - \overline{\varepsilon_{m < t < n}} \quad (12.3.1)$$

Figure 12.3.1a shows the raw value of strain obtained during the bending tests described in section 6.2.1. The zero error was calculated (with $m=8.128s$ and $n=13.056s$) and subtracted from the raw data to give that shown in Figure 12.3.1b.



(a)



(b)

— Front_Gauge — Bottom_Gauge — Back_Gauge — Top_Gauge

Figure 12.3.1: In (a) the raw strain gauge readings recording during the strain gauge reliability tests and (b) these strains adjusted for the zero error.

12.3.2 Force-displacement Curves efficiency

Figure 12.3.2 shows the raw data obtained from the 4-point-bend test on sample 1 of posterior struts, as recorded by material testing machine. These data were used to calculate the efficiency of the posterior struts.

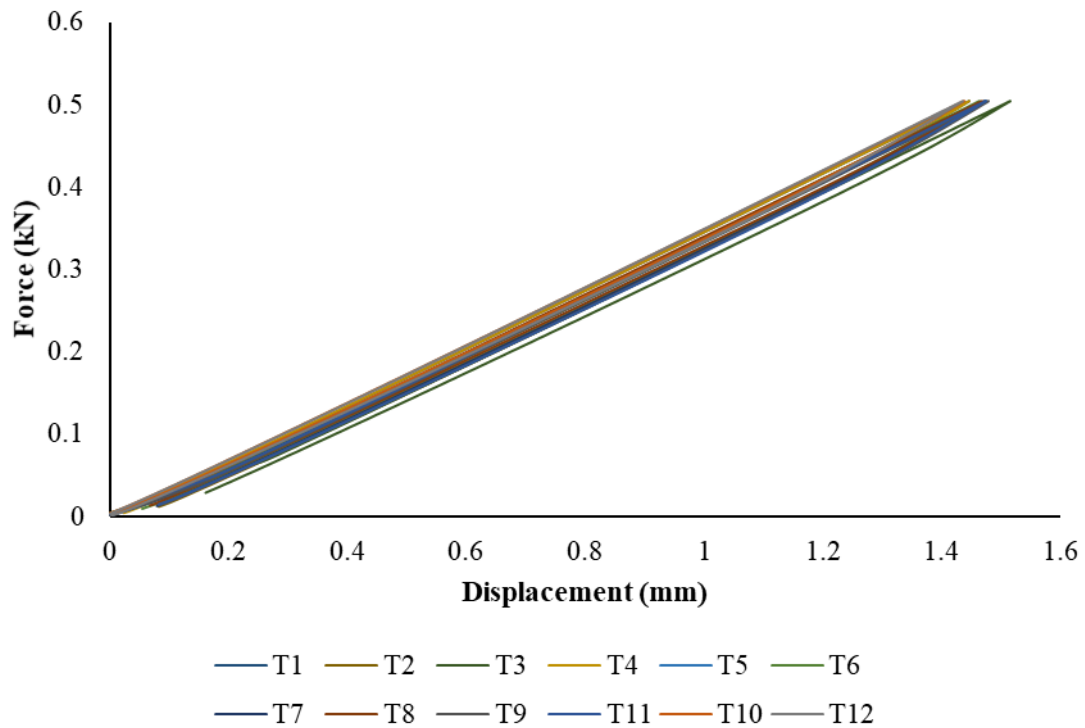


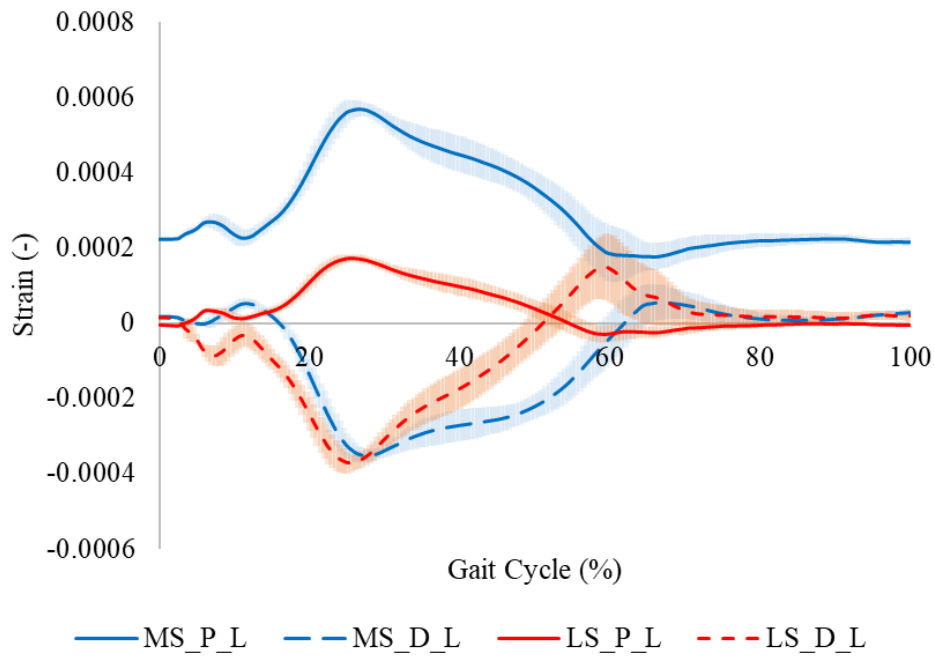
Figure 12.3.2: The force-displacement curves of 12 test repeats of 4-point-bending used to establish the efficiency of sample 1.

12.3.3 Mediolateral SGs

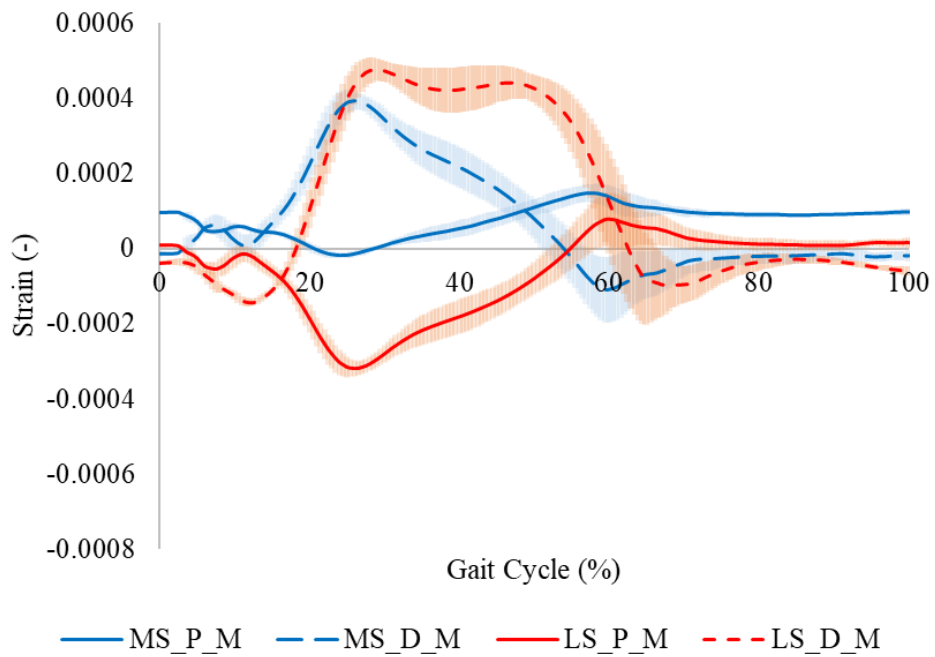
Figure 12.3.3 shows the strain values recorded at the medial and lateral locations on the struts. These values are one order of magnitude smaller than those experienced by the anteroposterior SGs. These represent motion of the struts in, approximately, the frontal plane.

The lateral locations (with reference to the PD-AFO limb) at the proximal end of the struts (LS_P_L and MS_P_L) was seen to experience small amounts of tensile strain as the PD-AFO entered the stance phase. These tensile strains reduced to a minimum at ~15% of the gait cycle and then increased to peak at ~30% of the gait cycle. At this point the strains reduced to ~0% strain. as the PD-AFO limb leaves stance phase at 60% of the gait cycle. The values for strain on the lateral side at the distal locations (LS_D_L and MS_D_L) behaved in a similar, but opposite, manner to those at the proximal locations (as the proximal locations became tensile the distal locations became compressive). This symmetry deviates at ~15% of the gait cycle where the distal strain on the medial strut (MS_D_L) became slightly tensile. The symmetry also deviated at ~50% of the cycle; the distal strain on the lateral strut (LS_D_L) continued to decrease from compression into tension.

The medial locations of strain were symmetrical to those of the lateral locations, when the lateral locations entered tension, the corresponding medial locations entered compression. The strain reading at the proximal location of the medial strut (MS_P_M), followed the symmetrical trend, with a positive or negative gradient, but at a greater magnitude.



(a)



(b)

Figure 12.3.3: The mean strain values $\pm 1SD$ at (a) the lateral side of the struts and (b) the medial side of the struts: on the medial strut, at the proximal (MS_P) and distal location (MS_D); and on the lateral strut, at the proximal (LS_P) and distal location (LS_D)

12.4 APPENDIX D

12.4.1 Compliance

To determine the compliance of the fixtures used for the experimental set up, in combination with the materials testing machine, a compression test was performed with the tibia and the aluminium fixture, both seen in Figure 7.3.3b. A displacement was applied up to a maximum force of 610N. The force was recorded with a 10kN loadcell at 50Hz. From the recorded force-displacement curve, the compliance, C , was found to be 0.48 ± 0.02 mm/kN using linear regression ($R^2=0.93$). To account for the machine's compliance in the experimental tests, (12.1.1 in appendix 12.1 was used where δ is the displacement, and P is the force at time i ..

12.4.2 Design Sensitivity

Table 12.4.1 shows the strain energy and rotational stiffness in the FE model, following the alteration of several design parameters, relative to the *baseline* model.

Table 12.4.1: Relative change in the strain energy and rotational stiffness, during early stance (10% of the gait cycle) and late stance (50% of the gait cycle) when compared to the baseline model, following the changes in design parameters (param.).

Parameter		% Change in strain energy				% Change in rotational stiffness			
		Early stance		Late stance		Early stance		Late stance	
Young's Moduli of	Param.	-40%	+40%	-40%	+40%	+40%	-40%	+40%	-40%
Carbon Fibre Layers	Change (%)	4	1	1	0	-10	-23	0	-15
Cuff Alignment	Param.	plan.	dors.	dors.	plan.	dors.	plan.	plan.	dors.
	Change (%)	12	-10	2	-3	8	-7	3	-2
Young's modulus of	Param.	-40%	+40%	-40%	+40%	+40%	-40%	+40%	-40%
Posterior Struts	Change (%)	89	-32	75	-30	37	-44	28	-34
Strut and Cuff	Param.	plan.	dors.	dors.	plan.	dors.	plan.	plan.	dors.
Alignment	Change (%)	50	-39	10	-11	39	-23	14	-10
Young's Moduli of	Param.	-40%	+40%	-40%	+40%	+40%	-40%	+40%	-40%
UD Carbon Fibre	Change (%)	1	-1	1	0	7	-10	7	-9
Plantar alignment of	Param.	plan.	dors.	plan.	dors.	dors.	plan.	dors.	plan.
toe region of base	Change (%)	0	0	0	0	0	0	2	-2
Addition/removal of	Param.	add.	rem.	add.	rem.	rem.	add.	rem.	add.
aramid	Change (%)	0	0	0	0	0	-3	2	-1
Young's Moduli of CT	Param.	-40%	+40%	-40%	+40%	+40%	-40%	+40%	-40%
Carbon Fibre	Change (%)	0	0	0	0	1	-2	1	-2
Plantar alignment of	Param.	plan.	dors.	plan.	dors.	dors.	plan.	dors.	plan.
whole base	Change (%)	0	-1	0	0	6	0	4	-4
Posterior strut cross-	Param.	-40%	+40%	-40%	+40%	+40%	-40%	+40%	-40%
sectional area	Change (%)	210	-45	168	-44	82	-78	61	-59
Uneven strut cross-	Param.	lat+	med+	lat+	med+	lat+	med+	med+	lat+
sectional area	Change (%)	-43	-46	-44	-44	82	80	61	61
Second Moment of Area	Param.	-40%	+40%	-40%	+40%	+40%	-40%	+40%	-40%
(±40%)	Change (%)	94	-17	82	-20	22	-54	21	-41

12.5 APPENDIX E

This section is supplementary to chapter 8.

12.5.1 Ligaments

Table 12.5.1 shows the ligaments included within the FE model, whose material properties could be determined from literature. Also listed is the number of springs used to approximate each ligament.

Table 12.5.1: Ligaments included within the FE model, and the reference used to determine there properties.

Ligament Name	No. of elements	Stiffness (N/mm)	Ref.
calcaneocuboid_bifurcate	4		[168]
calcaneonavicular_bifurcate	4	Non-linear	[165]
calcaneofibular_LCL	3		[164]
cunoIIInavicular_dorsal	3		[164]
cunoInavicular_dorsal	3		[164]
cunoInavicular_dorsal	3		[168]
long_plantar	10		[169] [166]
plantarfascia	10	Non-linear	[165]
talofibular_LCL_ant	3	Non-linear	[165]
talofibular_LCL_post	3	Non-linear	[165]
talotibia_post	3		[164]
tarsometatarsal_cuneI_tarsII_interos	0		[164]
tarsometatarsal_cuneII_tarsIII_dorsal	3		[164]
tarsometatarsal_cuneI_tarsI_dorsal	3		[164]
tarsometatarsal_cuneI_tarsII_dorsal	3	Non-linear	[165]
tibiocalcaneal_deltoid	3	Non-linear	[165]
tibiofibular_ant	3	Non-linear	[165]
tibiofibular_interos	3	Non-linear	[165]
tibiofibular_post	3	Non-linear	[165]
Tibiofibular_trasnverse	3		[167]
tibionavicular_deltoid	3		[167]
tibiotalar_deltoid_ant	3		[167]
tibiotalar_deltoid_post	3		[168]

The following ligament properties, shown in Table 12.5.2, were established by linearly scaling the material properties to that of the anterior-talofibular report by Funk et al. [165] using the areas reported by Mkandwire et al. [174, 197]. The area of the anterior-talofibular was reported to be 66.85mm².

Table 12.5.2: Ligament properties determined by scaling the area to that of the anterior-talofibular.

Name	No. of elements	Area Ratio	Ref.
calcanealocuboid_dorsal	5	0.16356	[169, 172]
calcaneocuboid_interosseous	3	1.158	[169, 173]
calcaneocuboid_plantar	7	1.57	[169, 172]
Calcaneonavicular_lateral	3	0.1469	[174]
calcaneonavicular_plantar	4	2.562	[169, 172]
cuboideonavicular_dorsal	3	0.208	[169, 174]
cuboideonavicular_plantar	3	0.442	[169, 174]
Cuboidnavicular_interos	3	0.223	[169, 174]
Cuneocuboid_plantar	3	0.11965	[174]
cuneoIIcuboid_interos	3	0.5179	[174]
cuneoIIIcuboid_dorsal_ant	3	0.11965	[174]
cuneoIIIcuboid_dorsal_post	3	0.21957	[174]
cunoIIInavicular_plantar	3	0.11	[169, 174]
cunoIInavicular_plantar	3	0.1288	[169, 174]
cunoInavicular_plantar	3	0.2	[169, 174]
intercuneiform_dorsal	6	0.22	[169, 174]
intercuneiform_interos	6	2.315	[169, 174]
intercuneiform_plantar	6	0.22	[169, 174]
talocalcaneal_lateral	3	0.109	[169, 174]
talocalcaneal_medial	3	0.237	[169, 174]
Talocalcaneal_interos	3	1.158	[169, 173]
Talocalcaneal_post	3	0.238	[169, 174]
talocalcaneal_ant_cervical	3	0.229	[169, 173]
talonavicular_dorsal	5	0.559	[169, 174]
tarsometatarsal_cuneoII_tarsII_dorsal	3	0.178	[174]
tarsometatarsal_cuneoI_tarsI_medial	3	0.411	[174]
tarsometatarsal_cuneoI_tarsI_plantar	3	0.307876	[174]
tarsometatarsal_cuneoII_tarsII_plantar	0	0	[169, 198]

Table 12.5.3 shows ligaments included for which there was no data. As such they were assumed to be similar to other ligaments with data.

Table 12.5.3: Ligament properties assigned from nearby ligament properties

Name	No. of elements	Assumed the same as
prox_phalI_dist_phalI_dorsal	3	tarsometatarsal_cuneIItarsII_dorsal
prox_phalI_dist_phalI_plantar	3	tarsometatarsal_cuneIItarsII_dorsal
prox_phalI_prox_phalII_dorsal	3	tarsometatarsal_cuneIItarsII_dorsal
prox_phalI_prox_phalII_plantar	3	tarsometatarsal_cuneIItarsII_dorsal
prox_phalII_dist_phalII_dorsal	3	tarsometatarsal_cuneIItarsII_dorsal
prox_phalII_dist_phalII_plantar	3	tarsometatarsal_cuneIItarsII_dorsal
prox_phalII_prox_phalIII_dorsal	3	tarsometatarsal_cuneIItarsII_dorsal
prox_phalII_prox_phalIII_plantar	3	tarsometatarsal_cuneIItarsII_dorsal
prox_phalIII_dist_phalIII_plantar	3	tarsometatarsal_cuneIItarsII_dorsal
prox_phalIII_prox_phalIV_dorsal	3	tarsometatarsal_cuneIItarsII_dorsal
prox_phalIII_prox_phalIV_plantar	3	tarsometatarsal_cuneIItarsII_dorsal
prox_phalIV_dist_phalIV_dorsal	3	tarsometatarsal_cuneIItarsII_dorsal
prox_phalIV_dist_phalIV_plantar	3	tarsometatarsal_cuneIItarsII_dorsal
prox_phalIV_prox_phalV_dorsal	3	tarsometatarsal_cuneIItarsII_dorsal
prox_phalIV_prox_phalV_plantar	3	tarsometatarsal_cuneIItarsII_dorsal
prox_phalV_dist_phalV_dorsal	3	tarsometatarsal_cuneIItarsII_dorsal
prox_phalV_dist_phalV_plantar	3	tarsometatarsal_cuneIItarsII_dorsal
tarsometatarsal_cuneIItarsII_interos	0	tarsometatarsal_cuneIItarsII_dorsal
tarsometatarsal_cuneIItarsII_plantar	3	tarsometatarsal_cuneIItarsII_dorsal
tarsometatarsal_cuneIItarsIII_plantar	3	tarsometatarsal_cuneIItarsII_interos
tarsometatarsal_cubetarsIV_dorsal	3	cubetarsV_dorsal
tarsometatarsal_cubetarsIV_plantar	3	cubetarsIV_dorsal
tarsometatarsal_cuneIItarsIII_plantar	3	tarsometatarsal_cuneIItarsII_dorsal
tarsometatarsal_cubetarsV_dorsal	3	cubetarsV_dorsal
tarsometatarsal_cubetarsV_lateral	3	cubetarsV_dorsal
		Lisfrance (interos)
tarsometatarsal_cubetarsV_plantar	3	tarsometatarsal_cuneIItarsII_dorsal

12.5.2 Lower Limb Only Simulation

Figure 12.5.1 shows the final position of the lower limb, when simulation 10% of the gait cycle.

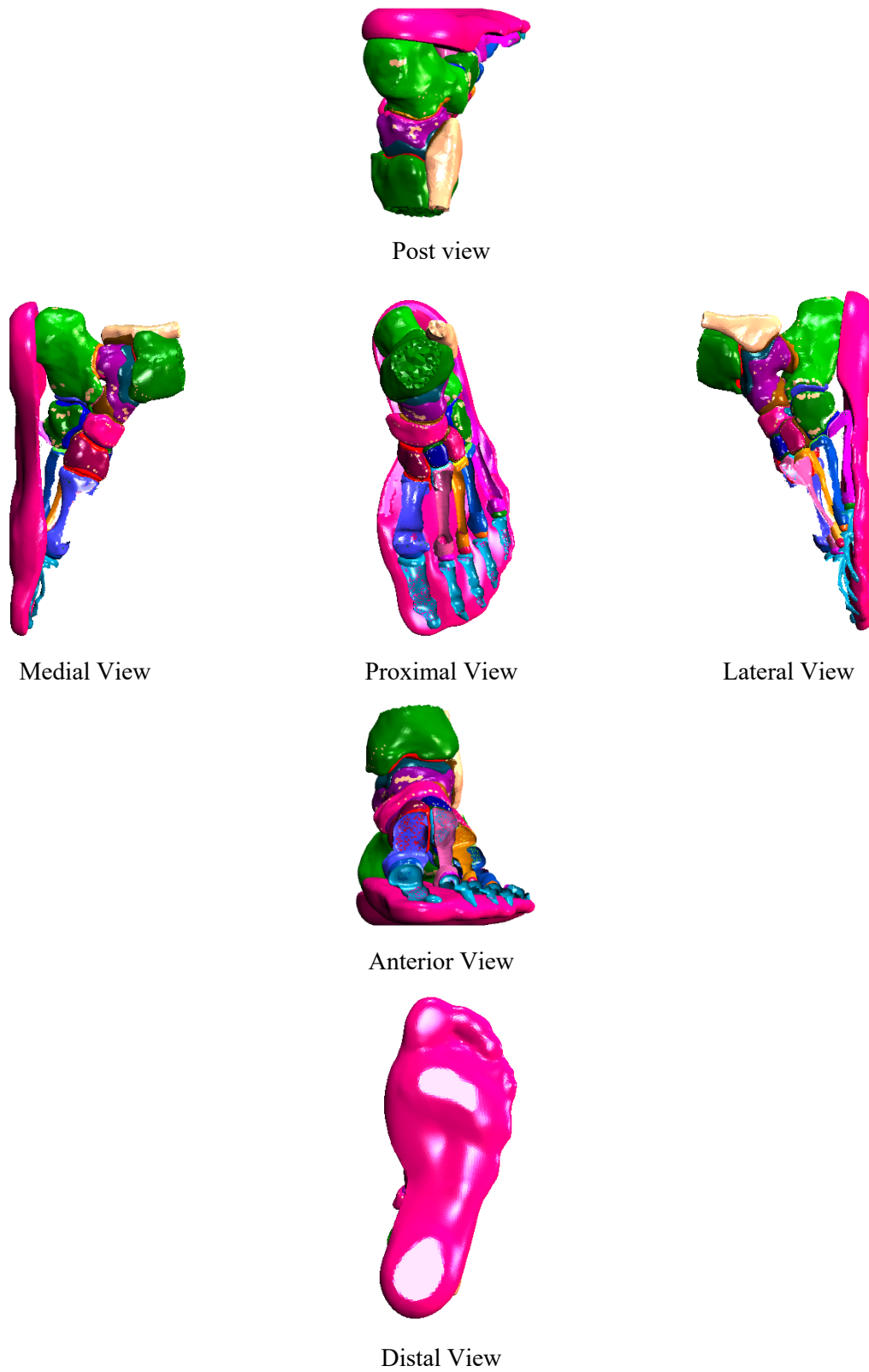


Figure 12.5.1: The lower Limb only upon completeion of sumlation at 10% of the gait cycle

12.5.3 Cartilage Contact Stress

Figure 12.5.2 shows the contact normal stress observed on the talar cartilage surfaces when the selected point in gait was simulated in the lower limb only.

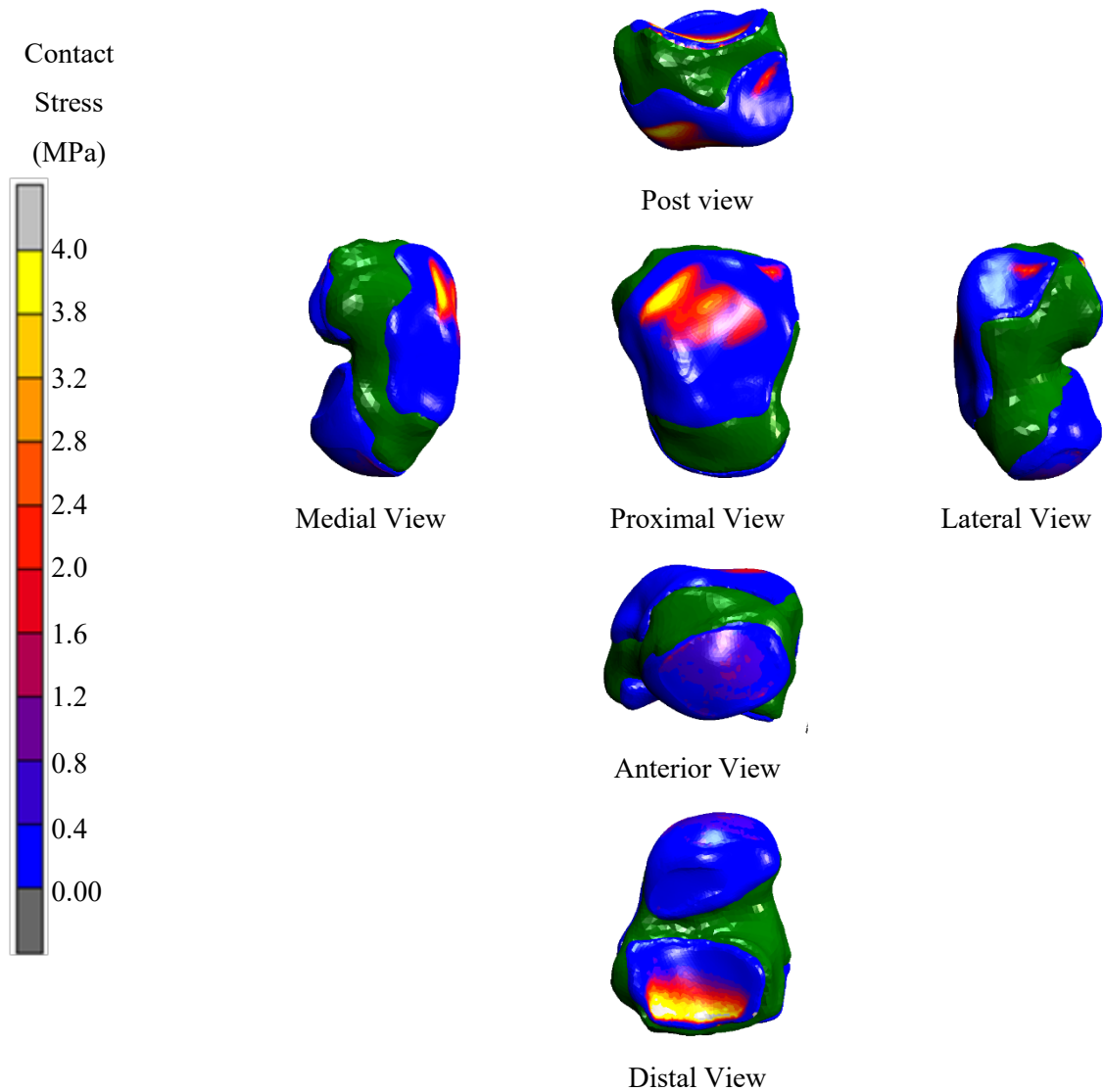


Figure 12.5.2: The contact normal stress on the talar cartilage surfaces, observed during the FE simulation of the lower limb only, at 10% of the gait cycle.

Figure 12.5.3 shows the contact normal stress on the calcaneal cartilage surfaces at 10% of the gait cycle in the lower limb only.

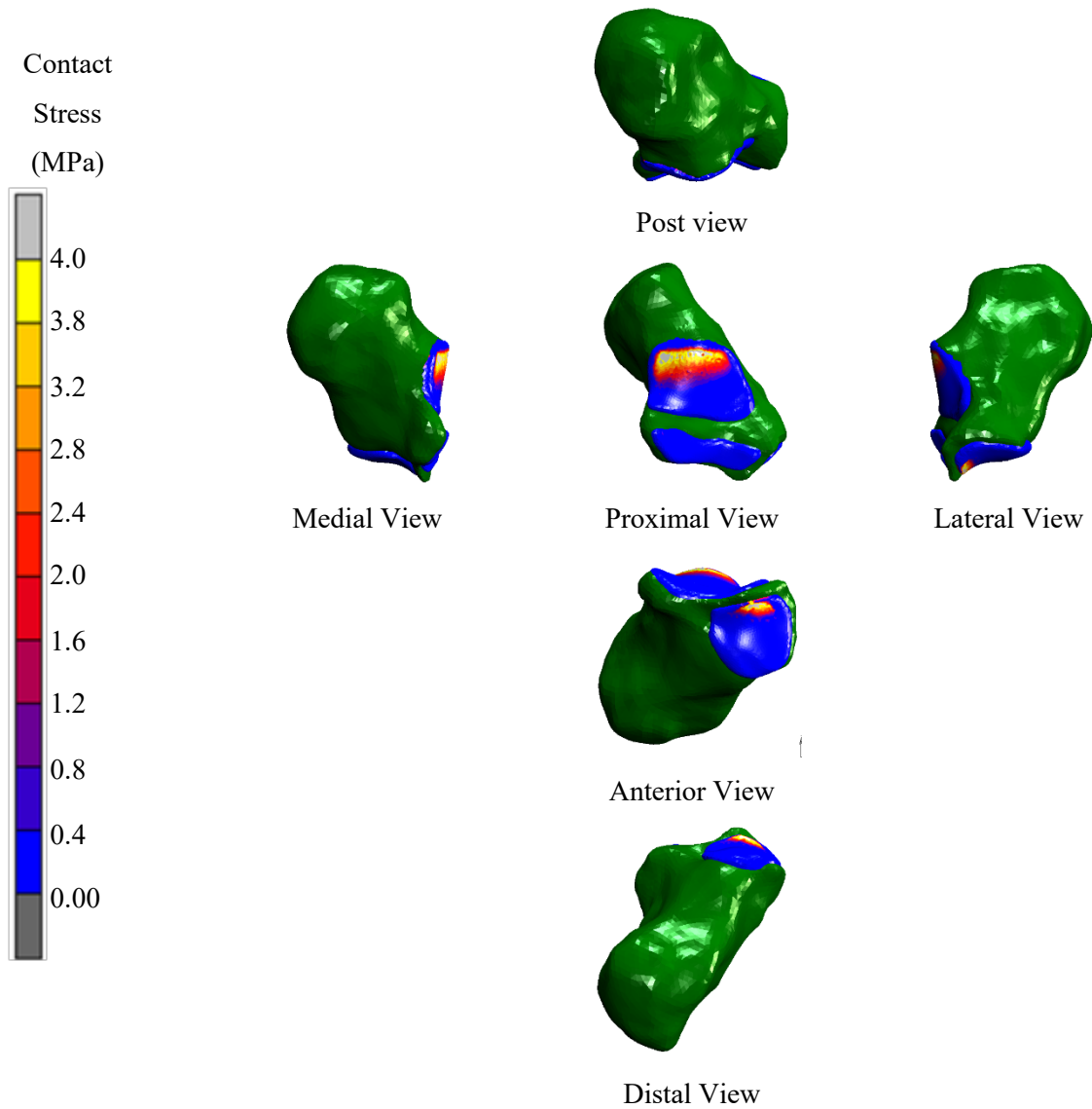


Figure 12.5.3: The contact normal stress on the calcaneal cartilage surfaces, observed during the FE simulation of the lower limb only, at 10% of the gait cycle

12.6 APPENDIX F

This section is supplementary to Chapter 9.

12.6.1 Limb in PD-AFO Model

Figure 12.6.1 shows the different views of final combined FE model of the lower limb and PD-AFO.

The combined model is positioned in the initial orientation to simulate 10% of the gait cycle.

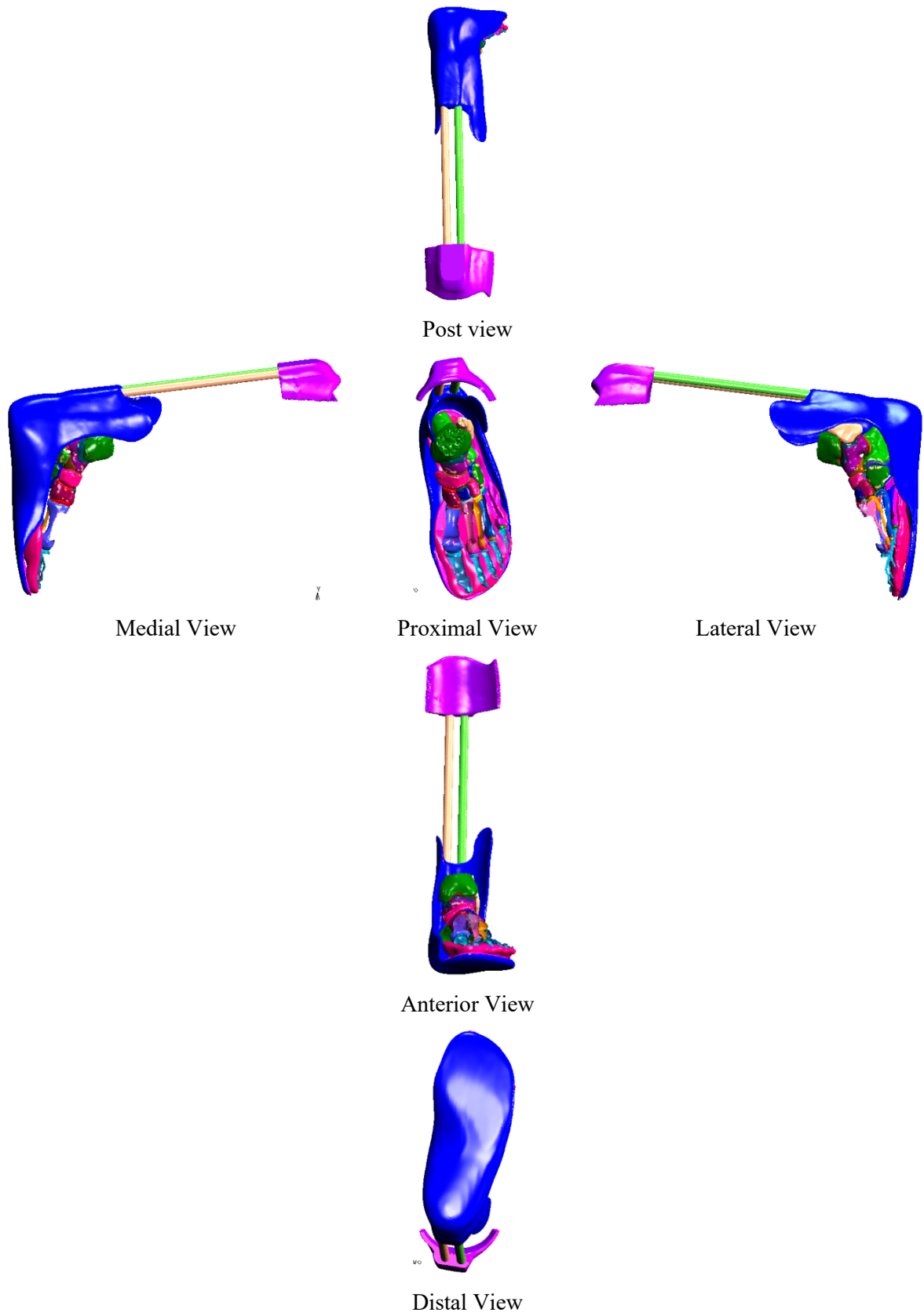


Figure 12.6.1: Views of the FE model of the lower limb within the PD-AFO positioned to simulate 10% of the gait cycle.

12.6.2 Tibia cross-sectional area

To calculate the average circular cross-section of the tibia, to use for the tibia truss, equation (12.6.1) was used. The volume, V , of the tibia was obtained in Autodesk Inventor from the solid meshed tibia, generated by segmenting scans. The volume was 434000mm^3 . The length, l , of the tibia was assumed to be the same as the length of the long axis of the tibia, with a value of 406mm . This gave an average cross-sectional area, $\overline{A_{c/s}}$, of 1070mm^2 , and a diameter of 36mm .

$$\overline{A_{c/s}} = \frac{V}{l} \tag{12.6.1}$$

12.6.3 Calf Contact

Figure 12.6.2 shows the Von Mises stress distribution obtained following the compression of the calf region of the lower leg with an applied displacement of up to 20mm, when assigned the properties from (a) Avril et al. (b) Dai et al. (c) the maximum values from Lima et al. and (d) the minimum values from Lima et al.

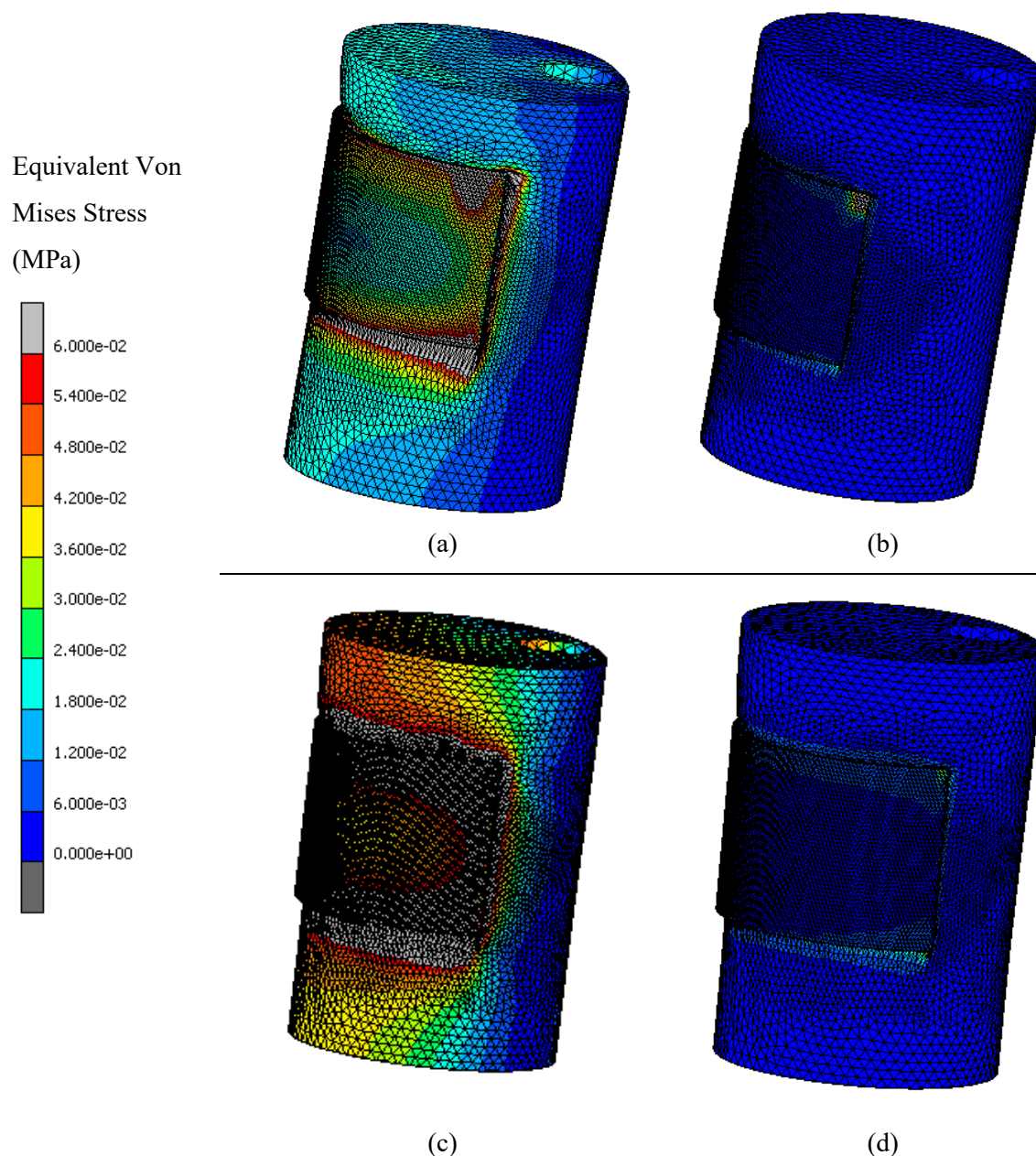


Figure 12.6.2: The equivalent Von Mises stress observed following compression of the idealised meshed calf with (a) Avril 2010 properties, (b) Dai 1999 properties, (c) maximum values in the range provided by Lima et al. and (d) minimum values in the range provided by Lima et al.

The stiffness used to define the properties of the 30 springs representing the calf, was derived from the force-displacement curve shown in Figure 12.6.3. These properties were those that gave the most comparative results between the meshed model and spring model, the results of which are shown in Figure 9.3.1 in chapter 8 in the main text.

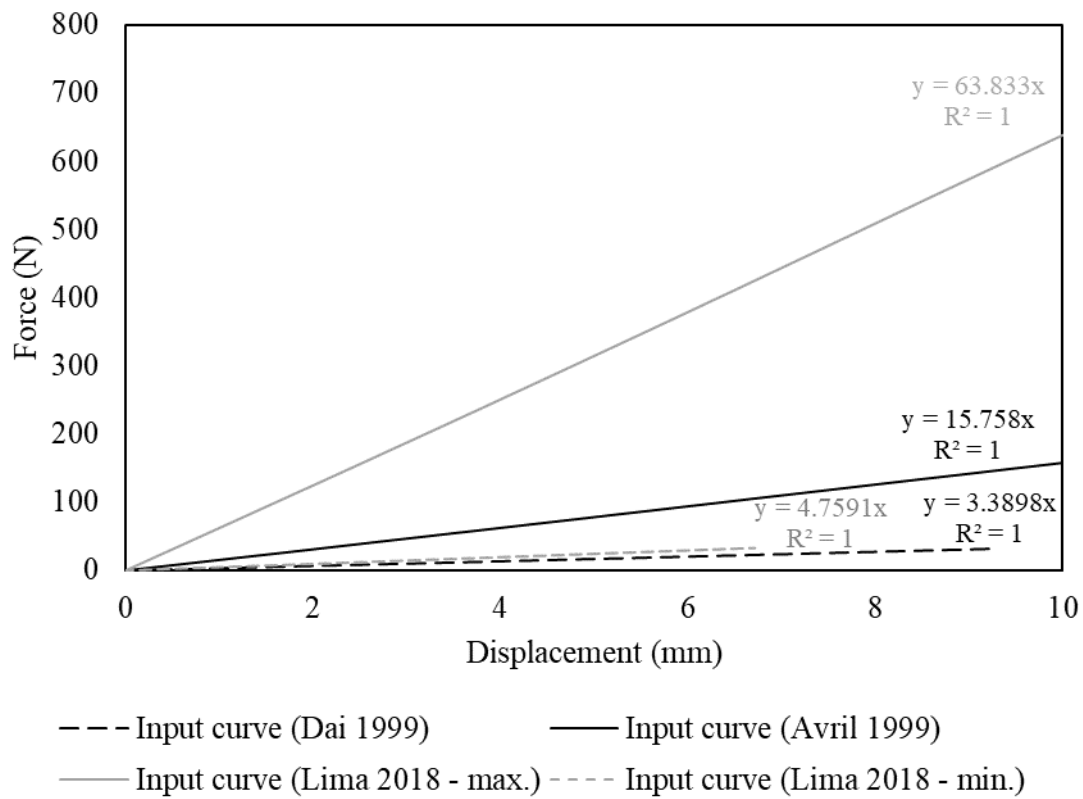


Figure 12.6.3: The force-displacement curve used to define the material properties of the spring in the combined PD-AFO – lower limb FE model.

Table 12.6.1 shows the CPU time, in seconds, for the simulation of compression of the calf, when modelling with a meshed body and when modelling with springs, for each set of material properties. For all material properties, using the spring model resulted in less than 9% of the CPU time than when run using the meshed model.

Table 12.6.1: The CPU time for each set of material properties, when run with the meshed calf model and the spring mode.

Material Properties Reference		CPU time (seconds)	
		Meshed Calf	Spring Model
Avril et al. 2010	[187]	25,626	2,199
Dai et al. 1999	[186]	14,897	547
Lima et al. 2018 (max. values)	[188]	62,464	806
Lima et al. 2018 (min. values)	[188]	27,514	658

12.6.4 Contact Stresses

Figure 12.6.4 shows the talus and its cartilage of the combined model, when simulating 10% of the gait cycle with the PD-AFO.

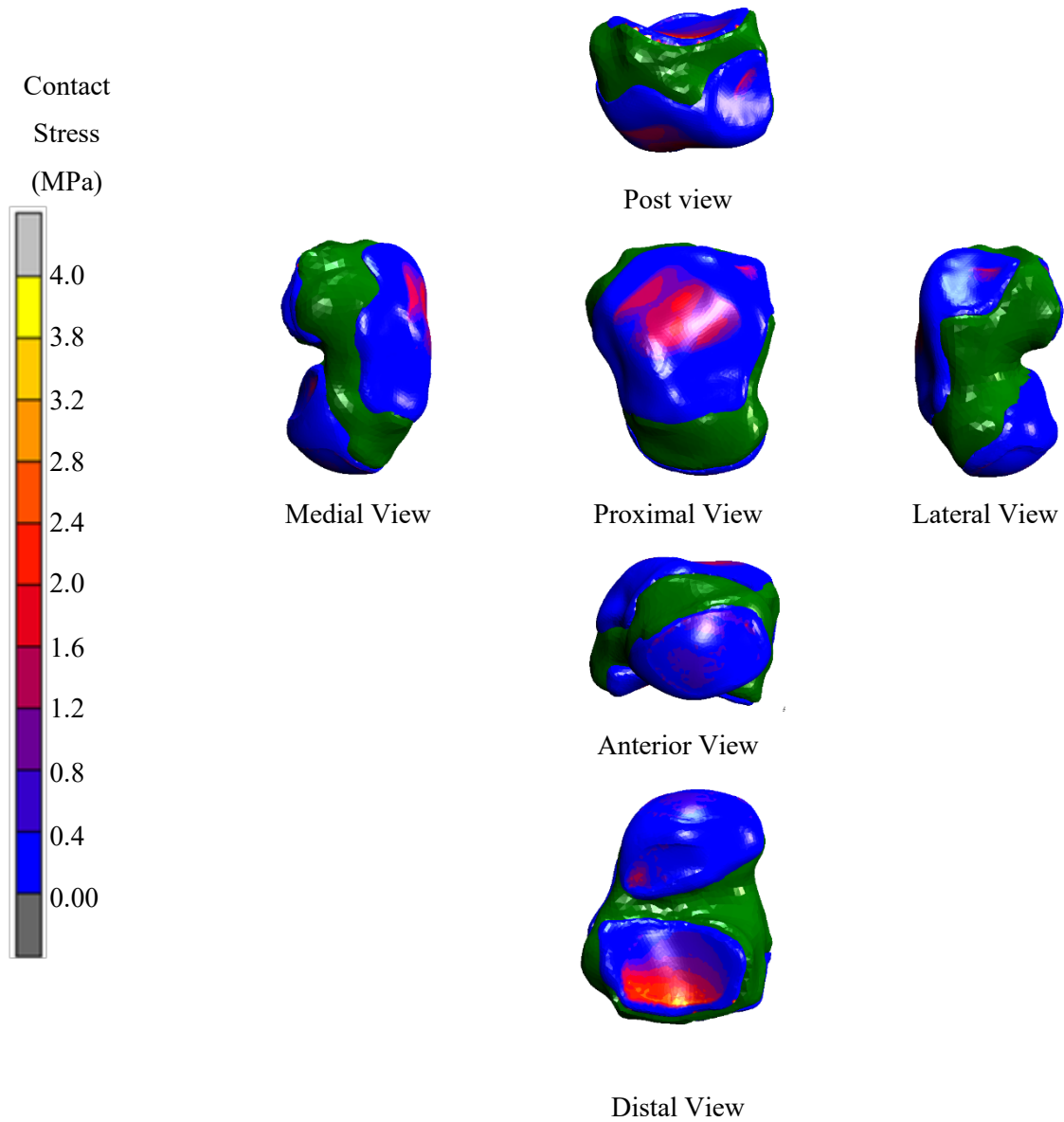


Figure 12.6.4: The contact normal stress on the talar cartilage surfaces, observed during the FE simulation at 10% of the gait cycle for the lower limb when in the PD-AFO

Figure 12.6.5 shows the calcaneus and its cartilage, when simulating 10% of the gait cycle with the PD-AFO.

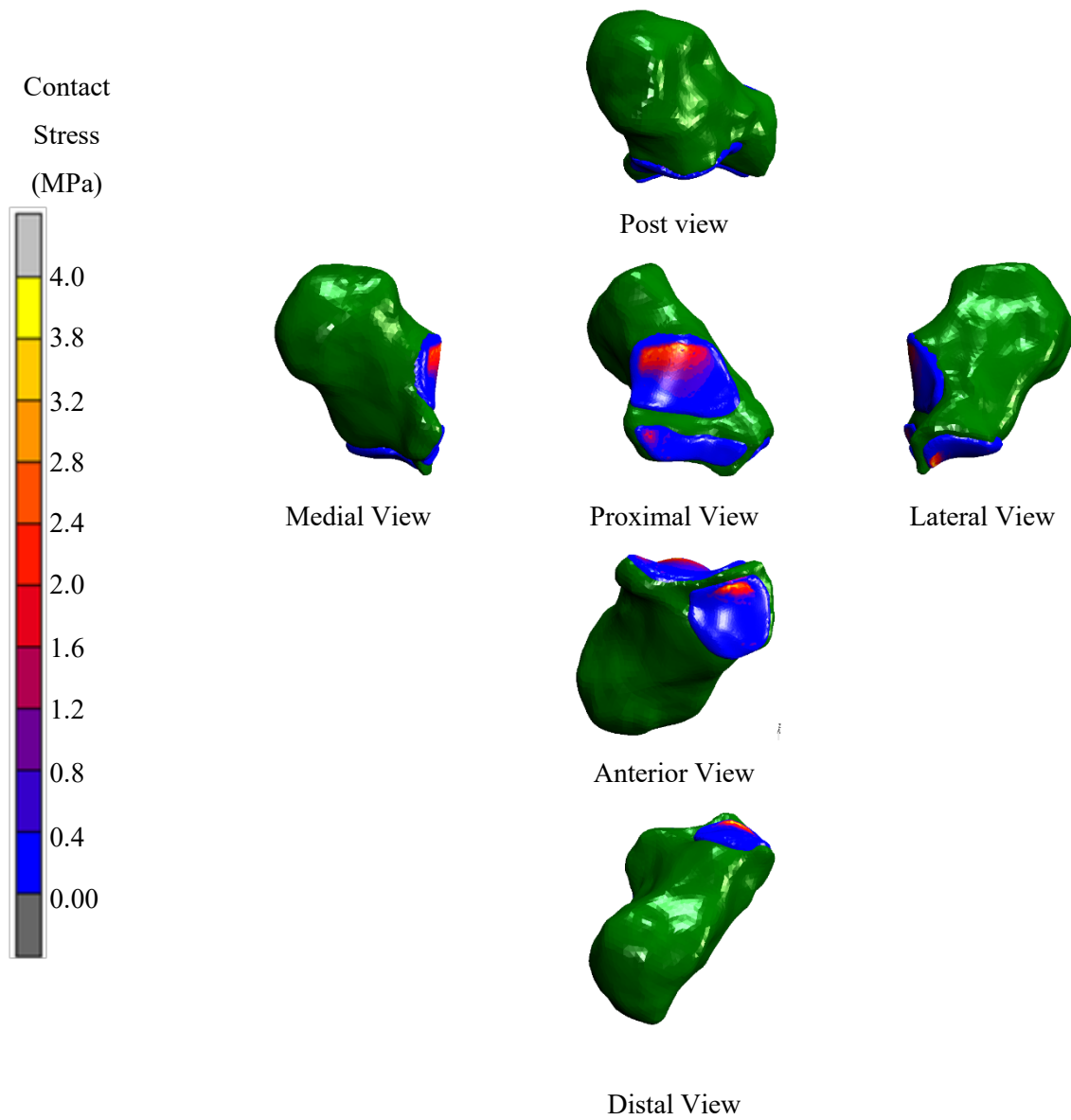


Figure 12.6.5: The contact normal stress on the calcaneal cartilage surfaces, observed during the FE simulation for 10% of the gait cycle for the lower limb when in the PD-AFO.

12.7 APPENDIX G

Figure 12.7.1 to Figure 12.7.15 show the permissions to reproduce all figures within this thesis that are not Open Access.

02/09/2021		RightsLink Printable License	
WOLTERS KLUWER HEALTH, INC. LICENSE TERMS AND CONDITIONS			
Sep 02, 2021			
This Agreement between Imperial College London – Kirstie Edwards ("You") and Wolters Kluwer Health, Inc. ("Wolters Kluwer Health, Inc.") consists of your license details and the terms and conditions provided by Wolters Kluwer Health, Inc. and Copyright Clearance Center.			
License Number	5131470164253		
License date	Aug 17, 2021		
Licensed Content Publisher	Wolters Kluwer Health, Inc.		
Licensed Content Publication	The Journal of Trauma and Acute Care Surgery		
Licensed Content Title	The Modern "Deck-Slip" Injury—Calcaneal Blast Fractures From Vehicle Explosions		
Licensed Content Author	Arul Ramasamy, Adam M Hill, Rhodri Phillip, et al		
Licensed Content Date	Dec 1, 2011		
Licensed Content Volume	71		
Licensed Content Issue	6		
Type of Use	Dissertation/Thesis		
Requestor type	University/College		
https://s1100.copyright.com/CustomAdmin/PLF.jsp?ref=6f6b3c23-4ead-4e29-a966-886e4d63534			
1/6			
02/09/2021		RightsLink Printable License	
Sponsorship	No Sponsorship		
Format	Print and electronic		
Will this be posted online?	Yes, on a secure website		
Portion	Figures/tables/illustrations		
Number of figures/tables/illustrations	1		
Author of this Wolters Kluwer article	No		
Will you be translating?	No		
Intend to modify/change the content	No		
Title	The Mechanical Response of a Passive-Dynamic Ankle-Foot-Orthosis and its Interaction with the Lower Limb during Gait		
Institution name	Imperial College London		
Expected presentation date	Aug 2021		
Portions	Figure 1 on page 1695		
Requestor Location	Imperial College London UREN, Imperial College London White City Campus 86 Wood Lane London, W120BZ United Kingdom Attn: Imperial College London		
Publisher Tax ID	13-2932696		
https://s1100.copyright.com/CustomAdmin/PLF.jsp?ref=6f6b3c23-4ead-4e29-a966-886e4d63534			
2/6			

Figure 12.7.1: Permission to reproduce Figure 1.2.1 in Chapter 1 [3].

02092021 Rightlink Primable License

WOLTERS KLUWER HEALTH, INC. LICENSE TERMS AND CONDITIONS

Sep 02, 2021

This Agreement between Imperial College London -- Kirstie Edwards ("You") and Wolters Kluwer Health, Inc. ("Wolters Kluwer Health, Inc.") consists of your license details and the terms and conditions provided by Wolters Kluwer Health, Inc. and Copyright Clearance Center.

License Number 513147077007

License date Aug 17, 2021

Licensed Content Publisher Wolters Kluwer Health, Inc.

Licensed Content Publication Journal of Bone & Joint Surgery

Licensed Content Title Comparative Effect of Orthosis Design on Functional Performance

Licensed Content Author Jeanne C. Patzkowski, Ryan V. Blanck, Johnny G. Owens, et al

Licensed Content Date Mar 21, 2012

Licensed Content Volume 94

Licensed Content Issue 6

Type of Use Dissertation/Thesis

Requestor type University/College

https://is.100.copyright.com/CustomAdmin/PLF.jsp?ref=156089_0edf-458b-b468-96197db1d1

02092021 Rightlink Primable License

Sponsorship No Sponsorship

Format Print and electronic

Will this be posted online? Yes, on a secure website

Portion Figures/tables/illustrations

Number of figures/tables/illustrations 1

Author of this Wolters Kluwer article No

Will you be translating? No

Intend to modify/change the content No

Title The Mechanical Response of a Passive-Dynamic Ankle-Foot-Orthosis and its Interaction with the Lower Limb during Gait

Institution name Imperial College London

Expected presentation date Aug 2021

Portions Figure 1 page 508

Requestor Location Imperial College London
UREN, Imperial College London
White City Campus
86 Wood Lane
London, W120BZ
United Kingdom
Attn: Imperial College London

Publisher Tax ID 13-2932696

https://is.100.copyright.com/CustomAdmin/PLF.jsp?ref=156089_0edf-458b-b468-96197db1d1

Figure 12.7.2: Permission to reproduce Figure 1.3.1 in chapter 1 [18]

ELSEVIER LICENSE TERMS AND CONDITIONS	
May 31, 2021	
This Agreement between Imperial College London – Kristie Edwards ('Your') and Elsevier ('Elsevier') consists of your license details and the terms and conditions provided by Elsevier and Copyright Clearance Center.	
License Number	4904801493483
License date	Sep 09, 2020
Licensed Content Publisher	Elsevier
Licensed Content Publication	Journal of Biomechanics
Licensed Content Title	ISB recommendation on definitions of joint coordinate system of ankle, hip, and spine
Licensed Content Author	Ge Wu, Sorin Siegler, Paul Allard, Chris Kirtley, Alberto Leonardo, Dieter Krosshaum, Mike White, Daryll D Lima, Luca Cristofolini, Hartmut Witte, Oskar Schmid, Jan Stokes
Licensed Content Date	Apr 1, 2002
Licensed Content Volume	35
Licensed Content Issue	4
Licensed Content Pages	6
Start Page	543
End Page	548

Type of Use	reuse in a thesis/dissertation
Portion	figures/tables/illustrations
Number of figures/tables/illustrations	2
Format	both print and electronic
Are you the author of this Elsevier article?	No
Will you be translating?	No
Title	Characterisation of a Passive Dynamic Ankle Foot Orthosis
Institution name	Imperial College London
Expected presentation date	Mar 2021
Portions	Figure 1 and Figure 2
Requestor Location	Imperial College London UREN, Imperial College London White City Campus 86 Wood Lane London, W120BZ United Kingdom Attn: Imperial College London
Publisher Tax ID	GB 494 6272 12
Total	0.00 GBP
Terms and Conditions	

INTRODUCTION

1. The publisher for this copyrighted material is Elsevier. By clicking "accept" in connection with completing this licensing transaction, you agree that the following terms and conditions apply to this transaction along with the Billing and Payment terms and conditions established by Copyright Clearance Center, Inc. ("CCC"), at the time that you opened your Rightslink account and that are available at any time at <http://www.copyright.com>.

Figure 12.7.3: Permission to reproduce Figure 2.3.1Chapter 2[27].

WOLTERS KLUWER HEALTH, INC. LICENSE TERMS AND CONDITIONS	
May 31, 2021	
This Agreement between Imperial College London -- Kristie Edwards ("You") and Wolters Kluwer Health, Inc. ("Wolters Kluwer Health, Inc.") consists of your license details and the terms and conditions provided by Wolters Kluwer Health, Inc. and Copyright Clearance Center.	
License Number	4991341024121
License date	Jan 17, 2021
Licensed Content Publisher	Wolters Kluwer Health, Inc.
Licensed Content Publication	Clinical Orthopaedics and Related Research
Licensed Content Title	Can an Integrated Orthotic and Rehabilitation Program Decrease Pain and Improve Function After Lower Extremity Trauma?
Licensed Content Author	Katherine Redigrew, Jeanne Putzkowski, Jason Wilken, et al
Licensed Content Date	Oct 1, 2014
Licensed Content Volume	472
Licensed Content Issue	10
Type of Use	Dissertation/Thesis
Requestor type	University/College
Sponsorship	No Sponsorship
Format	Print and electronic
Will this be posted online?	Yes, on a secure website
Portion	Figures/tables/illustrations
Number of figures/tables/illustrations	1
Author of this Wolters Kluwer article	No
Will you be translating?	No
Intend to modify/change the content	No
Title	The Mechanical Response of a Passive-Dynamic Ankle-Foot-Orthosis and its Interaction with the Lower Limb during Gait
Institution name	Imperial College London
Expected presentation date	Mar 2021
Portions	Figure 2A-D
Requestor Location	Imperial College London UREN, Imperial College London White City Campus 86 Wood Lane London, W120BZ United Kingdom Attn: Imperial College London
Total	0.00 GBP
Terms and Conditions	
Wolters Kluwer Health Inc. Terms and Conditions	
1. Duration of License: Permission is granted for a one-time use only. Rights herein do not apply to future reproductions, editions, revisions, or other derivative works. This	

Figure 12.7.4: Permission to reproduce Figure 3.3.1 in Chapter 3 [21].

WOLTERS KLUWER HEALTH, INC. LICENSE TERMS AND CONDITIONS	
May 31, 2021	
This Agreement between Imperial College London – Kirstie Edwards ("You") and Wolters Kluwer Health, Inc. ("Wolters Kluwer Health, Inc.") consists of your license details and the terms and conditions provided by Wolters Kluwer Health, Inc. and Copyright Clearance Center.	
License Number	4987651409371
License date	Jan 14, 2021
Licensed Content Publisher	Wolters Kluwer Health, Inc.
Licensed Content Publication	Clinical Orthopedics and Related Research
Licensed Content Title	How Does Ankle-foot Orthosis Stiffness Affect Gait in Patients With Lower Limb Salvage?
Licensed Content Author	Elizabeth Esposito, Ryan Blanck, Nicole Harper, et al
Licensed Content Date	Oct 1, 2014
Licensed Content Volume	472
Licensed Content Issue	10
Type of Use	Dissertation/Thesis
Requestor type	University/College
Sponsorship	No Sponsorship
Format	Print and electronic

Will this be posted online?	Yes, on a secure website
Portion	Figures/tables/illustrations
Number of figures/tables/illustrations	2
Author of this Wolters Kluwer article	No
Will you be translating?	No
Intend to modify/change the content	No
Title	The Mechanical Response of a Passive-Dynamic Ankle-Foot-Orthosis and its Interaction with the Lower Limb during Gait
Institution name	Imperial College London
Expected presentation date	Mar 2021
Portions	Fig. 1 on page 3028 Fig. 6 on page 3033
Requestor Location	Imperial College London UREN, Imperial College London White City Campus 86 Wood Lane London, W120BZ United Kingdom Attn: Imperial College London
Total	0.00 GBP
Terms and Conditions	

Wolters Kluwer Health Inc. Terms and Conditions

1. **Duration of License:** Permission is granted for a one time use only. Rights herein do not apply to future reproductions, editions, revisions, or other derivative works. This

Figure 12.7.5: Permission to reproduce Figure 3.3.3 and Figure 3.4.2 in Chapter 3 [56].

Order Number: 1091764
Order Date: 20 Jan 2021

Payment Information

Kirstie Edwards
kge12@ic.ac.uk
Payment method: Invoice

Billing Address:
Miss Kirstie Edwards
Imperial College London
URBN, Imperial College Lo
ndon
White City Campus
86 Wood Lane
London, W120BZ
United Kingdom
+44 7787502026
kge12@ic.ac.uk

Customer Location:
Miss Kirstie Edwards
Imperial College London
URBN, Imperial College Lo
ndon
White City Campus
86 Wood Lane
London, W120BZ
United Kingdom

Order Details

1. Journal of biomechanical engineering

Billing Status:
Open

Order license ID 1091764-1
Order detail status Completed
ISSN 0148-0731
Type of use Republish in a thesis/dissertation
Publisher AMERICAN SOCIETY OF MECHANICAL ENGINEERS,
Charity/aph/vol/figure
Portion
0.00 GBP
Replication Permission

LICENSED CONTENT

Publication Title Journal of biomechanical engineering
Country United States of America
Author/Editor AMERICAN SOCIETY OF MECHANICAL ENGINEERS
Publication Type Journal
Date 01/01/1977
Language English

REQUEST DETAILS

Portion Type Charity/aph/vol/figure
Number of charts / graphs / tables / figures requested 2
Format (select all that apply) Print:Electronic
Copies for the disabled? No

Distribution U.K. and Commonwealth (excluding Canada)
Translation Original language of publication
Copies for the disabled? No

Who will republish the content? Academic institution
Duration of Use Current edition and up to 5 years
Lifetime Unit Quantity Up to 499
Rights Requested Main product
Currency GBP
Minor editing privileges? No
Incidental promotional use? No

NEW WORK DETAILS

Title The Mechanical Response of a Passive-Dynamic Ankle-Foot-Orthosis and Its Interaction with the Lower Limb during Gait
Instructor name Kirstie Edwards
The requesting person / organization to appear on the license Kirstie Edwards

ADDITIONAL DETAILS

REUSE CONTENT DETAILS
Title, description or numeric reference of the portion(s) Figure 3 and Figure 4
Editor of portion(s) N/A
Volume of serial or monograph 140
Page or page range of portion 3-4
Title of the article/chapter the portion is from Assessment of Characteristics of Ankle-Foot Orthoses
Author of portion(s) AMERICAN SOCIETY OF MECHANICAL ENGINEERS,
Publication date of portion 2018-04-30

American Society of Mechanical Engineers ASME Special Terms
Permission is granted for the specific use of the ASME Figures 3.4 only as stated herein and does not permit further use of the materials without proper authorization. As is customary, we request that you ensure proper acknowledgment of the exact source of this material, the authors, and ASME as original publisher, in compliance with the STM Permission guidelines all fees are waived for the first 3 figures.

Total Items: 1
Subtotal: 0.00 GBP
Order Total: 0.00 GBP

Figure 12.7.6: Permission to reproduce Figure 3.4.1 in Chapter 3 and Figure 6.1.2 in Chapter 6 [63].

Order Number: 1091090
Order Date: 18 Jan 2021

Payment Information

Billing Address: Kirstie Edwards kge12@ic.ac.uk Payment method: Invoice	Customer Location: Miss Kirstie Edwards Imperial College London Imperial College Lo UBEN, Imperial College Lo ndon White City Campus 86 Wood Lane London, W120BZ United Kingdom +44 7787502026 kge12@ic.ac.uk
---	---

Order Details

1. Journal of biomechanics

Article: The effect of ankle foot orthosis alignment on walking in individuals treated for traumatic lower extremity injuries.

Order license ID: 1091090-1
Order detail status: Completed
ISSN: 0021-9290
Type of use: Republish in a thesis/dissertation
Publisher: PEGCAMON
Portion: Charly/graph/table/figure
Billing Status: Open

LICENSED CONTENT

Publication Title	Journal of biomechanics	Rightsholder	Elsevier Science & Technology Journals
Article Title	The effect of ankle foot orthosis alignment on walking in individuals treated for traumatic lower extremity injuries.	Publication Type	Journal
Author/Editor	UNIVERSITY OF MICHIGAN, AMERICAN SOCIETY OF BIOMECHANICS, EUROPEAN SOCIETY OF BIOMECHANICS.	Start Page	51
Date	01/07/1968	End Page	57
Language	English	Volume	61

Country: United Kingdom of Great Britain and Northern Ireland

REQUEST DETAILS

Portion Type	Charly/graph/table/figure	Distribution	Worldwide
Number of charts / graphs / tables / figures requested	1	Translation	Original language of publication
Format (select all that apply)	Print, Electronic	Copies for the disabled?	No
Who will republish the content?	Academic institution	Minor editing privileges?	No
Duration of Use	Life of current edition	Incidental promotional user?	No
Lifetime Unit Quantity	Up to 499	Currency	GBP
Rights Requested	Main product		

NEW WORK DETAILS

Title: The effect of ankle foot orthosis alignment on walking in individuals treated for traumatic lower extremity injuries
Institution name: Imperial College London
Expected presentation date: 2021-03-30

ADDITIONAL DETAILS

Instructor name: Kirstie Edwards
The requesting person / organization to appear on the license: Completed

REUSE CONTENT DETAILS

Title, description or numeric reference of the portion(s)	Figure 2	Title of the article/chapter the portion is from	The effect of ankle foot orthosis alignment on walking in individuals treated for traumatic lower extremity injuries.
Editor of portion(s)	Brown, Starr E.; Russell Esposito, Elizabeth; Wilken, Jason M.	Author of portion(s)	Brown, Starr E.; Russell Esposito, Elizabeth; Wilken, Jason M.
Volume of serial or monograph	61	Publication date of portion	2017-08-16
Page or page range of portion	54		

Elsevier Science & Technology Journals Terms and Conditions

Elsevier publishes Open Access articles in both its Open Access journals and via its Open Access articles option in subscription journals, for which an author selects a user license permitting certain types of reuse without permission. Before proceeding please check if the article is Open Access on <http://www.sciencedirect.com> and refer to the user license for the individual article. Any reuse not included in the user license terms will require permission. You must always fully and appropriately credit the author and source. If any part of the material to be used (for example, figures) has appeared in the Elsevier publication for which you are seeking permission, we will credit or acknowledge to another source it is the responsibility of the user to ensure their reuse complies with the terms and conditions determined by the rights holder. Please contact permissions@elsevier.com with any queries.

Total Items: 1
Subtotal: 0.00 GBP
Order Total: 0.00 GBP

Figure 12.7.7: Permission to reproduce Figure 3.4.3 in Chapter 3.[38].

Order Number: 1091092
Order Date: 18 Jan 2021

Payment Information

Kirstie Edwards
kge12@ic.ac.uk
Payment method: Invoice

Billing Address:
Miss Kirstie Edwards
Imperial College London
Imperial College Lo
UEN, Imperial College Lo
ndon

Customer Location:
Miss Kirstie Edwards
Imperial College London
UEN, Imperial College Lo
ndon
Write City Campus
86 Wood Lane
London, W120BZ
United Kingdom
+44 7787502026
kge12@ic.ac.uk

Order Details

1. Gait & posture

Article: Ankle-foot orthosis bending axis influences running mechanics.

Order license ID 1091092-1

Order detail status Completed

ISSN 0966-6362

Type of use Republish in a thesis/dissertation

Publisher ELSEVIER BV

Portion Image/photo/illustration

Billing Status:
Open

0.00 GBP
Republishing Permission

LICENSED CONTENT

Publication Title	Rightsholder	Elsevier Science & Technology Journals
Gait & posture Ankle-foot orthosis bending axis influences running mechanics.	Elsevier Science & Technology Journals	Journal
Author/Editor	Publication Type	147
North American Society of Gait and Clinical Movement Analysis, European Society of Movement Analysis in Children, Società italiana di analisi del movimento in dinica.	Start Page	152
Date	End Page	56
01/01/1993	Volume	
Language English		
Country Netherlands		

REQUEST DETAILS

Portion Type	Image/photo/illustratio n	Distribution Translation	Worldwide Original language of publication
Number of Images / photos / Illustrations Format (select all that apply)	1	Print, Electronic	No
Who will republish the content?	Academic institution	Minor editing privileges?	No
Duration of Use	Life of current edition	Incidental promotional use?	No
Lifetime Unit Quantity	Up to 499	Currency	GBP
Rights Requested	Main product		

NEW WORK DETAILS

Title	Institution name	Expected presentation date
The Mechanical Response of a Passive- Dynamic Ankle-Foot- Orthosis and its Interaction with the Lower Limb during Gait	Imperial College London	2021-03-30

ADDITIONAL DETAILS

Instructor name
Kirstie Edwards
The requesting person
/ organization to
appear on the license

REUSE CONTENT DETAILS

Title, description or numeric reference of the portion(s)	Title of the article/chapter the portion is from	Author of portion(s)
Figure 1	Ankle-foot orthosis bending axis influences running mechanics.	Russell Esposto, Elizabeth, Ranz, Elynn C, Schnidtbauer, Kelly A., Nepurue, Richard R., Wilken, Jason M.
Volume of serial or monograph	Publication date of portion	Russell Esposto, Elizabeth, Ranz, Elynn C, Schnidtbauer, Kelly A., Nepurue, Richard R., Wilken, Jason M.
56	2017-07-01	
Page or page range of portion		
149		

Elsevier Science & Technology Journals Terms and Conditions

Elsevier publishes Open Access articles in both its Open Access Journals and via its Open Access articles option in subscription journals, for which an author selects a user license permitting certain types of reuse without permission. Before proceeding please check if the article is Open Access on <http://www.sciencedirect.com> and refer to the user license for the individual article. Any reuse not included in the user license terms will require permission. You must always fully and appropriately credit the author and source. If any part of the material to be used (for example, figures) has appeared in the Elsevier publication for which you are seeking permission, with credit or acknowledgement to another source it is the responsibility of the user to ensure their reuse complies with the terms and conditions determined by the rights holder. Please contact permissions@elsevier.com with any queries.

Total Items: 1

Subtotal: 0.00 GBP
Order Total: 0.00 GBP

Figure 12.7.8: Permission to reproduce Figure 3.4.4 in Chapter 3 [54].

WOLTERS KLUWER HEALTH, INC. LICENSE TERMS AND CONDITIONS	
May 31, 2021	
This Agreement between Imperial College London – Kirstie Edwards ("You"), and Wolters Kluwer Health, Inc. ("Wolters Kluwer Health, Inc.") consists of your license details and the terms and conditions provided by Wolters Kluwer Health, Inc. and Copyright Clearance Center.	
License Number	5014801348056
License date	Feb 23, 2021
Licensed Content Publisher	Wolters Kluwer Health, Inc.
Licensed Content Publication	Journal of Prosthetics & Orthotics
Licensed Content Title	Plantar Pressure Changes with Use of an Interpid Dynamic Exoskeletal Orthosis
Licensed Content Author	Julianne Stewart, Tatiana Djafarzadeh, Richard Miltenberger, et al
Licensed Content Date	Oct 10, 2019
Licensed Content Volume	32
Licensed Content Issue	1
Type of Use	Dissertation Thesis
Requestor type	University/College
Sponsorship	No Sponsorship
Format	Print and electronic

Will this be posted online?	Yes, on a secure website
Portion	Figures/tables/illustrations
Number of figures/tables/illustrations	1
Author of this Wolters Kluwer article	No
Will you be translating?	No
Intend to modify/change the content	No
Title	The Mechanical Response of a Passive-Dynamic Ankle-Foot-Orthosis and its Interaction with the Lower Limb during Gait
Institution name	Imperial College London
Expected presentation date	Mar 2021
Portions	Figure 3 page 4
Requestor Location	Imperial College London UREN, Imperial College London White City Campus 86 Wood Lane London, W120BZ United Kingdom Attn: Imperial College London
Publisher Tax ID	13-2932696
Total	0.00 GBP
Terms and Conditions	Wolters Kluwer Health Inc. Terms and Conditions

Figure 12.7.9: Permission to reproduce Figure 5.2.1 in Chapter 5 [59].

WOLTERS KLUWER HEALTH, INC. LICENSE TERMS AND CONDITIONS

May 31, 2021

This Agreement between Imperial College London – Kirstie Edwards (“You”) and Wolters Kluwer Health, Inc. (“Wolters Kluwer Health, Inc.”) consists of your license details and the terms and conditions provided by Wolters Kluwer Health, Inc. and Copyright Clearance Center.

License Number	5020170294163
License date	Mar 01, 2021
Licensed Content Publisher	Wolters Kluwer Health, Inc.
Licensed Content Publication	Clinical Orthopaedics and Related Research
Licensed Content Title	How Does Ankle-foot Orthosis Stiffness Affect Gait in Patients With Lower Limb Salvage?
Licensed Content Author	Elizabeth Exposito, Ryan Blanck, Nicole Harper, et al
Licensed Content Date	Oct 1, 2014
Licensed Content Volume	472
Licensed Content Issue	10
Type of Use	Dissertation/Thesis
Requestor Type	University/College
Sponsorship	No Sponsorship
Format	Print and electronic

Will this be posted online?	Yes, on a secure website
Portion	Figures/tables/illustrations
Number of figures/tables/illustrations	1
Author of this Wolters Kluwer article	No
Will you be translating?	No
Intend to modify/change the content	No
Title	The Mechanical Response of a Passive-Dynamic Ankle-Foot-Orthosis and its Interaction with the Lower Limb during Gait
Institution name	Imperial College London
Expected presentation date	Mar 2021
Portions	Figure 5 - ankle power on page 3033
Requestor Location	Imperial College London UREN, Imperial College London White City Campus 86 Wood Lane London, W120BZ United Kingdom Attn: Imperial College London
Publisher Tax ID	13-2932696
Total	0.00 GBP
Terms and Conditions	

Wolters Kluwer Health Inc. Terms and Conditions

Figure 12.7.10: Permission to reproduce Figure 6.1.1a in Chapter 6 [56].

This Agreement between Imperial College London – Kirstie Edwards ("You") and Elsevier ("Elsevier") consists of your license details and the terms and conditions provided by Elsevier and Copyright Clearance Center.

May 31, 2021

ELSEVIER LICENSE
TERMS AND CONDITIONS

License Number 5020170018509

License date Mar 01, 2021

Licensed Content Publisher Elsevier

Licensed Content Publication Gait & Posture

Licensed Content Title Ankle-foot orthosis bending axis influences running mechanics

Licensed Content Author Elizabeth Russell Esposito, Eilyn C. Ranz Kelly A. Schindlbauer, Richard R. Neptune, Jason M. Wilken

Licensed Content Date Jul 1, 2017

Licensed Content Volume 56

Licensed Content Issue n/a

Licensed Content Pages 6

Start Page 147

End Page 152

Type of Use reuse in a thesis/dissertation

Portion figures/tables/illustrations

Number of figures/tables/illustrations 1

Format both print and electronic

Are you the author of this Elsevier article? No

Will you be translating? No

Title The Mechanical Response of a Passive-Dynamic Ankle-Foot-Orthosis and its Interaction with the Lower Limb during Gait

Institution name Imperial College London

Expected presentation date Mar 2021

Portions Figure 2 - ankle power of affected limb - on page 150

Requestor Location Imperial College London
UREN, Imperial College London
White City Campus
86 Wood Lane
London, W120BZ
United Kingdom
Attn: Imperial College London

Publisher Tax ID GB 494 6272 12

Total 0.00 GBP

Terms and Conditions

INTRODUCTION

1. The publisher for this copyrighted material is Elsevier. By clicking "accept" in connection with completing this licensing transaction, you agree that the following terms and conditions apply to this transaction (along with the Billing and Payment terms and conditions established by Copyright Clearance Center, Inc. ("CCC"), at the time that you opened your Rightslink account and that are available at any time at <http://myaccount.copyright.com>).

GENERAL TERMS

Figure 12.7.11: Permission to reproduce Figure 6.1.1b in Chapter 6 [54].

Order Number: 1091763
Order Date: 20 Jan 2021

Payment Information

Billing Address:
Kirstie Edwards
kge12@ic.ac.uk
Payment method: Invoice
Miss Kirstie Edwards
Imperial College London
Imperial College Lo
n
URBN, Imperial College Lo
ndon
Customer Location:
Miss Kirstie Edwards
Imperial College London
URBN, Imperial College Lo
ndon
White City Campus
86 Wood Lane
London, W120BZ
United Kingdom
+44 7787502026
kge12@ic.ac.uk

Order Details

1. Journal of biomechanical engineering

Order license ID 1091763-1
Order detail status Completed
ISSN 0148-0731
Type of use Republish in a thesis/dissertation
Publisher AMERICAN SOCIETY OF MECHANICAL ENGINEERS,
Charlygraphable/figure
Portion Republish in a thesis/dissertation
0.00 GBP
Reproduction Permission

LICENSED CONTENT

Publication Title Journal of biomechanical engineering
Country United States of America
Author/Editor AMERICAN SOCIETY OF MECHANICAL ENGINEERS
Publication Type Journal
Language English

REQUEST DETAILS

Portion Type Chart/graph/table/figure
Number of charts / graphs / tables / figures requested 1
Format (select all that apply) Print, Electronic
Distribution Translation
Worldwide Original language of publication
Copies for the disabled? No
Print, Electronic apply

Who will republish the content? Academic institution
Duration of Use Life of current edition
Lifetime Unit Quantity Up to 499
Rights requested Main product
NEW WORK DETAILS
Title The Mechanical Response of a Passive-Dynamic Ankle-Foot Orthosis and its Interaction with the Lower Limb during Gait
Institution name Imperial College London
Expected presentation date 2021-03-30
Minor editing privileges? No
Incidental promotional use? No
Currency GBP

ADDITIONAL DETAILS

Instructor name Kirstie Edwards
The requesting person / organization to appear on the license Kirstie Edwards

REUSE CONTENT DETAILS

Title, description or numeric reference of the portion(s) Figure 3
Editor of portion(s) N/A
Volume of serial or monograph N/A
Page or page range of portion 3
Title of the article/chapter the portion is from Assessment of a Virtual Functional Prototyping Process for the Rapid Manufacture of Passive Dynamic Ankle-Foot Orthoses
Author of portion(s) AMERICAN SOCIETY OF MECHANICAL ENGINEERS
Publication date of portion 2013-09-20

American Society of Mechanical Engineers ASME Special Terms

Permission is granted for the specific use of the ASME Figure 3 only as stated therein and does not permit further use of the materials without proper authorization. As is customary, we request that you ensure proper acknowledgment of the exact sources of this material, the authors, and ASME as original publisher.

Total Items: 1

Subtotal: 0.00 GBP
Order Total: 0.00 GBP

Figure 12.7.12: Permission to reproduce Figure 7.2.1 in Chapter 7 [105].

Order Number: 110063
Order Date: 28 Feb 2021

Payment Information

Kristie Edwards
kge12@cc.cuk
Payment method: Invoice

Billing Address:
Miss Kristie Edwards
Imperial College London
Imperial College Lo
ndon

Customer Location:
Miss Kristie Edwards
Imperial College London
Imperial College Lo
ndon
White City Campus
86 Wood Lane
London, W1T 2BZ
United Kingdom
+44 7787502026
kge12@cc.cuk

Order Details

1. S.A.E. transactions

Billing Status:
Open

Order license ID 110063-1
Order detail status Completed
ISSN 0096-726X
Type of use Republish in a thesis/dissertation
Publisher Society of Automotive Engineers
Portion Char/graph/table/figure
Republish in a thesis/dissertation
Char/graph/table/figure
0.00 GBP
Replication Permission

LICENSED CONTENT

Publication Title S.A.E. transactions
Date 01/01/1927
Language English
Rightsholder SAE International
Publication Type Journal

REQUEST DETAILS

Portion Type Char/graph/table/figure
Number of charts / graphs / tables / figures requested 2
Format (select all that apply) Print, Electronic
Who will republish the contents? Academic institution
Duration of Use Life of current edition
Lifetime Unit Quantity Up to 499
Currency GBP

RIGHTS REQUESTED
NEW WORK DETAILS

Main product
Title The Mechanical Response of a Passive-Dynamic Ankle-Foot Orthosis and its Interaction with the Lower Limb during Gait
Institution name Imperial College London
Expected presentation date 2021-03-01
Instructor name Kristie Edwards

ADDITIONAL DETAILS

The requesting person / organization to appear on the license
Kristie Edwards

REUSE CONTENT DETAILS

Title, description or numeric reference of the portion(s) Figure 11 and Figure 12
Editor of portion(s) N/A
Volume of serial or monograph 106
Page or page range of portion 3750-3751
Title of the article/chapter the portion is from Improvement of Numerical AnkleFoot Model: Modeling of Deformable Bone
Author of portion(s) Beaugonin, Muriel
Publication date of portion Heig, Eberhard Casarl, Dominique
1997-01-01

Total Items: 1

Subtotal: 0.00 GBP
Order Total: 0.00 GBP

Figure 12.7.13: Permission to reproduce Fig 1.2.2a and Fig 1.2.2b in Chapter 8 [147].

ELSEVIER LICENSE
TERMS AND CONDITIONS

May 31, 2021

This Agreement between Imperial College London – Kirstie Edwards ('Your') and Elsevier ('Elsevier') consists of your license details and the terms and conditions provided by Elsevier and Copyright Clearance Center.

License Number 5024120216756

License date Mar 08, 2021

Licensed Content Publisher Elsevier

Licensed Content Publication Experimental Gerontology

Licensed Content Title Achilles tendon loading is lower in older adults than young adults across a broad range of walking speeds

Licensed Content Author Anahid Ebrahimi, Isaac F. Loegering, Jack A. Martin, Robin L. Pomerooy, Joshua D. Roth, Darryl G. Thelen

Licensed Content Date Aug 1, 2020

Licensed Content Volume 137

Licensed Content Issue n/a

Licensed Content Pages 1

Start Page 110966

End Page 0

Type of Use reuse in a thesis/dissertation

Portion figures/tables/illustrations

Number of figures/tables/illustrations 1

Format both print and electronic

Are you the author of this Elsevier article? No

Will you be translating? No

Title The Mechanical Response of a Passive-Dynamic Ankle-Foot-Orthosis and its Interaction with the Lower Limb during Gait

Institution name Imperial College London

Expected presentation date Mar 2021

Portions Figure 2 page 4

Requestor Location Imperial College London
UREN, Imperial College London
White City Campus
86 Wood Lane
London, W120BZ
United Kingdom
Attn: Imperial College London

Publisher Tax ID GB 494 6272 12

Total 0.00 GBP

Terms and Conditions

INTRODUCTION

1. The publisher for this copyrighted material is Elsevier. By clicking "accept" in connection with completing this licensing transaction, you agree that the following terms and conditions apply to this transaction (along with the Billing and Payment terms and conditions established by Copyright Clearance Center, Inc. ("CCC"), at the time that you opened your Rightslink account and that are available at any time at <http://myaccount.copyright.com>).

GENERAL TERMS

Figure 12.7.14: Permission to reproduce Fig 1.3.9 in chapter 8 [175].

informa
healthcare

Modelling the interaction of ankle-foot orthosis and foot by finite element methods to design an optimized sole in steppage gait

Author: N. Jamshidi, H. Hanife, et al

Publication: JOURNAL OF MEDICAL ENGINEERING AND TECHNOLOGY

Publisher: Taylor & Francis

Date: Feb 1, 2010

Rights managed by Taylor & Francis

Thesis/Dissertation Reuse Request

Taylor & Francis is pleased to offer reuses of its content for a thesis or dissertation free of charge contingent on resubmission of permission request if work is published.

BACK

CLOSE

Figure 12.7.15: Permission to reproduce Figure 9.1.3 in chapter 9[183]
